**SANDIA REPORT**
SAND2016-2895
Unlimited Release

# Summary of Externally-Driven Cavern Oil Mixing Research at SNL Including Work Performed at ASU/Notre Dame and UMASS-Dartmouth

Steven W. Webb
Canyon Ridge Consulting LLC

Prepared by
Sandia National Laboratories
Albuquerque, New Mexico 87185 and Livermore, California 94550

Sandia National Laboratories is a multi-program laboratory managed and operated by Sandia Corporation, a wholly owned subsidiary of Lockheed Martin Corporation, for the U.S. Department of Energy's National Nuclear Security Administration under contract DE-AC04-94AL85000.



Issued by Sandia National Laboratories, operated for the United States Department of Energy by Sandia Corporation.



Available to DOE and DOE contractors from
U.S. Department of Energy
Office of Scientific and Technical Information
P.O. Box 62
Oak Ridge, TN 37831

Telephone: (865) 576-8401
Facsimile: (865) 576-5728
E-Mail: reports@osti.gov
Online ordering: http://www.osti.gov/scitech

Available to the public from
U.S. Department of Commerce
National Technical Information Service
5301 Shawnee Rd
Alexandria, VA 22312

Telephone: (800) 553-6847
Facsimile: (703) 605-6900
E-Mail: orders@ntis.gov
Online order: http://www.ntis.gov/search

SAND 2016-2895
Unlimited Release

# Summary of Externally-Driven Cavern Oil Mixing Research at SNL Including Work Performed at ASU/Notre Dame and UMass-Dartmouth

Stephen W. Webb
Canyon Ridge Consulting LLC
Sandia Park, New Mexico 87047

## Abstract

Sandia National Laboratories is investigating oil mixing in underground storage caverns as part of the Strategic Petroleum Reserve (SPR) program. Oil mixing in caverns can be classified as internally-driven or externally driven. In externally-driven mixing, which is addressed in this report, processes external to the cavern and the underground environment such as the introduction and removal of fluids can cause mixing of the oil. Miscible and immiscible mixing processes are discussed. As part of this investigation, research into the fundamental mixing processes for layered caverns has been conducted by Professor H.J.S. Fernando and associates at Arizona State University (ASU) (2006-2009) and at the University of Notre Dame (2010-2012) for miscible mixing from jets. Additional research for immiscible mixing at an interface due to fluid injection was conducted at the University of Massachusetts - Dartmouth. The results of the research conducted at Sandia National Laboratories and at ASU/Notre Dame and UMass-Dartmouth are summarized in this report.

## Acknowledgments

The author wishes to thank the various other people that contributed to this research program including Tim O'Hern, Dave Lord, and Imane Khalil at Sandia National Laboratories. The work could not have been done without the support of Dave Borns, the department manager at Sandia. Thanks also go to Kayla Streit and Carolyn Kirby who obtained permissions for the figures and tables as necessary. The author also wants to thank the various universities that assisted with the research effort.

The research conducted at Arizona State University (ASU) and at the University of Notre Dame was under the direction of Professor H.J.S. Fernando and included students Darren Gest and Suhas Pol at ASU and Chinmoy Nath at Notre Dame. Professor Sergey Voropayev provided invaluable assistance and insight at both institutions.

Professor Peter Friedman directed the research at the University of Massachusetts – Dartmouth as performed by student Allen Beaune.

Funding for this work was provided under the Sandia National Laboratories contract with the U.S. Department of Energy for Engineering Support of the U.S. Strategic Petroleum Reserve.

## Table of Contents

## List of Figures

## List of Tables

## Nomenclature

Nomenclature is included in each chapter as appropriate.

## Executive Summary

Sandia National Laboratories is investigating oil mixing in underground storage caverns as part of the Strategic Petroleum Reserve (SPR) program. Oil mixing in caverns can be classified as internally-driven or externally driven. In externally-driven mixing, which is the subject of this report, the introduction and removal of fluids (oil and brine in the underlying brine layer) drives the mixing behavior of the oil such as during degas. Research into the fundamental mixing processes has been conducted at Sandia National Laboratories, Arizona State University, the University of Notre Dame, and at the University of Massachusetts Dartmouth.

A literature review was conducted for jet and plume mixing for miscible fluids (oil into oil, water into brine) to understand the important physical processes and the state of predictive methods. Many of the models are limited to container aspect ratio of about 1.0, which is much different than the SPR cavern dimensions. Some approaches do consider container aspect ratios similar to SPR caverns, which may be useful for SPR-specific model development.

Models developed at Sandia include the Simple Degas Mixing Model, computational fluid dynamics (CFD) simulations, and the simplified Mixing Layers Model. All of these models provide insight into oil mixing in caverns. The influence of density differences on mixing. However, detailed experimental data for confirmation of cavern processes are lacking.

In order to obtain pertinent experimental data for cavern processes, preliminary jet mixing studies were performed at Arizona State University in 2009. This study was followed by comprehensive jet mixing studies were performed at the University of Notre Dame. Experiments were conducted that detail the behavior of a confined jet. Mixing between the jet and the resident fluid was also investigated for a uniform resident fluid using water and water-brine mixtures. A simple mathematical model was developed that compares well to the data.

The work conducted at SNL, Arizona State University, and the University of Notre Dame has formed a good base of knowledge about oil mixing in SPR caverns. With this knowledge, development of a degas simulation program similar to CaveMan is proposed. The prediction of degas performance, and modification of degas operations as a result, can have a significant impact on SPR operations.

For immiscible fluid mixing (oil and brine), a number of situations have been investigated including oil and brine withdrawal near oil-brine interface, or selective withdrawal, oil injection into brine layer; and oil injection just above oil-brine interface. Work conducted into selective withdrawal and jet mixing at the oil-brine interface resulted in SPR criteria that can be used to avoid immiscible mixing in these situations. Preliminary investigation of oil-brine mixing for oil injected into the brine layer has been performed, but additional study is needed to develop any predictive models.

# 1 Introduction

## Purpose and Scope of Report

Sandia National Laboratories is investigating oil mixing in underground storage caverns as part of the Strategic Petroleum Reserve (SPR) program. Oil mixing in caverns can be classified as internally-driven or externally driven. In internally-driven mixing, processes internal to the cavern and the underground environment such as heat, concentration, and density gradients can cause mixing of the oil. In externally-driven mixing, the introduction and removal of fluids (oil and brine in the underlying brine layer) drive the mixing behavior of the oil. The present report presents an overview of externally-driven mixing processes. An overview / summary of cavern oil mixing research for both cases is given by Webb (2016a). Internally-driven mixing is addressed in a companion report (Webb, 2016b).

As part of this investigation, research into the fundamental mixing processes has been conducted at Sandia National Laboratories, Arizona State University, the University of Notre Dame, and at the University of Massachusetts Dartmouth. Stephen Webb, David Lord, and Imane Khalil performed some analytical / numerical modeling of mixing processes in the oil layer. Tim O'Hern at Sandia directed a number of experimental research efforts including selective withdrawal and immiscible jet mixing. Professor H.J.S. Fernando and associates at Arizona State University (ASU) (2006-2009) and at the University of Notre Dame (ND) (2010-2012) performed research into both internally-driven and externally-driven oil mixing in a single fluid with possible miscible interfaces, or layering. Professor Peter Friedman and associates at the University of Massachusetts Dartmouth performed some experiments related to mixing from a downward-directed jet impacting an immiscible interface, such as oil injected into the bottom of the oil layer in a cavern near the oil-brine interface.

Water-brine mixing in the brine layer, which is complicated by the effects of leaching, is not directly discussed in this report although some aspects of the research are applicable to this situation. In addition, emulsions that may form as a result of immiscible fluid mixing are not addressed.

# MISCIBLE FLUID MIXING

# 2 Externally-Driven Mixing Scenarios

Externally-driven oil mixing, which is caused by the introduction and/or extraction of oil and brine in a cavern, can occur under a number of operational scenarios including filling, degas, and oil exchange (injection and withdrawal) between caverns. The primary externally-driven mixing scenarios are cavern filling and cavern degas. Both scenarios involve the introduction of oil into the cavern through an inlet jet. In degassing, fluid is withdrawn from the cavern at a different location so the oil inventory is essentially constant. The discussion below is from Lord and Rudeen (2007), who developed the simple degas cavern mixing model.

The degasification scenario is discussed in more detail below because it has been more widely studied. The filling scenario is similar and is not discussed explicitly.

## 2.1 Degasification at the SPR

The vapor pressure in oil stored in underground salt caverns at SPR increases with time. While not a problem during underground storage, vapor pressure increase poses an environmental safety risk when the oil is transferred to surface storage terminals where containment pressure is near atmospheric pressure. The oil bubble point (BP) pressure, or the pressure where gas starts to come out of solution, is an important parameter that is measured during degas. Typical BPs range up to 20 psia before degas, indicating that significant gas will evolve when the oil is transferred to surface oil storage tanks. Degas operations are performed to reduce the BP to about 12 psia. Oil degasification is done on a cavern basis well in advance of delivery.

Current oil degasification at SPR is achieved by flashing the crude in a processing plant to separate volatile gases where the excess gas is incinerated on-site and processed oil is re-injected into the cavern. A simple schematic of this concept is shown in Figure 2-1. The hanging string in the cavern to be degassed is positioned so that it terminates in the oil several feet above the oil-brine interface. The oil flows up the hanging string and into the degas plant where the oil passes through a flash drum that separates the oil into a liquid and a gas stream. The degassed oil is re-injected into the top of the cavern as a jet or plume.

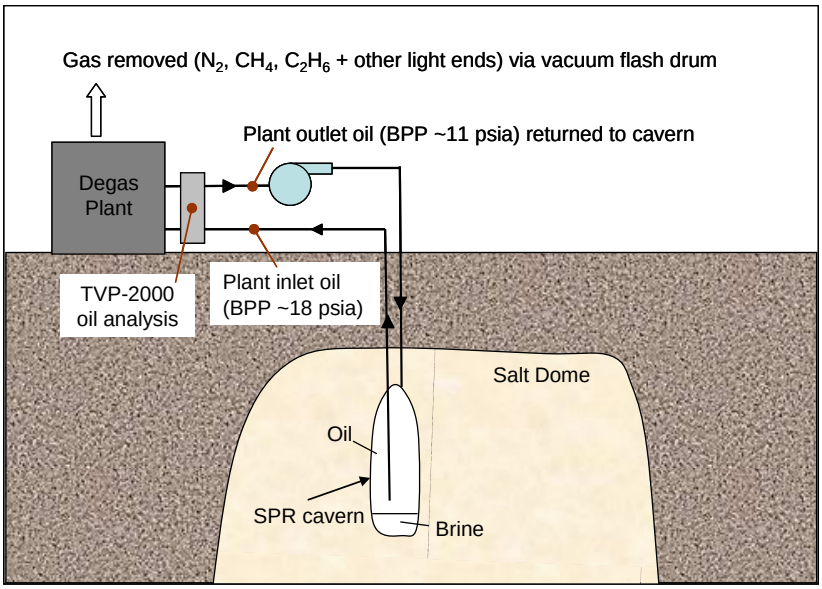


**Figure 2-1. Schematic of Operational Degas (Lord and Rudeen, 2007)**

## 2.2 Cavern Scale Mixing

Performance curves are defined in this report as degas plant inlet and outlet bubble point (BP) pressure histories overlaid on a single figure where time is represented as the processed oil volume fraction. The volume fraction (*VF*) is defined as the cumulative volume of oil processed divided by a representative cavern volume, in this case the oil volume at the start of degas. The inlet BP pressure is the more important parameter. The inlet BP pressure is measured at the inlet of the degas plant and is a measure of the in-situ BP of the oil in the cavern at the hanging string.

Evaluation of the degas performance curves led to the conclusion that there is some degree of cavern scale mixing of oil during degasification. The spectrum of possible in-cavern mixing scenarios is depicted conceptually in Figure 2-2- ranging from ideal plug flow to partial mixing (fingering or localized interface mixing) to complete mixing. Corresponding examples of actual performance curves are also shown in the figure. Ideal plug flow is depicted on the left extreme, while complete mixing is depicted on the right extreme. The interface between gassy oil and processed oil remains distinct and intact during the entire processing time, and it moves downward as the volume of oil processed increases. This scenario is the most efficient mixing scenario for the current degas configuration, as no processed oil is drawn into the plant. Cavern BH114 exhibited a plant performance curve that suggests nearly ideal plug flow. On the opposite end of the mixing spectrum, a completely mixed scenario supports no such barrier between gassy oil and processed oil, rapidly distributing processed oil throughout the cavern so that it appears in the plant inlet in gradually increasing amounts as the cavern volume is degassed. This is the least efficient scenario for degassing purposes, requiring a relatively large

volume of oil processed for effective removal of gas to project specifications. Cavern BH101 exhibited a performance curve that suggests nearly complete mixing. The wide range of possibilities between these extremes is depicted as intermediate mixing. In this scenario, some degree of effective plug flow is experienced early in processing. At some volume fraction, a significant decrease in plant inlet bubble point is observed, which implies the arrival of a mixture of gassy and processed oil. The processing efficiency of an intermediate mixing case falls between the plug flow and completely mixed. BH102 and BH103 performance curves suggest intermediate mixing.

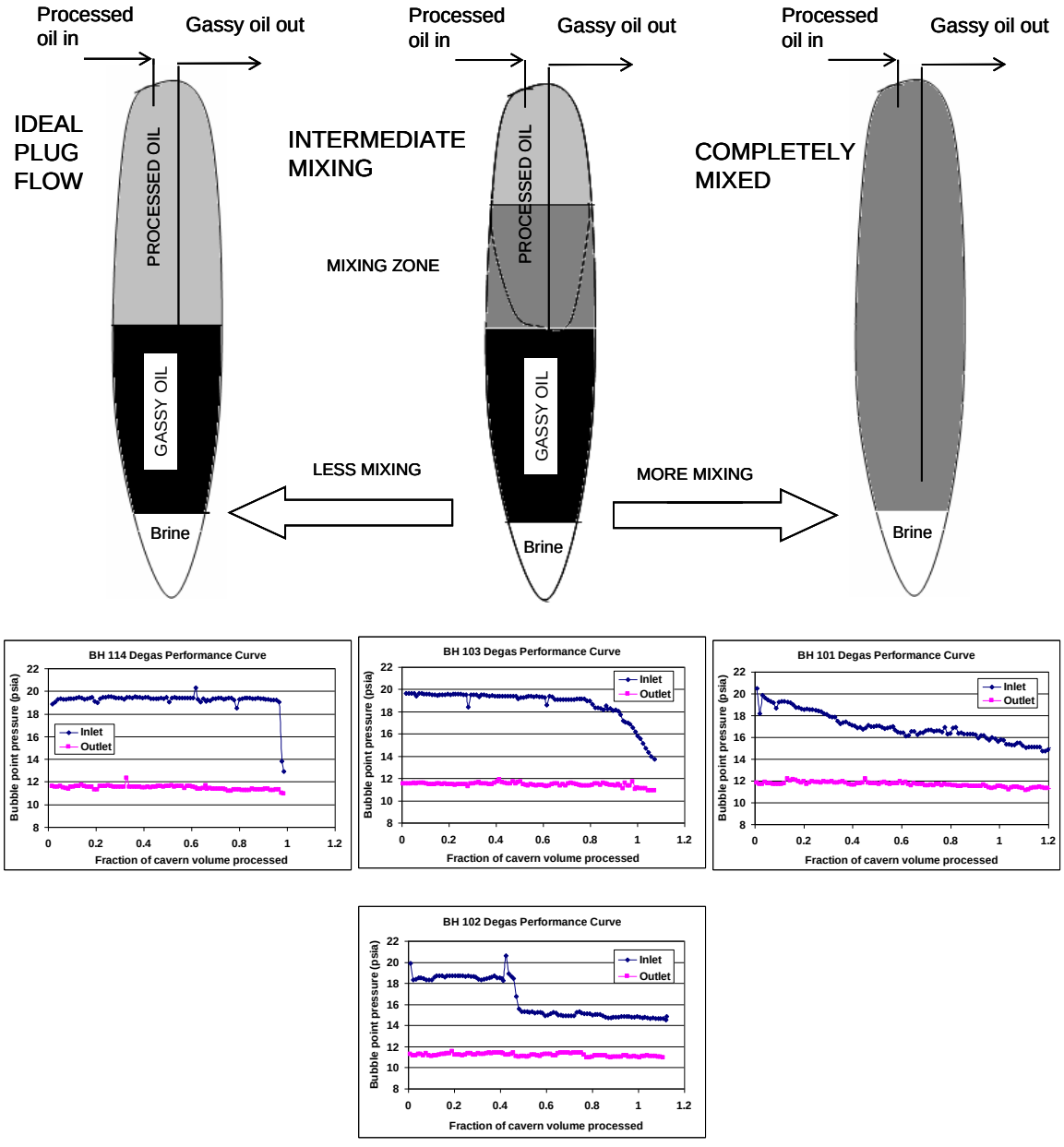


**Figure 2-2. Conceptual Representations of Possible Mixing Scenarios (Lord and Rudeen, 2007)**

## 2.3 Simple Degas Mixing Model

A simple degas cavern mixing model, referred to here as the SDM model, is presented as a means to test the viability of several ideal model configurations to simulate observed behavior.

### 2.3.1 SDM Model Bounding Cases

Sample SDM model output performance curves for the bounding cases of complete mixing and plug flow are overlaid in Figure 2-3. Both models were run to $VF$ = 1.24. Note that the completely mixed model shows a continuous decrease in plant inlet bubble point pressure ($BP_I$) throughout processing, while the plug flow model breaks at $VF$ = 1.0 and then remains at $BP_I$ = $BP_O$ = 11 psia. By comparison, the completely mixed plant inlet (and consequently cavern average) is 13.4 psia at $VF$ = 1.2. These two performance curves define the boundaries of expected behavior for the real systems, with the area marked in Figure 2-3 as "region of possible non-ideal mixing performance curves." Also, the post-degas in-situ bubble point should be generally bounded by the complete mixing performance curve from above and the diagonal dotted line representing the best-case plug flow from below, marked in Figure 2-3 as "region of non-ideal mixing cavern average BP."

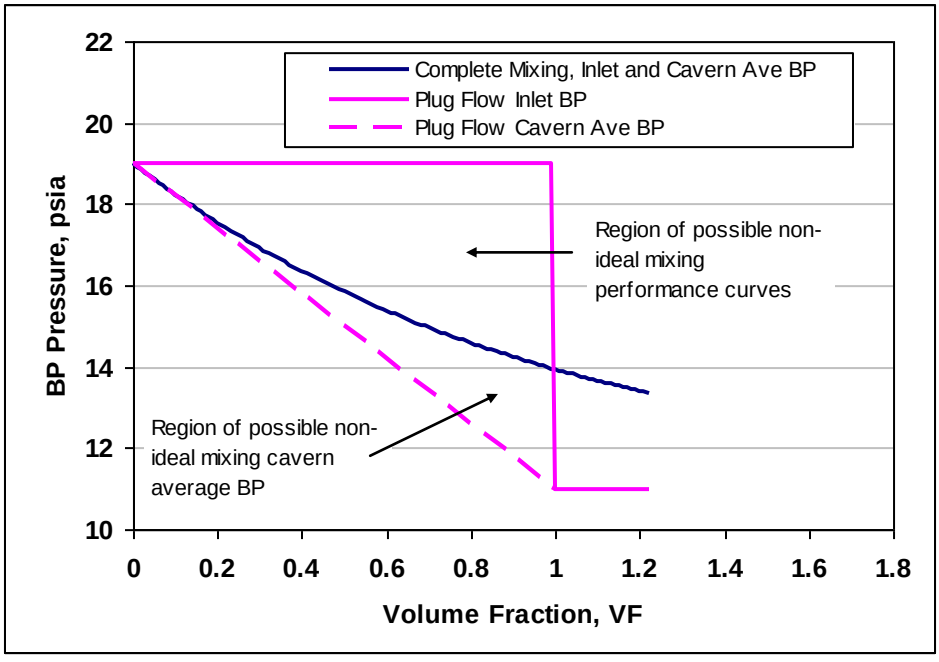


**Figure 2-3. SDM Model Results Showing $BP_I$ Histories (Performance Curves) for Complete Mixing and Plug Flow Bounding Cases (Lord and Rudeen, 2007)**

### 2.3.2 SDM Model Intermediate Cases

Inspection of the real performance curves shown earlier reveals that only a few of the caverns resemble either of the bounding cases. Many exhibit some sort of intermediate behavior with a break in inlet bubble point occurring sometime in the middle of processing, behaving almost as a plug flow cavern until the break, and then proceeding with something between plug flow and mixed for the remainder of processing. The SDM model was configured so that it can simulate a mixing barrier that moves downward with volume fraction processed, starting from an arbitrary point and reaching a completely mixed state before *VF* = 1.0. The cavern is divided into two zones separated by a mixing boundary in early processing. Plug flow occurs in the bottom zone, while either mixing or plug flow occur in the top zone (this model does not distinguish between the two mixing modes in the top of the cavern). At some point during processing, the mixing boundary is eliminated either because it is drawn into the intake at the bottom of the cavern or it simply breaks apart. After this point, the cavern is completely mixed and proceeds as such for the remainder of processing.

Running a case with the SDM model in which the mixing barrier breaks down at an arbitrary point (*VF* = 0.5) during processing yields the performance curves shown in Figure 2-4. Plant inlet BP is 19 psi until *VF* = 0.5 at which point the entire cavern mixes to a uniform state. The new starting point either goes to plug flow again, shown as the horizontal line, or complete mixing, which is the gradually decreasing BP. The dotted lines represent the cavern-average BPP for the ideal plug flow model—the lower bound for cavern BPP if the processing was stopped at the corresponding *VF*.

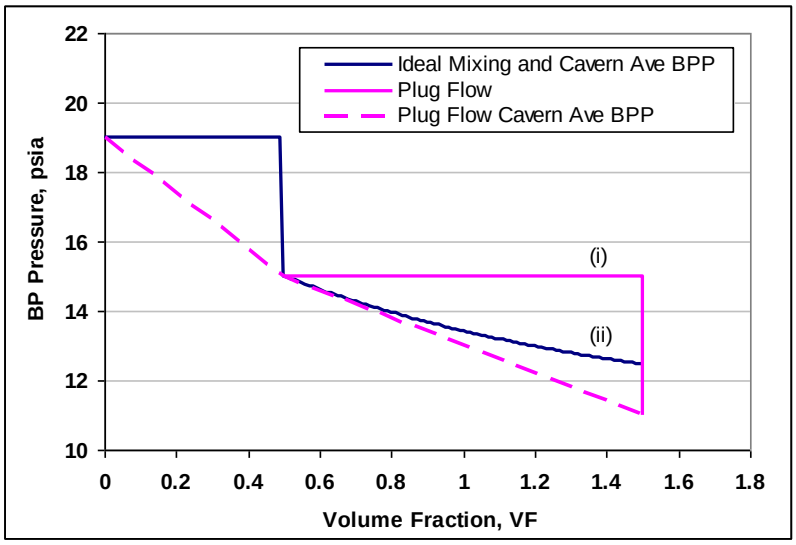


**Figure 2-4. SDM Model Performance Curves Depicting Plug Flow Until *VF* = 0.5, at Which Point the Entire Cavern Mixes and Proceeds with Either (i) Plug Flow or (ii) Complete Mixing until *VF* = 1.5 (Lord and Rudeen, 2007)**

### 2.3.3 Data-Model Comparisons

Several specific cases of measured data versus SDM model results are explored. Note that the model is not used in a predictive manner here, but rather in a post-process analysis to see if real system behavior is at least quantitatively consistent with the features of the simple conceptual cavern mixing models.

The cases presented in Figure 2-5 are:

a. Plug flow vs. BH104.
b. Complete mixing vs. BH101.
c. Intermediate model vs. BH102.
d. Intermediate model vs. BH113.

As can be seen, the SDM model does a good job of predicting the system behavior indicating that the mixing conceptual model is correct.

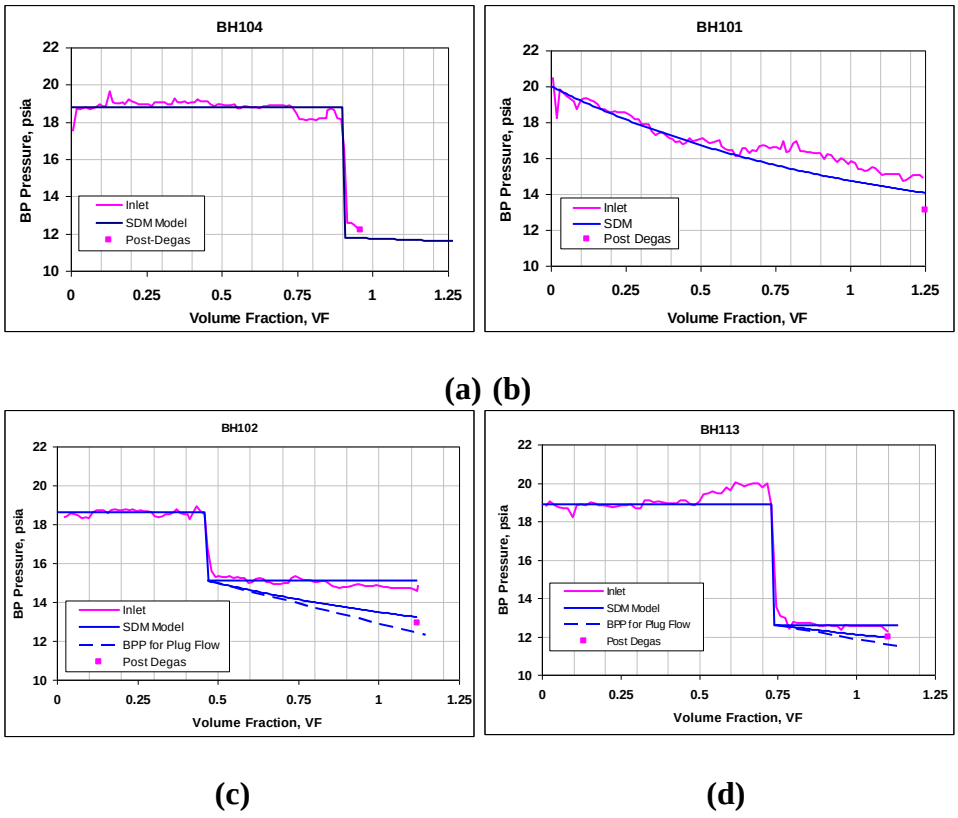


**Figure 2-5. SDM Model Performance Curves For Plug Flow (BH104), Complete Mixing (BH101), and Intermediate Mixing (BH102 and BH113) (Lord and Rudeen, 2007)**

## 2.4 Summary Comments on SDM Ideal Plug Flow and Mixing Modeling

The ideal plug flow and mixing models discussed above and implemented in the SDM model appear to capture many of the features of cavern mixing. Perhaps the most useful feature of the ideal models is that they can set bounds for the expected performance of the real degas systems, with plug flow rendering the highest efficiency, and complete mixing rendering the lowest efficiency. Also interesting is the finding that the magnitude of drop in inlet bubble point pressure that occurs when the performance curve breaks in the real systems corresponds reasonably well with simple mixing theory. The SDM model may be useful in this sense for putting bounds on (i) the expected magnitude of BPP drop according to the value of *VF* when the break occurs, and (ii) the bounds on expected in-situ BPP as a function of processing from the break point forward. An important limitation in the SDM is that it cannot predict when a break will occur, or how a system will respond to changes in operational parameters like string configuration or pumping rates.

# 3 Externally-Driven Mixing Mechanisms

Externally-driven oil mixing, which is caused by the introduction and/or extraction of oil and brine in a cavern, can occur under a number of operational scenarios including filling, degas, and oil exchange (injection and withdrawal) between caverns. In the oil injection scenario, an inlet jet or plume of oil is introduced into the cavern. Depending on the density difference between the inlet oil and the resident oil, the inlet jet or plume will sink or rise and mix with the resident oil. For oil injection, oil can be withdrawn at a different location (degas) or brine can be withdrawn from the brine layer (oil filling or exchange). There are two oil withdrawal scenarios. In the first one, which is operational during degas as described above, oil is withdrawn and injected into the oil layer. In the second scenario, water/brine is injected into the brine layer and oil is withdrawn from the oil layer.

For oil injection, oil mixing can be beneficial or detrimental to operations depending on the scenario. During filling and oil exchange, mixing is probably beneficial because the process will minimize layering and produce a more uniform oil in the cavern. During degas, however, mixing is detrimental. As discussed below, oil layering increases the efficiency of degas. In addition, if the oil injection string is too close to the oil-brine interface, detrimental entrainment of brine into the oil layer may occur. Therefore, understanding the oil mixing processes in a cavern is important to operations.

For oil withdrawal, the primary concern is the proximity of the oil-brine interface to the oil withdrawal string. If the oil withdrawal location is too close to but still above the oil-brine interface, selective withdrawal may occur such that brine is entrained into the oil, which would be detrimental.

Most of these externally-driven scenarios involve an inlet jet of oil injected into the resident oil layer. The research at Sandia National Laboratories and at ASU and ND concentrated on the fluid mixing mechanisms in the degas scenario because of the significance of this process to cavern operations including the time and cost. However, the processes involved are also important in cavern filling and in other operational scenarios.

Oil mixing mechanisms include the mixing that occurs due to the inlet jet or plume as well as the mixing due to unstable fluid stratification of a heavier fluid over a lighter fluid (Rayleigh-Taylor instability) that could be caused by the injection of a heavier fluid jet into a lighter fluid. Both mechanisms are discussed in this chapter along with an evaluation of the Coriolis force.

## 3.1 Jet Mixing

In the oil injection scenario, oil is injected as a jet into the resident oil. The behavior of the injected fluid jet depends on the density difference between the injected and resident oil. In the discussion that follows, the general characteristics of a buoyant jet are discussed for three cases. Assuming that the inlet buoyant jet is discharged downward as in SPR caverns, the three cases are

a. Less Dense Jet
   In this case, buoyancy is in the opposite direction of the initial jet momentum, which is often referred to as a negatively-buoyant jet. Because buoyancy and the initial momentum are in opposite directions, the jet will "turn around", and a penetration distance of the jet into the ambient fluid can be determined depending on the initial momentum and buoyancy of the jet. A less dense jet is probably encountered in caverns that exhibit ideal plug flow and possibly in intermediate mixing cases as described in Chapter 2. This condition is also often referred to as a fountain.
b. Neutral Jet
   In this case, there is no buoyancy difference between the jet and the ambient fluid. This condition is probably rarely encountered in SPR caverns because the oil is degassed, which will change the oil composition and temperature.
c. More Dense Jet
   For this condition, buoyancy is in the same direction of the initial jet momentum, or a positively-buoyant jet. Because buoyancy and the initial momentum are in the same direction, the jet will continue downward until it encounters either a denser ambient fluid if the ambient is stratified or layered, the oil-brine interface in SPR caverns, or cavern walls. A more dense jet is probably encountered in caverns that exhibit complete mixing and possibly in intermediate mixing cases as described in Chapter 2.

Note that a downward-directed jet of lower density is equivalent to an upward-directed jet of higher density.

The discussion of jet mixing is separated into the following sections:

1. General jet and plume behavior in uniform and stratified environments.
2. Simple entrainment numerical model for the prediction of jet and plume behavior.
3. Fluid entrainment across interfaces.
4. Effect of confinement.
5. Enclosure Models.

Each section discusses applicability to SPR caverns.

An example of the behavior of injection of a jet into a layered system, which is very similar to possible scenarios at SPR, is seen in experiments conducted by Kumagai (1984); this experiment is also discussed in more detail later in this report. In his experiments, he had a fresh water layer over a salt water layer in a tank and injected a denser salt water jet into the upper layer. Processes that influence the results are the entrainment of the upper layer fluid (fresh water) into the heavier (denser salt water) jet, which reduces the density of the jet to be less than that of the lower layer, and the impact of the jet on the layered interface, which is not initially penetrated, including entrainment across the interface.

The time evolution is shown in Figure 3-1. The inlet jet fluid was dyed for visualization purposes. In Figure 3-1a, the inlet jet impacts the layered surface but does not penetrate it due to the entrainment of fresh water into the jet. The jet fluid spreads out laterally along the interface. The process continues in Figure 3-1b and c as more and more of the jet fluid spreads out along the interface creating a slightly heavier upper layer with some stratification. The original interface is slightly depressed by the inlet jet.

In time, the upper layer density increases due the introduction of the denser jet. With this increased upper-layer density, the jet density at the interface increases such that it penetrates the layer interface. In Figure 3-1d, the inlet jet penetrates the interface, continues through the bottom layer all the way to the bottom of the tank, and spreads out along the bottom, forming yet another layer as seen in Figure 3-1e. Figure 3-1f shows the final configuration of a 3-layered system consisting of the original top layer, which is denser than fresh water due to the jet, a middle layer, which is essentially the original bottom layer, and a new bottom layer that is mostly from the inlet jet with fluid entrained from both of the above layers.

In the following sections, general results for jets and plumes will be discussed. The case of a uniform resident fluid will be presented first followed by resident-fluid stratification and layering effects. Representative studies are discussed so the reader will have a general knowledge of the basic concepts and approaches, but a thorough literature search and summary is not included.

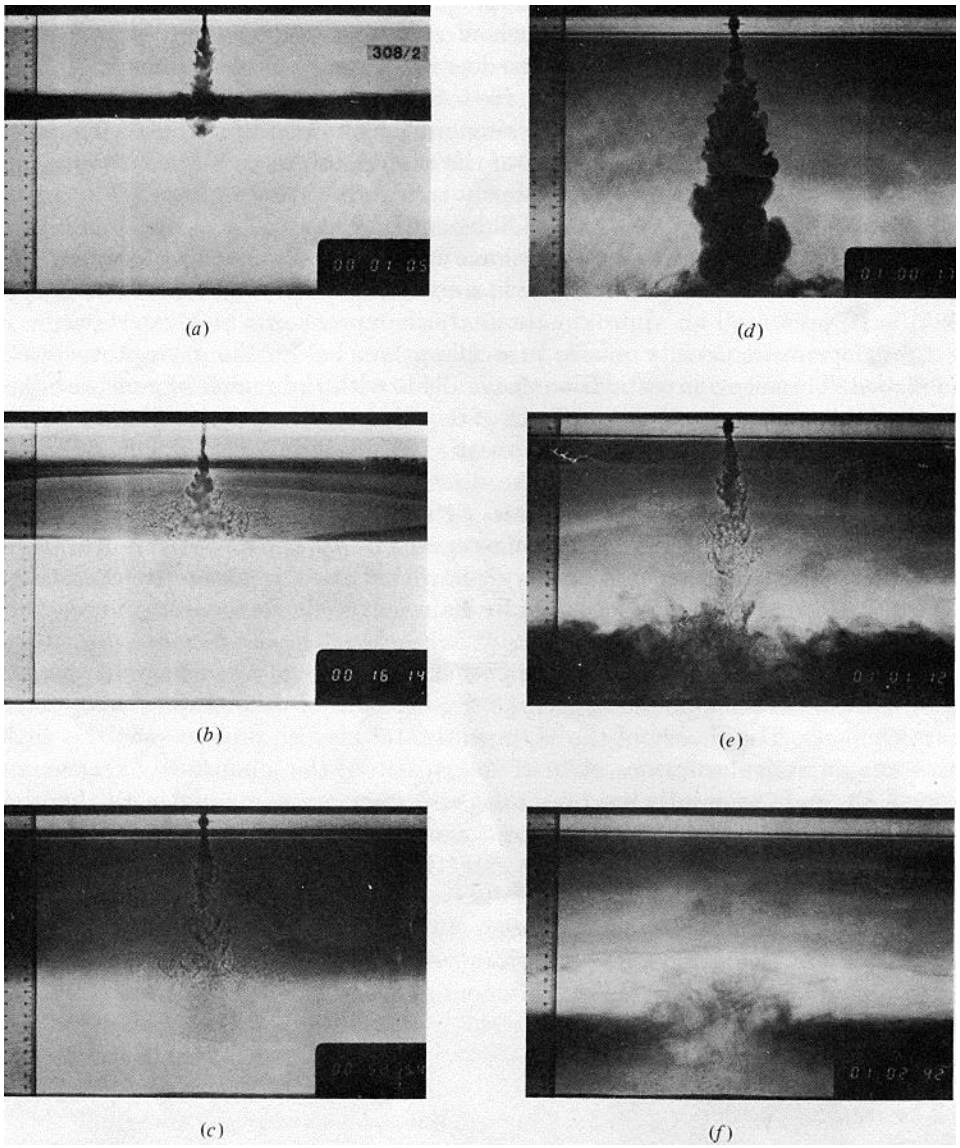


**Figure 3-1. Jet Mixing Results from Kumagai (1984)**

Shadowgraph showing the evolution of a layered system due to the introduction of a plume of dense salt solution of $\rho = 1.1344$ g/ml at $F = 14.1$ cm$^4$/s$^3$. Upper layer was initially fresh water 8.24 cm deep. Lower layer is salt solution of $\rho_2 = 1.0161$ g/ml. The time from the start in hours, minutes and seconds is indicated by the clock at the bottom. Depressions of the interface formed by the impingement of the plume are apparent in (*a*)–(*c*), which also show the rise of the first front. (*c*) shows a state just before the beginning of the penetration of the plume. (*d*), (*e*) and (*f*) show the spread of the plume fluid after penetration, made visible by the addition of dye. (*f*) shows the resulting three-layer structure.

### 3.1.1 General Buoyant Jet and Plume Behavior

The discussion below follows the classic dimensionless presentation of Fischer et al. (1979). In addition to the discussion in Fischer et al. (1979), Chen and Rodi (1980) review buoyant jet experimental data. The two presentations are essentially equivalent. The Fischer et al. (1979) outline will be followed below because it is easier to understand. The discussion below assumes a less dense jet initially directed vertically upward (positively-buoyant), or equivalently a more dense jet directed downward. Only round jets will be treated here. Results for plane jets are also given in in the above references.

In general, a jet is dominated by momentum over buoyancy while a plume is dominated by buoyancy over momentum. A buoyant jet has both jet and plume characteristics as the flow transitions between the two cases. Around the injection location, the buoyant jet behaves like a neutral buoyancy jet as the jet momentum dominates the buoyancy effects. As the jet momentum is lost, the behavior is similar to a plume where buoyancy effects dominate.

General relationships for the mass flux, momentum flux, and the buoyancy flux through a plane normal to the jet axis are given below.

Mass Flux

$$\rho\mu = \int_A \rho\, u\, dA$$

Momentum Flux

$$\rho m = \int_A \rho\, u^2\, dA$$

Buoyancy Flux

$$\rho\beta = \int_A g\, \Delta\rho\, u\, dA$$

where *u* is the time-averaged velocity in the axial direction and Δρ is the density difference between the jet and the surrounding fluid. Note that the effective gravitational acceleration is often used, or

$$g' = g\frac{\Delta\rho}{\rho}$$

Specific values of the terms are used, which are the integral values divided by the fluid density.

For a round jet, the density-scaled jet volumetric flow velocity, momentum, and buoyancy flux at the jet exit are given below assuming a "top hat" (uniform) velocity profile

$$Q = \pi\, r^2 u$$

$$M = Qu = \pi\, r^2 u^2$$

$$B = g\,\frac{(\rho_j - \rho_0)}{\rho_0} Q = g_o' Q = \pi\, r^2 u\; g\;\frac{(\rho_j - \rho_0)}{\rho_0}$$

where $r$ is the jet nozzle radius, $g_0'$ is the jet exit value of $g'$, $u$ is the assumed uniform jet exit velocity, $\rho_j$ and $\rho_0$ are the jet exit and ambient densities, and $g$ is the gravitational constant. These variables are frequently used in the discussion that follows.

An equivalent Reynolds number can be expressed as

$$Re = \frac{M^{1/2}}{\nu}$$

where $\nu$ is the kinematic viscosity.

### 3.1.1.1 Uniform Environment

#### 3.1.1.1.1 General Behavior

**Neutral Jet**

At the exit of the pipe, there is a zone of flow establishment (ZFE) for a neutral jet that is about 6 diameters long where shear between the jet and the resident fluid establishes a velocity profile in the jet. For a turbulent jet with a Reynolds number ($M^{1/2}/\nu$) greater than about 4000, the mean centerline jet velocity, $w_m$, downstream of the ZFE as a function of distance is given by

$$\frac{u_m Q}{M} = 7.0\left(\frac{l_Q}{Z}\right)$$

where the constant of 7.0 is based on the experimental data of a number of investigations as shown in Figure 3-2. The length scale for a turbulent jet, $l_Q$, is given by

$$l_Q = \frac{Q}{M^{1/2}} = (\pi)^{1/2}\, r = 1.77\, r$$

which will be discussed later. The centerline equation can also be written as

$$u_m = 7.0\frac{M^{1/2}}{Z} = 7.0\ \frac{\pi^{1/2}\, r\, u}{Z} = 12.4\, u\, \left(\frac{r}{Z}\right) = 6.2\, u\, \left(\frac{d}{Z}\right)$$

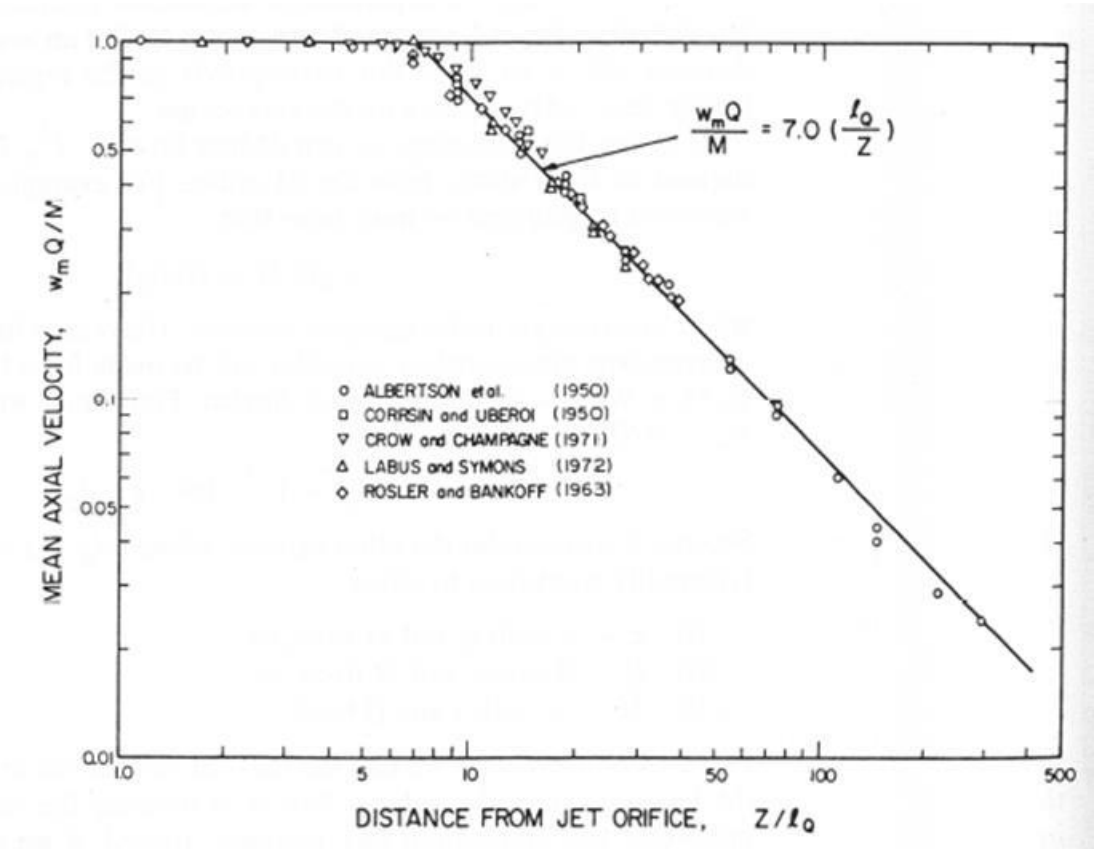


**Figure 3-2. Decay of Peak Jet Velocity for a Round Turbulent Jet (Fischer et al., 1979)**

The volume flux of the jet, which includes entrainment of the ambient fluid and is related to dilution of any initial concentration in the jet, is dependent on the velocity variation and the concentration distribution. Using a Gaussian distribution for the local variation of the mean density and mean concentration, which is supported by data after the zone of flow establishment (ZFE) of about six jet diameters, the velocity and concentration distributions can be written as

$$u = u_m exp[-(y/b_w)^2]$$

$$C = C_m exp[-(y/b_T)^2]$$

where $y$ is the distance from the jet centerline and $b_w$ and $b_T$ are the respective values of $y$ where the velocity and concentration are 37% (=1/e) of the maximum value.

Radial velocity data for a turbulent jet are shown in Figure 3-3 where *x* is the axial distance from the nozzle in this figure.

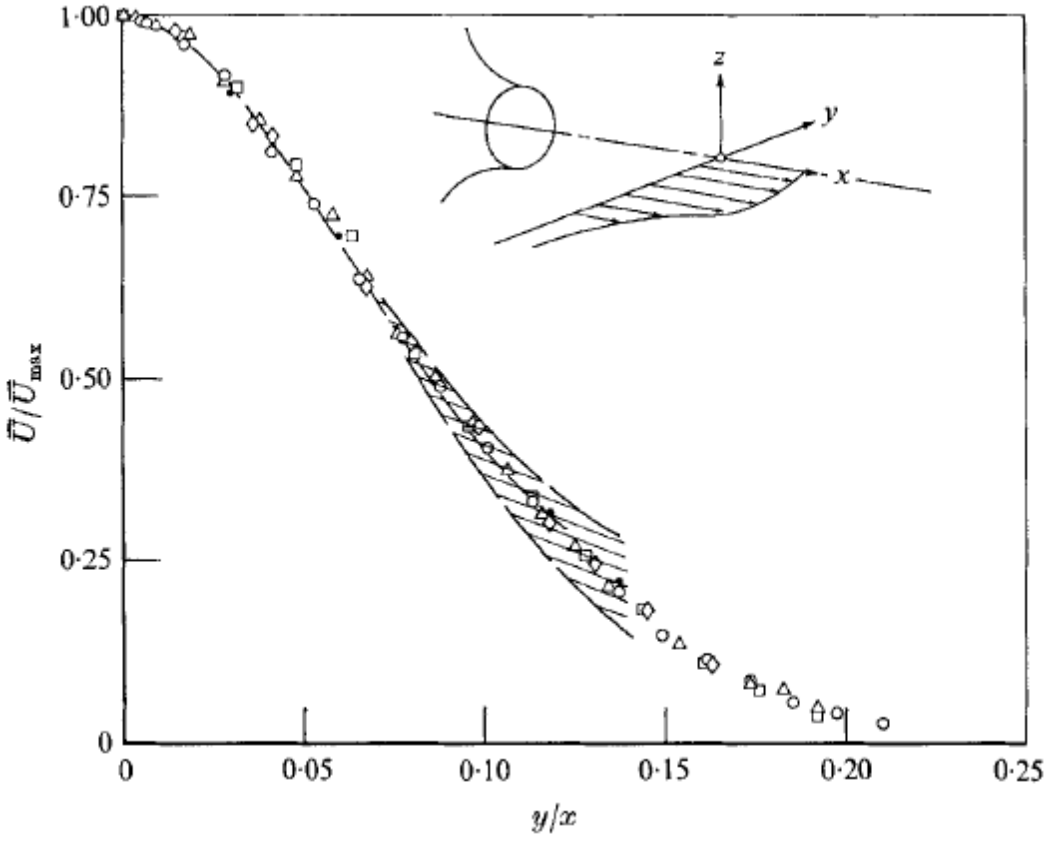


**Figure 3-3. Mean Radial Velocity Profile for a Jet (Wygnanski and Fiedler, 1969)**

Based on further analysis (Wygnanski and Fiedler, 1969), the mean velocity profile fits the Gaussian distribution well up to a *y/x* (radial to axial) ratio of approximately 0.1.

Values of the velocity and concentration distribution parameters $b_w/Z$ and $b_T/Z$ are remarkably constant for turbulent round jets. Based on the data from 13 investigations, the values of $b_w/Z$ and $b_T/Z$ are 0.107 ± 0.003 and 0.127 ± 0.004, respectively, as tabulated by Fischer et al. (1979), and the ratio

$$\frac{b_T}{b_w} = \lambda = 1.19$$

Using these results, the volumetric flow of the jet can be written as

$$\frac{\mu}{Q} = 0.25\left(\frac{Z}{l_Q}\right) \quad Z \gg l_Q$$

or

$$\mu = 0.44\, Z\, r\, u \quad Z \gg l_Q$$

The first equation is also equal to the ratio of the initial concentration value in the jet assuming a uniform initial distribution, $C_0$, divided by the average concentration of a tracer in the jet, $C_{av}$, or

$$\frac{C_0}{C_{av}} = \frac{\mu}{Q}$$

Figure 3-4 shows data-model comparisons for the relative volume flux of the jet from Fischer et al. (1979).

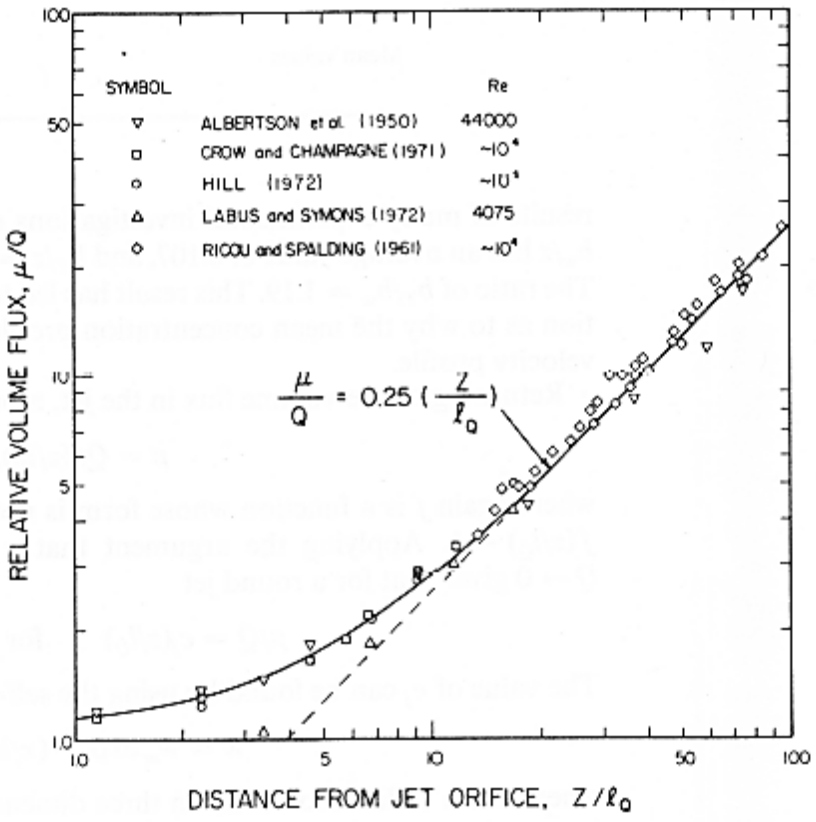


**Figure 3-4. Dilution Factor Along the Axis for a Round Turbulent Jet (Fischer et al., 1979)**

**Neutral Plume**

Similarly, for a neutral plume, i.e., a plume that is solely driven by buoyancy, the far-field velocity distribution on the centerline is a function of distance from the origin and the buoyancy flux and can be written as

$$u_m = 4.7\left(\frac{B}{Z}\right)^{1/3} \quad Z \gg \nu^{3/2}/B^{1/2}$$

or

$$u_m = 6.9\left(\frac{g'r^2\,u}{Z}\right)^{1/3} \quad Z \gg \nu^{3/2}/B^{1/2}$$

based on data-model comparisons given in Rouse et al (1952) where the greater than sign indicates that the plume is fully turbulent.

The length scale for a plume is

$$l_M = \frac{M^{3/4}}{B^{1/2}} = \frac{(\pi)^{1/4}\,r^{1/2}\,u}{{g_0}'^{1/2}}$$

where, as discussed earlier, $g_0'$ is the reduced gravity at the buoyant plume nozzle.

Other relationships for a round plume are as follows:

Total plume momentum flux

$$m = 0.35\,B^{2/3}Z^{4/3}$$

Mass flow rate

$$\mu = 0.15B^{1/3}Z^{5/3}$$

These equations can be combined to yield

$$\mu = c_p m^{1/2} Z$$

where $c_p$ is the growth coefficient of plumes. From data-model comparisons, this value is equal to about 0.254, which is very similar to the jet growth coefficient of 0.25 as seen earlier.

Similar to the jet, the above equation combined with the assumption of a Gaussian profile for the velocity implies

$$\sqrt{2\pi}b_w = c_p Z$$

Measured values of $b_w/Z$ and $b_T/Z$ for a round plume are 0.100 ± 0.005 and 0.120 ± 0.003, respectively, as tabulated by Fischer et al. (1979), and the ratio

$$\frac{b_T}{b_w} = \lambda = 1.20$$

which is very close to the value for a pure jet of 1.19.

For a round plume, the plume mass flow rate and dilution equations can also be combined by eliminating Z from the equations. The result is the plume Richardson number as given by

$$Ri_p = \mu \frac{B^{1/2}}{m^{5/4}}$$

which represents the ratio of buoyancy to inertial forces. Using the above equations for $\mu$ and $m$, the expression becomes

$$Ri_p = \frac{0.15}{0.35^{5/4}} = 0.557$$

which is a constant.

**Buoyant jets**

For a buoyant jet, the behavior is a combination of a jet and a plume.

There are two appropriate length scales for the buoyant jet. As discussed earlier, the appropriate length scale for a turbulent jet is

$$l_Q = \frac{Q}{M^{1/2}} = (\pi)^{1/2}\, r$$

The length scale for a plume is

$$l_M = \frac{M^{3/4}}{B^{1/2}} = \frac{(\pi)^{1/4}\, r^{1/2}\, u}{{g_0}'^{1/2}}$$

The ratio of the plume and jet length scales, $l_Q/l_M$, is the jet Richardson number, which is equal to

$$Ri = \frac{l_Q}{l_M} = \frac{Q\, B^{1/2}}{M^{5/4}} = (\pi)^{1/4}\left(\frac{{g'}_0\, r}{u^2}\right)^{1/2} = \left(\frac{\pi}{4}\right)^{1/4}\left(\frac{{g'}_0\, D}{u^2}\right)^{\frac{1}{2}} = \left(\frac{\pi}{4}\right)^{1/4}\frac{1}{Fr_d}$$

and is related to the inverse of the Froude number. $Fr_d$ is the jet densimetric Froude number, or

$$Fr_d = \left(\frac{u^2}{g'_0\, D}\right)^{1/2}$$

So

$$l_M = \frac{(\pi)^{1/4}\, r^{1/2}\, u}{{g_0}'^{1/2}} = \frac{(\pi/4)^{1/4}\, D^{1/2}\, u}{{g_0}'^{1/2}} = \left(\frac{\pi}{4}\right)^{1/4} D\, Fr_d$$

or

$$\frac{l_M}{D} = \left(\frac{\pi}{4}\right)^{1/4} Fr_d$$

Sometimes the Froude number is defined as the square of the above value, or

$$Fr = \left(\frac{u^2}{g'_0\, D}\right)$$

Similarly, the Richardson number is sometimes defined as

$$Ri = \frac{g'_0\, D}{u^2}$$

without the ($\pi$/4) factor and in terms of $u^2$, not $u$.

In order to keep the definitions straight, the following notation will be used

$$Fr_1 = \left(\frac{u^2}{g'_0\, D}\right)^{1/2} = \frac{u}{(g'_0\, D)^{1/2}}$$

$$Fr_2 = \left(\frac{u^2}{g'_0\, D}\right)$$

and

$$Ri_1 = \left(\frac{\pi}{4}\right)^{1/4} \left(\frac{g'_0\, D}{u^2}\right)^{\frac{1}{2}} = \left(\frac{\pi}{4}\right)^{1/4} \frac{1}{Fr_1}$$

$$Ri_2 = \left(\frac{\pi}{4}\right)^{1/2} \left(\frac{g'_0\, D}{u^2}\right) = \left(\frac{\pi}{4}\right)^{1/2} \frac{1}{Fr_2}$$

The absence of the ($\pi/4$) factor will be noted at that particular time.

$l_Q$ and $l_M$ are the length scales for the initial volume flux and the transition from a jet to a plume. The initial volume flux length scale, $l_Q$, is on the order of the initial jet diameter as discussed above, which is usually negligible compared to the transition or plume length scale, $l_M$. Thus, the length scale $l_M$ is commonly used to normalize Z.

The round jet volume flux and length scale can be made dimensionless as

Volume flux

$$\bar{\mu} = \frac{\mu B^{1/2}}{R_p M^{5/4}} = \frac{\mu}{Q}\left(\frac{Ri}{R_p}\right)$$

Length scale

$$\zeta = \frac{c_p}{R_p}\left(\frac{Z}{l_M}\right) = c_p\left(\frac{Z}{l_Q}\right)\left(\frac{Ri}{R_p}\right)$$

Using the jet zone relationship given earlier

$$\frac{\mu}{Q} = 0.25\left(\frac{Z}{l_Q}\right) \quad Z \gg l_Q$$

the dimensionless jet volume flux in the near-field region becomes

$$\bar{\mu} = \zeta \quad \zeta \ll 1$$

In the far-field plume zone,

$$\mu = 0.15 B^{1/3} Z^{5/3}$$

as given earlier becomes

$$\bar{\mu} = \frac{0.15\, R_p^{2/3}}{c_p^{5/3}} \zeta^{5/3} = \zeta^{5/3} \quad \zeta \gg 1$$

These results are straight lines on a plot of $\bar{\mu}$ vs $\zeta$ as shown in Figure 3-5, which also includes experimental data for different values of the jet Richardson number for a jet where buoyancy acts in the direction of the jet.

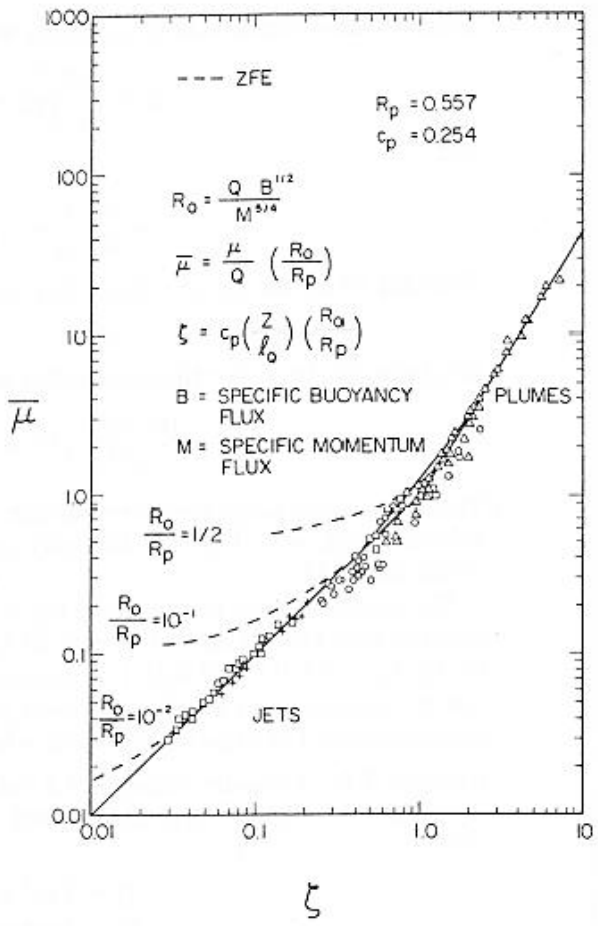


**Figure 3-5. Dilution For a Round Turbulent Buoyant Jet Including Experimental Data of Ricou and Spalding (1961) (Fischer et al., 1979)**

Papanicolaou and List (1988) performed detailed measurements on round vertical buoyant jets, and their results generally agree with those values above with slightly different numerical values. The most glaring difference is the concentration to velocity width ratio, $\lambda$. For a jet, their value of 1.194 is close to the value of 1.19 mentioned above. However, their value of 1.067 for a plume is much smaller than the value of 1.20. This smaller value has been generally used in later studies.

Experiments for buoyant jets are discussed in the next few sections.

#### 3.1.1.1.2 Buoyant Jet Experimental Data

Negatively- and positively-buoyant jets in a uniform ambient fluid will be discussed separately below because their behavior is different.

### *Negatively-Buoyant Jets or Fountains*

The first investigation into the behavior of negatively-buoyant jets was performed by Turner (1966) as summarized below. Other investigations include Abraham (1967), Pantzlaff and Leuptow (1999), and Kokkalis and Papanicolaou (2006), Papanicolaou and Kokkalis (2008). Each study is discussed separately below.

#### Turner (1966)

Turner (1966) was the first to investigate the scenario for an upward directed heavier fluid jet or fountain, or equivalently a downward directed lighter jet, in a uniform environment as depicted in Figure 3-6.

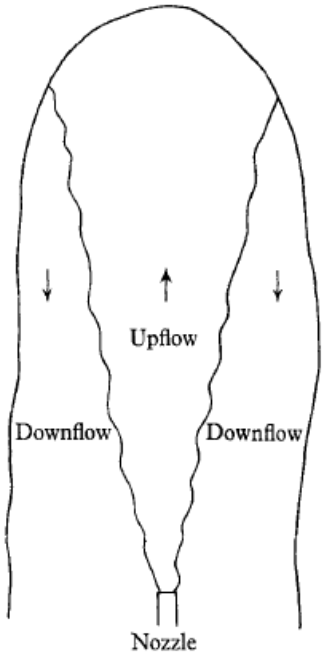


**Figure 3-6. Schematic of Upward-Directed Heavy Buoyant Jet (Turner, 1966)**

The jet rise height oscillates in time as shown in Figure 3-7 with a mean rise height of Z.

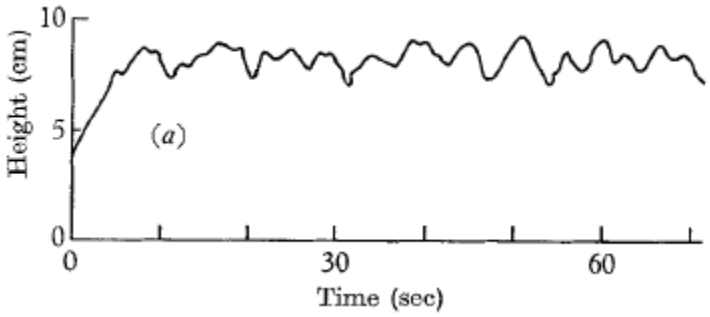


**Figure 3-7. Oscillation of Buoyant Jet Height (Turner, 1966)**

Using the same variables discussed in the previous section, the mean height of the jet rise can be written as

$$\frac{Z}{l_M} = C$$

Using the relationship derived earlier

$$\frac{l_M}{D} = \left(\frac{\pi}{4}\right)^{1/4} Fr_1$$

so

$$\frac{Z}{\mathrm{D}} = C\ \left(\frac{\pi}{4}\right)^{1/4} Fr_1 = \ C\ \left(\frac{\pi}{4}\right)^{1/4} {Fr_2}^{1/2}$$

which will be derived again below. Using the nomenclature of Turner,

$$V = \pi\, r^2 u$$

$$\Delta = g\ \frac{\left(\rho_j - \rho_0\right)}{\rho_0} = {g'}_0$$

in the definition of $l_M$, the jet rise height can be written as

$$Z = C\ \pi^{-3/4}\ V\ \Delta^{-1/2}\ r^{-3/2}$$

The data obtained by Turner (1966) are shown in Figure 3-8.

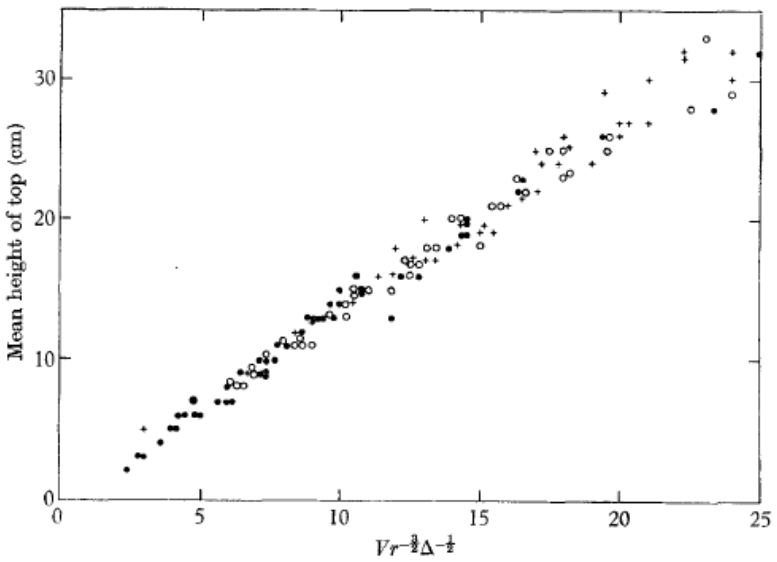


**Figure 3-8. Mean Height of Buoyant Jets (Turner, 1966)**

The x-axis is simply $l_M \pi^{3/4}$. According to Turner (1966), the constant C is equal to 1.85 based on a straight-line fit to these data, so

$$Z = C\,\pi^{-3/4}\,V\,\Delta^{-1/2}\,r^{-3/2} = 1.85\,\pi^{-3/4}\,V\,\Delta^{-1/2}\,r^{-3/2} = 0.784\,V\,\Delta^{-1/2}\,r^{-3/2}$$

Note that there seems to be a slight curvature in the data even though a straight-line fit is proposed.

The result

$$Z = 0.784\,V\,\Delta^{-1/2}\,r^{-3/2}$$

can be rewritten in terms of Froude number. By expanding the individual terms, the above expression can be rewritten as

$$Z = 0.784\,\frac{\pi}{2^{1/2}}\;\;{Fr_2}^{1/2}\,D$$

or

$$\frac{Z}{D} = 1.74\,{Fr_2}^{1/2} = 1.74\,Fr_1$$

In terms of Richardson number

$$\frac{Z}{D} = 1.64\,{Ri_2}^{-1/2} = \;1.64\,{Ri_1}^{-1}$$

As discussed earlier, the mean jet rise height is *Z*. The ratio of initial jet rise height to the steady mean value, *Z*, varied within a small range with a mean value of 1.43 as shown in Figure 3-7.

There is a definite problem with the above equation – it does *not* fit the data in Figure 3-8 as is obvious by inserting the maximum value on the x-axis of 25, which leads to a predicted mean height of 19.6 cm, well below the height of 30-35 cm from the figure.

There are other presentations of the data from later publications involving Turner directly. In Baines et al. (1990), the fit to Turner's data is given by

$$\frac{Z}{r} = 2.46\ Fr_{1,r}$$

where the characteristic length is r instead of *D*. This expression can be rewritten as

$$\frac{Z}{D} = 1.74\ Fr_1 = 1.74\ {Fr_2}^{1/2}$$

which is the same as given earlier. This relationship supposedly fits the Turner data and the data of 3 other investigations, although the 3 Turner data points in Figure 3-9 (denoted by "T") all seem to be above the line suggesting that the Turner data are suspect.

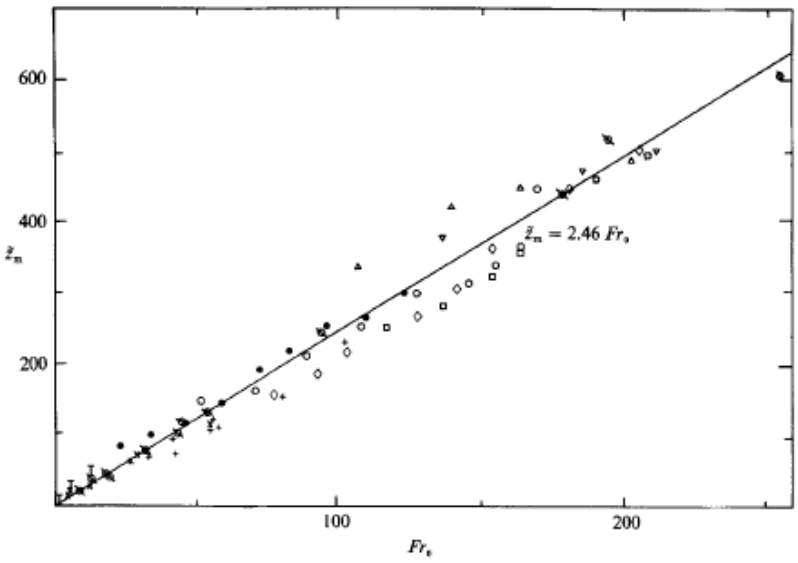


**Figure 3-9. Dimensionless Rise Height for a Buoyant Jet From Numerous Studies (Baines et al., 1990)**

More recently, Friedman and Katz (2000) contacted Turner about his 1966 data. Turner responded that there is a scale error on his earlier plot above. He provided Friedman and Katz corrected results, and the revised data are well fit by the relationship

$$\frac{Z}{D} = 2.2\left(\pi/4\right)^{-1/2} Ri_2^{\ -1/2}$$

where the ($\pi/4$) factor has been added due to different definitions of $Ri_2$, or

$$\frac{Z}{D} = 2.2\ Fr_2^{\ 1/2}$$

or

$$\frac{Z}{r} = 3.11\ Fr_{1,r}$$

which is 26% higher than the original fit, and this revised equation is probably the best fit to the Turner data. The Friedman and Katz (2000) paper and plot are discussed later in this report in Chapter 11.

Kokkalis and Papanicolaou (2006) also noted the discrepancy in the constant from Turner (1966); apparently they were unaware of the Friedman and Katz (2000) paper. They re-evaluated the constant C using the data plot presented earlier and came up with a constant of 3.17 instead of 1.85 as discussed later. Because the plot is in error as noted above, this new constant is not appropriate.

**Abraham (1967)**

Abraham (1967) developed a theoretical relationship for the time-averaged height for a negatively-buoyant jet based on some previous data for a submerged jet. His final relationship for the time-averaged rise distance is

$$\frac{Z}{D} = 1.94\ {Fr_2}^{1/2}$$

where

$$Fr_2 = \frac{u_0^2}{\frac{(\rho_j - \rho_0)gD}{\rho_j}}$$

Note that the $\Delta\rho/\rho$ term is slightly different than used by Turner (1966) in that the reference density is $\rho_j$ instead of $\rho_0$. This slight difference will be neglected below.

The original Turner (1966) result is

$$\frac{Z}{D} = 1.74\ Fr_1 = 1.74\ {Fr_2}^{1/2}$$

although the constant should probably be 2.2 instead of 1.74 as discussed in the previous section.

Abraham (1967) also compared his relationship to that of Priestley and Ball (1955) using his entrainment assumptions resulting in

$$\frac{Z}{D} = 1.86\ {Fr_2}^{1/2}$$

and Morton (1959a,b)

$$\frac{Z}{D} = 1.45\ {Fr_2}^{1/2}$$

as well as the Turner (1966) relationship as summarized in Table 3-1.

**Table 3-1. Comparison of Various Models with Turner (1966) Data**

| *Theoretical Solution* | *Value Compared to Original Turner Eqn* | *Value Compared to Revised Turner Eqn* |
|---|---|---|
| *Priestly and Ball (1955)* | *107%* | *85%* |
| *Morton (1959a,b)* | *84%* | *66%* |
| *Abraham (1967)* | *111%* | *88%* |

**Pantzlaff and Leuptow (1999)**

Pantzlaff and Leuptow (1999) investigated negatively (heavier jet directed upwards) and positively (lighter jet directed upwards) buoyant jets. The negatively-buoyant jet results will be discussed in this section, while the positively buoyant jets will be discussed in the next section.

For a negatively-buoyant jet, the experimental results in dimensionless form are presented in Figure 3-10, where *M* is the same as in earlier discussions, *F* is equal to the buoyancy flux, *B*, and *h* is equivalent to *Z*.

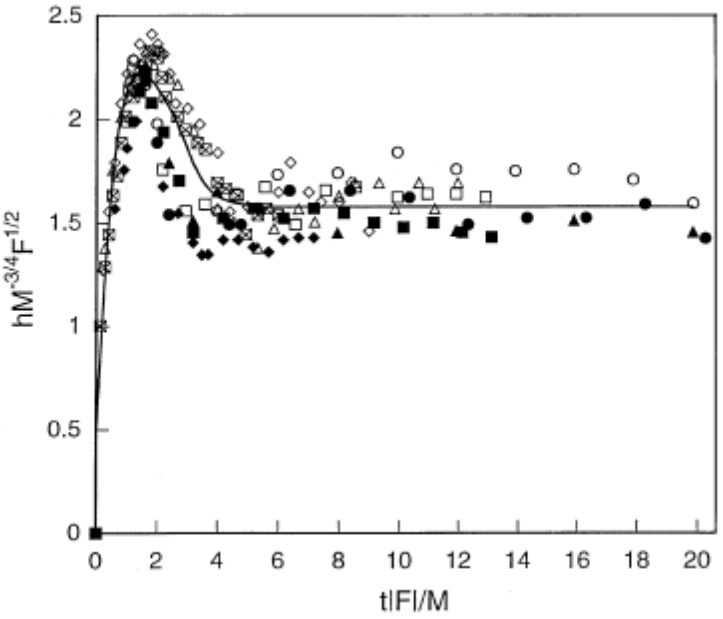


**Figure 3-10. Jet Penetration Height Using Similarity Variables (Pantzlaff and Leuptow, 1999)**

The asymptotic results for long times are where *Z* is equivalent to *h* in the above figure

$$Z = 1.6\,\frac{M^{3/4}}{F^{1/2}} = 1.6\,\frac{M^{3/4}}{B^{1/2}} = 1.6\,l_M$$

or

$$\frac{Z}{D} = 1.6\,\left(\frac{\pi}{4}\right)^{1/4} Fr_1 = 1.5\,Fr_1 = 1.5\,Fr_2^{1/2}$$

Note that the Froude number definition in Pantzlaff and Leuptow (1999) is different than used earlier, or

$$Fr_{Pantzlaff} = \frac{u^2}{r_0 g(1-\rho_0/\rho)} \sim 2\,Fr_2$$

so that any *Fr* number comparisons using their data need to have the Fr numbers modified.

These data will be compared to those from other investigations in Figure 3-12 (noted as P&L (1999)). The jet penetration height is generally lower than from other investigations, which Pantzlaff and Leuptow (1999) attribute to the finite size of tank and nozzle conditions.

**Kokkalis and Papanicolaou (2006)**

Kokkalis and Papanicolaou (2006) performed some experiments on a lighter jet injected downward into a heavier resident fluid similar to the SPR geometry for circular and non-circular jets. Two methods of introducing buoyancy were used – salt concentration and temperature.

They summarized the existing data at that time and plotted the normalized mean jet penetration distance as a function of the jet Richardson number, $Ri_1$, as shown below in Figure 3-11.

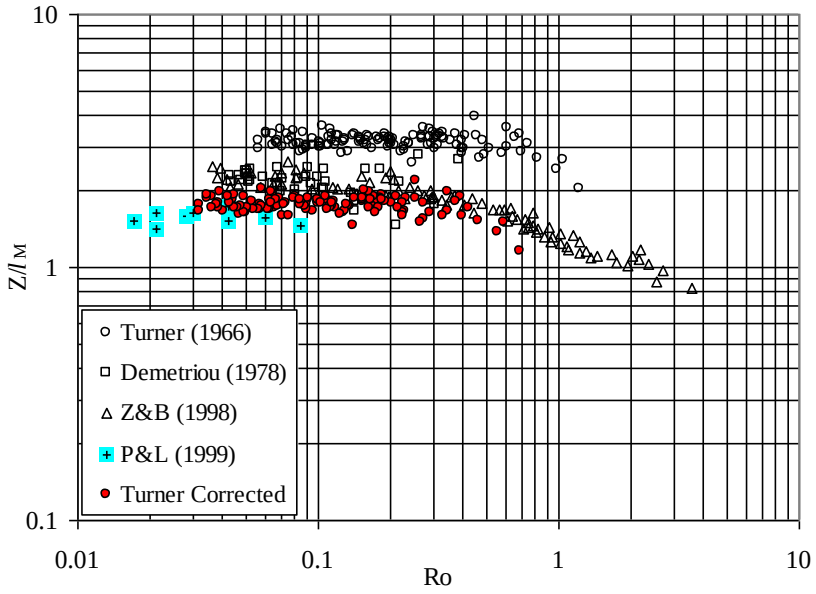


**Figure 3-11. Normalized Jet Penetration Distance vs. Richardson Number for Literature Data (based on Kokkalis and Papanicolaou, 2006; revised by Papanicolaou, 2015)**

They noted the discrepancy in the plot given from Turner (1966) as discussed above. They re-evaluated the constant *C* in the equation for the Turner (1966) data as being 3.17 instead of 1.85, or

$$\frac{Z}{\mathrm{D}} = C\ \left(\frac{\pi}{4}\right)^{1/4} Fr_1 = 3.17\ \left(\frac{\pi}{4}\right)^{1/4} Fr_1 = 2.98\ Fr_1$$

A value of 3.17 for the constant C is much larger than the values from other investigations, which range between 1.57 and 2.40. The top cluster of points in Figure 3-12 is mainly from Turner (1966) with a constant *C* of 3.17 while the Turner data with the a constant C of 1.85 is noted in filled-in diamonds; the lower cluster of points is from other studies. As discussed above, the Turner data figure has a scale error, so the constant of 3.17 for Turner's data is inappropriate, and the top grouping of points should be ignored.

Figure 3-11 presents the results as $Z/\ l_M$ as a function of the Richardson number. Using the expression

$$l_M = \left(\frac{\pi}{4}\right)^{1/4} Fr_1\ D$$

gives

$$\frac{Z}{D} = C\ \left(\frac{\pi}{4}\right)^{1/2} \frac{1}{Ri_1} = C\ \left(\frac{\pi}{4}\right)^{1/4} Fr_1 = 0.94\ C\ Fr_1$$

where *C* is the $Z/\ l_M$ value from the figure. For a $Z/\ l_M$ value of 2.0, which is the asymptotic value at low Richardson number, the results are

$$\frac{Z}{D} = 1.77 \frac{1}{Ri_1} = 1.88\ Fr_1 = 1.88\ {Fr_2}^{1/2}$$

which is similar to the other correlations.

Figure 3-12 summarizes the jet penetration data from Kokkalis and Papanicolaou (2006) for circular nozzles. The mean jet penetration depth, *Z*, and the maximum jet penetration depth, $Z_{max}$, are shown as a function of jet Richardson number ($Ri_1$) and the two buoyant jet length scales, $l_Q$ and $l_M$. Note that the penetration depths divided by the buoyant length scale, $l_M$, asymptotes to constant values as the jet Richardson number decreases, while the penetration depths divided by the jet length scale, $l_Q$, keeps increasing. Thus, the $l_M$ length scale is more useful to predict buoyant jet penetration depths. The ratio $Z_{max}/Z$ is approximately equal to 1.5, similar to the 1.43 value reported by Turner (1966).

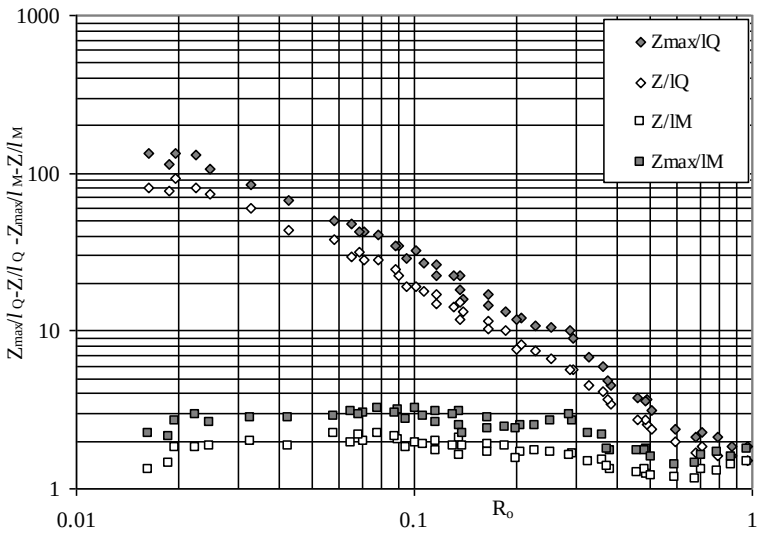


**Figure 3-12. Normalized Maximum and Mean Penetration Depths for Round Buoyant Jets (based on Kokkalis and Papanicolaou, 2006; revised by Papanicolaou, 2015)**

### Papanicolaou and Kokkalis (2008)

This paper is an extension of the earlier paper by Kokkalis and Papanicolaou (2006) discussed above. An updated version of Figure 3-11 is shown below in Figure 3-13.

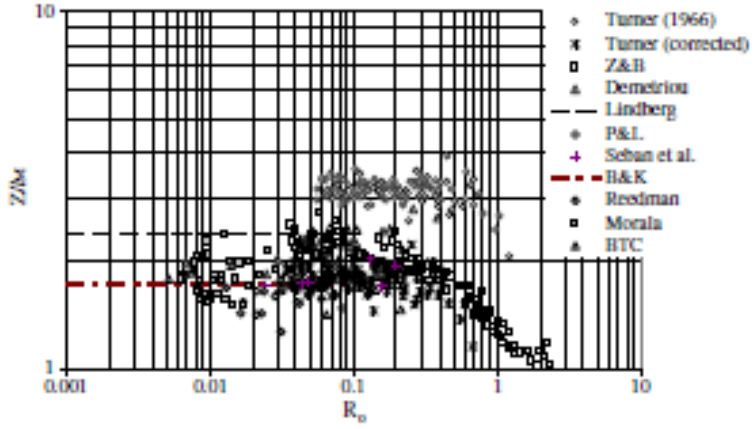


**Figure 3-13. Updated Normalized Jet Penetration Distance vs. Richardson Number for Literature Data (Papanicolaou and Kokkalis, 2008)**

The Lindberg and B&K (Bloomfield and Kerr) data are shown by lines because the initial jet Richardson number information is not available. As discussed earlier, the Turner data shown in the plots is in error and should be ignored.

The jet buoyancy from density differences was introduced in two ways – salt and heat. Buoyancy is preserved during mixing for the salt case but not for the case of heat due to the non-linear thermal expansion coefficient of water. Nevertheless, both types of buoyancy lead to similar behavior, especially as the temperature difference is reduced in the hot water case.

The salt-induced buoyancy data are shown in Figure 3-14a where the solid circles and open circles are the maximum and mean penetration depths, respectively. The data are generally consistent with previous investigations in that the dimensionless mean and maximum penetration distances at low Richardson numbers are approximately 2 and 3, respectively. The squares and crosses are model predictions using a 1-d ODE set of entrainment equations that will be discussed in a later section.

The data and model predictions from the heated jet case are shown in Figure 3-14b. The maximum penetration depth could not be ascertained from the experiment due to fluid mixing in the jet plenum. Note that the mean penetration depth for the hot water case is greater than for the salt case because buoyancy is not preserved for hot water, thereby reducing the buoyancy.

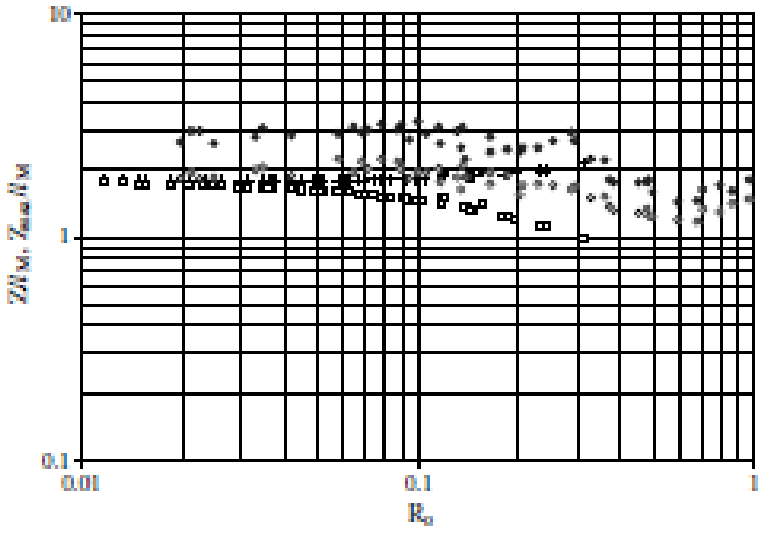


(a) Salt Cases

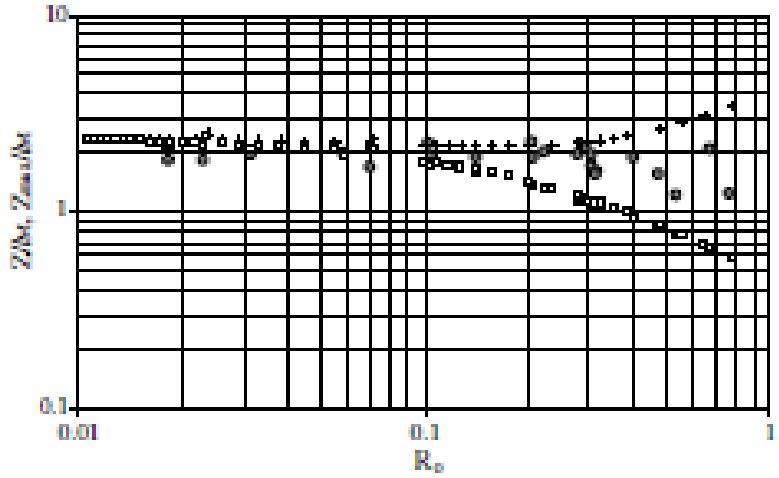


(b) Hot Water Cases

**Figure 3-14. Penetration Depths vs Richardson Number for Round Buoyant Jets (Papanicolaou and Kokkalis, 2008)**

### *Positively-Buoyant Jets*

The investigation by Pantzlaff and Leuptow (1999) for positively-buoyant jets will be discussed in this section.

#### Pantzlaff and Leuptow (1999)

The case of a positively-buoyant jet, such as a heavy jet directed downwards, or equivalently a lighter jet directed upwards, is discussed in this section. Pantzlaff and Leuptow (1999) looked at positively buoyant jets as in a light jet directed upwards as shown in Figure 3-15.

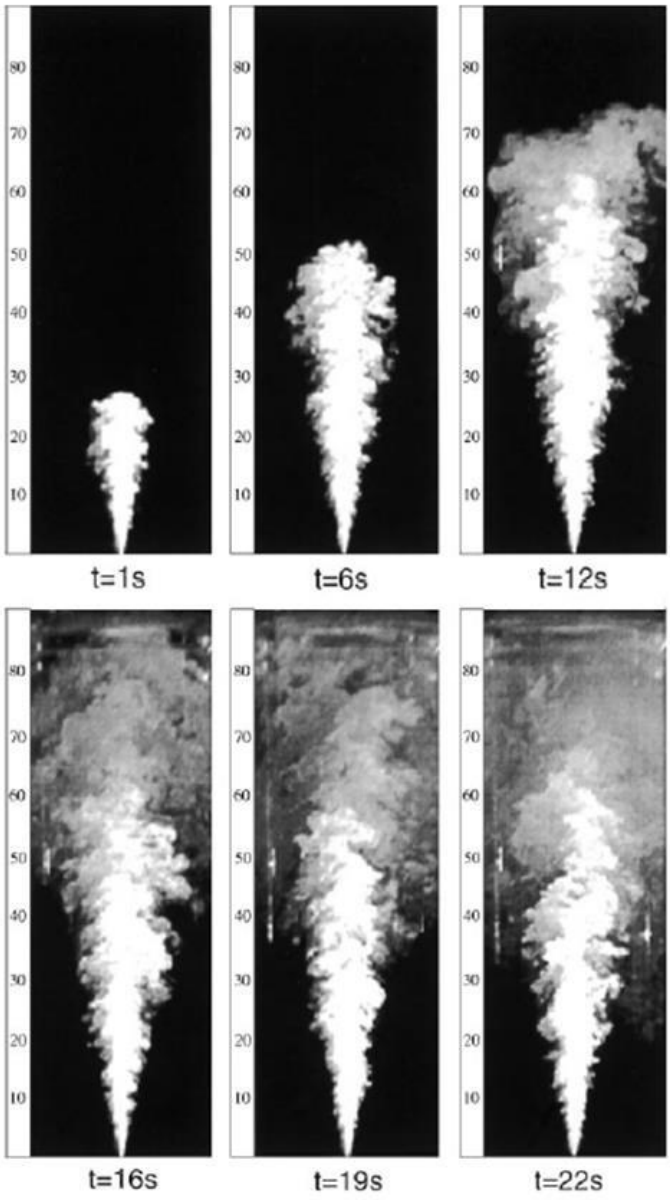


**Figure 3-15. Positively Bouyant Jet Behavior (Pantzlaff and Leuptow, 1999)**

Figure 3-16 and Figure 3-17 show the time-dependent data

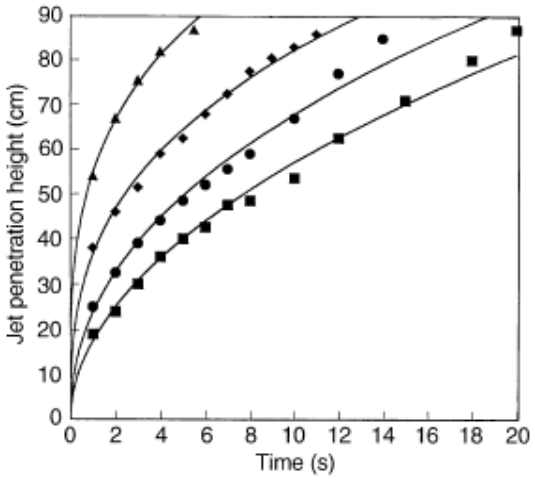


**Figure 3-16. Time-Dependent Jet Penetration Data (Pantzlaff and Lueptow, 1999)**

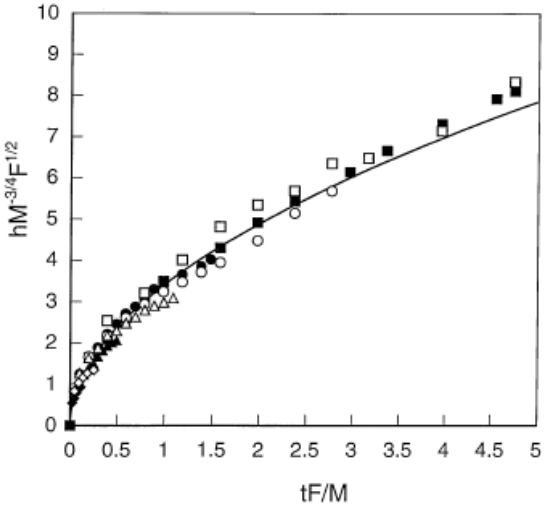


**Figure 3-17. Normalized Jet Penetration Data (Pantzlaff and Lueptow, 1999)**

Pantzlaff and Leuptow (1999) fit the data to the following relationship

$$Z\frac{F^{1/2}}{M^{3/4}} = Z\frac{B^{1/2}}{M^{3/4}} = \frac{Z}{l_M} = 3.4\left(\frac{Bt}{M}\right)^{0.52}$$

The collapse of the data into a single curve supports the previous scaling ratio of $Z/l_M$ originally used by Turner (1966) applies to these data as well. Note that the ratio increases with time to values of 8 or more. In contrast, negatively-buoyant jets have maximum ratios of 2 to 3.

For the case of a neutral jet, Turner (1962) developed a relationship that the jet penetration from a transient jet is proportional to $t^{1/2}$, which is supported by the above relationship.

### 3.1.1.2 Stratified Environment

If the resident fluid is stratified, the jet penetration depth will be affected. The stratified resident fluid will be entrained into the buoyant jet, which will alter the jet density differently compared to a uniform resident fluid. In the discussion that follows, a linear density distribution in the resident fluid is assumed. Note again that Fischer et al. (1979) assume a lighter jet directed upward from the bottom, which is equivalent to the SPR situation for a denser jet directed downward.

In the case of SPR, the resident fluid may be slightly stratified, either due to the initial conditions or during injection of the jet fluid. As discussed in Webb (2016a), the resident oil density increases with depth due to the increase in pressure even if the temperature increases with depth, which is typically seen in SPR temperature logs. However, the injected fluid density also increases with pressure, complicating the analysis. For the present discussion, the effect of pressure on the fluid density will be ignored.

#### 3.1.1.2.1 General Behavior

For the case of resident fluid stratification, the vertical density distribution is assumed to be given by

$$\rho = \rho_0(1 - \varepsilon(z))$$

$$\frac{1}{\rho_0}\frac{d\rho}{dz} = \frac{-d\varepsilon}{dz} = -\varepsilon'(z)$$

where $\rho_0$ is the resident fluid density at $z$=0 and $(d\varepsilon/dz)^{-1}$ is the characteristic length of density stratification.

Often the density gradient is expressed in terms of the Brunt-Vaisala buoyancy frequency, $N$

$$N^2 = -g\frac{1}{\rho_0}\frac{d\rho}{dz}$$

or

$$N^2 = g\epsilon'$$

Turner (1973, pg.11) discusses the parameter in more detail.

The jet behavior for a vertical downward directed initially positively-buoyant jet discharged into a linearly stratified fluid is shown in  from Fan (1967). In this case, the initial jet density is 1.024 g/ml; the ambient density at the nozzle is 1.007 g/ml. The ambient density at the

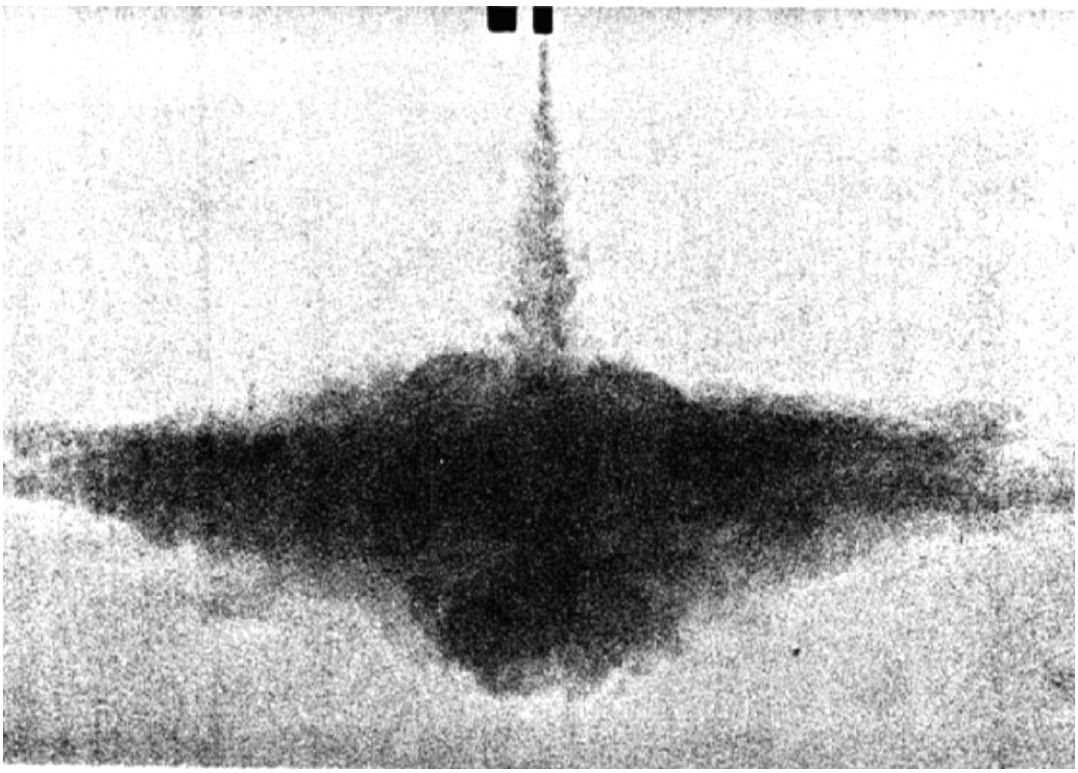

**Figure 3-18. Vertical Buoyant Jet Discharged Into a Linearly Stratified Environment (Fan, 1967)**

terminal (maximum) depth is 1.023 g/ml. Note that the jet overshoots the spreading distance where the jet spreads out horizontally.

As discussed by Fischer et al. (1979), the terminal (maximum) penetration distance for a round simple jet injected into a stratified environment is related to the jet length scale

$$L_{jet} \sim (M/g\varepsilon')^{1/4}$$

or

$$L_{jet} \sim M^{1/4}/N^{1/2}$$

while for a simple plume, the maximum penetration distance is proportional to the plume length scale

$$L_{plume} \sim B^{1/4}/(g\varepsilon')^{3/8}$$

or

$$L_{plume} \sim B^{1/4}/N^{3/4}$$

In both cases, the maximum penetration distance is approximately 3.8 times the appropriate length scale based on data-model comparisons discussed in Fischer et al. (1979).

Similar to the buoyant jet in a uniform environment, the ratio of the length scales is an important parameter. In the case of a stratified environment, the length scale ratio is

$$S = \left(\frac{L_{jet}}{L_{plume}}\right)^8 = M^2 g\varepsilon'/B^2 = (MN/B)^2$$

Note that Fischer et al. (1979) call this parameter *N*, not *S*. In order to avoid confusion with the Brunt-Vaisala buoyancy frequency, *N*, List (1982) uses the symbol *S* instead of *N*, which is followed here. For a linear density gradient, the parameter *S* and the initial jet Froude number or Richardson number are the important parameters.

Using the relationships given earlier

$$\zeta = \frac{c_p}{Ri_p}\left(\frac{Z}{l_M}\right)$$

and

$$l_M = \frac{M^{3/4}}{B^{1/2}}$$

the dimensionless asymptotic rise height for small and large values of *S* can be written as

$$\zeta_T = d_p S^{-3/8} \quad S \ll 1$$

$$\zeta_T = d_j S^{-1/4} \quad S \gg 1$$

where the values of $d_p$ and $d_j$ are both equal to 1.7 consistent with the earlier equations above.

The mean dilution at the maximum height can also be calculated using entrainment assumptions given later in this section as stated by Fischer et al. (1979). The resulting equations are

$$\bar{\mu}_T = e_p S^{-5/8} \quad S \ll 1$$

$$\bar{\mu}_T = e_j S^{-1/4} \quad S \gg 1$$

where $e_p$ is equal to 1.5 and $e_j$ has a value of 1.2.

The above sets of equations can be combined, and the results are on lines parallel to the pure jet and pure plume lines previously shown in Figure 3-5 as given below in Figure 3-19. Note the strong influence of different stratification values of *S* (*N* shown on figure).

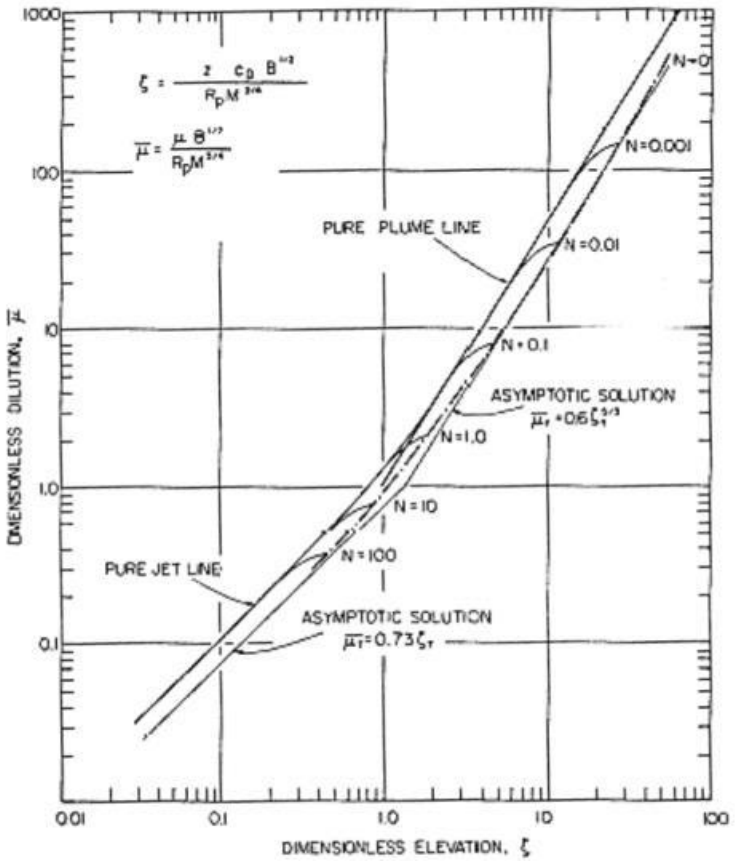


**Figure 3-19. Jet Dilution in a Linearly Stratified Environment (Fischer et al., 1979)**

Buoyant jets in a stratified environment exhibit dependency on the initial jet buoyancy similar to uniform environmental conditions described in the previous sections. However, in the case of stratified flows, the fluid buoyancy may change signs during the flow depending on the conditions at the jet nozzle and the environmental stratification.

For the stratified environment case, a couple of recent investigations for initially negatively- and positively-buoyant jets will be discussed. The applicability to SPR cavern conditions is somewhat limited. The experiments conducted to date use a linearly-stratified environment, whereas any stratification in SPR caverns is likely to be in discrete layers. Still, the effect of environmental stratification on buoyant jets may be significant for SPR.

### 3.1.1.2.2 Experimental Data

**Negatively- and Positively-Buoyant Jets**

**Overview of Papanicolaou Investigations**

Papanicolaou and Stamoulis (2010) and Konstantinidou and Papanicolaou (2003) performed experiments and analysis of buoyant jets discharging into a stratified environment. They defined the ambient fluid stratification as a function of the Brunt-Vaisala buoyancy frequency, *N*, where

$$N^2 = -\frac{g}{\rho_0}\frac{d\rho}{dz} = \frac{gd\varepsilon}{dz} = g\varepsilon'(z)$$

Note that Papanicolaou and Stamoulis (2010) use $N^2$ while Konstantinidou and Papanicolaou (2003) use *N* for the square of the buoyancy frequency. The discussion in Papanicolaou and Stamoulis (2010) follows the presentation in Fischer et al. (1979).

The length scales are written as

Jet

$$\frac{Z}{L_j} = C_j$$

$$L_j = \frac{M^{1/4}}{N^{1/2}}$$

Plume

$$\frac{Z}{L_p} = C_p$$

$$L_p = \frac{B^{1/4}}{N^{3/4}}$$

Then for a buoyant jet with finite values of *M* and *B*

$$\frac{Z}{L_j}\ and\ \frac{Z}{L_p} = f\left[\frac{M}{B}N\right].$$

or the ratio of the length scales discussed earlier.

For a jet, the value of $C_j$ can be determined from data where the buoyancy is small, or when $(M/B)N >> 1$. Similarly, the value of $C_p$ can be evaluated from data where the buoyancy is significant, or when $(M/B)N << 1$.

## Konstantinidou and Papanicolaou (2003)

Konstantinidou and Papanicolaou (2003) obtained data for round and orthogonal jets discharging into a stratified environment for initially positively-buoyant jets. As mentioned above, $N^{1/2}$ in this paper is equal to $N$ above. The data for the round jet are shown in Figure 3-20 where $Z_m$, or $Z$, is the terminal rise height or depth of the buoyant jet and $H_s$ is the spreading height.. They also proposed values of the entrainment coefficient and the width ratio as a function of $MN/B$ that will be discussed later.

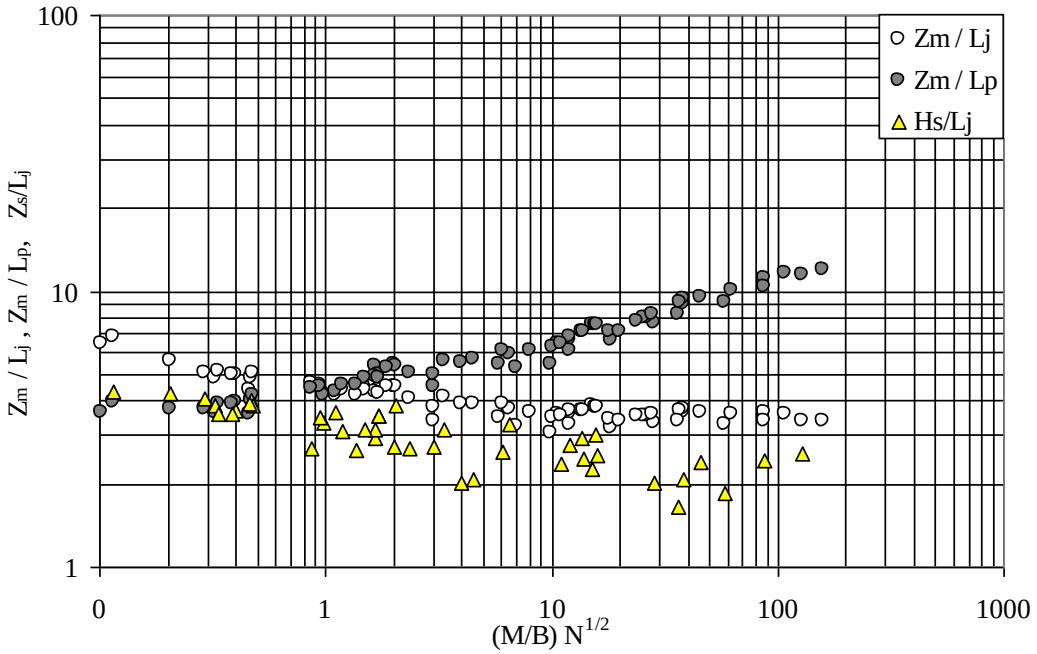


**Figure 3-20. Dimensionless Rise Height for Round Buoyant Jets (based on Konstantinidou and Papanicolaou, 2003; revised by Papanicolaou, 2015)**

From the results as plotted in Figure 3-20, the jet and plume mean rise height constants for stratified conditions can be determined from the appropriate regions on the graph (jet - $(M/B)N >> 1$; plume - $(M/B)N << 1$) are equal to

$$\frac{Z}{L_j} = 3.55 \quad jet$$

$$\frac{Z}{L_p} = 4.00 \quad plume$$

respectively.

## Papanicolaou and Stamoulis (2010)

Papanicolaou and Stamoulis (2010) conducted additional experiments using the same experimental setup as above for 4 different circular jets. They also obtained data for initially positively- and negatively-buoyant jets. The initially positively-buoyant jet will become neutral and then negatively-bouyant with depth in a stratified environment as denser fluid is entrained. The behavior of these two types of jets is shown below in Figure 3-21. As expected, the penetration depth of the initially positively-buoyant jet is larger than the initially negatively-buoyant jet.

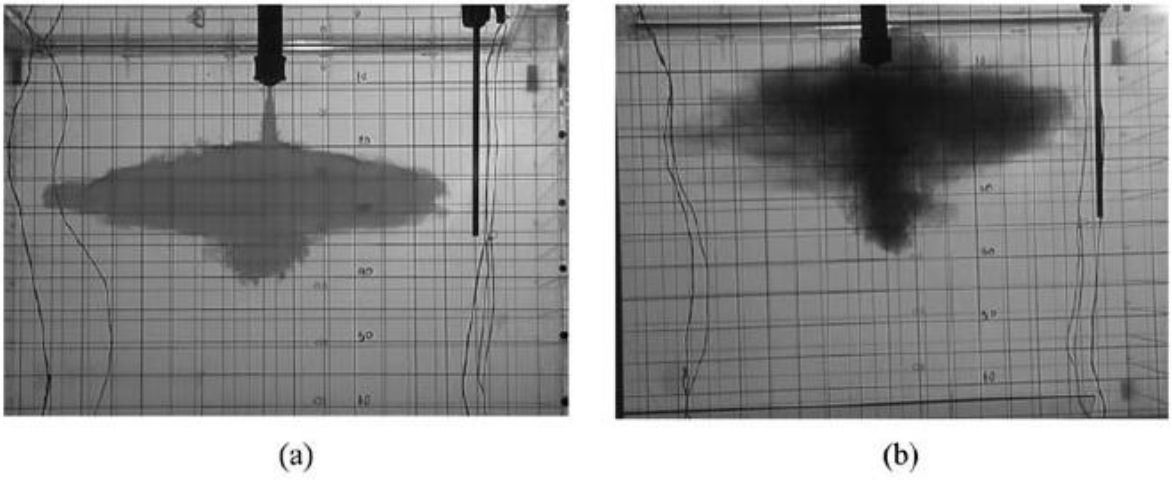


**Figure 3-21. Photographs of an initially (a) positively-buoyant jet (b) negatively-buoyant jet or fountain in stratified ambient (Papanicolaou and Stamoulis, 2010)**

Dimensionless constants for the terminal rise height as a function of the appropriate length scale are listed in Table 3-2 from previous experiments including the values from Fischer et al. (1979) discussed earlier where $Z$ is the terminal (maximum) height and $Z_s$ is the spreading height. All of the previous data are for positively-buoyant jets except for the last row, which is Bloomfield and Kerr (1998) for negatively-buoyant jets ($B < 0$ at source).

Figure 3-22 shows the experimental data obtained by Papanicolaou and Stamoulis (2010) along with the Bloomfield and Kerr (1998) data. The terminal (maximum) depth and the spreading depth are shown. For positively-buoyant jets, the depth increases as $MN/B \rightarrow 0$; for negatively-buoyant jet, the depth decreases towards 0 as $MN/B \rightarrow 0$. The data from Papanicolaou and Stamoulis (2010) are consistently greater than the Bloomfield and Kerr (1998) data possibly due to the small tank used by Bloomfield and Kerr (1998).

**Table 3-2. Constants From Other Investigations (after Papanicolaou and Stamoulis, 2010)**

| ***Author*** | $Z/L_j$ | $Z_s/L_j$ | $Z/L_p$ | $Z_s/L_p$ | ***Description*** |
|---|---|---|---|---|---|
| *Fan (1967)* | *3.41* | | | | *MN/B > 10* |
| *Abraham and Eysink (1969)* | *3.29* | | | | *MN/B=7-18* |
| *Wong and Wright (1988)* | *3.60* | | *4.46* | | *Rectangular and Circular tank* |
| *Papanicolaou et al. (1990)* | *3.46* | | *4.60* | | *MN/B>10; MN/B<1* |
| *Konstantinidou and Papanicolaou (2003)* | *3.55* | *2.38* | *3.97* | *2.99* | *MN/B>10; MN/B<1* |
| ***Average Values*** | *3.46* | | *4.34* | | |
| *Fischer et al. (1979)* | *3.80* | | *3.80* | | |
| *Chen and Rodi (1980)* | *3.80* | | *5.00* | | |
| *Morton et al. (1956)* | | | *3.81* | | *Including virtual origin* |
| *Bloomfield and Kerr (1998)* | *2.94* | *1.55* | | | *B=0 at source; MN/B=∞* |
| *Bloomfield and Kerr (1998)* | *2.88* | *1.35* | | | *B<0 at source; MN/\|B\|>10* |

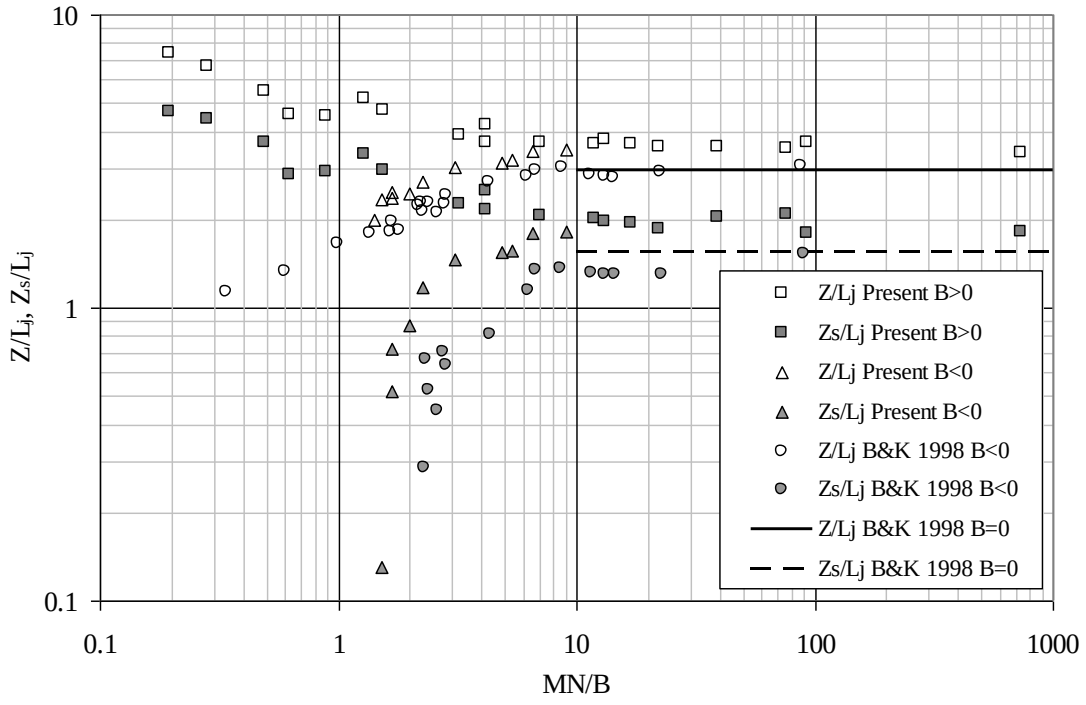


**Figure 3-22. Normalized Jet Penetration Terminal and Spreading Height vs. (MN/B) Including Comparison to Bloomfield and Kerr (1998) Data (based on Papanicolaou and Stamoulis, 2010; revised by Papanicolaou, 2015)**

The maximum and spreading heights from Papanicolaou and Stamoulis (2010) as a function of *MN/B* are shown in Figure 3-22 and Table 3-3. The asymptotic results for $MN/B > 10$ (jet) are $Z/L_j \sim 3.58$ and $Z_s/L_j \sim 1.94$. For $MN/B < 1$ (plume), the $Z/L_j$ ratio varies with $(MN/B)^{-1/4}$ as predicted.

**Table 3-3. Data Comparison With Bloomfield and Kerr (1998) (after Papanicolaou and Stamoulis, 2010)**

| ***MN/B > 10*** | $Z/L_j$ | $Z_s/L_j$ |
|---|---|---|
| *Bloomfield and Kerr* | *2.88±0.10* | *1.35±0.10* |
| *Papanicolaou and Stamoulis* | *3.58±0.12* | *1.94±0.11* |

### 3.1.1.3 Application to SPR

The above general relationships for jets and plumes given in section 3.1.1.1 will be applied to a modeled SPR cavern with the following conditions. Note that these relationships are for unconstrained jets and plumes without any wall effects, which would be present in SPR caverns. The influence of confinement is briefly discussed later in this chapter.

The modeled cavern is 2000 ft high with a uniform diameter of 200 ft. The degas inlet mass flow rate is 130,000 BBL/day for a cavern turnover time of 85.9 days. Various values are listed in Table 3-4.

**Table 3-4. Assumed SPR Cavern Parameters**

| ***Parameter*** | ***Value*** |
|---|---|
| *Cavern Diameter* | *200 ft* |
| *Cavern Height* | *2000 ft* |
| *Cavern Capacity* | *11.2 MBBL* |
| *Pipe ID* | *9.75 inches* |
| *Flow Rate* | *130,000 BBL/day =8.45 $ft^3/s$* |
| *Exit Velocity* | *16.3 ft/s* |
| *Density of Injected Oil* | *1%, 0.1%, 0.01% and 0% lighter than resident oil* |
| *Viscosity* | *5 centistokes = $5.2x10^{-5}$ $ft^2/s$* |

**Unconfined Relationships**

The basic buoyant jet and plume parameters for 1% lighter oil are calculated below

$$Q = \pi\, r^2 u = 8.45\ ft^3/s$$

$$M = Qu = \pi\, r^2 u^2 = 138\ ft^4/s^2$$

$$g' = g\frac{\Delta\rho}{\rho} = 0.32\ ft/s^2$$

$$B = g\ \frac{(\rho_j - \rho_0)}{\rho_0} Q = g'Q = \pi\, r^2 u\ g\ \frac{(\rho_j - \rho_0)}{\rho_0} = \pm 2.72\ ft^4/s^3$$

$$Re = \frac{M^{1/2}}{\nu} = 220{,}000$$

The various length scales are

Jet length scale

$$l_Q = \frac{Q}{M^{1/2}} = (\pi)^{1/2}\, r = 1.77\, r = 0.72\ ft$$

Plume length scale

$$l_M = \frac{M^{3/4}}{B^{1/2}} = \frac{(\pi)^{1/4}\, r^{1/2}\, u}{{g_0}'^{1/2}} = 24.4\ ft$$

The jet centerline velocity as a function of distance is

$$\frac{u_m Q}{M} = 1\ \ for\ \frac{Z}{l_Q} < 7$$

$$\frac{u_m Q}{M} = 7.0\left(\frac{l_Q}{Z}\right)\ \ for\ \frac{Z}{l_Q} > 7$$

$$u_m = \frac{\mathrm{M}}{Q} = 16.3\ ft/s\ \ for\ Z < 5$$

$$u_m = 7.0\left(\frac{M}{Q}\right)\left(\frac{l_Q}{Z}\right) = \frac{82.3}{Z} ft/s\ \ for\ Z > 5$$

Using a Gaussian distribution, the radial velocity distribution is given by

$$u = u_m exp[-(x/b_w)^2]$$

where *x* is the distance from the jet centerline or the jet radius. The value of $b_w/Z$ to the (1/e) distance is approximately 0.107 as discussed earlier, so $b_w$ = 0.107 *Z*. Based on Figure 3-3, the value for 2 $b_w$ will be used as the approximate jet total radius, or $b_{w,max}$ = 0.214 *Z*.

The total volume flux of the jet is given by

$$\frac{\mu}{Q} = 0.25\left(\frac{Z}{l_Q}\right) \quad Z \gg l_Q$$

or

$$\mu = 2.93\, Z \gg 0.72 \text{ ft}$$

For a neutral plume, the far-field velocity distribution on the centerline is a function of distance from the origin and the buoyancy flux and can be written as

$$u_m = 4.7\left(\frac{B}{Z}\right)^{1/3} \quad Z \gg \nu^{3/2}/B^{1/2}$$

where $\nu$ is the fluid viscosity and the greater than sign indicates that the plume is fully turbulent. The Z dimension is

$$Z \gg \frac{\nu^{3/2}}{B^{1/2}} = 2.4\, x\, 10^{-7}\, ft$$

so

$$u_m = 6.56\, \mathrm{Z}^{-1/3}\, ft/s$$

The total plume volume flux is given by

$$\mu = 0.15 B^{1/3} Z^{5/3} = 0.209\, Z^{5/3}\, ft^3/s$$

For a plume, the width is slightly different than a pure jet, or $b_w/Z$ is 0.100 so $b_w$ =0.100 *Z*. As above, 2 widths will be used for the total radius, or $b_{w,max}$ =0.200 *Z*.

The volume flux and length scales will be normalized as discussed earlier and shown in Figure 3-5, or

Normalized Volume Flux

$$\bar{\mu} = \frac{\mu B^{1/2}}{Ri_p M^{5/4}} = \frac{\mu}{Q}\left(\frac{Ri_1}{Ri_p}\right)$$

Normalized Length scale

$$\zeta = \frac{c_p}{Ri_p}\left(\frac{Z}{l_M}\right) = c_p\left(\frac{Z}{l_Q}\right)\left(\frac{Ri_1}{Ri_p}\right)$$

where $c_p$ = 0.254 and $Ri_p$ =0.557.

The dimensionless jet volume flux in the near-field region becomes

$$\bar{\mu} = \zeta \quad \zeta \ll 1$$

In the far-field plume zone,

$$\bar{\mu} = \frac{0.15\, R_p^{2/3}}{c_p^{5/3}}\zeta^{5/3} = \zeta^{5/3} \quad \zeta \gg 1$$

The two curves intersect at $\bar{\mu} = \zeta$ =1, or

$$\frac{Z}{l_M} = \left(\frac{Ri_p}{c_p}\right) = 2.19$$

or

$$\frac{Z}{l_Q} = \left(\frac{Ri_p}{c_p\, Ri_1}\right) = \frac{2.19}{Ri_1}$$

Four different jets directed downward will be analyzed. The first three will all be lighter than the resident fluid and will have different degrees of buoyancy. The fourth jet will be neutrally buoyant.

**Buoyant Jets**

The buoyancy will be parameterized as the density difference between the jet and the resident fluid divided by the resident fluid value. Negatively-buoyant jets will be discussed first.

**0.01 (1%) Density Difference**

Results for the density difference of 0.01 (1%) are shown below in Table 3-5.

**Table 3-5. Results for 0.01 (1%) Lighter Jet**

| ***Parameter*** | ***Value*** |
|---|---|
| $l_Q$ | *0.72 ft* |
| $l_M$ | *24.4 ft* |
| $Ri_1$ | *0.0295* |
| $Ri_2$ | *0.0087* |
| $Fr_1$ | *31.9* |
| $Fr_2$ | *1016* |

Using Turner's revised correlation

$$\frac{Z}{D} = 2.2\ |Fr_2|^{1/2} = 2.2\ Fr_1$$

The downward-directed buoyant jet will descend to a depth of 57 ft below the jet outlet before reversing directions. In a 2000 high cavern with a diameter of 200 ft, the normalized $Z/D_{cavern}$ is 0.285.

The behavior of the buoyant jet will be evaluated based on the dimensionless jet/plume volumetric flux vs dimensionless distance shown earlier in Figure 3-5. Note that there may be a discontinuity in the jet vs. plume equations – only the pure jet and pure plume relationships are used.

The dimensionless plot for the present conditions is shown in Figure 3-23. The buoyant jet behaves as a pure jet for $\zeta < 1$ and as a plume for $\zeta > 1$. In dimensional units, the transition is at $Z$=2.19 $l_M$, or at 53.4 ft, which is just before the jet/plume reverses direction. The predicted jet/plume centerline velocity is given in Figure 3-24, while the estimated radius of the jet/plume is shown in Figure 3-25. Note that at the final depth of 57 ft, the jet/plume radius is only about 12 ft giving a cavern to jet/plume area ratio of 69. Therefore, confinement effects are expected to be minimal.

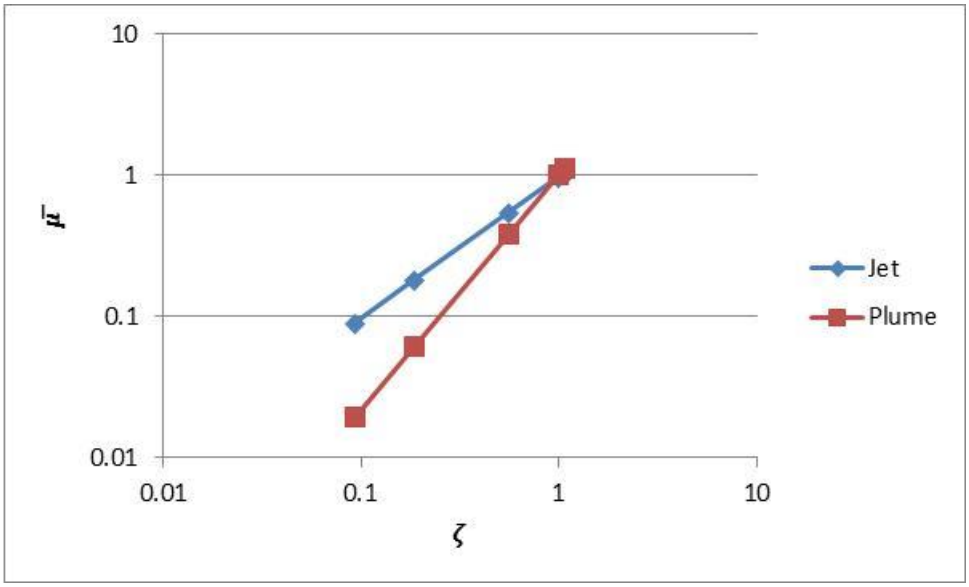


**Figure 3-23. Dimensionless Jet/Plume Characteristics for a Relative Density of 0.01**

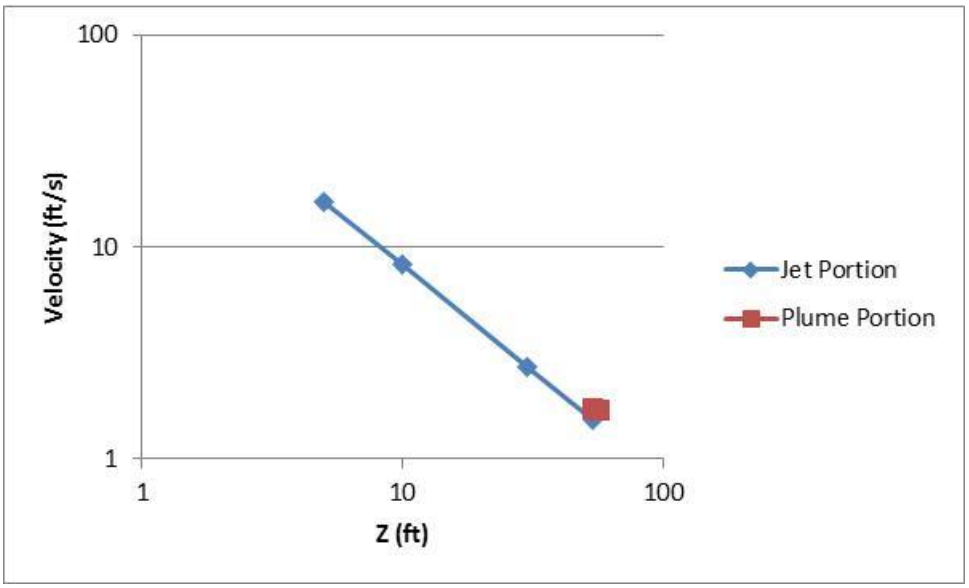


**Figure 3-24. Jet/Plume Centerline Velocity for a Relative Density of 0.01**

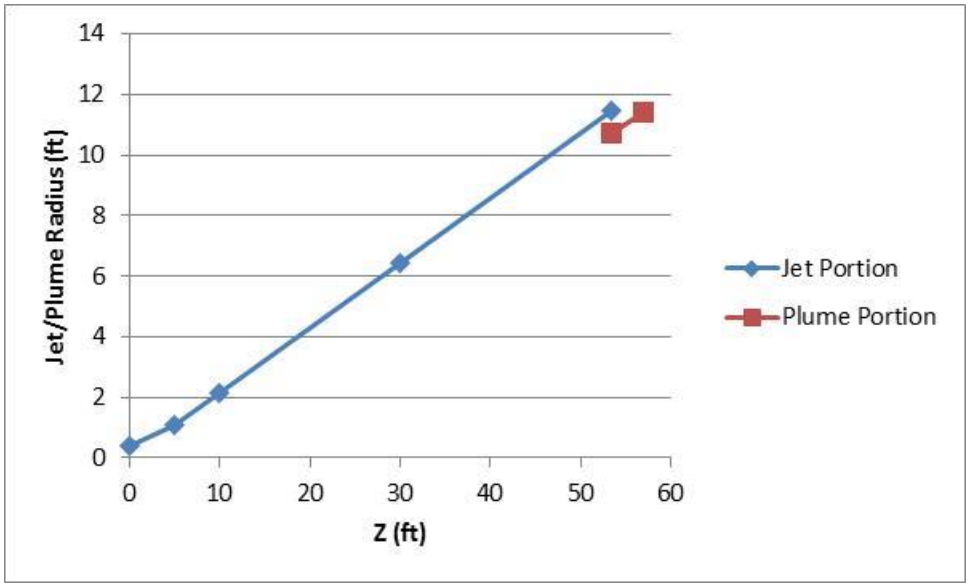


**Figure 3-25. Jet/Plume Radius for a Relative Density of 0.01**

### 0.001 (0.1%) Density Difference

Results for the density difference of 0.001 (0.1%) are shown in Table 3-6 below.

**Table 3-6. Results for 0.001 (0.1%) Lighter Jet**

| ***Parameter*** | ***Value*** |
|---|---|
| $l_Q$ | *0.72 ft* |
| $l_M$ | *77.1 ft* |
| $Ri_1$ | *0.0093* |
| $Ri_2$ | $8.75x10^{-5}$ |
| $Fr_1$ | *101* |
| $Fr_2$ | *10160* |

Again using Turner's revised correlation, the downward-directed buoyant jet will descend to a depth of 180 ft below the jet outlet before reversing directions. In a 2000 ft high cavern with a diameter of 200 ft, the normalized $L/D_{cavern}$ is 0.9.

The dimensionless plot for the present conditions is shown in Figure 3-26. The buoyant jet behaves as a pure jet for $\zeta < 1$ and as a plume for $\zeta > 1$. In dimensional units, the transition is at $Z$=2.19 $l_M$, or at 169 ft, which is just before the jet/plume reverses direction. The predicted jet/plume centerline velocity is given in Figure 3-27, while the estimated radius of the jet/plume is shown in Figure 3-28. Note that at the final depth of 180 ft, the jet/plume radius is about 36 ft for a cavern to jet/plume area ratio of 7.7. Therefore, confinement effects are expected to be small.

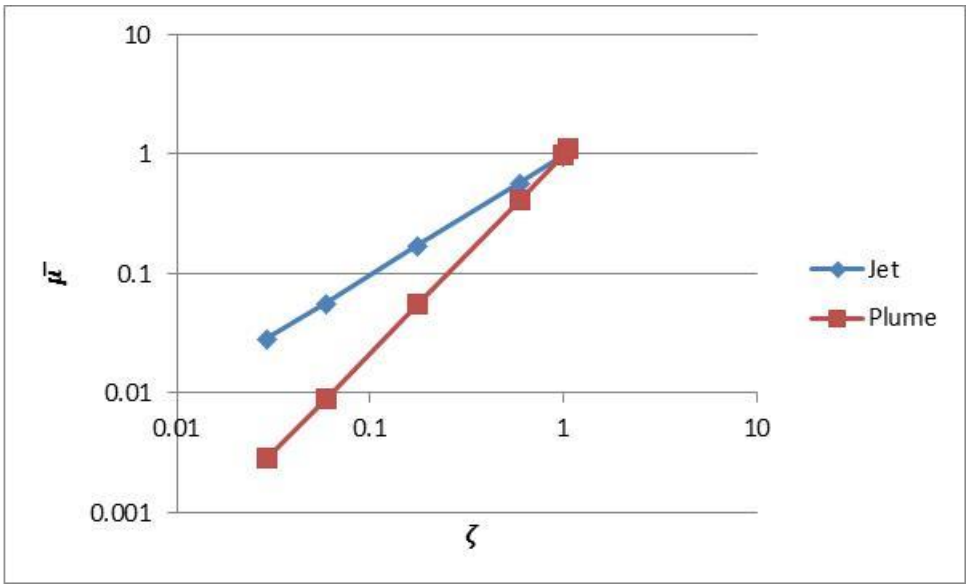


**Figure 3-26. Dimensionless Jet/Plume Characteristics for a Relative Density of 0.001**

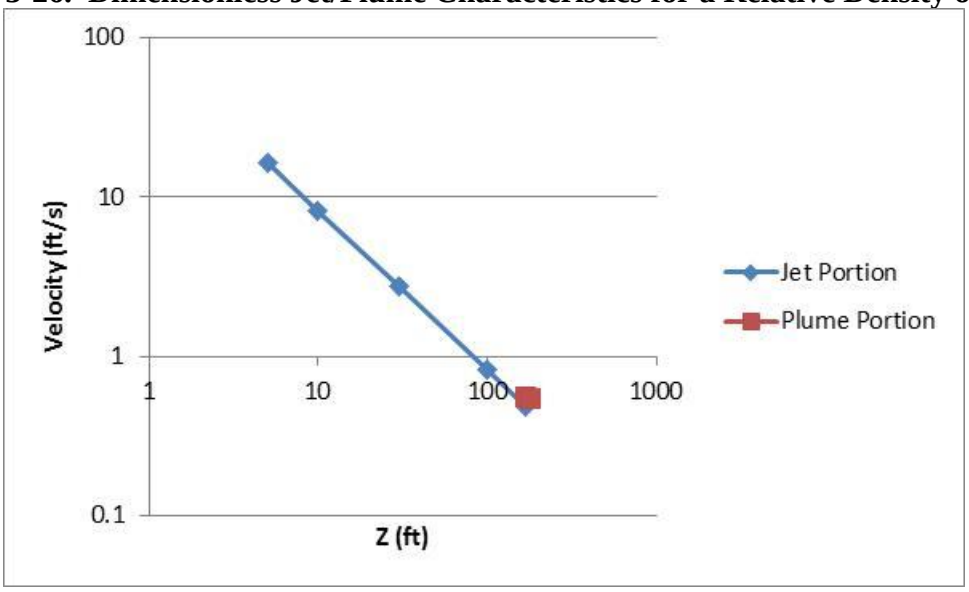


**Figure 3-27. Jet/Plume Centerline Velocity for a Relative Density of 0.001**

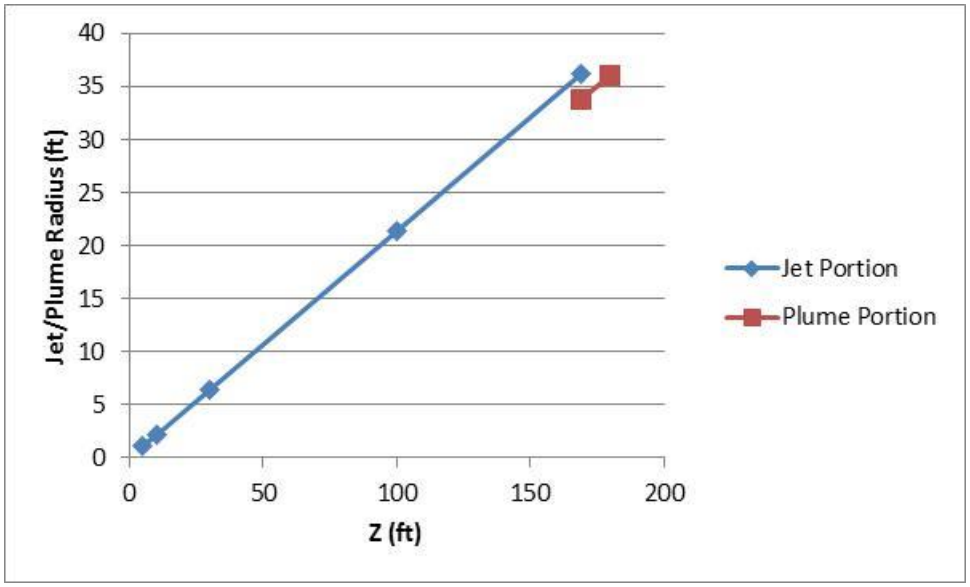


**Figure 3-28. Jet/Plume Radius for a Relative Density of 0.001**

### 0.0001 (0.01%) Density Difference

Results for the density difference of 0.0001 (0.01%) are shown below in Table 3-7.

**Table 3-7. Results for 0.0001 (0.01%) Lighter Jet**

| ***Parameter*** | ***Value*** |
|---|---|
| $l_Q$ | *0.72 ft* |
| $l_M$ | *244. ft* |
| $Ri_1$ | *0.0030* |
| $Ri_2$ | $8.75x10^{-6}$ |
| $Fr_1$ | *319* |
| $Fr_2$ | *101600* |

From Turner's revised correlation, the downward-directed buoyant jet will descend to a depth of 570 ft below the jet outlet before reversing directions. In a 2000 ft high cavern with a diameter of 200 ft, the normalized $L/D_{cavern}$ is 2.85.

The dimensionless plot for the present conditions is shown in Figure 3-29. The buoyant jet behaves as a pure jet for $\zeta < 1$ and as a plume for $\zeta > 1$. In dimensional units, the transition is at $Z$=2.19 $l_M$, or at 535 ft, which is again just before the jet/plume reverses direction. The predicted jet/plume centerline velocity is given in Figure 3-30, while the estimated radius of the jet/plume is shown in Figure 3-31. Note that at the final depth of 570 ft, the jet/plume radius is about 118 ft, or larger than the cavern radius. Therefore, confinement effects are expected to be significant.

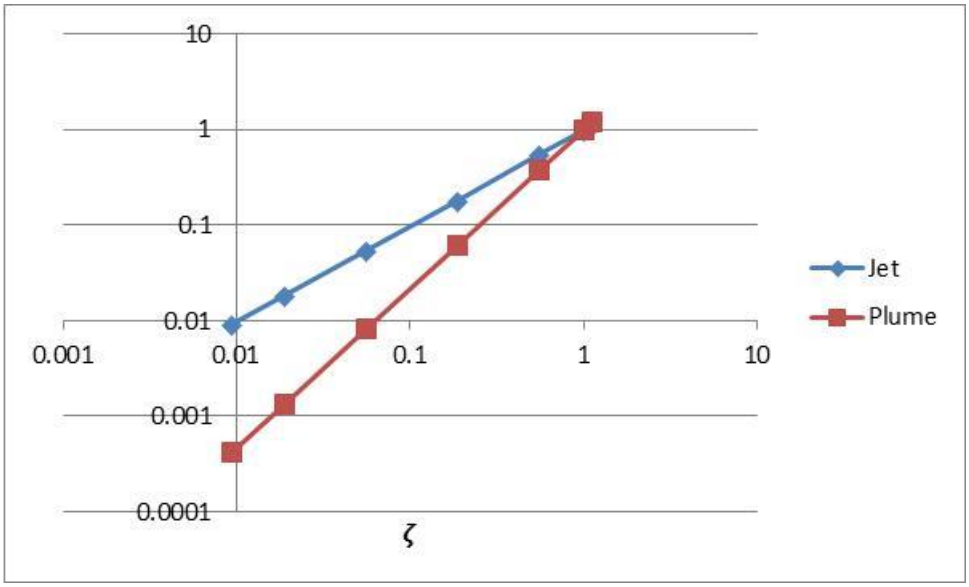


**Figure 3-29. Dimensionless Jet/Plume Characteristics for a Relative Density of 0.0001**

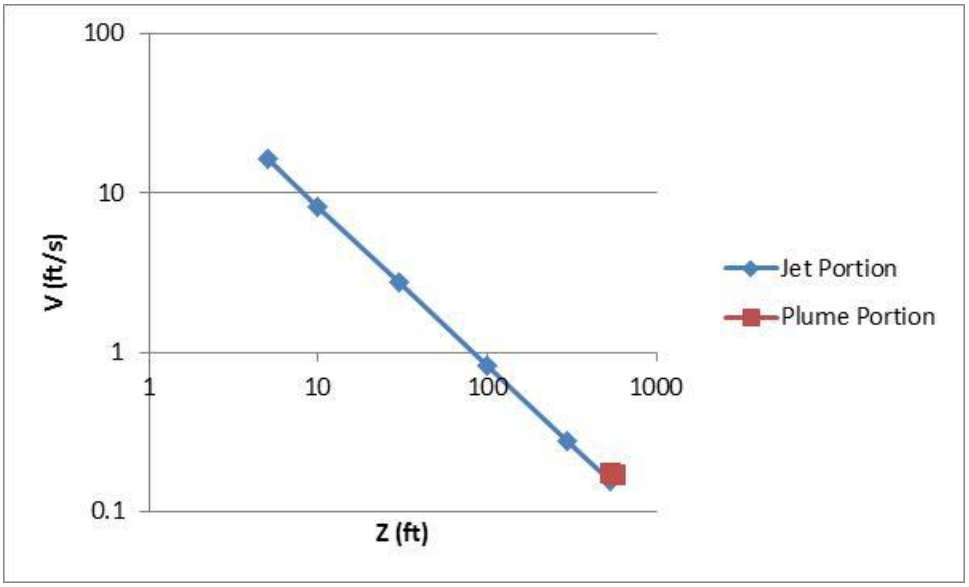


**Figure 3-30. Jet/Plume Centerline Velocity for a Relative Density of 0.0001**

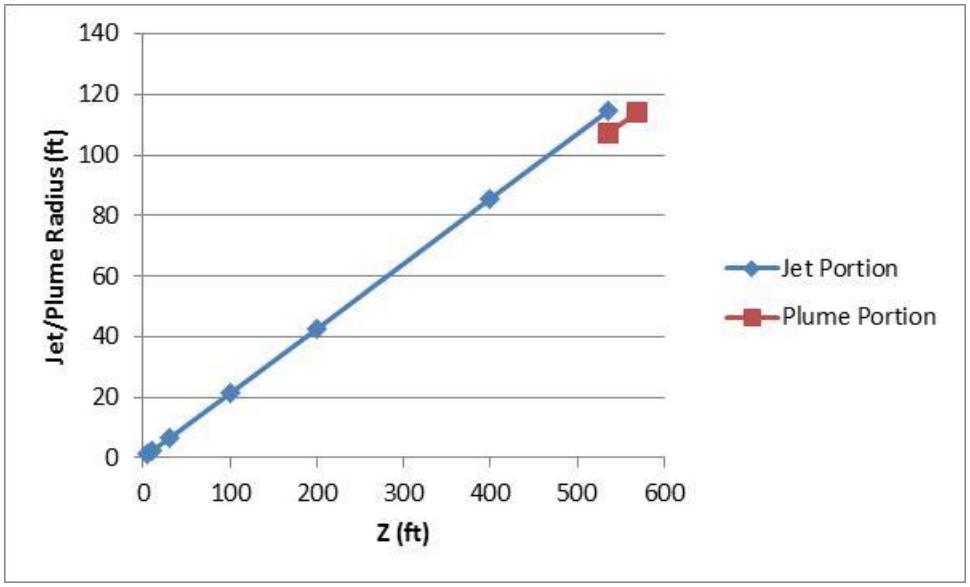


**Figure 3-31. Jet/Plume Half-width for a Relative Density of 0.0001**

### Heavier or Neutral Jet

The behavior of a neutral or heavier jet should be similar to the jet portion of the 0.0001 (0.01%) density difference jet except the jet will not turn around. The effect of confinement is significant at the larger distances.

### Summary

For negatively-buoyant jets in an SPR cavern, density differences of greater than 0.1% are expected to behave like free jets, and confinement is expected to have minimal effect on the jet behavior. For smaller density differences and for neutral and positively-buoyant jets, the effect of confinement is expected to be significant.

### 3.1.2 Entrainment Numerical Approach

Many of the above empirical relationships for jets and plumes implicitly include the entrainment of outside fluid into the jet or plume. While the empirical relationships may be appropriate for the particular conditions, such as uniform ambient or linear stratification, application to more general boundary conditions such as encountered in SPR caverns requires numerical integration and specification of entrainment. The entrainment approach is discussed in the following sections.

#### 3.1.2.1 Entrainment Equations

A fundamental calculation of the entrainment of fluid into a jet or plume is difficult and necessitates a detailed fluid flow and turbulence simulation. A simple assumption that the entrainment inflow is related to some characteristic velocity in the jet or plume was used by Morton et al. (1956) in their classic plume paper and by Turner (1986) for buoyant jets. This assumption has been used successfully since then. Relating the entrainment to the local centerline jet velocity results in the entrainment equation

$$\frac{d\mu}{dz} = 2\pi b_w \alpha_G u_c$$

where $\mu$ is the specific mass flux discussed earlier, $\alpha_G$ is the Gaussian entrainment coefficient, $b_w$ is the jet/plume radius, and $u_c$ is the local centerline jet velocity.

The mass, momentum, and buoyancy conservation equations for Gaussian profiles using the Boussinesq approximation are (Turner, 1986)

$$\frac{d}{dz}(b_w^2 u_c) = 2 b_w \alpha_G u_c$$

$$\frac{d}{dz}\left(\frac{1}{2} b_w^2 \mathrm{u}_c^2 \rho\right) = \lambda^2 \, b_w^2 g(\rho_0 - \rho)/\rho_1$$

$$\frac{d}{dz}\left(\frac{\lambda^2 b_w^2 u_c \, g(\rho_0 - \rho)/\rho_1}{1+\lambda^2}\right) = -b_w^2 u_c \, N^2(z)$$

where $\rho_0$ is the ambient density, $\rho_1$ is a fixed reference density, and $\rho$ is the plume density at distance $z$, and

$$N^2 = -\frac{g}{\rho_1}\left(\frac{d\rho_0}{dz}\right).$$

$$u = u_c \exp\left[-\left(\frac{r}{b_w}\right)^2\right]$$

$$\theta = \theta_c \exp\left[-\left(\frac{r}{b_\theta}\right)^2\right]$$

In this case, $b_\theta$ is equivalent to $b_T$ in earlier discussions.

Note that turbulent contributions are not included in the conservation equations. Dimensionless analysis and experimental data lead to the following relationships for a pure jet as discussed earlier

$$b_w = 0.107\, z$$

$$b_\theta = 0.126\, z$$

$$\lambda = \frac{b_\theta}{b_w} = 1.2$$

The variable $\alpha_G$ is the Gaussian entrainment coefficient relating the entrainment to the vertical velocity in the jet or plume.

Wang and Law (2002) present a second-order integral model that includes turbulent contributions. Turbulent and streamwise pressure gradient contributions to the momentum flux are about 10% for jets and plumes. Some investigations include this turbulent contribution.

Using the above relationships, the mass continuity equation can be easily solved resulting in the following entrainment value for a pure jet in a uniform environment as given by Turner (1986), or

$$\frac{\mathrm{d}b_w}{\mathrm{dz}} = 2\ \alpha_{G,jet}$$

$$\alpha_{G,jet} = 0.0535$$

Similarly, using pure plume relationships given earlier, the Gaussian plume entrainment coefficient in a uniform environment is

$$\frac{\mathrm{d}b_w}{\mathrm{dz}} = \frac{6}{5}\ \alpha_{G,plume}$$

$$\alpha_{G,plume} = 0.0833$$

The assumed velocity and density profiles will affect the value of the entrainment coefficient and the conservation equations. Common assumptions for the profiles include top-hat (uniform) and Gaussian profiles. For a top-hat assumption, the conservation equations are slightly modified as shown by Morton et al. (1956), Fischer et al., (1979) and others. Per Carazzo et al. (2008), the

entrainment coefficients for Gaussian profiles ($\alpha_G$) and top-hat profiles ($\alpha_{TH}$) are related to each other as

$$\alpha_G = \alpha_{TH}/2^{1/2}$$

Corresponding top hat values for a jet and plume in a uniform environment would be

$$\alpha_{TH,jet} = 0.0757$$

$$\alpha_{TH,plume} = 0.118$$

A number of investigators have solved the conservation equations for buoyant jets and plumes to estimate the entrainment coefficient for different conditions as will be discussed subsequently. Sometimes a virtual origin is used where the source term extrapolates to zero (Morton, et al., 1956, Papanicolaou and Kokkalis, 2008).

## Entrainment and Concentration/Velocity Width Ratio Models

### Entrainment

Positively-buoyant jets

The above values of the entrainment coefficient are for pure jets and pure plumes and not specifically for buoyant jets. Buoyant jets transform into plumes at larger distances, so the value of the entrainment coefficient should reflect this transition. Priestley and Ball (1955) proposed that the buoyancy effect on entrainment coefficient is proportional to the square of the local jet Richardson number. Fischer et al. (1979) suggested the relationship

$$\alpha_{buoyant\ jet} = \alpha_{jet} - \left(\alpha_{jet} - \alpha_{plume}\right)\left(Ri_1/Ri_p\right)^2$$

or

$$\alpha_{buoyant\ jet} = \alpha_{jet} - \left(\alpha_{jet} - \alpha_{plume}\right)\left(Fr_p/Fr_1\right)^2$$

where the Richardson number and Froude number are local values. Because $\alpha_{plume}$ is generally greater than $\alpha_{jet}$, the second term is positive and $\alpha_{buoyant\ jet}$ increases with increasing local Richardson number or decreasing local Froude number. As discussed by Fischer et al. (1979), the above equation can run into problems in density stratified flow in that the entrainment can become zero.

An alternative for density stratified flows is (Fischer et al., 1979)

$$\alpha = \alpha_{jet} exp\left[ln\left(\frac{\alpha_{plume}}{\alpha_{jet}}\right)\left(\frac{Ri_1}{Ri_p}\right)^2\right]$$

or

$$\alpha = \alpha_{jet} exp\left[ln\left(\frac{\alpha_{plume}}{\alpha_{jet}}\right)\left(\frac{Fr_p}{Fr_1}\right)^2\right]$$

Figure 3-32 from Fischer et al. (1979) presents the volume flux vs. elevation for stratified conditions for *N* (or *S*) =0.001 where MTT is the constant value of the Gaussian plume entrainment coefficient (0.0833), EXP is the exponential form given above, and PBF is the squared version given above. Note that the results given earlier in Figure 3-19 used the exponential form given above. The EXP and PBF forms perform similarly.

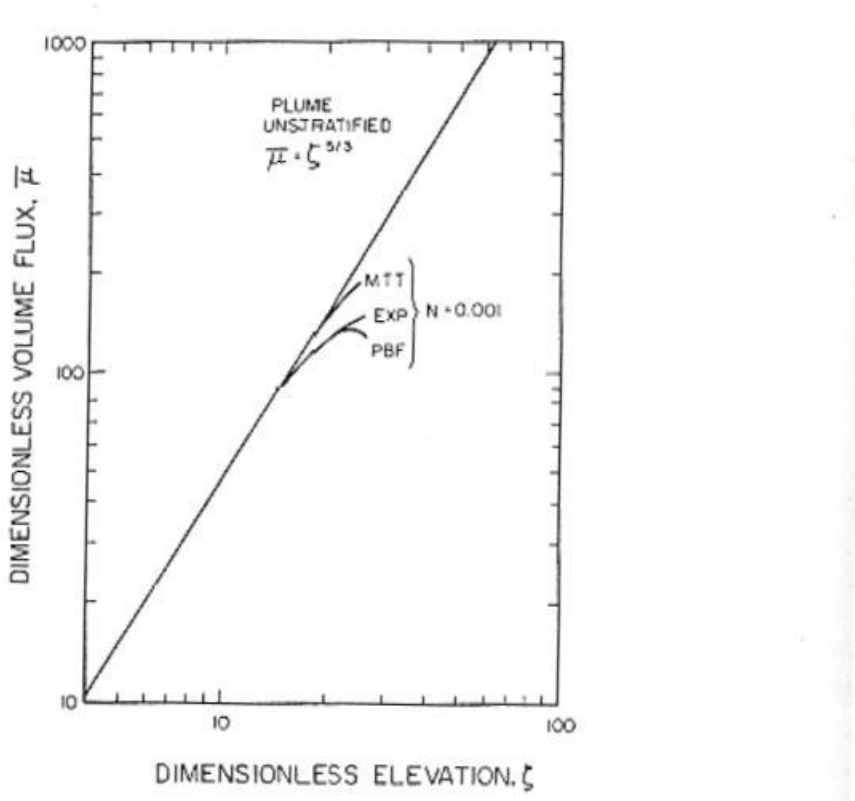


**Figure 3-32. Terminal Height Predictions for Different Entrainment Models (Fischer et al., 1979)**

List and Imberger (1973) derive an entrainment function that is a function of local inverse Froude number that supports the Priestley and Ball (1955) hypothesis. The entrainment function is used to develop the volume flux of a buoyant jet as a function of distance from the origin and the inverse Froude number. No value of the entrainment coefficient, $\alpha$, was developed.

Wang and Law (2002) developed a second-order integral model for buoyant jets injected into a uniform fluid that includes turbulent contributions. They also calculated the entrainment coefficient of a jet / plume as a function of Richardson number from their experiments for neutral and positively-buoyant jets and compared the results to the earlier equations above as shown in Figure 3-33. Note that the List (1982) curve is simply the exponential model given above.

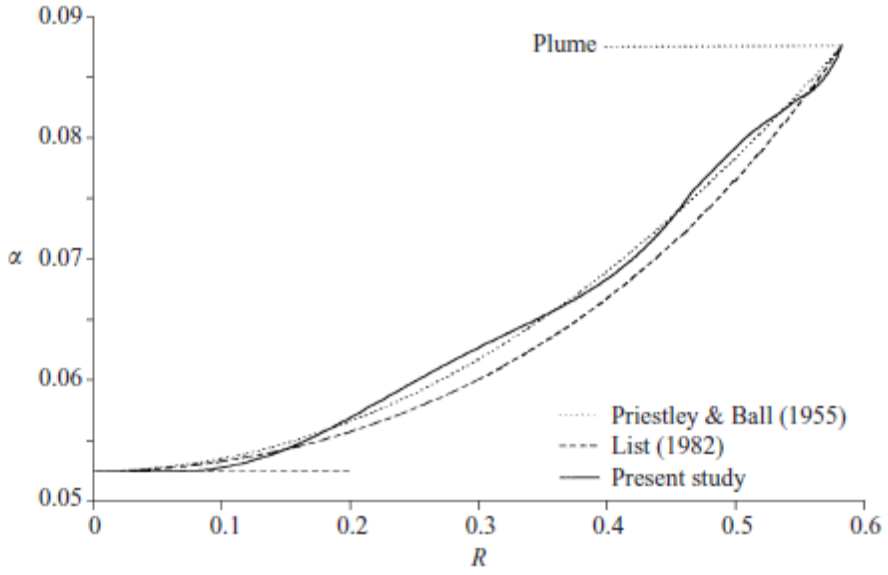


**Figure 3-33. Variation of Gaussian Entrainment Coefficient for Buoyant Jets For Various Models (Wang and Law, 2002)**

Both relationships are in good agreement with the experimental curve. They use the Priestley and Ball (1955) relationship for their second-order model with Gaussian entrainment coefficients of 0.0525 for jets, 0.0875 for plumes, and an $Ri_p$ value of 0.584.

**Negatively-buoyant jets**

Jirka (2004) presents an entrainment model for positively- and negatively-buoyant jets in a homogeneous environment that merges the pure jet and pure plume entrainment coefficients with a blending function that agrees reasonably well with Wang and Law (2002) results as shown below in Figure 3-34. Note that the entrainment function is mirrored around the simple jet value so the entrainment is much lower for negatively-buoyant jets than for positively-buoyant jets. A simple linear function is used in the transition region.

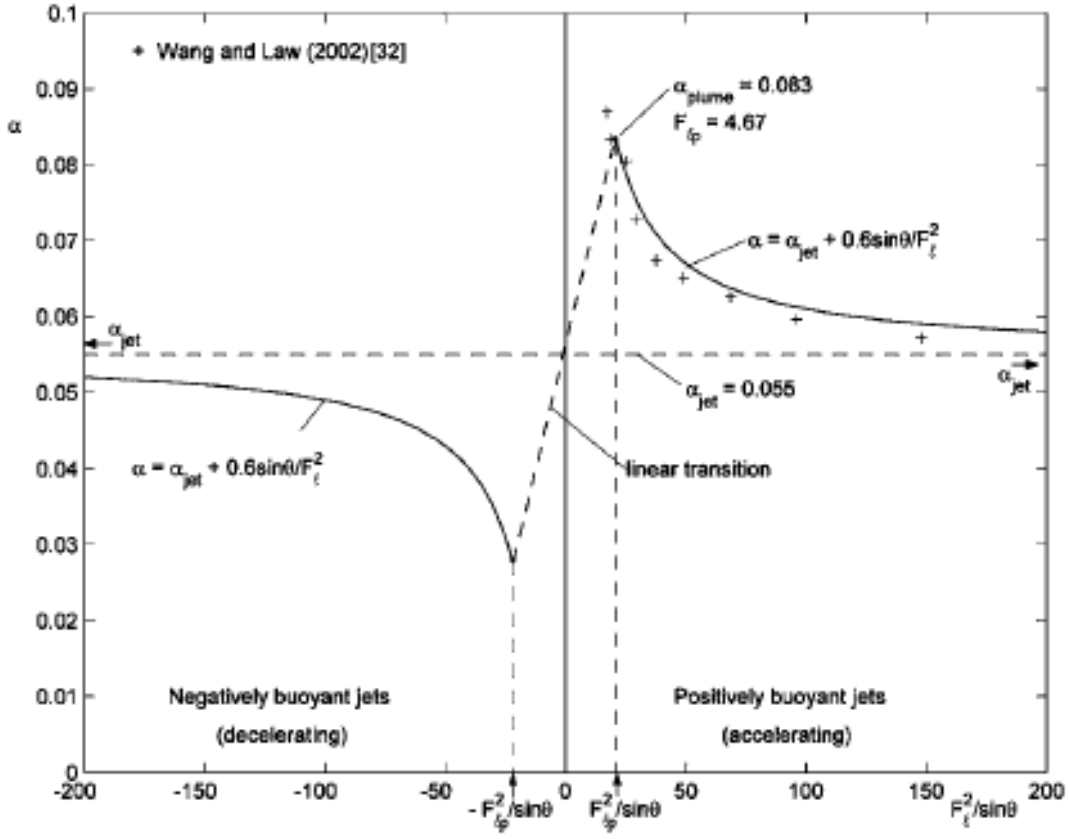


**Figure 3-34. Simple Gaussian Entrainment Function For Homogeneous Ambient (Jirka, 2004)**

Jirka (2004) also used this entrainment function for stratified environment conditions.

Recent work on entrainment models for negatively-bouyant jets has been performed by Kaminski et al. (2005). They investigated the situation of a collapsing fountain similar to a volcanic eruption where an initially negatively buoyant jet is driven upwards. As the initial momentum of the buoyant jet is dissipated, the jet falls downward to earth. This condition is also sometimes called a collapsing fountain. A top-hat entrainment coefficient of 0.057 (Gaussian value of 0.040), which is much smaller than from other investigations, was found, but

which agrees with the entrainment function proposed by Jirka (2004) as shown above. The difference between their value and others in the literature motivated them to revisit the entrainment coefficient for buoyant jets.

Note that Pantzlaff and Lueptow (1999) derive a top hat entrainment coefficient of 0.055 (Gaussian value of 0.039) for a negatively-buoyant jet. The difference between that value and typical values for positively-buoyant jets has been attributed to their small experimental apparatus, but it may just be due to a negatively-buoyant jet as the value is similar to those of Kaminski et al. (2005) and the Jirka (2004) function discussed above.

Kaminski et al. (2005) revisited the Priestly and Ball (1955) analysis using a slightly different approach similar to Morton et al. (1956). The resulting entrainment coefficient is given by

$$\alpha_{Top-Hat} = Ri_2' \left(1 - \frac{1}{A}\right) + \frac{1}{2} R \frac{d \ln A}{dz} + \frac{1}{2} C$$

where

$$Ri_2' = \frac{g' R}{u^2}$$

and R is the top-hat radial length scale, and A and C are derived values.

Values of A and C have been inferred from experimental data. The values of A range between 1.10 and 1.80, which increase with z. Values of C range between 0.10 and 0.14 with a derived constant value of 0.135 (Carazzo et al., 2010). Note that for a pure momentum jet, the Richardson number is zero, and $\alpha_{Top\text{-}Hat,jet}$ is equal to C/2, or 0.0675, or a Gaussian value of 0.048.

The variation of C as a function of distance is given by Carazzo et al. (2006)

*Z/D* > 10

$$A_j = 2.45 - 1.05 \exp(-0.00465 \frac{z}{D})$$

$$A_p = 1.42 - 4.42 \exp(-0.2188 \frac{z}{D})$$

Expressions for *Z/D* < 10 are discussed in Carazzo et al. (2008a).

The resulting top-hat entrainment coefficients as a function of distance from the exit normalized by $l_M$, the plume length scale, are shown below in Figure 3-35 for jets and plumes including measurements. The lower solid line is for jets, while the upper solid line is for plumes. The dashed lines should be ignored.

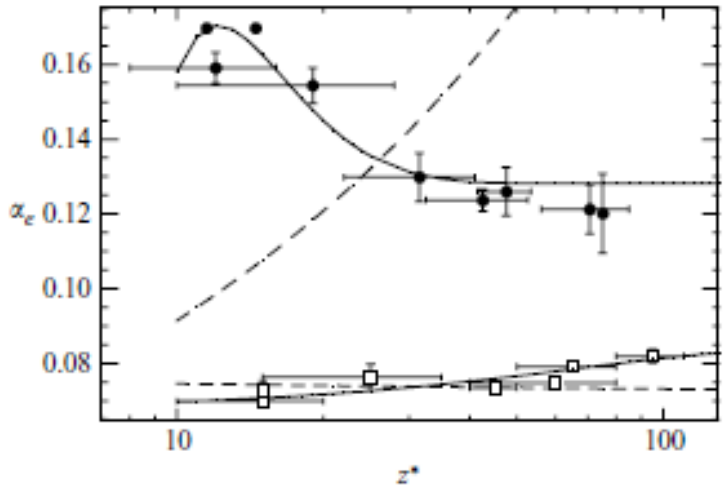


**Figure 3-35. Variation of the Top-Hat Entrainment Coefficient for Jets and Plumes (Carazzo et al., 2006)**

Note that a top-hat entrainment coefficient of 0.08 and 0.16 as shown above is equivalent to Gaussian entrainment coefficients of 0.057 and 0.0.113, respectively.

For a forced plume or a buoyant jet, the variation of *A* as a function of distance is given by Carazzo et al., (2008b),

$$A = A_j + \frac{(A_p - A_j)}{4}\left(\frac{Z}{l_m} - 1\right)$$

where $l_M$ is the plume length scale discussed earlier

$$l_M = \frac{M^{3/4}}{B^{1/2}} = \pi^{1/4} Ri_{1,r}^{-1/2} r_0$$

and the Richardson number definition does not have the ($\pi/4$) factor and is in terms of radius. In the region 1 <= $Z/l_M$ <= 5 where $Z/ l_M$ <1 is considered as a pure jet while z/ $l_M$ > 5 is considered to be a pure plume. This model was further developed by Carazzo et al. (2010) for the case of negatively-buoyant jets.

**Concentration/Velocity Width Ratio**

The concentration to velocity plume width ratio ($\lambda=b_T/b_w$) is also variable. Wang and Lee used the following equation for the variation of $\lambda$ in a buoyant jet

$$\lambda_{buoyant\ jet} = \lambda_{jet} - \left(\lambda_{jet} - \lambda_{plume}\right)\left(Ri/Ri_p\right)^{1.5}$$

where the local Richardson number is defined as

$$Ri = \frac{\mu\, B^{1/2}}{m^{5/4}}$$

which was given earlier for a neutral plume. The value varies from 0 for a neutral jet to a constant value for plumes. The parameters used by Wang and Lee (2002) are from their experiments and are $\lambda_{jet}$=1.23, $\lambda_{plume}$=1.04, and $R_p$=0.584, which are similar to the Papanicolaou and List (1988) values. The comparison of their experimental data to the above relationship is given in Figure 3-36.

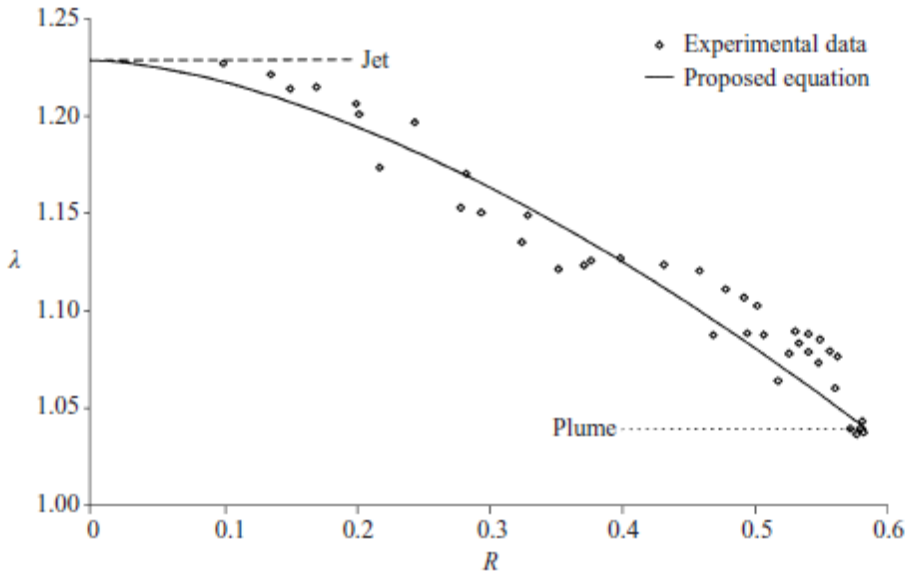


**Figure 3-36. Concentration to Velocity Ratio, $\lambda$, as a function of Local Richardson Number, (Wang and Law, 2002)**

### 3.1.2.2 Numerical Results

A number of investigations have integrated the entrainment equations, or their equivalent, and compared the results to data. Some of the results are summarized in the following sections.

#### 3.1.2.2.1 Uniform Environment

Positively- and negatively-buoyant jets in a uniform ambient fluid will be discussed separately because their behavior is different.

**Positively buoyant**

Jirka (2004) presents results of vertical positively-buoyant jet simulations using typical values for the entrainment coefficients and the variation with local Froude number as presented earlier. His results for the jet-plume behavior dilution are compared to experimental data in Figure 3-37. This figure is similar to that shown before as Figure 3-5 but with slightly different axes. Note the good agreement for the pure jet, pure plume, and the transition region. The behavior of positively-buoyant jets seems to be reasonably well predicted.

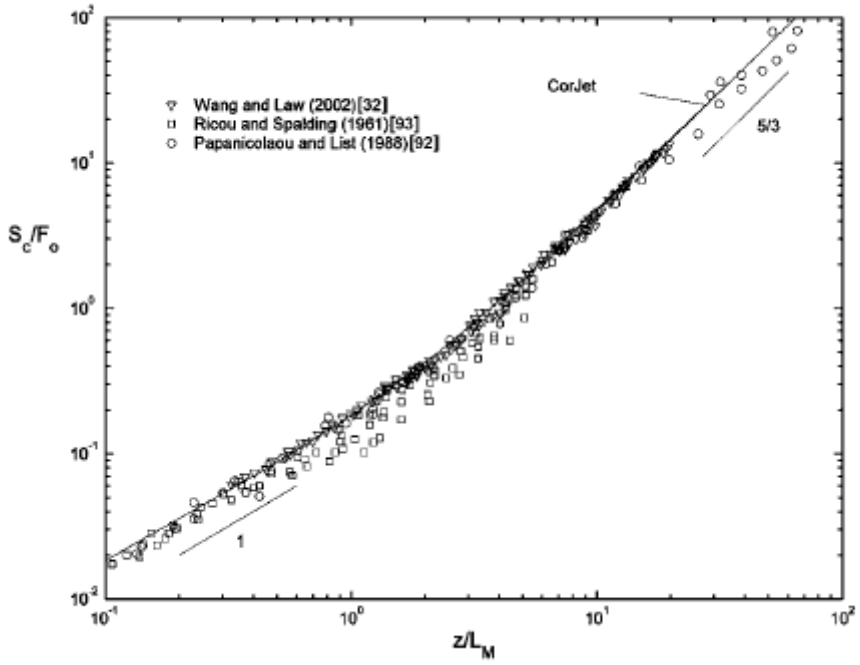


**Figure 3-37. Predicted Centerline Dilution for Positively-Buoyant Vertical Jet (Jirka, 2004)**

**Negatively-buoyant**

For negatively-buoyant jets, or fountains, the situation is less clear. The conservation equations presented earlier are only directly applicable for the negatively-buoyant jet until it changes direction. Predictions can be made for the maximum penetration depth, but when the buoyant jet changes directions and falls back upon itself, the simple model is not appropriate due to the incorrect specification of the entrained fluid.

Various investigators have integrated the conservations equations and assumed that the maximum depth is the maximum penetration depth of the buoyant jet or is the spreading depth. For the maximum penetration depth, Jirka (2004) compares his predictions with data for the maximum penetration depth in a uniform environment as shown in Figure 3-38, which show very good agreement. Note that the value of the entrainment constant is smaller for a negatively-buoyant jet than for a positively-buoyant jet as prescribed by his entrainment function discussed earlier.

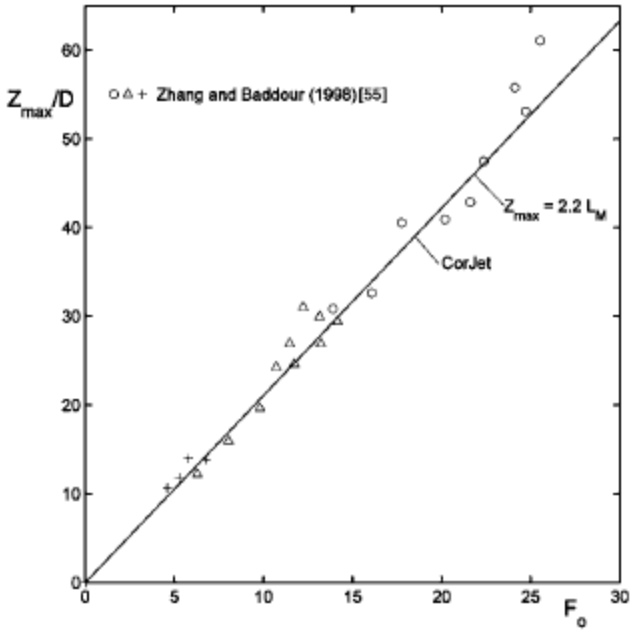


**Figure 3-38. Maximum Buoyant Jet Penetration Depth Data-Model Comparison (Jirka, 2004)**

Kokkalis and Papanicolaou (2006) and Papanicolaou and Kokkalis (2008) performed experiments on a lighter jet injected downward into a heavier resident fluid as discussed earlier. Two methods of introducing buoyancy were used – salt concentration and temperature.

The salt-induced buoyancy data are shown in Figure 3-39 (shown earlier as Figure 3-14) where the solid circles and open circles are the maximum and mean penetration depths, respectively. The data are generally consistent with previous investigations in that the dimensionless mean and maximum penetration distances at low Richardson numbers are approximately 2 and 3, respectively. The squares no virtual origin) and crosses (with virtual origin) are model predictions using the entrainment equations and are generally below the experimental data. The predicted values of the mean penetration depth at low Richardson numbers less than 0.1 is less than 2 for typical values of entrainment and width parameters.

Data-model comparisons for the hot-water buoyancy data are also shown in Figure 3-39. The maximum penetration depth could not be ascertained from these experiments as discussed earlier. The predicted mean penetration depth is slightly higher than the experimental data.

For low initial Richardson numbers, $Ri_{1,0}$, less than 1, the results are listed below in Table 3-8 along with the entrainment constants.

**Table 3-8. Numerical Results of Penetration Depth (Papanicolaou and Kokkalis, 2008)**

| Type | Profile | $\alpha_j/\alpha_p$ | $\lambda_j/\lambda_p$ | $Z/l_M\ (z_0=0)$ | $Z/l_M\ (z_0=3.28D)$ |
|---|---|---|---|---|---|
| Saltwater jet | Gaussian | 0.0545/0.0875 | 1.20/1.067 | 1.74 | 1.78 |
| Saltwater jet | Top-hat | 0.076/0.120 | 1 | 1.84 | 1.87 |
| Heated jet | Gaussian | 0.545/0.0875 | 1.20/1.067 | 2.26 | 2.33 |

The numerical simulations do not consider the reverse flow that occurs in a negatively-buoyant jet. Instead, the penetration depth is calculated and is compared to mean and maximum penetration depth data using different values of the entrainment coefficient.

In order to reproduce the mean penetration depth for the salt-water cases, the Gaussian jet entrainment coefficient has to be reduced 0.04 (Kokkalis and Papanicolaou, 2006). To reproduce the maximum penetration depth, the Gaussian jet entrainment coefficient had to be reduced further to a value of 0.025 (Papanicolaou and Kokkalis, 2008).

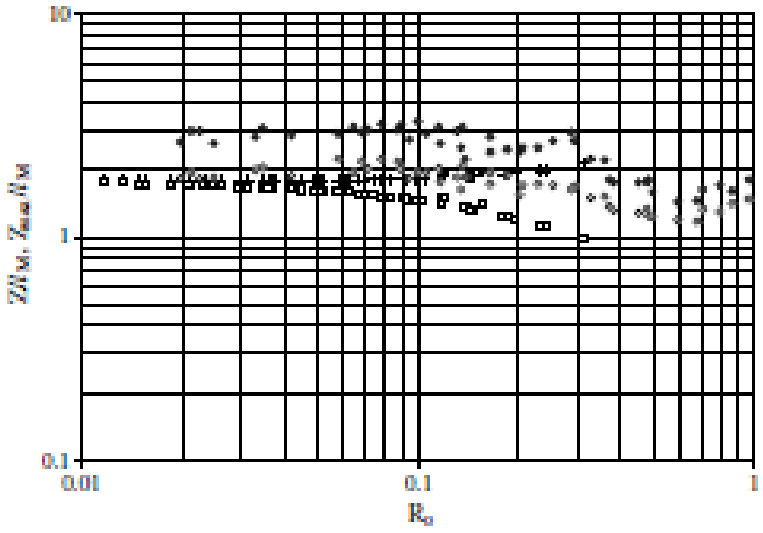


(a) Salt Cases

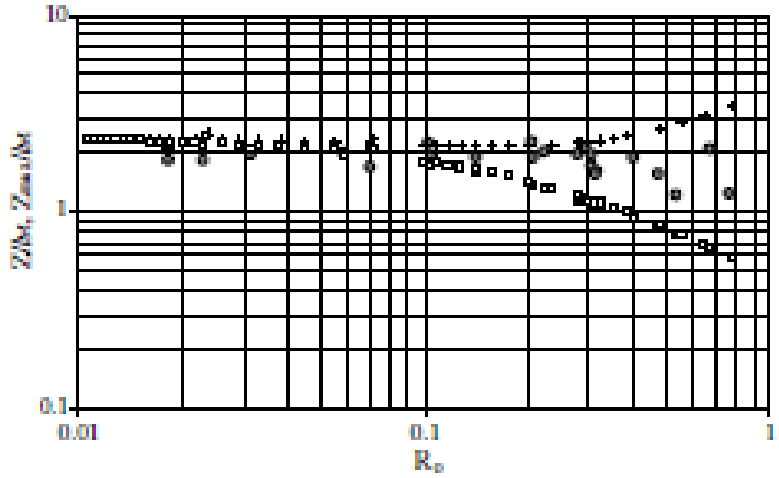


(b) Hot Water Cases

**Figure 3-39. Penetration Depths vs Richardson Number for Round Buoyant Jets (Papanicolaou and Kokkalis, 2008)**

Papanicolaou, Papakonstantis, and Christodoulou (2008) investigated the entrainment coefficient for negatively buoyant jets in uniform and stratified environments including angled jets. They used Gaussian and top hat entrainment formulations where the entrainment coefficient is varied according to the Priestley and Ball relationship given earlier and included the turbulent contributions to the earlier entrainment equations based on the work of Wang and Law (2002). The model calculates the maximum penetration depth and then assumes no further mixing as the jet goes to the spreading elevation. Only vertical jet results in a uniform environment are discussed in this section. They predict the spreading depth of the plume as opposed to the maximum plume height. In Figure 3-40, the maximum depth of the buoyant jet is given by the solids squares; model predictions are not presented for the maximum penetration depth. The open squares designate the spreading depth, which is the depth to be predicted by the model.

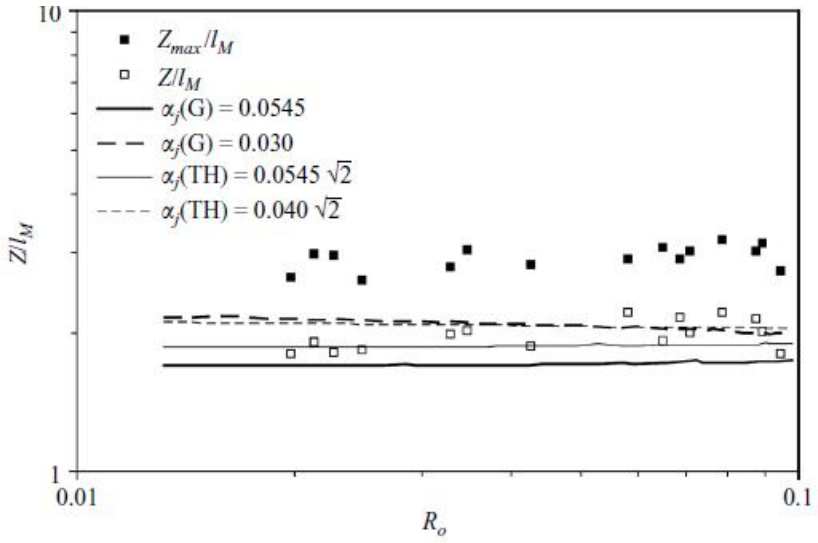


**Figure 3-40. Data-Model Comparisons for Gaussian and Top-Hat Models and Papanicolaou and Kokkalis (2008) data for a Uniform Environment (Papanicolaou, Papakonstantis, and Christodoulou, 2008)**

A top-hat value of the entrainment coefficient of 0.40 $2^{1/2}$ (=0.0566) (Gaussian=0.40), which has been proposed by Kaminsky et al. (2005) for collapsing fountains as discussed earlier, fits the spreading data reasonably well for these negatively buoyant jets. This entrainment coefficient is significantly less than the typical value for positively buoyant jets of 0.0545 $2^{1/2}$ (=0.0771) (Gaussian=0.0545); results for this value underpredict the spreading depth data.

As mentioned previously, the above conservation equations and entrainment values implicitly assume a positively-buoyant jet and are not applicable to the reverse-flow portion of a negatively-buoyant jet such as a fountain when the flow reverses. Carazzo et al. (2010) have developed a "confined" top-hat set of conservation equations that are applicable to negatively-buoyant jets in a uniform environment. The upward and downward flow regions are calculated. The set of equations is much more complicated than given above due to the fluid counterflow and will not be presented here. Comparison between the measured buoyant jet velocities as a function of radius for a number of cases and the fitting function used in the model is shown in Figure 3-41. Comparison of the predicted and measured steady-state heights is shown in Figure 3-42.

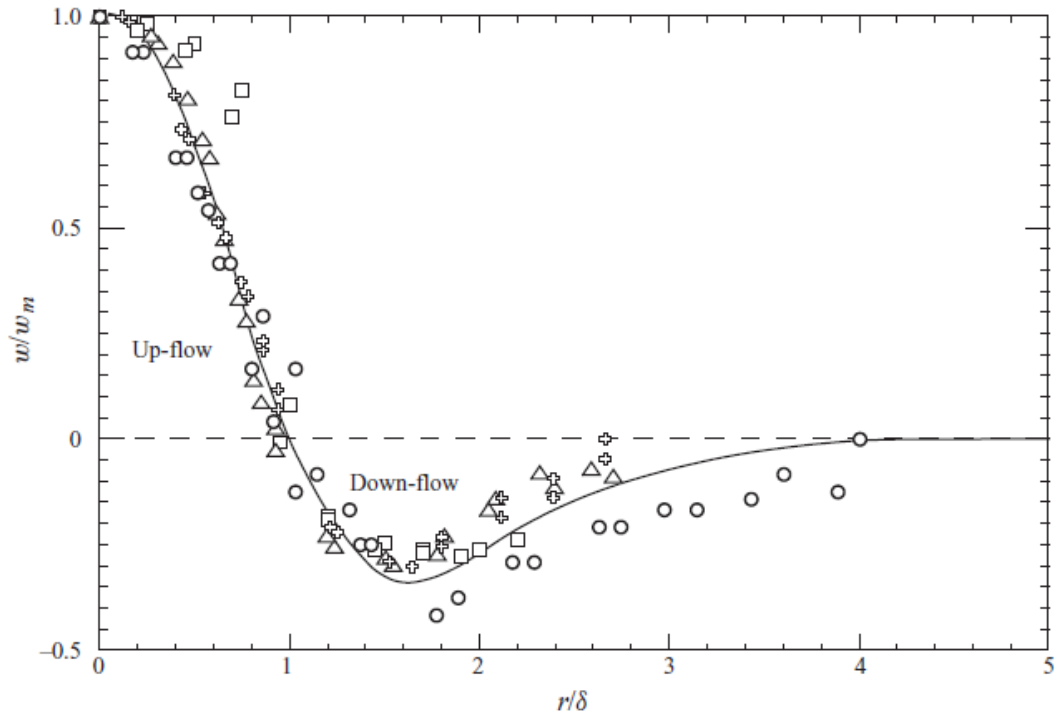


**Figure 3-41. Mean Vertical Velocity Data and Model Comparison for Fountain Model (Carazzo et al., 2010)**

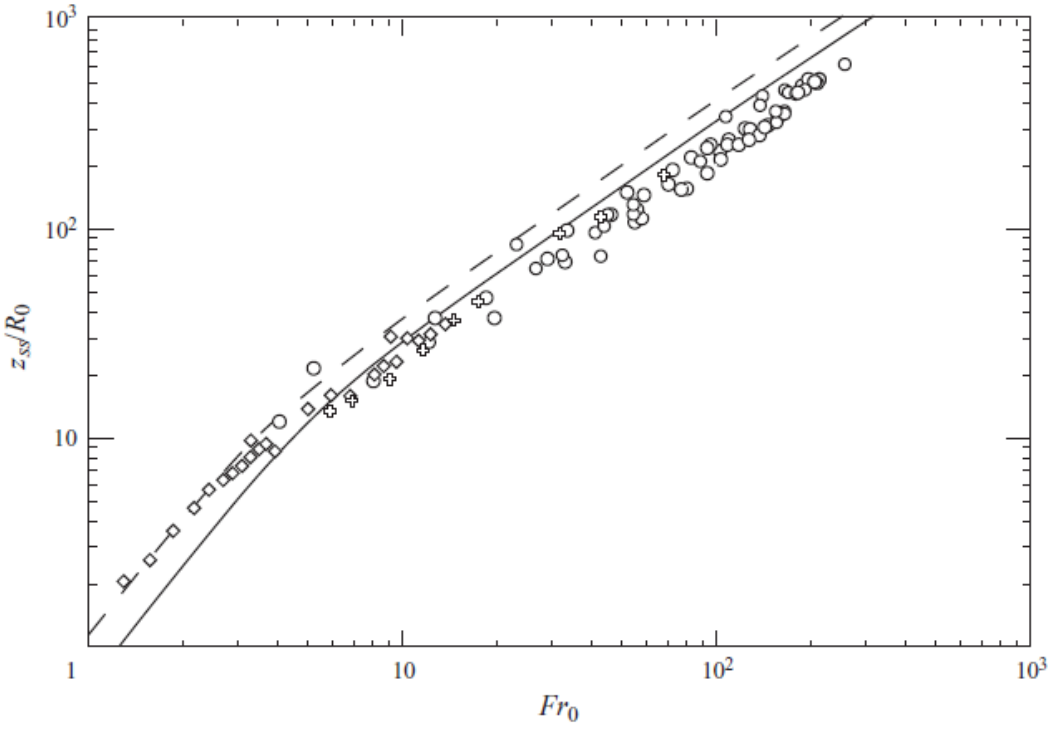


**Figure 3-42. Data-Model Comparison for the Steady-State Heights for Fountain Model (solid line) (Carazzo et al., 2010)**

### 3.1.2.2.2 Linearly-stratified Environment

As discussed earlier, Konstantinidou and Papanicolaou (2003) obtained data where $N^{1/2}$ in their paper is equal to $N$ above. They proposed values of the entrainment coefficient and the width ratio as a function of $MN/B$ as given below in Table 3-9. Note that no data-model comparison is presented but that the values of the entrainment coefficients are similar to those given by others.

They used the earlier conservations equations to predict the maximum penetration depth of the negatively-buoyant jet, and then they assumed that there was no more entrainment and the jet rose to the location consistent with its buoyancy at the maximum penetration depth.

**Table 3-9. Numerical Values of Gaussian Entrainment Coefficient, $\alpha$, and Concentration to Velocity Width Ratio, $\lambda$ (Konstantinidou and Papanicolaou, 2003)**

| Flow regime | $\alpha$ | $\lambda$ |
|---|---|---|
| $(M/B)N^{1/2} < 0.10$ | 0.0875 | 1.067 |
| $(M/B)N^{1/2} > 2$ | 0.025 | 1.194 |
| $0.10 < (M/B)N^{1/2} < 2$ | $\alpha_p \exp\left[\ln\left(\frac{0.025}{\alpha_p}\right)\left(\frac{(M/B)N^{1/2}}{2}\right)^2\right]$ | $\lambda_p \exp\left[\ln\left(\frac{\lambda_p}{\lambda_j}\right)\left(\frac{(M/B)N^{1/2}}{2}\right)^2\right]$ |

For the plume region ($MN/B < 0.1$), the typical plume values for the entrainment and the width ratio seem to be appropriate. However, in the jet region ($MN/B > 2$), the Gaussian entrainment value needs to be reduced from a typical value of 0.0545 to 0.025.

Papanicolaou, Papakonstantis, and Christodoulou (2008) investigated the entrainment coefficient for negatively buoyant jets in uniform and stratified environments including angled jets. Details were given earlier. Only the vertical jet results for a stratified environment are discussed in this section.

The results for the maximum height ($Z_m$) and the spreading height ($Z_s$) for a negatively buoyant jet in a stratified environment are shown in Figure 3-43 where the jet length scale, $L_j$, is

$$L_j = \frac{M^{1/4}}{N^{1/2}}$$

The results are a function of $(M/B)N$ as seen before.

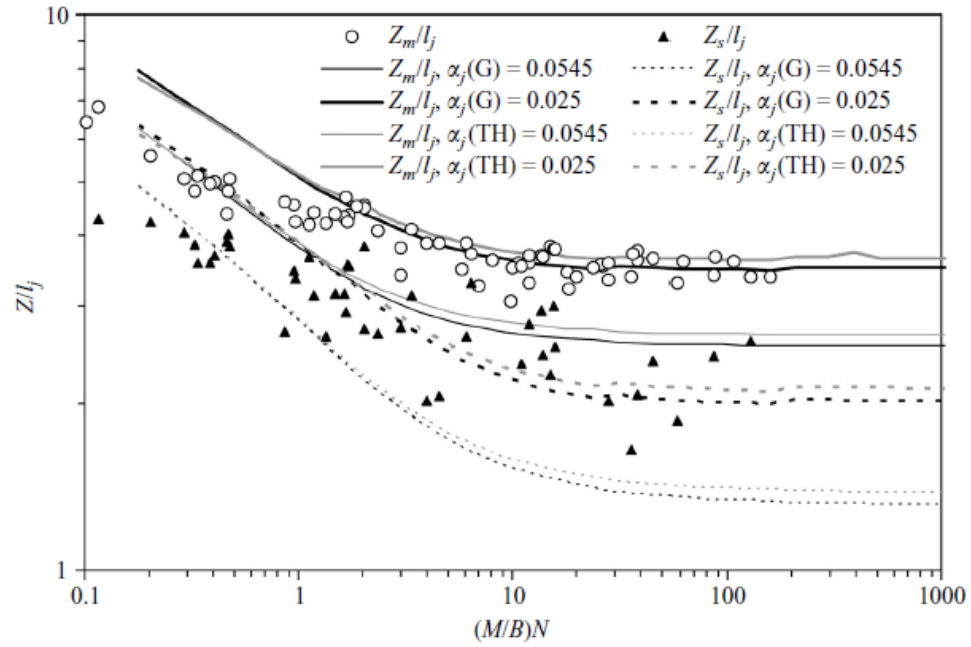


**Figure 3-43. Data-Model Comparisons for Gaussian and Top-Hat Models and Konstantinidou and Papanicolaou (2003) data for a Stratified Environment (Papanicolaou, Papakonstantis, and Christodoulou, 2008)**

Note that for $MN/B << 1$ the flow is a plume, while for $MN/B >> 1$, the flow is a jet.

The results from the Gaussian and Top-Hat models with the same entrainment value are very similar. The value of the jet entrainment coefficient, $\alpha_j$, decreases from 0.0545 to 0.025 (Gaussian values) as the data go from the plume region ($MN/B << 1$) to the jet region ($MN/B >> 1$). The model is able to predict both the terminal rise penetration depth as well as the spreading depth.

### 3.1.2.3 Application to SPR

The above entrainment numerical approaches probably have limited application to SPR because they are only directly applicable to unconfined jets. However, these approaches could conceivably be used to simulate SPR-specific confined flow data to obtain SPR-specific values of the entrainment coefficients.

### 3.1.3 Entrainment Across Density Interfaces

#### 3.1.3.1 Experimental Data

Turner (1968) was the first to investigate mixing across a density interface. He used grid-generated turbulence in a layered system and measured the mixing across a density interface for cases where the density difference was due to salinity or heat. Typical qualitative results when both layers are stirred are shown in Figure 3-44. The mixing rate across the interface is approximately proportional to $Ri^{-3/2}$ for salt and $Ri^{-1}$ for heat where Ri is a Richardson number,

$$Ri = g\frac{\Delta\rho}{\rho}\frac{1}{l\,n^2}$$

where $l$ and $n$ are a fixed but unknown length scale and the frequency of oscillation of the stirring grid, respectively. No quantitative relationships were developed from these data.

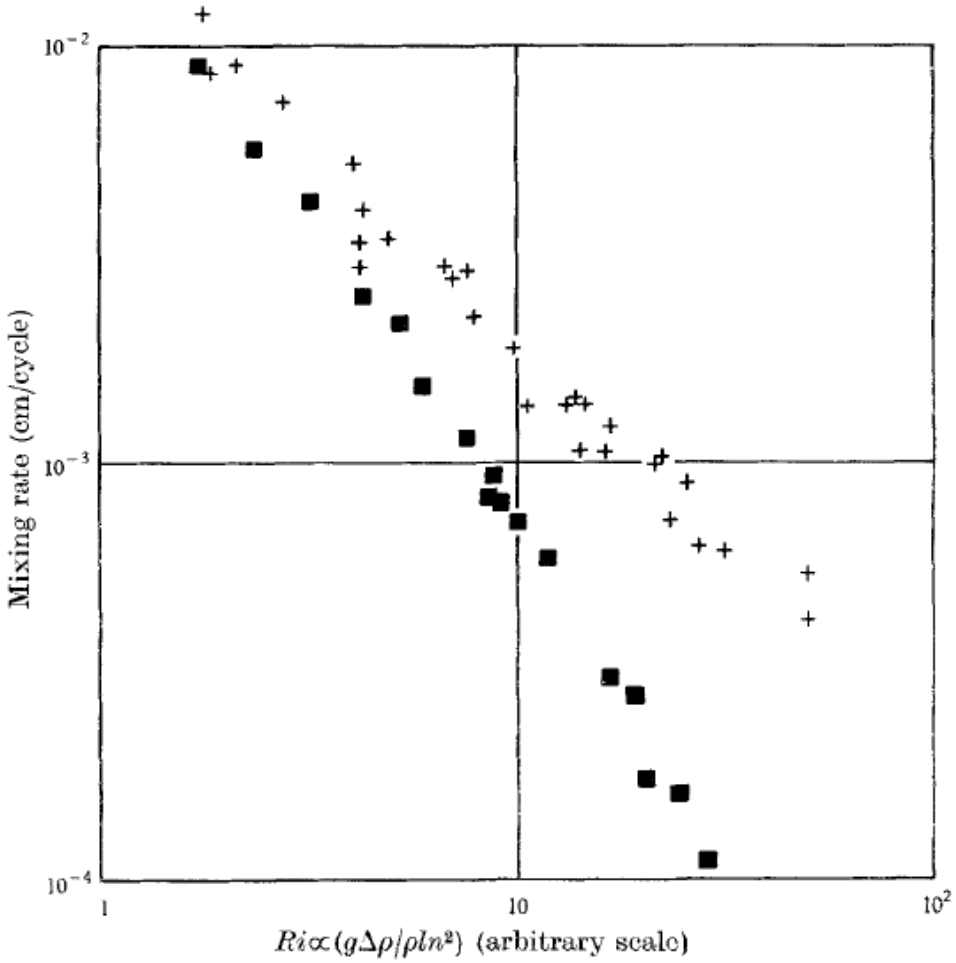


**Figure 3-44. Mixing or Entrainment Rate Across Interface vs. Richardson Number for heat (+) and salt (■)(Turner, 1968)**

Baines (1975) took the experiments one step further by using a positively-buoyant jet that impacts a density interface as shown in Figure 3-45.

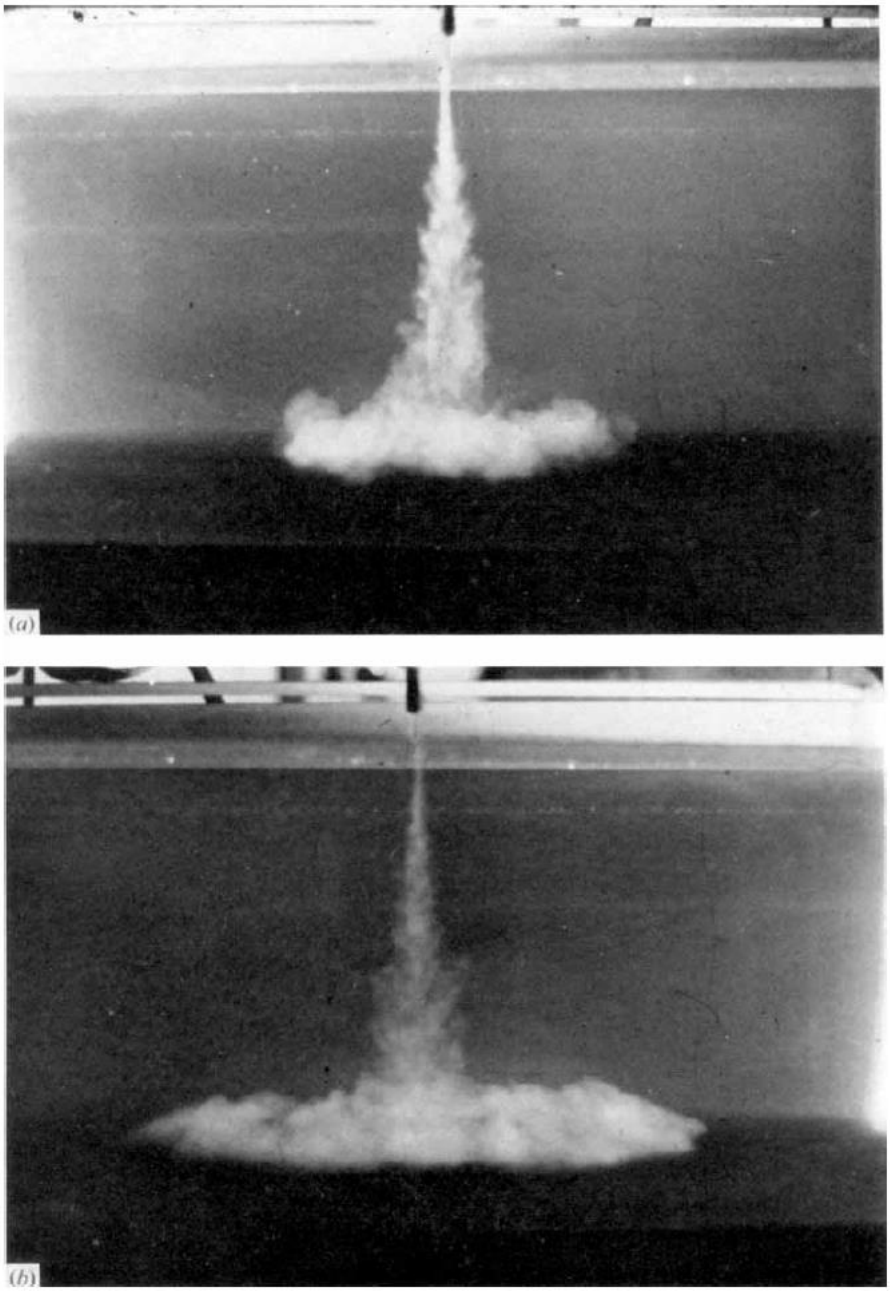


**Figure 3-45. Time Lapse of Plume Striking an Interface (a) 0 secs; (b) 2 secs (Baines, 1975)**

The observed entrainment volume flux and buoyancy flux are defined by dimensionless parameters at the interface

Froude number

$$Fr_1 = \frac{u_I}{(g_I' b_I)^{1/2}}$$

Entrainment volume flux

$$\frac{Q^*}{u_I b_I^2}$$

Entrainment buoyancy flux

$$\frac{B^*}{B_0}$$

where the subscript *I* indicates the values at or across the interface, and *Q** is the volume flux entrained, and

$$B^* = g_I' Q^*$$

and $B_0$ is the plume buoyancy at the jet/plume exit.

Interface conditions are calculated using standard Gaussian plume entrainment equations and a Gaussian plume entrainment coefficient, $\alpha_G$, of 0.093 from experimental data. Note that the value derived from the experimental data has a range of 0.084 to 0.100. Baines (1975) also developed equations for the density distribution in the enclosure based on the work of Baines and Turner (1969), which is discussed in a subsequent section. Note that the model of Baines and Turner (1969) assumes that the inlet plume is a source of buoyancy only with zero mass and momentum.

Results for the entrainment volume flux (note *F* in figure is *B* above, $\Delta$ is *g'*, and *w* is *u* above) are shown in Figure 3-46 - the entrainment flux is proportional to $Fr_1^3$, or $Ri_1^{-3/2}$. Baines (1975) also developed relationships for the velocity parameters for Turner's (1968) data, which is shown also shown. Baines (1975) notes that the good agreement with Turner's (1968) data is fortuitous but that the two results show the same general characteristics. An important difference is that the data of Turner (1968) show a maximum value of the entrainment volume flux while the experiments of Baines (1975) do not show this behavior. As given by Baines et al. (1993), the straight line equation is

$$\frac{Q_e}{w_I b_I^2} = 0.047\, Fr$$

The maximum value of the Froude number is when the impinging jet density is the same as the lower layer. In this case,

$$Fr_{1,max} = \left(\frac{5}{4\alpha_G}\right)^{1/2}$$

or 3.66 using the entrainment coefficient given above. Note that the experiments indicate a limiting Froude number of 3.8 as discussed by Baines (1975).

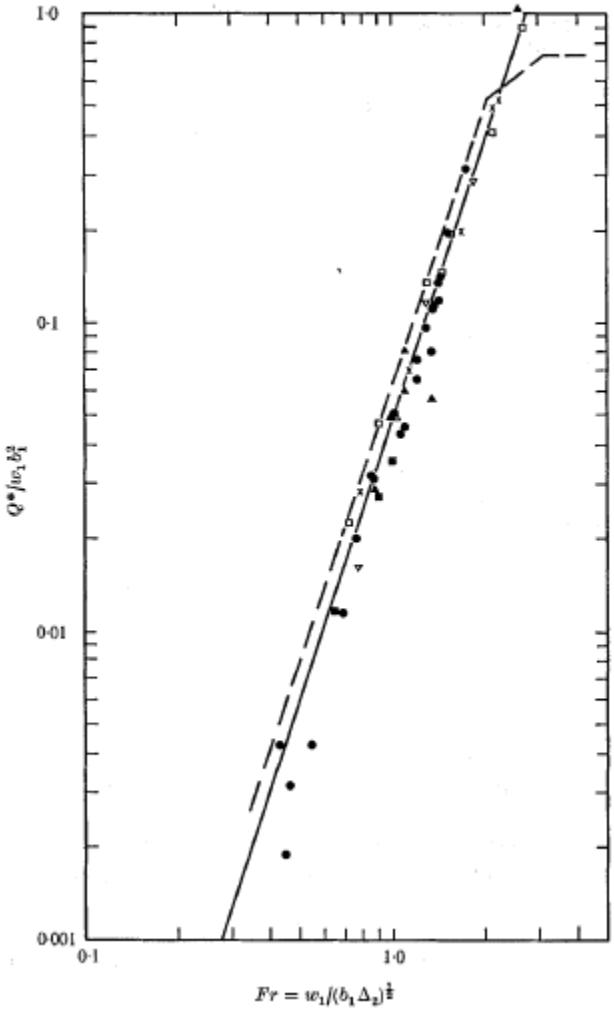


**Figure 3-46. Entrainment Volume Flux for Jets and Plumes, - - - transformed Turner (1968) data, — slope of 3 for data (Baines, 1975)**

Figure 3-47 gives the entrainment buoyancy flux data and a straight-line fit, so

$$\frac{B^*}{B_0} = \text{constant } Fr_1$$

where the constant is about 0.41.

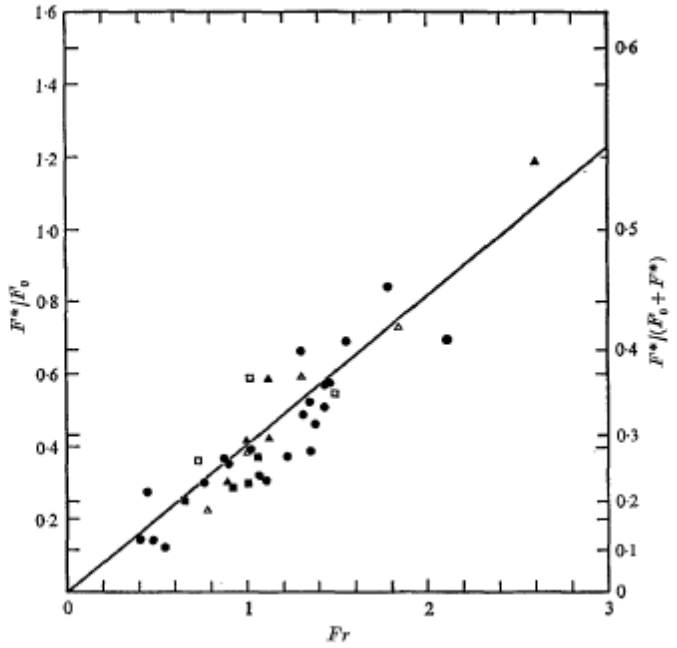


**Figure 3-47. Entrainment Buoyancy Flux (Baines, 1975)**

**Kumagi (1984)**

Kumagi (1984) performed experiments with a fresh water layer over a salt water layer in a tank that were briefly described earlier. He injected a positively-buoyant denser salt water jet into the upper layer and watched the evolution of the layering. The time evolution is shown in Figure 3-48. The inlet jet fluid was dyed for visualization purposes. In Figure 3-48a, the inlet jet impacts the layered surface but does not penetrate it due to the entrainment of fresh water into the jet. The jet fluid spreads out laterally along the interface. The process continues in Figure 3-48b and c as more and more of the jet fluid spreads out along the interface creating a slightly heavier upper layer with some stratification. The original interface is slightly depressed by the inlet jet.

In time, the upper layer density increases due the introduction of the denser jet. With this increased upper-layer density, the jet density at the interface increases such that it penetrates the layer interface. In Figure 3-48d, the inlet jet penetrates the interface, continues through the bottom layer all the way to the bottom of the tank, and spreads out along the bottom, forming yet

another layer as seen in Figure 3-48e. Figure 3-48f shows the final configuration of a 3-layered system consisting of the original top layer, which is denser than fresh water due to the jet, a middle layer, which is essentially the original bottom layer, and a new bottom layer that is mostly from the inlet jet with fluid entrained from both of the above layers.

Similar to Baines (1975), Kumagi (1984) modeled his experiments using entrainment equations. However, he assumed top-hat profiles for the entrainment equations rather than the Gaussian entrainment equations used by Baines (1975). Note that the $Fr_1$ number at the interface is $2^{5/4}$ (2.38) times larger for a Gaussian profile than for a top-hat profile, so the difference in entrainment equations and the Froude numbers needs to be considered in comparing the results. The top-hat entrainment coefficient, $\alpha_{TH}$, estimated from experimental data is 0.127 for top-hat profile, which is equivalent to an $\alpha_G$ of 0.090. Note that Baines (1975) and Baines and Turner (1969) used Gaussian entrainment coefficients of 0.100 and 0.093, respectively. Kumagi (1984) also developed equations for evolution of layer buoyancies assuming that the injected fluid is only a source of buoyancy with zero mass and momentum.

From his experiments, the entrainment rate across an interface is a function of the Froude number at the interface, $Fr_{1,I}$

$$Fr_{1,I} = \frac{u_I}{(g'_I b_I)^{1/2}}$$

as follows

$$\frac{Q^*}{b_I^2 u_I} = f\left(Fr_{1,I}\right) = \frac{Fr_{1,I}^3}{1 + 3.1Fr_{1,I}^2 + 1.8Fr_{1,I}^3}$$

as shown in Figure 3-49 where $Q^*$ is the total volume flux due to entrainment divided by the width of the plume, $b_I$, squared and the plume velocity at the interface, $u_I$, as calculated by the entrainment equations.

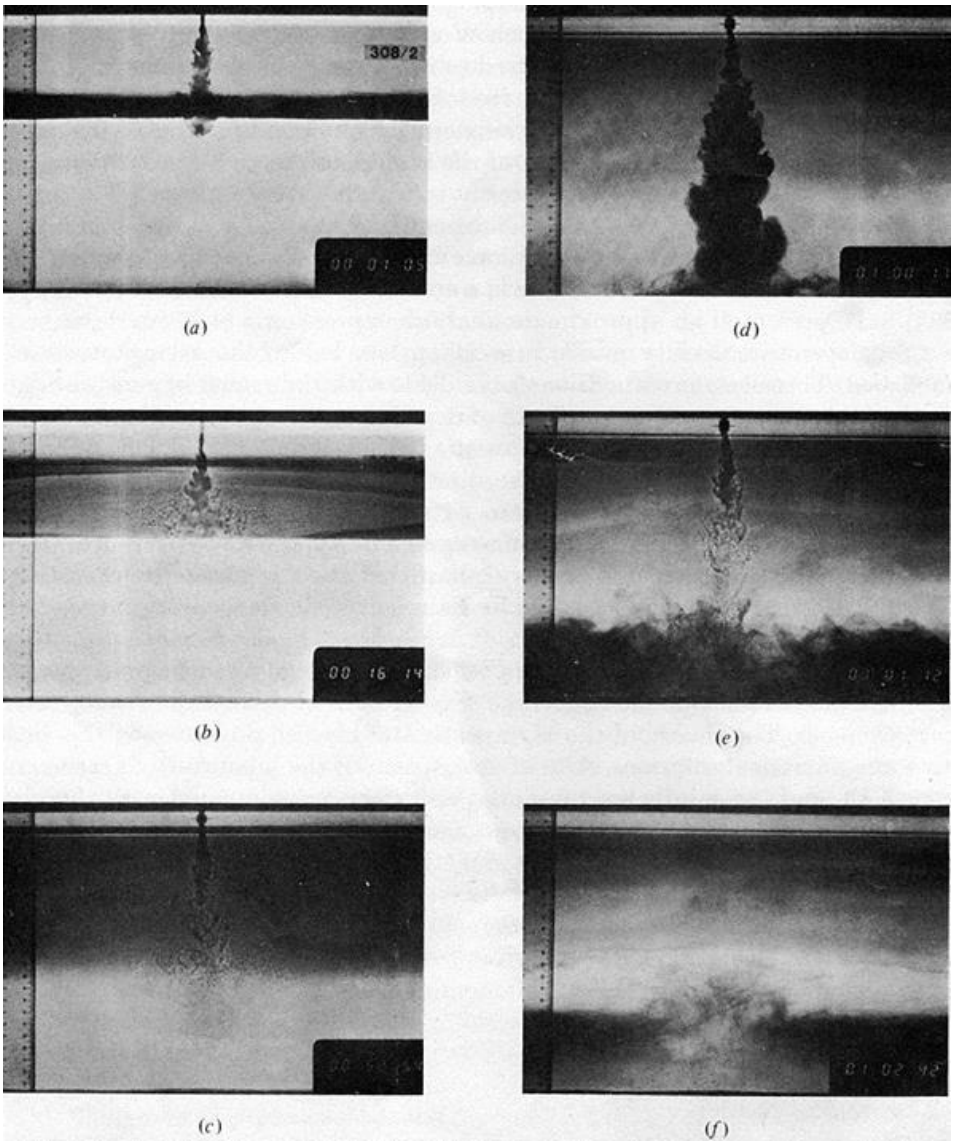


**Figure 3-48. Development of Layered System (Kumagi, 1984)**

Shadowgraph showing the evolution of a layered system due to the introduction of a plume of dense salt solution of $\rho = 1.1344$ g/ml at $F = 14.1$ cm$^4$/s$^3$. Upper layer was initially fresh water 8.24 cm deep. Lower layer is salt solution of $\rho_2 = 1.0161$ g/ml. The time from the start in hours, minutes and seconds is indicated by the clock at the bottom. Depressions of the interface formed by the impingement of the plume are apparent in (*a*)–(*c*), which also show the rise of the first front. (*c*) shows a state just before the beginning of the penetration of the plume. (*d*), (*e*) and (*f*) show the spread of the plume fluid after penetration, made visible by the addition of dye. (*f*) shows the resulting three-layer structure.

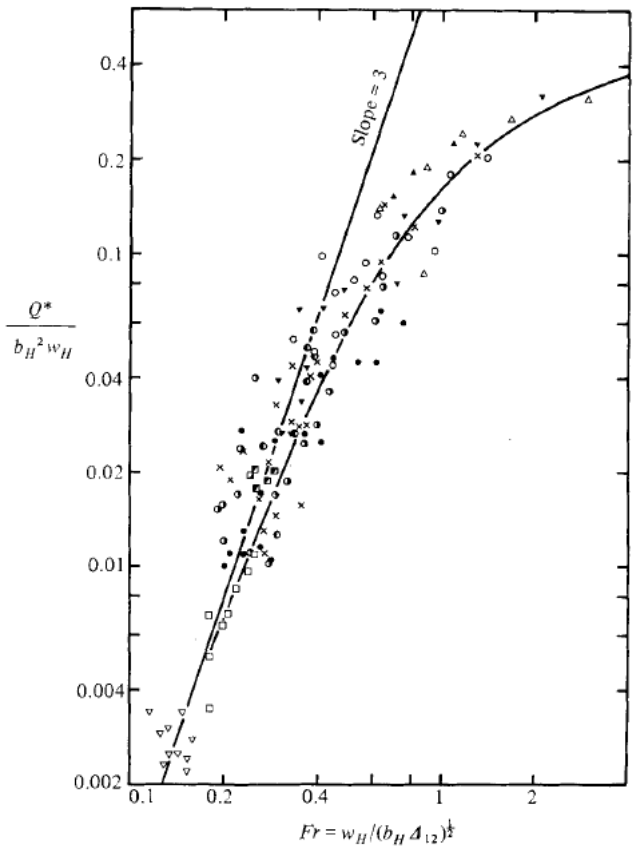


**Figure 3-49. Entrainment Volume Flux Across Interface vs. Froude Number (Kumagi, 1984)**

Note that as the Froude number goes to << 1, the entrainment value is proportional to the $Fr_{1,I}$ number to the third power, similar to the Baines (1975) results. However, as the $Fr_{1,I}$ number goes to infinity, the curve-fit asymptote goes to 0.56. The observed maximum value is 0.32 at a $Fr_{1,I}$ number of around 3. This behavior is similar to the presentation of the Turner (1968) data by Baines (1975) as discussed above.

The buoyancy flux across the interface is fit by a complex equation that is discussed in Kumagi (1984). The data-model comparison is given in Figure 3-50. The straight line in the figure is from Baines (1975).

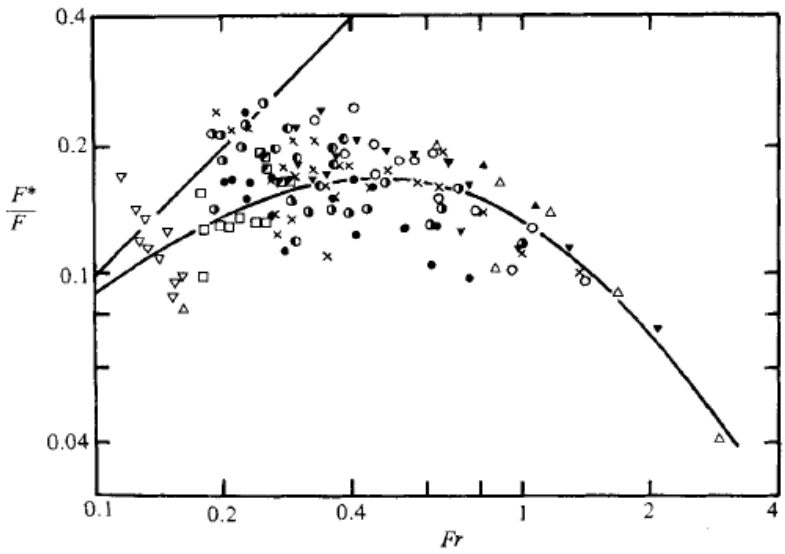


**Figure 3-50. Bouyancy Flux Across Interface vs. Froude Number (Kumagi, 1984)**

**Larson and Jonsson (1994, 1996)**

Larson and Jonsson (1994, 1996) performed experiments on a positively-buoyant jet impacting the density interface of a two-layer system. Due to mixing at the interface, the system eventually evolves into a three-layer system similar to Kumagi (1984). They parameterize the results in terms of a mixing efficiency and parameters at the jet nozzle exit.

The mixing efficiency, which is the ratio of rate of change in potential energy divided by the rate of change in kinetic energy, is calculated according to the equation

$$\eta = \frac{\Delta P}{\Delta K} = \frac{\Delta m \Delta z g A / \Delta t}{\frac{1}{2}\rho u_0^3 A_0}$$

$$\Delta m = \frac{\Delta m_1 + \Delta m_2}{2}$$

where various terms are defined in Figure 3-51. The mixing efficiency as a function of the Froude number of the intermediate layer is shown in Figure 3-52, where the Froude number is defined as

$$Fr_l = \frac{u_0}{\left(\frac{\Delta\rho}{\rho} g d_0\right)^{1/2}}$$

where the density difference is across the layers, and $u_o$ and $d_o$ are the velocity at the nozzle exit and the diameter of the nozzle, respectively.

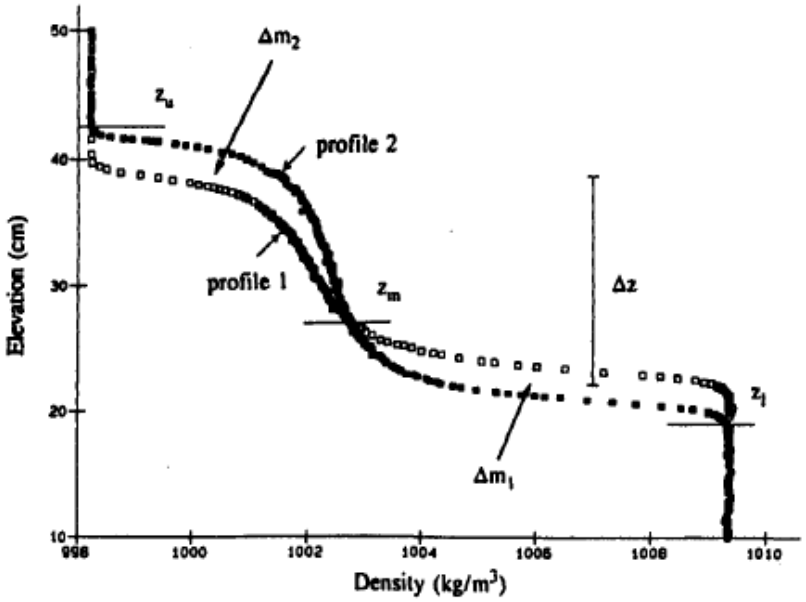


**Figure 3-51. Variable Definitions for Mixing Efficiency Determination (Larson and Jonsson, 1994)**

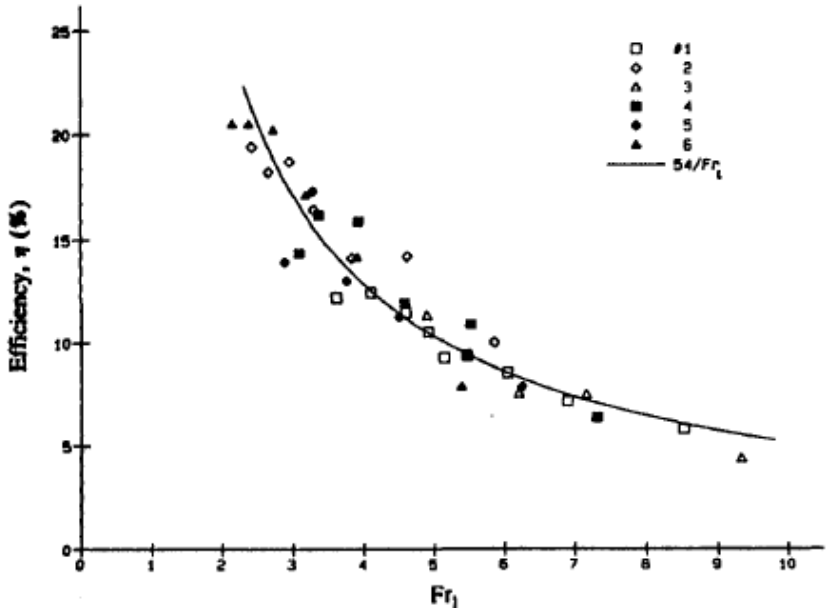


**Figure 3-52. Mixing Efficiency as a Function of Froude Number (Larson and Jonsson, 1994)**

Note that the Froude number is based on initial exit jet velocity, nozzle diameter, density differences, and layer depth, not the values at the density interface. Comparison of these results to those from other studies is complicated by the fact that these results use jet exit parameters while other studies use estimated parameters at the density interface. Nevertheless, they present transient data of the vertical density evolution for 6 different experimental conditions that could prove valuable for validation of other models.

#### 3.1.3.2 Application to SPR

The relationships for entrainment across interfaces discussed above are probably applicable to SPR in limited situations. The jet parameters at the interface need to be known to use the above relationships. The entrainment equations discussed earlier can probably only be used for minimum confinement effects.

### 3.1.4 Effect of Confinement

As indicated above, there may be a significant effect of jet/plume confinement in the SPR geometry. These effects are discussed in this section.

#### 3.1.4.1 Jet Characteristics

#### Hussein et al. (1994) Model

Hussein et al. (1994) investigated turbulent jet characteristics, and they developed a simple momentum balance to evaluate the effects of jet confinement due to the finite dimensions of their experimental device. The return flow 'steals momentum from the jet', which modifies the jet characteristics from that in an infinite domain. They assumed that the momentum integral at each section is equal to the rate of momentum addition from the jet. They divided the flow into the jet flow and the counter-current return flow as depicted in Figure 3-53. Equating the jet and return mass flow rates, and assuming that the jet velocity profile is Gaussian while the return velocity profile is uniform, they developed the relationship

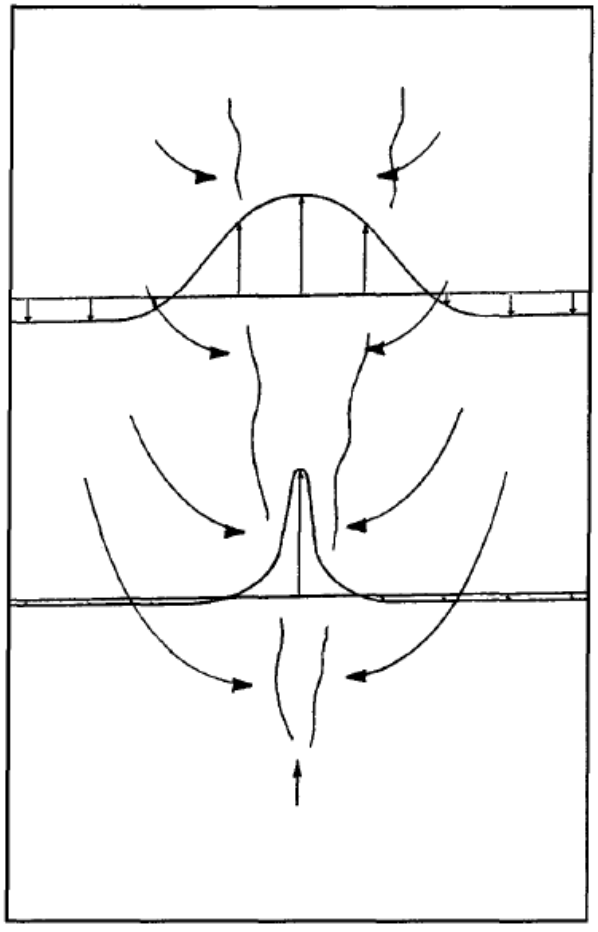

**Figure 3-53. Confined Jet Flow Pattern (Hussein, Capp, and George, 1994)**

$$\frac{M}{M_0} = \left[1 + \frac{16}{\pi B^2}\left(\frac{Z}{D}\right)^2 \frac{A_0}{A_R}\right]^{-1}$$

where $D$ is the jet exit diameter, $A_0$ is the jet exit area, $A_R$ is the area of "room", and $B$ is a constant that is equal to 6.5 from Hussein data and is the constant in the jet velocity decay equation.

This equation can be rewritten as

$$\frac{M}{M_0} = \left[1 + \frac{16}{\pi B^2}\left(\frac{Z}{D_R}\right)^2\right]^{-1}$$

where $D_R$ is the effective diameter of the room and the jet diameter cancels out.

The momentum ratio as a function of $Z/D_R$ is shown in Figure 3-54. The impact on confinement is 10% on momentum for a cavern depth of $Z/D_R$~1.0 ($Z$~200 ft for cavern diameter of 200 ft) and 50% for a cavern depth of $Z/D_R$~3.0 ($Z$~600 ft). The plume depths for the three jet density differences discussed earlier are also plotted.

For a downward-directed light jet in a cavern with a 200 ft cavern diameter, the effect of confinement is small for a density difference of 0.01 (1%) because the maximum jet depth is about 57 ft in which case the momentum ratio is 0.99. For smaller density differences, the effect is larger. For a density difference of 0.001 (0.1%), the jet depth is 180 ft, and the momentum ratio is 91%. For a density difference of 0.0001 (0.01%), the jet depth is 570 ft, and the momentum ratio is about 50%. Confinement effects are significant for the smallest density difference of 0.0001 (0.01%) and may be important for the intermediate density difference of 0.001 (0.1%) similar to earlier conclusions regarding the jet / cavern diameter ratio.

The effect of confinement might also be important in some of the buoyant jet experiments discussed earlier. Using this relationship, the effect of confinement can be estimated for various experiments including those given by Kokkalis and Papanicolaou (2006). The results using the vessel height as the maximum distance are shown in Table 3-10. The momentum values indicate that the Turner (1966) and Pantzlaff and Lueptow (1999) results may be influenced by confinement, while the effect of confinement is much smaller for the other investigations.

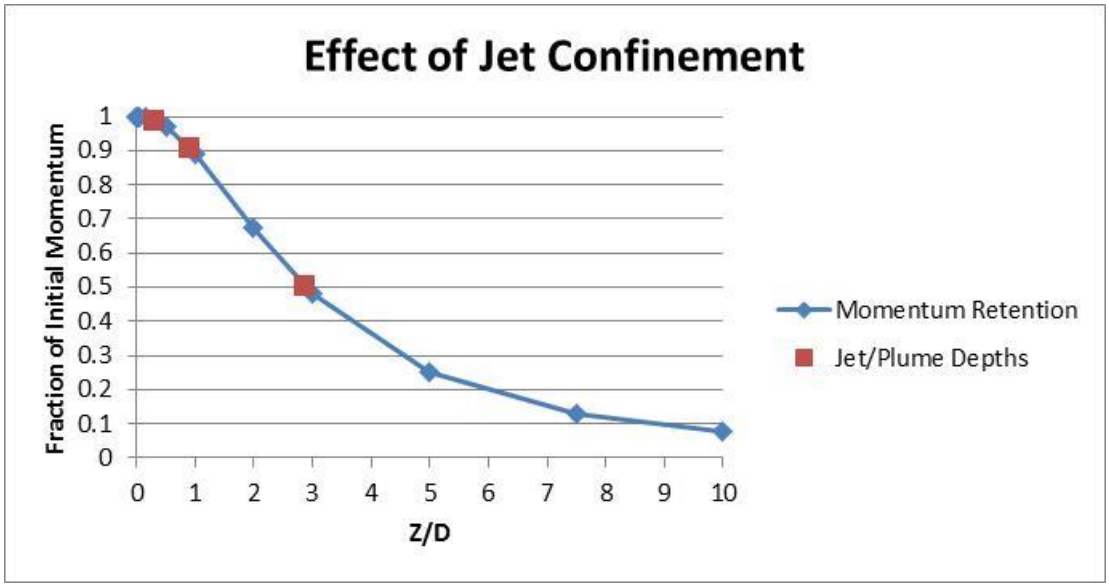


**Figure 3-54. Effect of Jet Confinement**

**Table 3-10. Evaluation of Minimum Momentum Retention For Various Experiments**

| Investigation | Horizontal Dimensions (m) | Effective Diameter (m) $(4A/\pi)^{1/2}$ | Height (m) | H/D | Nozzle Diameters (cm) | $A_{nozzle}/A$ | $M/M_0$ |
|---|---|---|---|---|---|---|---|
| Turner (1966) | 0.45 x 0.45 | 0.51 | 1.4 | 2.76 | 0.65<br>0.96<br>1.4 | 1.6e-4<br>3.5e-4<br>7.5e-4 | 0.53 |
| Pantzlaff and Lueptow (1999) | cylinder | 0.295 | 0.87 | 2.95 | 0.508 | 3.0e-4 | 0.49 |
| Demetriou (1978)[a] | 1.2 x 1.2 | 1.35 | 1.55 | 1.14 | - | - | 0.86 |
| Zhang and Baddour (1998)[a] | 1 x 1 | 1.13 | 1 | 0.89 | - | - | 0.91 |
| Lindberg (1994)[a] | 3.64 x 0.405 | 1.37 | 0.508 | 0.37 | - | - | 0.98 |
| Bloomfield and Kerr (2000)[a] | 0.40 x 0.40 | 0.45 | 0.70 | 1.55 | - | - | 0.78 |
| Kokkalis and Papanicolaou (2006) | 0.80 x 0.80 | 0.90 | 0.94 | 1.04 | 0.5<br>1.0<br>1.5<br>2.0 | 3.1e-5<br>1.2e-4<br>2.8e-4<br>4.9e-4 | 0.89 |

[a]Kokkalis and Papanicolaou (2006)

## Risso and Fabre (1997)

Risso and Fabre (1997) investigated turbulence in confined jets. In their experiments, which are schematically shown in Figure 3-55, they injected a neutral jet upward into a cylindrical tube that is closed at the top. The flow exited through an annulus at the bottom of the tube such that there was countercurrent flow. They used 2 different tubes; the dimensions are listed in Table 3-11. These experiments are of particular interest because the length-to-diameter ratios of the tanks are 6.7 to 9.6, similar to idealized SPR cavern ratios.

**Table 3-11. Risso and Fabre (1997) Experimental Parameters**

| | *Nozzle Diameter (d)* | *Tank Diameter (D)* | *$\alpha$=d/D* | *Tank Height (H)* | *$\gamma$= H/D* | *Annular ID (D')* | *$\beta$= $d^2/(D^2-D'^2)$* | *Re* |
|---|---|---|---|---|---|---|---|---|
| *Tank 1* | *15 mm*[1] | *77 mm* | *0.195* | *600 mm* | *7.7* | *70 mm* | *0.22* | *150,000* |
| *2/3-scale Tank* | | | *0.186* | | *6.7*<br>*8.1*<br>*9.6* | | *0.22* | *20,000*<br>*45,000*<br>*95,000* |

[1]-reported nozzle diameter is 10 mm; 15 mm was back-calculated from the various ratios listed in the paper. The nozzle diameter for the 2/3-scale tank is probably 10 mm.

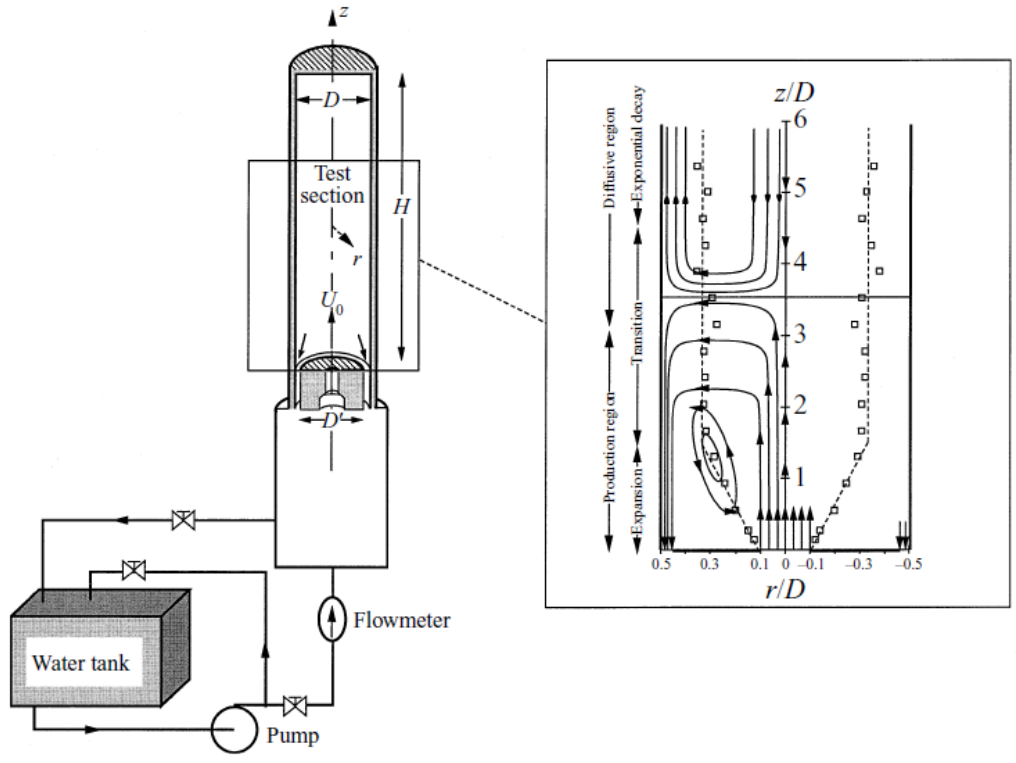


**Figure 3-55. Experimental Setup and Qualitative Results (Risso and Fabre, 1997)**

The centerline velocity decay for the Risso and Fabre (1997) data is given in Figure 3-56 where it is shown to be Reynolds number invariant (symbols are for a Reynolds number range from 22000 to 150000. In addition, the centerline velocity goes to zero at a z/D value of about 3.6 and slightly negative after that before it recovers to zero. Note that the velocity profile is also independent of the length of the tube.

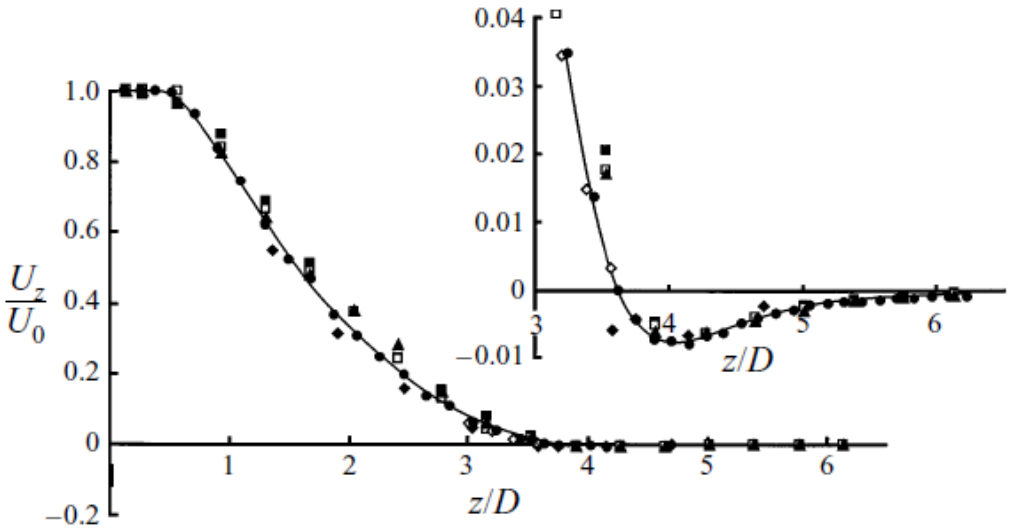


**Figure 3-56. Mean Centerline Velocity normalized by Enclosure Diameter for Various Reynolds Numbers (Risso and Fabre, 1997)**

Figure 3-57 shows the centerline velocity vs the distance normalized by the jet diameter including those from other sources. The nozzle to tank diameter ratio (*d/D*) is denoted by the variable $\alpha$. The solid diamonds are for a free jet. The centerline velocity is obviously a function of the container diameter, *D*. Note that the 3.6*D* value where the velocity goes to zero is supported by the other investigations. For $\alpha$=0.195 (solid circles), 0.186 (open circles and open squares), and 0.087 (solid squares), 3.6D corresponds to z/d of 18.5, 19.4, and 41.4, which is in line with the data shown. Thus, the *z/D* scaling for the jet centerline velocity is more appropriate for confined jet flow that *z/d*.

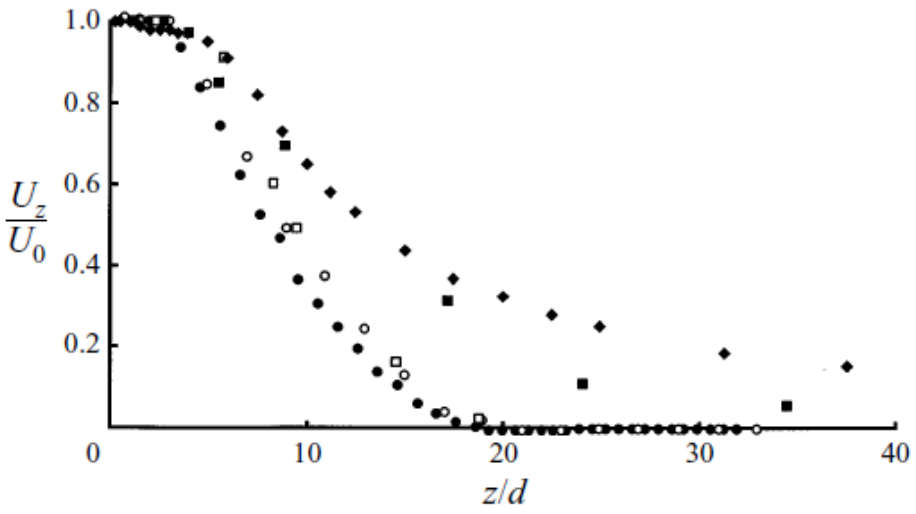


**Figure 3-57. Mean Jet Velocity Normalized to Jet Diameter, d (Risso and Fabre, 1997)**

The radial velocity profiles at z=0.4*D*, 1.3*D*, and 2.7*D* are given in Figure 3-58a-c, respectively. The velocity normalized by the exit velocity is shown by solids squares. The RMS axial and radial velocities are shown by solid diamonds and open triangles, respectively. Close to the jet exit (0.4D), the jet velocity is almost uniform as expected. Further downstream, the velocity profiles have a Gaussian shape, and the velocities cross zero at +-0.3D in the radial direction as depicted in Figure 3-55 earlier.

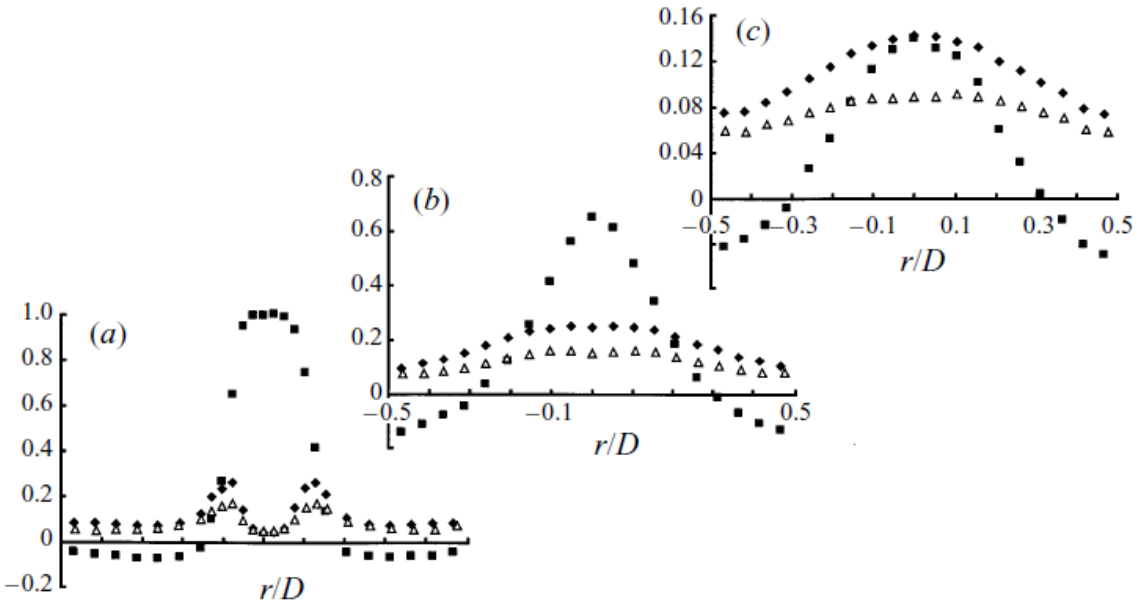


**Figure 3-58. Mean and r.m.s. Velocities at Various Distances Downstream (a) 0.4D; (b) 1.3D; (c) 2.7D (Risso and Fabre, 1997)**

### 3.1.4.2 Application to SPR

Confinement effects are expected to be significant in SPR caverns as confirmed in this section. The value of 0.3D for the effective radius of the jet can be compared to the previous simplistic results for various negatively buoyant jets. For the simplified cavern geometry with a diameter of 200 ft, this effective radius value is about 60 ft. For density differences of 0.01, 0.001, and 0.0001, the jet radius at reversal is about 12, 36, and 116 ft, respectively. Consistent with the momentum analysis given earlier, minimal confinement effects are expected for the first 2 cases, while significant effects are expected for the last case.

In addition to the simplistic jet radius comparison, the Risso and Fabre (1997) results show that the jet characteristics are significantly changed by to confinement conditions similar to those encountered in SPR caverns. Therefore, addition research is needed in this area.

### 3.1.5 Integral Models for Enclosures

In addition to the individual models described above for jet entrainment and entrainment across interfaces, integral models for enclosures have been developed based on the above concepts. Note that the most of the models for entrainment across a density interface described above also rely on entrainment conservation equations and other models to estimate conditions at the interface. In these models, the effect of confinement on the jet characteristics has not been explicitly addressed.

#### 3.1.5.1 Existing Models

**Positively-Buoyant Jets**

Baines and Turner (1969) developed an enclosure model as depicted in Figure 3-59. The source at the bottom is buoyancy only; the mass addition component is ignored so the total mass in the system is constant. Gaussian entrainment equations are used, and the entrainment coefficient is evaluated from the experimental data for the time when the jet front reaches the lower boundary. The descent of the front from the top surface is also predicted. From the experimental data, the Gaussian entrainment coefficient is estimated to be equal to 0.100.

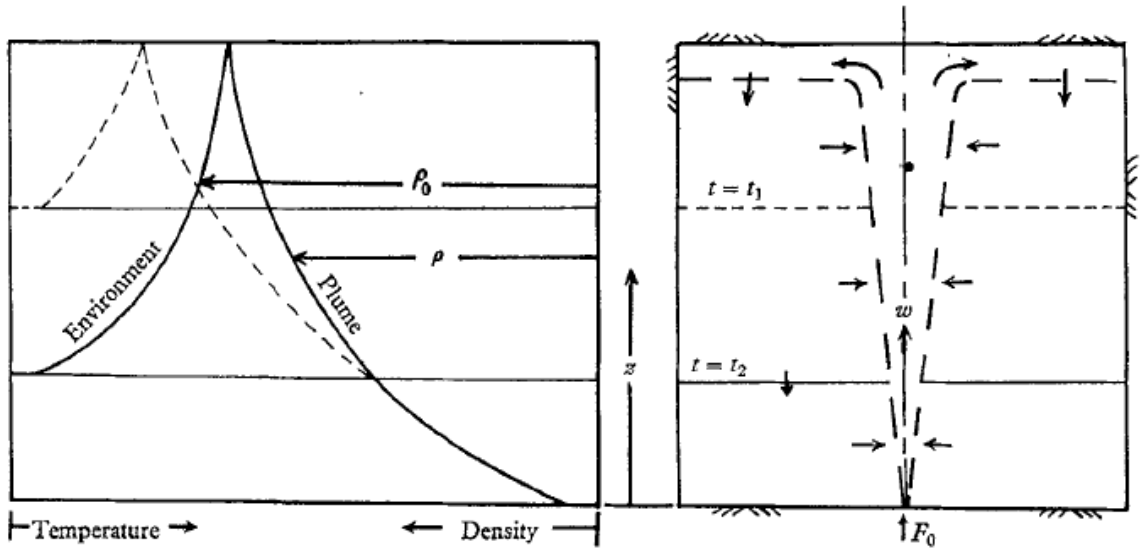


**Figure 3-59. Model Schematic (Baines and Turner, 1969)**

Germeles (1975) developed a model for mixing in tanks including the effect of plumes for LNG storage tanks for two miscible fluids. The schematic for an upward and centered lighter plume injected into a heavier fluid is shown in Figure 3-60.

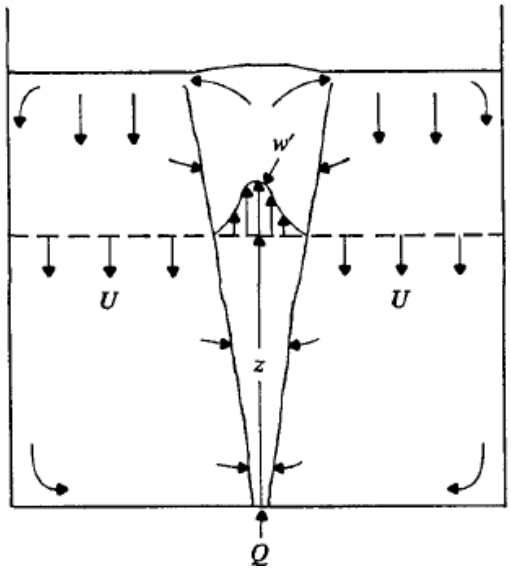


**Figure 3-60. Schematic of Germeles Model for Mixing of Two Miscible Fluids (Germeles, 1975)**

He used Gaussian entrainment equations and the filling-box model of Baines and Turner (1969) modified to include the mass source term of the injection. The resulting equations were integrated to give the final prediction. He also performed some experiments to validate his model. Of interest is a top-fill vertically downward directed jet where the injected fluid is about 6% heavier than the initial fluid in the tank, or a positively-buoyant jet. The entrainment coefficient is based on an ideal jet near the top fluid surface ($\alpha_G$=0.057) and an ideal plume at lower elevations ($\alpha_G$=0.082). The data-model comparison is shown in Figure 3-61 with good results where $\zeta$ is the dimensionless tank height and x are the data at $\tau$ = 1.0.

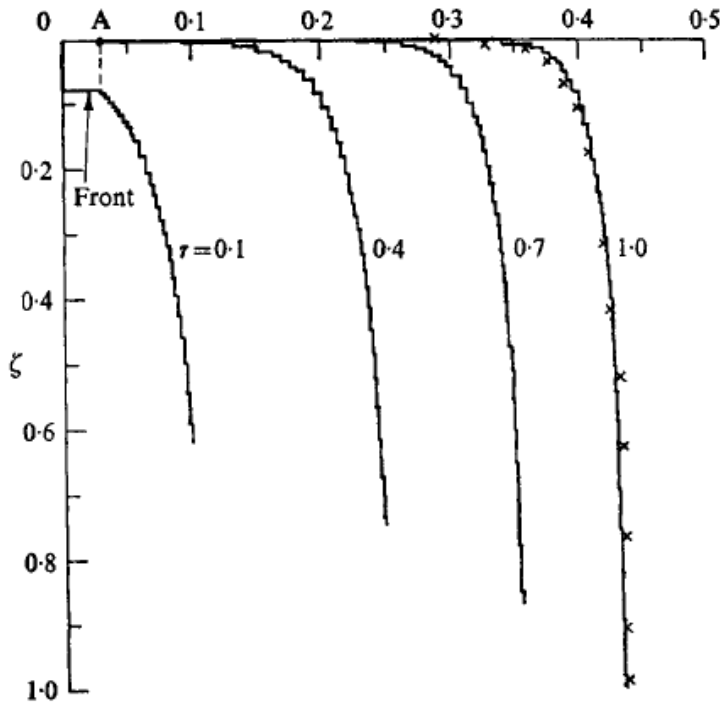


**Figure 3-61. Comparison of Germeles Model with Experimental Results (Germeles, 1975)**

As discussed earlier, Larson and Jonsson (1994) performed experiments and developed an empirical model for a lighter downward directed jet where the ambient fluid is layered. However, the results are presented as correlations and are not modeled by conservation equations to estimate an entrainment coefficient.

Worster and Huppert (1983) developed another conservation equation model ignoring the injection mass flux (buoyancy source only). They give an analytical approximation to the model that compares well to the full model solved using the Germeles (1975) numerical method for an upward-directed lighter jet.

Caulfield and Woods (2002) developed a model for mixing in a room that includes the inlet mass flow and a single outflow using the numerical scheme of Germeles (1975). They compared their model results to the Baines and Turner (1969) experimental data with good results using a Gaussian entrainment coefficient of 0.100.

Hunt et al. (2001) developed a model for stratification in rooms from jets and plumes for positive buoyancy conditions. Of particular interest is a relationship between the jet operating parameters and environmental stratification for well-mixed conditions. For example, for an aspect ratio of 8, which is typical of SPR caverns, the critical jet length should be less than 10 times the cavern height to retain stratification, or less than one enclosure diameter. Presumably this height could

be replaced by the distance to layering in the resident fluid. While the parameters are probably not directly applicable to SPR caverns, the concept might be of interest.

van Sommeren et al. (2012, 2013, 2014) performed experiments and scaling arguments for turbulent mixing in a narrow vertical tank of aspect ratio 40 with injection at the top of the tank. The initial fluid in the tank is fresh water and the injected fluid is denser salt water. The injected fluid is distributed evenly over the top of the tank so it is not a jet but a plug of denser fluid. This situation is similar to that when a fluid jet reaches the outer walls and stops as discussed later. Mixing between the denser injected fluid and the lighter resident fluid is by diffusive turbulence such as after the vertical motion of the jet is stopped. The turbulent diffusion process is modeled.

In van Sommerton et al. (2012), the injected fluid volume was also extracted at the bottom of the tank similar to SPR cavern operation. Evolution of the mixed region with time is presented and scaled. van Sommerton et al. (2013) added fluid injected at the bottom of the tank as opposed to fluid extraction such that countercurrent flow was established in the tank with net outflow out the top. van Sommerton et al. (2014) examine mixing and transport of a passive scalar at the bottom or top of the tank imposed on the mean flow for the van Sommerton et al. (2013) case with fluid injected at the bottom of the tank. The results from van Sommerton et al. (2012) may be useful to quantify turbulent diffusion values for confined jet applications such as SPR.

Cardoso and Woods (1993) extended the filling box of Baines and Turner (1969). Baines and Turner (1969) assumed an initially uniform environment. Cardoso and Woods (1993) consider an initially linearly stratified environment as shown in Figure 3-62. As with Baines and Turner (1969), the plume is considered to only be a source of buoyancy with no source of mass or momentum.

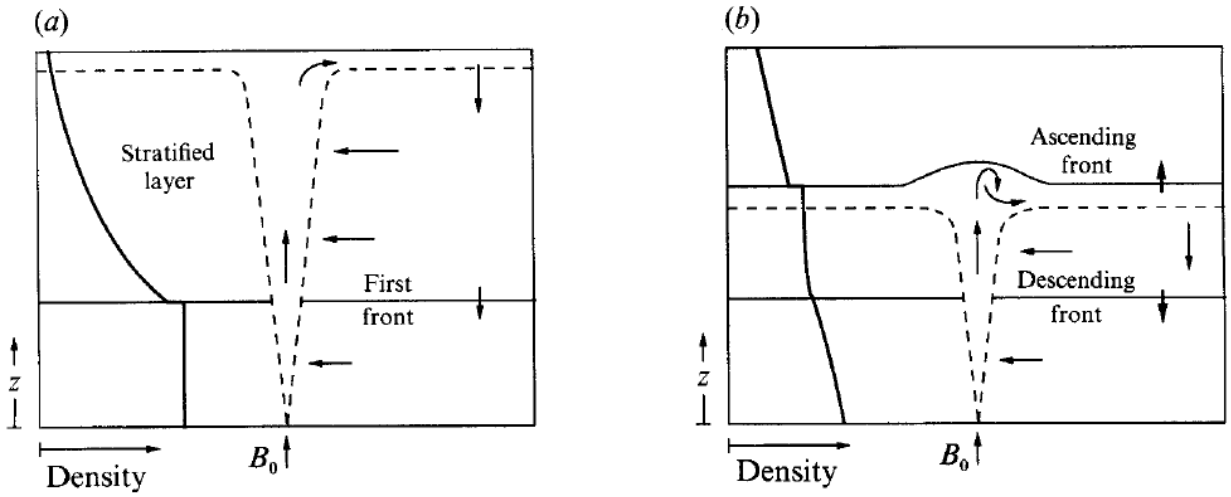


**Figure 3-62. Different Enclosure Conditions Analyzed (a) Uniform Environment (Baines and Turner, 1969); (b) Linearly Stratified Environment (Cardoso and Woods, 1993) (Cardoso and Woods (1993)**

Manins (1979) also extended the filling box model of Baines and Turner (1969) and delineated the conditions for application. Assumptions include a Prandtl number of order 1 or greater, half-width from plume centerline to outer wall about 1.2 times the height, and a large Rayleigh number. Only a buoyancy source is used for the plume with no mass or momentum source. The extension of the Baines and Turner (1969) model relates to the bottom boundary condition, which can act as a buoyancy sink or source for applications such as in the atmospheric boundary layer or internal heat generation in the earth's mantle.

In addition, Fragos and Papanicolaou (2006) investigated a downward flowing heavy plume into a uniform fluid in an enclosure. For nozzle $Ri_1$ number greater than 0.10, the normalized interface elevation vs. normalized time data collapsed into a single curve. Model predictions using the entrainment equations with a plume Gaussian entrainment coefficient of 0.0875 resulted in good data-model comparisons.

Of significant interest to SPR cavern mixing is the work of Barnett (1991). Barnett (1991) investigated positively-buoyant jets injected into a closed cylinder. Denser fluid (salt solution) was injected downward into an initially fresh water filled cylindrical tank 4.5 cm in radius and 131 cm high (H/D ~ 14.6). He measured the salt concentration vs time and depth. This aspect ratio is similar to SPR caverns. The only significant difference is that the cylinder was closed at the bottom so the flow entered and exited at the top of the cylinder. The impact of this difference will be addressed later in this report.

Barnett (1991) found that the jet/plume formed three regions as shown in Figure 3-63. The jet/plume region existed up to h/r of 5.78 (or h/D = 2.89) where the jet/plume hits the wall and dissipates. Following the plume region is a mixing region where the plume velocity dissipates and the fluid mixes. Finally, there is a convective region for the buoyancy. The total jet length seems to be similar to that seen by Risso and Fabre (1997) discussed earlier.

He developed a numerical model for the plume region based on the entrainment equations discussed earlier in this section including the development of stratification. Models for the mixing and convective regions were also developed. In the mixing region, a conservation of buoyancy equation was used to get the buoyancy, which is uniform in the mixing region, versus time. The convective region is simply convection with a constant eddy diffusivity.

Figure 3-64 compares the model prediction with experimental data for one experiment. The agreement between the model and the data is reasonable good considering the assumptions in the model and the uncertainty in the data. Finally, Figure 3-65 shows the results for three different equivalent experiments and the model prediction for a given time. The agreement is reasonable, and the experimental data show the variation in the data for the same experimental conditions.

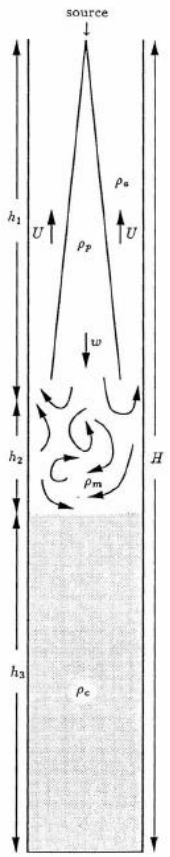


**Figure 3-63. Jet/Plume Regions Observed (Barnett, 1991)**

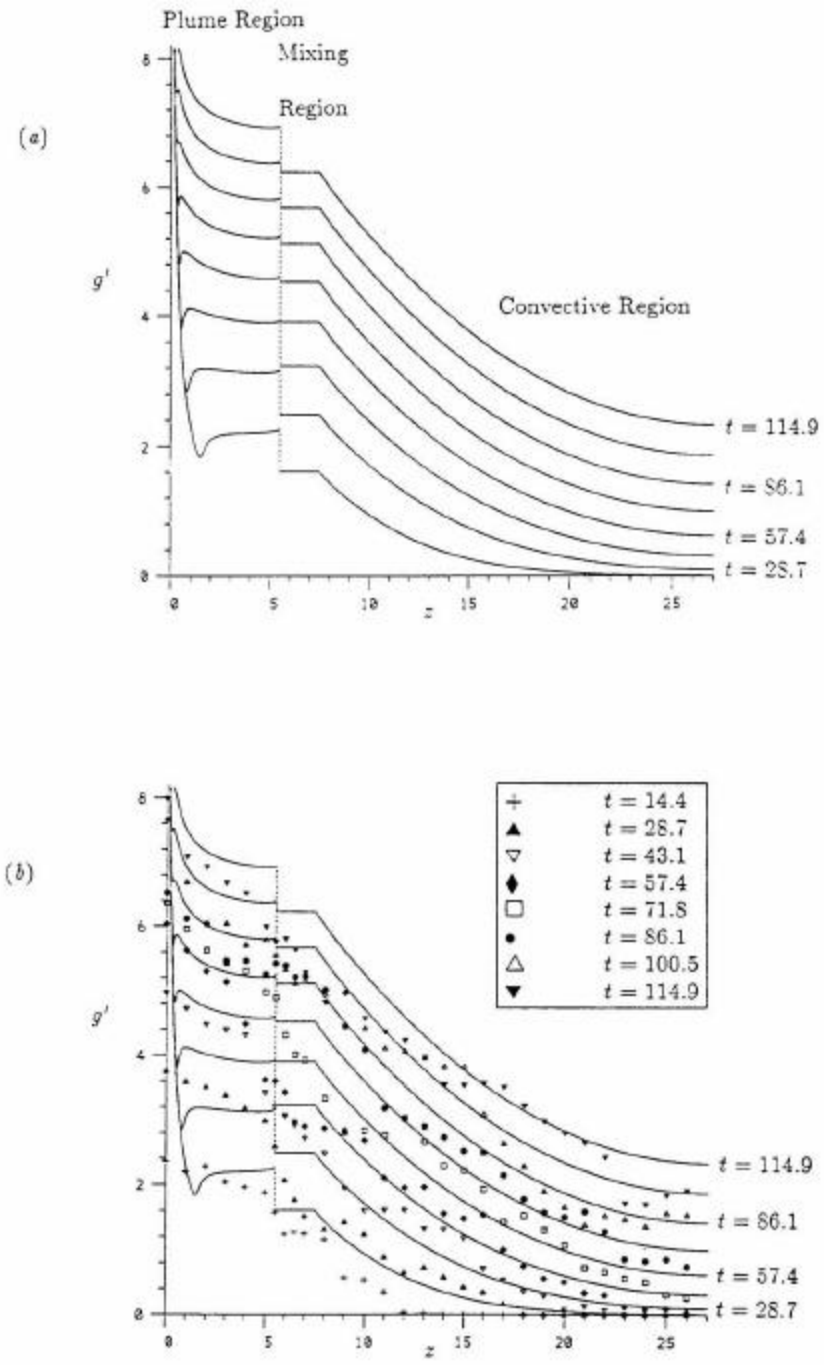


**Figure 3-64. Barnett Model Results (a) Numerical Solution and (b) Data-Model Comparison (Barnett, 1991)**

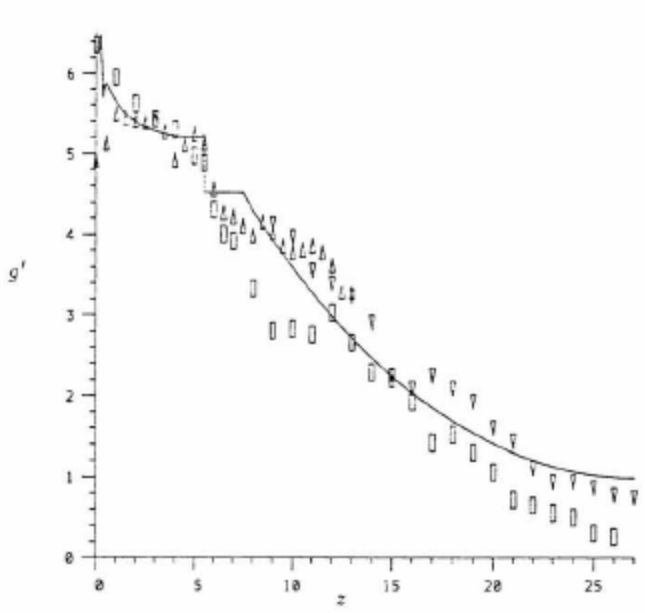


**Figure 3-65. Comparison of Barnett Numerical Solution For Three Similar Experiments at a Single Time (Barnett, 1991)**

**Negatively-buoyant jets**

Baines obtained data and developed models for open (Baines et al., 1990) and closed (Baines et al., 1993) volumes with negatively-buoyant jets. These models basically differ in where the fluid is withdrawn. For an open chamber, the fluid level rises with time. This model can be applied to situations in a region where fluid is added by the jet and is withdrawn downstream of the advancing fluid interface similar to an SPR cavern with top injection and bottom withdrawal. For a closed chamber, the fluid level is constant, and fluid is added and withdrawn at the inlet plane. In addition, for a closed chamber, co-flow and counter-flow cases are investigated where the outflow is withdrawn opposite the inlet. Each model will be summarized below.

**Open chamber**

Baines et al., (1990) investigated negatively-buoyant jets, or fountains, injected into an open chamber as depicted in Figure 3-66. They used the experimental data obtained by Turner (1966), which was discussed earlier, and data from Campbell and Turner (1989). The data are for a turbulent salt water jet injected upward from the bottom of the enclosure into fresh water. Due to the negatively-buoyant jet, the jet initially drops and then rises back upon itself.

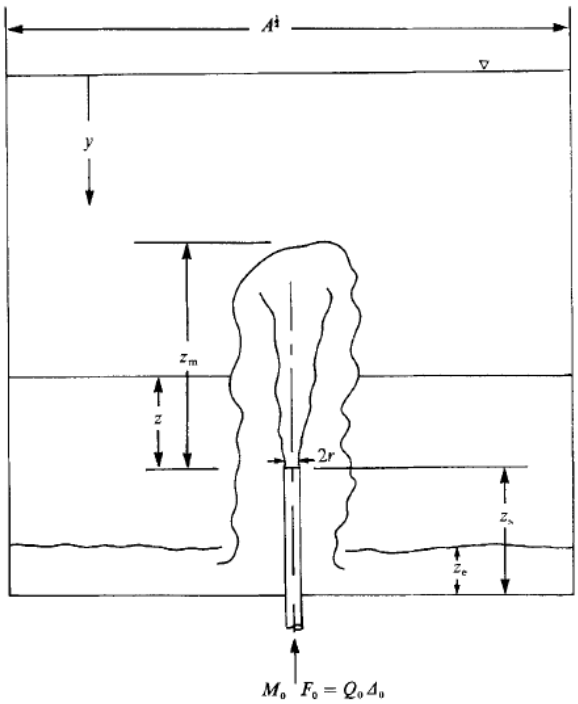


**Figure 3-66. Open Chamber Model for Fountains (Baines et al., 1990)**

Figure 3-67, which is from the closed chamber investigation of Baines et al. (1993), shows the general behavior of the fluid in the enclosure. In this figure, the interface is the dark line below the jet. The initial jet behavior is shown in (a) – note the mixed layer just above the interface as the initial front is developing. In (b), the front has formed and is advancing upward. Note that the jet deforms the interface. In (c), the front has risen high enough that the interface is essentially flat. The height of the negatively-buoyant jet or fountain increases with time due to the increased density of the fluid entrained into the jet.

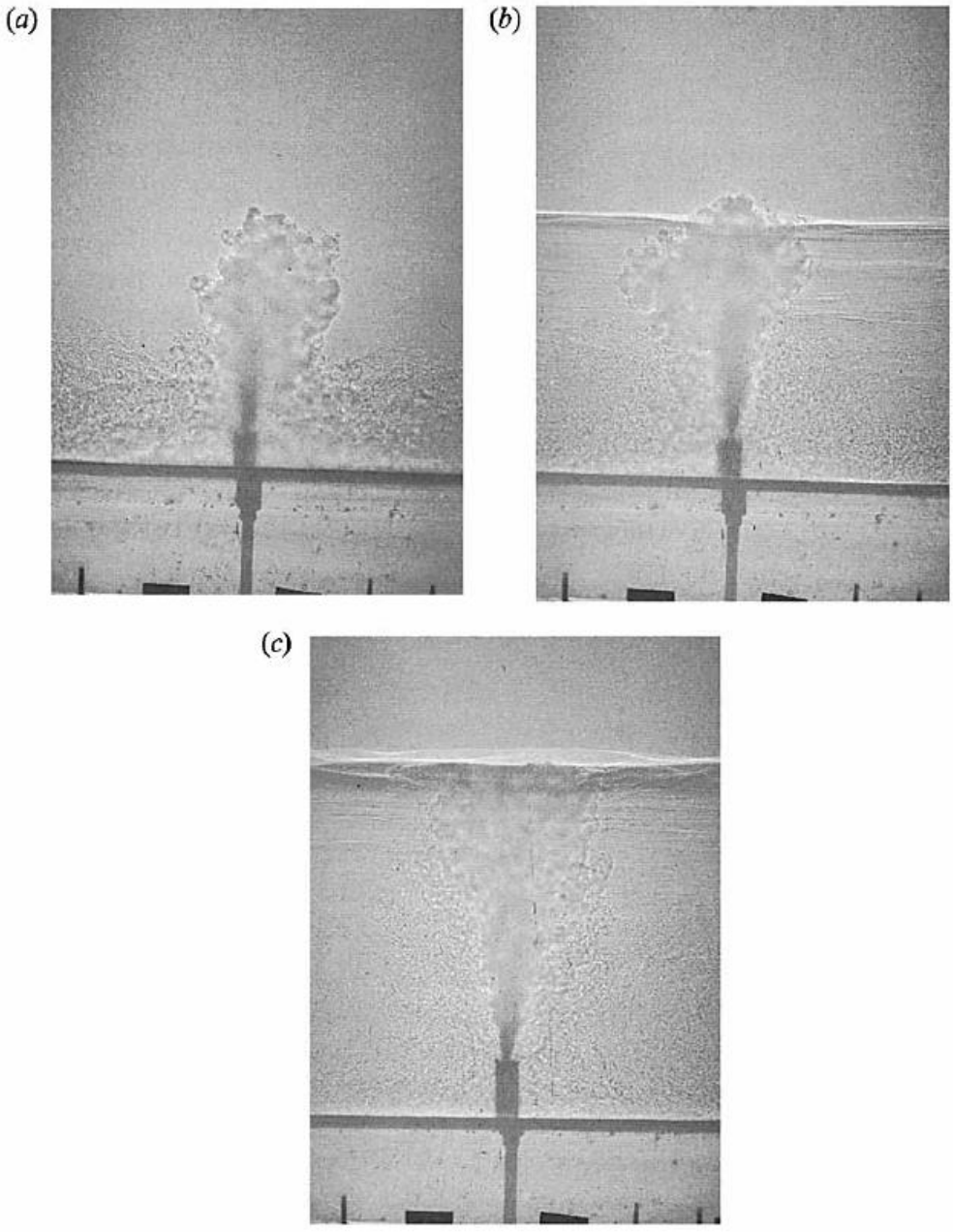


**Figure 3-67. Fountain Behavior in an Enclosure (Baines et al., 1993)**

The locations of various fronts and of the fountain are shown in Figure 3-68 for a given open chamber experiment. The slope of the initial front location is equal to the volume flux over the enclosure area. The second front, which was seeded at about 90 minutes into the experiment, has a similar slope. The location of the top of the fountain increases at about one-half the rate of the front as derived in the paper.

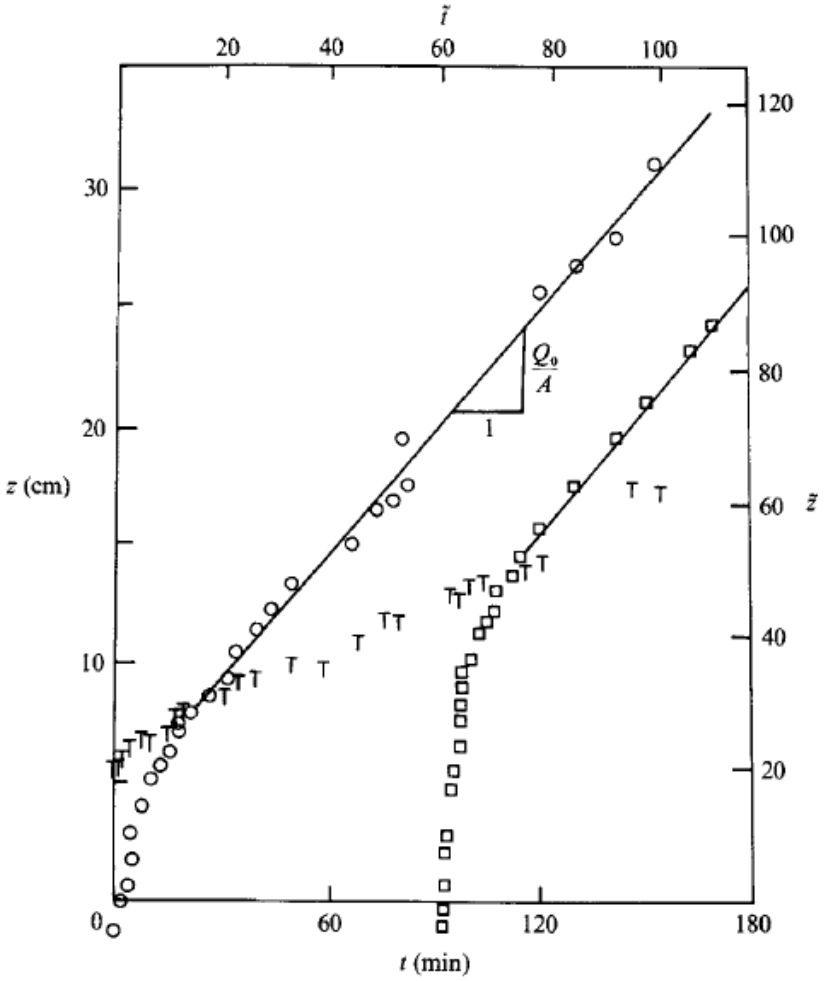


**Figure 3-68. Distances of Fronts for Fountain in Open Chamber (Baines et al., 1990)**

The elevation of the first front is used to estimate the entrainment rate into the fountain. Because the jet rises and then falls back on itself in the coordinate system shown, the entrainment equations given earlier can't be used directly. Based on unpublished data, the entrained flux into a vertical fountain increases linearly with depth below the top of the fountain, or

$$\frac{Q_e}{Q_0 Fr_{r,0}} = C - B\left(\frac{z}{r_0 Fr_{r,0}}\right)$$

This equation leads to an entrainment rate expression

$$q_e = -\frac{dQ_e}{dz} = B\frac{Q_0}{r_0}$$

which is the only fitting parameter in the analysis. Of note is that the average entrainment rate is independent of the Froude number according to this equation.

Expressions for the rise of the initial front have been fit to the experimental data to determine the value of the constant B, which has been determined to be 0.25 with no dependence on the Froude number. An expression for the rise of the top of the fountain is also derived. Both are only applicable until the front reaches the top of the fountain. Figure 3-69 compares the equation for the front with B equal to 0.25 and the equation for the top of the fountain for the same experiment shown in Figure 3-68. The fit is seen to be very good. After the front passes the top of the fountain, the front rises at a rate equal to the volumetric inflow of the jet, and the top of the fountain rises at one-half that value.

Equations are also derived for the density distribution below the front as a function of time. Figure 3-70 compares the predicted density distribution to the equations for the same experiment. The agreement is very good.

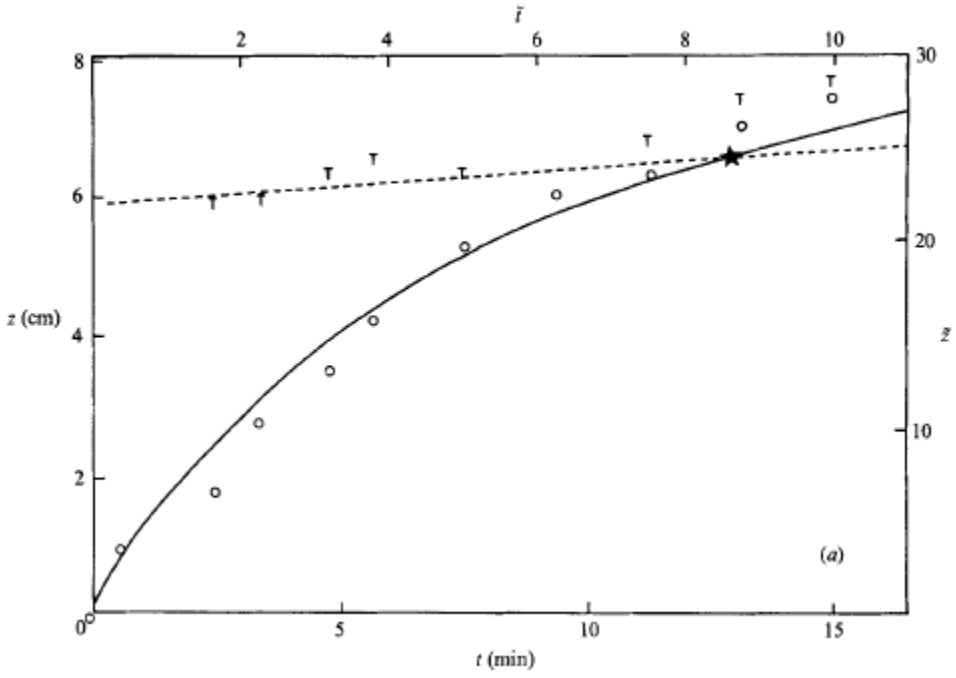


**Figure 3-69. Elevation of Front (o) and Top of Fountain (T) Including Model Predictions for an Open Chamber (Baines et al., 1990)**

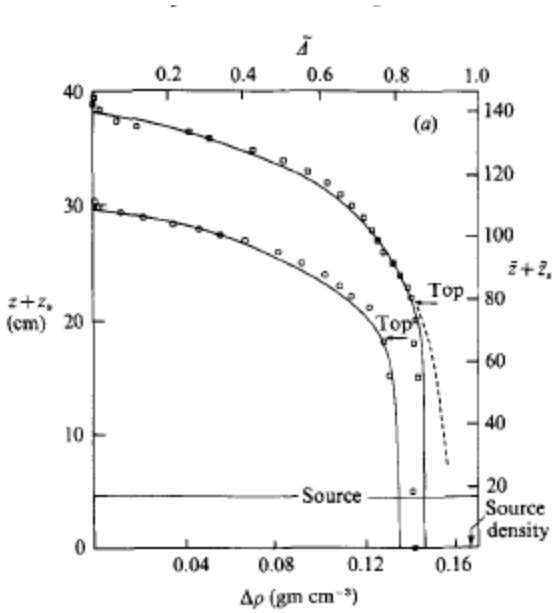


**Figure 3-70. Density Profiles For a Fountain in an Open Chamber (Baines et al., 1990)**

**Closed chamber**

For the closed chamber, the Baines et al. (1993) model is schematically depicted in Figure 3-71. Flow is injected and withdrawn at the inlet plane at the bottom of the enclosure. An external source, $Q_1$, can be specified so the conditions can be co-flow, counterflow, or constant volume. The difference between the injet jet volume flow and the external source is extracted from the enclosure at the elevation of the inlet. Thus, in the case of constant volume, the source volume flux is extracted from the enclosure at the bottom and there is no upper source.

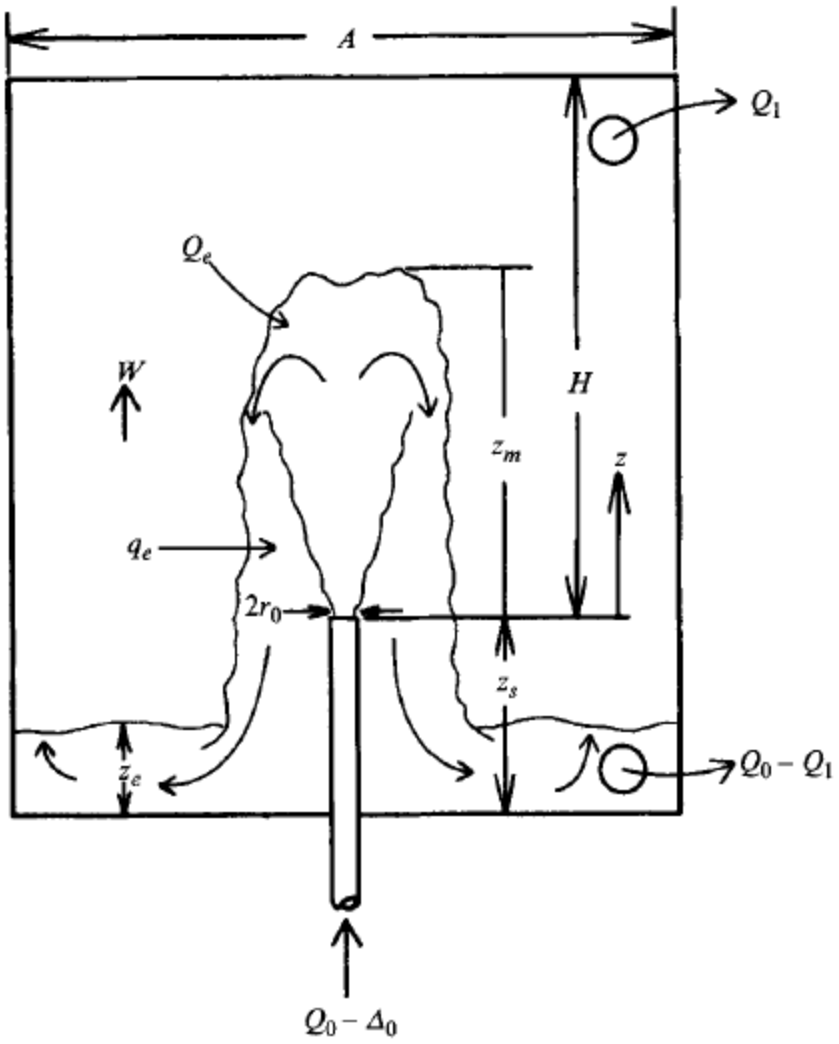


**Figure 3-71. Closed Chamber Model for Fountains (Baines et al., 1993)**

As mentioned in the discussion of the open chamber investigation, the entrainment is assumed to be given by the expression

$$\frac{Q_e}{Q_0 Fr_{r,0}} = C - B\left(\frac{z}{r_0 Fr_{r,0}}\right)$$

Figure 3-72 presents data for the closed chamber case. The value of the entrainment ratio at z equals zero is given by the jet rise equation in a uniform environment from Turner (1966), or

$$\frac{Z}{r} = 2.46\left|Fr_{1,r}\right|$$

and C/B is equal to about 2.46. As discussed earlier, this value should be about 3.11. The value of B is 0.25 from the open chamber results, so the expected straight-line relationship is

$$\frac{Q_e}{Q_0 Fr_{r,0}} = 0.611 - 0.25\left(\frac{z}{r_0 Fr_{r,0}}\right)$$

The data seem to correspond to that line pretty well. Deviation at the larger z values, or as the front reaches the top of the fountain, is due to the reduction in the buoyancy force as the entrained fluid becomes less dense.

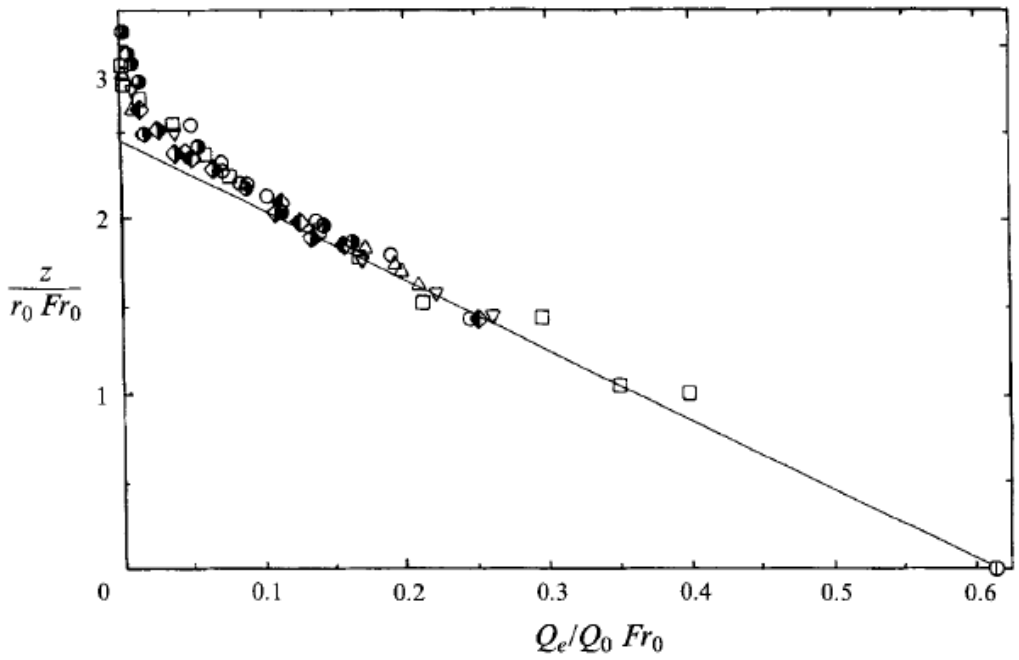


**Figure 3-72. Entrainment Flux Into a Fountain (Baines et al., 1993)**

The interface entrainment can be recast into variable relating the predicted jet geometry at the interface to the entrainment similar to previous analyses of Baines (1975) and Kumagi (1984), which were discussed earlier. Using the standard entrainment equations and a Gaussian entrainment parameter of 0.057, the entrainment data from the previous figure and from other measurements are given in Figure 3-73.

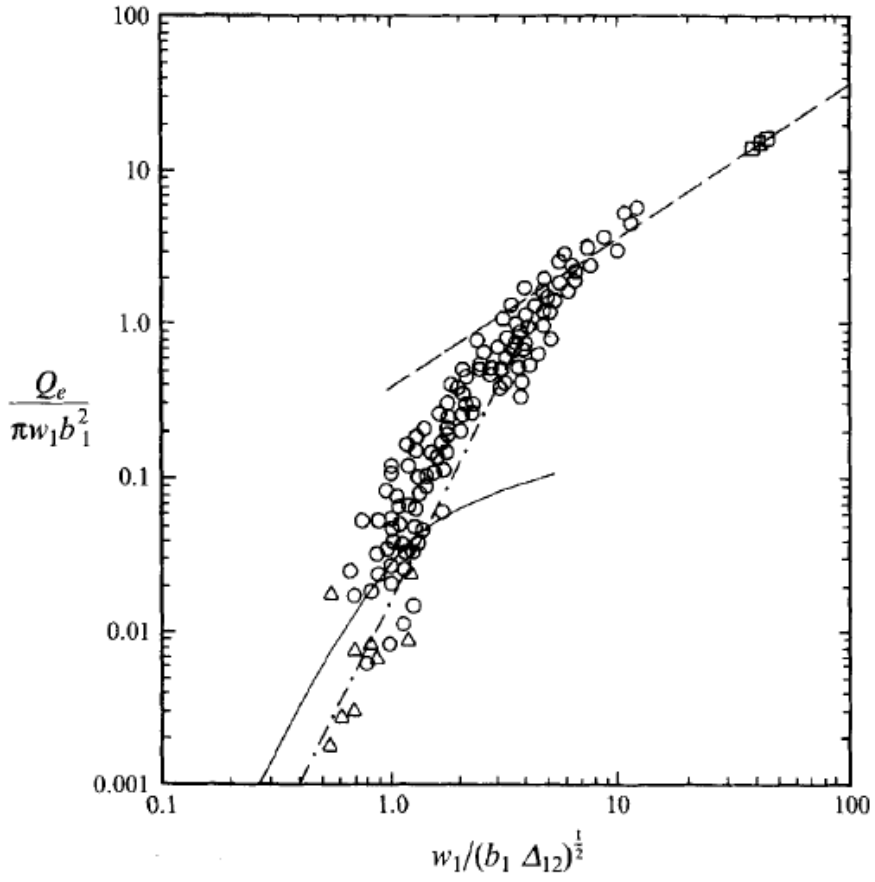


**Figure 3-73. Entrainment Rate Into a Fountain in Closed Chamber (Baines et al., 1993)**

The various lines include the previous relationships from Baines (1975) (dash-dot line) and from Kumagi (1984) (sloid line). The top long-dash line is given by

$$\frac{Q_e}{Q} = 0.363\ Fr_{r,i}$$

The fit to the entrainment rate data can be split into two regions. For $Fr_{r,i} > 5$, the above equation is applicable. For $Fr_{r,i} < 5$, the following expression is appropriate

$$\frac{Q_e}{\pi u_1 b_1} = 0.08\ Fr_1^3$$

where

$$Fr_1 = \frac{u_1}{(b_1 \Delta_{12})^{1/2}}$$

and $u_1$ is the centerline jet velocity, $b_1$ is the jet radius where the velocity goes to (1/e) of the centerline value, and $\Delta_{12}$ is the density difference between the jet and the fluid above interface. The interface parameters are calculated using the entrainment equations with a constant Gaussian entrainment coefficient of 0.057 for a jet ($\alpha$) considering momentum flux at source and momentum reduction by buoyancy. Note that the above entrainment equation has the same cubic relationship as Baines (1975) and Kumagi (1984) with a larger constant.

Models for the position of the front and the mean buoyancy below the interface are derived in the paper; data-model comparisons are shown in Figure 3-74 to Figure 3-76 showing very good agreement.

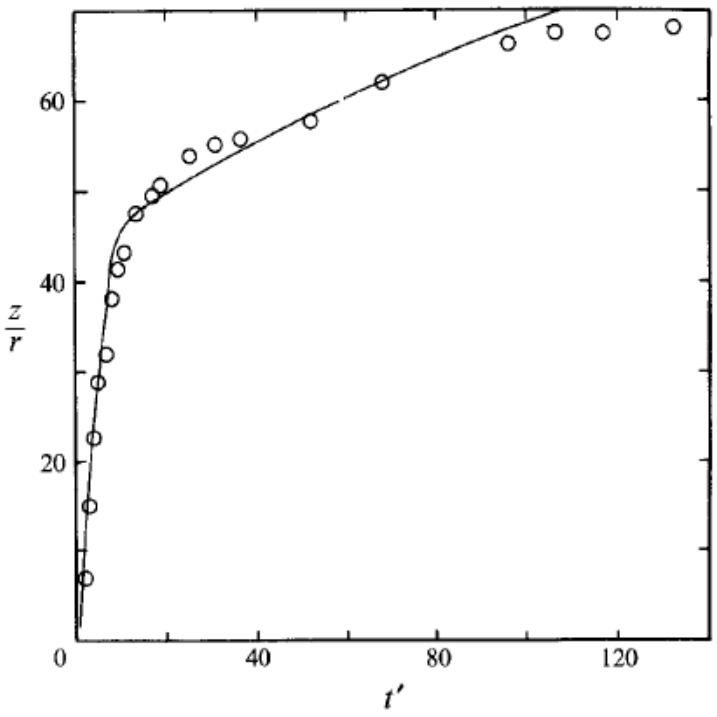


**Figure 3-74. Position of the First Front in a Closed Chamber (Baines et al., 1993)**

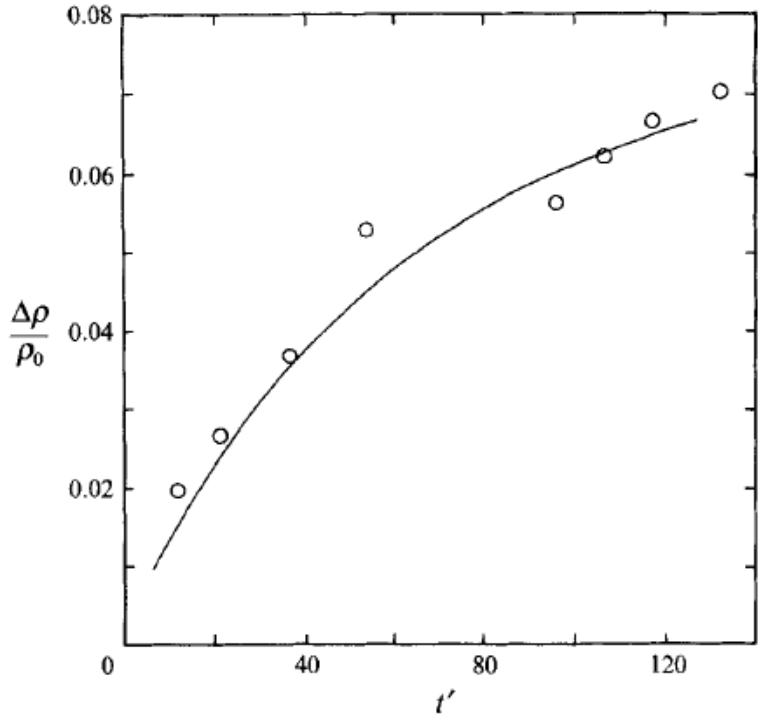


**Figure 3-75. Buoyancy Difference Across the Front in a Closed Chamber (Baines et al., 1993)**

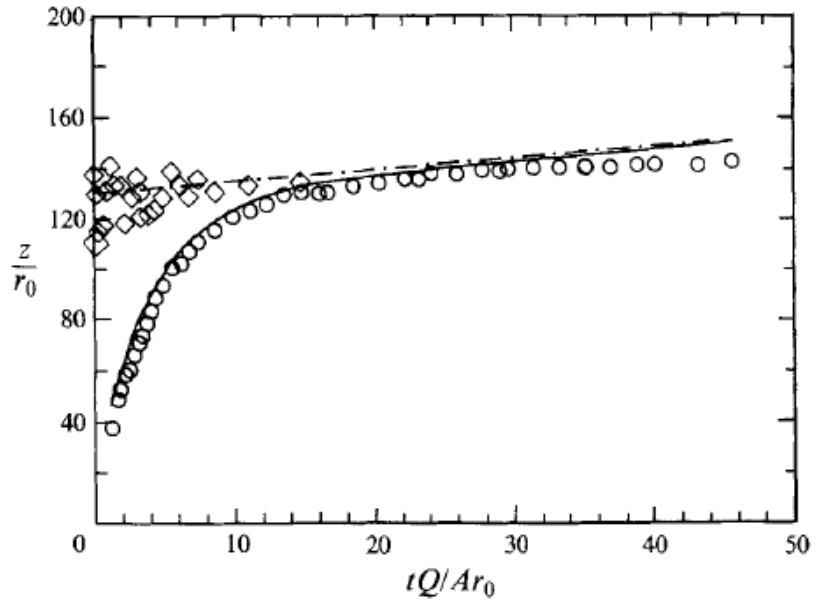


**Figure 3-76. Data-Model Comparisons for the Position of the Front (o) and the Top of the Fountain (◇) (Baines et al., 1993)**

#### 3.1.5.2 Application to SPR

Some of the enclosure models above may be applicable to SPR. The model of Barnett (1991) may be very useful for neutral and positively-buoyant jets in that the geometry is very similar to SPR caverns. Splitting the behavior into 3 regions may be very useful. The work of van Sommerton et al. (2012) in the turbulent diffusion region could be used. The open chamber model of Baines et al. (1993) may be of some use for negatively-buoyant jets for entrainment into the jet and for entrainment across interfaces. Any use of the jet entrainment function would need to be validated for SPR-specific geometry and conditions.

## 3.2 Rayleigh-Taylor Instability

Rayleigh-Taylor instability occurs when a fluid of a higher density is placed over a fluid of a lighter density in the vertical direction. Such a situation can occur in SPR caverns when a fluid of a different density is introduced into the cavern during filling or degas operations. The fluids mix by interchange of "packets" of fluids that penetrate the other.

### 3.2.1 Cook and Dimotakis

Cook and Dimotakis (2001) performed some instructive Direct Numerical Simulations (DNS) of Rayleigh-Taylor instability for miscible fluids in an enclosure. The cross-sectional area is a square of transverse dimension $L$ with an enclosure height 2.46 $L$; the initial interface in the middle. The Schmidt number was specified as 1.0 to approximate gas mixing. The density ratio of the fluids was 3.0 for these simulations.

In this case, the half-height of the enclosure, which is appropriate for the growth of the mixing layer from the initial interface, is 1.23 times the enclosure width, and the results are considered to be unconfined. Figure 3-77 shows the mixing of the two fluids out to a non-dimensional time of $t/\tau = 4.63$, where $\tau$ is the characteristic mixing time

$$\tau = \left(\frac{L}{A\ g}\right)^{1/2}$$

and $L$ is the is the transverse dimension and $A$ is the Atwood number.

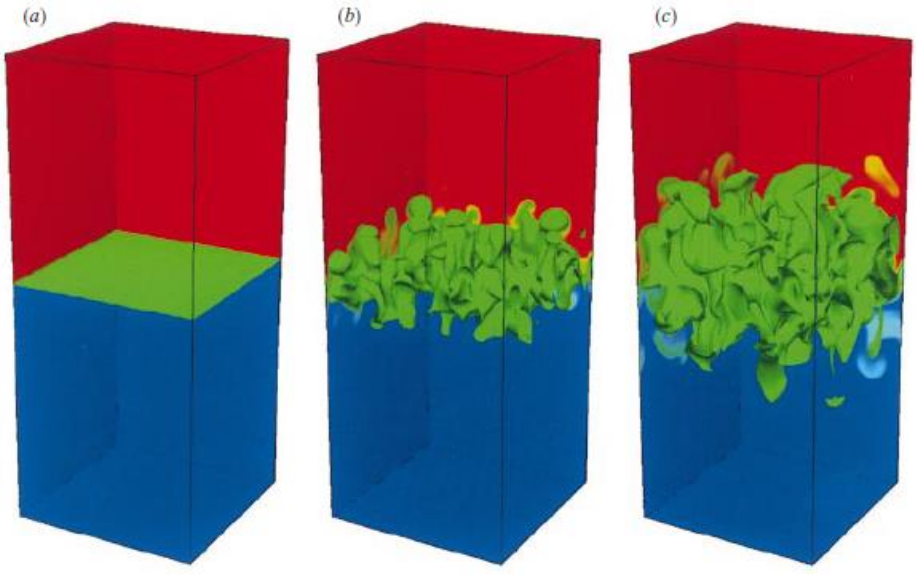


**Figure 3-77. Time-evolution of Rayleigh-Taylor Instability. Pure heavy fluid is red, pure light fluid is blue, intermediate (equal light and heavy) fluid is green. Times for the images: (a) t/τ =0., (b) t/τ =3.44, (c) t/τ =4.63. (Cook and Dimotakis, 2001)**

The Atwood number, *A*, is basically the driving for mixing and is given by

$$A = \frac{\rho_2 - \rho_1}{\rho_2 + \rho_1} = \frac{\Delta\rho}{2\bar{\rho}}$$

Using R = $\rho_2/\rho_1$,

$$A = \frac{R-1}{R+1}$$

and the Atwood number for this case is equal to 0.5.

As shown in Figure 3-77, the fluids mix above and below the original interface. Three cases were run with different initial interface perturbation fields where the length-scale of the perturbations got smaller with each case. The results for Case C, which had the smallest perturbation length-scale, are shown above.

Figure 3-78 shows the extent of vertical mixing for Case C, where z/L is the normalized distance above and below the initial interface position. Mixing seems to be essentially linear between the two fronts that propagate away from the initial interface.

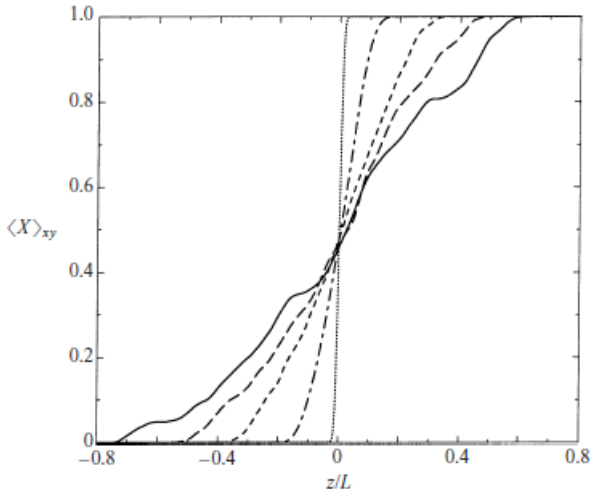


**Figure 3-78. Time-evolution of horizontally-averaged mole fraction. Lines are for t/τ = 0., 2.26, 3.40, 3.95, 4.52 (Cook and Dimotakis, 2001)**

Figure 3-79 shows the distribution of the mixing profile as a function of normalized distance from the original interface for Case C. As mentioned above, the profile is essentially linear over much of the mixing zone with tails at both ends.

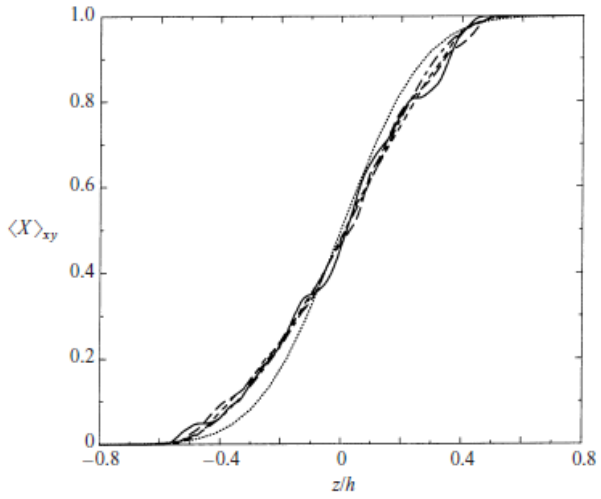


**Figure 3-79. Time-evolution of horizontally-averaged mole fraction. Lines are for t/τ = 0., 2.26, 3.40, 3.95, 4.52 (Cook and Dimotakis, 2001)**

Figure 3-80 shows the time evolution of the height of the mixing zone from the original interface. At early times ($t/\tau < \sim 1$), the growth of the mixing zone is diffusive and is proportional to $t^{1/2}$. At later times ($t/\tau > \sim 1$), mixing grows at a much faster rate and is proportional to $t^2$.

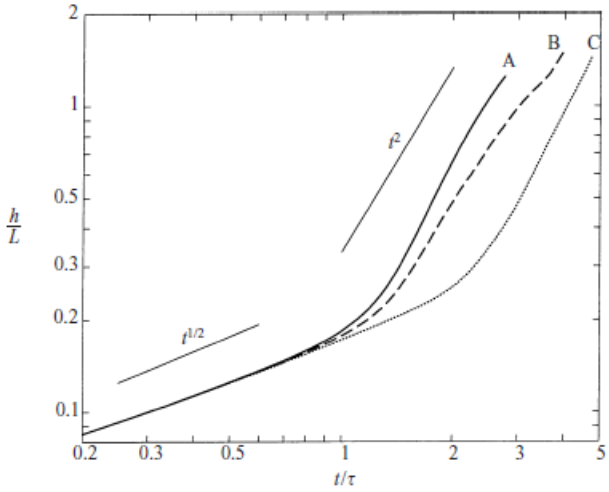


**Figure 3-80. Mixing zone height evolution. (Cook and Dimotakis, 2001)**

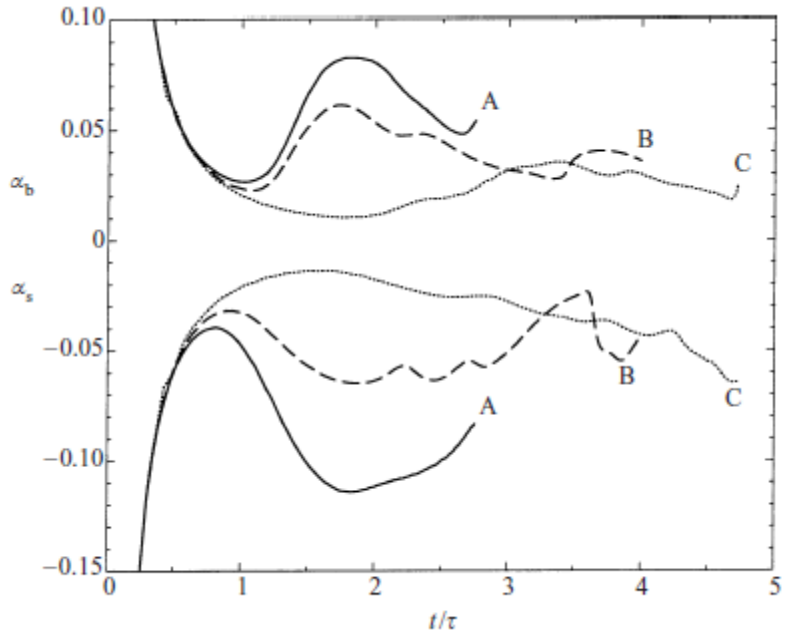


**Figure 3-81. Growth Coefficients, α. (Cook and Dimotakis, 2001)**

The depth of the mixing is given by

$$h = \alpha\, A\, g\, t^2$$

where $h$ is the depth of the mixing layer from the origin and $\alpha$ is the growth coefficient.

Values of the growth coefficient, $\alpha$, from the simulation are shown in Figure 3-81 where the top sets of lines are for bubbles, or the upward mixing, and the bottom set of lines are for the spikes, or the downward mixing. After the initial diffusive region ($t/\tau \leq 1$), the value of $\alpha$ is typically between 0.02 and 0.10. For Case C, after the initial diffusive region, the average value is about 0.03 for upward and downward mixing.

### 3.2.2 Linden et al.

Linden (Linden and Redondo, 1991, Linden et al., 1994) conducted physical experiments and numerical simulations at conditions more of interest to the present situation due the more moderate Atwood number. They conducted experiments in a tank 500 mm deep, 400 mm long, and 200 mm wide using brine and fresh water. In these experiments, the Atwood number varied between 1. x $10^{-4}$ and 5. x $10^{-2}$. Figure 3-82 shows the mixing zone behavior in an experiment where a small amount of milk was added to the bottom layer for visualization purposes. At $\tau$=0.5, the two-dimensional disturbance by the removal of the plate between the fluids is clearly seen. Three-dimensional behavior is clearly seen at the later times.

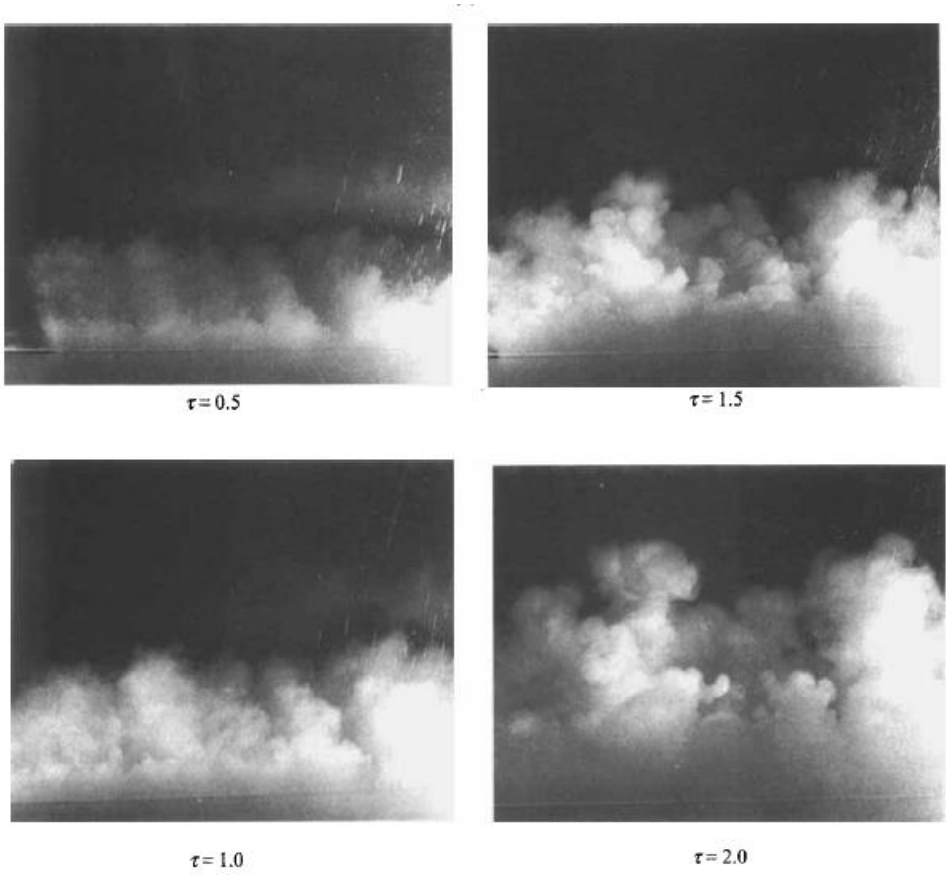


**Figure 3-82. Time evolution of interface mixing in experiments (Linden et al., 1994)**

Figure 3-83 shows the results from the experiments for the growth of the mixing zone height. The fit to the Linden et al. (1994) experimental data given on Figure 3-83 results in an $\alpha$ value of 0.044.

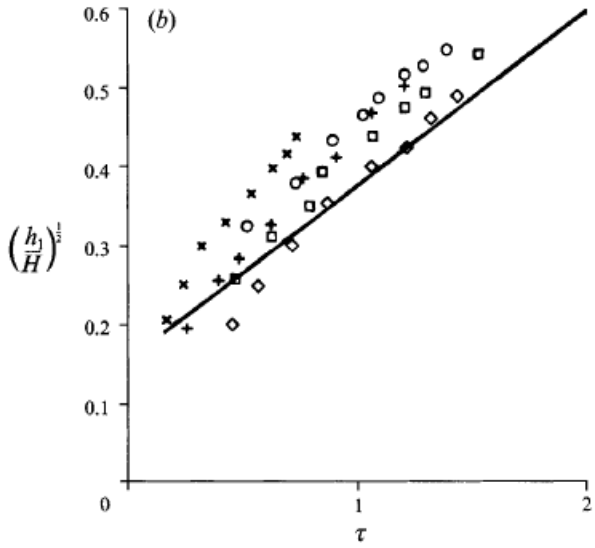


**Figure 3-83. Time evolution of mixing height (Linden et al., 1994)**

Note that Linden et al. (1991, 1994) use a different dimensionless time than used by others; in their results, they use the enclosure height as the characteristic dimension, or

$$\tau = \left(\frac{H}{A\,g}\right)^{1/2}$$

instead of the transverse dimension of the enclosure.

Linden and Redondo (1991) discuss the mixing efficiency of their experiments determined by the potential energy change. The potential energy is defined as

$$P \equiv g \int_0^H z\,(\rho(z) - \rho_2)\,dz$$

where $\rho_2$ is the density of the lower fluid and $H$ is the full height of both layers. The initial value of the potential energy is given by

$$P = \frac{3}{4} P_o$$

and

$$P_0 \equiv \frac{1}{2} g \Delta\rho H^2$$

For no mixing between the fluids, the final value of P is ¼ $P_o$ while for complete mixing with a final uniform density the final value of P is ½ $P_o$. The mixing efficiency is defined as

$$\eta \equiv \frac{P - \frac{1}{4}P_o}{\frac{1}{2}P_o}$$

The mixing efficiency as a function of Atwood number in their experiments varies from values less than 10% to about 50%. Note that for complete mixing, the value of mixing efficiency would be 50%.

The mixing efficiency values given by Linden and Redondo (1991) above may be misleading. As discussed by Linden et al. (1994), the circulation induced by the removal of the fluid barrier in the experiment may have reduced the mixing efficiency in the experiments. The values from the numerical code are 47 and 48%, or practically complete mixing.

### 3.2.3 Dalziel et al. (2008)

The above investigations are for unconstrained mixing. However, in an SPR cavern, the presence of walls may influence the mixing process. Dalziel et al. (2008) investigated Rayleigh-Taylor mixing in a high aspect ratio vertical square tube both experimentally and numerically. The square tube is 50 mm on a side and 2 m long. The initial density interface is in the middle of the tube, so the aspect ratio relative to the initial interface location is (*H/2d*) is 20, or (*2d/H*) of 0.05. The experiments are for salt water over fresh water with Atwood numbers of 0.005, 0.01, 0.02, and 0.038.

Due to the experimental procedure where the tube was overturned after the fluids were in place, the initial unconfined mixing period where the mixing zone height is less than the tube width was not observed. The experimental results for an Atwood number of 0.01 are shown in Figure 3-84 including a close-up near the interface at an early time.

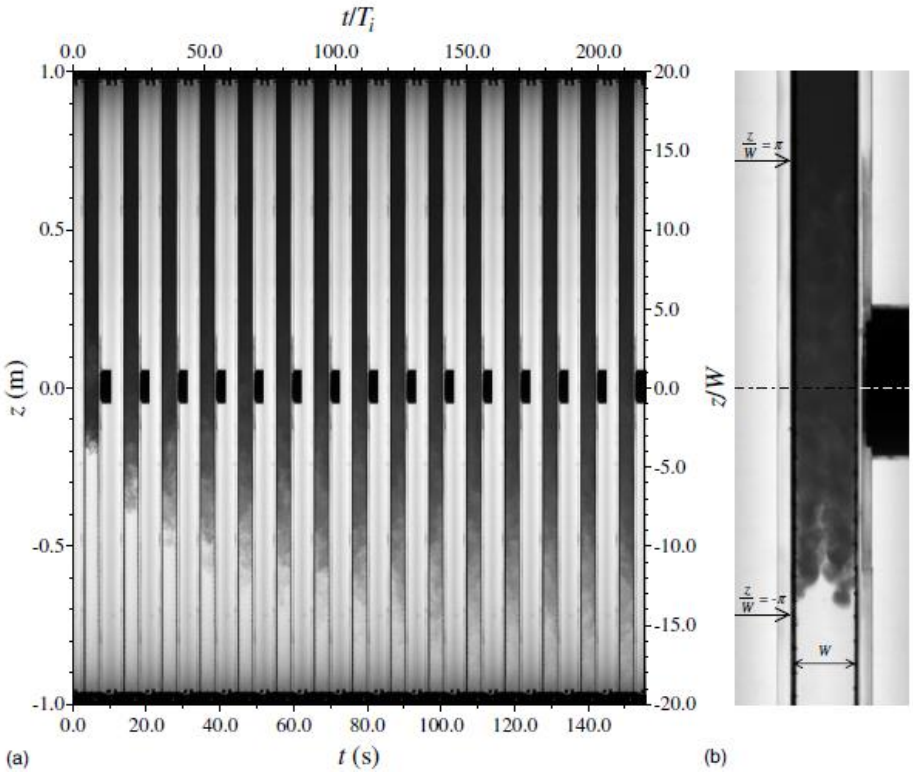


**Figure 3-84. Initial Instability Growth for A=0.01 (Dalziel et al., 2008)**

The height of the mixing zone for this experiment is shown in Figure 3-85 based on the concentration scale. Fits to various time functions are also shown.

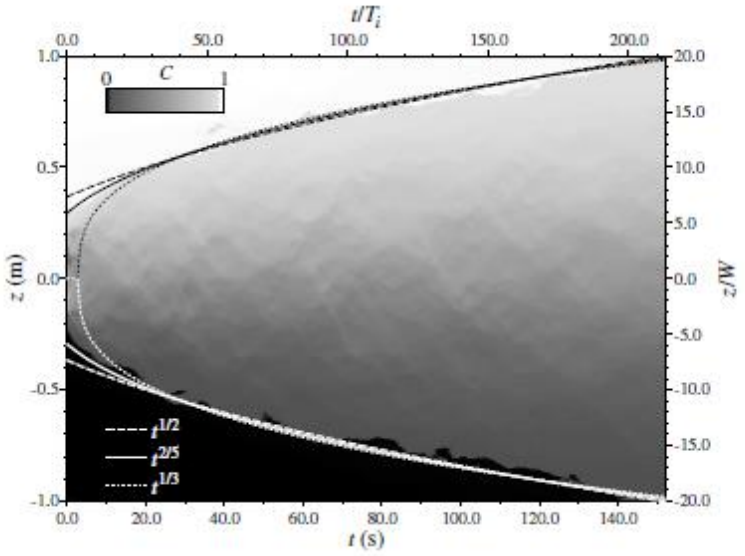


**Figure 3-85. Height of the Mixing Zone for A=0.01 (Dalziel et al., 2008)**

The initial unconstrained mixing is expected to follow the relationship

$$\frac{h}{W} = \alpha \left(\frac{t}{\tau}\right)^2$$

where

$$\tau = \left(\frac{W}{A\,g}\right)^{1/2}$$

and *W* is the transverse dimension. Subsequent to this unconstrained growth region, the growth relationship is given by

$$\frac{h}{W} = \alpha_{confined} \left(\frac{t}{\tau}\right)^{2/5}$$

where the transition is expected at h/W ~ 1. The mixing region growth for all the experiments is shown in Figure 3-86. Note that *W* is 0.050 m in these experiments. From these results, the value of $\alpha_{confined}$ in the above equation is approximately 2.4 from Figure 3-85. A comparison of the unconstrained and constrained growth rates is given in the next section.

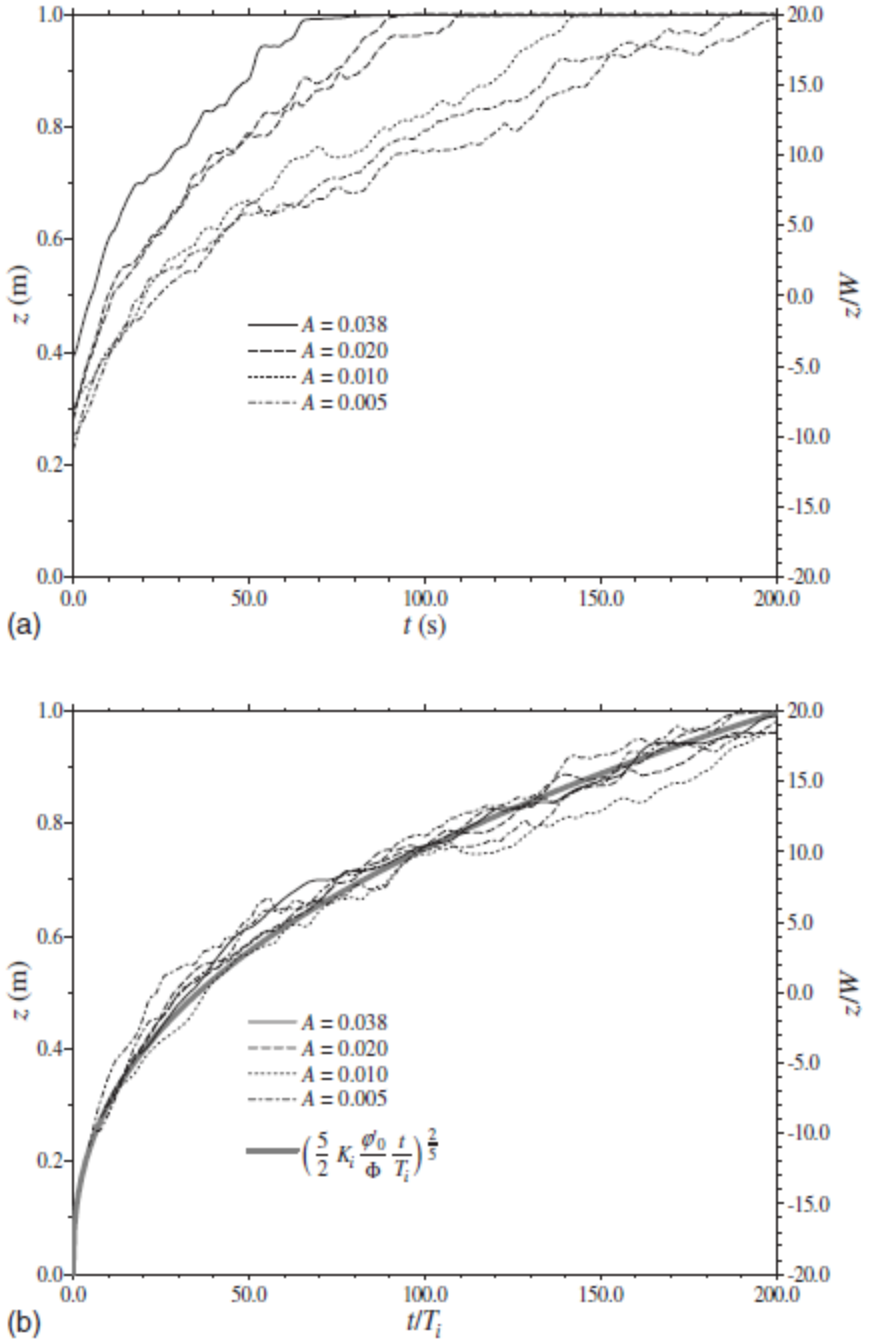


**Figure 3-86. Evolution of the Mixing Zone Height (a) experimental time (b) scaled time (Dalziel et al., 2008)**

Note that the mixing efficiency in these experiments is about 50%, or complete mixing.

### 3.2.4 Application to SPR

Based on the work of Dalziel et al. (2008) for constrained mixing, the characteristic time for the Rayleigh-Taylor mixing of two miscible fluids in an SPR cavern is given by

$$\tau = \left(\frac{\mathrm{W}}{A\,\mathrm{g}}\right)^{1/2}$$

where *W* is the transverse dimension (cavern diameter for SPR) and *A* is the Atwood number, which is given by

$$A = \frac{\rho_1 - \rho_2}{\rho_1 + \rho_2} = \frac{\Delta\rho}{2\bar{\rho}}$$

If W=200 feet, and $\Delta\rho/\bar{\rho}$=1% (A=0.005), the characteristic time is about 35 seconds. If $\Delta\rho/\bar{\rho}$=0.01% (A=0.0005), the characteristic time is about 350 seconds.

The initial, unconstrained depth of the mixing is approximately

$$h = \alpha\, A\, g\, t^2$$

or

$$\frac{h}{W} = \alpha \left(\frac{t}{\tau}\right)^2$$

where $\alpha$ is in the range 0.01 to 0.07. Note that the fit to the Linden et al. (1994) experimental data results in an $\alpha$ value of 0.044.

Based on the results of Dalziel et al. (2008), transition from unconstrained to constrained mixing will occur at *h/W* ~ 1, or *h*=200 feet. Using an α value of 0.04, transition will occur at about 175 seconds for a cavern diameter of 200 feet and $\Delta\rho/\bar{\rho}$=1% (*A*=0.005).

After the transition, the mixing height is proportional to the time to the 2/5 power, or

$$\frac{h}{W} = \alpha_{confined} \left(\frac{t}{\tau}\right)^{2/5}$$

Using the $\alpha_{confined}$ value of 2.4 and $\Delta\rho/\bar{\rho}$=1% (characteristic time of 35 seconds), and a total cavern height of 2000 feet, the mixing height will equal one-half the cavern height at about 220 seconds. The results seem to be contradictory in that the constrained growth seems to be faster than unconstrained growth.

The problem is seen in Figure 3-87 below, which plots the unconstrained and constrained relationships used above. The constrained relationship increases faster than the unconstrained relationship for dimensionless times less than about 13. Note that as shown earlier in Figure 3-85, the fit through the experimental data does not goes through 0 time, so there is an implied time offset where the fit might not be appropriate. In the present estimate, the transition between unconstrained and constrained growth will be made at an h/W of 1.0, which occurs at a dimensionless time of 5 for $\alpha$=0.04. Subsequently, the constrained curve will be zeroed out at the unconstrained results, or

$$\frac{h}{W} = \alpha_{confined} \left(\frac{t}{\tau}\right)^{2/5} - 4.57 + 1.0$$

where 1.0 is the unconstrained h/W value at the transition dimensionless time of 5 and 4.57 is the constrained h/W value for a dimensionless time of 5. This hybrid relationship is shown in Figure 3-88. So, in the present case, h/W equals 5, and the dimensionless time is 24.1, or a time of 840 seconds. In the overall scheme of SPR caverns, a time of 840 seconds, or 14 minutes, is negligible. Even if the Atwood number is 10 times smaller, the mixing time of 140 minutes is still insignificant for SPR caverns.

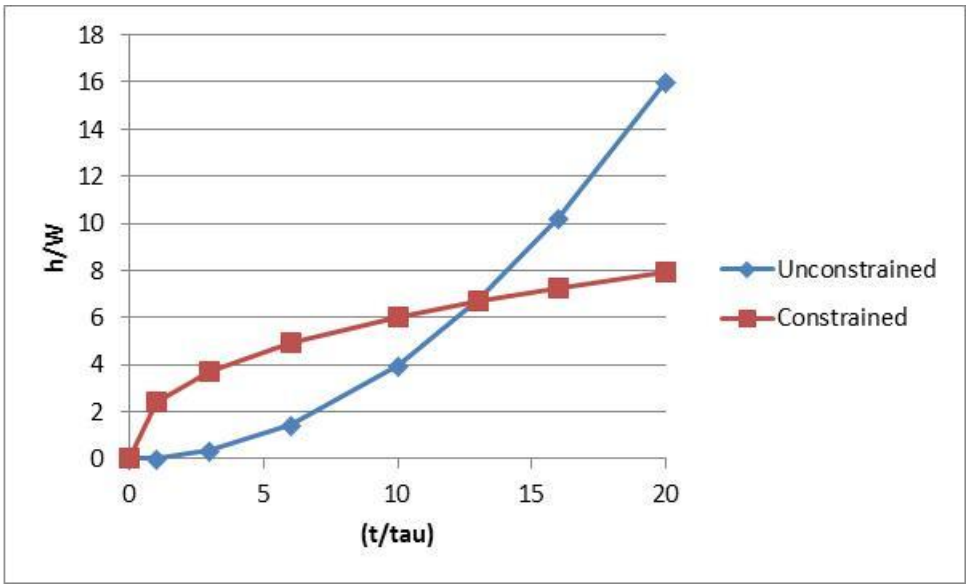


**Figure 3-87. Unconstrained and Constrained Relationships for Mixing Height**

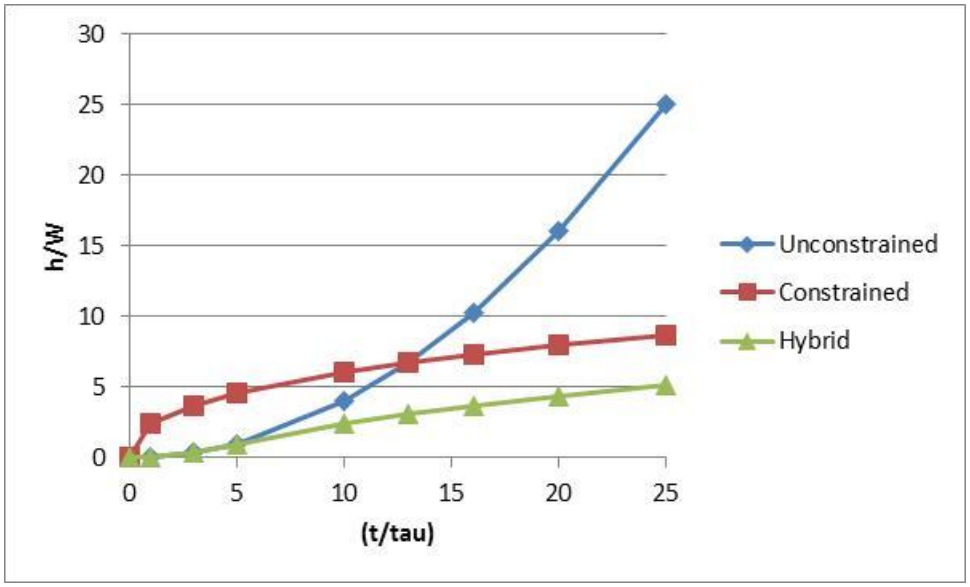


**Figure 3-88. Hybrid Mixing Height Relationship**

## 3.3 Coriolis Force

### 3.3.1 General Characteristics

The Coriolis force acceleration vector is the cross product of the vector components of the velocity and the Coriolis force. For the earth rotating on the north-south axis, consider a local coordinate system on a compass scale as shown in Figure 3-89. The x-axis is east, the y-axis is north, and the z-axis is straight up (Wikipedia, Coriolis effect). The rotation vector and the velocity vectors are given by

$$\Omega = \omega \begin{pmatrix} 0 \\ \cos\phi \\ \sin\phi \end{pmatrix}$$

$$\mathrm{V} = \begin{pmatrix} \mathrm{v}_x \\ \mathrm{v}_y \\ \mathrm{v}_z \end{pmatrix}$$

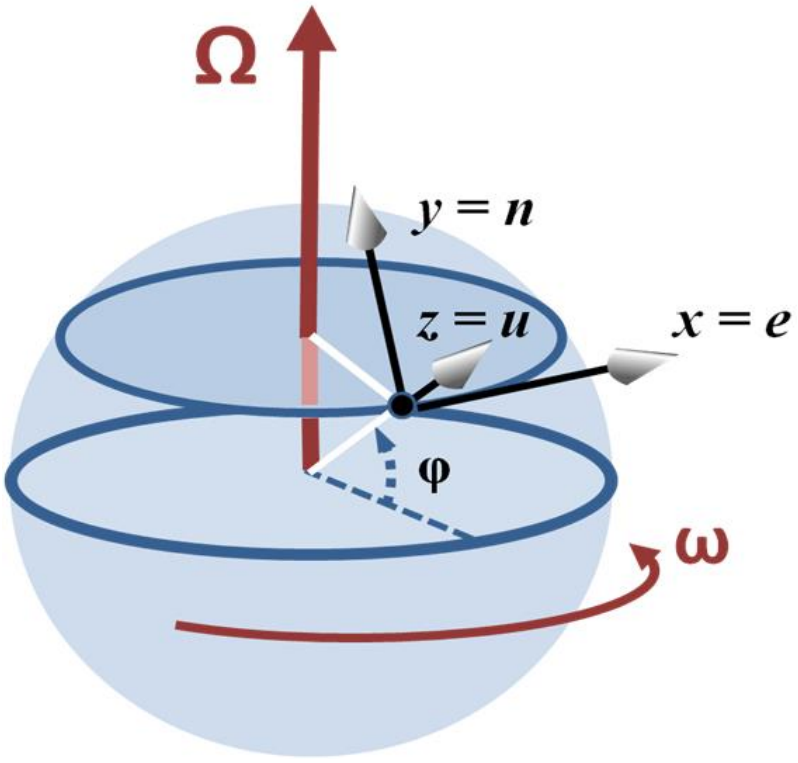


**Figure 3-89. Coriolis Force Coordinate System (Wikipedia – Coriolis Force)**

and the Coriolis acceleration is given by

$$a_C = -2\Omega \times V = 2\omega \begin{pmatrix} v_y \sin\phi - v_z \cos\phi \\ -v_x \sin\phi \\ v_x \cos\phi \end{pmatrix}$$

where $\phi$ is the latitude and ω is the planetary rotation angular velocity of 7.27 x $10^{-5}$ /sec. SPR caverns are located at latitudes of approximately 30°.

The Coriolis acceleration vector is

$$a_c \boldsymbol{i} = 2\omega\left(v_y \sin\phi - v_z \cos\phi\right) = 7.27\ x\ 10^{-5} v_y - 1.26\ x\ 10^{-4} v_z \ \left(\frac{1}{s}\right)$$

$$a_c \boldsymbol{j} = -2\omega\, v_x \sin\phi = 7.27\ x\ 10^{-5} v_x \ \left(\frac{1}{s}\right)$$

$$a_c \boldsymbol{k} = 2\omega\, v_x \cos\phi = 1.26\ x\ 10^{-4} v_x \ \left(\frac{1}{s}\right)$$

The vertical component of the Coriolis acceleration, 2 ω $v_x$ cos $\phi$, can be compared to the gravitational acceleration. Using a 1% criterion for the Coriolis force to be insignificant, and comparing the value to the gravitational acceleration of 32.2 ft/s$^2$ (9.8 m/s$^2$), $v_x$ would need to be 2500 ft/s (750 m/s) for the Coriolis force to be 1% of the gravitational force. For anything less, the Coriolis force in the vertical direction is less than 1% of the gravitational force, or negligible. Because the jet velocity is a maximum of 16.3 ft/s at the exit as given in Table 3-4, the vertical component of the Coriolis force is negligible.

The other components in the x and y directions may be important depending on the magnitude and duration. In consideration of these directions, the Rossby number is evaluated.

The dimensionless Rossby number is used to measure the importance of the Coriolis force, or

$$Ro = \frac{U}{Lf}$$

which is the ratio of the inertial forces to the Coriolis force where U is the characteristic velocity, L is the characteristic length scale, and f is the Coriolis frequency. The U/L ratio is the inverse of the fluid motion time scale, which is compared to the planetary rotational speed. A large Rossby force indicates that the effect of the Coriolis force is small, or that the fluid motion time scale is small compared to the planet rotational time scale. Similarly, a small Rossby number indicates that the Coriolis force may be important.

The Coriolis frequency can be written as

$$f = 2\omega sin\phi$$

where $\phi$ is the latitude and $\omega$ is the planetary rotation angular velocity of 7.27 x $10^{-5}$ /sec. SPR caverns are located at latitudes of approximately 30°, so $f$ = 7.27 x $10^{-5}$ /sec.

### 3.3.2 Application to SPR

The characteristic time of the SPR jet needs to be evaluated. We can use the velocity decay curve given by Risso and Fabre (1997) for a confined jet as shown earlier in Figure 3-56. For simplicity, a linear variation in the centerline velocity from $z$=0 to $z$=3.6 $D$ will be assumed, which underestimates the velocity in the near field. The time is simply the distance over the velocity, or

$$dt = \frac{dz}{u} = \frac{dz}{u_0\left(1. - \frac{z}{3.6\ D}\right)}$$

Integrating gives

$$\Delta t = -\frac{3.6\ D}{u_0}\log\left(1. - \frac{z}{3.6\ D}\right)\Big|_0^{z^*}$$

The result can't be integrated all the way to 3.6 $D$ because the velocity becomes zero and the time becomes infinite. Taking $z$* equal to 3.5 $D$ gives

$$\Delta t = \frac{5.6\ D}{U_0}$$

So, for $U_0$ of 16.3 ft/s and $D$ of 200 ft, the time is about 70 secs. The Rossby number is then

$$Ro = \frac{u}{Lf} = \frac{\frac{1}{70}\ \frac{1}{s}}{7.27\ x\ 10^{-5}\ \frac{1}{s}} = \sim 200$$

Because the Rossby number is large, the impact of the Coriolis force is small.

## 3.4 Summary

Current data and approaches to jet/plume behavior including interaction with interfaces are generally only directly applicable to situations without significant confinement such as would be present in SPR caverns. For negatively-buoyant jets in an SPR cavern, density differences of greater than 0.1% are expected to behave like free jets, and confinement is expected to have minimal effect on the jet behavior. For smaller density differences and for neutral and positively-buoyant jets, the effect of confinement is expected to be significant. Limited studies have investigated the influence of confinement on jet characteristics, but these studies are limited to a neutral jet (Risso and Fabre, 1997) and a positively-buoyant jet (Barnett, 1991). Negatively-buoyant jets in an enclosure have been studied by Baines et al. (1993), but the treatment is more empirical than theoretical regarding jet behavior.

Buoyant jet behavior is often analyzed through the entrainment numerical approach. This method probably has limited application to SPR because they are only directly applicable to unconfined jets. However, these approaches could conceivably be used to simulate SPR-specific confined flow data to obtain SPR-specific values of the entrainment coefficients.

Some of the enclosure models above may be applicable to SPR. The model of Barnett (1991) may be very useful for neutral and positively-buoyant jets in that the geometry is very similar to SPR caverns. The work of van Sommerton et al. (2012) in the turbulent diffusion region could be used. The open chamber model of Baines et al. (1993) may be of some use for negatively-buoyant jets for entrainment into the jet and for entrainment across interfaces. Any use of the jet entrainment function would need to be validated for SPR-specific geometry and conditions.

For Rayleigh-Taylor instabilities in SPR caverns, data for confined conditions indicate that the time scale for mixing in this case in small and essentially negligible compared to general SPR time scales.

In addition, the Coriolis force is small for SPR caverns and can be ignored.

## 3.5 Nomenclature

$A$ – flow area, constant

$b_T$ – thermal jet radial length scale

$b$, $b_w$ – velocity jet radial length scale

$B$ – buoyancy flux, constant

$c_p$ – plume growth coefficient

$C$ – concentration, constant

$d$ – diameter or constant

$D$ - diameter

$e$ - constant

$f$ - frequency

$Fr$ – Froude number

$g$ – acceleration due to gravity

$g'$ – effective gravitational acceleration

$h$, $H$ - height

$l_M$ – plume length scale for uniform environment

$l_Q$ – jet length scale for uniform environment

$L$ – length scale

$Ljet$ – jet length scale for stratified environment

$Lplume$ – plume length scale for stratified environment

$m$ - specific momentum flux, mass

$M$ – momentum flux

$N$ – Brunt-Vaisala frequency

$P$ – potential energy

$Q$ – volume flux

$r$ - radius

$R$ – length scale

$Re$ – Reynolds number of jet

$Ri$ – Richardson number

$Ro$ – Rossby number

$S$ – ratio of length scales to $8^{th}$ power for stratified environment

$t$ – time

$u$- axial velocity

v, V - velocity

$W$ – width

y – radial distance

z, Z – axial distance

$\alpha$ – entrainment coefficient, Rayleigh-Taylor growth factor

$\beta$ – specific buoyancy flux

$\varepsilon$ – density stratification parameter

$\varepsilon'$ - gradient of density stratification parameter

$\rho$ – density

$\rho_o$ – reference density

$\mu$ – specific volume flux

$\bar{\mu}$ - dimensionless specific volumetric flux

$\zeta$ – dimensionless length scale

$\nu$ – viscosity

$\rho_0$ – reservoir fluid density

$\Delta\rho$ – density difference

$\rho_j$ – jet density

$\lambda$ – jet thermal to velocity length scale ratio

$\eta$ – mixing efficiency

$\tau$ – time constant

$\phi$ - latitude

$\omega$ - angular velocity

Subscripts

0 – initial value

1 – value with velocity to 1st power

2 – value with velocity to 2nd power

av – average

d - densimetric

G – Gaussian

I - interface

j - jet

m – maximum, mixed

p – plume

R - room

s - spreading

T – mean value

TH – top hat value

Superscript

* – entrained value

# 4 CFD Simulations of Cavern Mixing

Simple cavern oil mixing simulations were performed by Webb (2009a) using the Fluent CFD code. In addition, Webb (2009b) compared some of the results in this section generated using Fluent with predictions from Star-CD to evaluate the difference due to CFD codes. Both memos in their entirety are included in this report in the Appendix.

## 4.1 Summary of CFD Simulations

A simple 2-d axisymmetric model of a full-scale cavern was developed by Webb (2009a). He used the Fluent computational fluid dynamics (CFD) code to investigate the effect of the inlet oil density on mixing and degas efficiency including uniform initial oil density and oil stratification. The model is simple by design, and these initial results provide some insight into cavern mixing processes during degas.

The modeled cavern is 2000 ft high with a uniform diameter of 200 ft as shown in Figure 4-1 with a total capacity of 11.2 MMB. No brine layer is assumed to be present so the entire volume is oil. The injection is located 100 ft from the top of the cavern while the outlet is 200 ft from the bottom. The inlet and outlet strings are concentric with the cavern with radii of 1.0 ft (bottom inlet/outlet) and 1.5 ft (top inlet/outlet). For this study, properties of diesel (density = 730 kg/m$^3$ (45.6 lb/ft$^3$), dynamic viscosity = 0.0024 Pa-s, kinematic viscosity = 3.3cSt, molecular diffusivity = $10^{-9}$ m$^2$/s) are used. The degas inlet mass flow rate is 175 kg/s (130,000 BBL/day) for a cavern turnover time of 85.9 days.

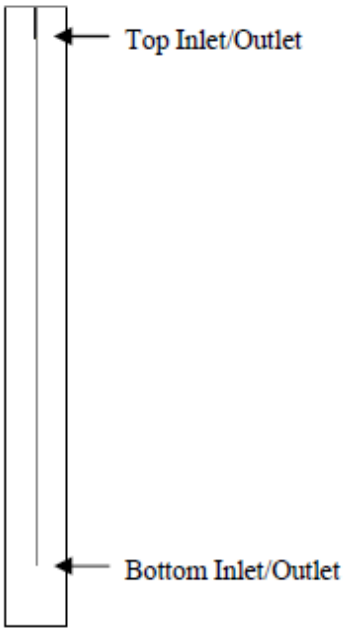


**Figure 4-1. Simplified Cavern Geometry**

## 4.2 Cavern Mixing and Degas Performance

Cavern mixing is dominated by two processes – mixing from the fluid jet as it enters the cavern at the inlet and mixing due to the buoyancy of the incoming fluid. As the fluid jet enters the cavern, mixing in the region just downstream of the inlet will occur. The length of this jet mixing region is affected by the buoyancy of the incoming fluid relative to the resident fluid. If the incoming fluid is lighter than the resident fluid, the incoming jet will reverse direction at some point and become a plume, and the mixed fluid will rise toward the top of the cavern. Conversely, if the incoming fluid is heavier than the resident fluid, the jet will continue downward toward the bottom of the cavern even when the jet momentum is dissipated. If the fluid densities are the same, the jet will continue downward until its momentum is dissipated, and mixing will occur in the region between the inlet and the position of jet momentum dissipation. Additional mixing may or may not occur if the jet/plume encounters a stratification boundary depending on the momentum of the jet/plume and the density difference across the stratification boundary. Mixing may also occur if the outlet location is located near a stratification boundary, which is often referred to as selective withdrawal, in which flow from the lower layer is "pulled up" into the outlet through the upper layer.

All of these mixing processes may affect the efficiency of any degas operation. Note that these processes are only approximated in this simple cavern degas mixing model. The geometry and inlet/outlet radii are greatly simplified as are the fluid properties. In addition, the nodalization used in the numerical model is not fine enough to capture all the details of the jet/plume mixing processes or the interactions between the fluid velocity and the stratification because the stratification boundary is often smeared by the numerics. Nevertheless, the present numerical model should give general trends and insight into degas operations.

The density of the injected fluid was kept constant during these simulations so the impact could be easily studied. Two types of plots are presented as shown in Figure 4-2.

1. The first plot shows the normalized bubble point (BP) at the outlet of the model, or at the degas plant. A normalized value of 1.0 is indicative of the pre-degas BP value, while a normalized value of 0.0 corresponds to the outlet BP value from the degas plant. A higher value of normalized BP indicates less mixing and better degas performance.
2. The second plot shows the fraction of processed oil in the entire cavern. If the value is 0.9, that indicates that 90% of the original oil in the cavern has been degassed. This value should increase as rapidly as possible, which indicates less mixing and better degas performance.

Lord and Rudeen (2007) have developed two cases for degas operations that tend to bound the results as discussed earlier. The best case for degas operations is plug flow. The injected oil pushes the initial resident fluid to the outlet, so the resident oil is processed first with no mixing between the two oils, so only a single cavern volume needs to be processed as shown

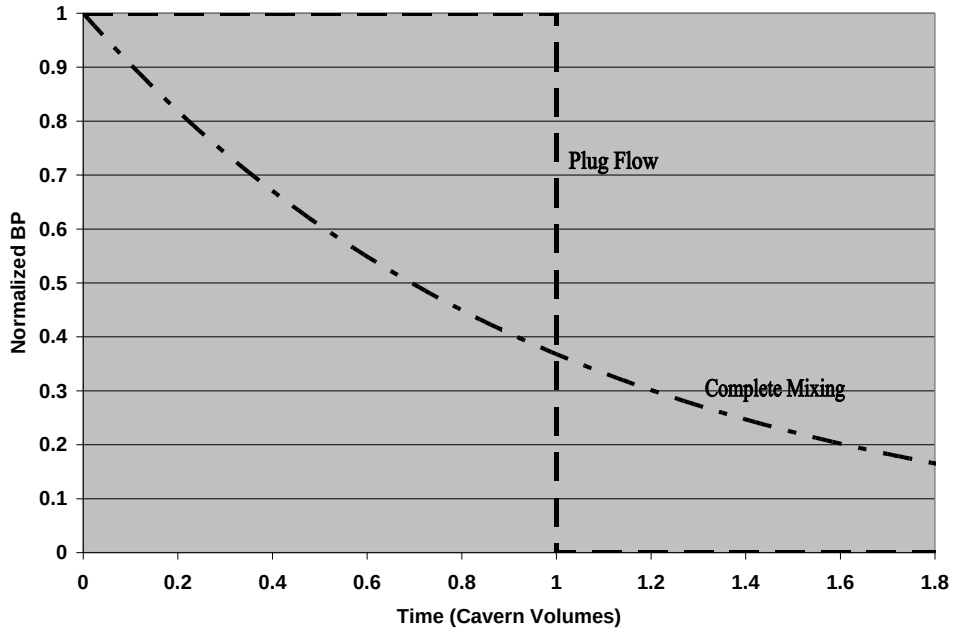


(a) Normalized Bubble Point (BP) Pressure Limits

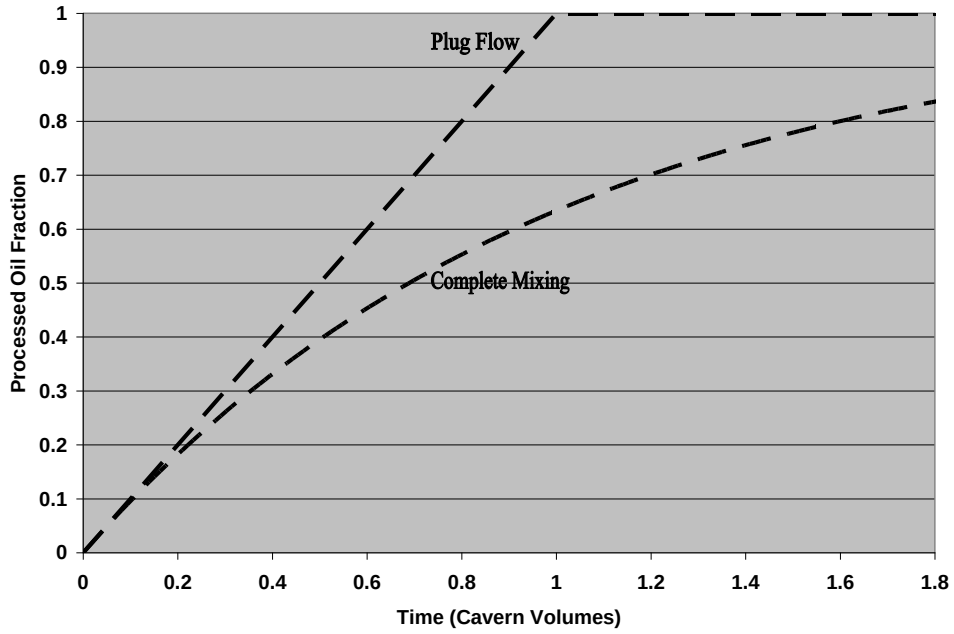


(b) Processed Oil Fraction Limits

**Figure 4-2. Plug Flow and Complete Mixing Limits for Degas Performance Curves**

by the "plug flow" line in Figure 4-2. The other limit is complete mixing of the injected fluid with the resident fluid. In this case, the withdrawn fluid includes some of the injected fluid, so the degas operation is less efficient than plug flow. This limit is shown in Figure 4-2 as the "complete mixing" line. In general, degas results should be between these two limits. Due to dead zones in the cavern and fluid stratification, degas performance can be below the complete mixing limit, but in general, complete mixing is the minimum degas performance. The difference is significant as can be seen for the time to process 80% of the oil. For the plug flow case, the time is 0.80 cavern volumes, while the time is 1.6 cavern volumes for the complete mixing case, or twice as long. The difference between the density of the injected fluid and the resident fluid varies from 0.0% (equal density), 0.01%, 0.1%, and 1.0% lighter and heavier.

Simulated degas performance results are shown below for the following cases of oil injection at the top of the cavern. Additional results are given in the Appendix.

1. Uniform Density Initial Conditions – all the oil initially in the cavern is at the same density with no stratification.
    a. Lighter oil injection at the top inlet – oil that is lighter than the original oil is added to the cavern near the top. Oil is withdrawn near the bottom of the cavern.
    b. Neutral density oil injection at the top inlet – the oil injected and the oil originally in the cavern are at the same density. Oil is added near the top of the cavern and withdrawn near the bottom of the cavern.
    c. Heavier oil injection at the top inlet – the oil injected near the top of the cavern is heavier than that initially in the cavern. Oil is withdrawn near the bottom.
2. Stratified Density Initial Conditions – the cavern is assumed to consist of equal volumes of a lighter oil over a heavier oil with a density difference of 0.1%.
    a. Injection of bottom layer oil at the top inlet – oil is withdrawn near the bottom of the cavern and injected near the top with no change in density. Because the oil in the bottom of the cavern is heavier than that in the top, the injected oil is heavier than the oil in the cavern at the injection location.
    b. Injection of lighter oil at the top inlet – oil that is lighter than either of the oil layers in the cavern is injected near the top of the cavern. Oil is withdrawn near the bottom of the cavern.

### 4.2.1 Uniform Density Initial Conditions

**Lighter Oil Injection**

The normalized BP and processed oil fraction results for injection of a lighter fluid at the top inlet are shown as a function of time in Figure 4-3. The difference between the density of the injected fluid and the resident fluid varies from 0.01% lighter, 0.1% lighter, to 1.0% lighter. The injected oil creates a jet that initially descends downward in the cavern. Due to the density difference, however, the jet turns around and rises to the top of the cavern as a plume. The processed oil fraction is relatively insensitive to the density difference as long as the injected fluid is lighter than the resident fluid.

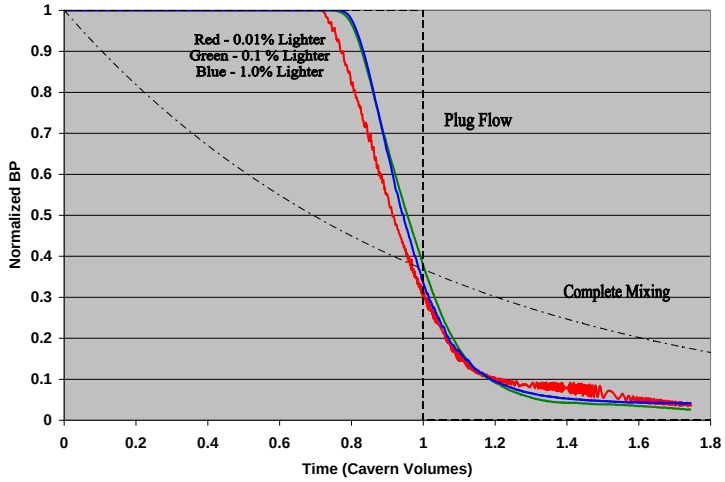


(a) Normalized BP Results

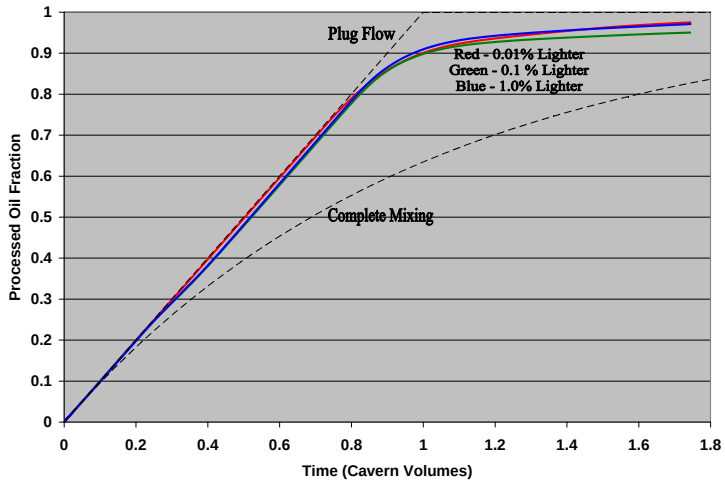


(b) Processed Oil Fraction Results

**Figure 4-3. Degas Performance Curve Results For Lighter Oil Injection – Top Inlet**

Both plots indicate a very efficient degas operation until about 80-85% of the resident fluid is processed similar to the plug flow case of Lord and Rudeen (2007). The difference after 0.85 cavern volumes is related to the outlet elevation and the fact that there is 90% of the resident fluid is above the outlet as well as dispersion of the plug flow "front" as seen in Figure 4-4.

Figure 4-4 shows contours of the injected oil mass fraction in the cavern as a function of time for the 0.1% lighter case. The mass fraction of initially resident oil to be degassed is simply 1.0 minus the injected oil fraction. Injection occurs near the top of the cavern while withdrawal occurs near the bottom. For the most efficient degas operation, the injected oil fraction should be minimized at the outlet in order to process the maximum amount of initially resident oil. The injected fluid is seen to rise to the top of the cavern, which pushes the resident oil to the outlet similar to plug flow conditions.

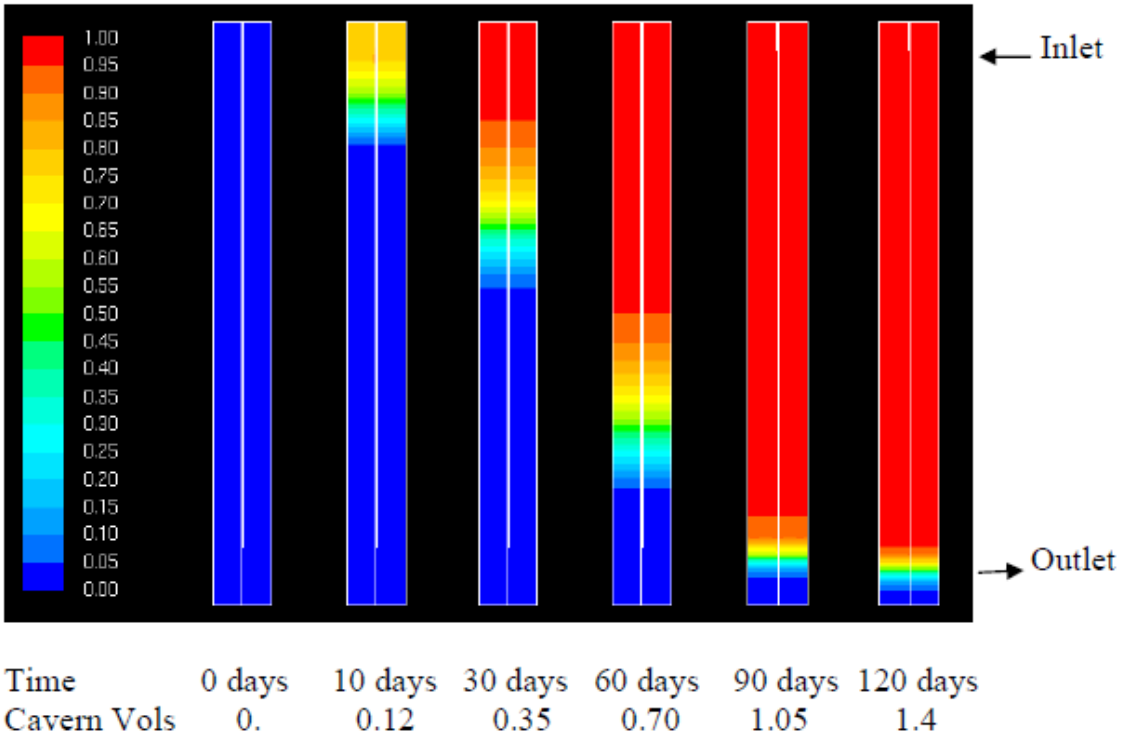


**Figure 4-4. Contours of Mass Fraction of Injected Fluid in Cavern (Lighter Oil Injection, Top Inlet)**

### Neutral Density Oil Injection

This case corresponds to the situation where the injected oil and the resident oil are at exactly the same density. The normalized BP and processed oil fraction results as a function of time for injection of a neutral density fluid at the top inlet are shown in Figure 4-5. The initial results are similar to plug flow up until about 0.5 cavern volumes; after that time, the results are about mid-way between plug flow and complete mixing.

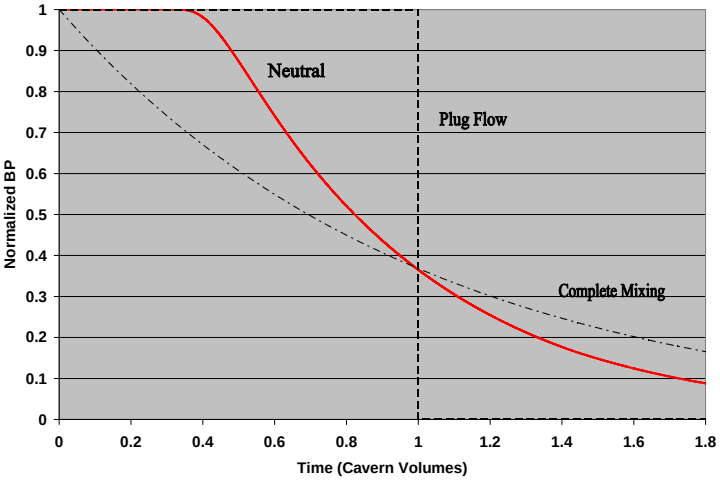


(a) Normalized BP Results

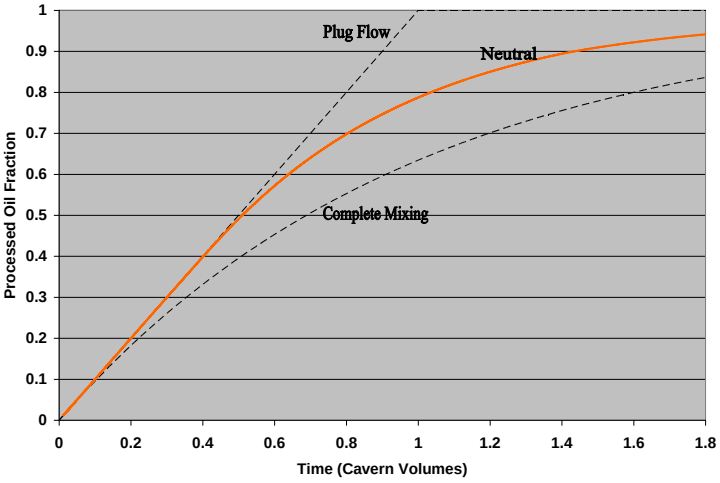


(b) Processed Oil Fraction Results

**Figure 4-5. Degas Performance Curve Results For Neutral Density Oil Injection – Top Inlet**

Figure 4-6 shows contours of the injected oil mass fraction in the cavern as a function of time for the neutral case. The initial jet of neutral density oil mixes about 1/3 of the cavern oil below the injection location. Below this location is a diffuse front of mixed oil. The front becomes more diffuse with time because there is no density difference between the injected and resident oil.

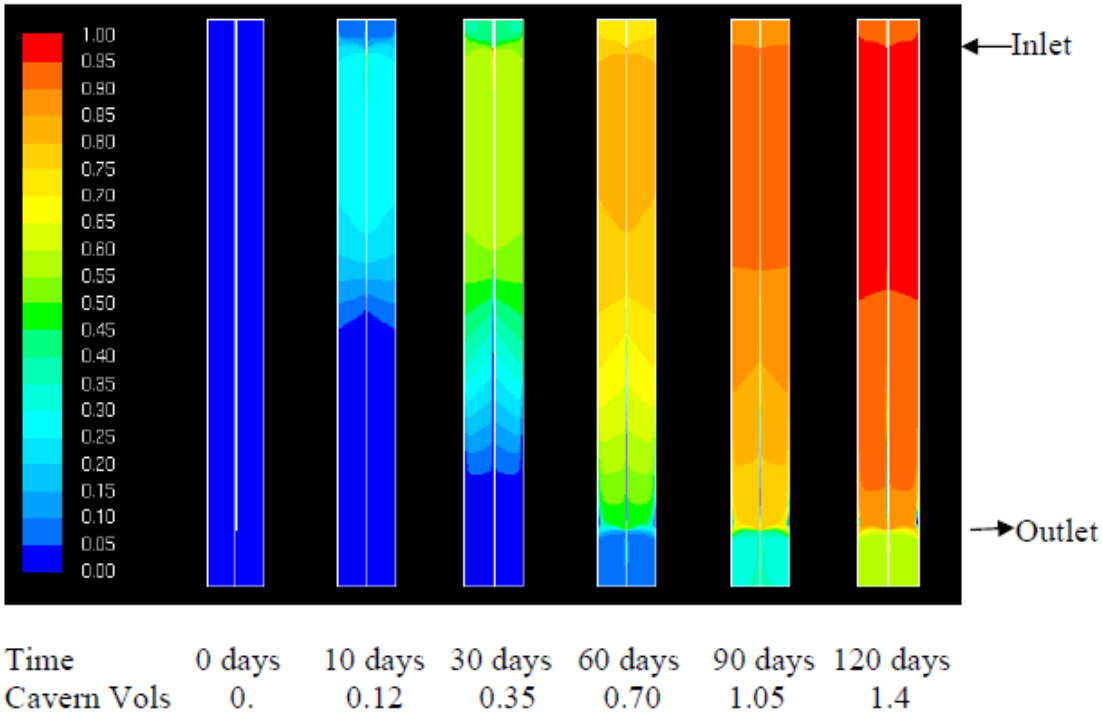


**Figure 4-6. Contours of Mass Fraction of Injected Fluid in Cavern (Neutral Density Oil Injection, Top Inlet)**

### Heavier Oil Injection – Top Inlet

The normalized BP and processed oil fraction results for injection of a heavier fluid are shown in Figure 4-7. The difference between the density of the injected fluid and the resident fluid varies from 0.01% heavier, 0.1% heavier, to 1.0% heavier. As shown in Figure 4-7, the results are similar to the complete mixing case with a minor influence on the density difference. The heavier injected fluid flows down to the bottom in the cavern promoting large scale mixing.

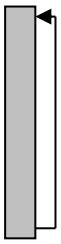

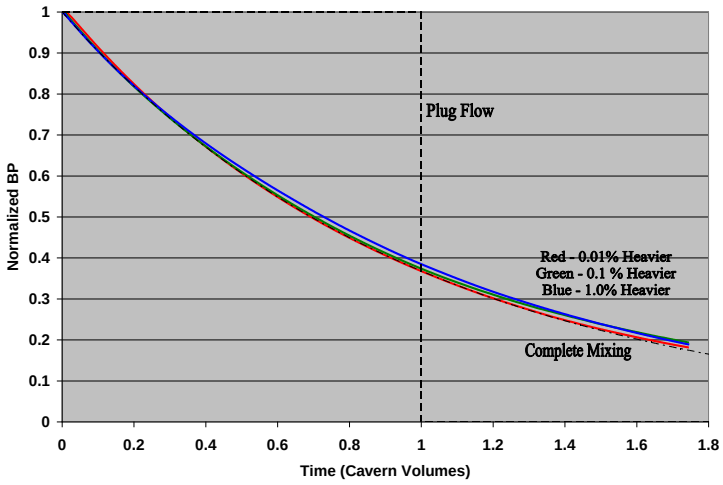


(a) Normalized BP Results

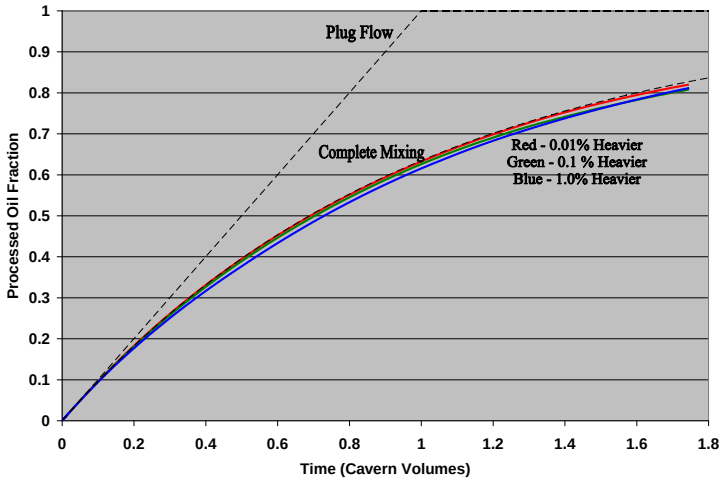


(b) Processed Oil Fraction Results

**Figure 4-7. Processed Oil Fraction vs. Time For Heavier Oil Injection – Top Inlet**

Figure 4-8 shows contours of the injected oil mass fraction in the cavern as a function of time for the 0.1% heavier case. The injected oil mixes with the resident oil immediately after injection. The results show an essentially uniform distribution of the injected oil below the inlet, or complete mixing in this region consistent with the degas performance curves shown above.

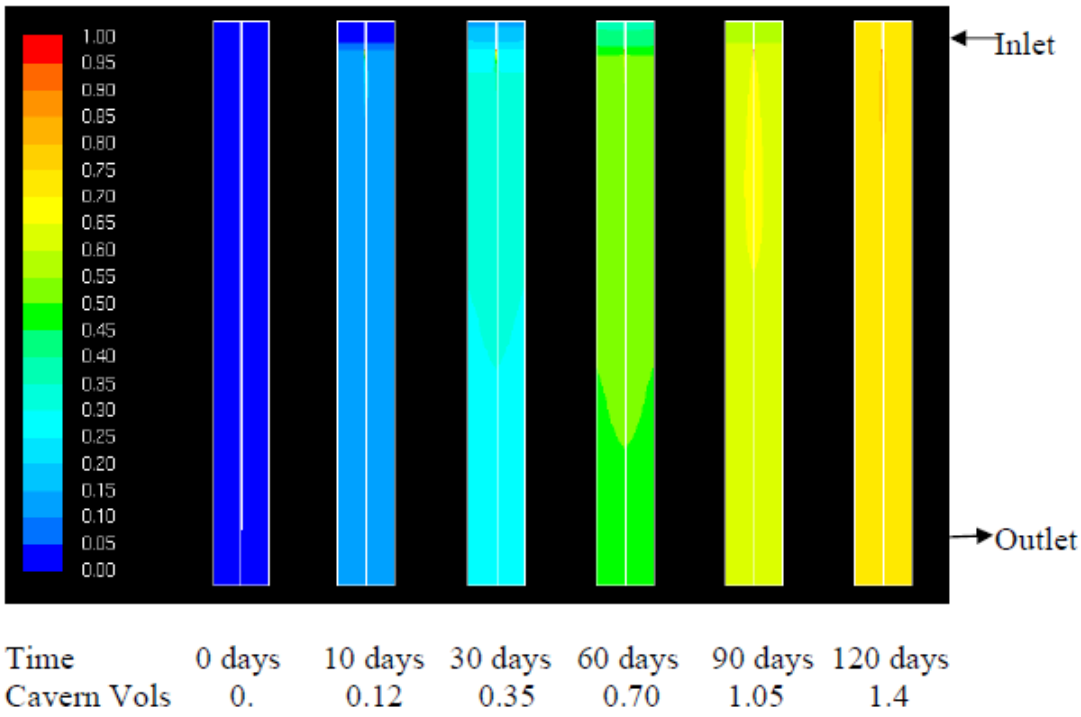


**Figure 4-8. Contours of Mass Fraction of Injected Fluid in Cavern (Heavier Oil Injection, Top Inlet)**

The above results can be converted to a temperature difference by using an approximate oil thermal expansion coefficient of 5. x $10^{-4}/^{o}$F (Meng et al., 2006, Frick, 1962). Therefore, a 0.01% density difference corresponds to a temperature difference of about 0.2 $^{o}$F. The degas performance curves for uniform density initial conditions have been replotted in Figure 4-9.

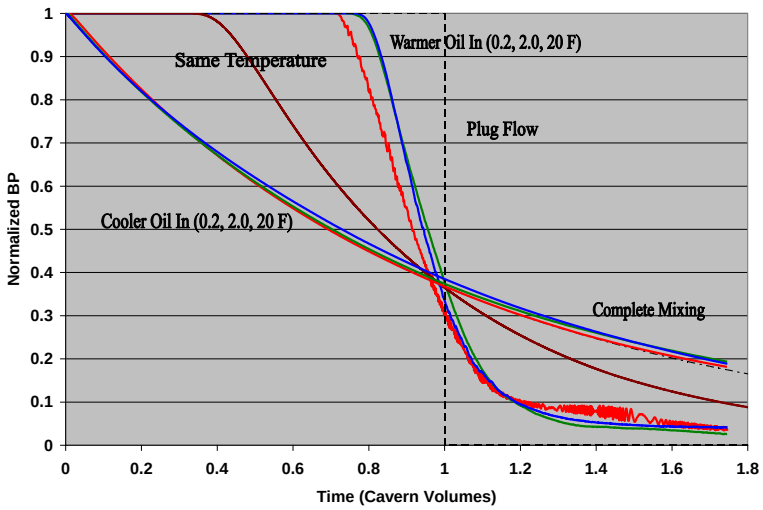


a) Normalized BP Results

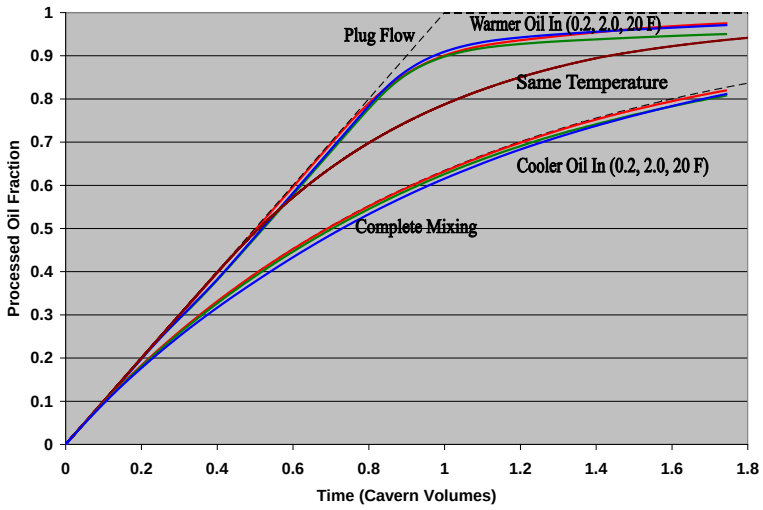


(b) Processed Oil Fraction Results

**Figure 4-9. Degas Performance Curves vs. Inlet Oil Temperature**

Calculated degas performance of a simplified cavern geometry with uniform initial density (no stratification) is strongly dependent on the density/temperature of the injected fluid. If the injected fluid is lighter/warmer than the resident fluid, degas proceeds similar to the plug flow model of Lord and Rudeen (2007). If the injected fluid is heavier/cooler than the resident fluid, large-scale mixing occurs and degas is similar to the complete mixing model of Lord and Rudeen (2007).

### 4.2.2 Stratified Density Initial Conditions

**2a / 2b - Inject Bottom Layer Into Top Inlet**

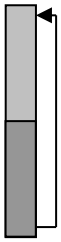

Oil is taken out of the bottom of the cavern and injected into the top with the injected density equal to the initial withdrawal density. The influence of the initial density stratification on degas performance is evaluated. As seen in Figure 4-10, the degas performance curves are initially similar to plug flow until about 35% of the oil is processed and then they go to the complete mixing curve, or when the stratification interface gets to the outlet location. The red curve shows the case of injecting the bottom layer oil into the top inlet. The green curve shows the reverse situation where the top layer oil is injected into the bottom inlet. Both curves give similar results.

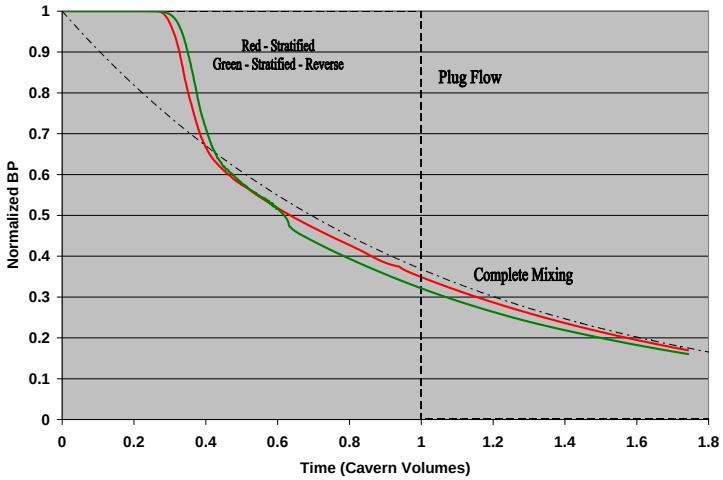


(a) Normalized BP Results

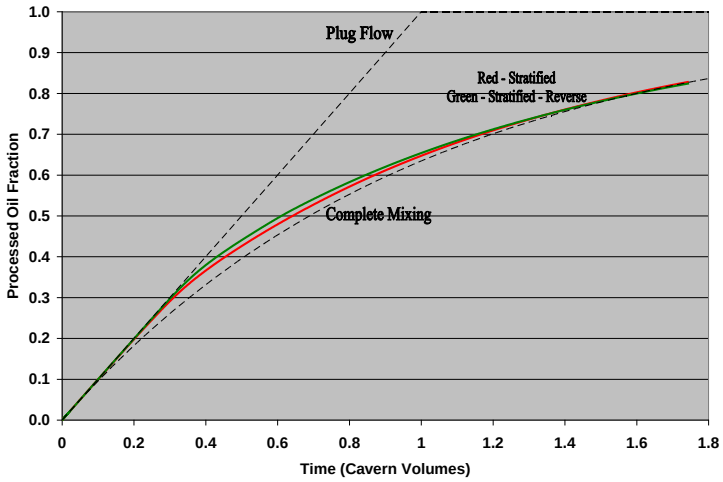


(b) Processed Oil Fraction Results

**Figure 4-10. Degas Performance Curve Results For Stratified Case**
**Inject Bottom Layer Into Top Inlet (Red) / Inject Top Layer Into Bottom Inlet (Green)**

Figure 4-11 shows the injected fluid mass fraction and density contours as a function of time for injection of the bottom layer oil into the top inlet (Red Curve above). The upper layer is well mixed but remains separate from the bottom layer. The bottom layer is withdrawn similar to plug flow until the well-mixed upper layer gets to the outlet; after that, the performance is similar to complete mixing.

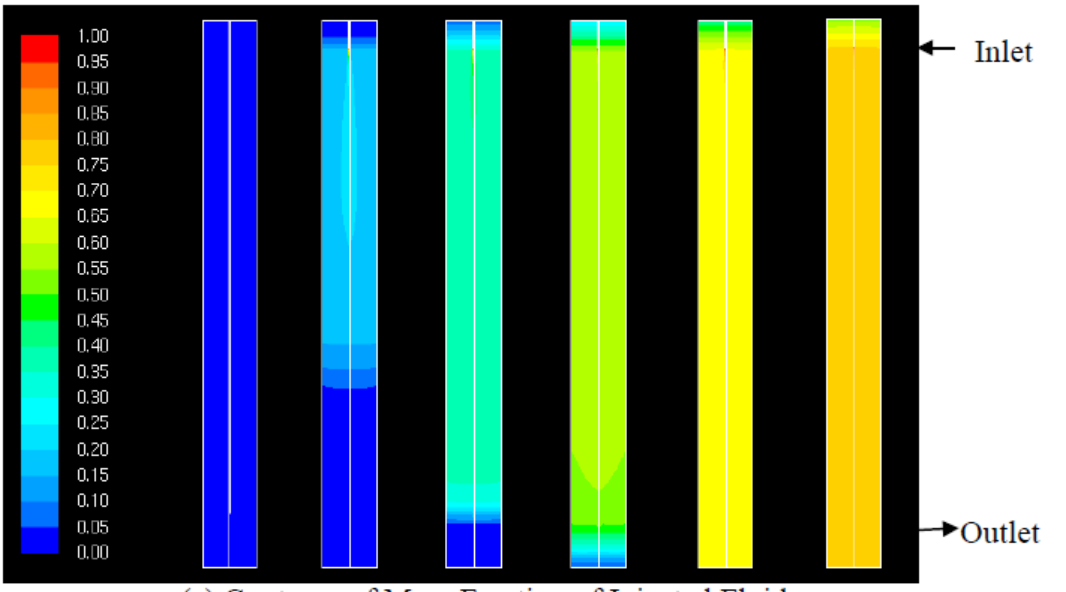


(a) Contours of Mass Fraction of Injected Fluid

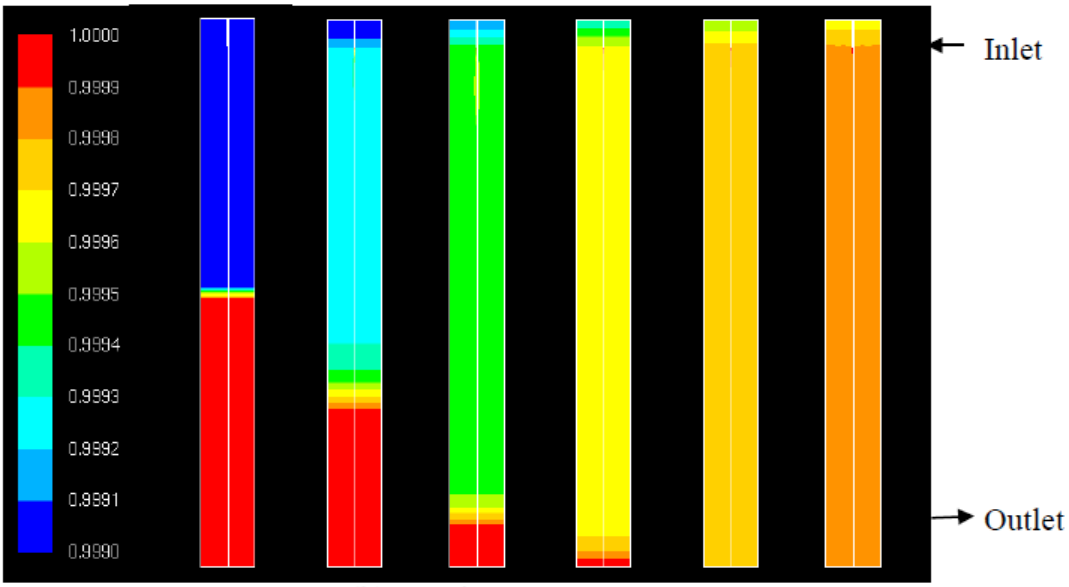


(b) Density Contours

| Time | 0 days | 10 days | 30 days | 60 days | 90 days | 120 days |
|---|---|---|---|---|---|---|
| Cavern Vols | 0. | 0.12 | 0.35 | 0.70 | 1.05 | 1.4 |

**Figure 4-11. Cavern Contours for Injection of Bottom Layer Into Top Inlet**

### 2c - Inject Lighter Fluid Into Top Inlet

In this case, an oil lighter than either the top or bottom oil layers is injected into the top inlet. The inlet oil is 0.1% lighter than the oil in the top layer, or 0.2% lighter than the bottom layer. As expected, the degas performance curves shown in Figure 4-12 are very similar to those for a lighter oil injection into a uniform density cavern. The degas performance is similar to plug flow until about 80% of the oil in the cavern has been processed.

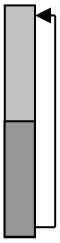

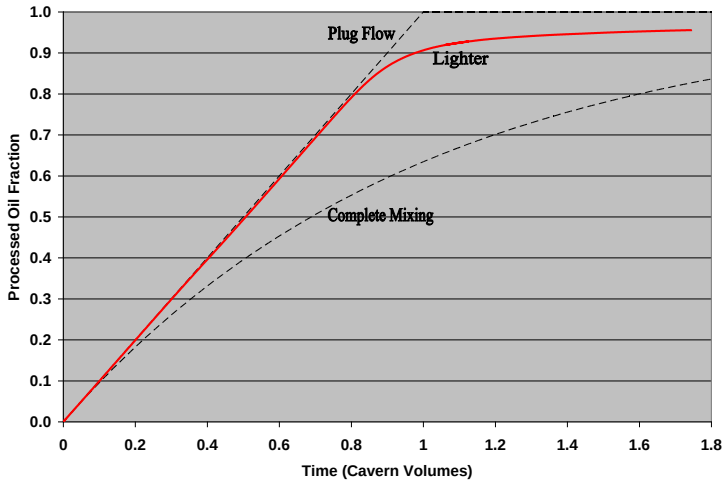


(a) Normalized BP Results

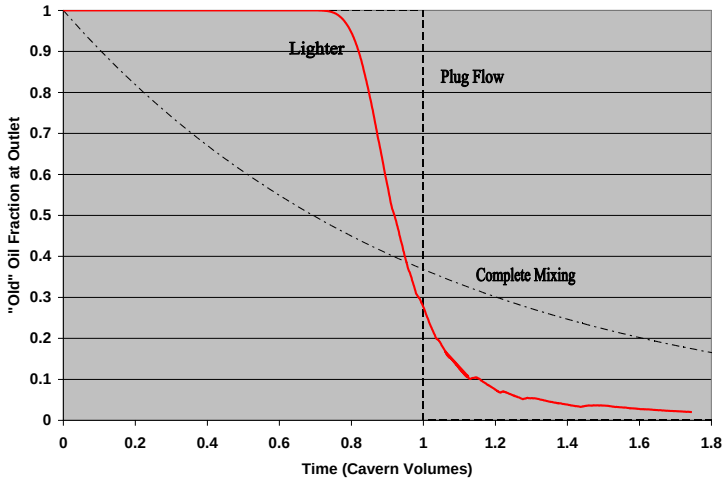


(b) Processed Oil Fraction Results

**Figure 4-12. Degas Performance Curve Results For Stratified Case Inject Lighter Oil Into Top Inlet**

Figure 4-13 shows the contours of the injection mass fraction in the cavern as well as the fluid density. The cavern acts like plug flow for most of the time consistent with the earlier case of lighter oil injection into a uniform density cavern.

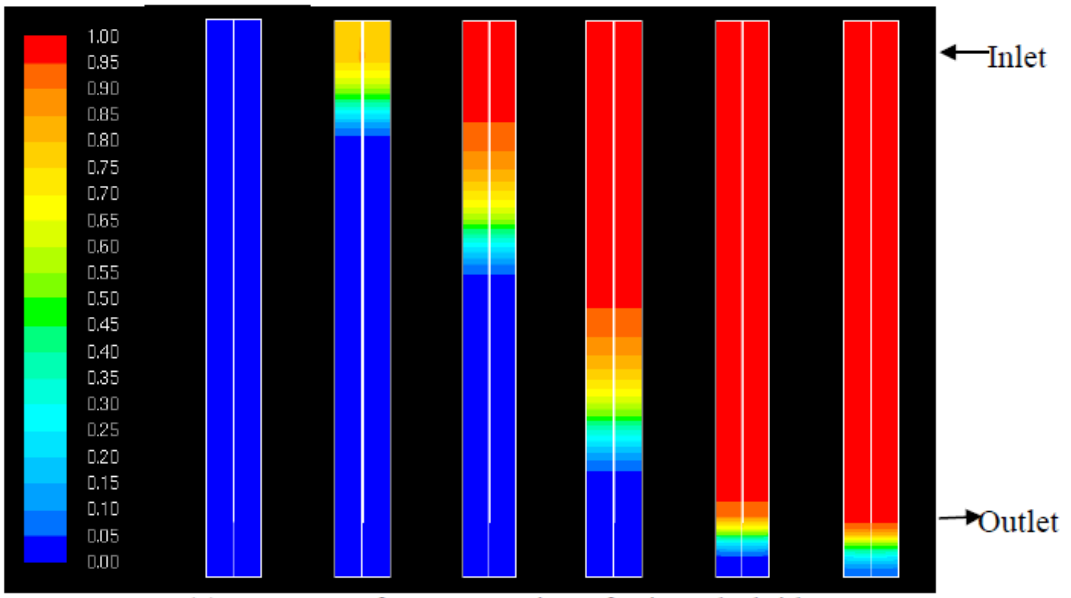


(a) Contours of Mass Fraction of Injected Fluid

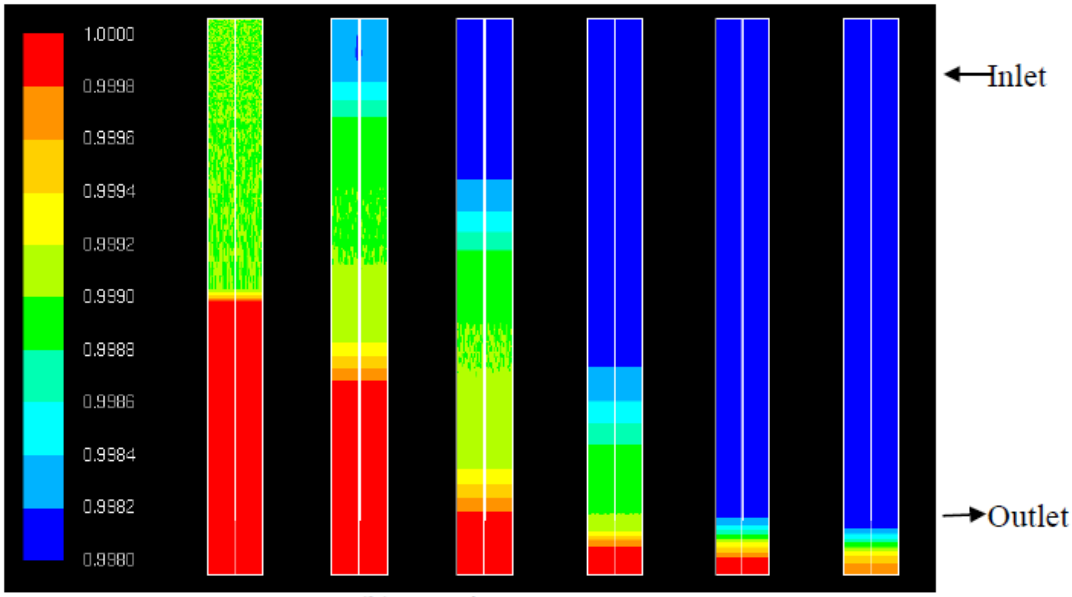


(b) Density Contours

| Time | 0 days | 10 days | 30 days | 60 days | 90 days | 120 days |
|---|---|---|---|---|---|---|
| Cavern Vols | 0. | 0.12 | 0.35 | 0.70 | 1.05 | 1.4 |

**Figure 4-13. Cavern Contours for Injection of Light Oil Into Top Inlet**

**Star-CD comparison**

Cavern mixing and degas performance has been simulated by the Fluent and Star-CD computer codes for a number of cases given by Webb (2009a) as given by Webb (2009b) – see the Appendix for the original memos. The results from both codes are essentially the same except for neutral density case. In this situation, the Star-CD results seem more physically realistic. In any event, the impact of this difference is probably small because any small density difference will significantly change the mixing behavior.

# 5 Water-Brine Mixing

## 5.1 O'Hern (2005) Data

O'Hern (2004, 2005a,b,c) conducted laboratory-scale experiments of water injected into brine for application to leaching. The rest of this section is from O'Hern (2005c) with some editing. More details about the diagnostics and details of the data analysis are given in O'Hern (2005c).

An experimental program was undertaken to study leaching plume behavior in the SPR. The goal was to determine the extent of mixing between injected raw water (fresh, brackish, or sea water) and the surrounding brine.

The experiment consisted of the large (35 inch ID) transparent cylindrical vessel that is a scale model of an SPR cavern that has been used in several previous studies. Saturated NaCl brine filled the lower portion of the vessel, sometimes with an overlying oil layer. Fresh water or unsaturated salt solutions were injected downward through an injection tube into the brine at prescribed flow rates and depths below the oil-brine interface. Flow rates were determined by scaling to match the ratio of buoyancy to momentum forces between the experiment and the SPR cavern. Initially, the momentum of the flow produces a downward jet of injected raw water below the tube end. Subsequently, the injected water jet entrains brine as buoyancy pulls the brine-raw water plume, with density lower than that of pure brine, up to the brine-oil or brine-air interface.

**Experimental Setup**

Figure 5-1 shows the basic experimental setup.

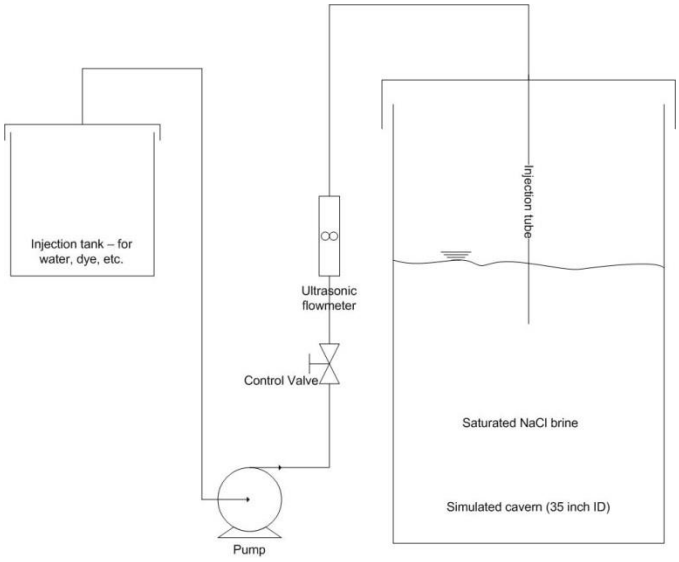


**Figure 5-1. Experimental setup. Two different injection tubes were used (0.83 and 0.15 inches ID).**

The experimental variables included density of injected raw water, diameter of injection tube, injection flow rate, and injection depth into the brine. One case was also run with an overlying oil layer.

**Experimental Procedure**

At the start of each test the large vessel was filled with saturated NaCl solution, the injection tube was positioned at the desired depth below the interface, and the injection tank was filled with the desired injection solution, i.e., water with dye or salt, and at the desired temperature. The brine was stirred then the tank was allowed to settle to a quiescent state as indicated by cessation of particle motion in the light sheet.

As shown in Figure 5-2, three camera positions were needed to cover the full extent of the plume from injection until it reached the vessel wall for the small injection tube. For the large tube the intermediate location (Position P2) was not needed). To start each experiment, the camera was located at Position P1, viewing the injection tube, the flow was initiated a few seconds later, and images were recorded at the rate of one per second. The flow was turned off after the rising plume was seen to reach the vessel walls or, when not clearly visible, after a few seconds more than the average time for the plume to reach the wall for those conditions. The tank was then stirred, the camera was moved to its new position, and the flow was repeated. For camera positions P2 and P3 (halfway between the injection tube and the wall and at the wall, respectively, and both just below the brine surface) images were recorded for an additional 30 seconds or so after flow was terminated in order to track the rising, spreading plume. In these locations follow-up images were recorded 10 minutes later as well.

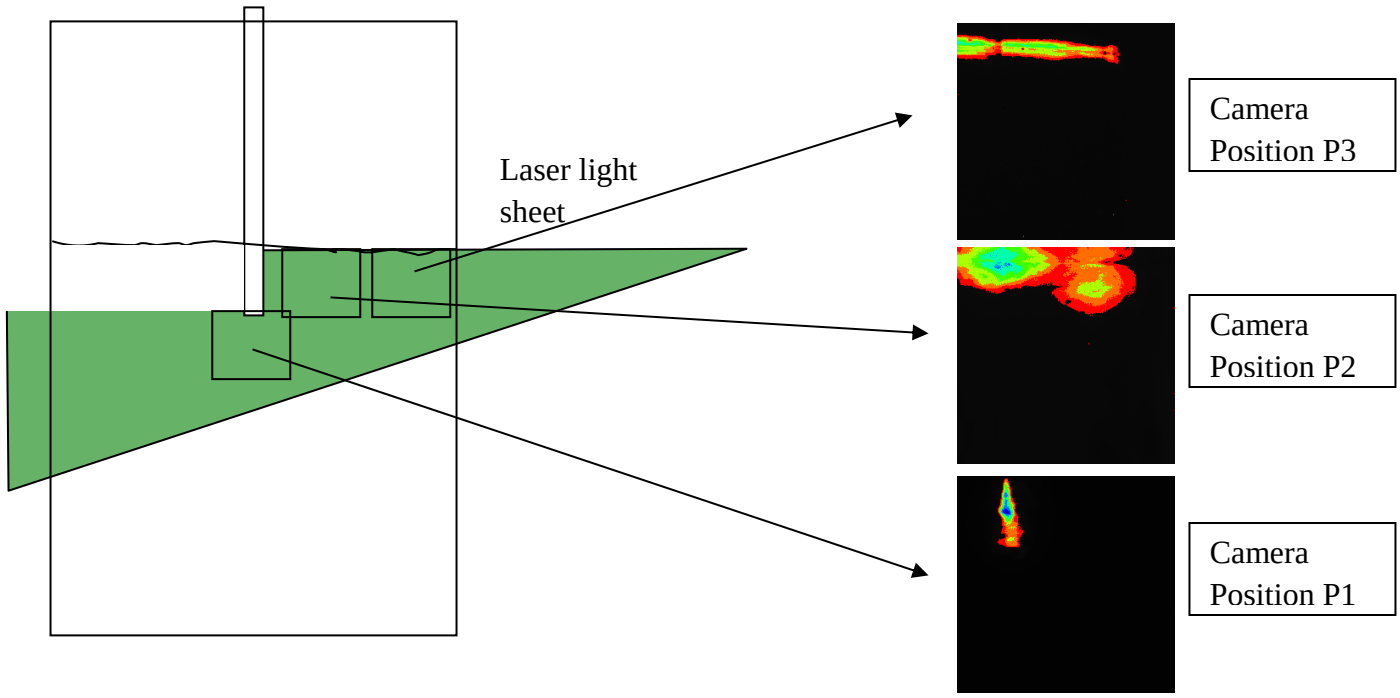


**Figure 5-2. Side view showing approximate camera locations. Actual raw data images are used to show sample data within each region. The images were taken in case 3_1_3 (see Table 1) and each was recorded during a different experimental run. False color in images provides a qualitative view of local concentration, with blue highest concentration of raw water and red lowest concentration. There were three camera positions, Camera Position 1 (P1) is at the end of the injection tube, Camera Position 2 (P2) is approximately halfway between the tube and the wall, and Camera Position 3 (P3) is at the wall.**

## Results and Discussion

Figure 5-3 through Figure 5-6 show some of the final data plots. Table 5-1 summarizes the cases that were run, including the measured run conditions and a listing of which images were useful (for Camera Position P1). The final data are in the form of Tecplot-ready column-separated-variable (CSV) files that have a file structure and units of x (cm), y (cm), raw water fraction (first image), raw water fraction (second image), …, raw water fraction (last image). For P2 and P3 the last column is data taken 10 minutes after the run ended, intended to show an average raw water concentration after the injection. There were a few cases where this was not recorded due to laser problems. The numbers of columns vary depending on how many images were taken and saved in that particular sequence. Table 1 lists which images show a well-established plume (based on watching movies of images and examining brightness in processed LIF data). These are the ones recommended for validation of simulations.

The measurement uncertainty is estimated to be ±15% of the measured value, e.g., a measured raw water fraction of 0.05 is expected to fall in the range 0.0425 to 0.0575. This relatively high degree of uncertainty is caused by several factors, including:

1. Since the entire flow could not be captured in one camera view, the camera was moved between image acquisitions. The 100% raw water reference $I_{peak}$ was visible only in images recorded at Camera Position P1. For Camera Positions P2 and P3 an assumed raw water intensity from the P1 images had to be used. There is generally good consistency in the measured concentration between the P2 and P3 images, indicating that this assumption is reasonable. An uncertainty of ±10% comes from the amount of variation typically seen in the peak intensity in the P1 images caused by laser fluctuations. Similar fluctuations were undoubtedly present in the P2 and P3 images but they did not contain a standard on which a measure of laser intensity could be made.
2. Remaining flow in tank after mixing despite efforts to run only when the tank was quiescent. The few cases where this was obvious, e.g., the plume fluid moving off-axis, were discarded, but there may still have been slight differences between tests due to this remnant flow.
3. Occasional bright reflections caused by floating debris at the top of the brine layer or bubbles in the plume itself. Any dust remained floating at the interface and, despite efforts to strain it all out, some remained. Strong reflections could make it through the optical filter, artificially indicating regions of high dye concentration.

Figure 5-7 shows the jet penetration from the P1 images as a function of injection velocity for the 0.15-in injection tube. The laboratory values are also scaled to cavern equivalent flowrate and penetration depth. Included in Figure 5-7 are predictions of a similarity-solution estimate of the penetration depth (Turner, 1979) for a downward-directed turbulent jet of buoyant liquid into a miscible liquid:

$$\frac{z_m}{D_1} = 1.85\left(\frac{\pi}{4}\right)^{\frac{1}{4}}\left[\frac{\rho_b U_1^2}{(\rho_b - \rho_o) g D_1}\right]^{\frac{1}{2}},\ U_1 = \frac{Q_1}{(\pi/4) D_1^2}, \tag{4}$$

*or, defining the Froude number* $Fr = \dfrac{\rho_b U_1^2}{(\rho_b - \rho_o) g D_1}$, *Equation (4) becomes*

$$\frac{z_m}{D_1} = 1.85\left(\frac{\pi}{4}\right)^{\frac{1}{4}} Fr^{\frac{1}{2}} \tag{5}$$

where $z_m$ is the penetration depth, $\rho_b$ and $\rho_o$ are the mass densities of the brine and raw water, respectively, $g$ is the gravitational acceleration, $Q_1$ is the volumetric flow rate of the raw water injection, $D_1$ is the inner diameter of the pipe, and $U_1$ is the average velocity of the raw water exiting the pipe end. The agreement between the experimental data and the model of Equation

(4) is generally good, although the observed penetration is lower than the model predicts for the high flow rate cases.

Examination of the flow images and the concentration at different locations in the tank has pointed out several characteristics of this flow and the effect of varying experimental parameters. Included in Table 1 is the peak raw water fraction in the plume as the flow approached the vessel wall in the P3 images. This value is taken from plots similar to the right-hand column of Figure 5. The concentration at the wall itself could not be measured as there was too much distortion by the curved tube to see the last few centimeters near the wall. Figure 5-8 shows the corresponding data for raw water concentration as the flow approached the wall. Note that the plots shown in Figure 5-8 included all of the experimental runs shown in Table 5-1, so multiple parameters vary between data points. All are included in order to determine obvious trends when varying a single parameter. None of the trends are strong. Observations of changing each parameter are:

1. Injection depth: The near-wall raw water concentration remains slightly higher when injection is shallower and becomes lower when injection is deeper. This is in agreement with expectations since shallower injection gives less mixing in the spreading plume.
2. Tube diameter: Experiments run with the larger diameter injection tube generally had lower raw water concentration in the plume as it approached the wall. This is thought to be due to more vigorous mixing in the tank caused by the larger injection plume.
3. Flow rate: No clear trend.
4. Density ratio: The ratio of injected raw water density to background brine density only varied over 0.834 – 0.864 (see Table 1). There is only a weak trend of higher raw water concentration with higher density ratio. The larger density ratio drives a stronger buoyant acceleration which may carry the plume fluid farther and faster before the plume becomes completely well mixed.
5. Oil Layer: Only one case was run with an overlying oil layer. There was no apparent difference between the plume behavior with or without the oil layer.

The data show some inconsistencies such as the P3 concentrations looking higher than the corresponding P2 concentration. These differences are within the experimental uncertainty (±15% for the P2 and P3 concentrations as presented above).

Instantaneous comparison of numerical simulations with experimental data is not too instructive because of the unsteady nature of the flow, i.e., there is no expectation that the flow in the experiment and the simulation will be synchronized. Therefore, it is not instructive to compare snapshots taken at a certain time after the initiation of raw water injection. For Camera Position P1, time averaged values are appropriate due to the strong mixing dynamics in the plume. For Camera Positions P2 and P3, the speed of the plume movement and the plume concentration profiles should be compared instead of results at a given time. Figure 9 shows representative time-averaged views of the plume at Camera Position P1. Initial plume computational validation has been done using such images (thanks to I. Khalil, 6141).

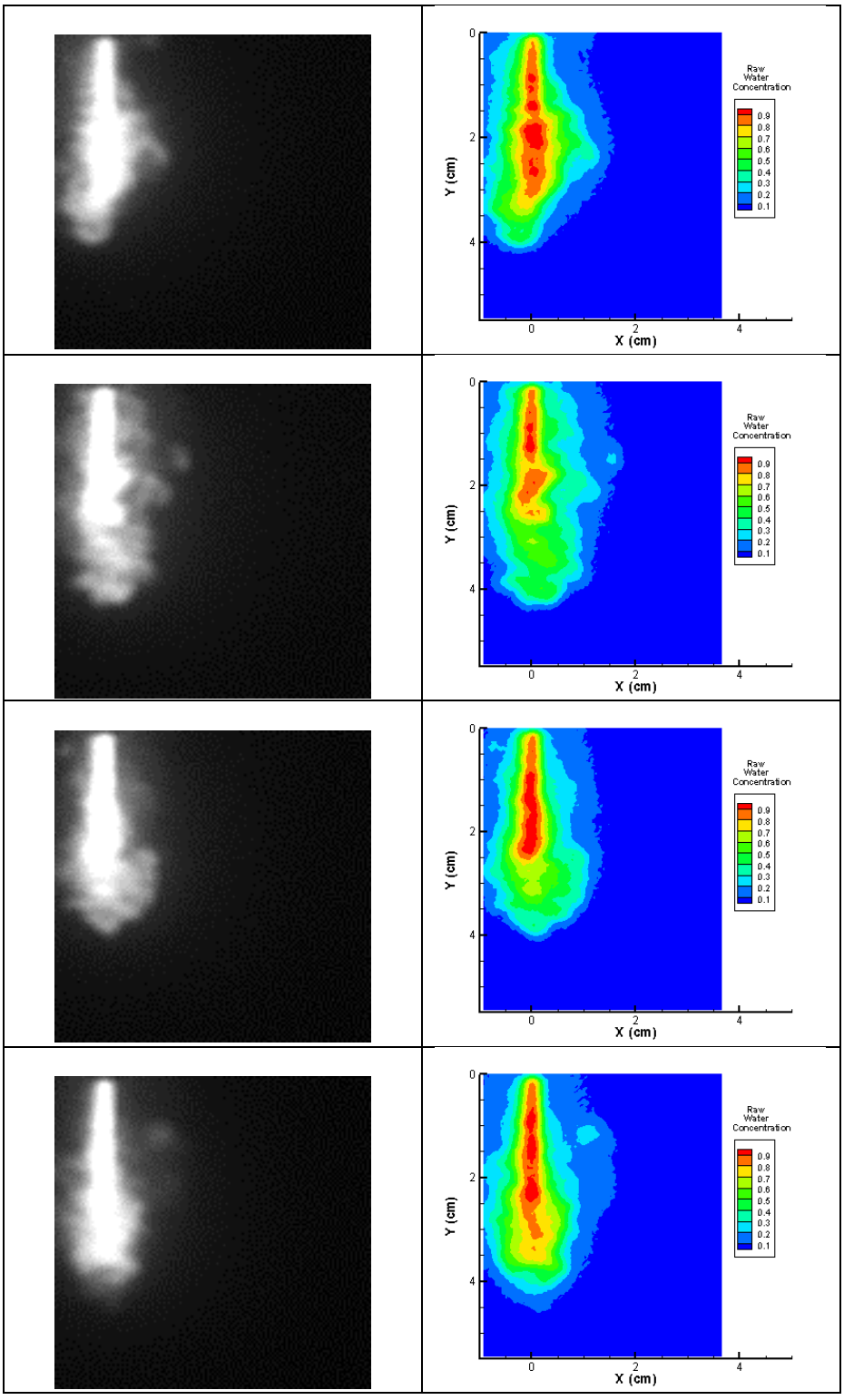


**Figure 5-3. Four consecutive PLIF images and their corresponding concentration contours showing raw water concentration in the injected plume at camera position P1. Camera timing is one second between frames. This series is from Test 3_2_5 (0.152 inch diameter injection tube, injection 9 inches below interface, injected raw water to brine density ratio = 0.838, flowrate equivalent to 99,000 ± 1000 bbl/day when scaled to SPR conditions)**

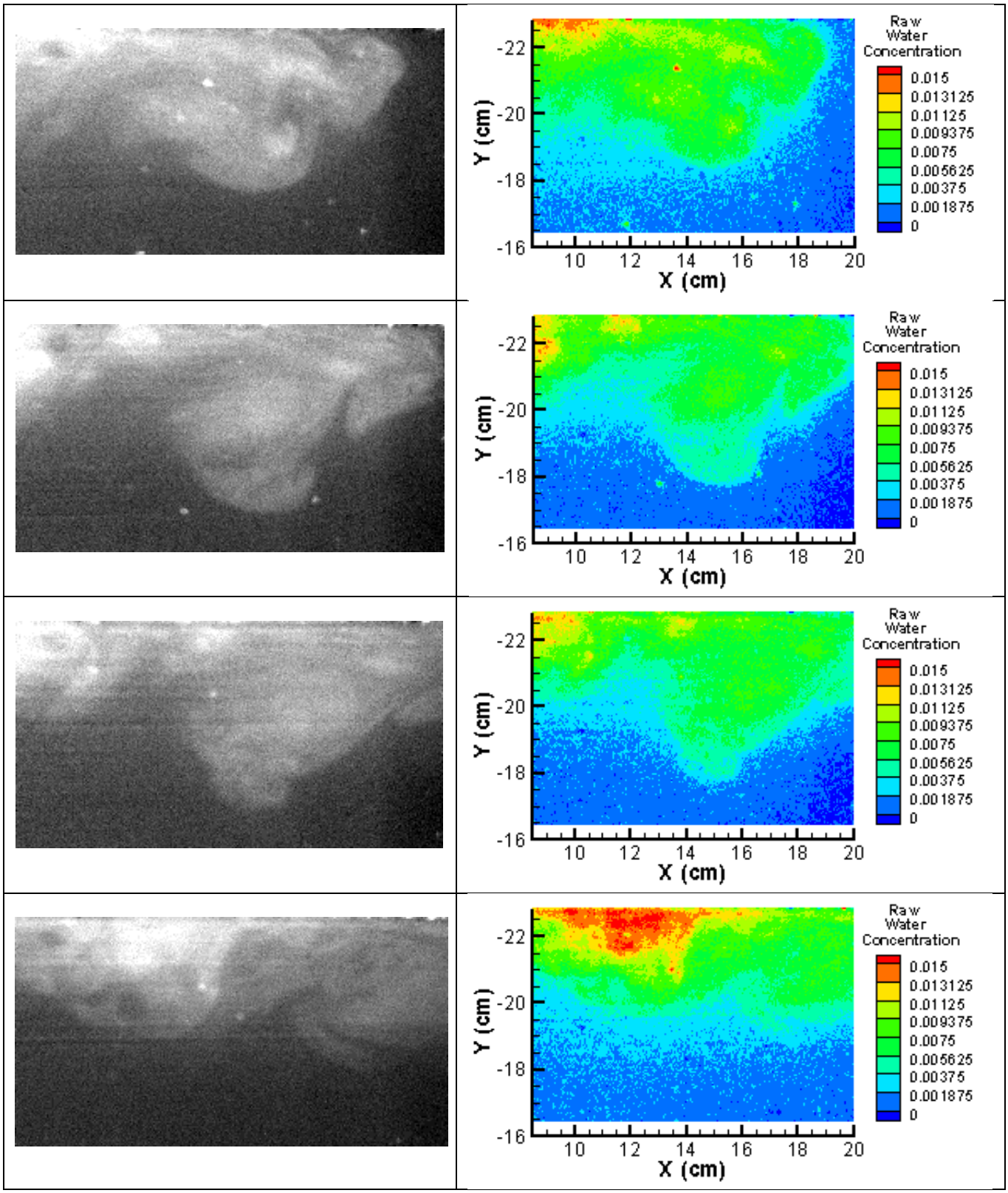


**Figure 5-4. Four consecutive PLIF images and their corresponding concentration contours showing raw water concentration in the injected plume at camera position P2. Camera timing is one second between frames. This series is from Test 3_2_5, same as Figure 5-2.**

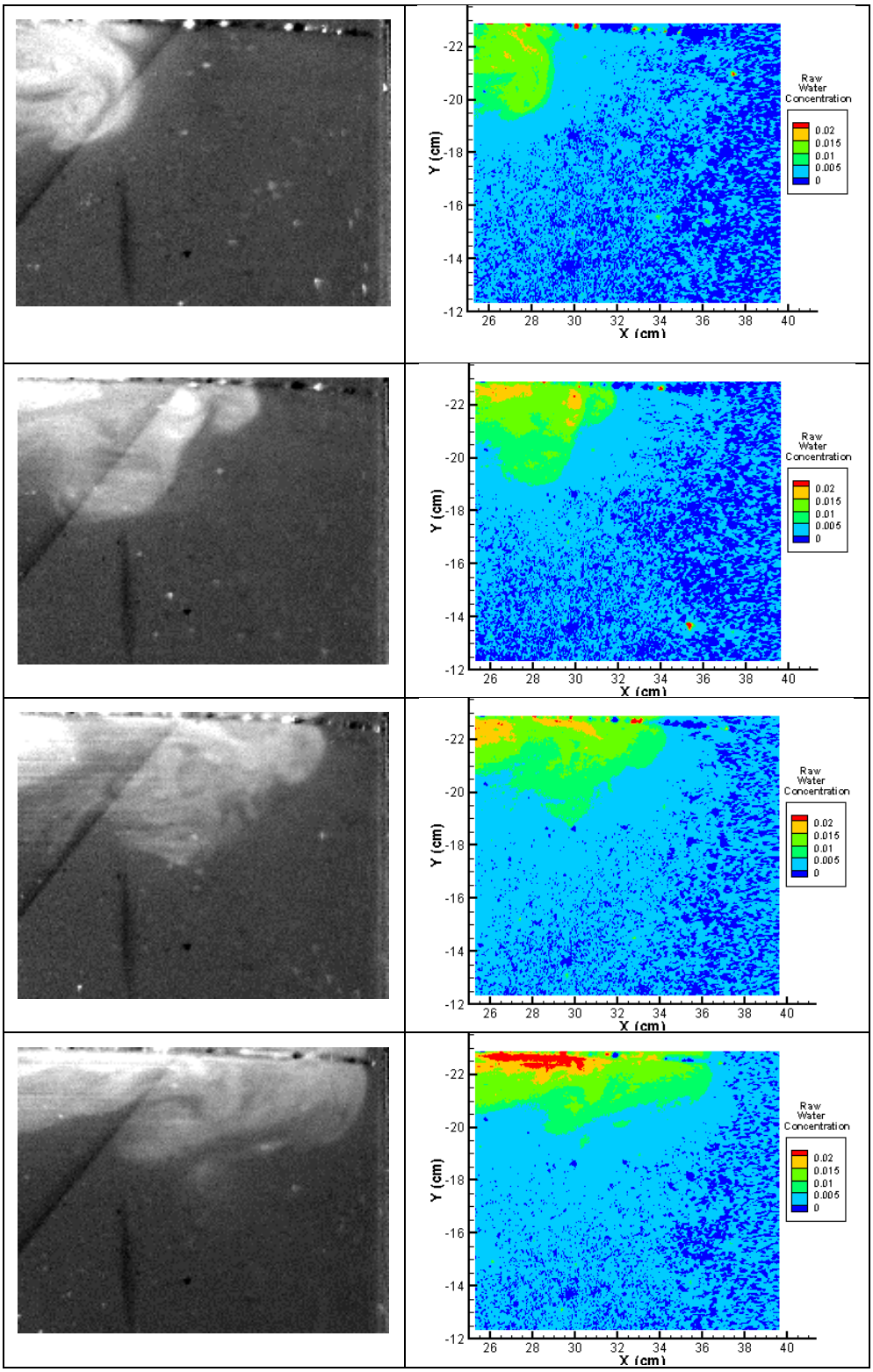


**Figure 5-5. Four consecutive PLIF images and their corresponding concentration contours showing raw water concentration in the injected plume at camera position P3. Camera timing is one second between frames. This series is from Test 3_2_5, same as Figures 5-2 and 5-3.**

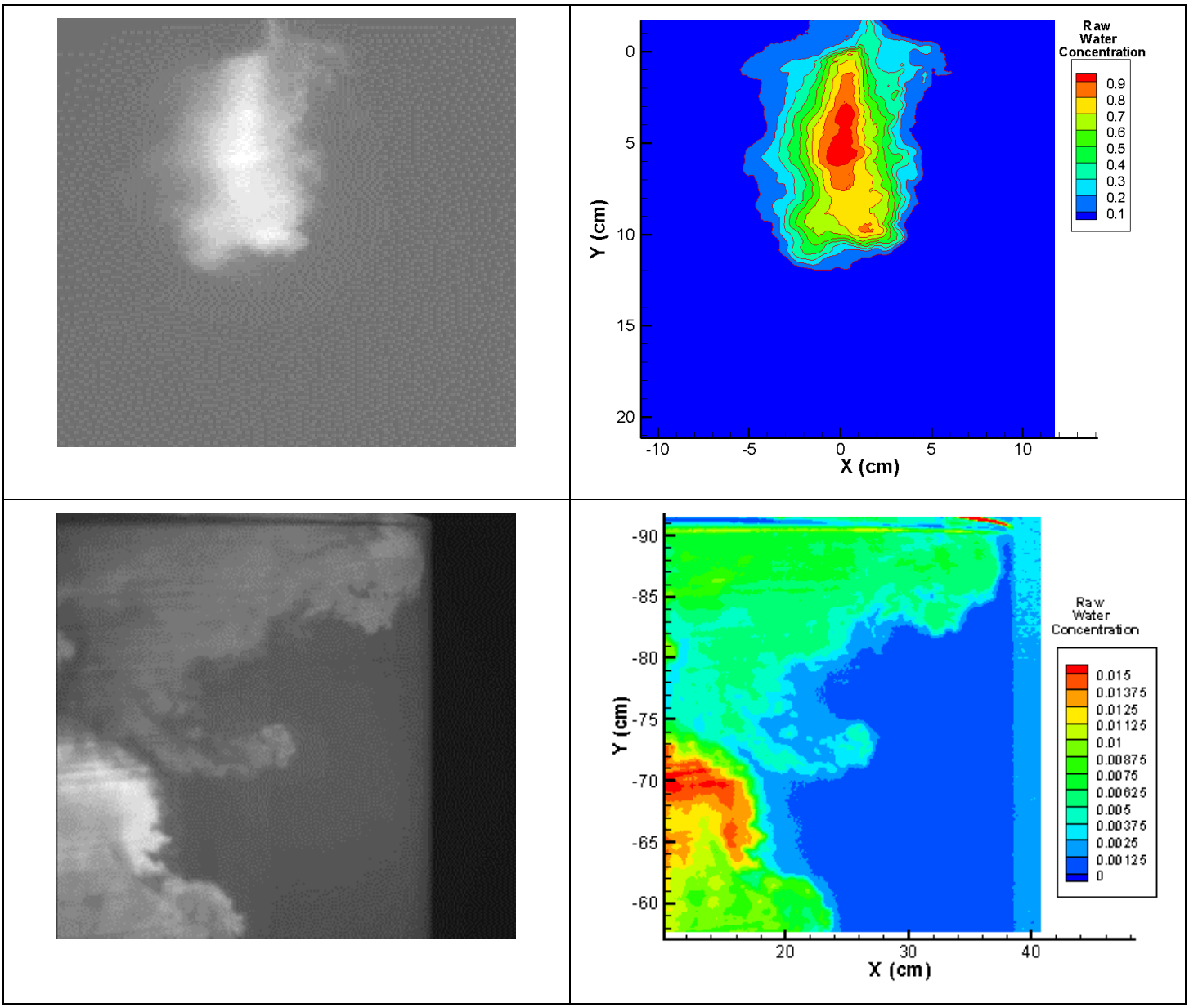


**Figure 5-6. Instantaneous photos of the plume at the two camera positions used for the larger injection tube cases and the corresponding raw water concentration fields. Data are from Test 1_1_3.**

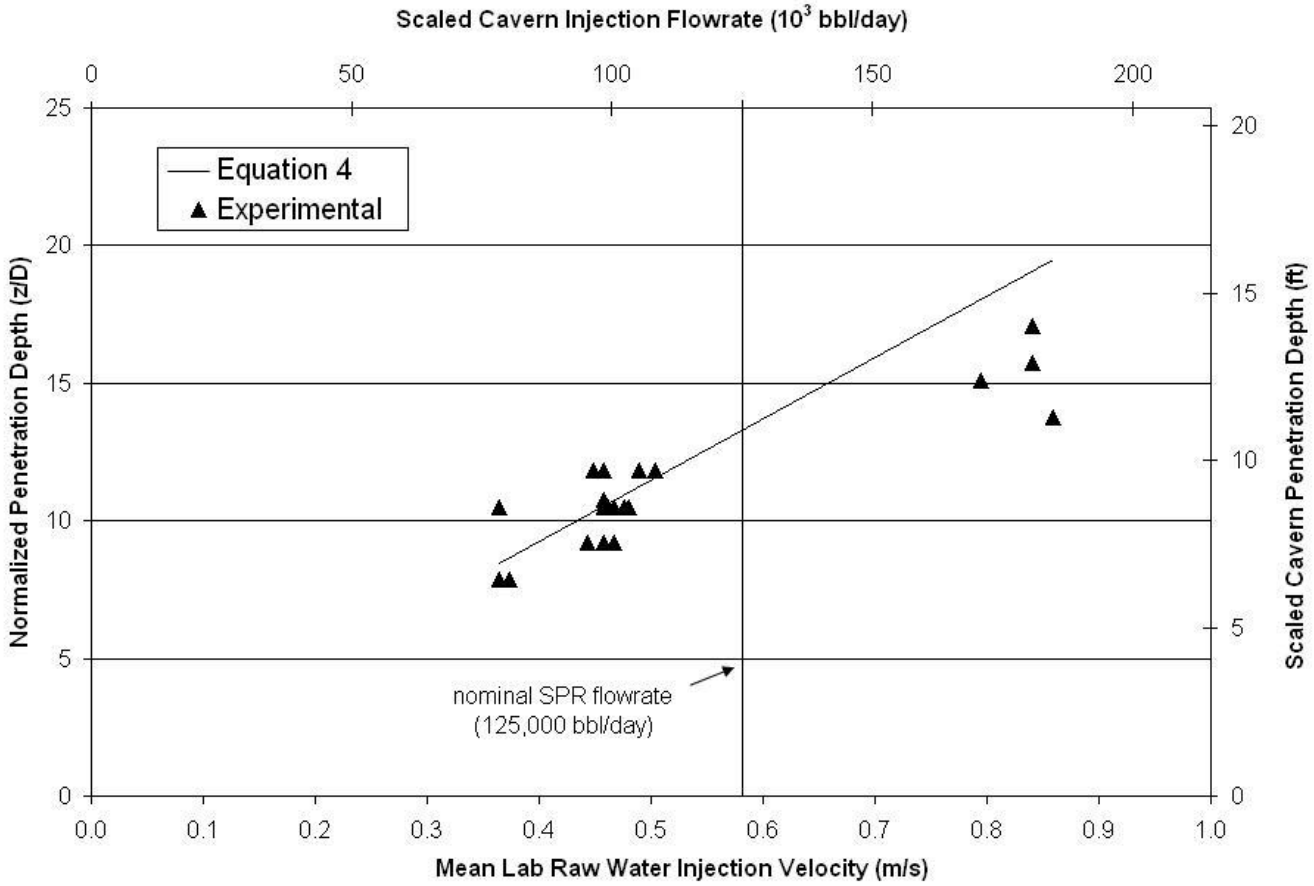


**Figure 5-7. Experimentally-determined jet penetration and predictions given by Equation 4 (Turner, 1979). All experimental data are for the small injection tube.**

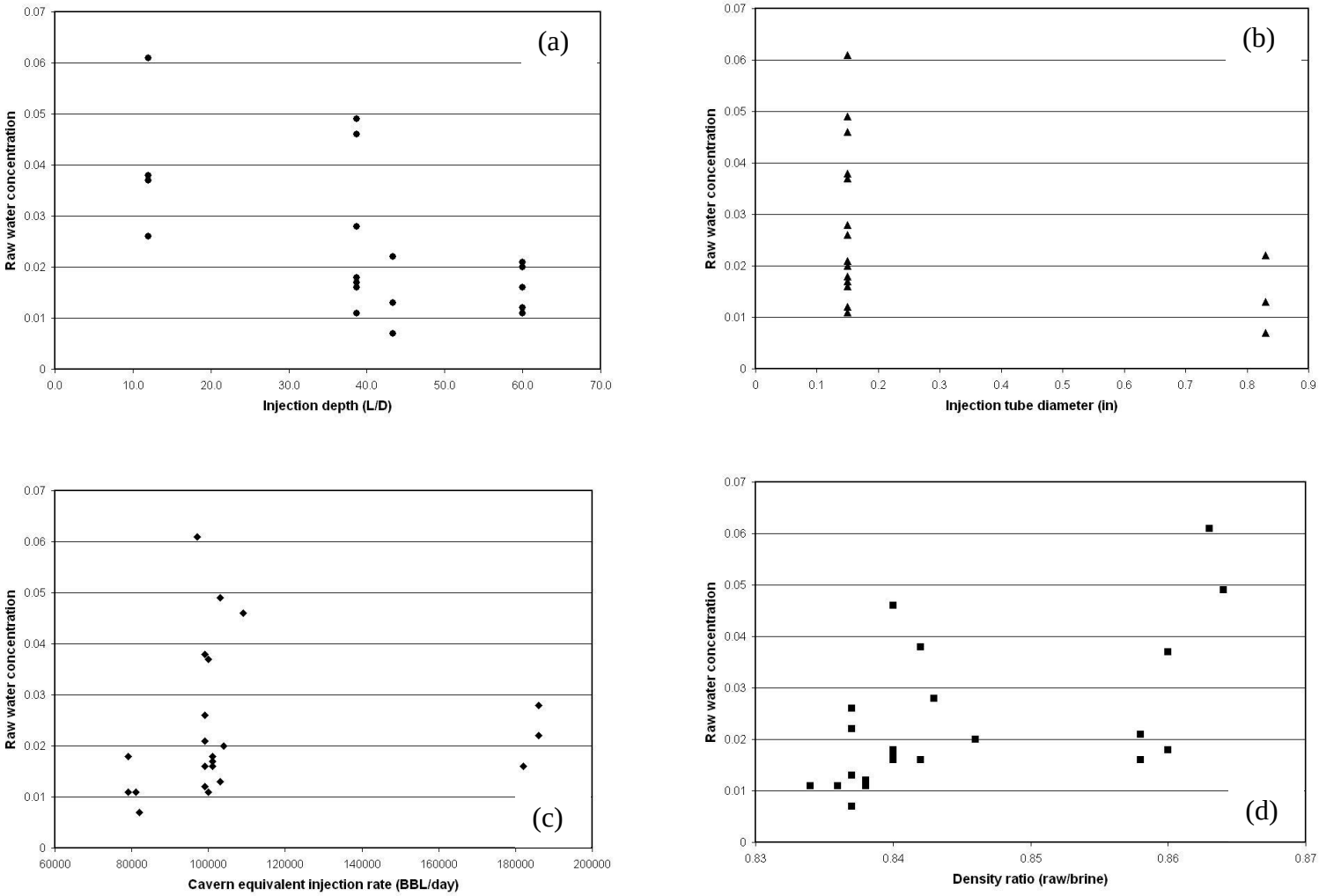


**Figure 5-8. Trends of concentration near wall with varying experimental parameters a) Injection depth b) Tube diameter c) Flow rate d) Density ratio.**

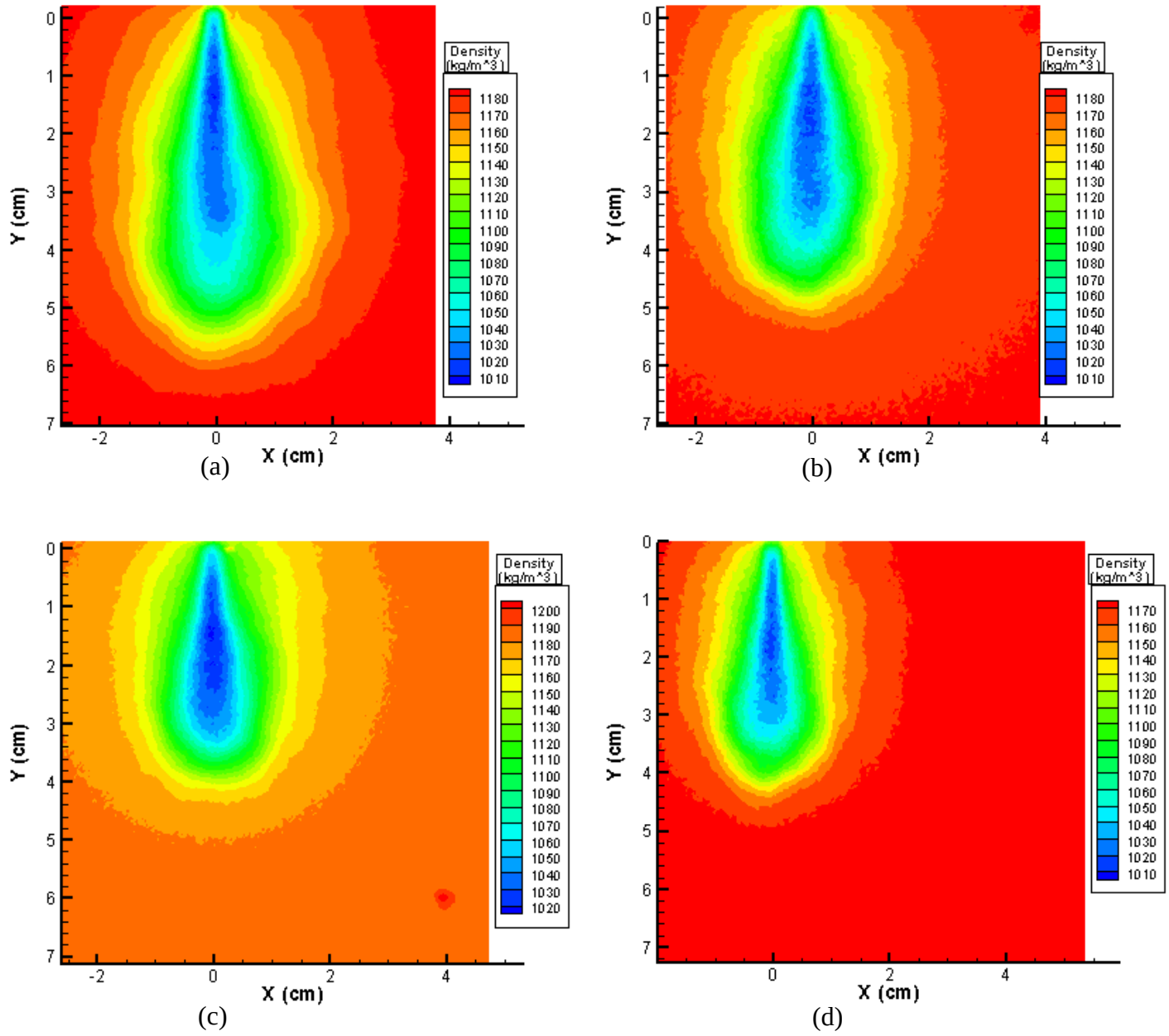


**Figure 5-9. Time-averaged plume density from Camera Position P1 image sequences. Data are from Tests (a) 3_3_3 (6/21/05) (b) 3_3_3 (6/23/05) (c) 3_2_3 (6/24/05) (d) 3_2_3 (6/27/05). Thanks to I. Khalil, 6141, for averaging images and converting from raw water concentration to density.**

**Table 5-1. Table of Experiments**

| Test ID | Date | Injection tube ID (in) | Target scaled cavern flowrate (bbl/day) | Actual scaled cavern flowrate (bbl/day) | Ratio of injected water to brine density ($\rho_r/\rho_b$) | Injected water density ($\rho_r$) | Brine density ($\rho_b$) | Injection depth (ft [in]) | useful P1 flow images (image #, columns in *.csv files) | Near wall raw water fraction |
|---|---|---|---|---|---|---|---|---|---|---|
| 1_1_3 | 8/3/2005 | 0.83 | 80000 | 82000 ± 1% | 0.838 | 1.000 | 1.194 | 3 [36] | 15-24, Q-Z | 0.007 |
| 1_2_3 | 8/3/2005 | 0.83 | 100000 | 103000 ± 1% | 0.838 | 1.000 | 1.194 | 3 [36] | 9-22 K-X | 0.013 |
| 1_3_3 | 8/3/2005 | 0.83 | 180000 | 186000 ± 1% | 0.838 | 1.000 | 1.194 | 3 [36] | 11-7, M-S | 0.022 |
| 3_1_3 | 6/24/2005 | 0.15 | 80000 | 79000 ± 1000 | 0.840 | 1.000 | 1.190 | 0.48 [5.8] | 11-44, H-AO | 0.018 |
| 3_1_3 | 7/18/2005 | 0.15 | 80000 | 79000 ± 500 | 0.838 | 1.000 | 1.194 | 0.48 [5.8] | 27-39, AC-AO | 0.011 |
| 3_1_3 | 7/20/2005 | 0.15 | 80000 | 81000 ± 500 | 0.836 | 1.000 | 1.196 | 0.48 [5.8] | 34-48, AJ-AX | 0.011 |
| 3_2_1 | 6/30/2005 | 0.15 | 100000 | 99000 ± 1000 | 0.842 | 1.000 | 1.188 | 0.15 [1.8] | 19-35 (no 25), U-AJ | 0.038 |
| 3_2_1 | 6/30/2005 | 0.15 | 100000 | 99000 ± 1000 | 0.842 | 1.000 | 1.188 | 0.15 [1.8] | 12-39, M-AN | 0.026 |
| 3_2_3 | 6/24/2005 | 0.15 | 100000 | 109000 ± 1000 | 0.840 | 1.000 | 1.190 | 0.48 [5.8] | 23-43, T-AN | 0.046 |
| 3_2_3 | 6/27/2005 | 0.15 | 100000 | 106000 ± 1000 | 0.846 | 1.000 | 1.182 | 0.48 [5.8] | 45-57, AT-BF | No P3 |
| 3_2_3 | 7/15/2005 | 0.15 | 100000 | 101000 ± 1000 | 0.840 | 1.000 | 1.190 | 0.48 [5.8] | 11-32, I-AD | 0.017 |
| 3_2_5 | 7/1/2005 | 0.15 | 100000 | 96000 ± 1000 | 0.847 | 1.000 | 1.181 | 0.75 [9] | 25-42 AA-AR | No P3 |
| 3_2_5 | 7/13/2005 | 0.15 | 100000 | 104000 ± 1000 | 0.846 | 1.000 | 1.182 | 0.75 [9] | 11-36, M-AL | 0.02 |
| 3_2_5 | 7/14/2005 | 0.15 | 100000 | 99000 ± 1000 | 0.838 | 1.000 | 1.193 | 0.75 [9] | 11-22, M-X | 0.012 |
| 3_2_5_O | 7/29/2005 | 0.15 | 100000 | 100000 ± 1000 | 0.834 | 1.000 | 1.199 | 0.75 [9] | 17-36, S-AL | 0.011 |
| 3_3_3 | 6/21/2005 | 0.15 | 180000 | 172000 ± 8000 | 0.837 | 1.000 | 1.195 | 0.48 [5.8] | 30-49, AF-AY | No P3 |
| 3_3_3 | 6/23/2005 | 0.15 | 180000 | 186000 ± 8000 | 0.843 | 1.000 | 1.186 | 0.48 [5.8] | 23-37 S-AG | 0.028 |

| Test ID | Date | Injection tube ID (in) | Target scaled cavern flowrate (bbl/day) | Actual scaled cavern flowrate (bbl/day) | Ratio of injected water to brine density ($\rho_r/\rho_b$) | Injected water density ($\rho_r$) | Brine density ($\rho_b$) | Injection depth (ft [in]) | useful P1 flow images (image #, columns in *.csv files) | Near wall raw water fraction |
|---|---|---|---|---|---|---|---|---|---|---|
| 3_3_3 | 7/20/2005 | 0.15 | 180000 | 182000 ± 4000 | 0.842 | 1.000 | 1.188 | 0.48 [5.8] | 18-33, T-AI | 0.016 |
| 3_3_3 | 7/21/2005 | 0.15 | 180000 | 182000 ± 4000 | 0.842 | 1.000 | 1.188 | 0.48 [5.8] | 20-31, V-AG | 0.016 |
| 3_3_3_R | 7/20/2005 | 0.15 | 180000 | 182000 ± 4000 | 0.842 | 1.000 | 1.188 | 0.48 [5.8] | 19-32 U-AH | No P3 |
| 4_2_1 | 6/29/2005 | 0.15 | 100000 | 97000 ± 1000 | 0.863 | 1.023 | 1.184 | 0.15 [1.8] | 18-31. T-AG | 0.061 |
| 4_2_1 | 7/26/2005 | 0.15 | 100000 | 100000 ± 1000 | 0.856 | 1.023 | 1.195 | 0.15 [1.8] | 16-33, R-AI | 0.037 |
| 4_2_3 | 6/28/2005 | 0.15 | 100000 | 103000 ± 1000 | 0.864 | 1.023 | 1.184 | 0.48 [5.8] | 19-36, T-AK | 0.049 |
| 4_2_3 | 7/15/2005 | 0.15 | 100000 | 101000 ± 1000 | 0.860 | 1.023 | 1.190 | 0.48 [5.8] | 14-34, P-AJ | 0.018 |
| 4_2_5 | 7/14/2005 | 0.15 | 100000 | 99000 ± 1000 | 0.858 | 1.023 | 1.193 | 0.75 [9] | 9-32, K-AH | 0.016 |
| 4_2_5_R | 7/14/2005 | 0.15 | 100000 | 99000 ± 1000 | 0.858 | 1.023 | 1.193 | 0.75 [9] | 7-28, F-AA | 0.021 |

## 5.2 Khalil and Webb (2006)

Khalil and Webb (2006) performed detailed Fluent simulations of the experimental data of O'Hern (2005c) for water injection into brine using the Large Eddy Simulation (LES) turbulence model. The experimental conditions are summarized below in Table 5-2. Note that for the smaller 0.15 inch tube, the outlet flow was laminar but the jet was tripped to get turbulent conditions. The flow for the larger 0.83 inch tube was turbulent. The jet depth for the buoyant jet compares reasonably well to the experimental data as listed in Table 5-3 and shown in Figure 5-10 for FLUENT Model 2.

The experimental jet penetration data are compared to the revised Turner correlation in Table 5-4. Even though the experimental and simulation jet penetration depths compare reasonably well as discussed above, the experimental jet is significantly shorter than predicted by the revised Turner correlation. In fact, the factor would need to be decreased by 26% (from 2.2 to 1.63) to bring the correlation in line with the data. The reason for this discrepancy may be the free surface top boundary condition and/or the depth of the injection, or it may be due to the low Reynolds number of the jet. These factors are included in the simulations but not in the correlation.

**Table 5-2. Summary of test runs**

| FLUENT Model # | Test ID | Test date | Injection tube ID (inch) | Injection depth (inch) | Target scaled cavern flowrate (bbl/day) | Lab velocity (m/sec) (ref) |
|---|---|---|---|---|---|---|
| 1 | 3_1_3 | 7/18/2005 | 0.15 | 5.8 | 80,000 | 0.37 |
| 2 | 3_2_3 | 6/24/2005 | 0.15 | 5.8 | 100,000 | 0.46 |
| 3 | 3_3_3 | 7/21/2005 | 0.15 | 5.8 | 180,000 | 0.83 |
| 4 | 3_2_1 | 7/26/2005 | 0.15 | 1.8 | 100,000 | 0.46 |
| 5 | 3_2_5 | 7/29/2005 | 0.15 | 9 | 100,000 | 0.46 |
| 6 | 1_1_3 | 8/3/2005 | 0.83 | 36 | 80,000 | 0.87 |
| 7 | 1_2_3 | 8/3/2005 | 0.83 | 36 | 100,000 | 1.08 |
| 8 | 1_3_3 | 8/3/2005 | 0.83 | 36 | 180,000 | 1.95 |

**Table 5-3. Plume length comparison**

| Test ID, Test date | FLUENT Model # | Experimental plume length (cm) | Simulation plume length (cm) | Error = (Sim-Data)/Data |
|---|---|---|---|---|
| 3_1_3, 7/18/05 | 1 | 3.0 | 2.8 | -7% |
| 3_2_3, 6/24/05 | 2 | 4.3 | 3.9 | -9% |
| 3_3_3, 7/21/05 | 3 | 6.2 | 6.2 | 0% |
| 3_2_1, 7/26/05 | 4 | 3.9 | 3.7 | -5% |
| 3_2_5, 7/29/05 | 5 | 4.3 | 3.4 | -18% |
| 1_1_3, 8/3/05 | 6 | 13.3 | 13.3 | 0% |
| 1_2_3, 8/3/05 | 7 | 17.4 | 16.3 | -6% |
| 1_3_3, 8/3/05 | 8 | 34.0 | 31.3 | -8% |

**Table 5-4. Plume length comparison details**

| Test ID, Test date | Injected water over brine density | $Fr_1$ Number | Turner Model Prediction (cm) | Experimental plume length (cm) | Error = (Pred-Data)/Data | Turner Constant |
|---|---|---|---|---|---|---|
| 3_1_3, 7/18/05 | 0.838 | 4.8 | 4.0 | 3.0 | 33% | 1.65 |
| 3_2_3, 6/24/05 | 0.840 | 5.9 | 4.9 | 4.3 | 14% | 1.93 |
| 3_3_3, 7/21/05 | 0.842 | 10.8 | 9.0 | 6.2 | 45% | 1.52 |
| 3_2_1, 7/26/05 | 0.842 | 6.0 | 5.0 | 3.9 | 28% | 1.72 |
| 3_2_5, 7/29/05 | 0.834 | 5.8 | 4.8 | 4.3 | 12% | 1.97 |
| 1_1_3, 8/3/05 | 0.838 | 4.7 | 21.7 | 13.3 | 63% | 1.35 |
| 1_2_3, 8/3/05 | 0.838 | 5.9 | 27.2 | 17.4 | 56% | 1.41 |
| 1_3_3, 8/3/05 | 0.838 | 10.7 | 49.4 | 34.0 | 45% | 1.51 |

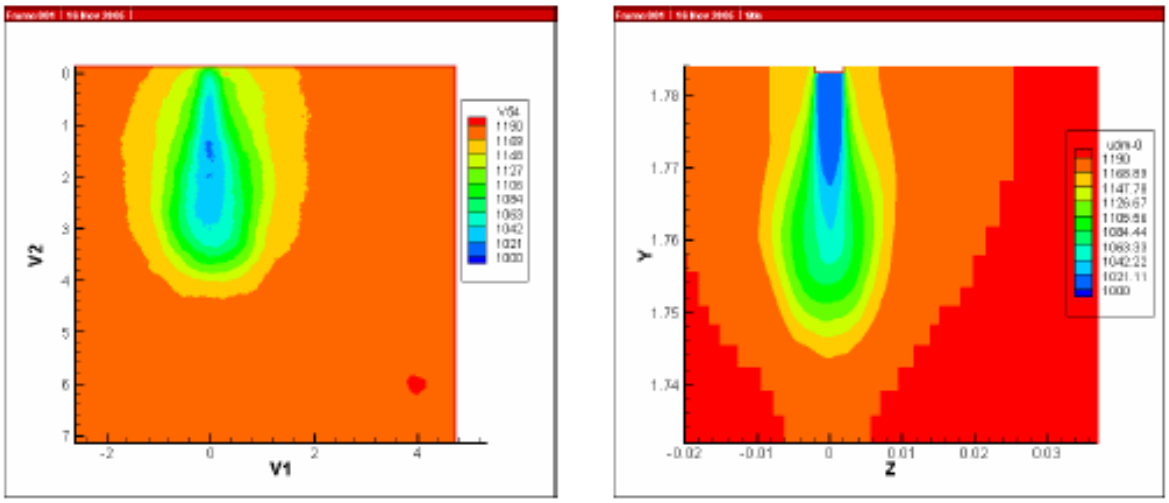


**Figure 5-10. Contours of time-average density (kg/m$^3$). Experimental Data on Left; FLUENT Results on Right.**

Khalil and Webb (2006) also presented details of the jet development and compared the results to the experimental data for 3 different camera positions as shown in Figure 5-11. Subsequently, however, Webb discovered that the frames at the free surface are incorrect. Khalil and Webb (2006) assumed that the camera positions were fixed in space. However, the vertical position of the frames was not fixed but was relative to the water surface (O'Hern, 2008).

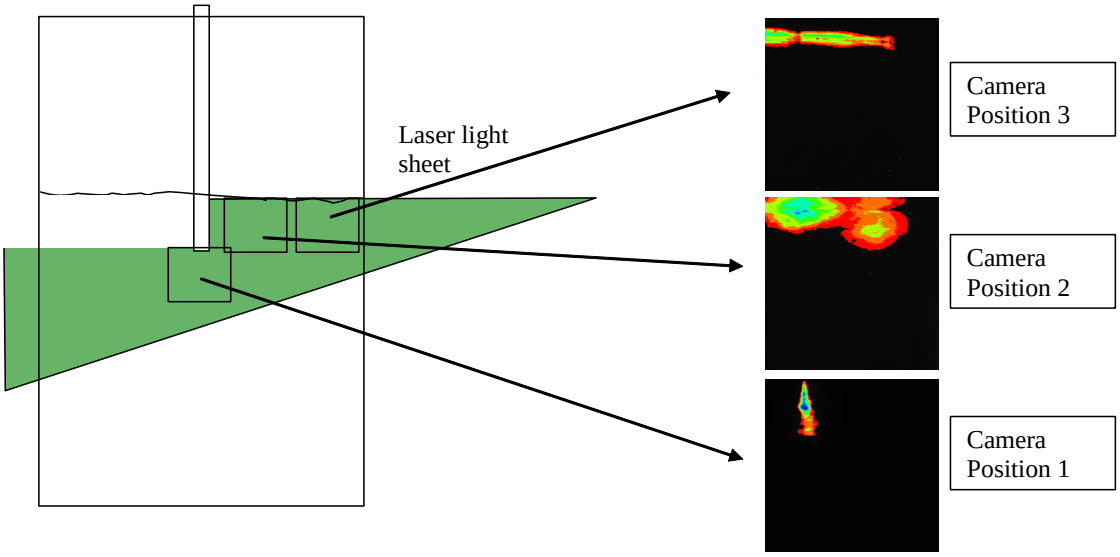


**Figure 5-11. Camera Positions for Experimental Data**

To illustrate the differences, Webb simulated Test ID 3_2_3 (Model 2) again in 2008. Figure 5-12 shows the complete mixing results. Figure 5-13 shows the assumed frame for Position P2 per Khalil and Webb (2006), which is significantly below the water surface as noted in Figure 5-14. Thus, the detailed comparison of the behavior of the mixing along the surface (camera positions P2 and P3) should be viewed with caution.

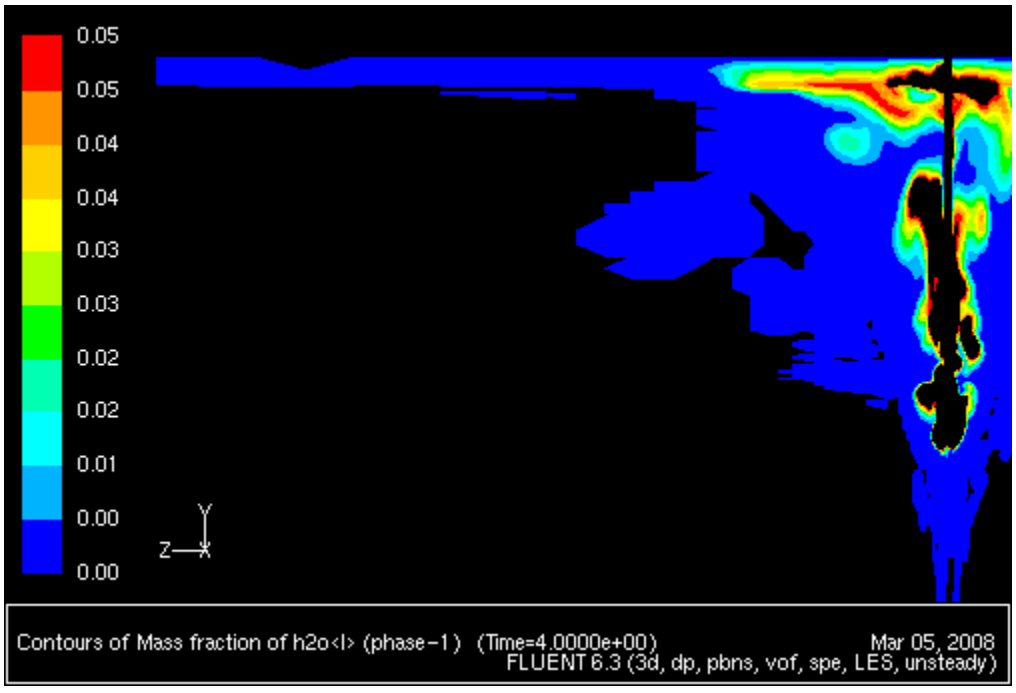


**Figure 5-12. Complete Mixing Results**

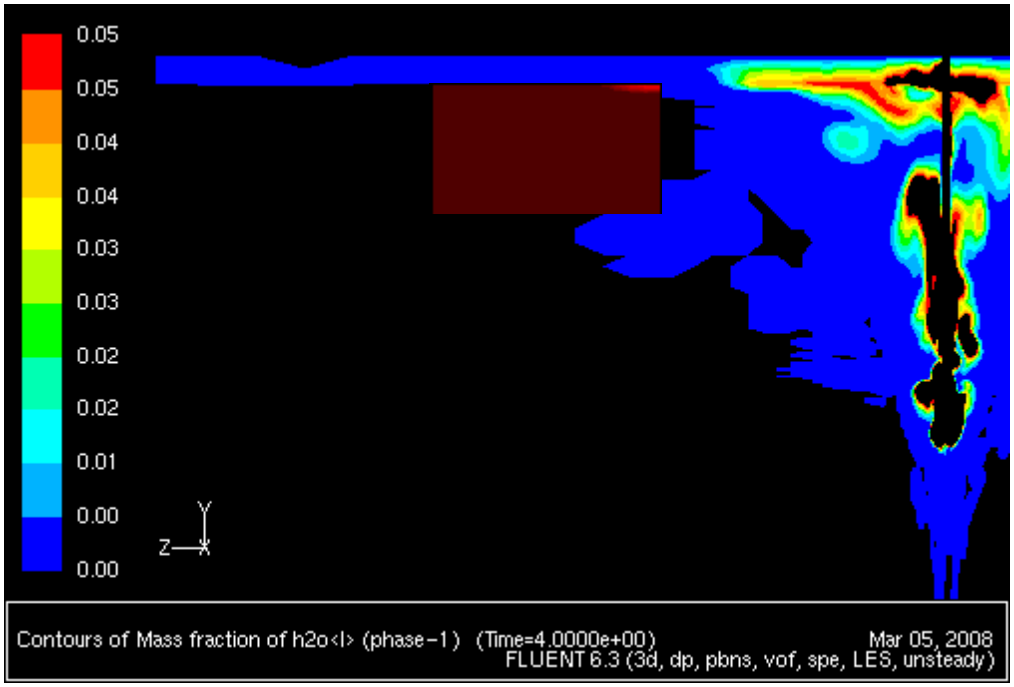


**Figure 5-13. Complete Mixing Results With Assumed P2 Position**


**Figure 5-14. P2 Mixing Results for Khalil and Webb Assumed P2 Position**

# 6 Mixing Layers Model

A mixing layers model for oil mixing in caverns was developed by Webb (Webb, 2010). The idea is that the cavern fluids initially consist of a lighter oil over a heavier oil. When the heavier oil is withdrawn from the cavern and passed through the degas plant it becomes even heavier. When this oil is injected into the top of the cavern, the density of the top layer (light oil plus degassed oil) will increase. When the top layer density equals the bottom layer density, the entire cavern will completely mix.

Assuming perfect mixing between different oils, the density of an oil mixture, $\rho_{\text{mixture}}$, is defined as

$$\rho_{\text{mixture}} = \sum_{i=1}^{n} \text{x}_\text{i}\rho_\text{i}$$

where $x_i$ is the volume fraction of oil i and $\rho_i$ is the density of oil i similar to a mixture of binary gases.

For simplicity, assume that there are only two oils in the top layer - the original light oil and the heavier degassed oil. As mentioned above, when the density of this mixed layer equals the density of the original heavier oil in the bottom of the cavern, $\rho_{\text{heavier}}$, the cavern will completely mix, or

$$\rho_{\text{heavier}} = \text{x}_{\text{degas}}\,\rho_{\text{degas}} + \,(1. - \text{x}_{\text{degas}})\rho_{\text{light}}$$

Rearranging gives the volume fraction of the light oil in the mixed layer when the density of the two layers are equal, or

$$x_{\text{degas}} = \frac{\rho_{\text{heavier}} - \,\rho_{\text{light}}}{\rho_{\text{degas}} - \,\rho_{\text{light}}}$$

For an initial light oil volume of $V_{\text{light}}$, the total volume of the degassed oil in the top layer is simply

$$V_{\text{degas-top layer}} = \,V_{\text{top layer}}\,\text{x}_{\text{degas}} \,= \frac{\text{V}_{\text{light}}}{(1. - \text{x}_{\text{degas}})}\,\text{x}_{\text{degas}}$$

and the fraction of the degassed oil volume corresponding to this volume is

$$\text{x}_{\text{degas}} = \frac{\text{V}_{\text{degas-top layer}}}{\text{V}_{\text{top layer}}} = \frac{\text{V}_{\text{light}}}{\text{V}_{\text{top layer}}}\,\frac{\text{x}_{\text{degas}}}{(1. - \text{x}_{\text{degas}})}$$

Now consider the case where you have mixing / entrainment between the layers due to the inlet jet. Assume that the heavier underlying oil is entrained into the upper layer and that the bottom layer density is unchanged. Calling the volume fraction of the entrained bottom fluid, which is at $\rho_{heavier}$, $x_{jet}$, the expression describing when the upper and lower layer densities are equal becomes

$$\rho_{\text{heavier}} = \mathrm{x}_{\text{degas,j}}\,\rho_{\text{degas}} + \mathrm{x}_{\text{jet}}\,\rho_{\text{heavier}} + \left(1. - \mathrm{x}_{\text{degas,j}} - \mathrm{x}_{\text{jet}}\right)\rho_{\text{light}}$$

with the solution

$$x_{\text{degas,j}} = \frac{\rho_{\text{heavier}} - \rho_{\text{light}}}{\rho_{\text{degas}} - \rho_{\text{light}}}\left(1. - \mathrm{x}_{\text{jet}}\right)$$

where $x_{degas,j}$ is the degas volume fraction including jet mixing. For an initial light oil volume of $V_{light}$, the total volume of the degassed oil in top layer is simply

$$V_{\text{degas-top layer,J}} = V_{\text{top layer}}\,\mathrm{x}_{\text{degas,J}} = \frac{\mathrm{V}_{\text{light}}}{\left(1. - \mathrm{x}_{\text{degas,j}} - \mathrm{x}_{\text{jet}}\right)}\,\mathrm{x}_{\text{degas,j}}$$

Substituting in

$$x_{\text{degas,j}} = \mathrm{x}_{\text{degas}}\left(1. - \mathrm{x}_{\text{jet}}\right)$$

The degas volume expression becomes

$$V_{\text{degas-top layer,j}} = V_{\text{top layer}}\,\mathrm{x}_{\text{degas,j}} = \frac{\mathrm{V}_{\text{light}}}{\left(1. - \mathrm{x}_{\text{degas}}\right)}\,\mathrm{x}_{\text{degas}}$$

which is equal to the degas volume fraction without jet mixing, so the degas volume fraction and degas fraction for complete cavern mixing is independent of the amount of jet mixing.

Using the oil properties listed in Webb and Lord (2010), an oil shrinkage number of 285 BBL/day (creep plus oil addition rate), and a degas flow rate of 130,000 BBL/day, the increase in oil density due to temperature and degas processes is about 0.0022, or 0.22 percent. The data from the cavern indicates that the transition occurs at 0.45 degassed cavern volumes (Webb and Lord, 2010). For initial volume fractions of the light oil of 5% (Webb and Lord, 2010) and 6.25% (Lord and Webb, 2010), the degas volume fraction for transition from plug flow to complete mixing is 0.45 and 0.57 cavern volumes, respectively. The mixing layers model curves for these two initial volume fractions are shown in Figure 6-1.

The cavern volumes are slightly different than given by Webb and Lord (2010). In Webb and Lord (2010), the cavern volume given was the total cavern volume of the upper layer, not just the degassed fraction. In contrast, the results here are for the degassed volume that is part of the upper layer, and the results are independent of any jet mixing as discussed above. The present

value is also more appropriate to compare with the cavern data than the value plotted in Webb and Lord (2010). The data-model comparison for both results is shown in Figure 6-2.

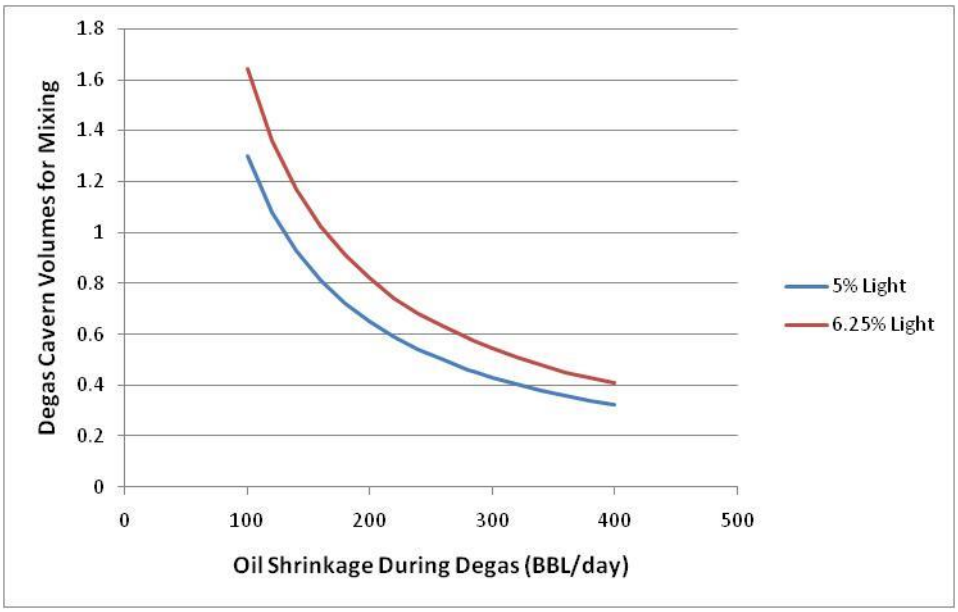


**Figure 6-1. BM106 Cavern Volumes for Complete Mixing vs. Oil Shrinkage Rate (Webb and Lord, 2010)**

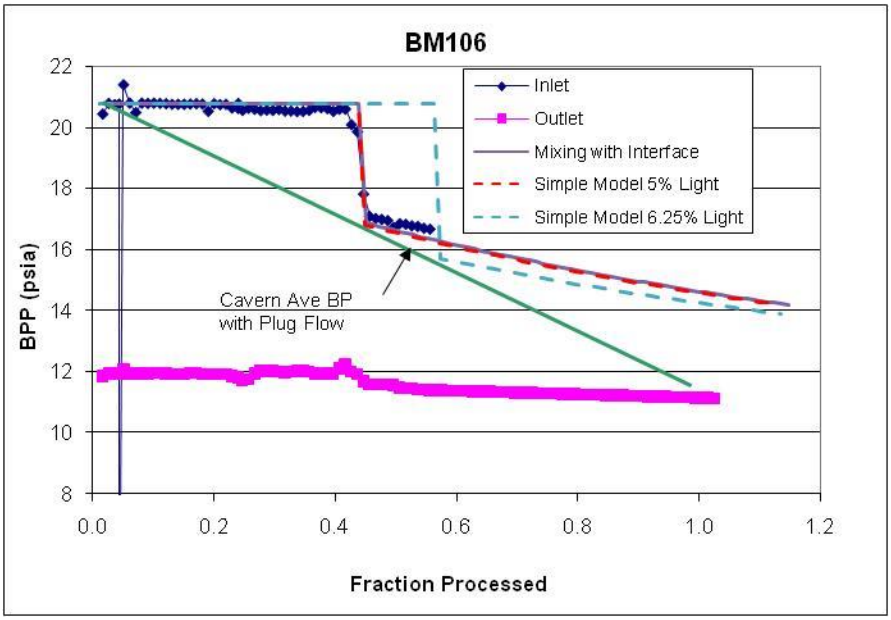


**Figure 6-2. Data-Model Comparison for BM106 Degas (Webb and Lord, 2010)**

# 7 Scaling issues

Dimensionless scaling of flow parameters and fluid properties is often used to go between full-scale conditions and laboratory-scale experiments. Scaling is also important in simulations in that the dimensionless number range of models and parameter values should be consistent. In externally-driven mixing, the Reynolds number and the Froude number (or Richardson number) are of primary concern.

In laboratory-scale experiments, it is often difficult to exactly match the Reynolds number, or ratio of inertial to viscous forces, between the experiment and the full-scale flow. The Reynolds number *Re* is defined as

$$Re = UD/\nu$$

where $U$ is the velocity, $D$ is a characteristic length (e.g., pipe diameter), and $\nu$ is the kinematic viscosity ($\nu = \mu/\rho$, with μ the absolute viscosity and ρ the density). Typical SPR inlet jet flows are 100,000 bbl/day of water or crude oil flowing through a 9.85 inch ID string, yielding inlet jet *Re* values on the order of $3.9 \times 10^5$ to $9 \times 10^5$, which cannot be achieved in a typical laboratory-scale experiments.

Instead, laboratory-scale experiments typically operate in a Reynolds number range that is considered to be fully turbulent although well below the full-scale value. The jet Reynolds number should indicate inertia-dominated, turbulent flows, so the flow physics should be the same, and increasing *Re* should not significantly change the flow or mixing behavior. The jet Reynolds number for this condition is discussed in Ungate et al. (1975), who state that the critical Re for a jet to be considered fully turbulent is on the order of 1500, and Dimotakis et al. (1983), who give a critical Re on the order of 2500-3000. However, more recent work by Dimotakis (2000) and Fernando (2011) indicate that there is a jet mixing transition at *Re* of approximately 10,000 where the flow becomes fully turbulent at all scales.

The Reynolds number question also applies to simulations. The Reynolds number range of experimental data used to develop and validate turbulence models, for example, is probably well below the range of full-scale conditions. Application outside of the range of validation should be performed with caution.

For buoyancy conditions in which the density of the inlet jet is different than the resident fluid, the Froude number, *Fr*, or ratio of momentum to buoyant force, is should be equal between the full-scale conditions and the laboratory setup. The Froude number is defined as:

$$Fr = \frac{\rho_i U^2}{(\rho_i - \rho_r) g d} \tag{2}$$

where $\rho_i$ is the injected oil density, $\rho_r$ is the resident oil density, $g$ is gravitational acceleration, $d$ is the injection pipe inner diameter, and $U$ is the mean injection velocity. Note that the Richardson number, which is often used, is simply the inverse of the Froude number. Equating $Fr$ between the lab and cavern conditions gives:

$$\frac{\rho_{i_{full}} U_{full}^2}{(\rho_i - \rho_r)_{full} g d_{full}} = \frac{\rho_{i_{lab}} U_{lab}^2}{(\rho_i - \rho_r)_{lab} g d_{lab}} \tag{3}$$

Geometric scaling is also sometimes employed, such as the aspect ratio of the full-scale cavern and that of the experiment. That scaling is straightforward.

Comparison of plume heights from small-scale data as described in Chapter 3 have been compared to large scale behavior by Turner (1986). Extrapolation of this plume height dependency is discussed by Turner (1986). Data-model comparisons for laboratory experiments, ice rink conditions, and oil fires as well as data for a volcano eruption are shown in Figure 7-1, and the small-scale relationship applies to the larger scales. Note that the nomenclature in this figure is somewhat different than given in Chapter 3 in that $Z_m$ is given in terms of $F$ and $G$ as

$$Z_m = 5\, F^{1/4} G^{-3/8}$$

Now

$$F = B/\pi$$

$$G = N^2$$

so

$$Z_m = 3.8\, B^{1/4} N^{-3/4}$$

which is the same expression given earlier for a plume. Data-model comparisons are very good at all physical scales.

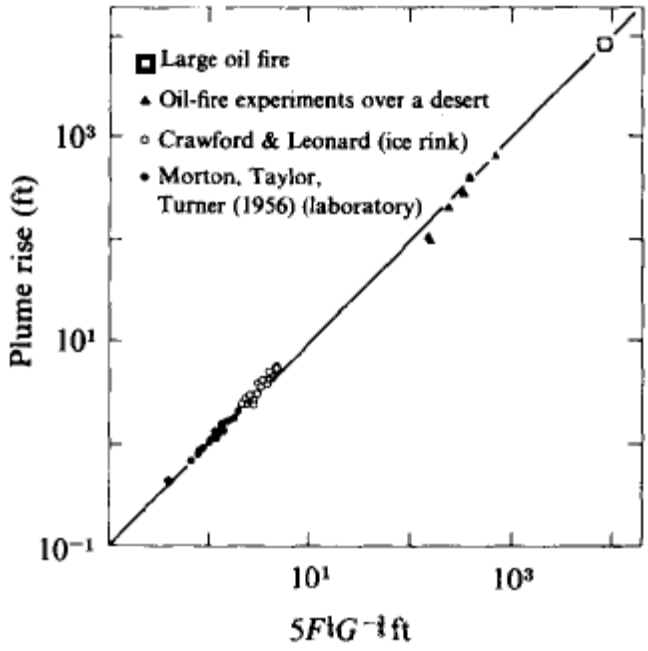


**Figure 7-1. Extrapolation of Plume Rise in Stratified Environments to Large Scales (Turner, 1986)**

# 8 Summary of Current Models for Externally-Driven Mixing

The SDM model developed by Lord and Rudeen (2007) is extremely useful in that it identifies the importance of mixing through comparison of the model results with field-scale degas data. However, the model does not predict mixing. The CFD model presented by Webb can theoretically predict mixing but validation questions remain including scaling issues and the turbulence model. The computer time for simulations is also of concern depending on the spatial fidelity of the model.

In order to obtain additional insight into the processes involved in cavern-scale mixing due to jet/plume fluid injection and to provide small-scale experimental data for model development and validation, a combined experimental and theoretical program for cavern-scale mixing during typical degas operations was initiated at Arizona State University (ASU) under Professor H.J.S. Fernando in 2006. In 2010, Professor Fernando moved to the University of Notre Dame (ND), where the program continued. Details of the work are given in a thesis and dissertations and are summarized in the next few chapters.

# 9 Studies Conducted at Arizona State University

## 9.1 Summary of Studies

Studies of double-diffusive convection as applied to SPR caverns were conducted by Suhas Pol under the direction of Professor Fernando at ASU as detailed in the internal mixing report (Webb, 2016b). In addition, preliminary jet mixing studies were performed by Suhas Pol and Darren Gest under Professor Fernando's direction as summarized in this section. The material in this section is from the dissertation of Pol (Pol, 2010) and the thesis of Gest (Gest, 2010) and has been slightly edited for this report. The original section numbers, etc., used by Pol have been retained. Copies of the original dissertation and thesis are in the SPR library.

Some changes and corrections have been made. They are

1. Equation 4.2.1 has been changed from

$$w_c = w_o e^{-(z-z)^*}$$

   to

$$w_c = w_o e^{-(z-z^*)}.$$

2. Some material has been added from Gest (2010) to section 4.4.
3. Some minor editing has been done.

# 4. Jets in a Confined Two-layer Stratified System

## 4.1 *Introduction*

The motivation for this part of the study was to understand mixing process occurring during the degas operations in SPR caverns. Extensive literature on free jets in homogenous or stratified fluids is available (Fischer et al. 1979, Abromovich & Schindel 1963), however, there are only a very few studies that report the effects of confinement on jets in homogeneous fluids (Risso et al. 1996, Voropayev et al. 2010). The effect of confinement on jets in stratified fluids also has been studied in a few studies (Gest 2010). The mean flow of a homogeneous jet issued in a confined narrow container tends to vanish at about *4D* from the inlet, creating a zone of diffusive turbulence. The apparatuses used in previous studies, however, did not have a fluid exit configuration similar to that of SPR caverns, and the excess fluid was simply collected upstream of the jet inlet (with a rising fluid level in the case of vertical container configurations). Further, the effects of a density gradient between the jet inlet and background fluid in the container have not been studied earlier. The present study was undertaken to simulate more closely the flow configuration of the SPR caverns and to understand the effects of density gradients between the jet exit and the background fluid downstream. In the following section, theoretical preliminaries of the jet interface interaction will be described, followed by an experiment conducted to investigate these theoretical ideas.

## 4.2 *Theoretical Considerations*

Fully turbulent jets issued in confined regions lose their momentum (~4 *D* from the inlet, where D is the diameter of the container) as a result of the adverse pressure gradients developed in the cylinder (Vorapayev et al. 2010). The resulting loss of momentum causes the residual flow to contain only zero mean flow turbulence, and thus leaving only the diffusive turbulence in the tank (Risso et al. 1997). The confinement effects are largely independent on the location of the boundaries normal to the axis of the jet, upstream or downstream, (Vorapayev et al. 2010). The absence of a normal wall downstream relieves the pressure gradients that develop due to confinement effects, and hence spare the jet from dissipating momentum. From the measurements made by Risso et al. (1997), in confined jets the variation of centerline streamwise velocity $w_c$ with the streamwise distance $z$ can be estimated as,

$$w_c = w_o e^{-(z-z^*)} \quad , \tag{4.2.1}$$

where $w_o$ is the jet exit (axial) velocity and $z^*$ is the distance from the inlet up to a virtual origin. From the data presented by Risso et al. (1997), for homogenous turbulent jets $z^* = 0.8D$.

When there is a density difference at the jet inlet (i.e., fluid at the jet inlet $\rho_{in}$ and the density $\rho_{b1}$of the fluid in the container are different), the buoyancy jump at the inlet $\Delta b_{in}$ needs to be taken in to account to predict the evolution of the flow. It can be hypothesized that for $\rho_{in} \ll$

$\rho_{b1}$that the momentum of the jet causes the formation of a mixed layer of fluid near the surface, since the jet lose its momentum and reverse the propagation direction after a certain distance. When a positively buoyant fluid is injected without confinement, it propagates to a certain distance, loses its momentum and then rises to the top. The distance to which it travels can be as (Turner 1966).

$$z_n = c_6 M^{1/2} F^{-1/2} \quad , \tag{4.2.2}$$

where M is the momentum flux, F the buoyancy flux and $c_6$~1.85 is a constant. When there is a pressure gradient introduced due to confinement, $z_n$ can be smaller, and help preserve the density interface. This latter problem has not been studied so far. On the other hand, when the jet is negatively buoyant, the combined forcing due to initial momentum flux and reinforcing buoyancy forces cause the jet to propagate farther against the adverse pressure gradient, thus making the density interface vulnerable to breakup by the jet. Below as a first step, we consider the case of $\rho_{in} = \rho_{b1}$, which is a neutrally stratified jet issuing into a two layer fluid.

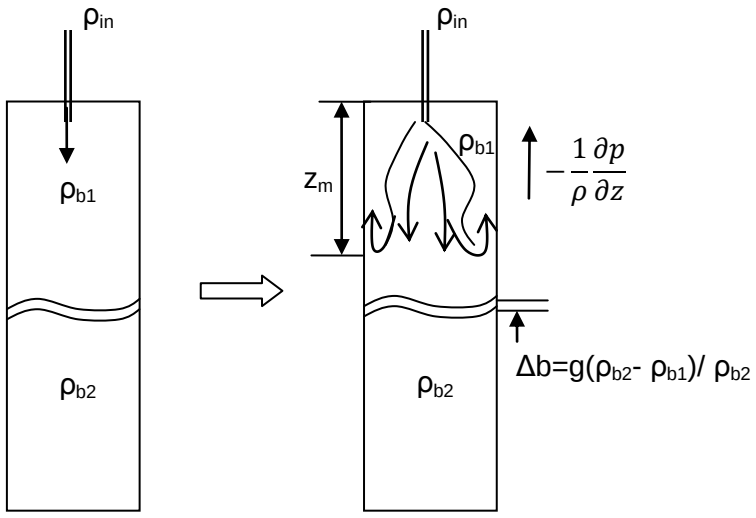


**FIGURE 4.2.1:** Discharging of a buoyant jet into a homogeneous fluid. Here the momentum of the jet is dissipated by the adverse pressure gradient and positive buoyancy of the jet.

4.3 *Neutral Jet in a Two-Layer Fluid*

Consider the case of a jet issuing into a confined environment. The decay of axial velocity can be written as

$$w_c = w_o e^{-n_1(z-z^*)} \quad , \tag{4.3.1}$$

where $n_1$ is an empirical coefficient. Now the upper layer density is the same as the jet density ($\rho_{in} = \rho_{b1}$), but the lower layer density ($\rho_{b2}$) causes a buoyancy jump $\Delta b = g(\rho_{b2} - \rho_{in})/\rho_{b2}$.

For a significant jump in buoyancy ( $\rho_{in} << \rho_{b2}$ ), one argument would be that the buoyancy and the inertial forces are in balance at the 'bouncing back' of jet from the interface, thus leading to

$$w_c^2 \sim \Delta b h_i \text{ for } h_i < 4D \tag{4.3.2}$$

where $h_i$ is the distance from the jet inlet up to the location where jet mixes the interface due to impingement. Beyond $z \geq h_i$, the mean fluid motion in the axial direction can be expected negligible. Substituting (4.3.1) in (4.3.2), we get,

$$h_i \Big/ e^{-2(h-z^*)n_1} \sim \frac{w_o^2}{\Delta b} \text{ for } h_i < 4D \tag{4.3.3}$$

which can be written as

$$h_i \Big/ D \sim \frac{w_o^2 e^{-2(h-z^*)n_1}}{\Delta b \; D} \tag{4.3.4}$$

Another way to estimate jet mixing at the interface is to consider the distance that interface moves from its original position $\Delta a$ upon initial (vigorous) jet mixing. This is illustrated in Figure 4.3.1. The jet penetrates the upper layer of depth $a$ and then impinges on the interface across which the buoyancy jump is $\Delta b$. The jet excessively decelerates over the distance than it would if the density interface was absent.

A balance of inertia forces at $z = a + \Delta a$ gives

$$\Delta a \sim \frac{w_o^2 e^{-2(a+\Delta a-z^*)n_1}}{\Delta b} \qquad \text{for } (a + \Delta a < 4D) \tag{4.3.5}$$

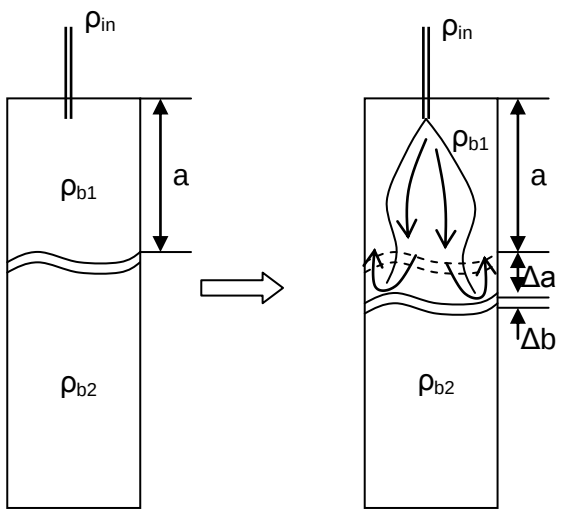


**FIGURE 4.3.1:** Schematic of mixing due to impingement of a jet on an interface of a two-layer stratified fluid with interface at a distance a, from the inlet.

4.4 *Experiments*

Figure 4.4.1 is a schematic of the experimental setup that was initially used in sink-source flow studies. It consisted of a closed cylindrical tank of small aspect ratio ($W/H$=1/10, $W$=12.07 cm, $H$=118.75 cm). The sides of the tank were made of Plexiglas to enable visualization and measurements. This tank was water sealed from all sides; nevertheless, the design permitted the placement of jet inlet, which was a blunt-nosed 0.13 cm inner diameter needle, at the center of the top lid. A separate outlet pipe was inserted from the top, offset from the center toward the sides such that excess fluid can be drawn out from a location close to the bottom of the tank, similar to SPR caverns flow configuration during degas operations.

For the experiments, a two layer stratified fluid with known buoyancy difference $\Delta b$ and the interface location was filled in the tank. Generally, a fresh water layer was placed atop a salt water layer of known salinity with the interface height minimized by very slow filing of the second layer. A turbulent jet ($Re$ > 4000) of known velocity consisting of fresh water was introduced from the top and its evolution was observed and measured. The change in location of the interface $\Delta a$ was estimated by noting the point at which a buoyancy jump is observed in the salinity of the outgoing fluid. The above case of experiments was considered since it simulates one of the most basic degas configurations. A simpler case which has already been reported by Risso et al. (1997) is the evolution of homogenous jets in low aspect ratio containers. Table 4.1 tabulates the experimental conditions for 27 experiments that were performed.

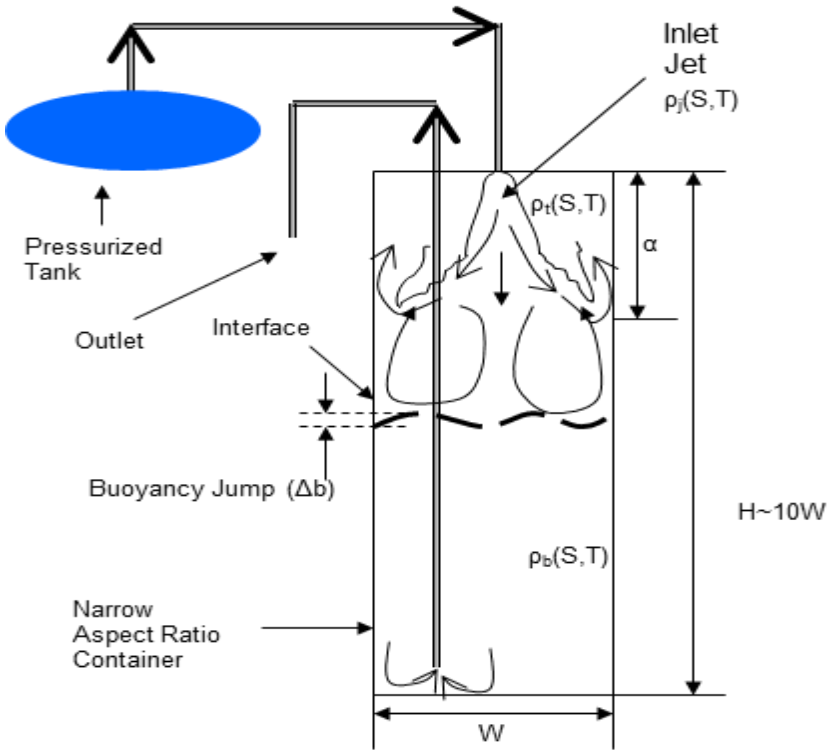


**FIGURE 4.4.1:** A schematic of the experimental setup for jet inlet/outlet studies. The setup consists of a narrow rectangular tank (*W/H*=10) with jet inlet at the top.

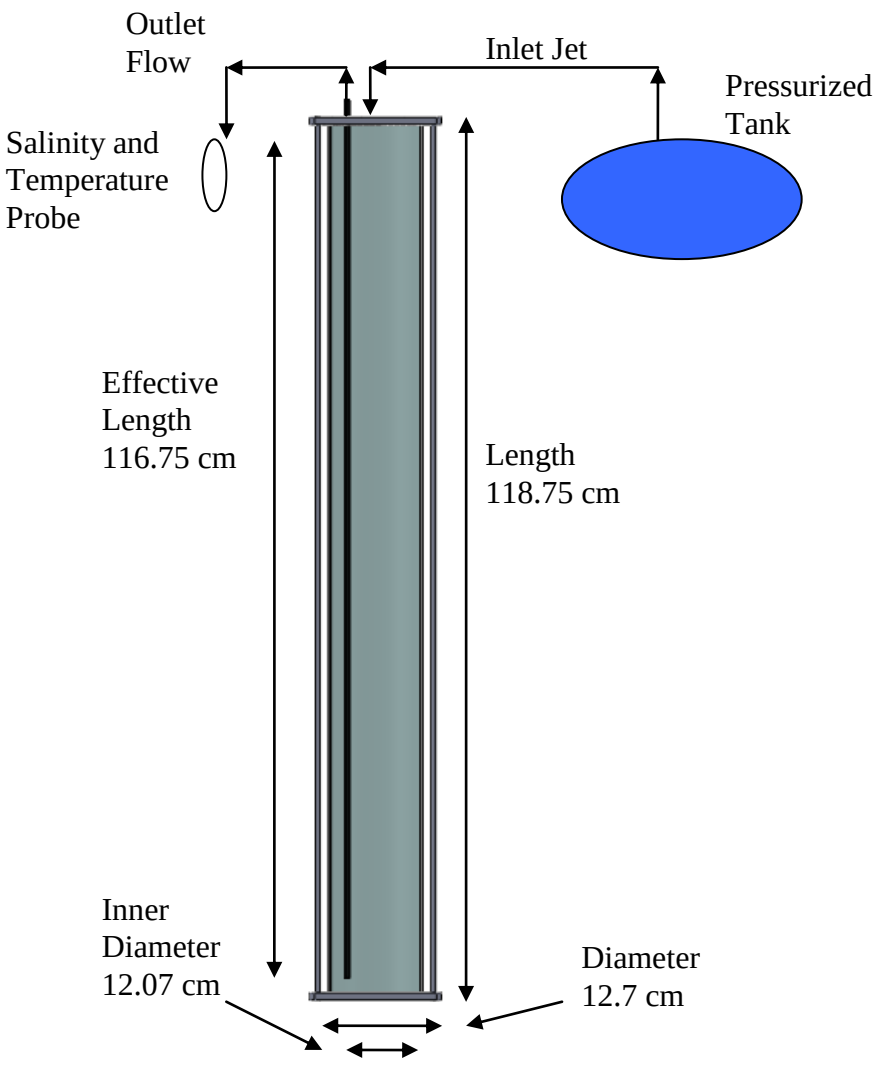


**FIGURE 4.4.2:** Experimental Dimensions (added; Figure 4.1 from Gest (2010))

| $h_{Uo}$ (cm) | Salinity (ppt) | Inlet Jet Velocity ($w_j$) (m s$^{-1}$) | Buoyancy Jump $\Delta b_o = \frac{g\Delta\rho_o}{\rho_o}$ (m s$^{-2}$) | $\frac{h_{Uo}}{D}$ | $Ri_{hU} = \frac{\Delta b h_U}{w_I^{\,2}}$ | $Ri_o = \frac{\Delta b h_U}{w_j^{\,2}}$ | $Re = \frac{w_j d_o}{\nu}$ |
|---|---|---|---|---|---|---|---|
| 9.0 | 148 | 8.86 | 1.08 | 0.7 | 0.005 | 0.001 | 12312 |
| 9.0 | 127 | 4.11 | 0.92 | 0.7 | 0.022 | 0.005 | 5720 |
| 10.0 | 78 | 7.12 | 0.57 | 0.8 | 0.006 | 0.001 | 9894 |
| 10.0 | 100 | 7.70 | 0.73 | 0.8 | 0.006 | 0.001 | 10708 |
| 10.5 | 110 | 6.47 | 0.80 | 0.9 | 0.011 | 0.002 | 8997 |
| 11.2 | 103 | 5.85 | 0.75 | 0.9 | 0.016 | 0.002 | 8128 |
| 12.2 | 123 | 5.89 | 0.90 | 1.0 | 0.024 | 0.003 | 8187 |
| 19.5 | 128 | 4.50 | 0.93 | 1.6 | 0.228 | 0.009 | 6251 |
| 20.0 | 75 | 6.24 | 0.55 | 1.7 | 0.077 | 0.003 | 8679 |
| 20.0 | 100 | 7.70 | 0.73 | 1.7 | 0.068 | 0.002 | 10708 |
| 20.5 | 148 | 3.95 | 1.08 | 1.7 | 0.423 | 0.014 | 5492 |
| 21.0 | 148 | 8.83 | 1.08 | 1.7 | 0.094 | 0.003 | 12272 |
| 28.5 | 98 | 8.33 | 0.71 | 2.4 | 0.330 | 0.003 | 11586 |
| 29.5 | 148 | 8.27 | 1.08 | 2.4 | 0.618 | 0.005 | 11494 |
| 29.5 | 125 | 5.25 | 0.91 | 2.4 | 1.292 | 0.010 | 7302 |
| 29.5 | 125 | 4.28 | 0.91 | 2.4 | 1.949 | 0.015 | 5944 |
| 30.0 | 75 | 6.24 | 0.55 | 2.5 | 0.608 | 0.004 | 8679 |
| 30.5 | 124 | 4.36 | 0.90 | 2.5 | 2.273 | 0.014 | 6057 |
| 31.2 | 163 | 6.59 | 1.19 | 2.6 | 1.503 | 0.009 | 9160 |
| 31.5 | 148 | 3.72 | 1.08 | 2.6 | 4.543 | 0.025 | 5168 |
| 32.0 | 158 | 4.12 | 1.15 | 2.7 | 4.373 | 0.022 | 5722 |
| 35.5 | 123 | 4.45 | 0.89 | 2.9 | 5.757 | 0.016 | 6192 |
| 35.5 | 150 | 4.51 | 1.09 | 2.9 | 6.852 | 0.019 | 6267 |
| 40.0 | 149 | 4.49 | 1.08 | 3.3 | 16.262 | 0.021 | 6247 |
| 40.7 | 126 | 4.36 | 0.92 | 3.4 | 16.732 | 0.020 | 6056 |
| 45.4 | 100 | 5.72 | 0.73 | 3.8 | 18.765 | 0.010 | 7956 |

**Table 4.1:** Jet experimental data and calculated variables. (Table 4.1 in Pol replaced with Table 5.1 from Gest (2010); the first 5 columns are the same; Gest added the last 3 columns where *Ri* is Richardson number, $w_j$ and $w_I$ are the jet and interface velocity, $d_0$ is the nozzle diameter, and $h_U$ is the upper layer height.)

The Particle Image Velocimetry (PIV) was attempted to obtain flow field information. The PIV system utilized a 532 nm laser-pulse generator in combination with cylindrical lenses to produce a light sheet in the vertical plane. The pulse generator was set to produce a pair of laser pulses separated by a time lag of 2000 µs with a frequency of 5 Hz for each pair. The fluid in the tank was seeded with Pliolite particles of size ~ 75 microns, which acted as tracers following the fluid flow. A high resolution camera was coupled with the laser pulse generator via synchronizer to capture images of moving particles illuminated by the laser light sheet. This allowed measurement of one horizontal and the vertical component of velocity at a rate of 5 Hz in a 2*D* plane located at the axis of the tank.

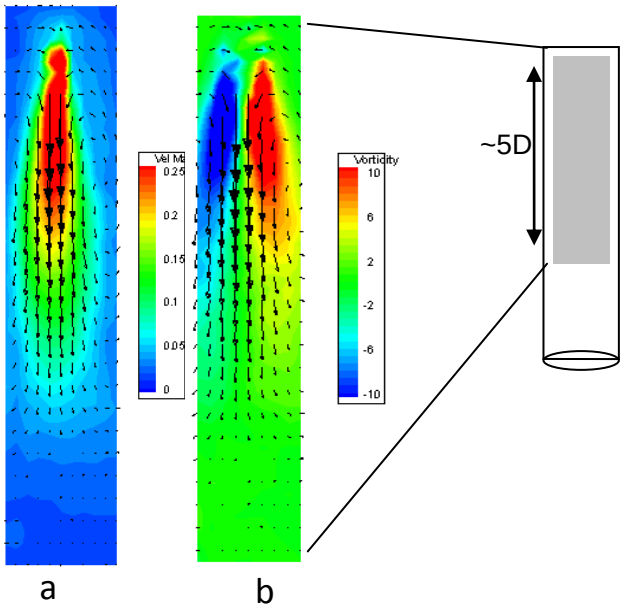


**FIGURE 4.4.2:** Contours of velocity magnitude overlain with velocity vectors (a) and contours of vorticity magnitude with velocity vectors for the case of homogenous jet inlet at Reynolds number *Re*~8000.

The changing mixed layer height both due to entrainment of the jet and the downward movement of the interface due to constant outflow rate gradually reduced the concentration of tracer particles, creating non-optimal conditions for PIV measurements. Further the problem was exacerbated by high variation in the velocity of the jet fluid within the low aspect ratio container, requiring constant modifying of the time lag between two laser pulses (2000 μs, was found to be optimal). Due to aforementioned reasons, PIV measurements for the experiments enlisted in table 3.4 could not be obtained successfully. Owing to the simplicity of the configuration, however, PIV measurements for the evolution of homogeneous jets in low aspect ratio was obtained.

Figure 4.4.2 is a snapshot of PIV measurements averaged over 45 seconds showing velocity vectors and contours of velocity and vorticity magnitude for a case where the jet *Re* ~ 8000. As expected from previous studies (Risso et al. 1997, Voropayev et al. 2010), it is clear that the jet loses nearly all its momentum at around a downstream distance of 4*D*. Since, velocity measurements of the stratified cases could not be obtained, the constant $n_1$ is set to 1 in (3.5.7) to estimate the centerline velocity.

4.5 *Experimental Results*

Based on the experiments conducted in collaboration with Gest (2010) described above the viability of the expression (4.3.5) could be evaluated based on direct measurements.

Figure 4.5.0 shows the experimental data reduction. The salinity at the outlet as a function of time is shown in Figure 4.5.0a. These results can be simply flipped to give the salinity as a function of percent volume, or equivalently height, in the vessel as shown in Figure 4.5.0.b. (This paragraph added as well as Figure 4.5.0; Figure 4.3 from Gest, 2010).

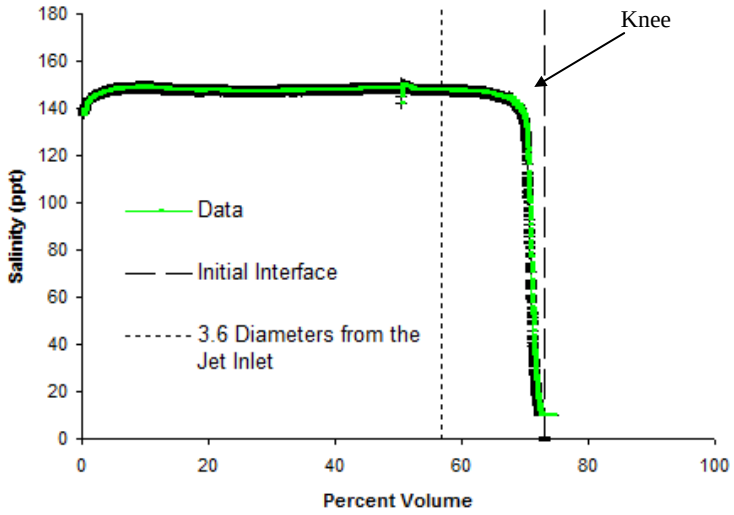


(*a*)

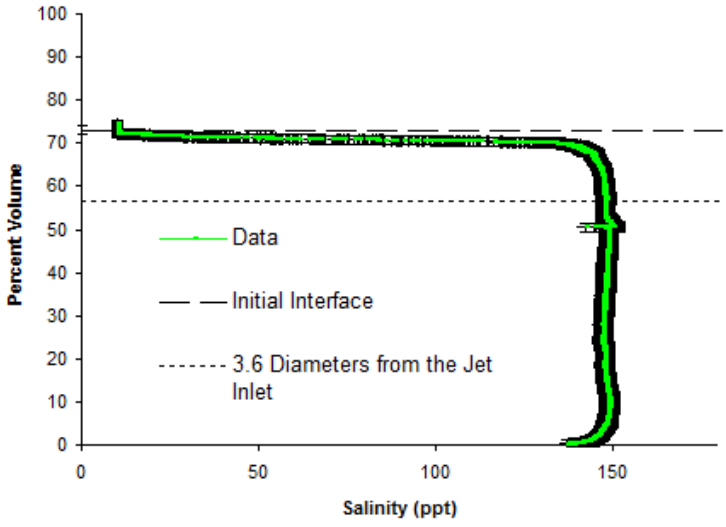


(*b*)

**FIGURE 4.5.0.** Experimental Data Reduction

The experimental parameters for these runs are given in Table 4.1, where the salinity of the bottom layer, jet inlet velocity, buoyancy jump, and the inverse aspect ratio of the upper layer *a/D* are given. For $\Delta a / a$ << 1, it is possible to write (4.3.5) as

$$\Delta a / a \sim \frac{w_o^2 e^{-2(a-z^*)n_1}}{\Delta b \; a} \sim \frac{1}{Ri_I} \tag{4.5.1}$$

where $Ri_I$ is the interfacial Richardson number based on the jet velocity at the interface, viz.,

$$Ri_I = \frac{\Delta b a}{w_I^2} . \tag{4.5.2}$$

Where interfacial velocity, $w_i$ , is given by,

$$w_I = w_o e^{(a-z^*)} \tag{4.5.3}$$

Figure 4.5.1 shows the variation of $\Delta a / a$ as a function of $Ri_I$ , and the data follows a best fit power law of the form

$$\frac{\Delta a}{a} \approx 0.1 \left( \frac{1}{Ri_I} \right)^{1/2} \tag{4.5.4}$$

indicating that the simple power law behavior proposed in (4.5.1) is not followed. This may be due to the dependence of interfacial velocity on the stability of the interface ( $Ri_I$ ) in which case it cannot be represented in terms of homogeneous fluids. Further work is warranted in delineating the correct interfacial velocity. Nevertheless, (4.5.3) can be used as a good engineering correlation for the jet penetration. If the density interface is located at $z > 4D$, then the diffusive turbulence dominates in the interfacial area, and the plug flow is expected to occur.

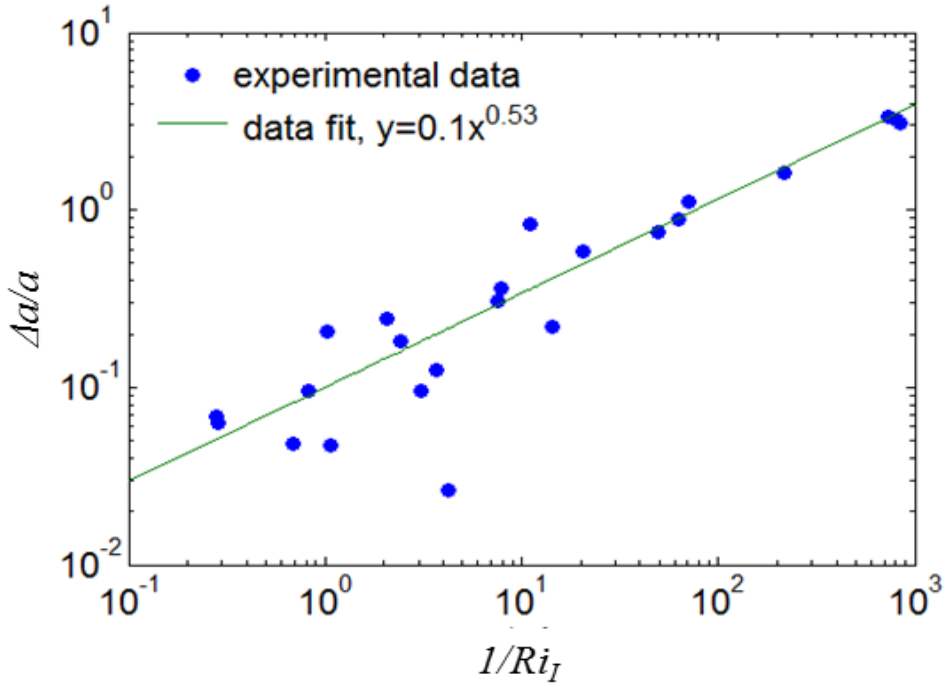


**FIGURE 4.5.1.** Variation of the normalized penetration depth with interfacial Richardson number.

## 5. Conclusions

A combined theoretical/experimental program was conducted with the aim of studying fluid dynamical phenomena occurring in the U.S. Strategic Petroleum Reserves (SPR), wherein oil from multiple sources is stored in underground salt caverns. These caverns are slender and tall, which are produced by 'solute mining' of subterranean salt deposits. The caverns extend from 2000 - 4000 ft. depth, with a diameter of about 200 ft. Thus, the cavern aspect ratio width / height is about 0.1. Owing to the presence of different oils, the petroleum in the caverns is stably stratified, but this stratification is subjected to the geothermal heat flux, which acts as natural forcing on caverns. The effect of a heat flux on a stable density (solute) gradient has been studied previously, but the present case differs in that the convection in caverns has a low aspect ratio and hence the width ($W$) is important.

In a series of experiments, the impact of a neutrally buoyant jet on a density interface was investigated. These experiments were conducted in collaboration with Gest (2010), where a jet was released to the upper layer of a two layer fluid contained in a low overall aspect ratio vessel while letting the fluid from the container exit from the bottom layer at a rate equal to the inflow. A tall pipe penetrating to the bottom layer was employed. The container was pressurized, so that the pressure is built by the jet causes the fluid from the lower layer to exit along the tall pipe.

This configuration mimicked the flow situation during degassing of SPR caverns. The jet impingement causes mixing at the interface according to the nature of the jet at the interface. If the distance to the interface $z > 4D$, $D$ being the width scale of the container, then the jet momentum is dissipated before reaching the interface. In this case the effect of jet on the interface can be treated as that of diffusive turbulence (without mean momentum), and hence can be considered weak (Fernando 1991). When $z < 4D$, however, the interaction of the mean momentum flux with interfacial buoyancy forces and tends to cause mixing at the interface depending on the local Richardson number. A simple balance of buoyancy forces resisting the inertia forces of the advancing jet could not explain the observed jet mixing behavior (i.e., the depth to which the interface advances as a result of initial mixing). The involvement of the container width as a variable, in addition to local parameters, is suspected to be the cause. An empirical correlation for the jet mixing distance was presented, for which theoretical foundation is yet to be developed.

## 9.2 Evaluation of Data

At first glance, the experimental data seem to be amenable to simulation and as validation data. However, there are some problems with the data. Note that time-dependent salinity data are available for most of the experiments listed in Table 4.1.

For example, let's look at the detailed and tabulated data for the two highlighted rows in Table 4.1 given earlier. The parameters look to be the same except for different inlet jet velocities, which would make the two experiments good candidates for model evaluation.

However, on further inspection, the data are not that similar. The higher velocity salinity information in Table 4.1 and the transient salinity data are considerably different as plotted in Figure 9-1. Note that the initial salinity profile in the experiments was not measured because the test section was capped off and the existing hole was too small for the probe (Gest, 2010). If one were to believe the tabular value and use that for the initial condition, the profile would be fresh water from the top down to 29.5 cm and then a salinity of 125 ppt to the bottom. The detailed data show that the maximum salinity is about 160 ppt – much greater than given in the table. In contrast, the lower velocity tabulated and detailed data are consistent as shown in Figure 9-2. The value of 125 ppt is reflected in the transient data, so presumably these data could be used for model evaluation.

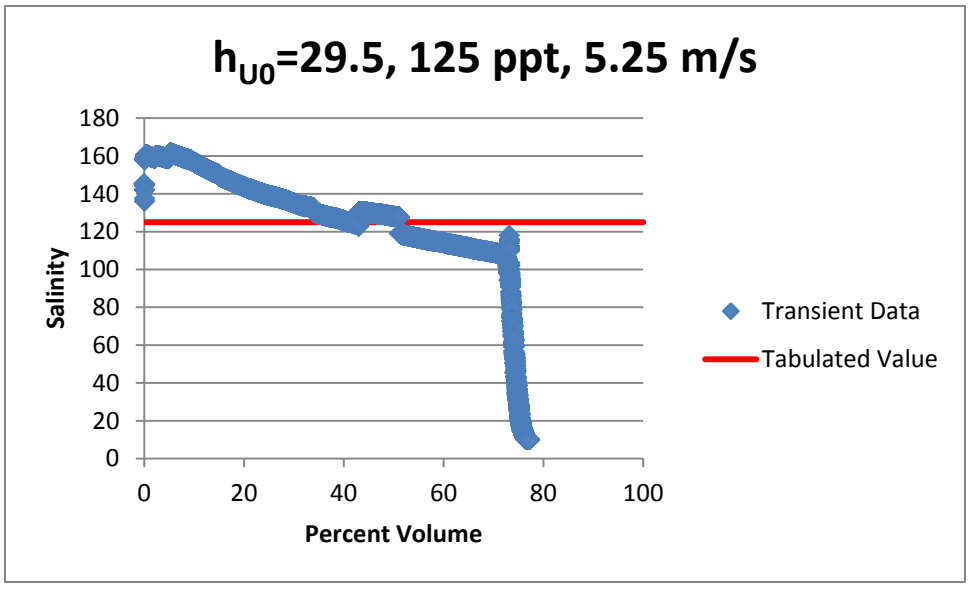


**Figure 9-1 Transient and Tabulated Data for Case 1**

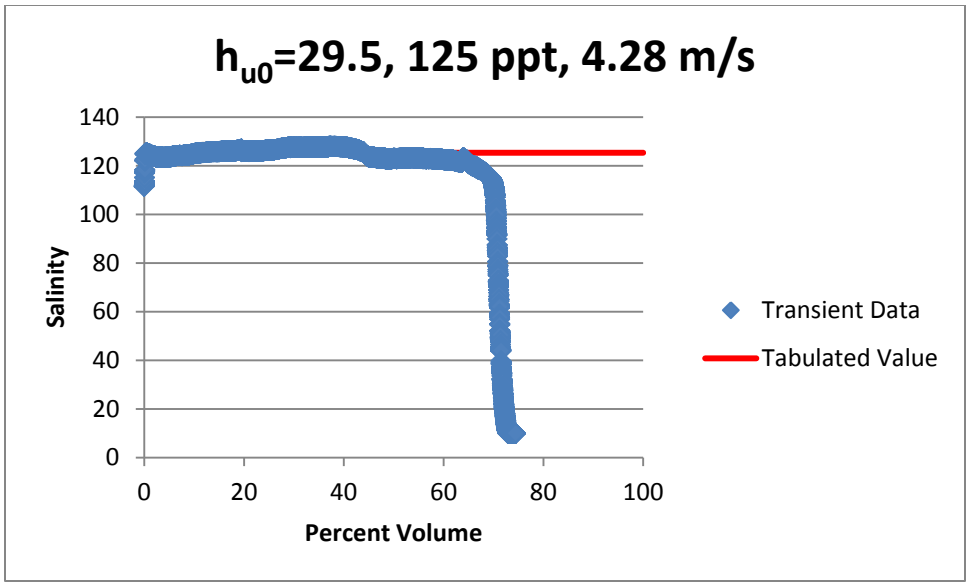


**Figure 9-2 Transient and Tabulated Data for Case 2**

Most of the data in Table 4.1 have been evaluated further. The ratio of the maximum measured salinity data from the time-dependent salinity data are compared to the initial salinity data from Table 4.1 in Figure 9-3. As can be seen, the maximum salinity data are often far greater than the initial salinity data indicating that the parameters in Table 4.1 may not be accurate.

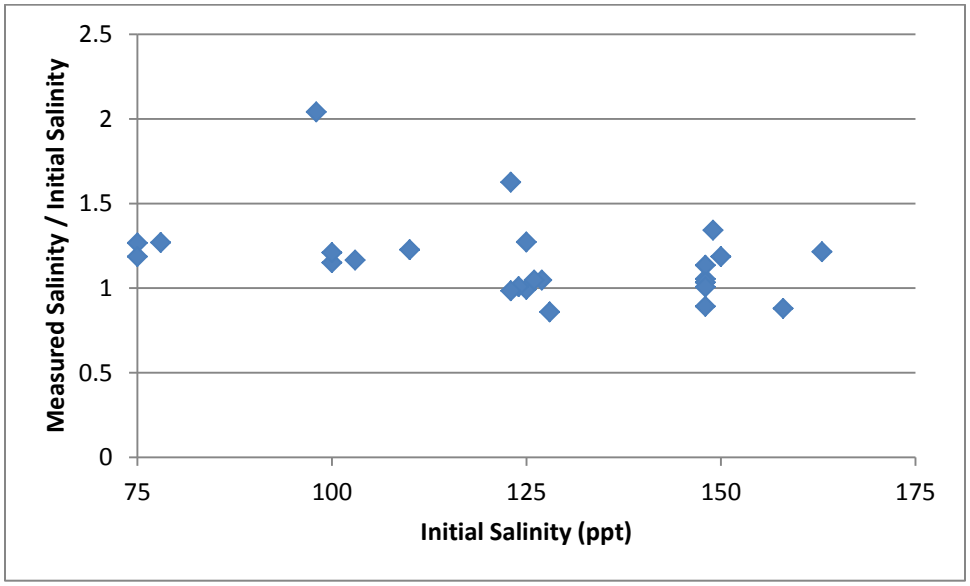


**Figure 9-3. Evaluation of ASU Salinity Data**

However, the problem of the initial conditions for the experiments is an open question. Which data do you select and what criteria do you use? Should a step function profile be assumed even though it was not directly measured? These problems call into question the usability of these experimental data for model evaluation and development. While these data may be qualitatively interesting, quantitative use is probably limited.

# 10 Studies Conducted at Notre Dame

This chapter includes material from the Ph.D. dissertation of Chinmoy Nath (10.1) as well as material from other studies conducted at the University of Notre Dame (10.2, 10.3) as given by Fernando (2012).

## 10.1 Chinmoy Nath Dissertation

This section is from the Ph.D. dissertation of Chinmoy Nath (Nath, 2013) with minor editing as noted. The full original dissertation is in the SPR library.

A number of these studies have been published – the appropriate publication is noted at the start of each subsection.

# Chapter 1: INTRODUCTION

### 1.1 Motivation

A fundamental understanding of the evolution and dynamics of turbulent jet inside a cylindrical cavity under a range of governing conditions is important for modeling and parameterization of mixing process of crude oil in SPR caverns. During the past several years the Sandia National Laboratories has supported research at University of Notre Dame (UND) aimed at understanding the evolution of turbulent jets in homogenous and stratified fluids, jet stoppage mechanism and mean flow characteristics. The comprehensive laboratory based research program was augmented by theoretical parameterizations carried out by the UND Environmental Fluid Dynamics (EFD) Laboratories to understand the precession of confined jets, turbulent mixing in stratified fluids and flow structures associated with jets in homogeneous fluids.

The author of this thesis was directly involved in the above-mentioned research program for the past four years, the results of which are summarized in journal publications, conference proceedings and in the following chapters.

### 1.2 Problem Statement

Although jet oscillations in long, two-dimensional, cavities have been documented for some 50 years (Molloy and Taylor, 1969), with more recent work delving into basic flow structures and characteristics of turbulence (Mataoui and Schiestel, 2009; Khoo et al., 1992; Villermaux and Hopfinger, 1994; Risso and Fabre, 1997; Liu et al., 1997, Lawson, 2001), no reliable parameterizations exist that can be used to extrapolate laboratory results to large cylindrical caverns. Confined round jets have also been used in a number of previous experiments (Sonin et al., 1986; Brown et al., 1990). In these studies, however, the main interest has been to obtain flow characteristics at distances larger than the jet penetrating distance $x>x^*$, in the region of

weak turbulence (Risso and Fabre, 1997). No general parameterizations are available for typical mean velocity at $x \leq x^*$.

As mentioned, a typical SPR cavern is cylindrical in shape, with roughly a diameter of 70 m and height 700 m (aspect ratio = width/height~0.1), holding about 10 million barrels of crude oil (Lord and Rudeen, 2007). The cavern top is usually at a depth of ~ 700 m. At such oil storage pressures, subsurface gases seeping into the cavern are absorbed and retained in crude oil, necessitating periodic degassing to prevent the deterioration of oil quality. As the nature dictates it, due to geothermal heat flux and stratification within the cavern, one or more stable layers separated by slight buoyancy jumps are formed in the caverns, which prevent mixing between the degassed fluid emanating from the jet and un-degassed bottom fluid that is being drawn out, if the density interfaces lay below the jet penetrating distance $x > x^*$. As prevention of such mixing greatly increases the efficiency of degassing (Voropayev et al., 2012), the jet penetration distance is a key engineering parameter in SPR degas-operations planning. Thus, the first part of this research is aimed at developing a fundamental understanding on the evolution and dynamics of axisymmetric turbulent jet in a low-aspect ratio cylindrical cavity filled with homogenous fluid.

During degassing operation, gas laden crude oil is removed from the bottom of the SPR cavern, and degassed oil is simultaneously injected near the top of the cavern as a vertical jet from round nozzle. The density (mostly temperature) of post-degassed oil in general differs from SPR caverns oil, and hence often the injected jet is either positively or negatively buoyant. It is of utmost importance to understand the effect of buoyancy on mixing characteristics of such jets as well as the efficiency of oil refilling. Thus, the second part of this research is aimed toward advancing a model for the mixing mechanism of buoyant jets in low-aspect ratio cavity, both in the laboratory and field conditions.

From the operational planning point of view, degassing procedure is expensive, and it takes about 3 months to degas and refill a cavern. In addition, in the real world, engineering constraints do not allow the placement of the jet nozzle at the cavern axis, and thus it is necessary to know the allowable nozzle offset from the cavern axis that would not cause significant increase of jet penetration depth. An increase in jet penetration depth could led to enhance mixing and a delayed cavern refilling time. Therefore, the third part of this research is dedicated to establishing the dependence of jet penetration depth and flow patterns on offset positioning of the jet. The aim is to extrapolate the results to SPR caverns.

## 1.3 Literature Review

In many applied problems, because of the presence of boundaries, fundamental assumptions of free jets are no longer valid. Owing to confinement, significant modifications occur in typical free jet flows. Presence of boundaries impact jet flow structure, and many new phenomena arise that require different approaches of study. The confinement of a jet may arise in different situations: (a) presence of solid walls (b) presence of free surface, and (d) presence of interfaces due to strong stratification.

### 1.3.1 Confined Jet

An experiment conducted by Villermaux and Hopfinger (1994) investigated axisymmetric circular jet in a rectangular cavity. The Reynolds number used for the experiment varied from 100 to 4000. Pitot tube and smoke visualization were employed to measure mean velocities and flow oscillations. The existence of separated recirculatory cells between the main flow and boundary walls was common for confined jet configurations. They proposed that the role of confinement is to establish a recirculating zone adjacent to the jet in the near field that convects large amplitude perturbations upstream. The oscillatory property of confined jets occurred over a range of Reynolds numbers in which free jets do not display low frequency oscillations. At higher Reynolds numbers (Re> 4000), the mean reattachment length was found to be independent of the Reynolds number.

A series of experiments were performed by Risso and Fabre (1997) using a jet moving upward along a vertical cylindrical tube filled with a homogeneous fluid. The container was axisymmetric with a low aspect ratio of about 1 to 12.8, and it had an inlet jet and a circular ring outlet, both on the bottom of the container. These experiments were carried out with much higher Reynolds numbers but the results showed that the Reynolds number did not affect the observed behavior of the jet, especially at the location where the mean velocity of the jet vanishes. They found that the velocity is constant up to $0.5D$, with $D$ being the diameter of the container. Turbulent diffusion then transfers momentum to the surrounding fluid, but the overall momentum decays due to a pressure gradient that develops in the tank. This pressure gradient also causes a much faster decay of velocity with distance. They found that the mean velocity is zero around $3.6D$ from the inlet. The negative velocity then increases from there to a maximum at $4.3D$, and then it slowly decreases to zero beyond that point. At a distance $3D$ the flow becomes dominated by turbulence, with the mean velocity having little effect on the motion anymore. If the tube is long enough for the turbulence to decay ($> 4.3D$), the flow characteristics of the jet do not seem to be influenced by the overall length of the container. In general, this diffusive turbulence does not seem affected by the Reynolds number, aspect ratio, or the ratio of inlet diameter to the outlet cross sectional diameter.

Mataoui et al (2003) conducted experiments with a turbulent plane jet issuing into a rectangular cavity and compared results with numerical data. Measurements were made using hot wire

anemometry, accompanied by smoke visualizations. The experiments were conducted with Re = 4000 to study the effect of confinement on the jet characteristics. They reported three flow regimes, depending on the location of jet exit inside the cavity: oscillatory regime, transitional regime and steady regime. The fundamental frequency in the oscillatory regime was found to increase linearly with the Reynolds number. Mataoui et al (2003) suggested a simple model based on coupling between velocity and pressure, which was proposed to be responsible for oscillatory behavior of the jet.

In previous literature, offset jet flow is divided into three major regions: (a) reverse flow region, (b) attachment region and (c) wall jet region. In different regions the flow structures, respectively, resembled free jets, backward facing step flow, and wall jets. Here a brief summary of literature review on wall jet and offset jet are presented.

### 1.3.2 Wall Jet and Offset Jet

An extensive review of wall jet literature prior to 1981 was done by Launder and Rodi (1981, 1983). The spread rate of the jet is determined by the spread of the jet half widths ($y_{0.5}$ and $z_{0.5}$) in the wall-normal and lateral directions. Launder and Rodi (1981, 1983) reviewed literature on turbulent wall-jets and determined that 3D turbulent wall jets spread much slower in the wall-normal direction than its 2D counterpart. The smaller spread rate is associated with a large lateral spread rate. Launder and Rodi (1981, 1983) determined that the spread in the lateral direction is $\sim 5$ times as large as that in the wall-normal direction. This anisotropic spread rate is characteristic of the 3D turbulent wall jet. Launder and Rodi (1983) argued that the large lateral spread is caused by the mean secondary flow in the 3D turbulent wall jet, and they examined the transport equation for the mean streamwise vorticity.

An experiment with a 2D offset jet using laser Doppler anemometry (LDA) and a pressure probe was performed by Nasr and Lai (1997, 1998). The experiments were conducted at a Reynolds number of 11,000. The jet exit diameter was employed as the appropriate length scales in this study. Some of the quantities reported are the static pressure, distributions of turbulence intensities and Reynolds shear stresses. The maximum mean streamwise velocity of the reversed flow was found to be about $0.27U_0$ ($U_0$ is jet exit velocity). One of the characteristics of the shear layer is the reattachment length, $x_r$. Nasr and Lai (1997) developed the following correlation using their own data and data from previous studies, $x_r/d = 2.63(h/d)^{0.855}$, where $h$ is the distance from the wall and $d$ is the nozzle diameter; this is consistent with the power law expression developed by other investigators. Nasr and Lai (1998) also reported that, downstream of the reattachment point, the velocity decay is much slower than that of a free jet but higher than a wall jet. According to them, the spatial distributions of turbulence intensities and Reynolds shear stresses show a high-turbulence recirculating flow region close to the nozzle plate between the jet and the offset plate. This indicates strong interactions between the flow in the reverse flow zone and the inner shear layer flow in the vicinity of the reattachment point.

Miozzi et al (2010) investigated experimentally a free-surface turbulent jet with and without the presence of a lateral wall. Experiments were conducted with a range of Reynolds number varying from 4000 to 10000. Velocity field measurements were performed by means of Feature Tracking called Optical Flows. The quantities reported were the maximum velocity, half-width velocity and the reattachment length. Miozzi et al (2010) reported that the presence of a free surface limits the entrainment of ambient fluid, thus resulting in a slower decay of centerline velocity than in free circular or plane jets. The presence of a lateral wall strongly modifies the shear layer in comparison to that in free jets. The result for reattachment point as a function of ($h$/$d$) showed quite good agreement with Nasr and Lai (1997) and other authors' work.

## 1.4 Approach And Objective

A laboratory based research program, augmented by theoretical modeling, is conducted to study the evolution of round turbulent jets discharging into a low-aspect ratio cylindrical cavity containing homogenous/stratified fluid in order to enhance our scientific understanding of crude oil mixing process in SPR caverns during degas.

As mentioned before in previous Sections 1.1 and 1.2, numerous factors (such as the jet velocity, cavern diameter, crude oil temperature, background stratification, sidewall heating, nozzle positioning, etc.) are responsible for crude oil mixing in SPR caverns. To comprehend this complicated mixing mechanism inside a huge underground facility, this research work is divided into three different steps. Initially starting with simplified conditions, conclusions derived at one step are implemented to understand mixing mechanism with additional complexities in next step.

In the first part, the evolution of a round turbulent jet released into a low-aspect-ratio cylindrical container filled with a homogeneous fluid is investigated experimentally. Digital video recordings and particle image velocimetry (PIV) are used to delineate and quantify flow structures and obtain flow parameters of consequence (velocity/vorticity, frequency of oscillations). In order to study different physical processes, a preliminary dimensional analysis was conducted first, followed by experimental and theoretical modeling. The main objectives of this part of the research program are as follows

- Study flow dynamics of axisymmetric turbulent jets in a low-aspect ratio cavity under varying conditions
- Understand and model the mechanisms responsible for jet mixing and jet stoppage
- Develop parameterizations for the frequency of flow oscillations and mean and turbulent flow velocities as a function of external parameters.

In the second part, we elucidate the important processes of turbulent buoyant jet mixing in a stratified fluid by conducting laboratory experiments with varying parameters coupled with theoretical modeling. Digital video recording, micro-scale conductivity probes and optical

refractometer are used for flow measurements.The theoretical modeling is done by using a control volume approach. The main objectives of the second part are as follows:

- Model the degas flow configuration in SPR caverns with the purpose of quantifying mixing processes of buoyant jets
- Derive parameterizations so that the results can be extrapolated to actual caverns.

In the third part, laboratory experiments are conducted to understand mixing mechanism associated with confined turbulent jets with the nozzle being offset from the center of a cylindrical configuration. The Particle Image Velocimetry (PIV), dye visualization and digital video recordings were employed for flow diagnostics. Three most important questions studied are:

- How do flow patterns respond to the increase of nozzle distance from the center axis?
- How do the jet penetration depth and jet spread rate change with the nozzle offset distance?
- Is there any critical offset threshold $\Delta_{critical}/D$ beyond which the jet penetration is undesirable?

Of interest are various changes that offset positioning of jet imposed on confined jet, and identify the implication for SPR cavern degas operations.

## 1.5 Outline Of The Thesis

Theoretical and Laboratory experiments on turbulent jets in low aspect ratio cavities are presented in this dissertation. The organization of this thesis is as follows.

Chapter 1 deals with the motivation, some background of the thesis and discussion about the problem. Next, a brief literature review with related work has been presented. In further sections objective and approach to the problem has been stated.

In Chapter 2, we discuss turbulent jet flow in a confined cavity in detail. In section 2.3, a description about experimental set-up and standard procedures for confined jet experiments are given. In section 2.4, useful main governing parameters for the jet mixing are identified, the effect of boundary conditions on jet stoppage distance is discussed, and a scaling analysis is presented. In section 2.5, basic flow characteristics such as jet precession, frequency of oscillations and other turbulent flow characteristics are presented.

In Chapter 3, a study of turbulent (positive/negative) buoyant jets injected vertically into a slender cylinder containing a stratified fluid is presented. We define experimental apparatus and methods employed in section 3.3. In section 3.4, qualitative observations and general flow behavior of buoyant jet mixing are described while section 3.5 gives results of measurements with positive and negative buoyant jet mixing, including the time evolution. In section 3.6 a mathematical model is advanced to explain the results, which is compared with the measurements.

In chapter 4, investigations of radial offset jets relative to the cavern axis are presented. Section 4.3 establishes relationships among important non-dimensional parameters for offset jet mixing. Section 4.4 starts with an explanation of different experimental facilities and instrumentations used to capture the impact of radial jet offset on flow structures. In section 4.5, the results obtained on velocity/vorticity fields, the effects on mixing length and the pressure drop due to jet offset are studied.

Finally, in Chapter 5, the main findings of our research are listed and its applications to the SPR cavern mixing problem are summarized together with recommendations for future work. The relevant appendices are given at the end of the dissertation.

# 2 PRECESSION OF CONFINED JETs IN HOMOGENOUS FLUIDs

Note - The material in this chapter has been published in Voropayev, S.I., X. Sanchez, C. Nath, S. Webb, and H.J.S. Fernando, "Evolution of a confined turbulent jet in a long cylindrical cavity: Homogeneous fluids," Physics of Fluids, 2011, 23(115106).

## 2.1 General Remark

In this chapter, a study of axisymmetric turbulent jets discharging into a homogenous fluid inside a long cylindrical cavity is discussed.

## 2.2 Introduction

The SPR caverns consist of a collection of approximately cylindrical caverns designed to store crude oil to meet emergency crises. Crude oil stored in these low aspect ratio (width/height ~0.1) caverns is periodically removed from the bottom, degassed and re-introduced near the top as a jet to maintain the oil quality. The jet nozzle diameter is much smaller than the cavern diameter. The cavern flow falls into the category of confined jet flows. Some of their features include the limited depth $x^*$ of jet penetration, rapid decrease of vertical velocity and a recirculating region between the jet and confining walls.

At high Reynolds numbers, confined jets often exhibit low frequency instability, oscillating behavior, large coherent structures and recirculating cells even when the flow boundary conditions are held symmetric and steady. The oscillatory phenomenon has been identified in numerous studies via direct velocity/pressure measurements, visualization and numerical simulations (Villermaux and Hopfinger, 1994; B.M. Gebert et al., 1998; Denisikhina et al., 2005). These oscillations lead to strong mixing in the upper part of caverns, and hence their characteristics are of importance for improving SPR performance and decreasing the cost of cavern degassing operations.

## 2.3 Experimental Set-up And Method

In most of the experiments, the flow was generated in a circular glass cylinder of length $L$=65 cm, inner diameter $D$=10 cm ($L>>D$) and thickness 0.5cm, with closed top and bottom. In some runs, a smaller cylinder ($D$=4.5 cm, $L$=45 cm) was used. To minimize optical distortions due to curvature, the cylinder was placed in a larger (75x75x25 $cm^3$) square Plexiglas tank filled with distilled water; see the schematic in figure 2.1. This tank (1) was painted black, and the water level (2) was above the top surface of the cylinder (3). In most cases, the 'bottom end' of the cylinder was sealed by a glass disk while the 'top end' was closed by a glass disk (4) with a small circular hole (diameter 1.5 cm) at the centre. The jet flow (5) inside the cylinder was generated using a conical round nozzle (6) placed at the centre of the hole in the top disk (4). The inner nozzle diameter was $d$=0.165 cm while the outer diameter was 0.5 cm, which is less than

the diameter of the hole in the glass disk (4). A precision calibrated pump (7) takes water from the larger tank and feeds the nozzle (6) with a relatively small volume flux $q$, generating an intense turbulent jet with a substantial momentum flux $J$. The same amount of fluid, but with negligible momentum, leaves the cylinder through the hole in the top cover (4). Although most of the measurements were conducted with both ends closed to better understand the mechanism of jet break up, additional experiments were conducted with different (top/bottom) boundary conditions.

The dimensional Cartesian coordinate ($x$, $y$, $z$) system used and associated dimensional velocity components ($u$, $v$, $w$) are shown in figure 2.1. The instantaneous velocity component is presented as a sum of the mean and fluctuating parts, i.e. $u = \bar{u} + u'$. A similar notation is used for dimensionless velocity, i.e. $U = \bar{U} + U'$. The velocity data were obtained mostly in the ($x$-$y$) plane along the cylinder axis using particle image velocimetry (PIV). In selected runs, to clarify the mechanism of jet oscillations, additional data on cross-flow velocity components were obtained in the ($y$-$z$) plane by interchanging the positions of the camera and laser.

To this end, the water in the cylinder was seeded with highly reflective Pliolite tracer particles (diameter $d_0$=100 μm) having a small response time ($d_0^2/18\nu$ <0.0005 s; Merzkirch, 1974), thus ensuring that particles follow fluid motion. A commercial PIV system (TSI Incorporated) was used, which includes: a Dual Nd:YAG Laser (8) (output 90 mJ/pulse, pulse duration 6 ns) with optics to produce a thin ($\Delta h \approx 0.3$ cm) horizontal light sheet (9) that spreads along the cylinder axis through a transparent gap (10), a Laser-Pulse Synchronizer and a CCD camera (11) (PIVCAM 10-30, 1024x1024 pixels). The camera, laser and the synchronizer were connected to a control computer, and data processing was conducted using the TSI PIV software package Insight™. Pairs of images were captured at a fixed frequency (15 Hz with 2.5 ms time shift in between) over the duration of the experiment (typically 30 s), and transferred to the computer. The duration was restricted by the number of image pairs (~450) that could be stored on the computer RAM. The data were later transferred to the hard drive, where the horizontal velocity and vertical vorticity fields were calculated from each pair of frames using Insight™.

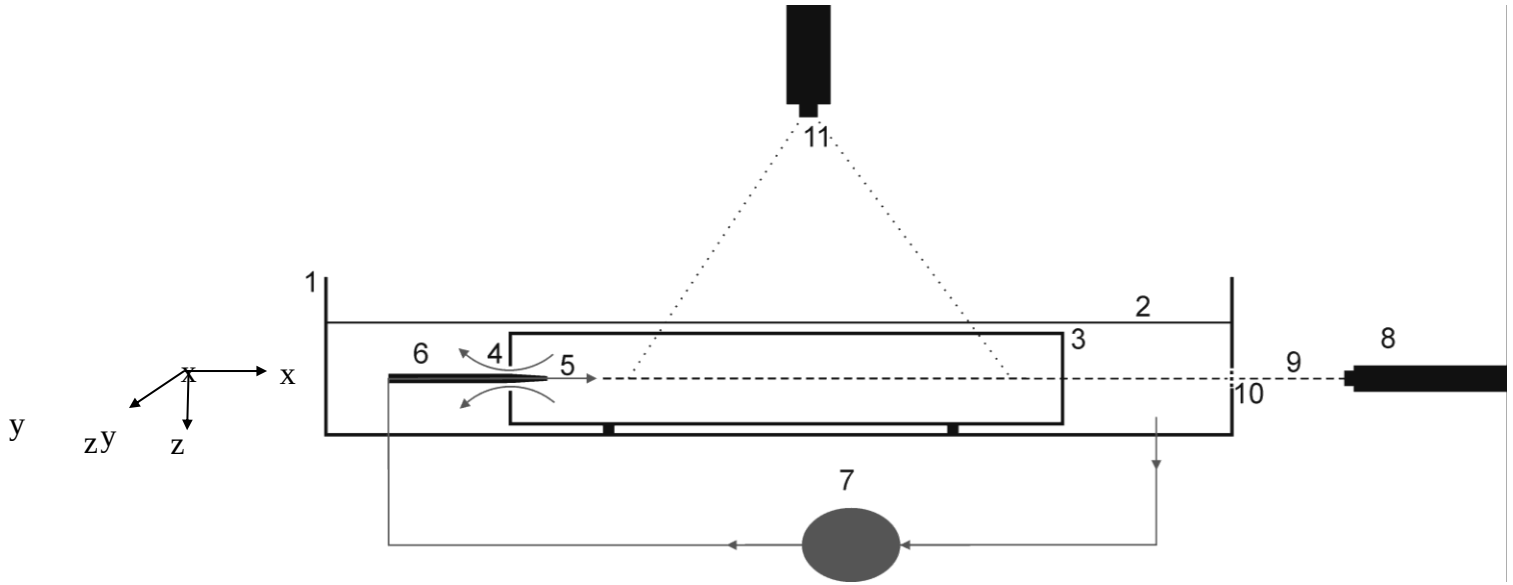


FIGURE 2.1: Experimental set-up: 1 - tank (75x75x25 $cm^3$) painted in black with water; 2 - water level inside the tank; 3 - glass cylinder (diameter $D$=10 cm, length $L$=65 cm) seeded with small Pliolite particles; 4 - small hole for outflow; 5 – inflow; 6 – nozzle ($d$=0.165 cm); 7 - calibrated pump; 8 – laser; 9 – horizontal light sheet; 10 - transparent gap; 11 - CCD (for PIV) or DVC (for video) camera. Cartesian coordinates ($x$, $y$, $z$) are shown to the left, with origin at the centre of the nozzle. In most experiments, only the horizontal ($u$, $v$) velocity components were measured in ($x$-$y$) plane along the cylinder axis. In some runs additional data on across flow velocity components ($v$, $w$) were obtained in a vertical plane ($y$-$z$). In the latter experiments, the camera and laser were interchanged.

The PIV images in the (*x*-*y*) plane had a space resolution of about 0.075 cm/pixel. The area of observations was 65x10 $cm^2$ with an interrogation area of 32x32 pixels, and the data were interpolated onto a grid (4x4 pixels). Numerous commercial (TSI) algorithms are available to calculate velocity fields from image pairs, but the standard Nyquist algorithm (50% overlap) produced the best results with minimum number of erroneous vectors. Obvious spurious vectors (<1-2%) were removed and substituted by 'averaged' interpolated values. No additional averaging or smoothing was used. Information was stored as vector files, on a 204x34 matrix (~0.3 cm spatial resolution) that contain digitized values of horizontal velocity components for each image pair (~450 vector files for each run). The resulting vector files were used in two ways. First, using Tecplot software, instantaneous and averaged velocity/vorticity fields were plotted (see examples below), and the analysis was done frame by frame or using Tecplot animation option. After preliminary analyses, the data from vector files were processed using Matlab.

In addition to PIV, digital video recordings were used for visual observations and analysis. Here the flow was seeded with larger Pliolite particles (diameter ~0.25 mm) but with a lower concentration than that used for PIV to prevent overlapping of particle 'streaks'. The camera used was DVC-3400 (DVC Company), and a 300mJ continuous laser was used for illuminating the flow field. The camera was free-running (frequency 10Hz) and particle streak images were obtained from these digital video recordings. This method was useful in mapping the global flow structure and for visually observing the period of flow oscillations. The recordings of duration 100-200 s were replayed at a slow speed (1-5 Hz) and analyzed manually; some characteristic images are given below (figure 2.5).

To better visualise the central part of the jet in selected runs, smaller tracer particles were introduced continuously at the nozzle. The resulting images give the streamlines issued from the nozzle and are used below (figure 2.3) to illustrate the jet structure. The DVC resolution was not enough for smaller tracer particles, for which a still digital camera of high resolution was used.

The experiments with PIV measurements and DVC recordings covered five jet Reynolds numbers (*Re*=10100, 12700, 15300, 17900, 23100; defined below). Each experiment was repeated five times to improve statistics. For averaging, the PIV data were processed by using 5 data segments (5x450 pairs of frames) for each run. To obtain more data on the frequency of flow oscillations, six additional experiments (*Re*=2800, 5900, 9100, 12200, 18400, 24600) were conducted where long DVC records were made; no PIV measurements were made in these runs. Although in most of experiments the cylinder was positioned horizontally (figure 2.1), for convenience, it is shown vertically in the following illustrations.

## 2.4 General Flow Behavior And Scaling Analysis

### 2.4.1 General Flow Behavior

Upon initiation, the jet propagates relatively quickly along the cylinder with a characteristic spherical front. Nevertheless, in contrast to unconfined jets, where the front propagates over large distances, the jet front in a low-aspect-ratio cylinder suddenly stops at some critical distance $x^*$ from the origin (see schematic in figure 2.2), loses its coherence and breaks down into smaller eddies forming, at $x \sim x^*$, the so-called weak 'diffusive turbulence' (Risso and Fabre, 1997). Thereafter, fluid motions decay rapidly with distance, and at $x > x^*$ the fluid visually appears still.

In the upper part of the cylinder, $x < x^*$, however, the motion remains energetic and large 'coherent' eddies are frequently visible in the flow surrounding the central part of the jet. Visually the flow never reaches a strict steady state but changes periodically with a characteristic frequency $f$ in rather complex manner.

To understand the general flow structure, extensive observations of DVC recordings and PIV measurements were made both along flow ($x$-$y$) and across flow ($y$-$z$) planes, and the results are summarized below.

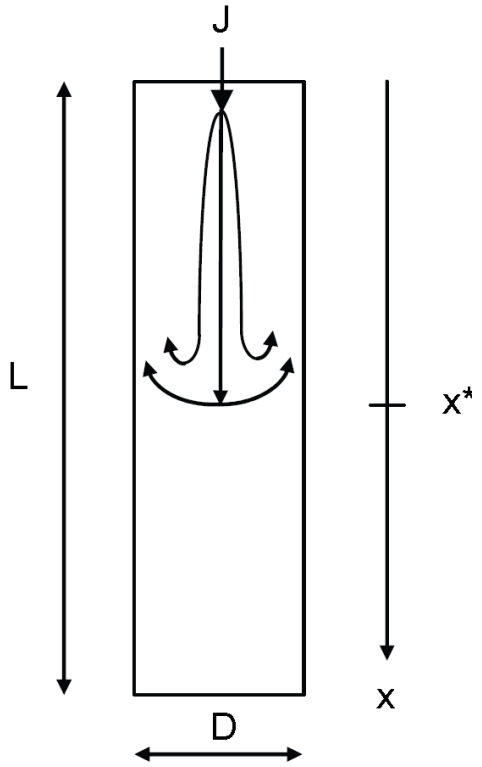

Figure 2.2: A schematic of mean flow in a long cylinder and external parameters

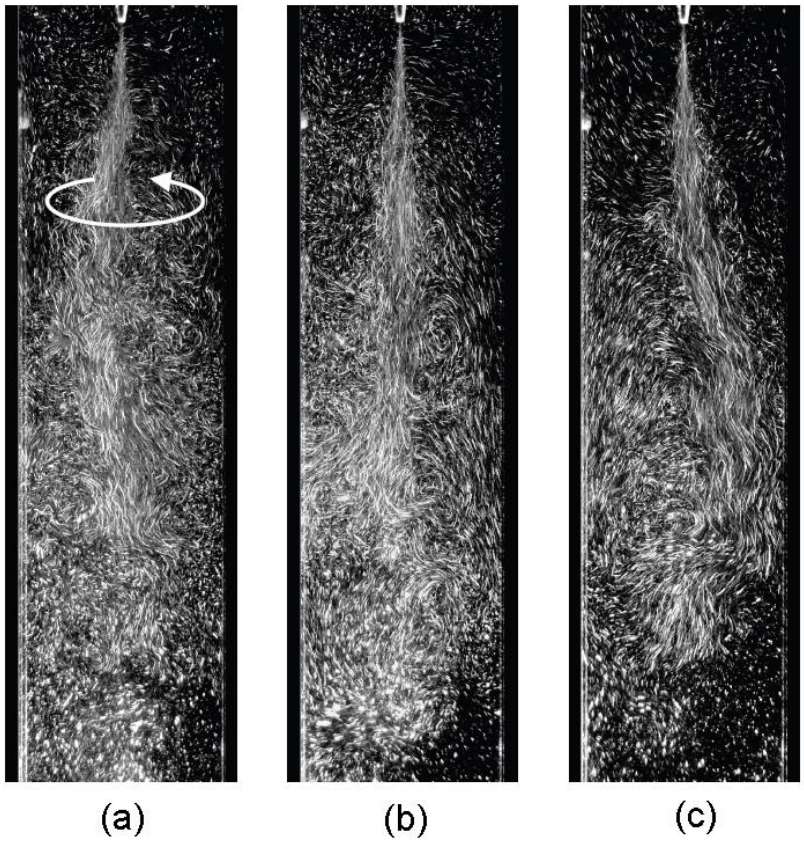


Figure 2.3: Particle streak images showing the central part of the jet at different times. In (a) - jet is tilted to the left and slowly rotates azimuthally (white arrow) around the cylinder axis, in (b) – jet continues its azimuthal rotation and becomes visible near the cylinder centreline, in (c) - it becomes tilted to the right. The direction of rotation changes periodically with time. In this experiment Re=10100 and an exposure of 0.05 s was used. To visualise the streamlines, smaller tracer particles were introduced directly into the nozzle.

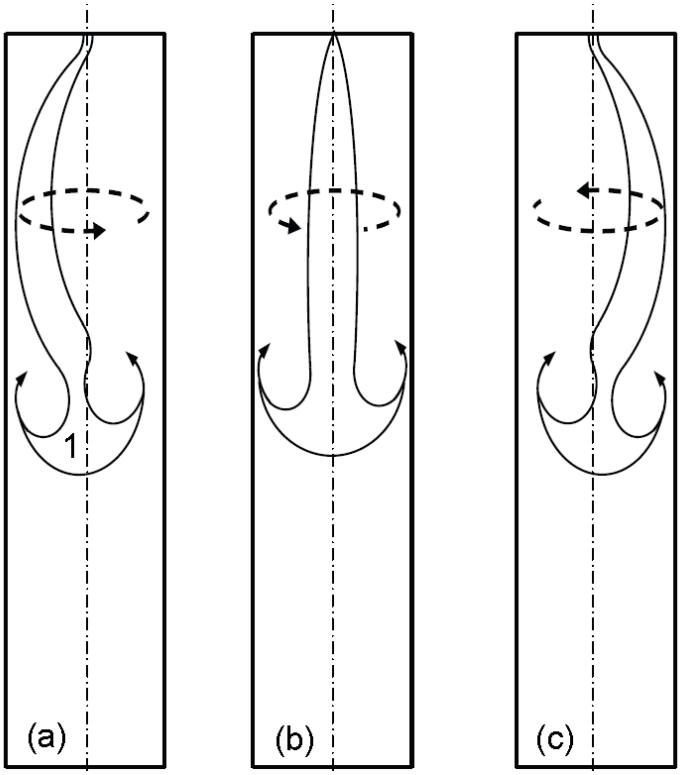


Figure 2.4: A schematic of periodic flow precession (a-c) around cylinder axis as observed in the (*x*-*y*) plane during half of the period. Observations show that this instability originates in the jet frontal area (1) and propagates upstream. The direction of precession (arrow) changes periodically.

Schematically, the established flow can be depicted as (i) primary jet flow with relatively high velocity, and (ii) secondary recirculation cell(s) with smaller velocities. Typical particle streak images showing mostly the central part of the jet in the (*x*-*y*) plane at different times are shown in figure 2.3. At the first glance, the jet appears to be simply oscillating periodically in the (*x*-*y*) plane, similar to flipping oscillations of two-dimensional jets. More detailed observations in the (*x*-*y*) plane and additional observations in (*y*-*z*) (see below), however, show that the jet is spiraling periodically around the cylinder axis (precessing mode). Such (azimuthal) precession has been observed previously in studies of flame stability in swirling flows with rapid expansion and later in similar flows with large expansion ratio and no upstream swirl (Nathan et al., 1998).

In figure 2.3(a) the jet is visible as deflected to the left and slowly rotates azimuthally around the cylinder axis, in (b) the jet continues its azimuthal rotation and becomes visible near the cylinder centreline, and in (c) the jet is deflected to the right. A schematic of periodic flow precession around the cylinder axis in the (*x*-*y*) plane is given in figure 2.4.

The analysis of DVC recordings shows that the flow is dominated by large eddies that arise rather spontaneously, grow in size due to merger of smaller eddies and form large recirculation cells adjacent to side walls (figure 2.5). Observations in the (*x*-*y*) plane show that cells reside for a while and then almost disappear only to recur (within the light sheet) in the opposite side after some time.

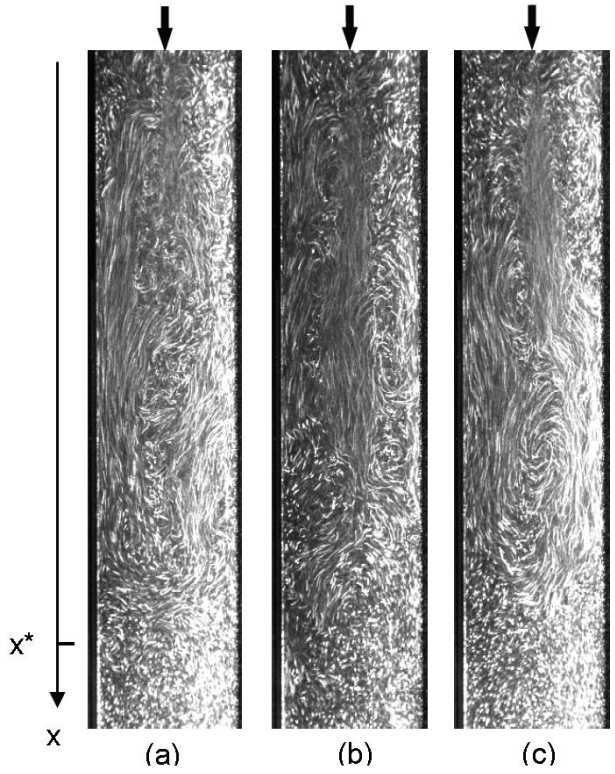


Figure 2.5: Typical particle streak images, showing large coherent eddies and periodic flow oscillations in the (*x*-*y*) plane. The flow was seeded with relatively large tracer particles and the central part of the jet is not well visible. In (a) – large recirculation cell is visible along the right side of the image, in (b) – two approximately symmetric cells are visible along both sides, in (c) – large cell is visible along the left side. The nozzle is shown by black arrow, Re=10100 and an exposure of 0.1 s was used.

As shown schematically in figure 2.6(a), the secondary flow is approximately axisymmetric with jet in the central part, accompanied by a toroidal recirculation cell, which is visible in the ($x$-$y$) plane as two symmetric elongated elliptical cells filled with smaller eddies. In (b) the flow loses its symmetry, the central jet migrates to the left, the toroidal cell is deformed and becomes visible in the ($x$-$y$) plane as two asymmetric cells – larger in the right and smaller in the left. In (c), the flow again passes through its approximately symmetric state, forming in (d) a large intense cell to the left and a small weaker cell to the right. Thereafter the process repeats itself. Symmetric state (a,c) is sometime unclear, and the flow vacillates between (b) and (d) by precessing along the cylinder axis as shown in figure 2.4.

The analysis of DVC recording and PIV images shows that at small distances $x<0.5D$ only a narrow energetic central jet remains nominally steady (figure 2.3), while the near-wall recirculation cells are formed periodically in the outer flow at $0.5D<x<3D$ (figure 2.5).

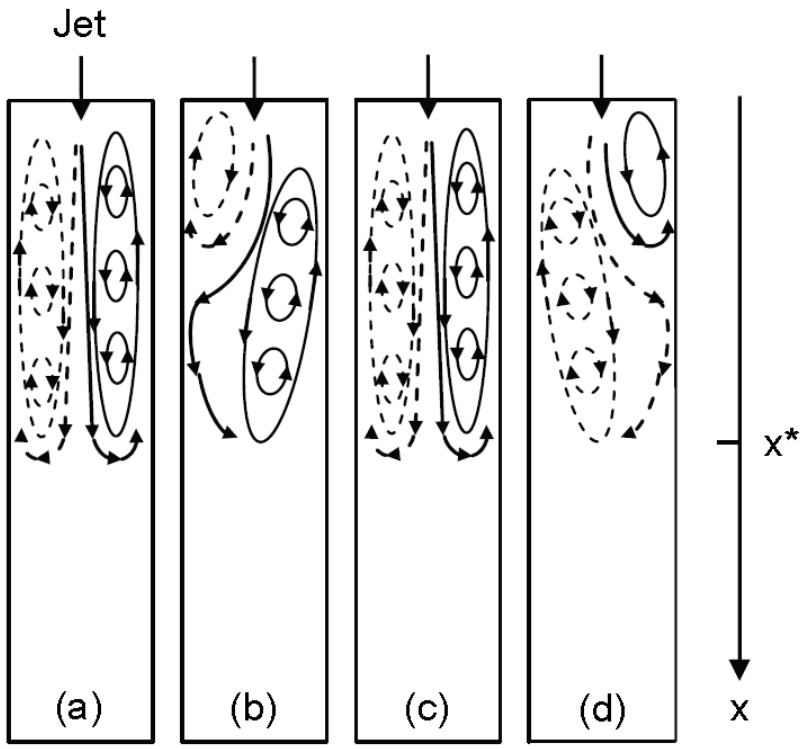


Figure 2.6: A schematic of the evolution of flow structures during an oscillation period in the x-y plane. Dashed and solid lines show clockwise and anticlockwise motions, respectively. (a) - the flow approximately is axisymmetric with toroidal recirculation cell, which is visible as two symmetric elongated elliptic cells carrying smaller eddies; (b) - the flow breaks its symmetry, toroidal cell is deformed and becomes visible as two asymmetric cells; (c) - the flow passes through its symmetric state, forming in (d) a large intense cell at the left and small weaker cell at the right; symmetric state (a, c) sometimes is not easily seen and the flow vacillates between (b) and (d) by precessing along the cylinder axis (figure 2.4).

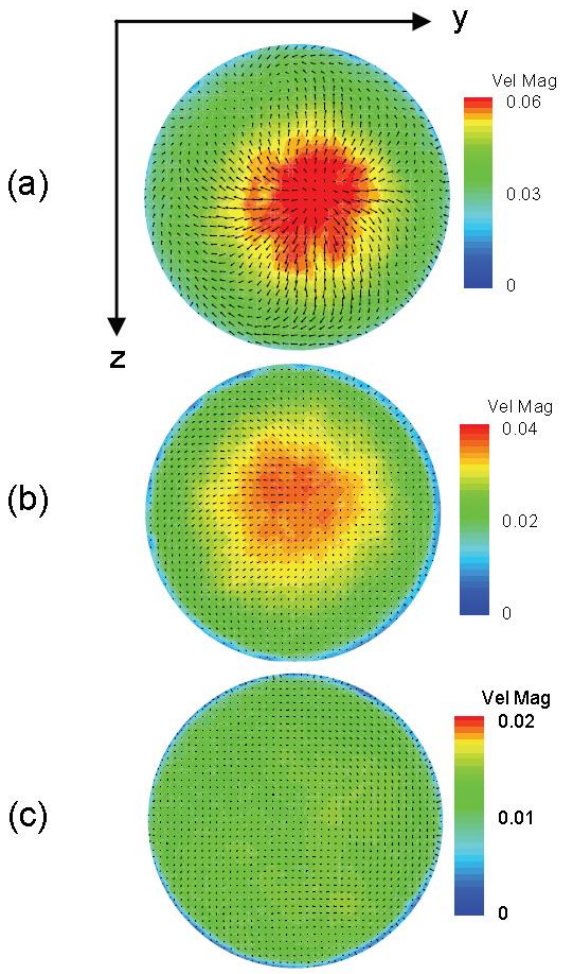


Figure 2.7: Transverse velocity magnitude (averaged over ~100 periods; color scale is in $ms^{-1}$) in (y-z) plane for different distances from the nozzle: $x/D$=1.5 (a), 2.5 (b), 3.5 (c). Note that the scale is different for each image, and the rapid decrease of transverse velocity at the jet axis.

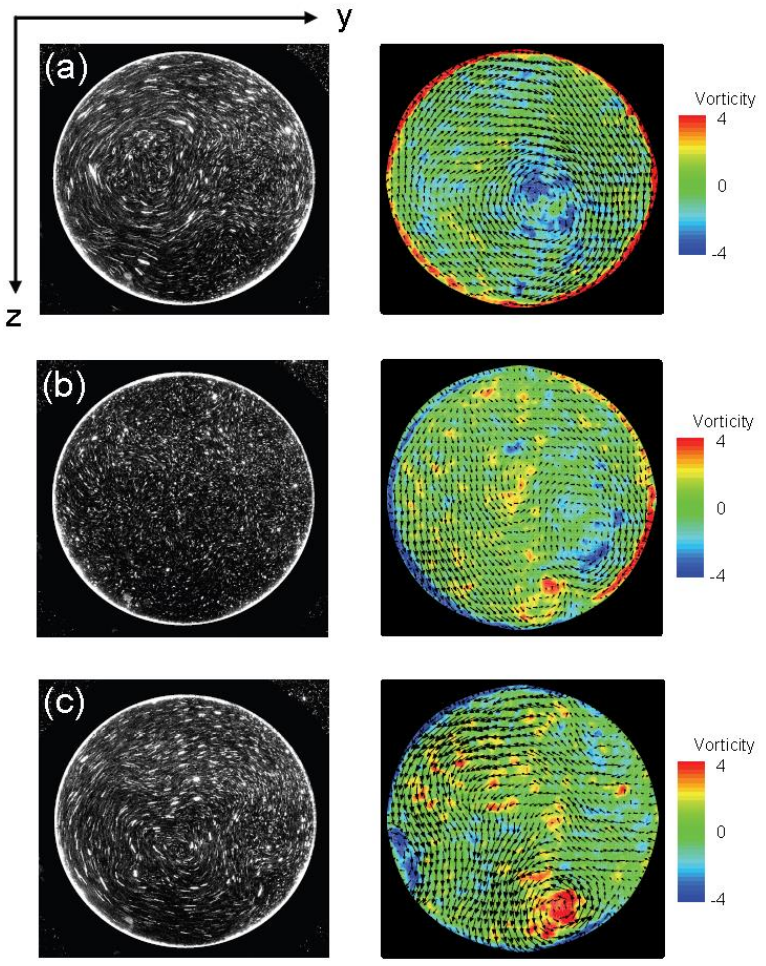


Figure 2.8: Left column - particle streak images in the (*y*-*z*) plane; Right column – PIV data for vorticity (different colors) and velocity (black arrows) in a transverse plane. (a) – fluid rotates mostly clockwise and the net angular momentum M is negative; (b) - direction of rotation changes and the net angular momentum is near zero; (c) - fluid rotates mostly counter clockwise and the net angular momentum is positive. Re=10100, X=*x*/*D* =3.5. Thin near-wall boundary layers with sharp variation of azimuthal vorticity are seen in vorticity data.

Figure 2.7 shows averaged PIV data of the transverse velocity magnitude in the across flow (*y*-*z*) plane for different distances from the origin. Axisymmetric diverging jet flow is visible near the cylinder axis at small and moderate distances (a, b). At larger distances (c) the jet is not evident and at $3D<x<4D$ the flow can be described as a spherical frontal area of size *D* in chaotic motion (see figure 2.2, 2.4). Visually the rotational flow instability originates in this frontal area, which periodically rotates slowly in one or another direction, initiating the deflection of upstream jet toward the wall followed by precession.

Typical streak images and PIV data for instantaneous across flow velocity (*v*, *w*) and axial vorticity are shown in figure 2.8. In figure 2.8(a), the fluid rotates mostly clockwise and the net angular momentum *M* in the along flow direction is negative. In figure 2.8(b), the direction of rotation changes and the net angular momentum is near zero. In figure 2.8(c) the net angular momentum is positive.

Using PIV data for across flow (*y*-*z*) velocity components (*v*, *w*), the (kinematic) angular momentum *M* (per unit length of the cylinder) was calculated as a function of time, *t*, as $M(t) = \iint_S [v(t)z - w(t)y]dydz$ (*S* – cylinder cross section), and the results are shown in figure 2.9.

As can be seen, *M* changes periodically from positive to negative, indicating periodic switching between clockwise and counter clockwise rotation. A typical period of $1/f \sim 10$ s is evident from this record, and spectral analysis gives $f=0.089$ Hz as the dominant frequency. This agrees well with the frequency of jet oscillations observed in the along flow (*x*-*y*) plane (see figure 2.16 below).

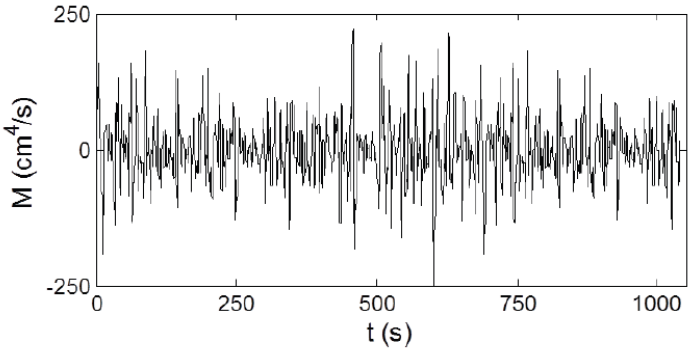


Figure 2.9: Kinematic angular momentum M (per unit cylinder length) as a function of time t (Re=10100, X=*x*/*D* =3.5).

Although *M* switches between positive and negative values (figure 2.9), detailed observations show that the fluid as a whole has only little rotation relative to the cylinder axis. Instead, eddies of opposite sign of rotation (swirl) are observed. They interact with each other in a complex manner, periodically forming one or two larger eddies with significant amount of swirl relative

to the eddy axis. These larger eddies precess by spiraling periodically relative to the cylinder axis. For smaller distances the results were more ‘noisy’ and the spectral peak was less sharp. Therein the axial jet velocity *u* is strong (see below) and PIV measurements of across flow (*v*, *w*) velocity are not accurate, since tracer particles crossing the light sheet are visible only for a very short time.

The description above is based on observations in two planes, whilst the real flow is three-dimensional. Nevertheless, extensive observations show that the flow is clearly unstable with a dominant rotational instability (precession mode), and the global flow structure changes periodically with a characteristic frequency *f*.

The physical mechanism that impedes jet propagation in a long cylinder is discussed next, precursor to developing scaling and similarity analyses. The evaluation of scaling using PIV and DVC measurements will be given thereafter.

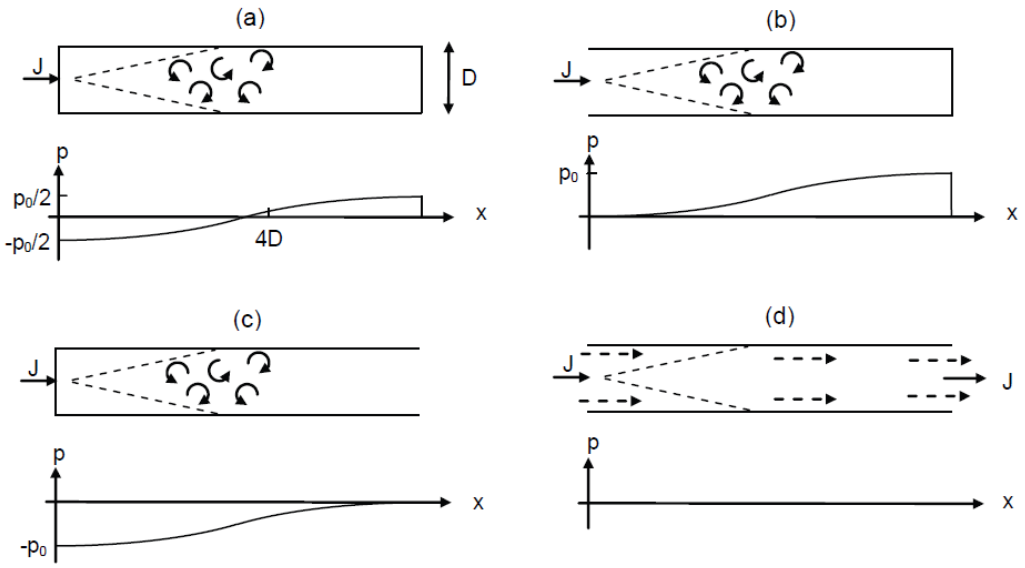


Figure 2.10: Schematics of flow patterns and mean gauge pressure p distributions (cross-sectional mean) for different boundary conditions based on momentum conservation considerations, assuming no viscous losses: (a) – closed top and bottom, (b) – open top, (c) – open bottom, (d) – open top and bottom. The pressure in (d) is equal to the outside pressure.

### 2.4.2 Boundary Conditions and Jet Dissolution

The driving force for this flow configuration is the (kinematic) momentum flux $J$ (force per unit mass) of the jet, which is related to the fluid velocity at nozzle exit (contributions from pressure and viscous stresses are negligible at the nozzle exit (Batchelor, 1970). For a free jet, the net momentum flux is conserved along the flow, which allows the jet to propagate a large distance from the origin. In contrast, the jet flow in a closed low aspect ratio cylinder stops at $x>x^*$. Prima facie this can be construed as due to side-wall influence, where the viscous drag reduces the axial velocity. Observations show, however, that velocity near the wall is in the opposite direction due to recirculation cells (see figure 2.6 and figure 2.11(a, b) below), axial momentum decay cannot be accounted by the lateral viscous friction, and hence pressure gradients induced by end walls remain the only possible mechanism for jet stoppage. This contrasts with the case of free jets, where outside pressure may be neglected (Schlichting, 1979).

To clarify the role of end wall boundary conditions, additional experiments were conducted with the same jet intensity $J$ but with different boundary conditions: both ends of the cylinder closed but with provisions for the flow to exit through a coaxial opening surrounding the nozzle (figure 2.10(a)); the top of the cylinder open and the bottom closed (figure 2.10(b)); bottom open while the top closed (figure 2.10(c)); and both top and bottom open (figure 2.10(d)).

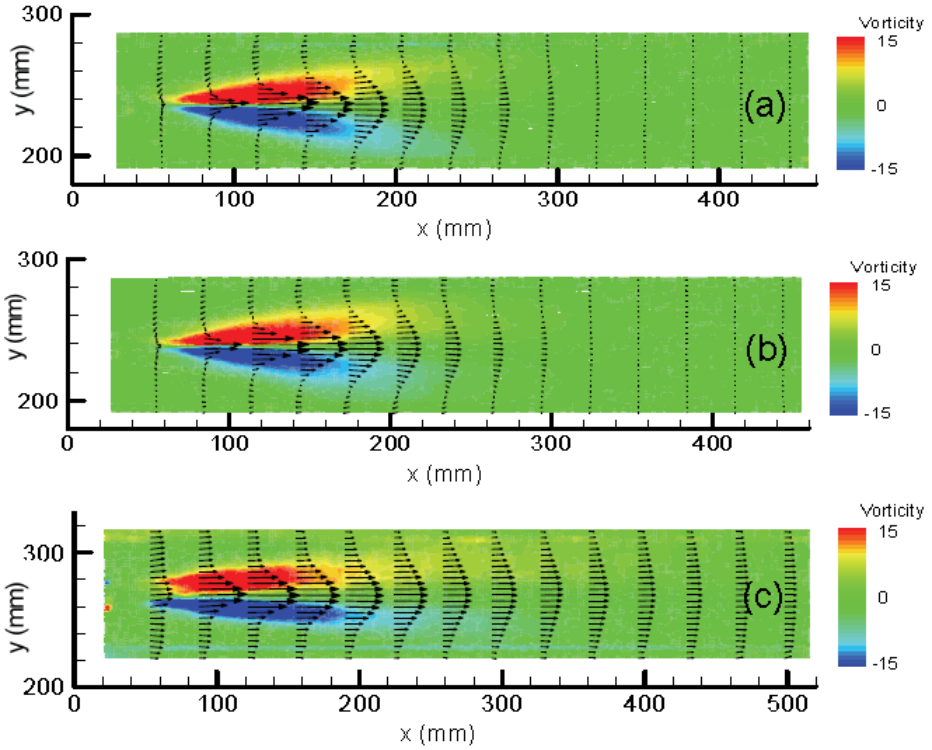


Figure 2.11: PIV data of mean axial velocity (arrows) and mean vorticity (color coding, in $s^{-1}$) for three experiments at Re=10100: (a) top open and bottom closed, (b) bottom open and top closed, (c) both top and bottom open. Ensemble averaging over 5x450 data frames was used. For clarity, only every eighth velocity profile is shown.

Observations showed that flows in (a-c) were visually identical, in that the stoppage of the jet at $x \approx x^*$ was followed by periodic jet oscillations with approximately the same frequency and global flow structure. Quantitative PIV data confirm this conclusion. Figures 2.11(a, b) show that the mean vorticity and mean axial velocity distributions are practically the same for cases where either the top or the bottom is closed. The case with both ends closed is indistinguishable from these two cases (not shown). The case of both open ends (figure 2.10(d)), however, showed completely different behaviour (figure 2.11(c)). After the jet was initiated, the flow in the entire cylinder started moving, soon establishing a flow much like that through a pipe. Once the steady flow was established, the flow did not have visible oscillations.

The above results can be explained by considering momentum flux transformation under different cylinder end conditions. When only the bottom of the cylinder is closed (e.g., figure 2.10(b)), the action of the momentum source $J$ leads to an opposing pressure distribution in the cylinder (see Cantwell, 1986, for a related discussion) with a mean (over the cylinder cross section) pressure $p$ distribution shown schematically in figure 2.10(b). If viscous losses near lateral boundaries are neglected, then the conservation of momentum determines the mean pressure $p_0$ at the bottom of the cylinder as

$$p_0 = \rho J / S, \qquad (2.1)$$

where $\rho$ is the fluid density and $S=\pi D^2/4$, so that the net force at the bottom is $\rho J$. The momentum flux $J$ transforms to a pressure distribution that opposes the motion, acts on the bottom/top of the cylinder and leads to the jet stoppage at some distance $x^*$.

For the case of figure 2.10(d), no such opposing pressure gradients are possible, hence the flow resistance is merely due to wall friction. Now the flow is free to preserve a significant amount of its momentum and stream through the cylinder (figure 2.11(c)).

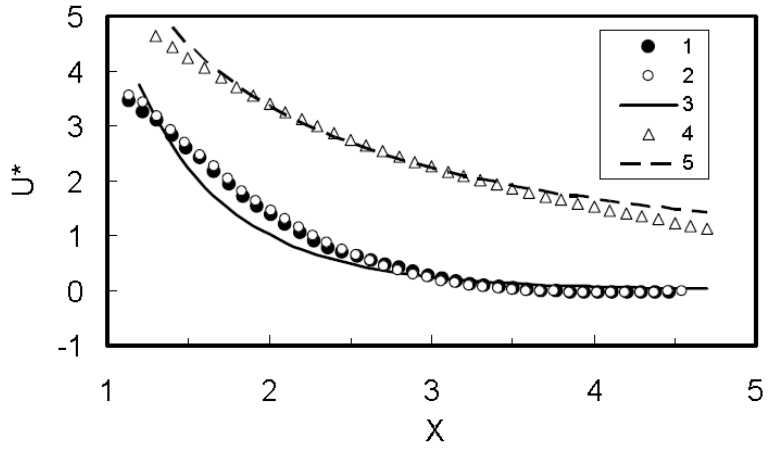


Figure 2.12: Decay of dimensionless axial velocity with distance for three experiments at Re=10100: (1) - top open and bottom closed, (2) - bottom open and top closed, (3) - equation (2.16) for both top and bottom closed, (4) - both top and bottom open, (5) - Schlichting's solution for a free turbulent jet.

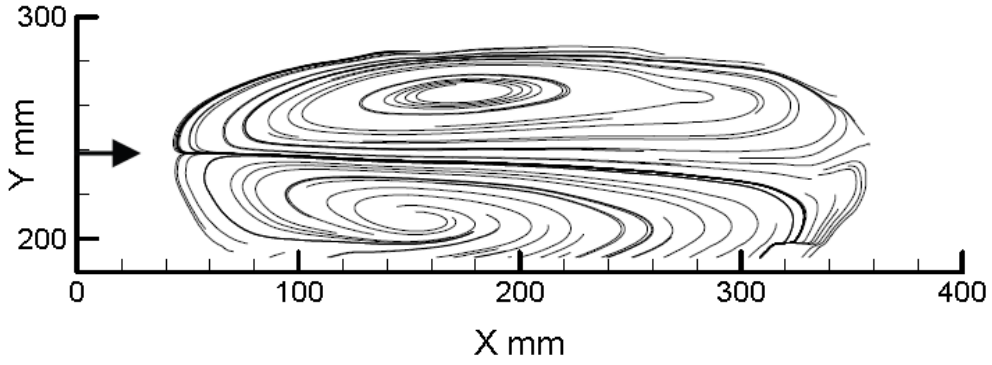


Figure 2.13: Selected mean streamlines for figure 2.11(a) (x-y plane). The mean flow is approximately axisymmetric and streamlines show the cross-section of toroidal recirculation cells of figure 2.6(a). Arrow shows the nozzle.

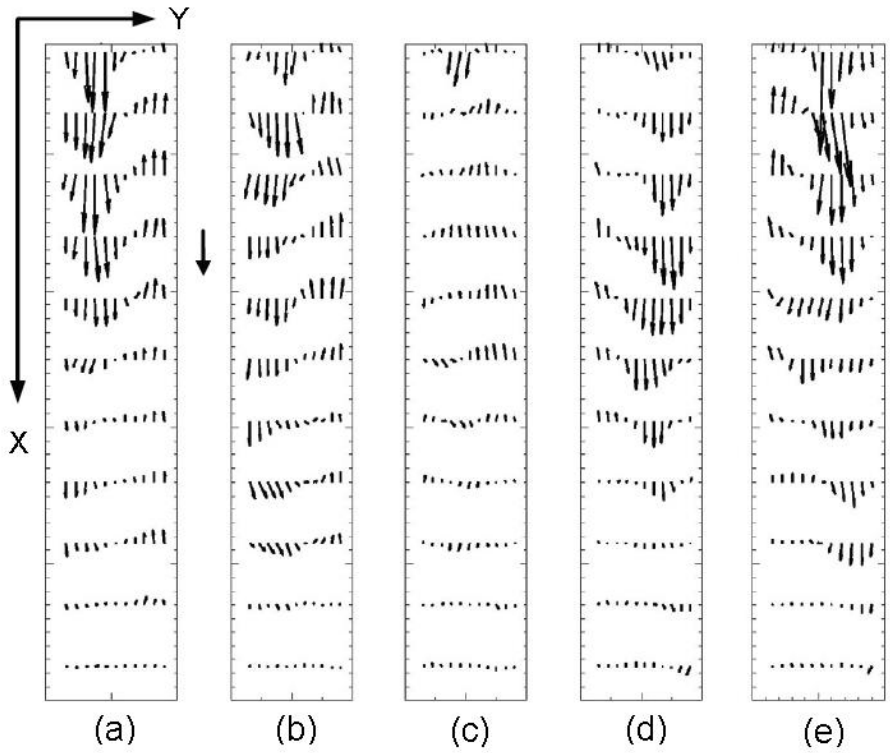


Figure 2.14: Instantaneous velocity (black arrows) maps for different times at Re=10100: t=0 (a), 1.3 (b), 2.6 (c), 3.9 (d), 5.2 s (e). The plots span half of the period of oscillations ($1/f \approx 10.4$ s). The velocity scale (10 $cms^{-1}$) is shown by solid vertical arrow between (a) and (b).

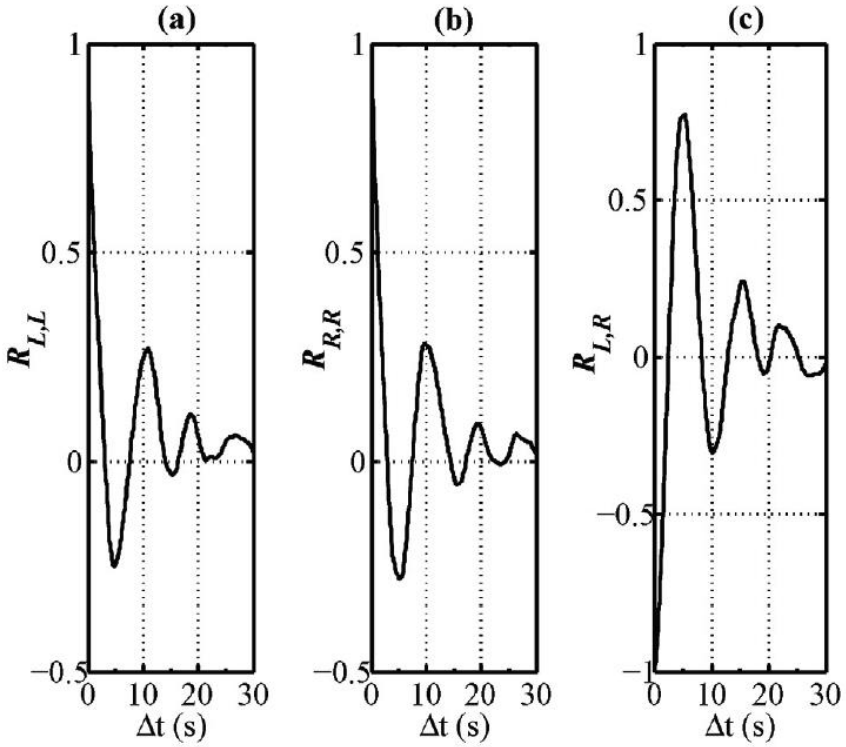


Figure 2.15: Time autocorrelations averaged over x. (a) - $R_{LL}$ at $y$=-0.25$D$, (b) - $R_{RR}$ at $y$=0.25$D$, (c) - cross-correlation $R_{LR}$ (between $y$=-0.25$D$ and $y$=0.25$D$). Re=10100. The time correlations show 1/f ≈10.4 s.

The decay of mean maximum axial velocity $u^*$ with axial distance x for three experiments with the same $Re$=10100, but different boundary conditions is shown in figure 2.12. Dimensionless velocity $U^* = u^* D / J^{1/2}$ and distance $X = x / D$ are used in this graph (see Section 2.4.3). The data for the two cases (1 and 2 in figure 2.12) where one end is closed are practically indistinguishable. Empirical parameterization (solid line 3) derived below for the case where both the top and the bottom are closed satisfactorily describes the data of 1 and 2. The case 4 of figure 2.12, where both ends are opened, demonstrates different behavior. This flow belongs to the class of Craya-Gurtet flows (Revuelta et al., 2004), and Schlichting's solution (Schlichting, 1979) for free turbulent jet (dashed line 5) satisfactorily describes its limiting behavior (figure 2.11(c)).

Based on the above observations, we conclude that the case of a jet issuing into a cylinder with both ends closed is generally similar to the case where only one end is closed. Using the mean velocity data shown in figure 2.11, streamlines in the ($x$-$y$) plane could be plotted; an example is shown in figure 2.13. The mean flow therein is approximately axisymmetric and evinces large toroidal recirculation cells, as was schematized in figure 2.6(a).

Before proceeding further, we present a scaling analysis and discuss some predictions.

### 2.4.3 Scaling Analysis

Consider jet-induced flow in a long cylinder of diameter $D$ and length $L$ ($>>D$), wherein at least one end is closed (figure 2.2). The jet is emanating from a round nozzle of diameter $d$ ($<<D$), with a volume flux $q$. The kinematic viscosity and density of the fluid are $\nu$ and $\rho$, respectively. The important governing dimensional parameters for the fully established flow are $q, d, D, L, \nu, \rho,$ and hence any flow characteristics $A_i$ can be represented as

$$A_i = \Phi_i(q, d, D, L, \nu, \rho, x, y), \tag{2.2}$$

where $x$ is the axial distance, $y$ the characteristic across flow distance and $\Phi_\iota$ are unknown functions.

Experiments show that for $L>>D$ the length of the cylinder is not important, given the mean motion stops at a finite distance $x^*<L$. Also, for $d<<D$, the volume flux $q$ and nozzle diameter $d$ are important only in a combined form,

$$J = q^2 / s, \quad s = \pi d^2 / 4, \tag{2.3}$$

which is the jet momentum flux (jet intensity). Following the standard approach (Batchelor, 1970; Schlichting, 1979; Davidson, 2004), we use the *kinematic* momentum flux (momentum flux per unit mass) because for incompressible homogeneous fluids the fluid density does not play a role in flow dynamics, except for determining the pressure as in equation (2.1).

In dimensionless form $J$ is equal to the jet Reynolds number (e.g., Batchelor, 1970)

$$Re = J^{1/2}/\nu \,. \tag{2.4}$$

When the flow is turbulent ($Re$>>1), the molecular viscosity is assumed unimportant in the spirit of the Reynolds number similarity, whence equation (2.2) can be reduced to five dimensional governing parameters

$$A_i = \Phi_i(D, J, \rho, x, y)\,, \tag{2.5}$$

three of which have independent dimensions. Thus, in dimensionless form only two independent parameters remain (cf., Barenblatt, 1996). Choosing the characteristic length $l$ and time $\tau$ scales

$$l = D, \quad \tau = D^2 / J^{1/2}\,, \tag{2.6}$$

the velocity scale is

$$l/\tau = J^{1/2}/D\,, \tag{2.7}$$

the turbulent (effective) viscosity

$$l^2/\tau = J^{1/2}\,, \tag{2.8}$$

and pressure

$$(l/\tau)^2 \rho = J\rho/D^2\,, \tag{2.9}$$

where equation (2.9) is consistent with equation (2.1). Using these scales and equation (2.5), certain predictions are possible.

For example, the mean dimensionless axial velocity $\overline{U} = \dfrac{\overline{u}}{J^{1/2}/D}$ becomes

$$\overline{U} = \overline{U}(X, Y)\,, \tag{2.10}$$

where $\overline{U}(X,Y)$ is a function of the dimensionless coordinates $X = x/D, \quad Y = y/D$. Similarly, the dimensionless critical distance $x^*$ and flow oscillation frequency $F$ becomes

$$X^* = x^*/D = C, \quad F = \frac{f}{J^{1/2}/D^2} = C^*\,, \tag{2.11}$$

where $C$ and $C^*$ are constants ($X$ and $Y$ are unimportant for $x^*$ and $F$). Note that $F$ can be interpreted as a Strouhal number, which is expected to be a constant for an inertially dominated flow. These predictions can be verified via measurements.

It is reiterated that the above predictions are valid only for narrow ($L/D>>1$) cylinders where $L$ can be neglected and self similarity is viable. For $L/D\sim1$, no complete similarity is expected, given the appearance of an additional length scale $L$ and this case is beyond the scope of this investigation. Similarly, when $d<<D$ (in our case $d/D\approx1/60$), the nozzle can be considered as a 'point' source of momentum flux $J$ (Schlichting, 1979; Batchelor, 1970), thus permitting exclusion of nozzle diameter from the analysis.

For two-dimensional flows, similar considerations yield the following, (Note: The second equation in 2.12 and 2.13 have been changed due to symbol conflicts in the equations in the original dissertation. The symbol *I* has been replaced by *J* to keep it from being confused with the first equation in 2.12.)

$$I=D, \quad \tau = D^{3/2} / J^{1/2} \quad , \tag{2.12}$$

where $J$ is the jet momentum flux per unit jet width, whence the predictions equivalent to equation (2.11) become

$$X^* = x^*/D=C_{2D},\ F= f / \tau = C^*_{2D} \quad . \tag{2.13}$$

In general, the coefficients $C_{2D}$, $C^*_{2D}$ may differ from $C$, $C^*$ in equation (2.11).

## 2.5 Basic Flow Characteristics

### 2.5.1 Frequency of Flow Oscillations

Quantitative data on f were obtained using DVC recordings and PIV data. First, relatively long (100-200 s) DVC recordings with frequency 10 Hz were made for each run. Then these recordings were replayed several times at a slow speed (1-5 Hz) and the mean (over the recording period) values of $f$ were obtained for each run. The scatter of the data for each run did not exceed ±10%. Thereafter, by using PIV data, instantaneous velocity profiles were plotted (e.g., figure 2.14) and the mean $f$ for each data set was obtained.

In addition, using the same PIV data, the time correlation function $R_{uu}(x, y, \Delta t)$

$$R_{uu}(x,y,\Delta t) = \frac{< u(x,y,t)u(x,y,t+\Delta t) >}{< u^2(x,y,t) >} \tag{2.14}$$

for the axial velocity $u$ at $y$=±0.25$D$ was calculated (<….> is the time averaging) for 1<$x/D$<3 and averaged over $x$. Typical time autocorrelations $R_{LL}(y, \Delta t)$ at $y$=-0.25$D$ (near the left side) and $R_{RR}(y, \Delta t)$ at $y$=0.25$D$ (near the right side) as well as time cross-correlations $R_{LR}(y, \Delta t)$ (between $y$=-0.25$D$ and $y$=0.25$D$) are shown in figure 2.15. The mean period 1/$f$ of flow oscillations for each run was obtained by calculating the time shift $\Delta t$ when the first maximum (for autocorrelation) or minimum (for cross-correlations) was observed.

The results of different methods are summarized in figure 2.16, where $f$ (in Hz) is plotted as a function of the frequency scale (6), $1/\tau = J^{1/2}/D^2$ for experiments with different jet intensities $J$. The agreement with equation (2.11) is clear, and the best fit gives $C$*=0.1 with regression coefficient $R^2$=0.96.

To our knowledge, no previous frequency data are available for 3D geometries, but some exist for 2D, and are included in figure 2.16 with appropriate adjustments. To make direct comparisons with the 3D data, equation (2.13) can be written as

$$F = \frac{f}{(J/H)^{1/2}/D^{3/2}} = \frac{f\beta^{1/2}}{J^{1/2}/D^2} == C^*_{2D}, \qquad (2.15)$$

where $J = IH$ is the net momentum flux, $\beta = H/D$ is the aspect ratio and $H$ the width of the 2D jet.

Using $f$ and $Re$ in (Villermaux and Hopfinger, 1994) (β=0.2, 0.3, $Re$=1000-3600) and (Mataoui and Schiestel, 2009) (β=1, $Re$=500-4000), the modified frequencies $f\beta^{1/2}$ were calculated and are shown in figure 2.16, which

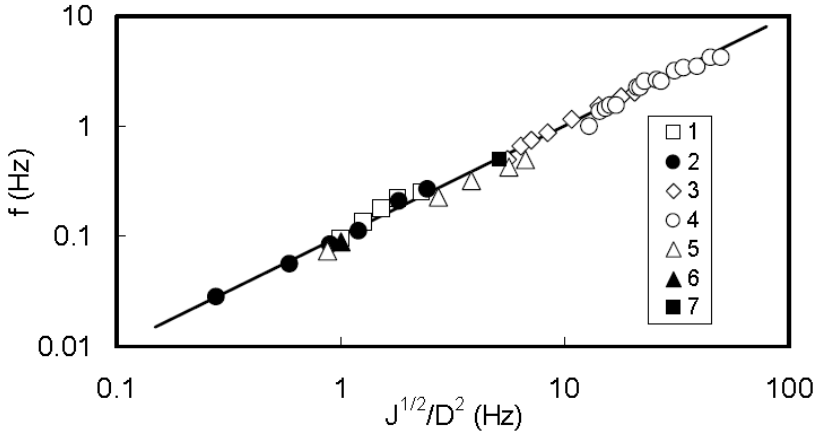


Figure 2.16: Frequency of oscillations f versus frequency scale. Symbols – experimental data, solid line - equation (2.11) with C*=0.1. Data from: (1) - present experiments, $d/D$=0.016 (PIV); (2) - present experiments, $d/D$=0.016 (DVC); (3) – Villermaux and Hopfinger, 1994 (β=0.2), (4)

– Villermaux and Hopfinger, 1994 (β=0.3), (5) – Mataoui and Schiestel, 2009 (β=1), (6) - present experiments, $d/D$=0.016 (angular momentum); (7) - present experiment, $d/D$=0.037 (DVC).

fall on our best fit (solid) line, indicating that coefficients in equations (2.11) and (2.15) are the same for both geometries. The fact that 2D experiments conducted using air jets give similar results to those of water jets strongly supports similarity scaling of Section 2.4.3.

### 2.5.2 Mean Flow Characteristics

The mean dimensionless centerline axial velocity $U^*(X) = \bar{U}(X, Y = 0)$ as a function of dimensionless distance $X$ is shown in figure 2.17 by the colored lines (1-5) for all runs conducted with the larger cylinder, $d/D$=0.016. The mean of all is shown by solid line (6), which illustrates approximate independence of Reynolds number. The data for the smaller cylinder $d/D$=0.037 are shown by open circles.

For comparison, data from previous work are also shown in figure 2.17 by crosses (8). These were taken from Risso and Fabre (1997), where a visually similar dimensionless velocity distribution could be found for $Re$=150000 and $d/D$=0.195. Nevertheless, there is one important difference: in Risso and Fabre (1997), the cylinder diameter $D$ and the nozzle exit velocity $u_0$ are used as length and velocity scales (hence invoking $d$ as an independent variable). We proposed the same length scale $D$ but a different velocity scale $J^{1/2} / D$, where the jet momentum flux $J$ is used as the sole parameter describing the jet, a composite of $u_0$ and $d$. In comparing our data with those of Risso and Fabre (1997), we have used $J^{1/2} / D$, and a satisfactory agreement was noted over a range of $d/D$ (0.016-0.195) and $Re$ (10000-150000), as shown in figure 2.17.

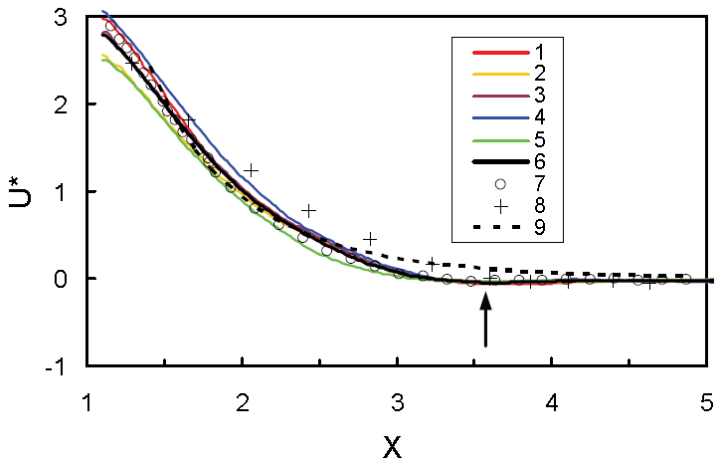


Figure 2.17: Decay of mean dimensionless axial velocity U* with dimensionless distance X are shown by colour lines (1-5) for $d/D$=0.016 at Re=10100 (1), 12700 (2), 15300 (3), 17900 (4), 23100 (5); (6) - mean over all experiments with larger cylinder, (7) - smaller cylinder, $d/D$=0.037, (8) - data from Risso and Fabre (1997), Re=150000, $d/D$=0.195, (9) - equation (2.16).

As can be seen, *U** smoothly decreases with X, crosses zero at X ≈ 3.2 and shows (see black arrow) a small but measurable negative value until X ≈ 3.6 before becoming close to invisible, yielding a critical distance X*≈3.6 and C≈3.6 for equation (2.11). The exact value of C is not very important, as it depends on the definition of X*. More importantly, X* remains approximately the same for different experimental conditions (figure 2.17), thus supporting our similarity arguments.

Empirically, the mean centreline axial velocity can be approximately fitted to the function

$$U^*(X) = \frac{A}{X\exp(X)} \quad , \tag{2.16}$$

which is shown in figure 2.17 by the dashed line (9), with the constant A=13.8. Note that equation (2.16) takes into account that, at small X, U* ought to decay inversely with X, as in a free jet. But at larger X it is expected to decay exponentially (Risso and Fabre (1997), Sonin et al., 1996; Brown et al., 1990).

To parameterize $\overline{U}(X,Y)$, it is possible to propose $\overline{U}(X,Y) = U^*(X) \times \overline{U}(Y)$ with $\overline{U}(Y) = \sin(BY)/BY$, which gives

$$\overline{U}(X,Y) = \frac{A}{X\exp(X)} \times \frac{\sin(BY)}{BY} \quad , \tag{2.17}$$

where B=const. figure 2.18 shows equation (2.17) with A=13.8 and B=10.2 by solid lines. In the near-wall thin boundary layer the measurement accuracy is modest and thus the velocity amplitude of reverse flow is most probably underestimated. For comparison, available data (Risso and Fabre, 1997) for transverse dimensionless mean axial velocity profiles are shown in figure 2.19, and equation (2.17) describes these data very well.

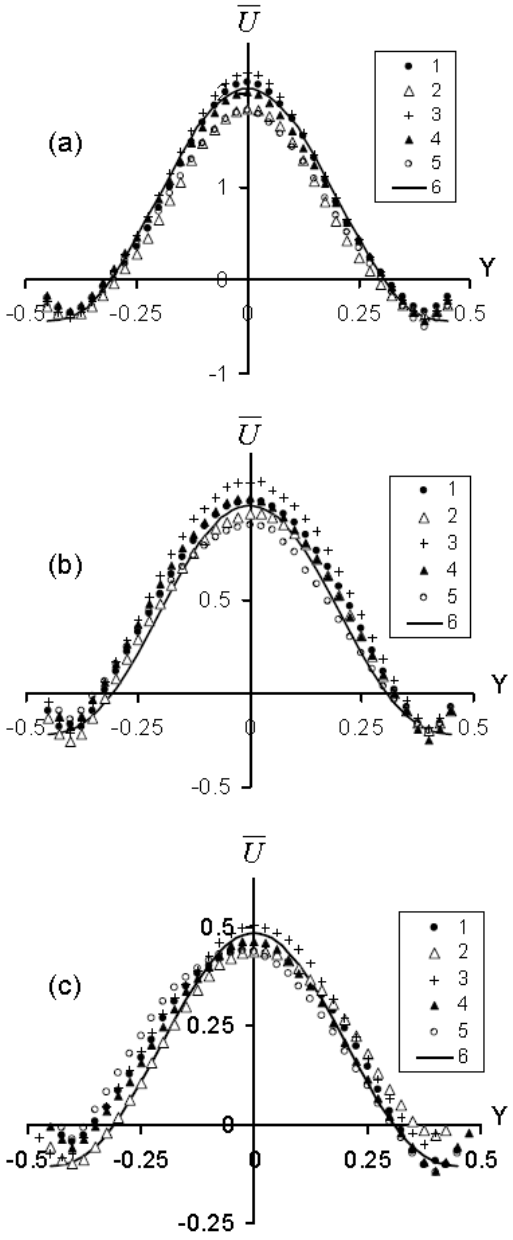


Figure 2.18: Transverse profiles of dimensionless mean axial velocity for different dimensionless axial distances: X=1.5 (a), 2 (b), 2.5 (c) and for Re=10100 (1), 12700 (2), 15300 (3), 17900 (4), 23100 (5). Solid line (6) is equation (2.17).

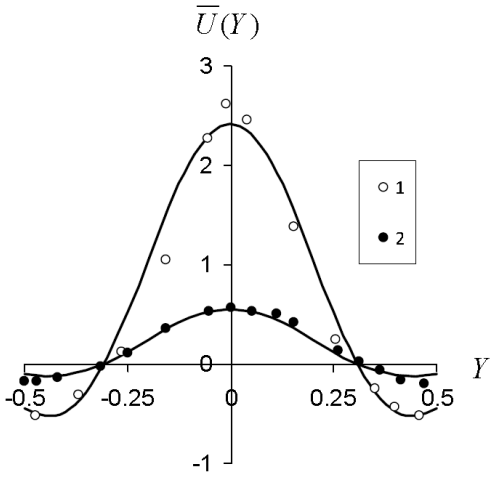


Figure 2.19: Transverse profiles of dimensionless mean axial velocity for X=1.3 (1), 2.7 (2). Symbols – experimental data from Risso and Fabre (1997) for Re=150000, *d*/*D*=0.195, solid line is equation (2.17).

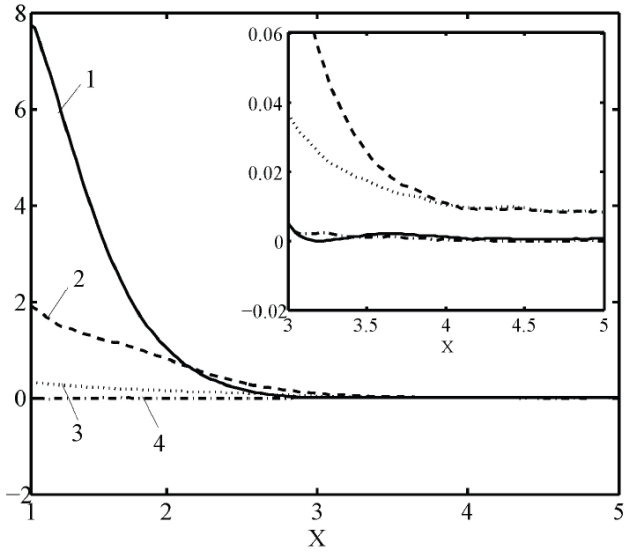


Figure 2.20: The maximum values of squared dimensionless mean axial velocity $U^{*2}$ and turbulence statistics of and versus X: (1) - $U^{*2}$, (2) - $\langle U'^2 \rangle$, (3) - $\langle V'^2 \rangle$, (4) - $\langle U'V' \rangle$. Averaged values over all experiments conducted at different Reynolds numbers are shown.

Although equation (2.17) does not capture the no-slip condition at a finite radial distance, it correctly describes the mean axial velocity profiles over a broad range of parameters, *Re* (10000-150000) and *d*/*D* (0.016-0.195), and employs a minimal number of empirical coefficients. It is expected to be a valuable formula in engineering applications.

### 2.5.3 Basic Turbulent Flow Characteristics

Although turbulent flow characteristics in similar geometries have been measured previously (Sonin et al. 1986; Brown et al., 1990), the main interest has been on flow characteristics at larger distances $X>X^*$, in the area of weak 'diffusive' turbulence with negligible mean velocity. To complement, here we present turbulence data at smaller distances, where the mean flow is present. The second order moments for $U'$ and $V'$ are shown in figure 2.20 as a function of *X*. The data for different Reynolds numbers satisfactorily collapsed (within ±10 %), and for clarity the average overall Reynolds numbers are shown. The mean values of $U^{*2}$ are also shown for comparison. For $U^*$ we used averaged data given by solid line (6) in figure 2.17. In figure 2.20, at smaller distances ($X<2$), only $<U'^2>$ is significant and it is comparable to $U^{*2}$ while $<V'^2>$ is smaller by a factor of 5. At larger distances both $U^{*2}$ and $<U'^2>$ decay in similar ways and are comparable. Beyond X≈3.6, all flow characteristics become very small. The cross-correlations $<U'V'>$ are negligibly small at all distances. Inset in figure 2.20 is an enlarged view of flow characteristics at X>3.

# 3 PENETRATION OF A CONFINED JET IN STRATIFIED FLUID

Note - This material has been published in Voropayev, S.I., C. Nath, and H.J.S Fernando, "Mixing by turbulent buoyant jets in slender containers," Physics Letters A, 2012, 376 (3213-3218).

Some clarification of terms is necessary. In the present chapter, positively-buoyant and negatively-buoyant refers to the direction of the buoyancy, not the relative value compared to the jet velocity as discussed earlier in Chapter 3. Therefore, in this chapter, a lighter jet directed downward is referred to as a positively-buoyant jet; in Chapter 3 of this report, that situation would be referred to as a negatively-buoyant jet because the buoyancy and velocity act in different directions. Similarly, a heavier jet directed downward is referred to as a negatively-buoyant jet; in Chapter 3, that situation would be referred to as a positively-buoyant jet.

## 3.1 General Remark

In this chapter, we present a study of a turbulent buoyant jet injected into stratified fluid inside a long cylindrical cavity. This chapter starts with the introduction in Section 3.2, while giving details of the experimental setup in section 3.3. In section 3.4, a description of the qualitative flow behavior of a buoyant jet is presented. In section 3.5 results of a buoyant jet mixing with stratified fluid as a function of time is reported. The working fluid is water, and salt is used to change its density to obtain either a positively or negatively buoyant jet. This chapter concludes with section 3.6, where a theoretical model is proposed, permitting the calculation of vertical density distribution as a function of time. Also, criteria for different penetration depths with positive and negative buoyant jets are discussed.

## 3.2 Introduction

In the previous chapter, the jet flow in a long cylinder under neutrally stratified conditions was studied in detail (Voropayev et al., 2011). At high Reynolds numbers, the resulting flow belongs to the confined jets flows (Melloy and Taylor, 1969; Khoo et al., 1992; Villermaux and Hopfinger, 1994; Risso and Fabre, 1997; Mataoui and Schiestel, 2009), wherein the jet penetrates only a limited distance, while exerting energetic periodic oscillations. PIV measurements (Voropayev et al., 2011) include the frequency of jet oscillations, jet break-up (stoppage) distance, mean and turbulence characteristics and the influence of end-walls. The results were expressed using the characteristic length, $D$, and velocity, $J^{1/2}/D$, scales, where $J$ is the jet kinematic momentum flux, which is proportional to jet Reynolds number, and $D$ the container width. In particular it was shown that the jet stoppage distance $l$ does not depend on $J$, container length $L$, fluid viscosity and density, top/bottom boundary conditions and other parameters, but mostly depends on the container diameter $D$, viz.,

$$l = C_0 D, \tag{3.1}$$

where $C_0 \approx 3.2$ when $l$ is defined as the distance where the mean axial jet velocity diminishes to zero (see figure 17, 20 in Voropayev et al., 2011 for details).

In this section, the results obtained from the previous part (Voropayev et al., 2011) have been extended to the case of buoyant jets, and the evolution of the jet and container fluid density are investigated experimentally. Results of mixing of positive and negatively buoyant jets with the ambient fluid as a function of time are reported here. Guided by the experimental results, a theoretical model is developed and verified experimentally.

### 3.3 Experimental Set-up And Method

Experiments were conducted using a long (length $L$=118.5 cm) vertical Plexiglas cylinder of circular cross section (diameter $D$=12 cm) with closed top and bottom (figure 3.1). Working fluid is distilled water at room temperature, the density $\rho$ of which was adjusted by changing the water salinity $S$. The equation of state takes the form

$$\rho = \rho^*(1 + \beta S), \tag{3.2}$$

where $\rho^*$=1 g cm$^{-3}$, $S$ – salinity (in ‰) and $\beta \approx 0.0008$ (‰)$^{-1}$ at 20 $^0$C.

As shown in figure 3.1, the jet flow inside the cylinder (1) was generated using a round nozzle (2) placed at the cylinder centreline. The inner nozzle diameter is $d$=0.165 cm and its exit is 3 cm below the water level in the cylinder. A precision pump (3) feeds the nozzle (2) with a volume flux $Q$ from a reservoir (4) filled with water of density $\rho_0$ (salinity $S_0$), thus generating a turbulent jet with Reynolds number $\mathrm{Re} = 4Q/\pi d\nu$ ($\nu$ - kinematic viscosity). The same amount of fluid, but with negligible momentum, leaves the cylinder through a long vertical pipe (5) of diameter 0.5 cm. It takes fluid from near the bottom and pumps it to the reservoir (6). Initially the cylinder is filled with a fluid of density $\rho_1$ (salinity $S_1$), and at time $t$=0 a jet of density $\rho_0$ is initiated. The jet fluid mixes with the fluid of density $\rho_1$ contained in the cylinder, and a mixed fluid of density $\rho=\rho(t)$ leaves the cylinder via pipe (5). In this study, the main interest is the characteristics of $\rho(t)$. Considering that oil in SPR caverns may either be lighter ($\rho_0<\rho_1$) or heavier ($\rho_0>\rho_1$) than the cavern oil, both positively and negatively buoyant jets were studied.

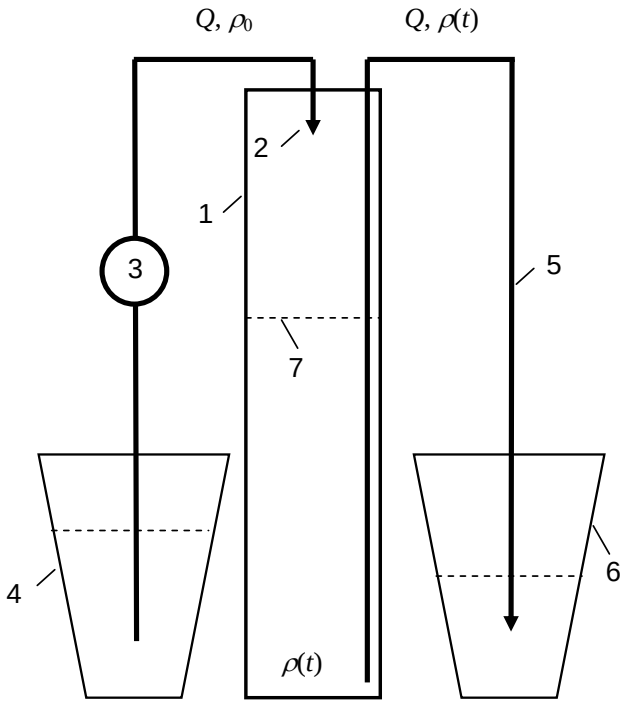


Figure 3.1: Schematic of the experimental set-up: 1 – long cylinder (length $L$=118.5 cm, diameter $D$=12 cm), closed at the top and bottom, initially filled with water of density $\rho_1$; 2 – vertical jet nozzle (diameter $d$=0.165 cm); 3 - precision water pump to control the volume flux $Q$; 4 – reservoir with jet water of density $\rho_0$; 5 – long tube to collect the exiting fluid from the bottom of the cylinder of density $\rho(t)$; 6 – reservoir to collect and measure $\rho(t)$ of the exiting fluid; 7 – jet stoppage boundary.

To clarify the general flow structure, digital video camera (DVC-3400) recordings were made, by adding small amounts of fluorescent dye to the jet, thus allowing visual flow observations and analysis. A vertical planar laser sheet was used for illumination, and recordings were made from the side. Instantaneous contours of dye concentration were obtained using the 'ImageJ' software.

Experiments with density measurements were conducted thereafter, for which the experimental parameters are given in Table 3.3-1 (in calculating Re we took into account that viscosity depends on salinity). In six experiments the jet fluid was lighter (fresh water, $S_0$=0) than the cylinder fluid (salt water, $S_1$=15-103 ‰) whereas in three experiments the jet fluid was heavier (salt water, $S_0$=15-100 ‰) than the cylinder fluid (fresh water, $S_1$=0).

Before each run, the cylinder was filled with fluid of salinity S1 (density $\rho_1$). At t=0 the jet (salinity $S_0$, density $\rho_0$) was initiated and the salinity $S(t)$ [density $\rho(t)$] of fluid exiting at the cavern bottom was measured as a function of time. To measure the salinity, small samples of fluid (~5 ml) were taken out of the cylinder bottom periodically (initially with time interval of ~2 min and later ~5 min) by the pipe 5 (see figure 3.1), and their salinity was measured by a refractometer (Leica Inc.). Each run continued until the salinity of the mixed fluid $S(t)$ became practically equal to the jet salinity $S_0$, which was typically about one hour.

TABLE 3.3-1

VALUES OF PARAMETERS IN EXPERIMENTS

| Run # | $S_0$ (‰) | $S_1$ (‰) | $Q$ ($cm^3s^{-1}$) | Re |
|---|---|---|---|---|
| 1 | 0 | 103 | 9.1 | 7020 |
| 2 | 0 | 50 | 9.1 | 7020 |
| 3 | 0 | 25 | 9.1 | 7020 |
| 4 | 0 | 15 | 9.3 | 7180 |
| 5 | 0 | 102 | 9.1 | 7020 |
| 6 | 0 | 49 | 18.2 | 14040 |
| 8 | 100 | 0 | 8.9 | 5870 |
| 10 | 50 | 0 | 9.1 | 6530 |
| 11 | 15 | 0 | 9.1 | 6900 |

In addition, 'instantaneous' density profiles $\rho(x)$ were measured in selected runs using a four-electrode micro-scale conductivity probe (Precision Measurement Eng. Inc.) mounted on a vertical traversing platform. When required, the jet was stopped for 2-3 min, a small hole was opened at the top of cylinder, and the conductivity data (used later for the calculation of $S$ and $\rho$) were taken as the probe traversed down. Thereafter, the probe was taken out from the cylinder, the hole was closed and the experiment continued. Such measurements were made only for positively buoyant jet, where periodic jet stoppage did not affect strongly the resulting stable density distribution. For negatively buoyant jet with unstable density distribution this method could lead to erroneous results.

### 3.4 Qualitative Observations and General Flow Behavior

A sequence of images showing the formation of a mixed layer of depth l in the upper part of the cylinder is given in figure 3.2 for a positively buoyant jet.

Upon initiation, the jet propagates relatively quickly along the cylinder (figure 3.2(a)) and reaches a maximum depth (figure 3.2(b)) at which time the jet front suddenly stops at some critical distance $l$ from the origin, similar to the case of a confined jet in a homogeneous fluid (Voropayev et al., 2011). In the stratified case, however, the jet fluid, although strongly diluted by entrainment, remains buoyant and the jet front bounces back somewhat (figure 3.2(c)). The entrainment at this time is mostly axial, occurring in a conical region highlighted by dye contour. The bottom boundary of this region soon transforms from spherical to almost horizontal, and a mixed layer of depth $l$ is formed (figure 3.2(d, e)). Beyond this region, fluid motions decay rapidly with distance, and the fluid visually appears as still, similar to the case of homogeneous fluid (Voropayev et al., 2011; Risso and Fabre, 1997). In the upper part of the cylinder, the motion remains energetic with large 'coherent' eddies, and it visually looks well mixed, thus building a stable vertical density distribution at the bottom of a mixed layer.

All these occur relatively fast, during the first 30-40 seconds of the experiment. Later, the mixed fluid slowly propagates down as a slab (see figure 3.2(f-h)) with a velocity that depends on the flux rate $Q$ of exiting fluid out of the pipe (5 in figure 3.1) and cylinder cross-sectional area $s = \pi D^2 / 4$. In all, for positively buoyant jets, a mixed layer of depth $l$ given by equation (3.1) builds up rapidly at the top, underlain by a region of negligible turbulence.

Observations of negative buoyant jets, however, showed different behavior. At short times, the flow development is very similar to that of positively buoyant jets (see figure 3.2(a-c)), and a mixed (by jet) layer of similar depth $l$ is rapidly formed near the top of the cylinder. The fluid in the upper mixed layer is now heavier than the underlying fluid, and unstable density stratification is formed in the cylinder. Ensuing convective instability leads to deep convection, and with time the convective mixed layer reaches the bottom of the cylinder, forming a turbulent layer that fills the entire cylinder of depth $L$; up to depth $l$, rapid mixing occurs by the jet action and below it by deep convection.

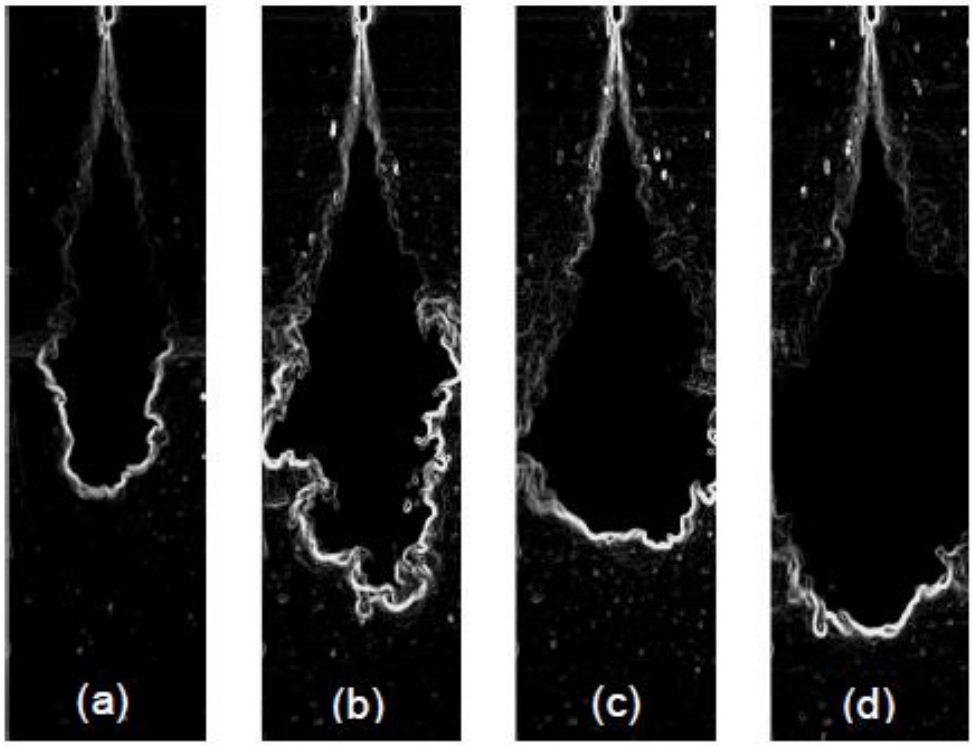


Figure 3.2: A sequence of images showing rapid formation of an upper mixed layer of depth *l*. Fluorescing dye was used for visualization. The width of the cylinder (*D*=12 cm) gives the length scale. Only the upper part of the cylinder is shown. Experimental parameters: Re=7020, $S_0$=0, $S_1$=105 $‰$; t=2.0 (a), 4.3 (b), 12.1 (c), 31.4 (d).

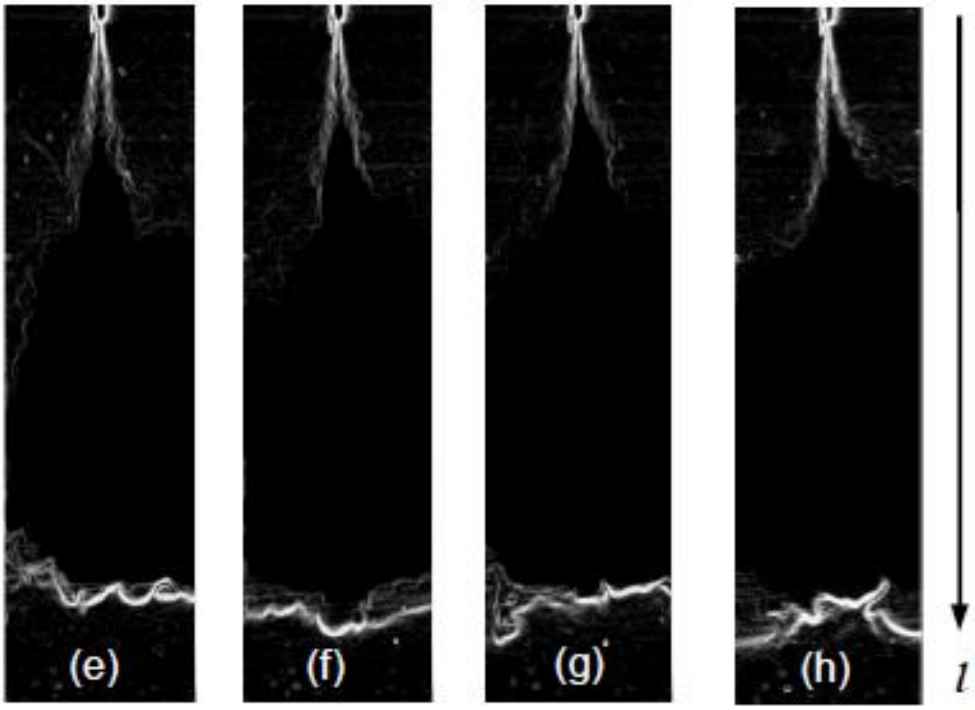


Figure 3.2: (continued) t=46.1 (e), 58.6 (f), 65.6 (g), 74.6 s (h).

### 3.5 Results Of Measurements

#### 3.5.1 Positively Buoyant Jets

In these experiments the cylinder was filled with salty (salinity $S_1$) water while fresh water (salinity $S_0$=0) was used as jet fluid. The dependences of exiting water salinity $S$ with time $t$ for all six runs conducted with positively buoyant jets are shown in figure 3.3. As seen in figure 3.3, in all runs $S(t)$ remains practically constant, and equal to the initial salinity of the cylinder (see Table 1) for a long time interval, $t$≈10-15 min. Thereafter the salinity starts decreasing sharply for 10<$t$<25 min and then more slowly, reaching asymptotically the salinity of the jet fluid $S_0$ at $t$≈30-60 min.

To affirm this general behavior the results of run #5, conducted under practically the same conditions as run #1 (see Table 1), are also given in figure 3.3; both measurements are in satisfactory agreement. The influence of $Q$ on $S(t)$ is also illustrated in figure 3.3 where the results for two runs (#2 and #6) conducted with approximately the same initial background salinity $S_1$ but different $Q$ are shown. The general behavior of $S(t)$ for run #2 in is very similar to that for runs #1 and #5, which were conducted with the same $Q$ as run #2. In contrast, comparison of runs #2 and #6 (figure 3.3) shows that the flux rate $Q$ change (increase in two times) leads to a proportional change (decrease in two times) of the time scale, while the salinity scale does not change. To summarize, the data shown in figure 3.3 for all six runs conducted for the positively buoyant jet indicate possible flow similarity, which will be addressed below.

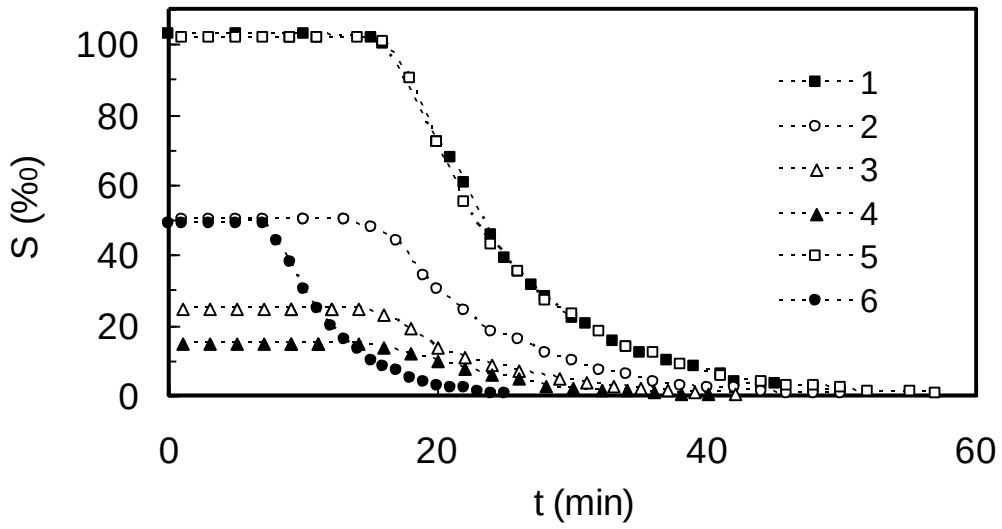


Figure 3.3: The dependences of exiting water salinity $S$ with time $t$ for all six runs (see Table 1) conducted with positively buoyant jets. Symbols – measurements, dashed lines – best fits.

### 3.5.2 Negatively Buoyant Jets

In these experiments the cylinder was filled with fresh water ($S_1$=0), while salty water ($S_0$) was used as the jet fluid (see Table 1). The exiting water salinity $S(t)$ as a function of time $t$ is shown in figure 3.4. First, consider run #8 with the largest jet salinity, and $S(t)$ here starts increasing promptly after the jet flow was initiated. With time, $S(t)$ increases smoothly and asymptotically reaches the jet salinity $S_0$ at $t\approx$110 min. Comparison with figure 3.3 shows that the time for $S(t)\approx S_0$ for the negatively buoyant jets is approximately twice as long as for the positively buoyant jet, given the same conditions. This is due to continuous and intense mixing of jet and background fluids.

Similar general behavior was observed for two runs (#10 and #11) conducted with smaller jet salinities (figure 3.4), except for some minor differences. At smaller jet salinities there is a noticeable time delay, $\Delta t$~2-4 min, between the jet initiation and the time for a measurable change of $S(t)$. This will be discussed later.

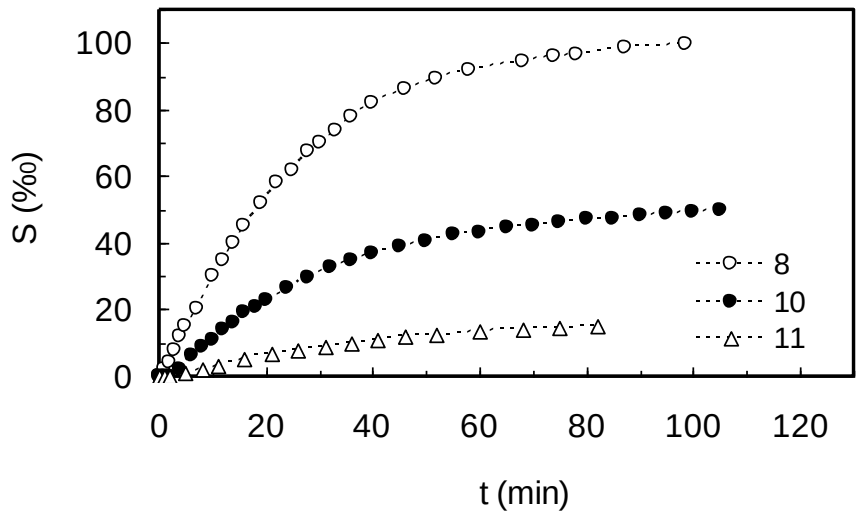


Figure 3.4: The dependence of the salinity S of exiting water with time t for all three runs (see Table 1) conducted with negatively buoyant jets. Dashed lines – best fits.

## 3.6 Mathematical Model and Comparison with Measurements

To explain the results of measurements, consider the model schematized in figure 3.5. Let a long vertical cylinder of diameter $D$ be filled with incompressible fluid of density $\rho_1$. At time $t=0$, a fluid of density $\rho_0$ is introduced as a jet from the top of cylinder, at $x=0$, the volume flux rate being $Q$. Simultaneously, fluid is removed from near the bottom at $x=L$ with the same flux rate $Q$. The interest is the density $\rho(x,t)$ of the fluid in the cylinder as a function of time, $t$, depth, $x$, and other external parameters. For simplicity, neglect the density variations in radial direction and consider the one-dimensional problem.

### 3.6.1 Positively Buoyant Jets($\rho_0 \le \rho_1$)

Observations (see e.g., figure 3.2 and figure 3.7 below) show that soon after the flow initiation the fluid in the upper part of the cylinder of depth $l$ is well mixed by the jet, and negligible mixing occurs beneath. Thus at $t>0$ the fluid density in the upper layer can be written as

$$\rho(x,t) = \rho(t), \quad 0 \le x < l, \tag{3.3}$$

where $l$ is the mixing depth. Below this level, at $x \ge l$, the entire fluid column of density $\rho(x,t)$ moves downward with the velocity (figure 3.5)

$$U = 4Q/\pi D^2. \tag{3.4}$$

For $0 \le x < l$ the balance of mass in the control volume $V_0=ls$, gives

$$V_0 \frac{d\rho(t)}{dt} = Q\left[\rho_0 - \rho(t)\right], \tag{3.5}$$

where $Q\rho_0$ is the mass flux at $x=0$ and $-Q\rho(t)$ at $x=l$.

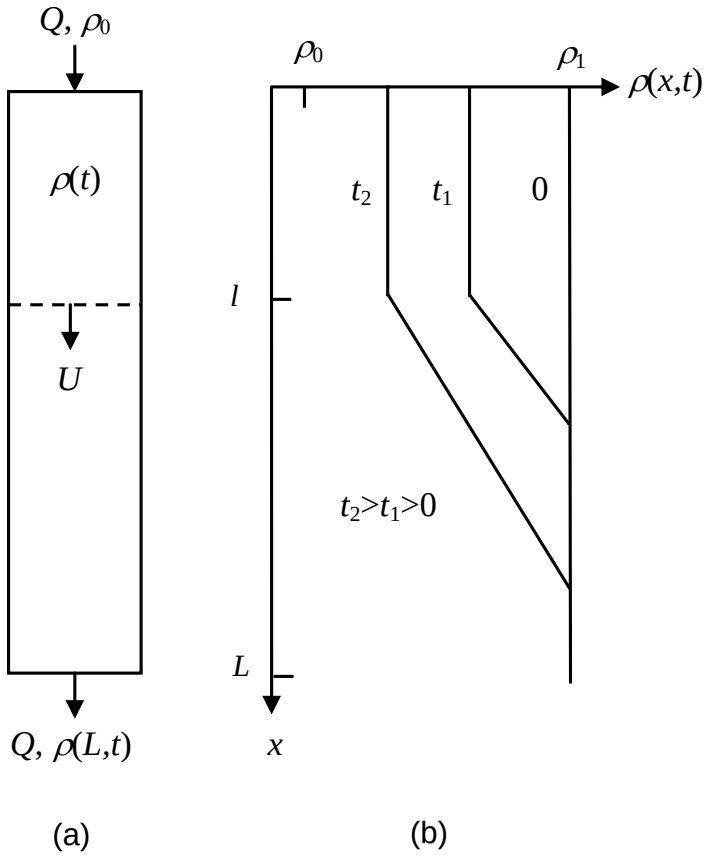


Figure 3.5: In (a) - flow schematic; in (b) - time evolution of vertical density profile for positively buoyant jet.

For the initial condition, $\rho(t)=\rho_1,\quad t=0$, the particular solution for equation (3.5) is given by

$$\rho(x,t)=\rho(t)=\rho_0+(\rho_1-\rho_0)\exp(-Ut/l),\quad 0\le x<l, \tag{3.6}$$

which can be used as the boundary conditions at $x=l$ for the function $\rho(x,\ t)$ for $x\ge l$.

Observations show that mixing at $x\ge l$ is negligible, and to find $\rho(x,\ t)$ at $x\ge l$ the conservation of mass can be used,

$$\frac{D\rho}{Dt}=\frac{\partial\rho}{\partial t}+U\frac{\partial\rho}{\partial x}=0, \tag{3.7}$$

where $D/Dt$ is the material derivative. The general solution for equation (3.7) has the form (see e.g., Whitham, 1974) $\rho(x,t)=\Phi(x-Ut)$, where $\Phi$ is an arbitrary function to be determined using the boundary condition from equation (3.6) at $x=l$. The resulting solution has the form

$$\rho(x,t)=\begin{cases}\rho_0+(\rho_1-\rho_0)\exp\left[(x-l-Ut)/l\right], & l\le x<l+Ut\\ \rho_0+(\rho_1-\rho_0)=\rho_1, & l+Ut\le x\end{cases}. \tag{3.8}$$

Note, that the cylinder length, $L\ge l$, does not enter the problem.

It is convenient to write equations (3.6) and (3.8) in dimensionless form using $(\rho_1-\rho_0)$, $l$ and $L/U$ as the density, length and time scales. In choosing $L/U$ as the time scale we took into account that in practice, during the refilling of SPR caverns, the time of oil processing is measured in units of time, $t_0=V/Q=L/U$, that is needed to recirculate one cavern volume $V=\pi D^2L/4$. Using the dimensionless density $R(x,t)=\left[\rho(x,t)-\rho_0\right]/(\rho_1-\rho_0)$, the dimensionless solution becomes

$$R(X,N)=\begin{cases}\exp(-NL/l), & 0\le X<1\\ \exp(X-1-NL/l), & 1\le X<1+NL/l\\ 1, & 1+NL/l\le X\end{cases}, \tag{3.9}$$

where the dimensionless time $N=t/t_0$ can be interpreted as the number of cavern volumes processed, $X=x/l$ the dimensionless depth and $l$ is given in equation (3.1).

In the experiments, the density of water taken at the level $x=L$ was measured as a function of time $t$. At $X=L/l$, the solution equation (3.9) gives the following dependence of dimensionless density $R$ on the dimensionless time $N$

$$R(X = L/l, N) = \begin{cases} 1 & , \quad N \le 1 - l/L \\ \exp[(1-N)L/l - 1], & 1 - l/L < N \end{cases}. \tag{3.10}$$

To compare equation (3.10) with the measurements, positively buoyant jet data shown in figure 3.3 were recalculated for all runs and are plotted in figure 3.6 using dimensionless variables *R* and *N*. As seen in figure 3.6, in dimensionless plots, data for all runs collapsed on the 'universal' curve, as) shown in equation (3.10) by the solid line.

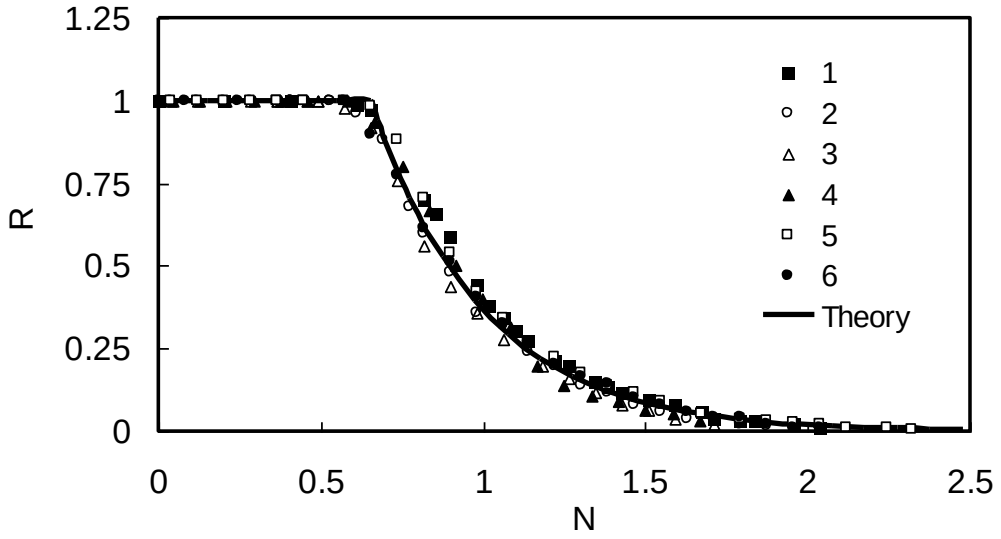


Figure 3.6: Same data as in figure 3.3, but in dimensionless coordinates *R* and *N*. Symbols – measurements, solid line –model prediction equation (3.10).

To further validate equation (3.9), vertical density profiles were measured in some runs and compared with the calculations; see figure 3.7 for a typical case, where a succession of profiles measured at different times in run #2 is shown by thin lines.

Using equation (3.9) the density profiles were calculated for the same times and are also shown by solid lines. The agreement is very good, although some differences between the measurements and calculations can be seen in the pycnocline area, $X>1$. These differences can be explained by the fact that the measured profiles are 'instantaneous' while calculated profiles reflect the mean behavior. Similar results were obtained for other runs.

### 3.6.2 Negatively Buoyant Jets ($\rho_0 > \rho_1$)

The solution of equation (3.9) is rather general, and can be applied for negatively buoyant jets as well. As discussed in Section 3.4, soon after jet initiation, heavy fluid of the jet mixes with the upper part of the container to a depth $l$. Convection prevails below this level, soon penetrating down to the container bottom at $x=L$. Neglecting the first approximation of the time for convection to penetrate to the bottom, it is reasonable to take the cavern length $L$ as the mixing depth instead of $l$ in equation (3.9). In the experiments, the salinity of exiting water taken at the level $x=L$ was measured as a function of time $t$. For $x=L$ and using $L$ instead of $l$, the solution of equation (3.9) gives

$$R(X=1,N)=\exp\left(-N\right), \quad N\geq 0 . \tag{3.11}$$

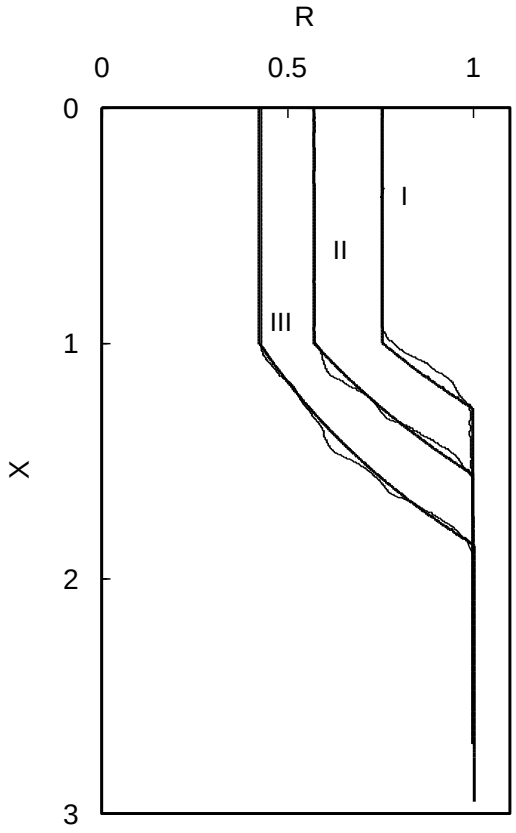


Figure 3.7: Comparison of measured (thin lines) and calculated (solid lines) vertical density profiles for run #2 for different times in dimensionless variables. The dimensionless density *R* is shown as a function of dimensionless depth *X* for different dimensionless times *N*=0.1 (I), 0.2 (II), 0.31 (III).

To compare equation (3.11) with measurements, the negatively buoyant jet data shown in figure 3.4 are replotted in figure 3.8(a) in the dimensionless variables *R* and *N;* equation (3.11) is shown by the solid line. Although at the largest value of salinity the agreement is satisfactory, some discrepancies are evident at smaller salinities. As mentioned in Section 3.5.2, there is a small time delay $\Delta t$ between the start of the experiment and for the occurrence of measurable changes in the salinity of exiting water (see figure 3.4). This was attributed to the time taken for the convective mixed layer to reach the bottom. The neglect of $\Delta t$ in the model may be a cause for the discrepancy observed.

The delay time $\Delta t$ can be estimated as follows. Observations show that at first the jet is mixing rapidly (and we neglect this time) to the depth $l$, and then much more slowly, during time $\Delta t$, by convection to a depth $(L\text{-}l)$. Separate experiments show that typical vertical convection velocity $u$ in a long cylinder of the length $L$ and diameter $D$ can be estimated as $u = C(bD)^{1/3}\left(L/D\right)^{n}$, where $b = g^{*}Q/s$ is the buoyancy flux, $g^{*} = g(\rho_0 - \rho_1)/\rho_0$, $g$ – gravity acceleration, $s = \pi D^2/4$ and $C \approx 0.05$, $n = 1/2$ were determined by observing the growth of the convective mixed layer as a function of time as well as by direct measurement of $u$ using particle image velocimetry. Estimating the delay time as $\Delta t = (L - l)/u$, we obtain the estimate

$$\Delta N = Q\Delta t / sL \approx C^{-1}\left(4/\pi\right)^{2/3}\left(1 - l/L\right)\left(Q^2/D^5 g^{*}\right)^{1/3}\left(D/L\right)^{1/2} \qquad (3.12)$$

for the dimensionless delay. Adjustment of measurements using $\Delta N$ improved the agreement between data and model predictions [figure 3.8(b)].

For the reasons explained at the end of Section 3.3 for negatively buoyant jets, no "instantaneous" density profiles were measured. Nevertheless, satisfactory agreement of measurements with similarity solution in figure 3.8 supports the idea that for negatively buoyant jets the whole water column is mixed.

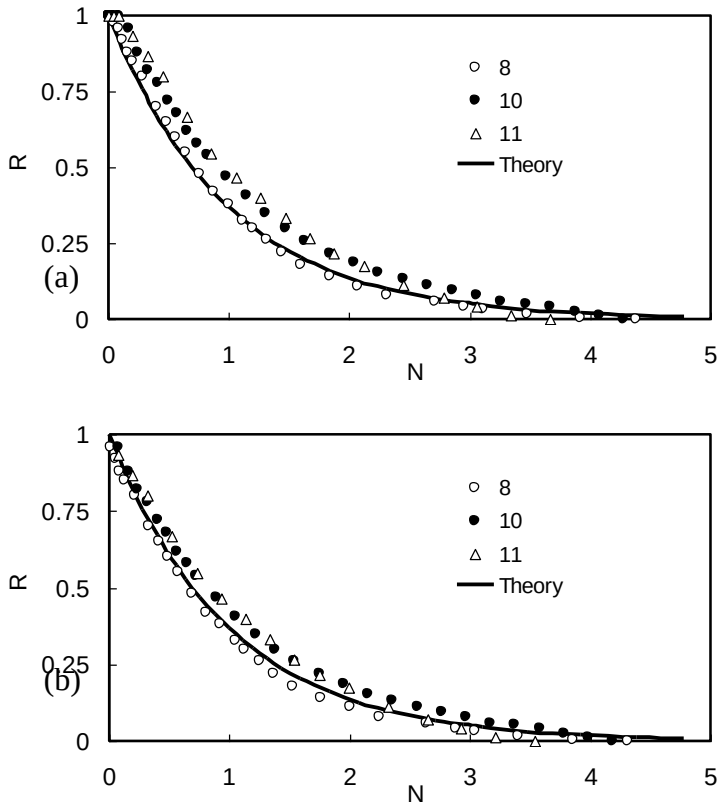


Figure 3.8: In (a) – the same data as in figure 3.4, but in dimensional coordinates *R* and *N*. Solid line – model prediction equation (3.11). In (b) – the same data as in (a), but with small corrections for the dimensionless time delay $\Delta N$. The solid line shows solution equation (3.11).

# 4 WALL ATTACHMENT OF OFFSET JET IN HOMOGENOUS FLUID

Note - This material has been published in Nath, C., S.I. Voropayev, D. Lord, and H.J.S. Fernando, “Offset Turbulent Jets in Low-Aspect Ratio Cavities,” J. Fluids Eng., 2014, 136:060911.

## 4.1 General Remark

A study of an offset turbulent jet injected into a homogenous fluid inside a low-aspect ratio cylindrical cavity is presented in this chapter. This chapter is divided into five sections. Section 4.2 starts with an introduction, and relationships among non-dimensional parameters are identified is section 4.3. In section 4.4 an overview of the offset jet test facility is reported. This chapter ends with section 4.5 discussing the experimental results with flow behavior, velocity measurements, mixing length variation and drop in pressure with respect to different radial offset distances.

## 4.2 Introduction

The release of a turbulent jet into a quiescent background has been the subject of extensive study, which can be broadly categorized into cases of unconfined (List, 1982) and confined jets (Blake and Powell, 1986). The latter considers the presence of confining walls, a case with widespread applications to combustors, fuel-injectors, and cooling water and pollution discharge systems in lakes. Confined jets can be further classified into four classes, based on their dynamical attributes: (a) a jet impinging on a solid wall (Broderson et al., 1986); (b) wall jets where the discharge is at a boundary (Launder and Rodi, 1983); (c) offset jet from a vertical wall issuing parallel to a closely located horizontal solid or a free-surface boundary (List, 1982; Bourque and Newman, 1960; Miozzi et al., 2009), and (d) jet injected into a cavity (Risso and Fabre, 1997). The above classification is similar to that of Gu (1996), with the exception that an additional class (d) has been included, studies of which have been reported in the past, though infrequently (Villermaux and Hopfinger, 1994).

Previous work on (a)-(d) has been on either two-dimensional or axisymmetric cases, and to our knowledge studies with nozzle offset from the axis of symmetry have not been reported. This part of the research addresses this issue, where penetration of a jet into a cylindrical container with and without nozzle offset is considered. The jet is injected at one end of the cylinder as a point momentum source while fluid is being withdrawn at the other end with the same volume rate as the supply rate but with negligible momentum. It can be considered as a special case of category (d). Previous studies show that confined jet flows, with jet at the axis of symmetry, exhibit a wide range of features: (a) the dissolution of the jet at a distance $l = 3.6D$ from the nozzle, where $D$ is the container diameter (Risso and Fabre, 1997); (b) the development of an adverse pressure gradient by the return flow between the jet and walls (Liberzon and Fernando,

submitted; (c) jet precession due to instabilities (Konig and Fiedler, 1991; Voropayev et al., 2011); and (iii) regions of fluid recirculation (Gu, 1996). With offset of the nozzle, the flow symmetry is broken, leading to complex flow patterns, which is studied in this chapter.

In the third and final part of this research, study was done to characterize the effect of offset positioning of the nozzle on flow structure, jet penetration depth, jet spreading rate and velocity field. In parallel, simple demonstrations of pressure distribution changes for different offset positions is presented.

### 4.3 Non-dimensional Parameters

Consider the discharge of a jet into a low aspect ratio cylindrical container. Here the aspect ratio is defined as $\Gamma = D/L$; $D$ is the cylinder diameter and $L$ the length of the container. The jet velocity is $u_0$, the nozzle diameter is $d_0$ and the coordinate system is indicated in figure 4.1(a). Thus the momentum and volume fluxes of the jet are, respectively, $J = (\pi \cdot d_0^2 \cdot u_0^2)/4$ and $Q = (\pi \cdot d_0^2 u_0)/4$. To mimic SPR flow configuration, fluid is extracted by a tube of diameter $d_e$ from the lower part of the cylinder, located at horizontal and vertical distances of $P_y$ and $P_x$, respectively, from the origin. The nozzle offset distance from the origin is $\Delta$ and $\nu$ is the kinematic viscosity. The mixing depth $l$ can be written as

$$l = f_1\left(d_0, u_0, \Delta, D, L, P_y, P_x, d_e, \nu\right), \quad l = f_2\left(J, \Delta, D, L, P_y, P_x, d_e, \nu\right), \tag{4.1}$$

where $f_1$, $f_2$…are functions. Note that $d_0$ and $u_0$ are replaced by $J$, assuming a point jet of high momentum and low flow rate, c.f., List (1982). The corresponding non-dimensional form is

$$\frac{l}{D} = F_1\left(\frac{\Delta}{D}, \frac{L}{D}, \frac{J^{1/2}}{\nu}, \frac{P_y}{D}, \frac{P_x}{D}, \frac{d_e}{D}\right), \tag{4.2}$$

where $F_1$ and $F_2$…are functions.

Some simplifications can be made with the following assumptions: (i) at high Reynolds numbers $\mathrm{Re} = \left(J^{1/2}/\nu\right)$, the Reynolds number similarity can be assumed; (ii) for $D<<L$, the length of the cavity is unimportant since the jet mean flow persists only until the depth x = $l$ <<$L$, (Risso and Fabre, 1997); (iii) for a point source jet, $d_0/D << 1$, the nozzle shape and jet diameter $d_0$ can be neglected, (Keane and Adrian, 1992); and (iv) since fluid withdrawal occurs at a location far from the jet break up, the exit conditions are unimportant i.e., $(P_x >> l; P_y = D)$. Thus equation (4.2) becomes

$$\frac{l}{D} = F_2\left(\frac{\Delta}{D}\right), \tag{4.3}$$

which is used to present the results of the study in terms of the dimensionless jet offset.

### 4.4 Experimental Setup and Method

Several cylindrical containers of low aspect ratios $\Gamma$ were used, depending on the application: Cylinder C1 ($L$= of 110 cm; $D$=10 cm, $\Gamma = 0.09$); Cylinder C2 ($L$=80 cm; $D$=10 cm, $\Gamma = 0.125$); Cylinder C3 ($L$=100 cm; $D$=10 cm, $\Gamma = 0.1$); and Cylinder C4 ($L$ = 30 cm; $D$ = 4.5 cm, $\Gamma = 0.15$). In each case, a peristaltic pump circulated water from the bottom of the cylinder to the jet at the top, and the momentum associated with the fluid sink at the bottom suction exit was negligible.

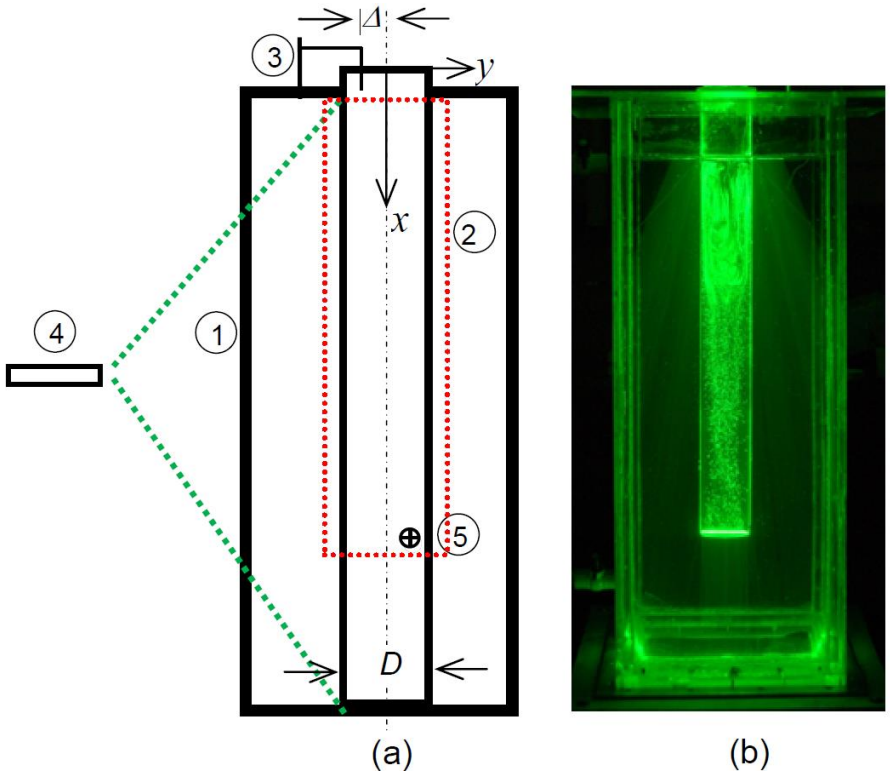


Figure 4.1: (a) Experimental set-up: 1 – Rectangular tank, 2 – glass cylinder (cylinder A; D=10 cm, L=110 cm) seeded with Pliolite particles, 3 – Nozzle ($d$=0.165 cm), 4 – Nd: YAG Laser, 5 – jet withdrawal position. The coordinate system used is also shown. 1(b) same setup with a shorter cylinder (cylinder B; $D$=10 cm, $L$=80 cm) fixed to the top cover was employed for streak photography. Tracer particles are shown inside the cylinder, illuminated by the laser sheet. The dashed box indicates the observational area for PIV.

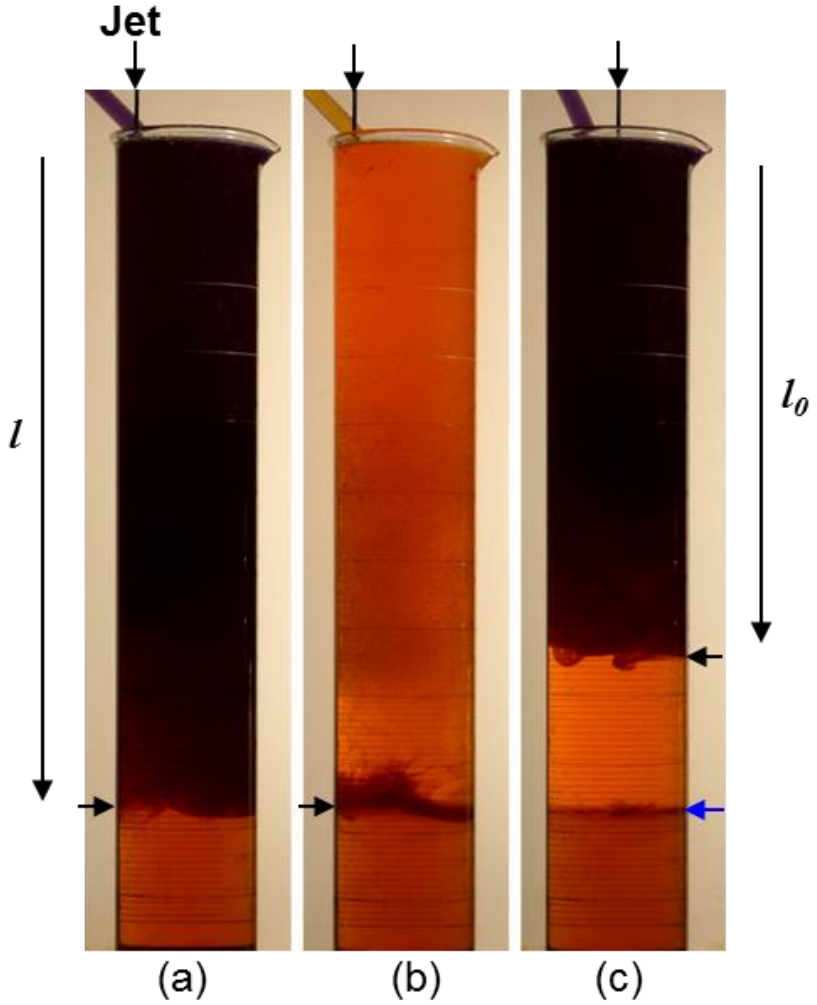


Figure 4.2: Photographs showing how the mixing depth l changes when the jet is shifted from the near wall position, $\Delta \approx D/2$ (a, b), to the centerline position, $\Delta \approx 0$ (c). Black vertical arrows at the top show the jet positions in (a-c); black horizontal arrows show the boundary between mixed and unmixed fluids in (a-c), and blue horizontal arrow in (c) shows the 'scar' from previous mixing in (a, b).

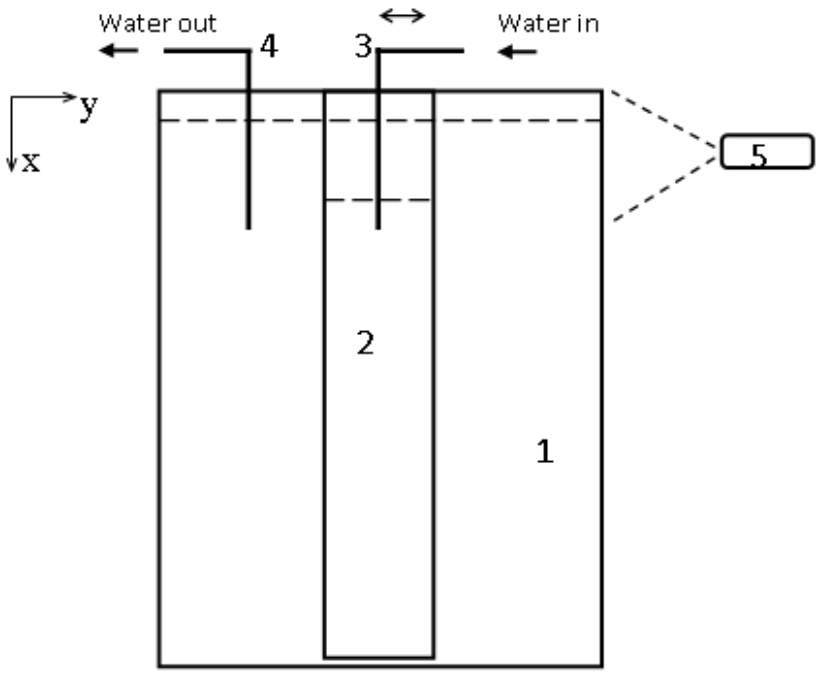


Figure 4.3: Experimental set-up: 1 – Cylindrical beaker with diameter *D1* = 20 cm and length *L1*=35 cm, 2 –glass cylinder (diameter *D*=4.5 cm, length *L*=30 cm) with both sided open 3 – Nozzle (diameter *d*=0.165 cm, capable of vertical and traverse movements), 4 – water suction pipe connected to calibrated pump, 5 – DVC camera used for video recording water level inside cylinder and beaker.

Dye visualization was conducted using cylinders C1 and C4. In one set of experiments, the working fluid was a solution of (20% by mass) hydrochloric acid (HCl) neutralized with (50% by mass) sodium hydroxide, with Thymol Blue added as a pH indicator, the pH of the resulting solution being close to 7. Further addition of alkaline solution would change the pH of the working fluid to (8.0-9.6), the indicator changing to the color blue. Addition of HCl would change pH to (1.2-2.8), with color yellow. The jet was then initiated, and after it reaches a quasi-steady state, a minute amount of HCl acid/Thymol Blue was added to the nozzle inlet line. The color of the jet mixing zone changes due to the acid-base reaction, allowing the evaluation of mixing length (figure 4.2). Video recordings (20 frames, frame rate~2 fps) were made at the center cross-section in the (x-y) plane by a DVC-3400 digital video camera, and from these recordings 6-8 best images for each run were selected with discernible jet borders that are visually untainted by recirculating background fluid. These selected images were processed using ImageJ software, which were later converted to readable MatLab file, from which the averaged mixing length was estimated with ± 4% uncertainty. The mixing length $l$ for individual offset positions was calculated by averaging data from ten identical runs.

To remove optical distortions during photography, Tanks C1 and C2 were placed inside a rectangular glass tank filled with water (25x25x100 $cm^3$). As illustrated in 4.1(a), the outer glass tank (1) was painted black inside (except visualization regions) and the experimental cylinder (2) was rigidly fixed to or suspended from the cover of the tank; see figure 4.1(a, b). Camera controls (exposure, gain, offset and frame rate) were carefully tuned by means of DVCview software. Recordings of ~ 600 frames at~10 fps were made, which were stored in the computer RAM for later frame by frame analysis.

The PIV measurements were performed using the Cylinders C1 and C3, immersed in the rectangular water tank. The jet was introduced from the top of the cylinder using an ‘L-shaped’ round nozzle (3) of diameter $d_0$=0.165 cm, which could be traversed vertically and horizontally. The same amount of fluid was drawn from the bottom of the cylinder without significantly disturbing basic flow patterns (exit diameter $de$ = 1 cm) and this fluid was reintroduced as the jet. Upon establishing a quasi-steady state, PIV images were taken using the CCD camera and stored for further analysis. To study the jet behavior at different offset locations, the nozzle, attached to a precision micrometer, was positioned at different radial locations, including near the wall. A standard PIV system (TSI Inc.) was used, which included a Dual Nd:YAG Laser (4) to illuminate the flow field, Laser-Pulse Synchronizer, 1 GB RAM computer, and a CCD camera (PIVCAM 10-30). The Laser-Pulse Synchronizer controlled the camera and sampling computer. A set of cylindrical lenses expanded the laser beam into a thin sheet (4) that illuminated a section along the cylinder axis, and PIV data were obtained in this (x-y) plane. The cylinder was sealed from the bottom, and the working fluid was seeded with neutrally buoyant Pliolite tracer particles.

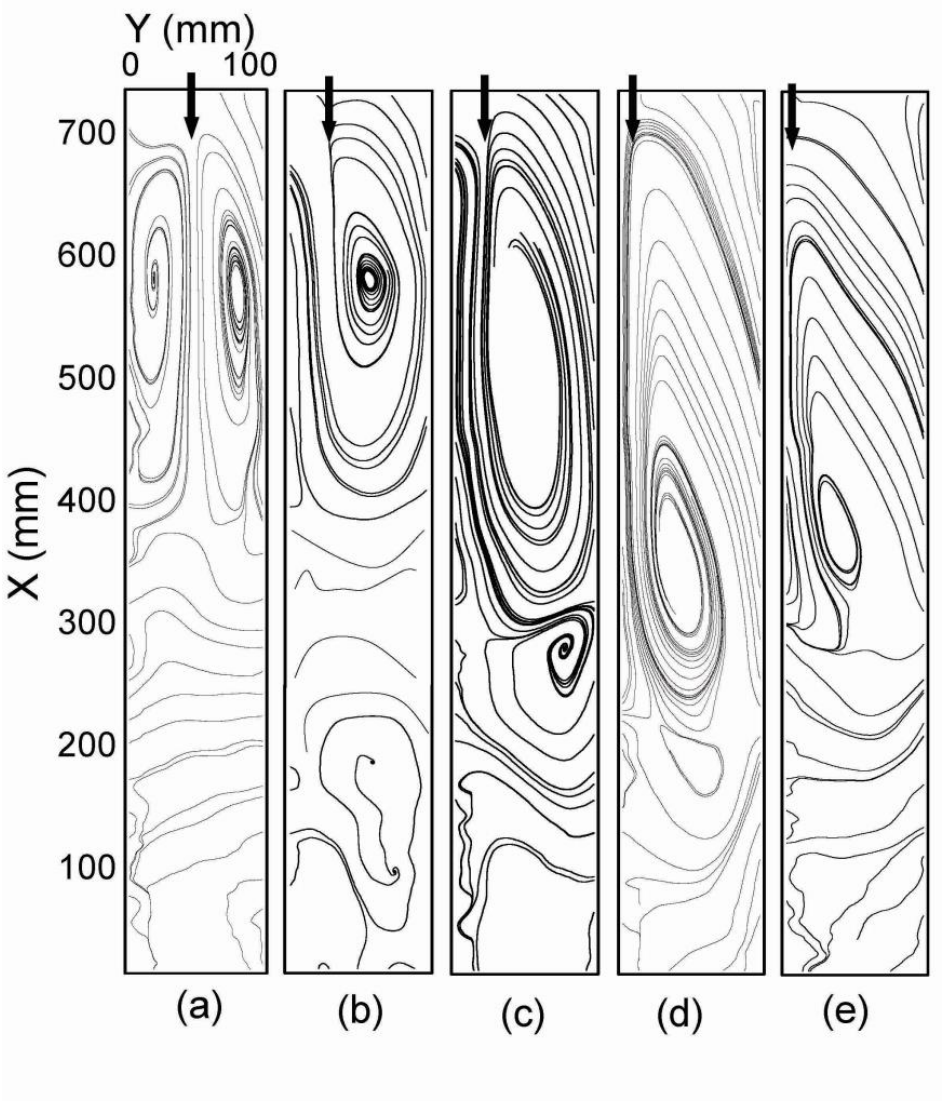


Figure 4.4: Contours of streamlines for different radial offset positions ($\Delta/D$): (a) 0, (b) 0.2, (c) 0.25, (d) 0.4 and (e) 0.49. Experiments conducted at the same Reynolds number of 10,000. The jet location is indicated in the figure.

The PIV horizontal velocity data obtained for the (*x*-*y*) plane were processed using the TSI PIV software package. Pairs of images were captured at 15 Hz, and 400 pairs were used for processing. The images had a space resolution of ~ 0.3 cm/pixel. The observations covered 70x10 $cm^2$ (shown in dotted box) in figure 4.1(a), and the interrogation area was 32x32 pixels, with data interpolated onto a grid of 8x8 pixels. Erroneous vectors (2%) were separated and substituted by interpolated values; and processed data were stored in vector files on a (232x34) matrix. During post-processing, Tecplot software was used to map instantaneous and averaged velocity/vorticity fields. Streamlines were computed using Tecplot's predictor-corrector integration algorithm. Data from the vector files were processed using Matlab for mean flow characteristics. The experiments were conducted at three Reynolds numbers (Re = 7,000, 10,000, 15,000).

One of the inherent limitations of PIV in measuring flows with very high velocity gradients is the difficulty of simultaneously obtaining data, with acceptable accuracy, in high and low velocity regions. Owing to large velocities, PIV particles are untraceable near the jet exit located in the observation area, leading to large errors in velocity measurements. Since the present study was not focused on the jet exit region, measurements made near the jet exit area were neglected. The uncertainties associated with PIV measurement has been discussed in more detail in previous studies (Adrian, 1991), which for the present case was estimated as ± 3%.

A set of experiments were also conducted to study the overall pressure difference in the tank introduced by jet injection as function of $\Delta/D$ . The cylinder C4, with both ends open (free ends), was placed vertically inside a cylindrical beaker of length $L_1$ = 35 cm and diameter of $D_1$ = 20 cm (see figure 4.3). The set up was filled with fresh water to a depth of $H$=35 cm, and the beaker and cylinder had the same water depths due to leakage at the cylinder bottom. A round nozzle was placed at the upper part of the cylinder, with $d_0$=0.165 cm, and a jet was discharged with a substantial momentum flux $J$ ~ 39,000 $cm^4s^{-2}$ at Re ~20,000. While the jet was being discharged, the water level in the cylinder dropped, raising the water level in the beaker. Video recordings were made at the center (*x*-*y*) cross-section, with a view of 640x480 pixels. For each experiment, about 600 frames (taken at ~10 fps) were analyzed using the DVCview software to evaluate the differential water height ($\Delta h$) between the inner and outer cylinder, which could be checked against the readings of a ruler placed in the background (uncertainty ± 0.5mm).

## 4.5 Experimental Results And Discussion

### 4.5.1 Flow Behavior

Previous studies on axisymmetric confined jets have shown that they undergo precessing motions with a well-defined frequency, thus exhibiting time varying flow with quasi-stationary character (Voropayev et al., 2011). The averaged streamline patterns (400 frames) for this case are shown in figure 4.4(a). Experiments with the displacement of jet nozzle show that only small changes to unsteady oscillations and recirculating streamline patterns occur as far as $\Delta/D<0.2$, but marked deviation to streamlines appeared when $\Delta/D$ approaches 0.2, shown in figure 4.4(b). The penetration depths of the jet in the two cases, however, are approximately the same $l \approx (3.3\text{-}3.6)D$, as will be discussed later. When the jet offset increases to $\Delta/D=0.25$, marked changes to streamlines as well as to penetration depth were observed.

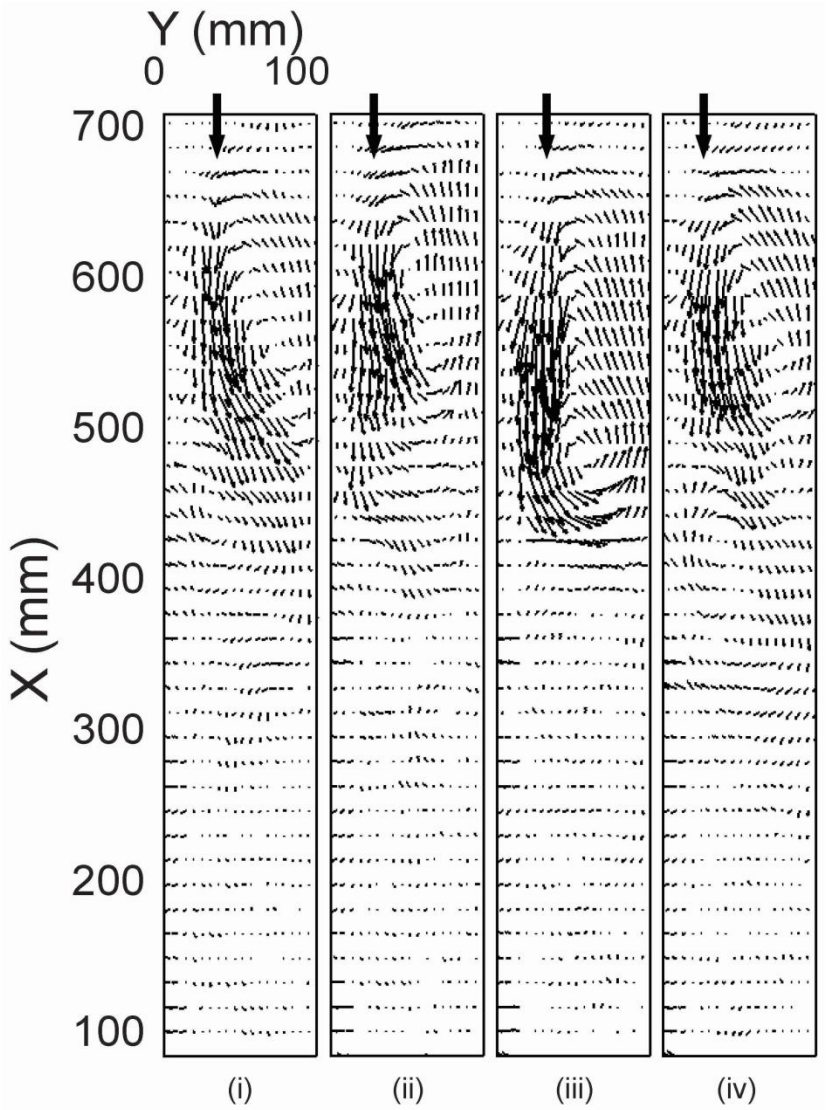


Figure 4.5 (a): Pair of velocity vectors shown for offset jet $\Delta/D$=0.2 in the *xy* plane for consecutive (i) 1st sec (ii) 2nd sec (iii) 3rd sec (iv) 4th sec after the flow reached some quasi-steady state. Reynolds Number = 10,000.

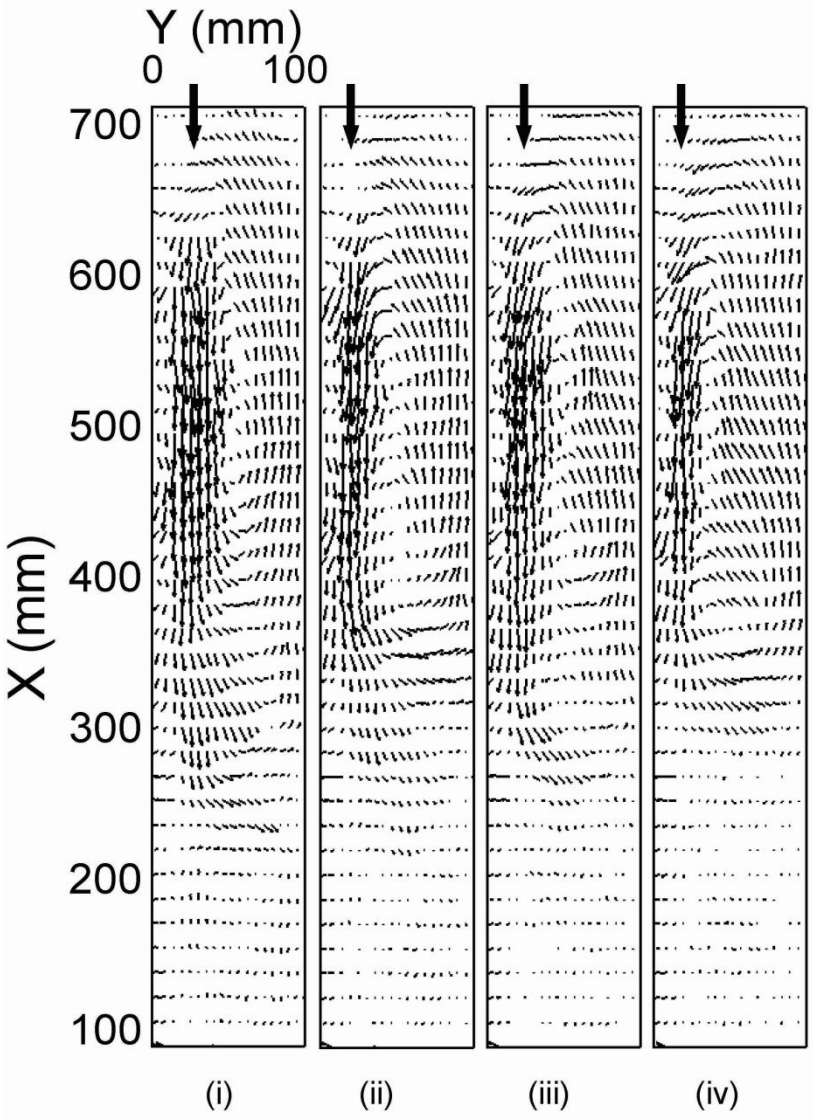


Figure 4.5(b): Pair of velocity vectors for offset jet $\Delta/D$=0.25 in the xy plane for consecutive (i) 1st sec (ii) 2nd sec (iii) 3rd sec (iv) 4th sec after the flow reached some quasi-steady state. Reynolds Number = 10,000.

The jet showed a steady attachment to the nearby wall with similarities to a wall jet, precessing motions disappear, the penetration depth increases, and on the average the jet separates out of the wall at some distance, forming a small, but oscillatory, tail or a recirculating region in figure 4.4(c). The penetration depth continues to increase with the increase of offset up to about $\Delta/D$=0.40 as show in figure 4.4(d), and then starts decreasing in figure 4.4(e).

Instantaneous velocity vectors shown in Figure 4.5(a, b) illustrate different degrees of unsteadiness for $\Delta/D$=0.2 and 0.25 cases. Here the data have been taken after the jet has been fully established. Note the flow vacillations in figure 4.5(a), which occur over the entire length of the jet, caused by precessing motions. Conversely, when $\Delta/D$=0.25 in figure 4.5(b), the attached portion of the jet remains steady, with the tail vacillating and leading to average streamlines of figure 4.4(c). The flow behaves similarly at $\Delta/D$=0.4 but the length of wall attachment is larger. The penetration depth in this case is $l \approx 5.2D$, about 40% increase from the axisymmetric case. Observations at $\Delta/D$=0.49 has some similarities to $\Delta/D$=0.4 as far as the flow structure is concerned, but the intensity of circulation and flow velocities are lesser, which is expected in view of the closeness of jet to the wall and hence enhanced viscous momentum losses.

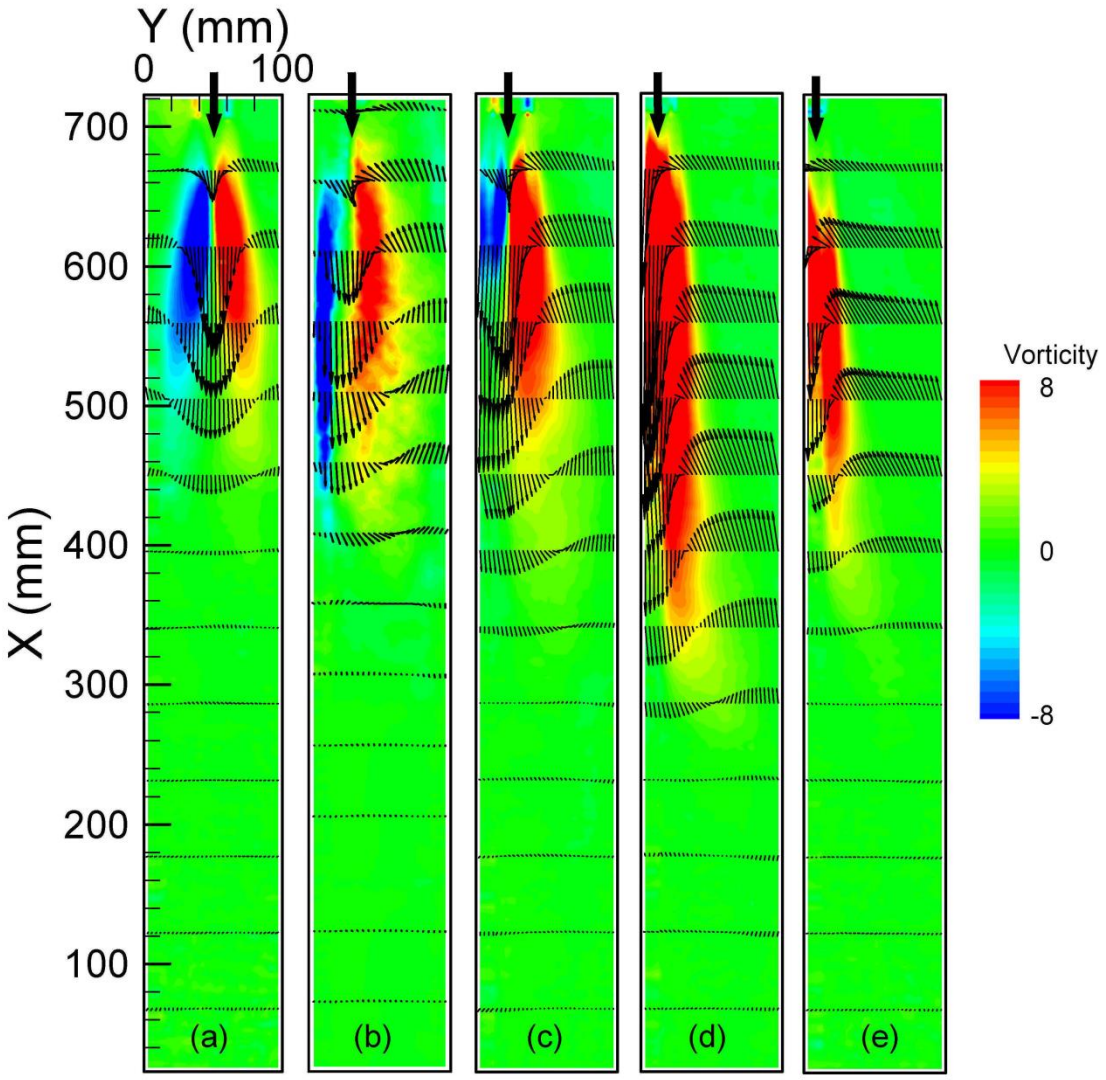


Figure 4.6: Mean velocity profiles in the *xy* plane for radial offset positions ($\Delta/D$): (a) 0, (b) 0.2, (c) 0.25, (d) 0.4 and (e) 0.49. Vorticity is measured in $s^{-1}$. Nozzle positions at the top of the cylinder for different radial positions are shown by an arrow.

Averaged mean velocity profiles are shown in figure 4.6 for different $\Delta/D$. The background red and blue colors represent positive and negative vorticities, respectively, and the arrow length represents the velocity magnitude (the data are averaged over 400 frames). Sometimes, the PIV images could not accurately capture flow fields near the wall ($y>0.4D$) because of the higher velocities, but the bulk of the flow could be well captured and analyzed. The approximately constant value of $l/D$ for $\Delta/D<0.2$, its increase thereafter, followed by a decrease are all clear from figure 4.6.

A sequence of particle streak images are shown in figure 4.7 for the case $\Delta/D=0.4$, the highest jet penetration. Note the stronger wall jet, the outer edge of which forms large (coherent) eddies that advect with the flow and the weaker outer flow rising in the opposite directions. These instantaneous images can be compared with figure 4.4(d) and figure 4.6(d) that show 'averaged' streamlines and velocity vectors, which are devoid of ubiquitous coherent structures evidenced in figure 4.7(b). Somewhat thicker shear layer between the two streams in figure 4.6(c, d) is a result of these structures that transfer momentum between downward and upward flows, which ultimately determine the jet separation point.

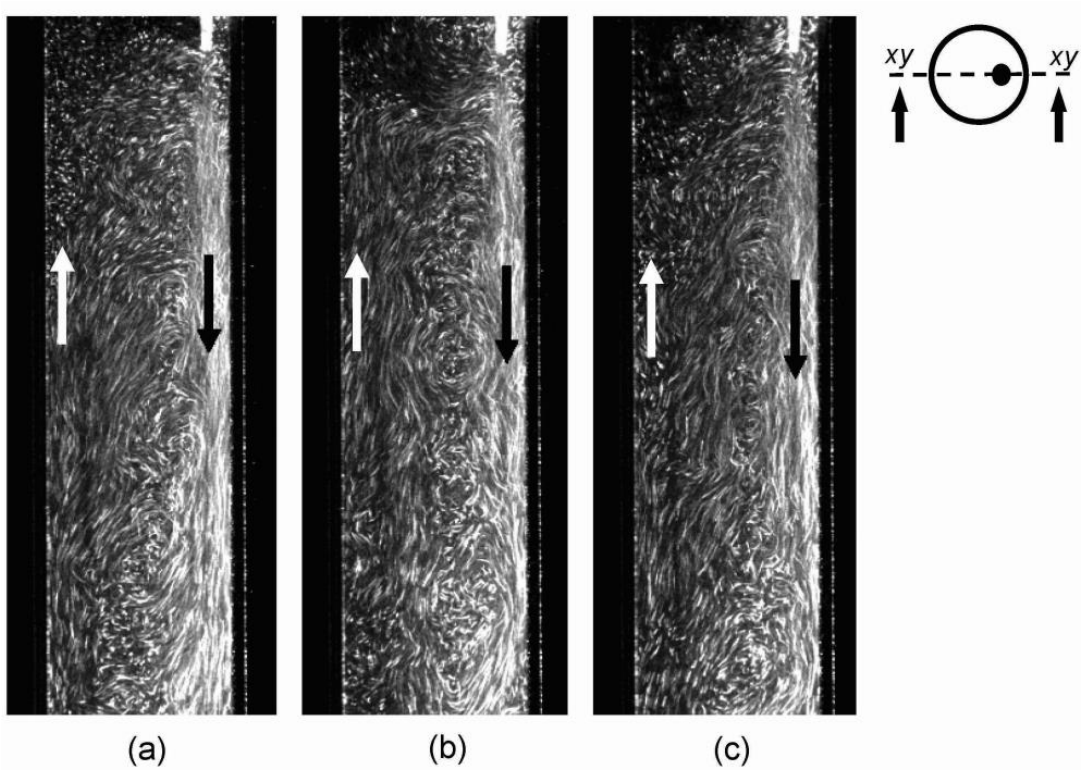


Figure 4.7: Sequence of particle streak images showing the formation of large-scale (coherent) eddies in the x-y plane for $\Delta/D$ = 0.4. Large eddies form clockwise circulation rather than oscillating between cylinder walls. In rightmost inset, the dotted line indicates laser sheet whereas the black dot is the nozzle position. Re=10,000. An exposure of 0.1 s was used.

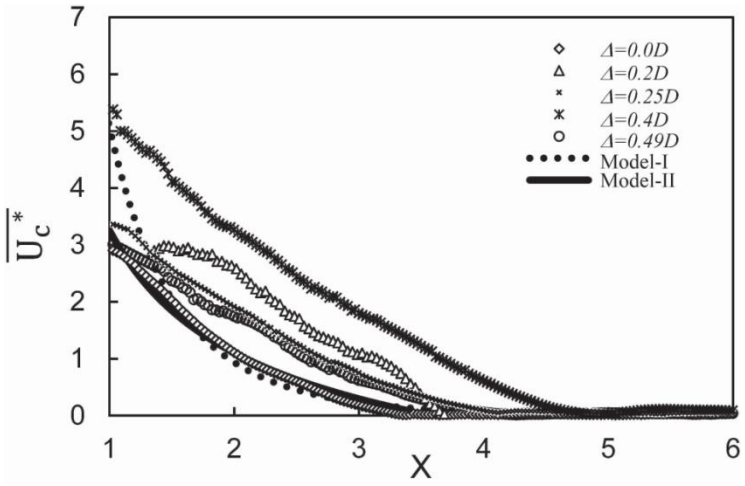


Figure 4.8: Decay of dimensionless maximum centerline mean velocity $\overline{U_c^*}$ in the *xy* plane along the dimensionless distance X = *x*/*D* for different radial offset positions of the nozzle. Comparisons between data for axisymmetric confined jet, estimates of Model-I (Voropayev et al., 2011) and that of Model-II (see Appendix A in this chapter) developed in this study are shown. The jet spreading angle β used in Model-II is experimentally found to be 0.14. This can be compared with unconfined axisymmetric jets, where the spreading angle is ~0.1 [15]. Note that for the magnification of figure shows that for $\Delta/D$ =0.4, $l_{max}$~ (5.1-5.3)*D*

### 4.5.2 Velocity Measurements

Shown in figure 4.8 is the dimensionless maximum centerline mean velocity $\overline{U_c^*}$ along the downstream dimensionless distance X = *x/D* for different offset positions. Here the centerline velocity $\overline{U_c}$ was obtained by averaging ~ 400 image pairs at a given offset position, and $\overline{U_c^*} = \overline{U_c} / U_Q$, where $U_Q = J^{1/2}/D$ is a velocity scale, ($U_Q$ ~ 10.1 cm/s; Re = 10,000). The mixing length for the nozzle position $\Delta/D$ =0 can be estimated as $l_{min}$~ (3.3– 3.6)*D*, and for the offset position $\Delta/D$ =0.4 (circles) as $l_{max}$~ (5.1-5.3)*D*. The data for 0<X<1 are excluded due to measurement difficulties at higher speeds. The results for the zero offset position were compared with the empirical expression of Voropayev et al. (2011) for the axisymmetric case, $\text{Model I} = A/X\exp(X)$ where A= 13.8. A new model that takes into account the details of pressure gradient development is given in the Appendix A in this chapter, of which the predictions are also included (Model-II), the latter being more successful in predictions. The faster decay of $\overline{U_c}$ for axisymmetric jet in comparison to an offset jet can be explained by the stronger pressure gradient due to pronounced restrictions on entrainment flow in the former. This aspect is further illustrated later, using the estimates of bottom pressure in the cylinder.

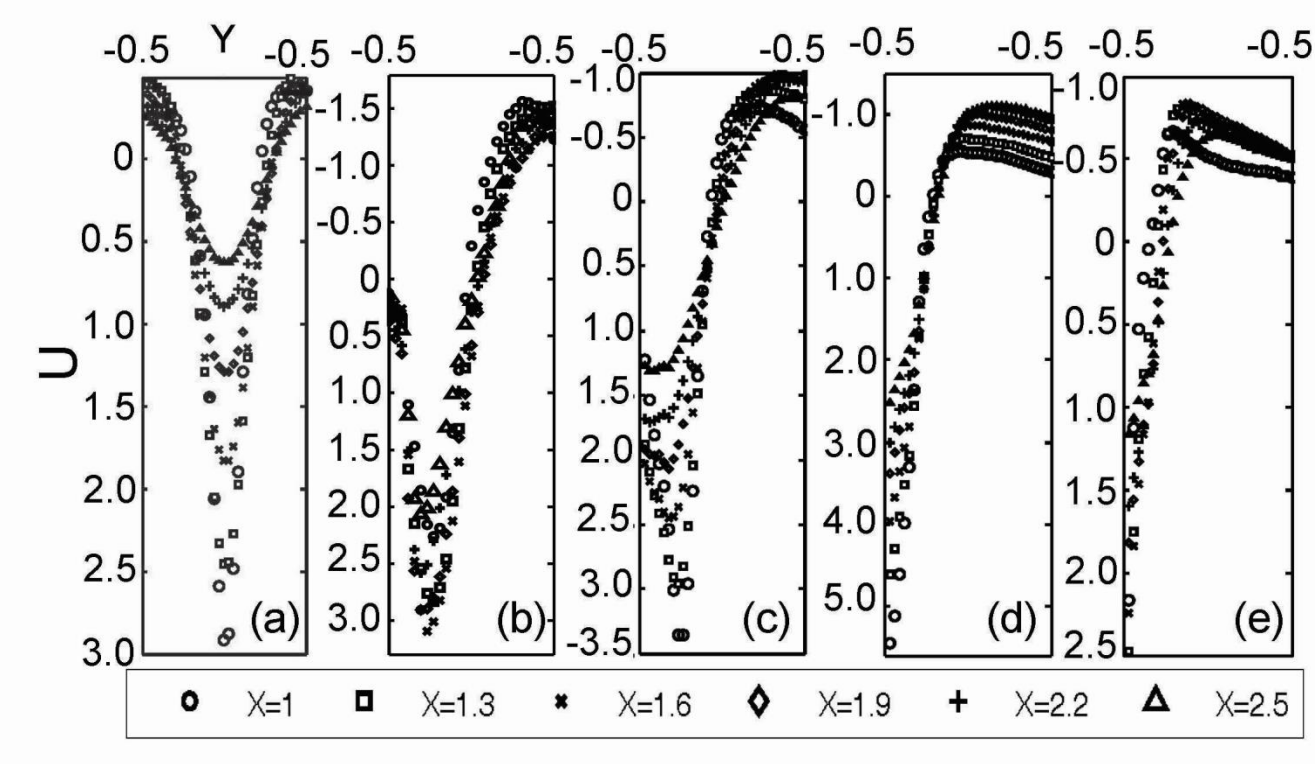


Figure 4.9: Transverse distribution of mean axial dimensionless velocity U in xy plane at different dimensionless distances from the nozzle for different radial offset positions ($\Delta/D$): (a) 0, (b) 0.2, (c) 0.25, (d) 0.4 and (e) 0.49. The symbols representing distances are shown in the bottom of the figure.

Figure 4.9 shows transverse mean axial velocity U, normalized by $U_Q$, at six dimensionless downstream distances (X = $x/D$ = 1, 1.3, 1.6, 1.9, 2.2 and 2.5) and various normalized transverse distances $y/D$ for different offset positions. Note that for axisymmetric jets the axial velocity decreases and half width increases with increasing distances in figure 4.9(a). For offsets jets shown in figure 4.9(b-e), however, although the transverse velocity decreases downstream, the increase of half width is less distinctive. Also, the approximate cross-sectional area available for the mean counter-flow at X=2.5 increases (assuming jet front maintains a spherical shape) in figure 4.9(a-e), a significant increase (35-90)% from the axisymmetric to the four offset positions Δ/D =0.2, 0.25 0.4 and 0.49. This increase allows the return flow to occur with a diminished adverse gradient.

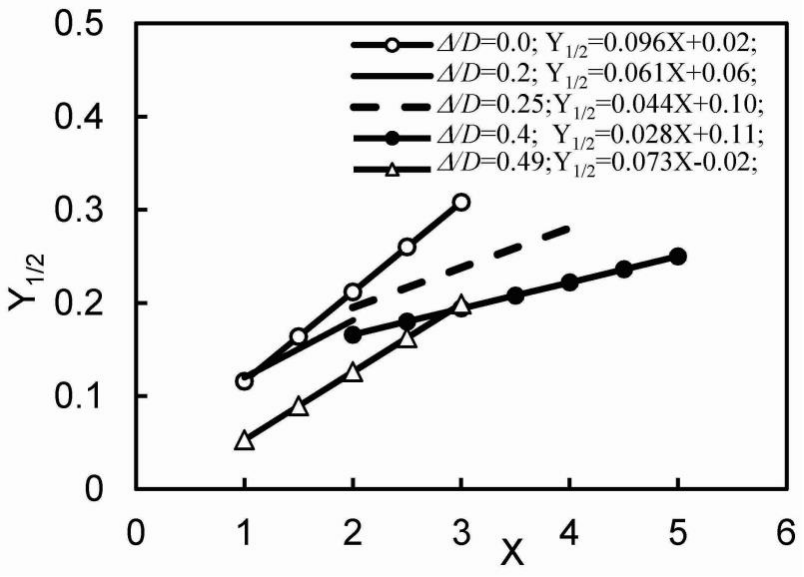


Figure 4.10: Variation of mean (normalized) velocity half-width ($Y_{1/2}$) for different radial offset positions ($\Delta/D$ = 0, 0.2, 0.25, 0.4 and 0.49) along X nozzle distance. Reynolds number = 10,000.

Figure 4.10 shows a comparison of mean velocity half-width $Y_{1/2}$ ($y_{1/2}/D$) as a function of X for $1D \leq X \leq 5.2D$ for different offset positions. Here the transverse distance at which the positive $\overline{U}$ reaches half of it maximum was considered as $y_{1/2}$. The best linear fits for $1D \leq X$ are shown, with numerical expressions in the inset, and for clarity individual data points have been omitted and only the best fits are shown. Note that only the data up to the maximum width of the jet is shown, and hence the best-fit lines have different lengths. The spread (slope) is largest at $\Delta/D=0$, and it reduces until $\Delta/D=0.4$ (where $l=l_{max}$) and again rises for $\Delta/D=0.49$. The $\Delta/D=0.4$ case has the most cross-sectional area for the return flow, and hence the adverse pressure gradient is expected to be smallest and the mixing depth largest.

For the first four cases the wall energy losses can be considered small and hence the momentum flux $J$ is approximately invariant with $x$. For the $\Delta/D=0.49$ case, intensified boundary-layer rates of strain dissipate jet momentum significantly, and hence the jet penetration is expected to be smaller than that for $\Delta/D=0.40$, although the former has a higher return flow area.

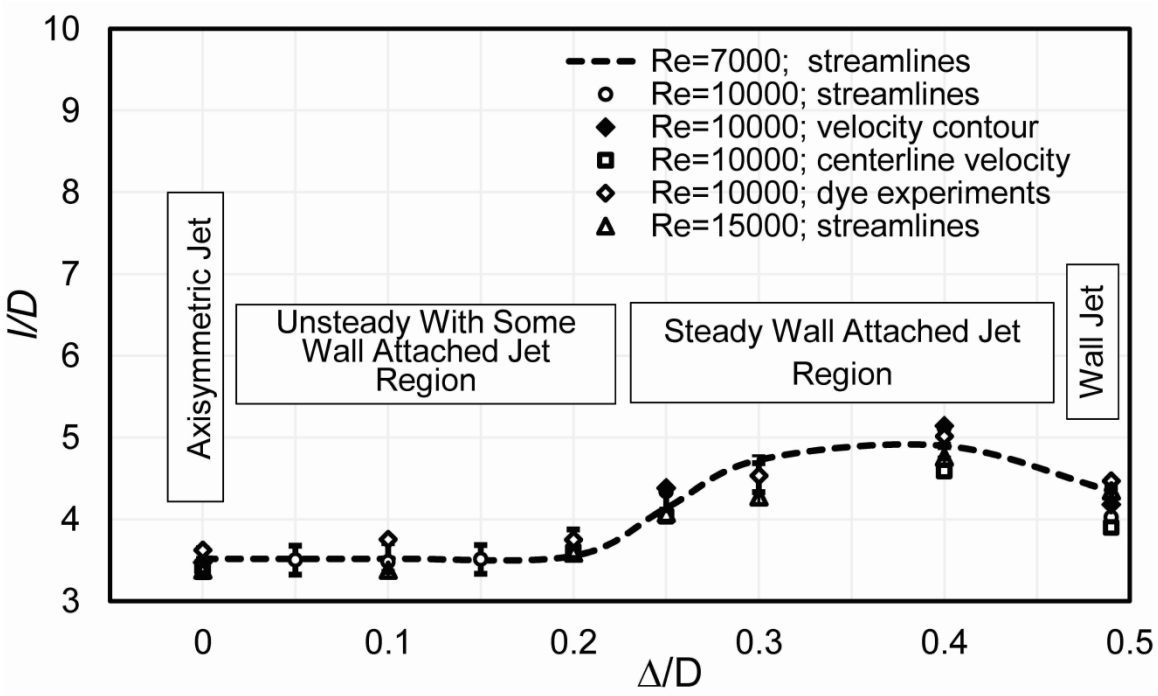


Figure 4.11: Dimensionless mixing length *l*/*D* in the flow as a function of different radial offset positions. Mixing lengths are calculated based on different criteria discussed in the text. Three Reynolds numbers have been used: Re = 7000, 10,000 and 15,000

### 4.5.3 Mixing Length

Figure 4.11 shows the dependence of dimensionless maximum mixing length $l/D$ on radial offset position $\Delta/D$ based on four different measurement criteria. The following criteria were used: (a) streamline-contour based evaluation, where the length of the largest circulatory cell (from TecPlot software) was considered as $l$, since large-scale circulation is primarily responsible for axial momentum transport up to the jet break-up; (b) the velocity magnitude contours for different offset positions were obtained, and length of the contour with maximum velocity for a given $\Delta/D$ was considered as $l$; (c) the location where the velocity along the jet-nozzle centerline is nearly zero was taken as $l$; (d) In the dye experiments, the side-view length of the cylindrical column wherein color changes occur due to jet injection was taken as $l$.

Overall, $l/D$ based on various criteria show a good agreement, as evident from figure 4.11. The minimum mixing length occurs at $\Delta/D=0$, for the axisymmetric case, and it remains unchanged (or slightly changed) for $\Delta<0.2D$, possibly because of small changes occurring to the vacillating flow and to the return flow area in this $\Delta/D$ range (c.f. figure 4.5(a) with figure 3 of. [41]). This is followed by a regime with steady wall flow and unsteadiness some distance away, as evident in figure 4.4(c) and figure 4.5(b), causing the mixing length to increase. A combination of steady three-dimensional jet flow near the wall and an increase of return flow area may be responsible for the largest mixing length occurring at $\Delta = 0.4D$ as shown in figure 4.4(d), figure 4.6(d) and figure 4.7. A further increase of $\Delta/D$ causes a decrease of $l/D$, possibly due to significant momentum loss from the jet at the thin wall boundary layer, shown in figure 4.4(e) and figure 4.6(e); also see the pressure measurements discussed below.

### 4.5.4 Pressure Drop

As discussed in Section 4.4, the momentum loss in the jet was demonstrated by a simple two-cylinder experiment shown in figure 4.12. The undisturbed water height in the cylinder and beaker is at 4cm on the ruler, and the system is hydrostatic. When the jet is present, a difference ($\Delta h$) of the water level heights is developed, which is dependent on $\Delta/D$, as evident from figure 4.12 (b, c) for $\Delta/D=0.0$ and 0.49, respectively.

The dependence of $\Delta h/D$ on $\Delta/D$ for Re=20,000 is shown figure 4.13. The $\Delta h$ (~2.4cm) is largest for axisymmetric jets, which drops about 4% in the range $0.0D<\Delta<0.2D$. When the jet is moved toward the cylindrical wall, $0.2D<\Delta<0.5D$, a drop of about 25 % from the $\Delta/D=0$ case is observed ($\Delta h$~1.6cm), which can be attributed to the loss of jet momentum due to wall influence. The results of adverse pressure gradient produced by jet entrainment starts decreasing when $\Delta/D>0.25$, due to jet deflection by wall effects and increase of the area available for the upward flow; figure 4.10. In general, an increase of area available for upward flow and conditions for higher wall drag reduce the adverse pressure gradient.

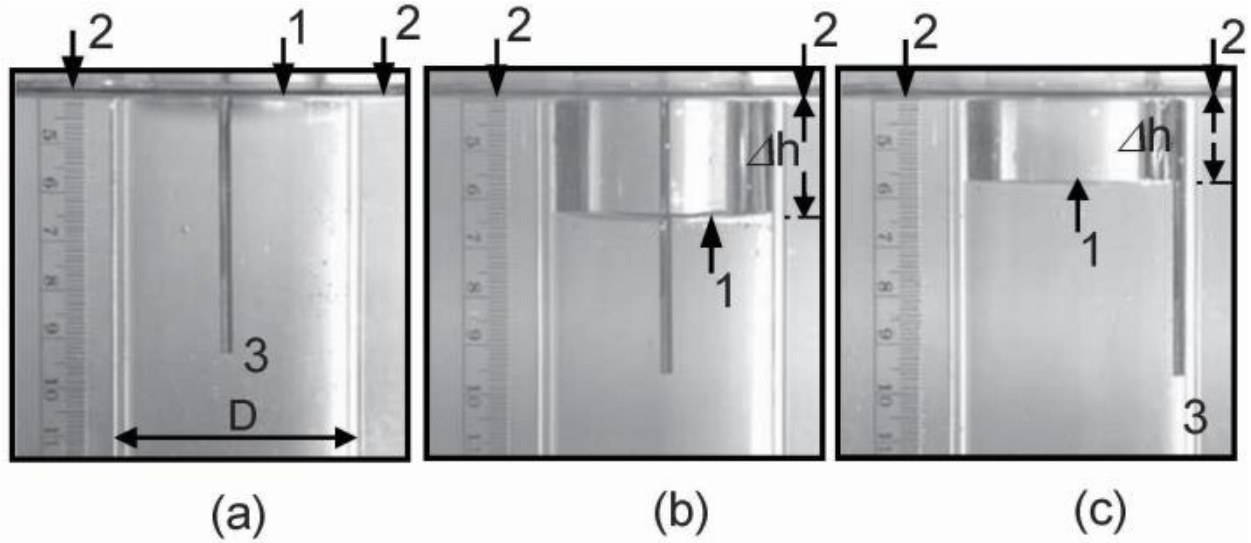


Figure 4.12: Images from DVC recordings for different radial positions of nozzle. A cylinder with an open bottom is in a larger beaker filled with water. (a) Initially the free surfaces of the cylinder (1) and beaker (2) coincide, but after the introduction of jet from nozzle exit (3), the water level in the cylinder drops by $\Delta h$. In (b), the jet is at the center and in (c) it is near the wall.

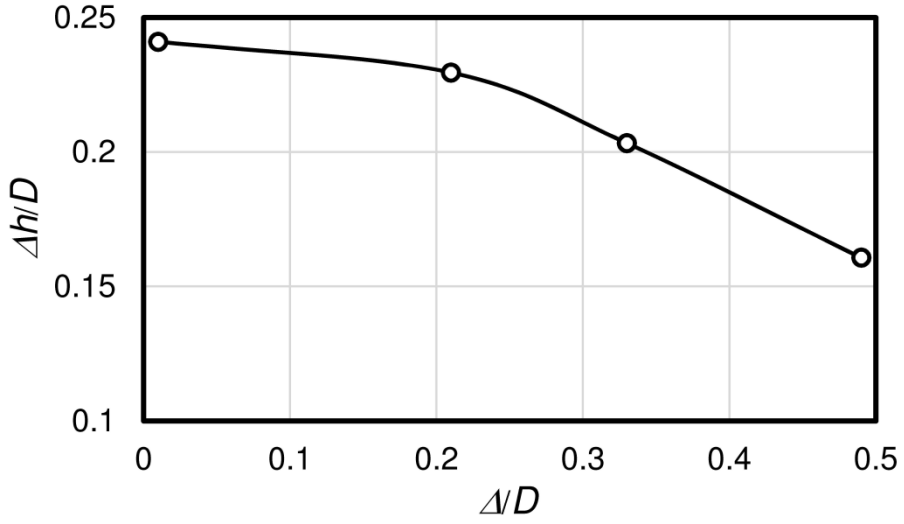


Figure 4.13: Variation of the difference in water level height $\Delta h$ (cm) between the cylinder and beaker as a function of different radial offset positions (where point shows measurement at $\Delta/D$ = 0.01, 0.21, 0.33, 0.49 and line represents best fit to measurements) Reynolds number: Re=20,000.

For the experiment in figure 4.12, the initial jet momentum flux was $J$=39,000 cm$^4$s$^{-2}$, and the increase of pressure at the bottom due to adverse pressure gradient causes flow of water from the cylinder to the beaker, and hence $\Delta h$. The drop in water level in the cylinder is clearly visible in (b) with $\Delta h$ ~2.4 cm, and in (c) with $\Delta h$ ~ 1.6 cm. In the latter case, the pressure drop due to viscous losses can be estimated as

$$\Delta p / \rho g = (J - J^*) / gS = 4(J - J^*) / \pi g D^2 , \qquad (4.4)$$

where $\Delta p$ is the pressure difference between the bottom of the cylinder and beaker, $S$ is the cross-section of the cylinder and $J^*$ is the net momentum loss due to viscous effects. For figure 4.12(c), $\Delta h$ = 1.6 cm, and using the value of $J$, it is possible to estimate $J^* \approx J/3$, a significant loss.

# 5 CONCLUSIONS AND RECOMMENDATIONS FOR FUTURE WORK

## 5.1. Conclusions: General Remark

In this chapter, a summary of all results and conclusions during this study are reported. As mentioned in section 1.4, three different set of experiments are used to investigate different aspects of the oil mixing problem in SPR caverns. In sections 5.1.1, section 5.1.2 and section 5.1.3, we present conclusions based on experimental and theoretical results, each derived from conducting different set of experiments. This chapter ends with some recommendations for future work.

### 5.1.1 Conclusion: Precession of Confined Jet In Homogenous Fluid

The evolution of a turbulent jet released into a low aspect ratio (width/height) cylinder under neutrally stratified conditions was investigated experimentally using PIV and digital imaging methods. The study was focused on: (i) observations of general flow structure and instabilities that lead to periodic oscillations intrinsic to jets; (ii) the roles of (top/bottom) boundary conditions and resulting pressure adjustments that cause jet to disintegrate into diffusive turbulence, and (iii) the parameterization of flow velocities and jet oscillating frequency.

Using scaling arguments and the assumption of Reynolds number similarity, the governing dimensional parameters were reduced to two: the jet intensity $J$ (kinematic momentum flux) and container width $D$, which leads to characteristic length $D$ and time $D^2/J^{1/2}$ scales. The scaling for the critical distance for jet disintegration and the frequency of flow oscillations was proposed and experimentally confirmed. The characteristics of rotational instability were addressed using angular momentum of the flow.

Based on experiments with different top/bottom conditions, it was argued that the principle results of our study, conducted using a jet issuing into a cylinder with both ends closed, should be valid to geometries with one end closed. For the former case, empirical parameterization was proposed for mean velocity distribution.

Using the scaling laws developed, useful estimates for flow quantities in the SPR caverns could be obtained. Typical parameters for laboratory experiments and SPR cavern are given in Table 5.1 ($1/f$ being the period of oscillations). Using (2.11) with $C$=3.6 and $C$*=0.1, the dimensional values of $x$* and $f$ for SPR caverns were calculated and are shown in Table 5.1.

TABLE 5.5-1

COMPARISON OF LABORATORY AND SPR FIELD PARAMETERS

| | L<br>cm | D<br>cm | q<br>$cm^3/s$ | d<br>cm | J<br>$cm^4/s^2$ | $\nu$<br>$cm^2/s$ | Re | $x^*$<br>cm | f<br>Hz | $J^{1/2}/D$<br>cm/s |
|---|---|---|---|---|---|---|---|---|---|---|
| SPR | $7x10^4$ | 7000 | $3x10^5$ | 25 | $1.8x10^8$ | 0.1 | $1.3x10^5$ | 25000 | $2.5x10^{-5}$ | 2 |
| Lab | 65 | 10 | 8-40 | 0.165 | $(1\text{-}65)x10^3$ | 0.01 | $(3\text{-}25)x10^3$ | 36 | 0.03-0.27 | 3-25 |



.

In SPR caverns, however, the crude oil is slightly stably (density) stratified with typical buoyancy frequencies in the range $N \approx 10^{-3}$-$10^{-4}$ $s^{-1}$. Vertical jet mixing in such cases can be characterized by the jet-cavern Froude number

$$Fr = u^* / DN = \frac{J^{1/2}}{D^2 N} U^*(X) = Fr_0 U^*(X), \tag{6.1}$$

where $u^*$ is the typical vertical velocity and $U^*(X)$ is given in equation (2.16). For $Fr \geq 1$, mixing may be significant, while it is insignificant for $Fr << 1$. Using $Fr_0 = J^{1/2} / D^2 N \approx 0.3$-$3$ as typical for SPR caverns, one arrives at the conclusion that an oil column of dimensionless depth $X^*$ is subjected to significant vertical velocities and prone to be well mixed. Also, in a low aspect ratio cavern, the flow is expected to oscillate with a period $1/f$, which is half a day. Such flow vacillations may induce additional mixing, considering SPR degas periods are ~3 months. To investigate the effects of stratification, additional work was conducted and the conclusions from the study are presented in the following section.

### 5.1.2 Conclusion: Penetration of Confined Jet in Stratified Fluids

The jet-induced mixing in a long cylindrical container was investigated experimentally, for the cases of negatively and positively buoyant jets. Based on observations, a theoretical model was proposed, which permits calculations of vertical density distribution in long vertical cylinders as a function of time. The most useful concept used for the model development is the mixing depth. For lighter (or neutral) jet the mixing depth is equal to the jet stopping distance $l$, which, for the considered geometry, depends only on the cavern diameter; see equation (3.1). For heaver jet fluid the mixing depth is equal to the length of cavern $L$. Denoting by $N^*$ the number of cavern volumes which is needed to be processed to obtain desired exiting density $R^*$, the following estimate follows from equation (3.10)

$$N^* = 1 - (l / L)(1 + \ln R^*). \tag{6.2}$$

Thus, the efficiency of refilling in SPR caverns strongly depends on the depth of mixing and for no mixing, $l / L \to 0$, equation (3.10) transforms into step function and the efficiency is maximum, while for complete mixing, $l / L \to 1$, it is minimum with exponential decay (equation (3.11)). To avoid complete mixing, the processed oil could be heated slightly to make it positively or neutrally buoyant before refilling. The use of additional diffuser at the nozzle exit with the purpose to decrease the mixing depth (equation (3.1)) also may be useful.

### 5.1.3 Conclusion: Wall Attachment of Offset Jet In Homogenous Fluid

Laboratory experiments were conducted to investigate the evolution of a point, turbulent, offset jet in a confined cylinder, a topic that has not been considered hitherto. The aim was to investigate the change of jet penetration (mixing) length and flow patterns as a function of the normalized offset distance. Particle Image Velocimetry and flow visualization were employed, and the experiments covered normalized offset distances $\Delta/D$ = 0.0, 0.2, 0.25, 0.4, and 0.49, Reynolds numbers Re = 7000, 10,000 and 15,000 and axial normalized measurement distances $1 \le (X = x/D) \le 7$.

When $\Delta/D$ = 0, the jet is nominally axisymmetric and precesses, as found in previous studies. In this case, the jet dissolves into diffusive turbulence at a distance $l \approx 3.6D$, which was the minimum of all $\Delta/D$ investigated. For $0 < \Delta/D \le 0.2$, the jet tends to attach to the cylinder wall but precesses while exhibiting some asymmetry with a jet dissolution distance of $l \approx (3.3\text{-}3.6)D$. The flow patterns significantly changed in $0.2 < \Delta/D < 0.25$, with the development of a steady stream near the wall and an oscillating tail. Theretofore, the jet hugged the closest sidewall and remained steady, and the maximum jet mixing length $l \approx 5.2D$ was observed at $\Delta/D$ = 0.4. In $0.25 \le \Delta/D \le 0.49$, wall effects play an important but variable role in the decay of jet momentum, and led to the drop in the adverse pressure gradient. The most jet momentum loss by wall friction occurred at $\Delta/D$ = 0.49.

Based on the results of this study, an engineering recommendation can be made for positioning a jet for SPR degassing. The most optimal would be a jet placed in $0 < \Delta < 0.20D$ to minimize mixing between processed oil injected by the jet and unprocessed oil being removed from the bottom of the cavern. This criterion is especially appropriate when density interfaces that separate two oil types are present, the destruction of which are due to jet impingement may cause a drastic drop in degassing efficiency due to mixing of degassed and unprocessed oil.

## 5.2 Recommendations for Future Work

Some recommendations for future studies of turbulent jet mixing in a confined cavity, with applications to SPR caverns, are summarized below:

- Present investigation of confined jets provides novel information on the effect of confinement on the mixing process and rotational instability. Modern applications of PIV techniques such as holographic PIV are able to measure three-dimensional velocity fields. This will provide more insight into the physics of jet flow and rotational instability in confined cavity.

- The present and previous confined jet studies were performed with smooth sidewall surfaces. It would be instructive to investigate how surface roughness affects flow structures.

- A Time-Resolved PIV technique can be employed to study the time scales and other temporal characteristics of the flow.

- Further studies can be performed to investigate the deviation of jet penetration depth and flow structures by varying the boundary conditions such as side and bottom wall heating.

- Further experimental work is needed to determine the effect of jet inclination to the cylinder axis, especially, its effect on jet mixing and rotational instabilities at different nozzle distances.

# Appendix A:
# SCALE FOR THE MEAN JET VELOCITY

## A.1 Scale For The Mean Jet Velocity

Consider an axisymmetric jet in a confined cavity with top-hat velocity $U$(x) at any $x$, as shown in figure A.1. The jet momentum flux is $J = \pi r_0^2 u_0^2$ and the volume flux $Q = \pi r_0^2 u_0$. The jet radius grows as $r_j = \beta x$ ($\beta$ is the jet spread angle) until it breaks up at $x = L_c$. Assuming that entrainment velocity into the jet follows the usual entrainment hypothesis, $u_e = \alpha_e U$, where $\alpha_e$ is the entrainment coefficient, the volume conservations implies

$$d(\pi U r_j^2) / dx = 2\pi r_j (\alpha_e U), \tag{A.1}$$

and the assumed (uniform) upward velocity $u_u$ at any $x$ is given by

$$\pi(R^2 - r_j^2) u_u = \int_0^x (\alpha_e U) 2\pi r_j dx \ . \tag{A.2}$$

Combining equations (A.1) and (A.2), and assuming that the jet is a momentum source with negligible initial volume flow $Q = \pi r_j^2 U$ we get

$$u_u = U r_j^2 / (R^2 - r_j^2) \ . \tag{A.3}$$

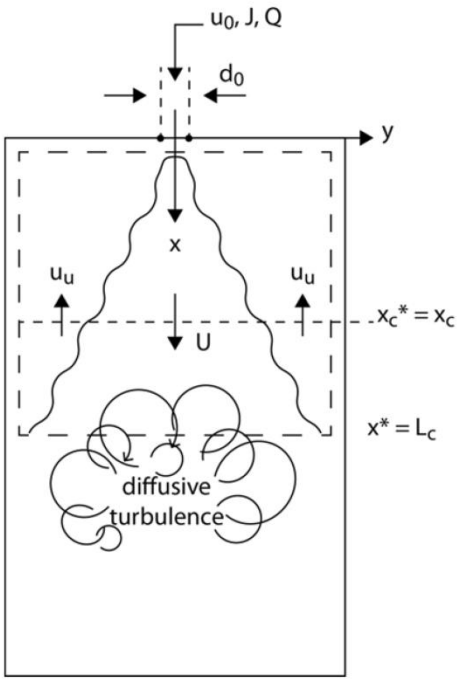


Figure A.1: Schematic of jet flow in a cylindrical cavity shown up to jet break-up distance $x=L_c$. The jet exit velocity and nozzle diameter is $u_0$ and $d_o$, respectively. Here the (uniform) upward velocity is denoted as $u_u$. The dash line indicates the control volume. Two control volumes are shown, one with the lower end at $x_c$ and the other at $L_c$.

Consider a control volume as shown by the dashed line, with the top coinciding with the jet origin, the bottom at a distance x*, and boundaries coinciding with cylinder walls. The momentum balance for the case of x*= x can be written as

$$-(P_x-P_0)\pi R^2/\rho=\pi(R^2-r_j^2)u_u^2+(\pi r_j^2 U)U-u_0(\pi r_0^2)u_0\,. \qquad \text{(A.4)}$$

For the special case of $x = L_c$, $U \approx u_u \approx 0$ , equation (A.4) reduces to $\pi R^2 \Delta P_x/\rho=J$ , where $\Delta P_x=p(x)-p_o$ is the pressure jump, $p_o$ being the pressure at the jet nozzle level. Assuming an uniform pressure gradient, the pressure at $x < L_c$ is given by

$$\Delta P_x/\rho=(J/\pi R^2)*(x/L_c)\ . \qquad \text{(A.5)}$$

Using equations (A.4), (A.5) and (A.3), we get

$$J\left(\frac{x}{L_c}\right) = -\pi(R^2 - r_j^2)\frac{U^2 r_j^4}{(R^2 - r_j^2)^2} - \pi r_j^2 U^2 + J, \tag{A.6}$$

which can be rearranged as

$$U = C_1 \frac{J^{1/2}}{x}\left(1 - \frac{x}{L_c}\right)^{1/2}\left(1 - \frac{C_2 x^2}{R^2}\right)^{1/2}, \tag{A.7}$$

where, $C_1 = 1/\sqrt{\pi\beta^2}$ and $C_2 = \beta^2$.

## Appendices B, C and D deleted

## 10.2 Mixing by Turbulent Buoyant Jets in Slender Containers In the Presence of Natural Convection

This work is not part of the dissertation of Nath (2013) but is from a report from Fernando (2012).

### 6.3 Effects of Jet Injection on Convection in Confined Cylinders

Experiments were conducted on convective turbulence from natural convection in confined containers and on influence of jets on kindred convective flows. Of interest was the scaling of convection (which is much different from the large aspect ratio case) and flow patterns caused by the jet/convection interaction. Particle Image Velocimetry (PIV) was used to deduce flow structures based on whole field velocity measurements and using a Microscale Conductivity-Temperature Instrument (MSCTI) for recording the temperature profiles. The experimental procedure and the results are summarized below.

#### 6.3.1 Experimental Setup

Experiments were performed using a (70 cm) long cylinder of diameter ($d$=10 cm) placed inside a vertical (100x45x45 $cm^3$) rectangular tank filled with water. The larger rectangular tank (1) was painted black inside (except visualization regions) and the cylinder (2) was fixed to the cover of the tank; see the schematic in Fig. 6.3.1.1.

The jet was introduced from the top of the cylinder using an 'L-shaped' round nozzle of diameter $d_j$=0.165 cm placed at the centre. A calibrated pump recirculated water from the lower half of the cylinder to the nozzle. A commercial PIV system was used for velocity measurements, which included a Dual Nd:YAG Laser (4), Laser-Pulse Synchronizer, 1 GB RAM computer, and a CCD camera (PIVCAM 10-30), for velocity field (Figure 6.3.1.1). The Laser-Pulse Synchronizer controlled the CCD camera and the sampling computer. A mirror tilted at $45^0$ angle deflected the laser beam perpendicular to the bottom of the cylinder, and a cylindrical glass rod was used to spread the beam into a sheet before entering the tank at a section along the cylinder axis. The cylinder fluid was seeded with Pliolite tracer particles.

The convection was generated by heating the walls of the cylinder by recirculating warm water in the outer tank. The hot water was added from the bottom inlet and mixed cooler water was drawn out from the top outlet at a constant volume rate. The water in the rectangular outer tank served dual purposes: it heats up the side walls of the cylinder and minimizes the optical deformation during measurements.

A MSCTI (3) probe from the PME Inc. was deployed to measure the temperature profiles inside the tank and cylinder. This instrument provides two analog voltage outputs, one from salinity and the other for temperature, in the range -5 volts to +5 volts. The MSCTI probe was mounted on an Aluminum structure capable of making vertical and traverse motion. The vertical travel of the

probe was precision controlled by an optical encoder mounted at the top of the frame. The data acquisition and control for the probe were made using Labview software on a separate computer.

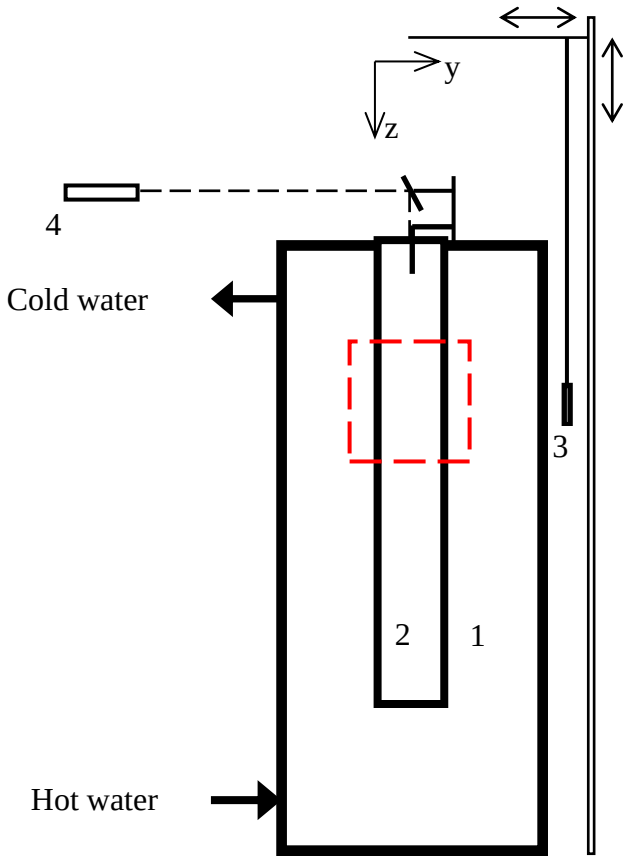


**Figure 6.3.1.1:** Experimental set-up: 1 – Rectangular tank (45x45x100 cm3) with three inside wall coated with black paint, 2 –glass cylinder (diameter *d*=10 cm, length *L*=70 cm) seeded with Pliolite particles, 3 – MSCTI probe for salinity and temperature measurements (capable of vertical and traverse movements) mounted on aluminum frame, 4 – laser emitting horizontal light beam deflected by mirror used for PIV measurements. Coordinates are shown at the top of the cylindrical beaker and red frame is the area of interest for study of convection with jets.

### 6.3.2 Methodology

To delineate the effects of jet on convection, the experiments were conducted in two different stages. First, the hot water was circulated in the rectangular tank and upon establishing convection PIV images were taken using CCD camera, which were stored for further analysis. Second, the jet was introduced by the L-shaped nozzle (with its tip 5 cm below water surface) while convection was in progress. MSCTI probe was used for temperature data before and after the jet was injected into the cylinder.

The PIV data on horizontal velocity were obtained in a vertical plane (y-z) passing through the cylinder axis. The data processing was conducted using TSI PIV software package (InsightTM). Pairs of images were captured at 15 Hz, and 200 pairs were used in processing. These images had a space resolution of ~ 0.075 cm/pixel. The area of observation was (18-36 x 10 $cm^2$) with interrogation area 32x32 pixels, and the data were interpolated onto a grid (8x8 pixels). Erroneous vectors (2%) were separated and substituted by interpolated values. Information was stored as vector files on a (98x32) matrix, which was used with Tecplot software to map instantaneous and averaged velocity fields. After preliminary analyses, the data from vector files were processed using Matlab for mean flow characteristics (200 frame pairs). The experiments were conducted at Reynolds numbers (~7500), with and without the jet. The temperature profiles from MSCTI were saved using labview software, which were later processed in Excel to obtain profiles.

In convection experiments without jets, a larger frame of view (from 0 to 3.8 *h/d*, *h* the depth and *d* the cylinder diameter) from the water surface was chosen to estimate the effect of cylindrical walls on convection. Since the velocity of seeded particles is extremely high near the nozzle, the area of interest was shifted 15 cm down from the surface (~1 to 3.5*h/d*) to study jet/convection interaction.

### 6.3.3 Results

The vertical velocity profiles were obtained using PIV Insight software and Tecplot as shown in Fig 6.3.3.1. As expected, a thin boundary layer (0.1 cm) was found to develop on heated vertical walls, with warm fluid rising along the wall and recirculating into the interior of the cylinder, after intruding along the top surface. Fig. 6.3.3.1 a shows representative profiles in the presence of the jet and convection and Fig. 6.3.3.1 b shows the same experiment but without the jet. Note that in Fig. 6.3.3.1.a the jet approximately loses it velocity at (~3.5-3.6d), and its oscillations due to global instability break the boundary layer and destroy convective cells. As such the jet dominates the flow evolution.

Figs. 6.3.3.2 (a,b) show temperature profiles in the outer tank, which is homogenously mixed by recirculating hot water. In Figure 6.3.3.2b, there are two profiles of temperature taken at the centre of the cylinder. The profile in blue was measured approximately 10-15 min after the initiation of recirculation of hot water in the outer cylinder. Temperature stratification usually builds up in the cylinder, but when the jet is introduced the convective patterns are broken up by the oscillations of the jet, and the profile becomes uniform (black). Careful observations show that up to (~3.5-3.8 *h/d*) there are substantial fluctuations, but thereafter profiles are more homogenous.

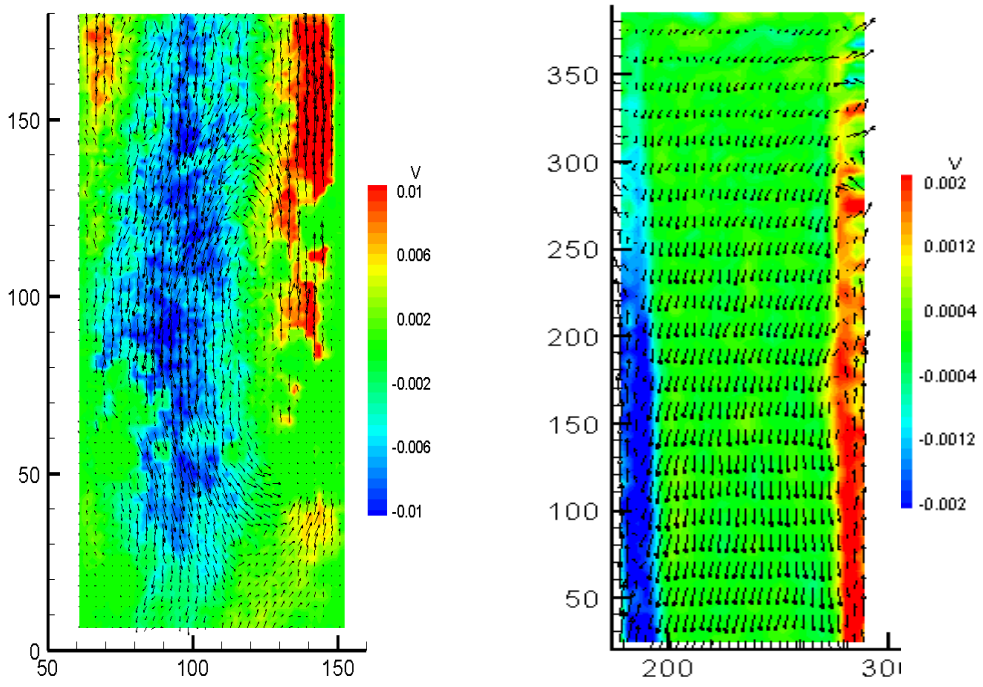


(a) (b)

**Figure 6.3.3.1:** Typical vertical velocity contour for (a) – convection with jet from 1.5 *h/d* to 3.5 *h/d*; (b) – convection in the absence of the jet from (0 to 3.8) *h/d*. Data are averaged over 200 data frames and velocity is in $ms^{-1}$. The horizontal and vertical axes are arbitrary, and depend on the camera location with respect to the tank (which is not the same for both cases as they are different experiments)

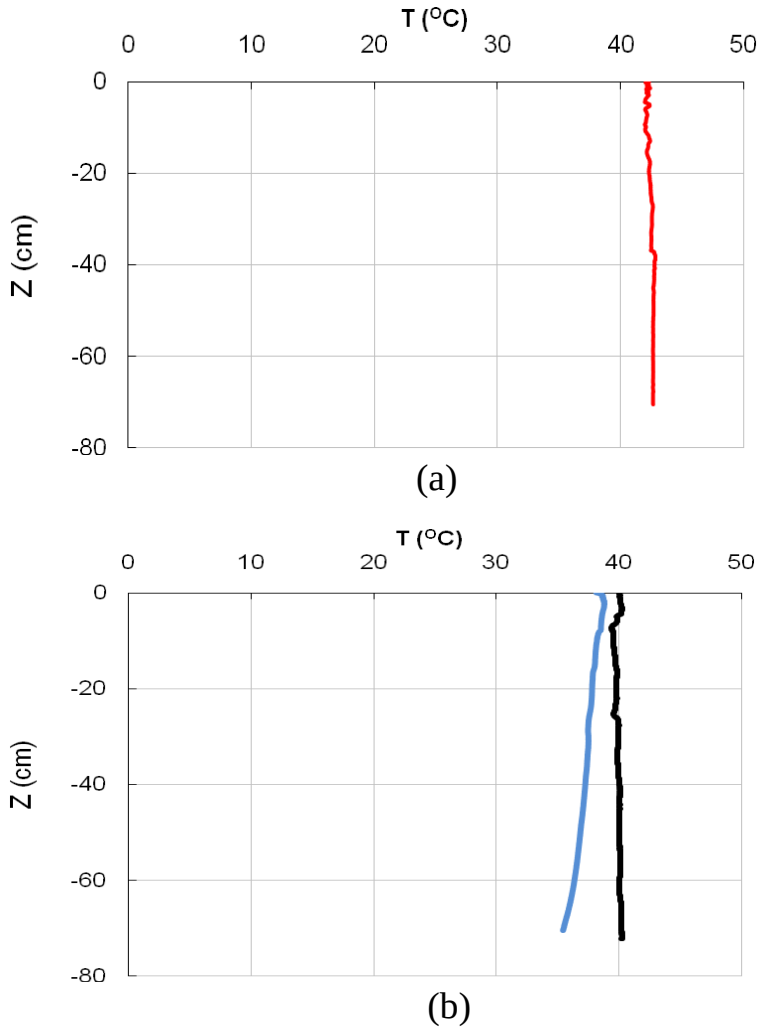


**Figure 6.3.3.2:** Typical temperature profiles in (a) the rectangular tank ~10-15 min after circulation of hot water begins (shown in red); (b) the cylindrical container before the jet is started (shown in blue). The profile after the jet is introduced is shown in black.

Fig. 6.3.3.3 presents the transverse profiles of mean axial velocity U, for different dimensionless distances Z during experiments conducted with and without the jet under convective conditions. When the jet is absent, there is a slight decrease of velocity in the vertical direction. On the contrary, in the experiments with convection and jet there is significant increase of velocity toward the surface, with the secondary circulation responsible for this flow. The influence of the jet is rather strong compared to that of convection, and the jet clearly dominates within the cylinder. Since the driving force can be represented by the temperature difference or an equivalent dynamical parameter, the buoyancy jump across the cylinder walls, where g is the gravitational acceleration and  the thermal expansion coefficient, there are two scaling velocities are possible, and, where z is the vertical coordinate. Transverse profiles of the vertical velocity

shown in Figure 6.3.3.3(a,c,e) clearly indicate that there is a variation of vertical velocity in the vertical direction, and hence the latter scaling may be most appropriate for the pure convection case. Note that in Figures 6.3.3.3 and 6.3.3.4 that positive z is vertically downward as shown in Figure 6.3.1.1. Thus, a negative velocity is actually vertically up, and a positive velocity is vertically down. Figure 6.3.3.4a clearly shows that this is indeed the case, where the scaling collapses the data aptly. This self-similarity of profiles is quite encouraging, and can be directly applicable to the cavern flows when density stratification is not present.

The same scaling cannot be applied when the jet is present, given that profiles show differing shapes (Figs. 6.3.3.3[b,d,f]) and do not collapse when scaled with the buoyancy scaling proposed (Fig. 6.3.3.4b). It appears that the flow is fully dominated by the jet for this case. A new scaling based on the jet momentum is in order, with more experiments to delineate criteria for momentum and buoyancy dominated cases, which for long cylinders nominally expected to be dependent on the length-scale. Beyond $L$, the cavern flow is dominated by convection and below it the flow is momentum dominated.

In summary, we have delineated scaling for turbulent convection induced in a cylindrical tank forced by a constant temperature difference between the walls and interior fluid. When a jet is forced, this self-similar behaviour is untenable and the flow is dominated by jet momentum. It is proposed that the jet is dominant for a length of order beyond which the convection takes over.

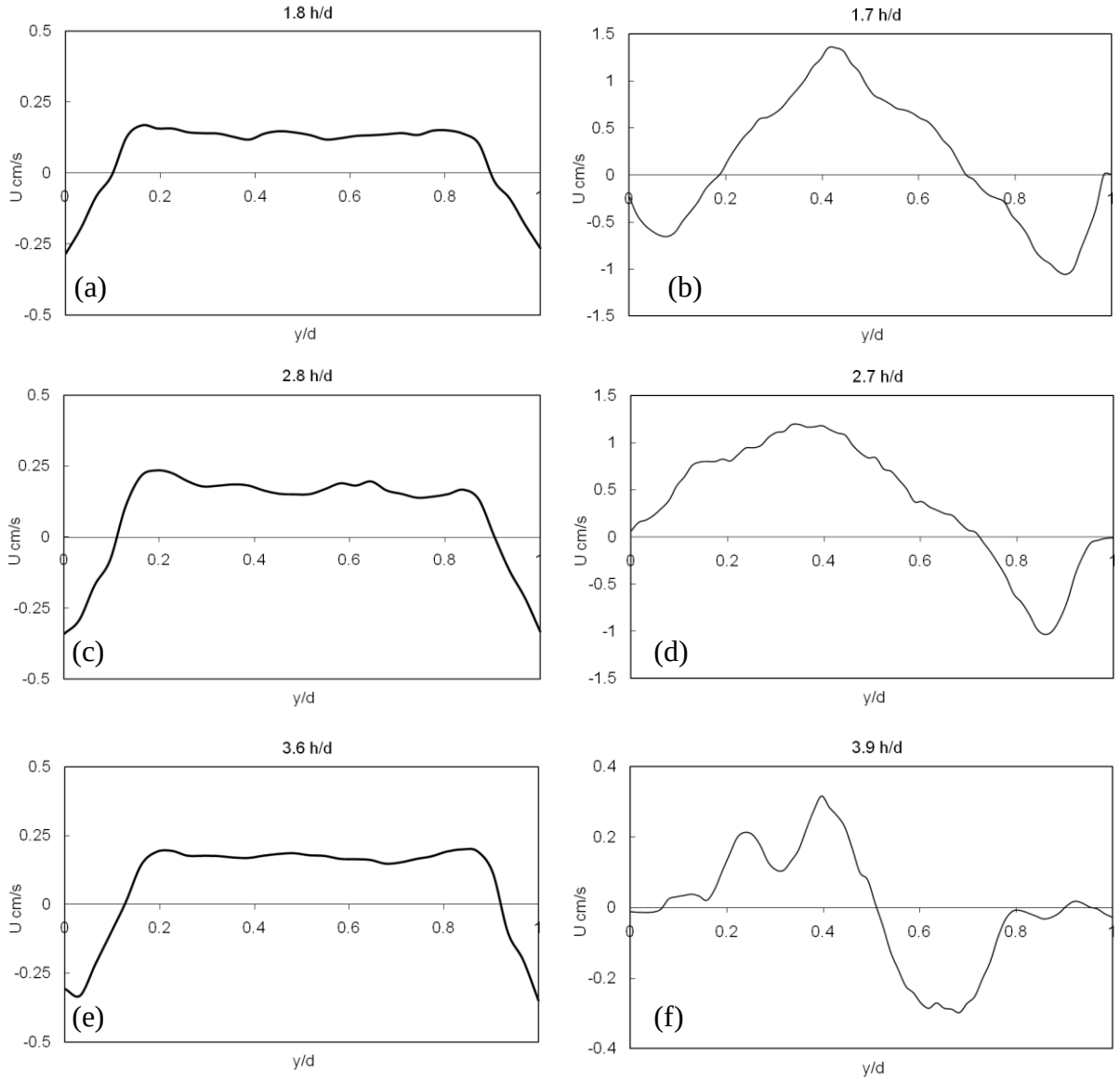


**Figure 6.3.3.3:** Mean vertical velocity profiles in the cylindrical tank at different depths for convection without the jet (a,c,e) and convection with the jet (b,d,f).

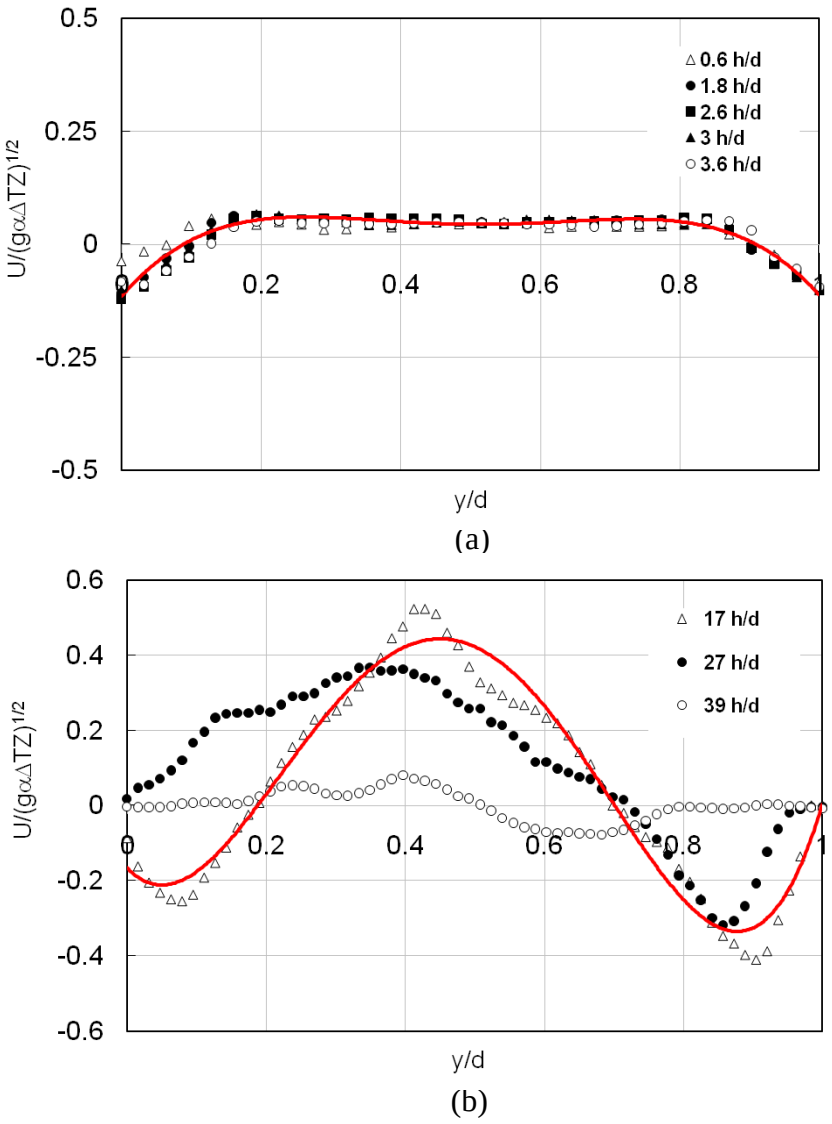


**Figure 6.3.3.4:** Mean velocity profiles normalized by the velocity scale and plotted against normalized radial distance for different depths. (a) convection without jets, (b) convection with jets.

## 10.3 Pressure Distribution in Confined Jet Flow

Note - This material has been published in Liberzon, D., and H.J.S. Fernando, 2014, "Pressure Distribution in Confined Jet Flow," J. Fluids Eng., 136 (031202).

This write-up below is not part of the dissertation of Nath (2013) but is from a report from Fernando (2012).

### 7.1 Abstract:

A momentum jet injected into a confined container breaks up to "diffusive turbulence" after travelling a critical distance. It has been argued that an adverse pressure gradient developing within the container, acting against the jet momentum flux, is responsible for this break up. Experimental evidence for this adverse pressure gradient is presented in this paper, supplemented by a control-volume analysis to explain the results. The rise of pressure from the jet-injection level to a location beyond the jet break up $(x_b)$ was shown to be proportional to the jet momentum flux. The overall (integrated) side-wall friction on a control volume was negligible, compared to the increase of pressure, if the flow control volume extends beyond $x_b$. For smaller lengths of the control volume, the side wall drag is not negligible compared to the pressure rise. The Reynolds number similarity was evident for jet Reynolds numbers above 6000. This work was motivated by its applications to degassing of crude oil stored in the U.S. Strategic Petroleum Reserves, which are slender salt caverns. To improve its quality, periodically oil is cycled through a degassing plant and injected back to the cavern as a jet, and the degassing time is critically dependent on jet dynamics.

### 7.2 Introduction

Motivated by applications to U.S. Strategic Petroleum Reserve (SPR), where close to seven hundred million gallons of crude oil are stored in underground caverns of nearly 200 ft. diameter and 2000 ft. height, Voropayev et al. (2011) conducted laboratory experiments on jet injection into long slender cylinders of the same aspect (width/height) ratio. The flow configuration used was the same as that in SPR degas operations, where oil contaminated by gaseous diffusion from the cavern walls is pumped out from below, degassed, and injected from the top, as shown in Figure 7.3.1 (Ehgartner et al. 2005). Voropayev et al. (2011) confirmed the previous findings of Risso and Fabre (1997) conducted using a similar flow configuration but without fluid withdrawal from the bottom: that the jet breaks down into "diffusive" turbulence devoid of any mean momentum, after travelling a distance of $x_b \approx 3.6D$. Voropayev et al. (2011) argued qualitatively that the jet break up occurs due to the development of an adverse pressure gradient, which acts against the jet momentum flux. This pressure gradient arguably develops when either one or both ends of the cylinder are closed. The presence of this pressure gradient has not been verified experimentally, although the velocity and turbulence structure of the jet and possible instabilities have been discussed in a number of studies (Risso and Fabre (1997), Villermaux &

Hopfinger (1994), Khoo et al. (1992), Liu et al. (1997), Mataouia and Schiestelb (2009) and Voropayev et al. (2011)). Verification of the presence of this pressure gradient is important not only in fundamental jet break up studies, but also in calculating forces on SPR caverns walls. The work presented herein was designed to capture this pressure gradient, if present, and to parameterize it using a simple model (section 7.3). The experiments are discussed in (Section 7.4) and the results in (Section 7.4). The paper concludes with a summary in (Section 7.5).

## 7.3 Model

Consider the flow configuration shown in Figure 7.3.1, where a jet of velocity $u_j$ is injected into a low aspect ratio, $D/H<<1$, container via a nozzle of diameter $d_j$. The inflow and outflow rates are equal, $Q=A_j u_j$, and the jet momentum is given by $J=A_j u_j^2$, where the cross sectional area is $A_j=\pi d_j^2/4$.

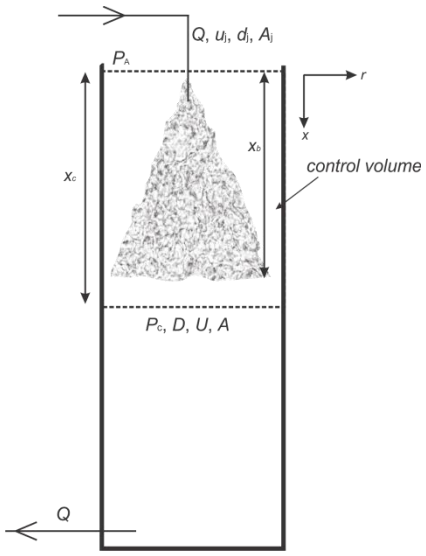


**Figure 7.3.1:** A schematics of the experimental configuration. Dashed line indicates the control volume

An arbitrary control volume (CV) is selected with a length $x_c$ and diameter $D$, as shown. The pressure at the top surface is $p=P_A$ (in the present case $P_A=0$, gauge) and at $x=x_c$, $p=P_C$. The sidewall drag FD on the CV can be represented by $C_D = \frac{F_D}{\frac{1}{2}\rho u_j^2 A_c}$, where $A_c$ is the CV area that coincides with the container walls, $A_c=\pi D x_c$, $C_D = C_D\,(Re_j, x_c/D)$ is the "effective" or bulk drag coefficient with its parameter dependencies are selected based on dimensional considerations, and $Re_j=u_j d_j/\nu$ is the jet Reynolds number. The mass conservation yields $Q=u_j A_j=UA$, where $U$ is the uniform advection velocity below the jet and $A$ the cylinder cross sectional area. The axial momentum balance yields

$$-(P_C - P_A)A - F_D = -\rho Q[u_j - U], \quad (7.3.1)$$

where $\rho$ is the density. After manipulation, (7.3.1) becomes

$$(P_C - P_A) = \rho u_j^2 \left(\frac{d_j}{D}\right)^2 \left[1 - \left(\frac{d_j}{D}\right)^2\right] - \frac{F_D}{A} \quad (7.3.2)$$

or

$$\frac{\Delta p}{\rho u_j^2} = \frac{(P_C - P_A)}{\rho u_j^2} = \left(\frac{d_j}{D}\right)^2 \left[1 - \left(\frac{d_j}{D}\right)^2\right] - 2C_D \frac{x_c}{D}. \quad (7.3.3)$$

The bulk drag coefficient $C_D(Re, x_c/D)$ appearing in the last term indicates possible dependence on the Reynolds number, in addition to that on $x_c/D$. In general, for negligible drag, $C_D=0$ and for $d_j/D<<1$, (7.3.3) becomes

$$\frac{(P_C - P_A)}{\rho u_j^2} = \left(\frac{d_j}{D}\right)^2 = \frac{A_j}{A}. \quad (7.3.4)$$

## 7.4 Experimental Setup

Considering that SPR caverns have $D/H \approx 0.1$, a slender cylinder of $D$=25.4 mm, $H$=575 mm ($D/H$=0.044) was used. It was made of clear Plexiglas with bottom end sealed, and the jet was introduced just below the water surface with a nozzle of $d_j$=1 mm (Figure 7.4.1). The water was filled to the full cylinder height, and the fluid was withdrawn at the same rate as the jet volume flux rate using a 3 mm diameter hole drilled at the side wall, close to the cylinder bottom. Estimates showed that to obtain a measurable pressure in the cylinder a flow rate of 0.1 L/min is necessary. After consideration of several alternative designs, the jet nozzle was supplied with tap water (pressure ~3 atm) and the fluid was removed by a centrifugal pump at the same volume rate as the jet. The parity between the in and out flow rates was ensured by two pressure-controlled metering valves located in the jet entry and exit lines. In all experiments, once the steady state was established, Thymol blue acid reagent dye was introduced to the jet for flow visualization, based on which the degeneration of the jet into diffusive turbulence at $x_b$=3.7$D$ was confirmed. The jet initially expanded rapidly with $x$, and then spread across the entire vessel diameter upon reaching $x_b$. Thereafter slow downward advection of colored fluid was clearly observed, confirming the observations of Voropayev et al. (2011). Pressure measurements were performed by a simple, custom made, gravitational manometer since available commercial transducers could not produce a stable response to small pressure differences generated in these experiments. Multiple brass tubes (1 mm in diameter each) were introduced into the cylinder at prescribed positions, functioning as pressure sensing ports. The ends penetrating outside were

connected to flexible 1 m long Tygon tubes, which were fixed vertically to a stand against a graduated backdrop, marked in mm. The differences between the water level inside the cylinder and each tube, h, were monitored. The readings were converted to pressure values by using

$$\Delta p = (P_C - P_A) = \rho g h \quad ,(7.4.1)$$

where $\rho$ is the water density and $g$ is the gravity. To achieve the required accuracy, the backdrop was imaged by a digital camera, processing each image using Matlab® for detecting the water column levels. Here the accuracy of h is governed by image resolution (Res) and meniscus inside the Tygon tubes. Capturing images at $Re_s$=0.72 pix/mm yielded an accuracy of 4 pix for $h$ and an error for $\Delta p$ of ± 1.5 Pa. Being limited by this relatively large absolute error, flow rates ranging between 0.1 and 0.7 L/min were required to obtain reliable results when expected pressure values, Pest, were estimated using (7.3.4). Values of Pest on the order of O(102 Pa) would keep the relative error below 10%.

To measure $\Delta p$ after the jet breakup ($x > x_b$), the pressure ports were positioned at $x/D$=4.33, 4.72 and 5.12 from the jet leading nozzle. Careful observations reveled that within the available accuracy pressure at different radial distances ($r/D$= 0.1, 0.3, 0.4) remains approximately constant. Hence, all pressure measurements in the stagnant area were performed at the center of the cylinder cross section.

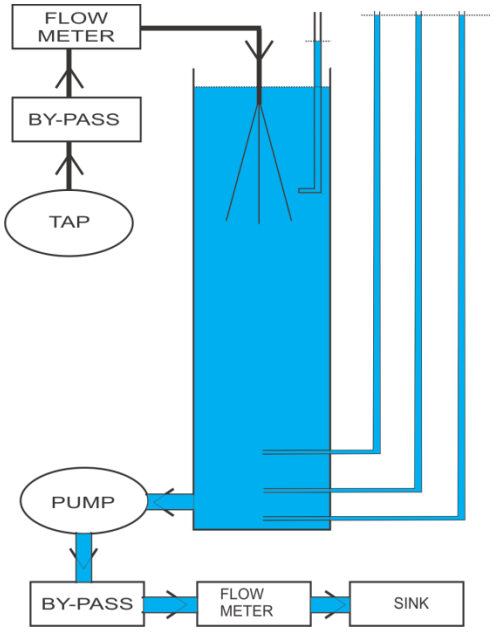


**Figure 7.4.1:** Experimental setup

To obtain pressure measurements in the active jet area ($x < x_b$) without causing significant disturbances to the flow, a slightly different pressure probe was introduced. Made of the same 1 mm in diameter brass tube, this probe was 200 mm long with a 90$^o$ bend, with sensing port

pointing toward the center of the cylinder cross section (Figure 7.4.1). The probe was introduced from the upper end of the cylinder extending down and could be lowered as desired. At each measurement depth the probe was fixed to eliminate any positioning or vibrations-related inaccuracies. The pressure was measured at total of 10 prescribed position, $x/D$=1.57, 1.97, 2.36, 2.76, 3.15, 3.54, 3.94, 4.33, 4.72 and 5.12 for each flow rate used, covering the full depth of the jet penetration and thereafter the diffusive turbulence.

## 7.5 Experimental Results

Figure 7.5.1 shows a dimensional plot of pressure distribution $\Delta p$ with distance $x/D$ conducted at different $Re_j$ numbers.

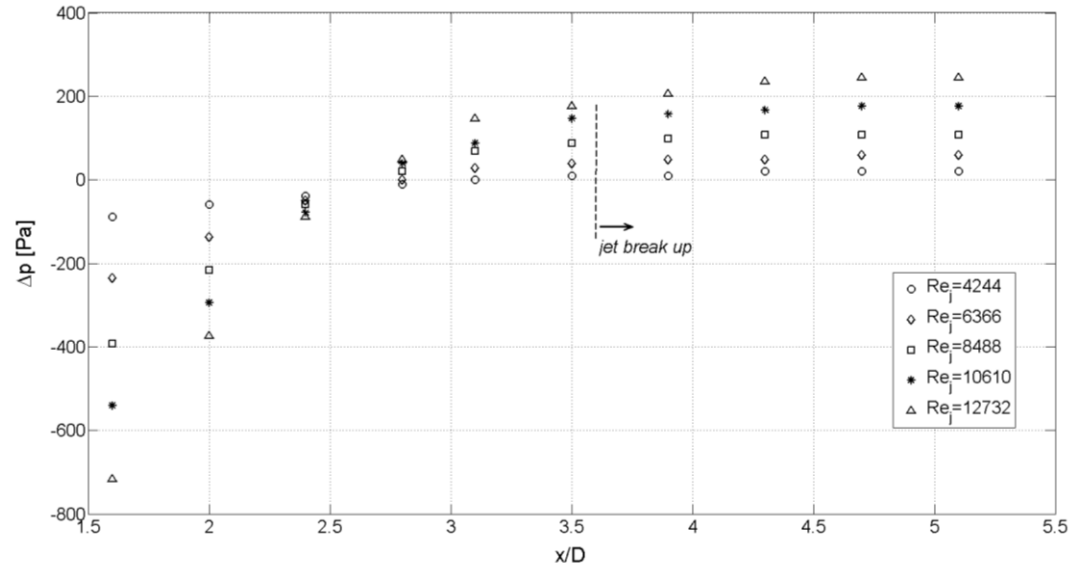


**Figure 7.5.1:** Pressure distribution as function of distance from the jet inlet nozzle

Note the clear development of an adverse pressure gradient in each case, and leveling of the pressure after the jet breaks up and advection established at $x \approx 3.7D$. Figure 7.5.2 shows the same plot, with pressure normalized by $\rho u_j^2$ in concurrence with (7.3.3) and (7.3.4).

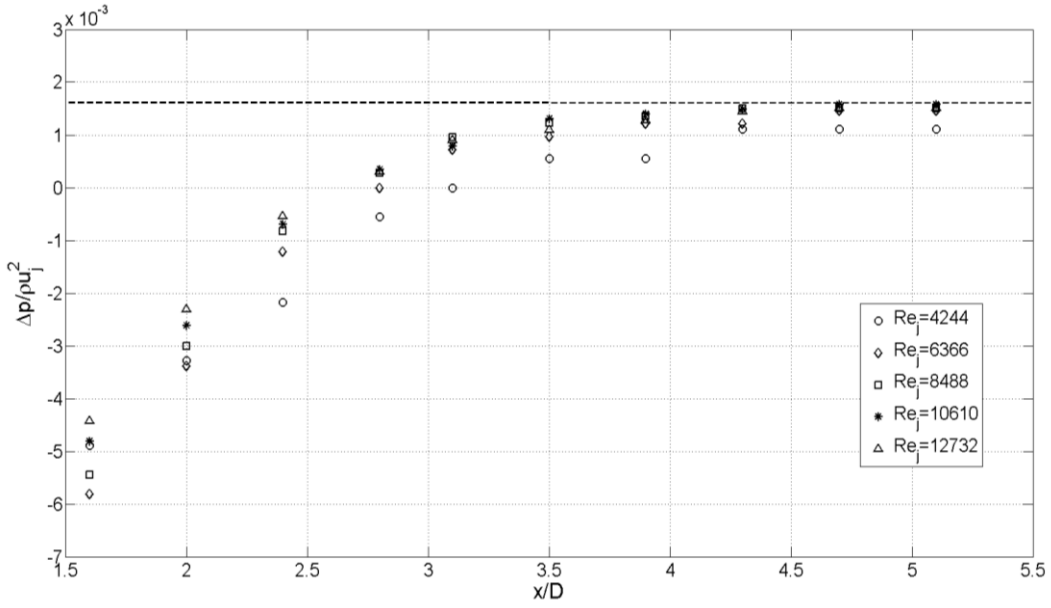


**Figure 7.5.2:** Normalized pressure distribution as a function of the distance from the jet inlet. Dashed line is the theoretical value for $C_D$ =0, 1.6x10-3, from (7.3.4).

Note the excellent collapse of data beyond $x=3.7D$, indicating a general agreement with (7.3.4), with little influence of $Re_j$ above 6000 or so. Given that $(d_j/D)\approx 1.6\text{x}10^{-3}$, the measured $\Delta p/\rho u_j^2$ is very small. The average value of $\Delta p/\rho u_j^2$ for $x/D>4$ was found to be $1.4\text{x}10^{-3}$, which is in agreement with the model prediction (7.3.4). Also the collapse of data at $Re_j>6000$ supports Reynolds number similarity (the independence of results on Reynolds numbers, at its higher values). The closeness of results to (7.3.4) indicate that the wall drag on the fluid is negligible compared to pressure gradient forcing.

For $x_c/D<3.7$, the effective drag coefficient can be evaluated as

$$C_D = \frac{1}{2}\left[\left(\frac{d_j}{D}\right)^2\left[1-\left(\frac{d_j}{D}\right)^2\right]-\frac{\Delta p}{\rho u_j^2}\right]\left(\frac{D}{x_c}\right) \qquad (7.5.1)$$

and Figure 7.5.3 shows a plot of $C_D$ versus $x_c/D<3.7$.

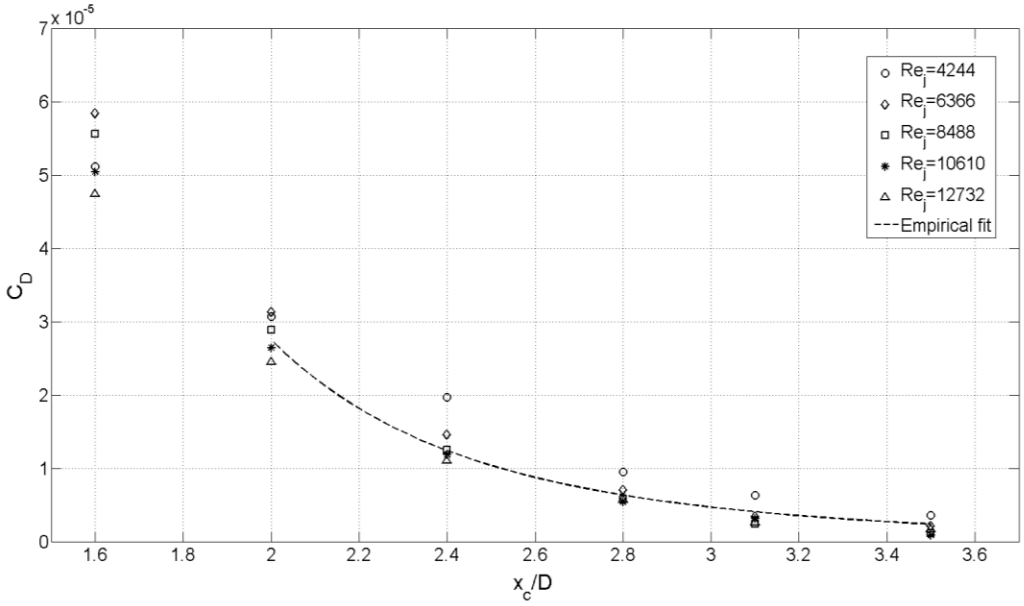


**Figure 7.5.3:** Drag coefficient distribution as a function of the distance from the jet inlet for xc<3.7.

A clear dependence of $C_D$ ($Re_j$, $x_c/D$) on $x_c/D$ can be seen, with little dependence of $C_D$ on $Re_j$ for $Re_j$>6000 for $x_c/D$>2. In the latter limit, the bulk $C_D$ can be presented using the empirical formula

$$C_D = 5.7 \times 10^{-4} \left(\frac{x_c}{D}\right)^{-\frac{13}{3}} \; for \; 1.6 < \frac{x_c}{D} < 3.7 \; and \; Re_j > 6000. \qquad (7.5.2)$$

## 7.6 Conclusions

Unlike for the case of free jets, the evolution of jets in confined low aspect ratio containers has received only little attention despite their important practical implications. In the latter case, the jet travels a distance of $x_b$~3.7D and breaks up to form diffusive turbulence (Risso and Fabre, 1997). Voropayev et al. (2011) argued that this break up is due to the development of an adverse pressure gradient as a result of jet confinement, which counteracts the momentum flux of the jet. The verification of the existence of this pressure gradient was the goal of this paper, complemented by the development of a control-volume-analysis based model for pressure distribution. Of particular interest was the case where the jet is injected at the center of one end and an equal volume flux is extracted from a level close to the other (capped) end. This configuration has applications to degassing of oil in U.S. strategic oil reserves.

The results clearly indicated the development of an adverse pressure gradient along the container, with the gage pressure after the jet break up (at distances $x > x_b$) being proportional to the jet momentum flux, $\rho u_j^2$, according to the model prediction (7.3.4). The result was independent of the jet Reynolds number for $Re_j$> 6000. The total side wall friction on a control

volume of length $x_c$ was found to be negligible (compared to the pressure gradient force) when $x_c > x_b$. For $x_c < x_b$, complex flow patterns that arise during jet interaction with confined ambient fluid in the cylinder and side walls, however, caused this drag to be significant vis-à-vis the pressure gradient force. As such, the normalized drag (drag coefficient) for $x_c < x_b$ was dependent on $x_c/D$, but as before $Re_j$ dependence was negligible for $Re_j > 6000$. An empirical relationship was proposed between the overall side-wall drag coefficient $C_D$ and normalized control volume length $x_c/D$ for $1.6 < x_c/D < 3.7$.

## 10.4 NOMENCLATURE

$a$ – distance of the interface from the jet inlet

A – dimensionless parameter, $N^3W^2/4q_o$

c, $c_1$,... $c_6$ – proportionality constants

$C_p$– heat capacity

$D$ – diameter of the container

f , $f_1$ , ... $f_6$ – undetermined functions

$fq_1$ , ... $fq_6$ – undetermined functions

$F$ – flux of buoyancy

$g$ – acceleration due to gravity, 9.81 $ms^{-2}$

$g_1$ – undetermined function

$h$ ,$h_i$ –height of the mixed layer

$h_c$ –critical mixed layer height beyond which wall effects become prominent

$H$ – total height of the container

$l$ – length scale

$M$ – flux of momentum

n, $n_1$, $n_2$ – empirically determined exponents

$N$ – Brunt-Vaisala frequency, $s^{-1}$

$p$ – pressure

$p_1$ – empirically determined exponent

$q_o$ – buoyancy flux

$Q$– heat flux, $W/m^2s$

$Ra$ – Rayleigh number, $(g\alpha\Delta T)^4/\nu\kappa_T N^6$

$Ri_I$ – interfacial Richardson number, $\Delta ba/w_i$

$Re$ – Reynolds number of jet, M/νD

$S$ – salinity, ‰ or gm/l

$t$ –time, s

$t_c$ –critical time beyond which wall effects become prominent

$t'$ – normalized time, Nt/A

$t^*$ – normalized time, Nt

$t_c^*$ – normalized critical time, $Nt_c$

$T$ – temperature, °C

$T_w$ – temperature at the wall, °C

$T_i$ – temperature of interior fluid, °C

$u'$ – characteristic velocity in an isotropic eddy in the horizontal plane

$w$ – convective velocity in z direction

$w'$ – characteristic velocity in an isotropic eddy in z direction

$w_*$ – convective velocity scale in z direction

$w_c$– velocity at the axis of jet

$w_I$– velocity of the jet at the location of the interface

$w_o$– velocity at jet inlet

$w_p$– along wall velocity

$W$ – total width of the tank

x – horizontal ordinate

z – vertical ordinate

$z_n$ – vertical distance up to buoyant jet mixes

$z^*$ – streamwise distance, 0.8D

$\alpha$ – expansion coefficient due to temperature

$\beta$ – expansion coefficient due to salinity

$\beta_1, \beta_2, \beta_3$ – proportionality constants

$\gamma_1, \gamma_2, \gamma_3$– proportionality constants

$\Gamma$ – aspect ratio, W/h

$\delta$ – width of the mixed layer

$\delta_i$ – interfacial distortions

$\Delta a$ – displacement of the interface due to mixed caused by the jet

$\Delta b$ – buoyancy jump at the density interface, $-g\Delta\rho/\rho_o$

$\Delta b_T$ – buoyancy jump due to temperature difference, $\Delta b_T = g\alpha(T_w - T_i)$

$\Delta S$ – salinity difference, ‰

$\Delta T$ – temperature difference, °C

$\eta$ – scaling parameter

$\eta_1$ – undetermined function

$\kappa_s$ – solute (salt) diffusivity, $m^2/s$

$\kappa_t$ – thermal diffusivity, $m^2/s$

$\lambda$ – potential energy (per unit area)

$\nu$ – kinematic viscosity, $m^2/s$

$\xi$ – normalized height with respect to width, h/W

$\xi_c$ – normalized critical height with respect to width, $h_c/W$

$\pi, \pi_1, \pi_2, \pi_3$– undetermined functions

$\rho$ – density, $kg/m^3$

$\rho_o$ – reference density, $kg/m^3$

$\rho_{in}$ – density of inlet jet fluid, $kg/m^3$

$\rho_b$ – density of background fluid, $kg/m^3$

$\rho_{b1}$ – density of lighter fluid layer in two-layer stratified fluid, $kg/m^3$

$\rho_{b2}$ – density of heavier fluid layer in two-layer stratified fluid, $kg/m^3$

$\sigma_w$– rms velocity in z direction

## 10.5 Applicability to SPR

The studies conducted at the university of Notre Dame under the direction of Professor H.J.S. Fernando have important implications for SPR caverns regarding flow behavior and mixing. Some implications have been described in subsection 5. The confined jet experiments described in subsection 2 show that a neutral jet will not penetrate more than 3.2 to 3.6 cavern diameters before the jet momentum is dissipated and a fundamental change in flow and mixing behavior occurs. The proper scaling of the flow for application to large systems such as SPR caverns has been derived, and approximate equations for the flow velocity in this jet dissipation region have been developed. The jet behavior is unsteady with typical SPR cavern periods of about ½ a day.

Subsection 3 discussed simple cavern mixing models for negatively- and positively-buoyant jets in SPR caverns; note that different definition of negatively- and positively-buoyant jets than given earlier in Chapter 3. Simple models give a very good description of cavern mixing including the density at the cavern outflow and the density profiles.

Hanging strings in SPR caverns are often not located on the center axis of the cavern – most are offset from the axis. Subsection 4 investigates the change in cavern mixing behavior due to offset hanging strings. If the hanging string is near the center, the effects are small. If the hanging string is near a cavern wall, mixing can be enhanced compared to a hanging string on the center axis.

Subsection 6 discusses experiments for simultaneous jet mixing and natural convection, which occur in SPR caverns. Preliminary results show the interaction between the cavern velocity caused by the jet and cavern velocity due to natural convection. Further work is necessary to properly scale the relationship between these two contributions.

The pressure distribution in the confined cylinder, which counteracts the incoming jet momentum, is discussed in subsection 7 for different cylinder boundary conditions. As discussed in subsection 2, the flow for many different boundary conditions is essentially the same. The pressure gradient was measured as a function of Reynolds number in a confined cylinder. Based on typical SPR jet parameters, the pressure gradient from the jet is negligible compared to the hydrostatic value.

# IMMISCIBLE FLUID MIXING

# 11 **UMass – Dartmouth**

The previous sections in this report all deal with miscible fluids, or fluids that can readily mix such as water and brine or two oils, and the mixing caused by external forces such as jets. The present chapter presents an investigation of mixing for immiscible fluids, such as oil and brine, due to jets. Other immiscible fluids studies are presented in subsequent chapters.

The present application for SPR is the injection of oil in a cavern downward near the oil-brine interface. Experiments were conducted at UMass – Dartmouth by Allen Beaune under the supervision of Professor Peter Friedman to correlate the mixing at the oil-brine interface in SPR caverns as a function of dimensionless numbers including the normalized separation distance between the jet exit and the oil-brine interface. In these experiments, the interaction between a downward-directed oil jet impinging on an interface which separates two immiscible fluids (oil and water-glycerin mixture) was investigated using a scaled model. The silicone oil represents the crude oil and the water glycerin mixture represents the brine. The effect of the separation distance between the interface and nozzle exit on mixing between the immiscible fluids was investigated at different jet flow conditions. The experimental setup investigated the flow structure and determined the dependence on the Richardson number and other controlling dimensionless parameters.

The rest of this section is background on mixing at an immiscible fluid interface based on work previously done by Professor Friedman. Following this background material, the new experimental work done by Allen Beaune (Beaune, 2011) is presented. This material is generally from the M.S. thesis of Allen Beaune, which is available in its original form in the SPR library. Much of the background has been deleted in the present presentation, and the experimental data are not included below. The data are included in the original thesis.

## 11.1 Background

Friedman and Katz (1999) looked at flow and mixing for a jet impinging on an immiscible interface, such as the oil-brine interface in an SPR cavern. From experiments with water jets impacting a fuel-water configuration as shown in Figure 11-1, they observed four flow regimes with increasing jet flow, where the interface Richardson number is defined as

$$Ri_i = D_i \frac{(\rho_2 - \rho_1)g}{\rho_2 U_i^2}$$

where the parameters are depicted in Figure 11-1 where $D_i$ is the jet diameter at the interface, $\rho_2$ is the jet density, $\rho_1$ is the impacted fluid density, and $U_i$ is the jet velocity at the interface. The impacting jet creates deformation of the interface of height, $h$, and diameter, $D_d$.

The experiments generally had the pipe exit at the fuel-water interface ($l_2$=0), so the outlet jet diameter and velocity are the interface values. Therefore, the Richardson number at the pipe exit

$$Ri_p = D_p \frac{(\rho_2 - \rho_1)g}{\rho_2 U_p^2}$$

which is the same as the interface Richardson number, $Ri_i$, in these experiments only. One series of experiments was conducted for $l_2 > 0$ for observation purposes only.

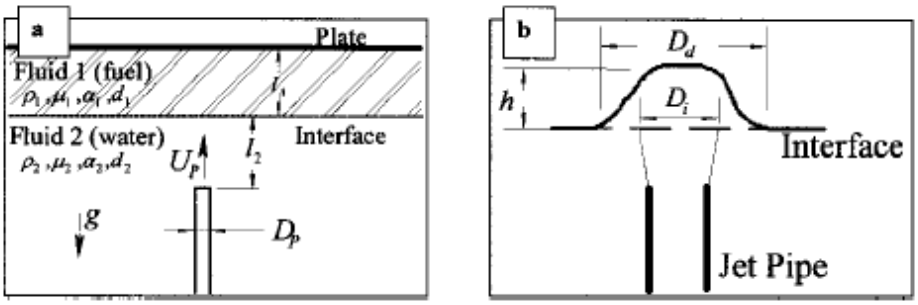


**Figure 11-1. Jet-Interface Geometry and Parameters (Friedman and Katz, 1999)**

The four flow regimes observed are as follows. A larger interface Richardson number corresponds to a higher density difference between the layers and an increased distance from the jet source as indicated by a larger jet diameter and a smaller jet velocity.

1. Flow regime 1 - smooth and stable deformation of the interface as shown in Figure 11-2a. This regime occurs when $Ri_i > 15$.
2. Flow regime 2 - flow separation at the edge of the interface and the formation of a lip as seen in Figure 11-2b. This regime occurs for $15 > Ri_i > 1.1$.
3. Flow regime 3 – Unstable jet penetration and an unstable interface as seen in Figure 11-2c. This regime occurs for $Ri_i < 1.1$ and an aspect ratio $< l_1/D_i$)
4. Flow Regime 4 - Efficient mixing between fluids per Figure 11-2d. This regime occurs when ($AR > l_1/D_i$)

Flow Regime 4 is particular to their experimental setup because an impingement plate was set up above the fuel layer.

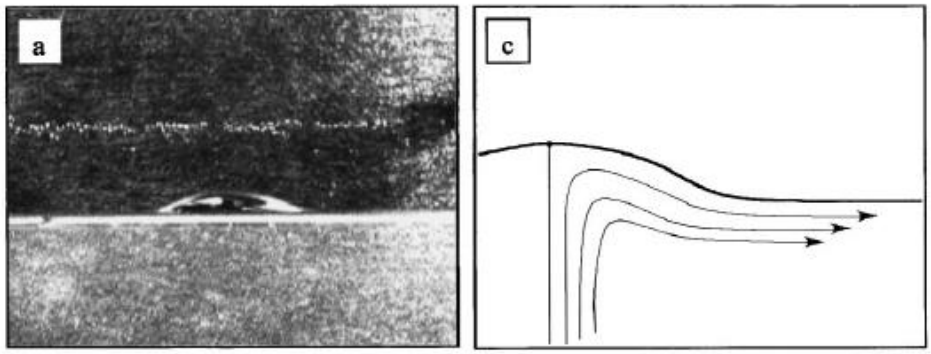


Flow Regime 1 – Smooth stable deformation of the interface ($Ri_i > 15$)

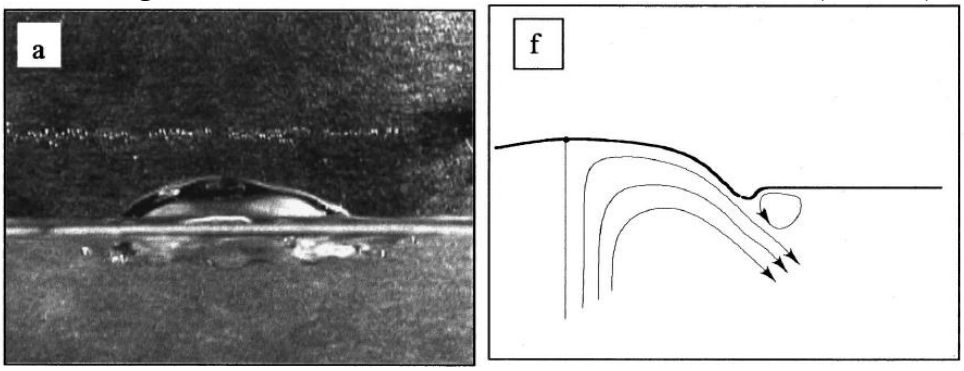


Flow Regime 2 – Flow separation at the edge of the interface ($15 > Ri_i > 1.1$)

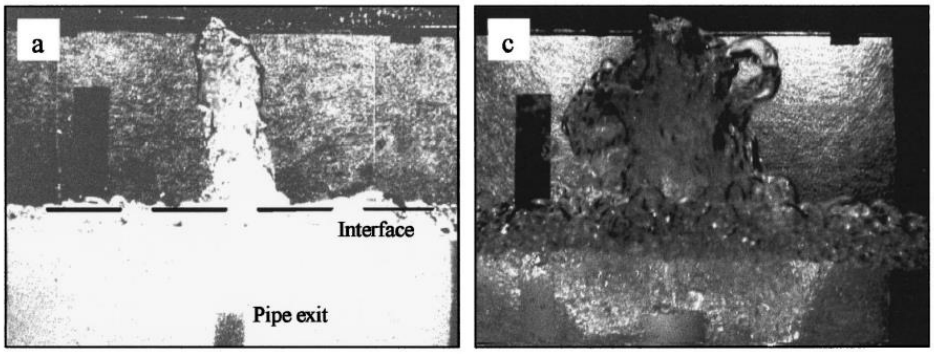


Flow regime 3 – Unstable jet penetration ($Ri_i < 1.1$ and AR < $l_1/D_i$)

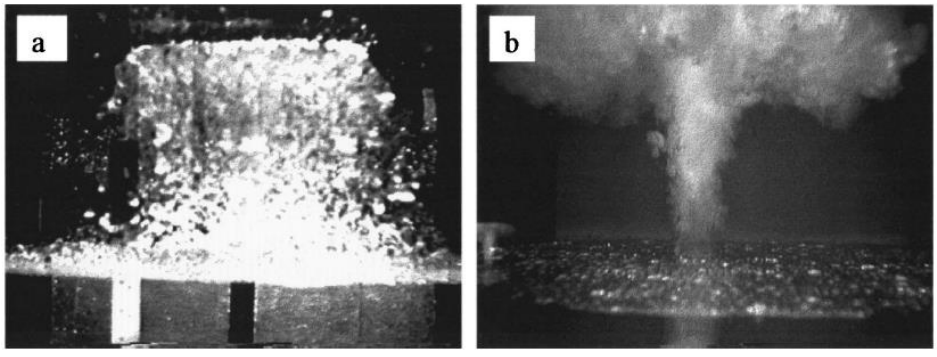


Flow Regime 4 - Efficient mixing between fluids (AR > $l_1/D_i$)

**Figure 11-2. Observed Flow Regimes (Friedman and Katz, 1999)**

In Flow Regimes 1 and 2, there is little or no mixing. Mixing generally starts in the transition between Flow Regimes 2 and 3, or at approximately $Ri_i$=1.1.

The aspect ratio (AR) of the interface, which is the height of the deformation divided by the diameter at the interface ($h/D_i$), is shown in Figure 11-3 where Dia is the pipe diameter, $D_p$. For high interface Richardson numbers and a stable interface, the aspect ratio is small such that the deformation depth of the interface is small. As the interface Richardson number decreases and the aspect ratio increases, the interface becomes more and more unstable. Note that an aspect ratio of 1.0 seems to be the approximate transition point for no mixing – mixing.

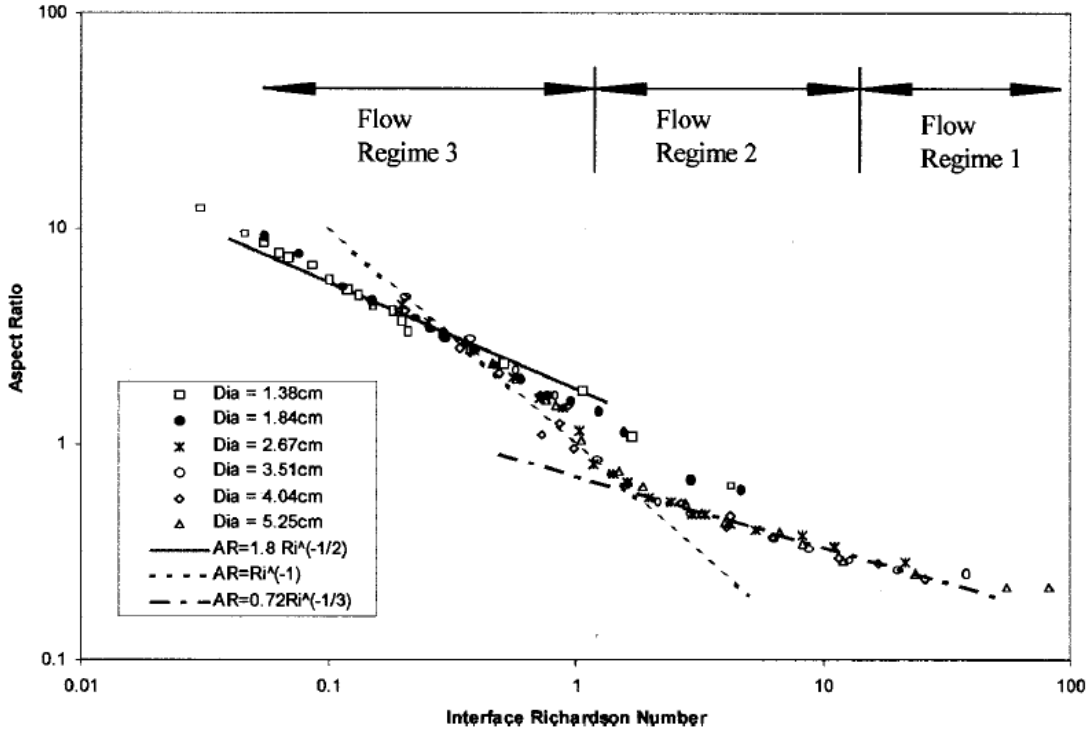


**Figure 11-3. Flow Regime Correlation (Friedman and Katz, 1999)**

Note that the above data and flow regime descriptions are for the pipe exit at the immiscible interface, or $l_2$=0.

Friedman and Katz (2000) extended their investigation into deformation at immiscible interfaces by using other experimental data for non-zero distances. For non-zero distances, they develop a spreading factor for the jet, which is defined as

$$F = \frac{U_i}{U_p} = \frac{D_p K_2}{l_2 - x_0}$$

where $x_0$ is the virtual origin and $K_2$ is an empirical spreading factor. From other studies, the values of $x/D_p$=-5 and $K_2$=6.7 are selected. Note that the value of $F$ is equal to 1.0 for miscible fountain flow and for interfaces in the near-field.

The interface Richardson number can be rewritten as

$$Ri_i = D_i \frac{(\rho_2 - \rho_1)g}{\rho_2 U_i^2} = D_i \frac{(\rho_2 - \rho_1)g}{\rho_2 U_p^2 F^2} = \frac{D_i}{D_p} \frac{Ri_p}{F^2}$$

Friedman and Katz (2000) correlate the interface deformation data with the parameter $Ri_p/F^2$, which as noted above is slightly different than the previously used $Ri_i$.

Their new correlation is based on their data ($l_2$=0) with those of others for immiscible flow ($l_2$>0) as well as miscible conditions such as jet rise height as considered earlier by Turner (1966). All the data form a couple of groups as shown in Figure 11-4. Interestingly, the data of Turner (1966) agree with the immiscible data as shown on the plot. Note that the Turner (1966) data used in this work is different than the original data. The authors contacted Turner, who admitted his original figure had a scale error. The revised data have been used by Friedman and Katz (2000). The data generally collapse with each other except for the Friedman and Katz data for $Ri_p/F^2$ > 2.

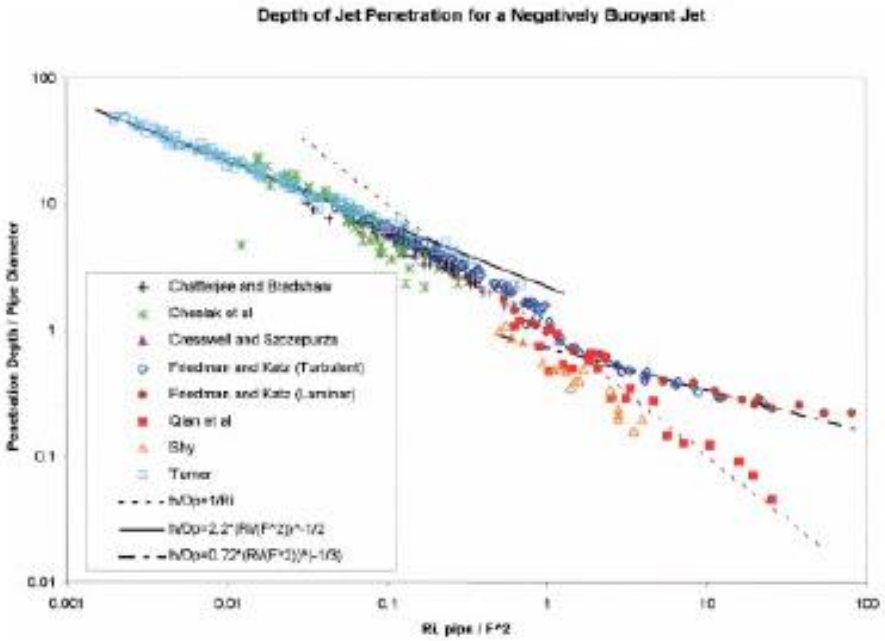


**Figure 11-4. Penetration Depth Correlation (Friedman and Katz, 2000) (Best Figure Available)**

## 11.2 Beaune Thesis

The original thesis (Beaune, 2011) including numbering is given in the following sections – some material deleted as noted. Some minor formatting has also been performed. The format for the references is unchanged from the original thesis.

# ABSTRACT


## The Effect of Spreading on a Vertically Directed Jet Impinging a Sharp Density Interface

by Allen Beaune

Experiments were performed to investigate phase mingling at a sharp density interface impinged by downward directed, laminar and turbulent, silicone oil jets. The interaction of the jet with the interface falls into distinct regimes that are governed almost entirely by the distance from the interface and the Richardson number, defined using the parameters at the jet exit. The effect of spreading as the jet passed through an identical fluid prior to the interface was quantified. The effect of separation on both the aspect ratio and the transition Richardson number are quantified for laminar flows. The effect of distance from the interface can be quantified in terms of a jet spreading factor, defined as the characteristic centerline velocity divided by the velocity at the pipe exit. As a result of conservation of momentum, the Richardson number varies inversely with the cube of the spreading factor. Experimental data demonstrates that the spreading factor of a turbulent jet can be approximated using classical decay of a self-similar jet with a virtual origin located 10 diameters upstream of the exit and an empirical jet spreading coefficient of 11. Surprisingly, these results are valid not only in the self-similar region, but from the pipe exit to a distance of about 35 diameters downstream of the pipe exit (the furthest distance investigated).

# LIST OF SYMBOLS AND DIMENSIONLESS NUMBERS

Subscripts:

| | |
|---|---|
| 1 | water glycerin mixture properties |
| 2 | silicone oil properties |
| p | pipe exit properties |
| i | interface properties |
| $\alpha$ | jet spreading rate |
| $\mu$ | dynamic viscosity |
| $\nu$ | kinematic viscosity |
| $\rho$ | density |
| $\Delta\rho$ | density difference ($\rho_2$-$\rho_1$) |
| b | radius of the jet |
| D | diameter |
| F | jet spreading velocity decay factor ($F=U_i/U_p$) |
| g | gravitational constant (9.8 m/s$^2$) |
| h | depth of interface deformation |
| K | empirical jet spreading coefficient |
| l | distance between jet exit and interface |
| U | average velocity |
| $x_0$ | downstream distance between jet exit and the virtual origin (negative = upstream position) |
| $l/D_p$ | diameters of separation |
| Re | Reynolds number ($Re = \rho UD/\mu$) |
| Ri | Richardson number ($Ri = D\Delta\rho g/(\rho U\text{^}2$ )) |
| AR | Aspect ratio ($AR = h/D_p$ ) |

# 1 Introduction

## 1.1
## 1.2 (Original sections 1.1 and 1.2 deleted – original thesis is in SPR Library)

### 1.3 Research Goal

During the filling process and recirculation, the interface separation distance from the fill pipe exit continually changes. Knowing the maximum flow rate, that can be used without having mingling, would speed the filling process and reduce costs. Therefore, this research is focused on determining the flow rate that causes mingling as a function of the separation distance.

### 1.4 Overview of Research

This research is an experimental investigation of the interaction between a downward-directed oil jet impinging on an interface which separates two immiscible fluids (oil and water-glycerin mixture) using a scaled model. The silicone oil represents the crude oil and the water glycerin mixture represents the brine solution. The effect of the separation distance between the interface and nozzle exit on mixing between the immiscible fluids was investigated. The experimental setup did investigate the flow structure and determined the dependence on the Richardson number and other controlling dimensionless parameters.

### 1.5 Other Applications

The scientific principles investigated in this research are applicable to other natural and man-made applications, including:

- Smoke stack emissions hitting a temperature inversion in the atmosphere
- A supersonic jet of oxygen impinging on molten iron in the steel making process
- Discharge of waste disposal systems
- Volcanoes and deep sea vents
- Seawater compensated fuel tanks on naval ships

# 2 Background and Theory

Free flows are fluid flows that are not confined by rigid surfaces and are produced by a combination of momentum and buoyant forces. They are able to spread and entrain the ambient fluid through which they flow and are classified into two types; plumes and jets depending on the main driving force. Plumes are predominantly driven by the density difference between the driven fluid and the ambient fluid whereas jets are predominantly driven by a source of momentum. Pure plumes have no initial momentum; likewise pure jets have no initial buoyancy. Further classification and controlling parameters can be found in (Ansong 2009).

The geometry in this study consisted of a neutrally buoyant jet that traveled through the ambient fluid and impinged on a sharp density interface. The ambient fluid was at the same temperate with no type of cross flow. When the jet reached the density interface it became a negatively buoyant jet/fountain, meaning the buoyant forces act in the opposite direction of the flow's momentum. Both laminar and turbulent, axisymmetric jets were considered.

## 2.1 Laminar and Turbulent Jets

The Reynolds number is the controlling parameter that determines whether the flow pattern is laminar or turbulent. As shown by (Lee and Chu) Reynolds number below 2000 is considered laminar and above is turbulent. A crucial difference between the flow patterns is the mixing and entrainment that occurs. Laminar flow has momentum dissipated only at the edges of the jet due to viscous effects, maintaining its high momentum core. Turbulent jets, in contrast shed large-scale eddies, with sizes on the order of the jet diameter that entrain much of ambient fluid as it flows. This redistributes momentum and causes the jet to spread more rapidly. In free flows, all laminar plumes and jets become unstable at some distance from the exit and subsequently become turbulent (Ansong).

### 2.1.1 Region of Flow Establishment vs. Region of Fully Established Flow

Similar to how flow in a pipe has a developing "entrance region" and a fully developed flow region, a jet has a region of flow establishment and region of fully developed flow. The region of flow establishment maintains almost all of its centerline velocity, maintaining a "top-hat" velocity profile. Although references differ on the length of the unaffected potential core, from about 1 diameter (White) to about 6 diameters of separation, (Lee and Chu) (Baines and Chu) this is considered the near field. The radius of the jet increases continuously after it exits the due to turbulent entrainment. In the zone of established flow, the flow becomes self-similar with the centerline velocity decaying linearly and the velocity following a Gaussian distribution (White) as shown in Figure 4.

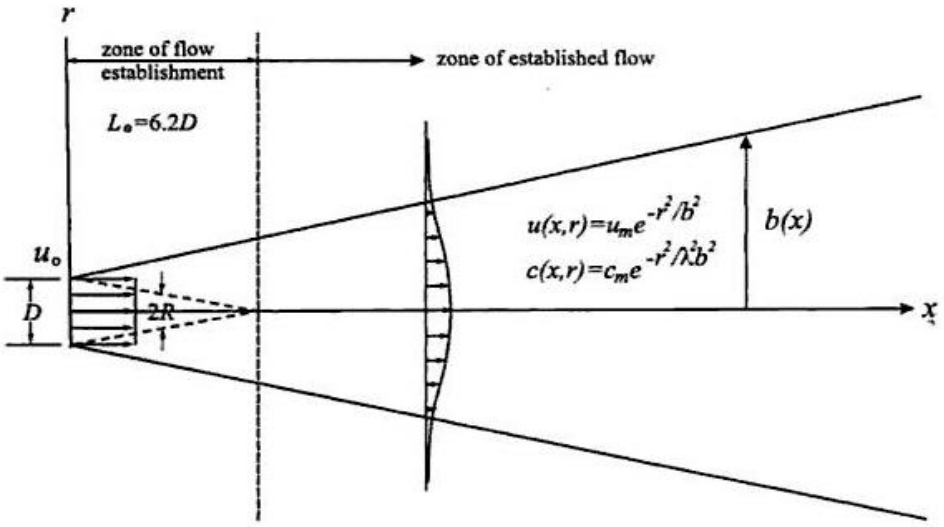


**Figure 4 Round Turbulent Jet Structure (Lee and Chu)**

### 2.1.2 Experiments with No Interface

Previous experiments have involved only pure jets; the jet fluid is the same as the ambient fluid with no density interface. These experiments, e.g. (Morton), that showed a turbulent plume of finite size, momentum, and buoyancy can be related to the flow from a virtual point source with infinite velocity, as well as the entrainment hypothesis. Along with (Abraham, Jet diffusion in stagnant ambient fluid) that said that a plume widens at a constant rate instead of a constant entrainment coefficient. This constant jet spreading rate, $\alpha$, is said to be 0.17 by (Lee and Chu) and 0.114 by (Baines and Chu) through experimental observation. Thus Equation 1 can be used to find the radius of the jet at any point in the region of fully established flow, where x is the distance from the jet exit and $x_0$ is the downstream distance between jet exit and the virtual origin.

$$b(x) = \alpha(x - x_0)$$

**Equation 1 Function for the Radius of a Free Flow Jet**

## 2.2 Fountains with Reversing Buoyancy

A negatively buoyant jet is characterized by a core in one direction surrounded by an annular flow in the opposite direction. The momentum is the dominant force until it is balanced by the buoyant force, after which it reverses direction and returns to a neutrally buoyant position. Just like a jet moving through a similar fluid, the outer fluid is entrained into the inner fluid. However in this case because buoyancy is involved, the momentum is not conserved because it is acted upon by an external force, namely gravity (Baines and Chu). A large amount of experimentation, (Papanicolaou and List) (Abraham, Jets with negative buoyancy in homogeneous fluids) (Albertson, Dai and Jensen) (J. S. Turner) et.al, has investigated reversing buoyancy fountains using miscible fluids, however these experiments involved entrainment of the ambient fluid even after passing the density interface. The present work has been

concentrated on both uniformly stratified fluid and sharp density interface separating immiscible fluids.

### 2.2.1 Dimensional Analysis

The behavior of a jet with reversing buoyancy impinging on an immiscible fluid interface is governed by the relationship (Friedman and Katz, The flow and mixing mechanisms caused by the impingement of an immiscible interface with a vertical jet):

$$\left( St, \frac{h}{D}, Bo \right) = F\left( Ri, Re, We, \phi, \frac{l}{D}, \frac{\mu_F}{\mu_S} \right)$$

**Equation 2 Functional Relationship of a Negatively Buoyant Fountain**

Where:

$St = fD/\bar{U}$ represents the Strouhal number – a dimensionless characteristic describing oscillating flow mechanisms,

$Bo = d^2 g\left(\rho_F - \rho_S\right)/\sigma$ represents the Bond number – a dimensionless ratio of surface tension forces to body forces,

$Ri = Dg\left(\rho_F - \rho_S\right)/\rho_F \bar{U}^2$ represents the Richardson number – the dimensionless ratio of buoyant forces to the inertial forces,

$Re = \rho_F \bar{U} D/\mu_F$ represents the Reynolds number – a dimensionless ratio of the inertial forces to the viscous forces,

$We = \rho_F \bar{U}^2 D/\sigma$ represents the Weber number – a dimensionless ratio of the inertial forces to the surface tension forces

The most important independent parameter in Equation 2 is the Richardson number (Friedman, Vandakoot and Meyer Jr.), which is the ratio of the buoyancy to inertial forces. A low Richardson number jet (<<1) is momentum dominated and is usually referred to as a pure jet, whereas a high Richardson number jet (>>1) is buoyancy dominated and is referred to as a pure plume. Moderate values are referred to as forced plumes or fountains. The effect of Reynolds number has been shown to be limited to determining whether the flow is laminar or turbulent (Friedman, Vandakoot and Meyer Jr.). For laminar flow, a Richardson number correction factor is necessary as the result of increased momentum, due to the non-uniform velocity profile (Friedman and Katz, The flow and mixing mechanisms caused by the impingement of an immiscible interface with a vertical jet).

### 2.2.2 Flow Regimes

The experiments of this research involved immiscible fluids and therefore the fluids remained separated, even though emulsification arose. We considered three of the four flow regimes first presented by (Friedman and Katz, The flow and mixing mechanisms caused by the impingement of an immiscible interface with a vertical jet). Briefly they are:

1. Flow regime 1 was characterized by a stable deformation in the interface and flow that remained attached to the interface as it flowed outward from the center, as shown in the Particle Image Velocimetry (PIV) vector map in Figure 5. This regime also included flow that made it to the interface with minimal velocity.

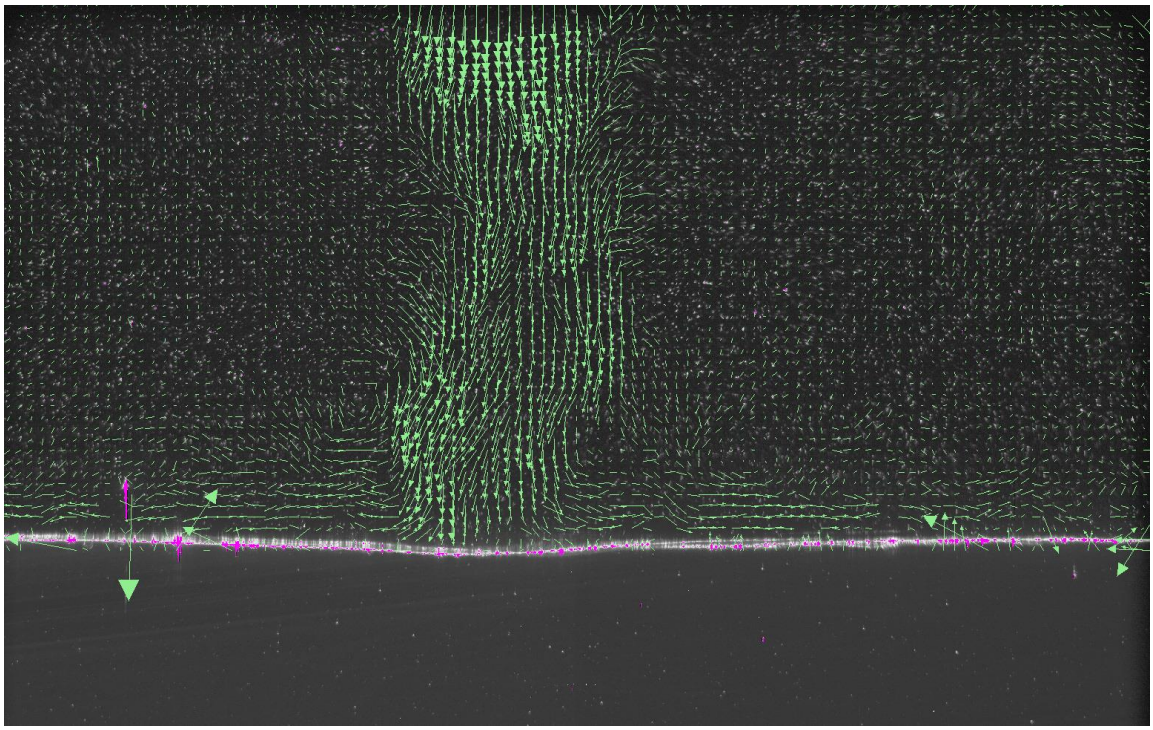

**Figure 5 A Turbulent Jet in Flow Regime 1**

2. Flow regime 2 was characterized by a stable deformation in the interface and flow that **separated from the interface** as it flowed outward from the center, as shown in the PIV vector map in Figure 6. As the flow separates it causes an annular "lip" of the impinged fluid to rise above the interface, this was used as the transition indicator from flow regime 1 to flow regime 2. Flow regime 2 occurred as the jet velocity was increased, thus decreasing the Richardson number. Fluid mixing can occur at the end of this regime as well as during the next regime.

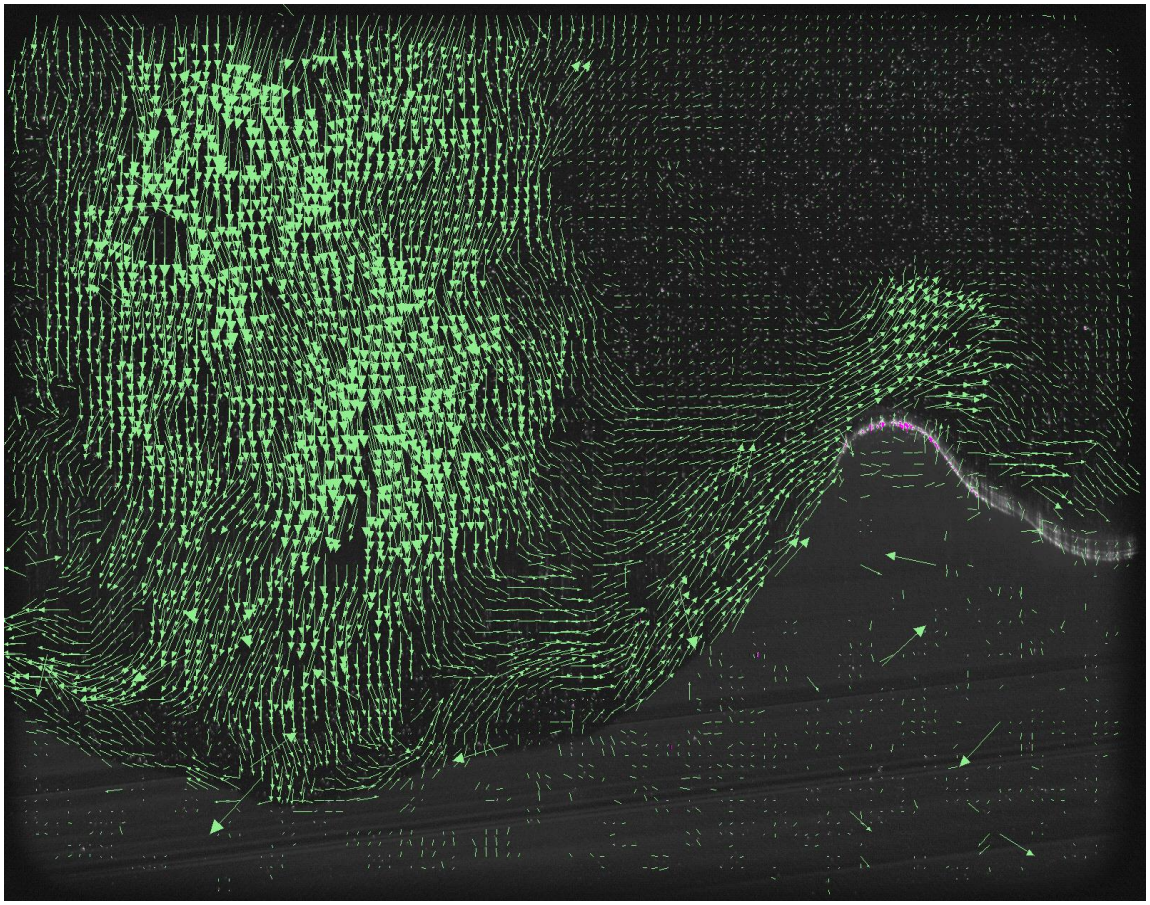

**Figure 6 Turbulent Jet in Flow Regime 2**

3. Flow regime 3 was characterized by an **unstable deformation in the interface.** As the cavity becomes deep and the sides more steep, it begins to collapse. This collapsing of the deformation cavity was used as the transition indicator from flow regime 2 to flow regime 3. Due to the dynamics of flow regime 3, it cannot be visualized in a single PIV and instead requires a series of images as shown in Figure 7. From top left, across to bottom right.

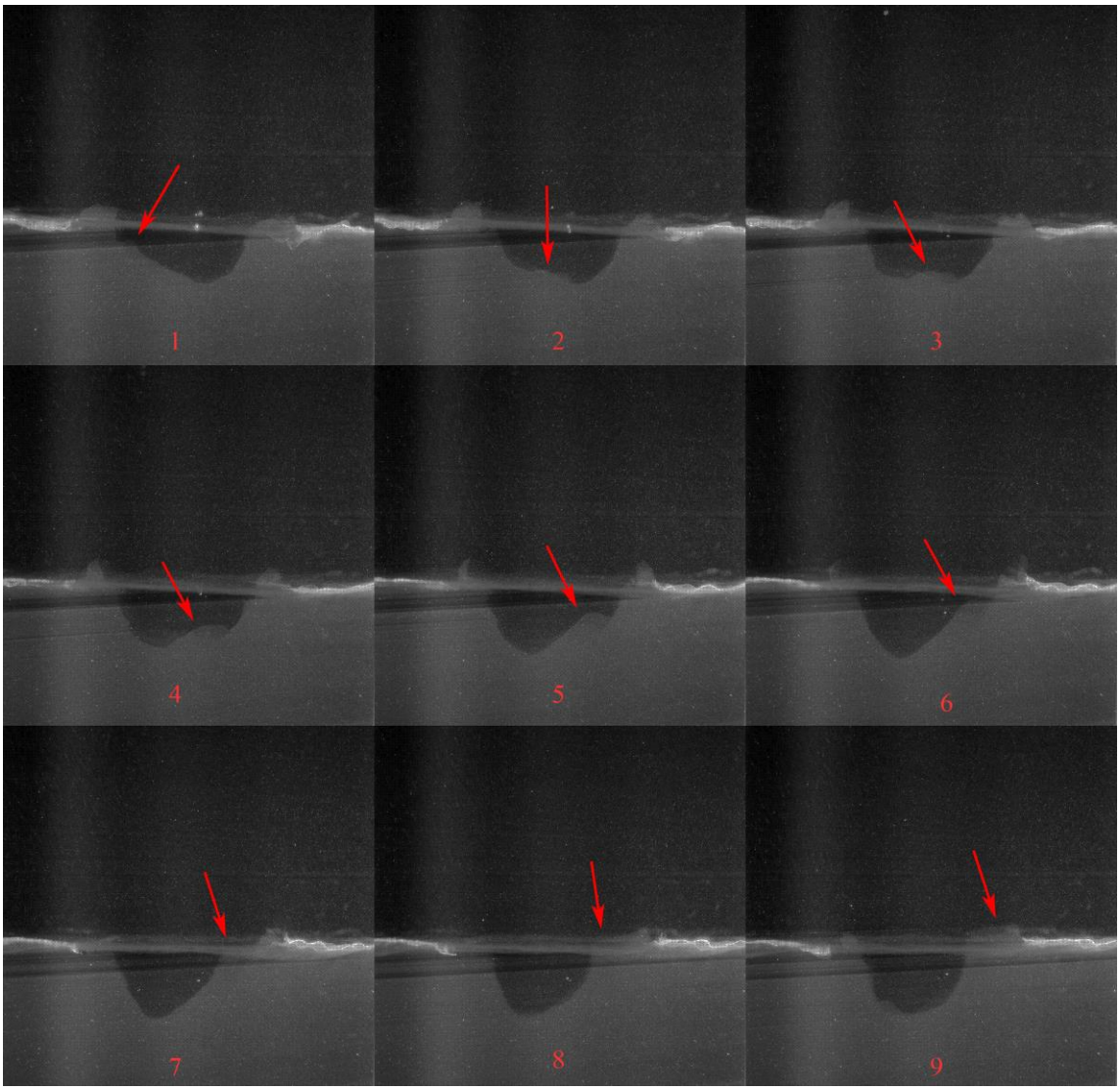


**Figure 7 Sequential Images of Regime 3**

In the turbulent experiments flow regime 3 was characterized by large momentum fluctuations rather than the collapsing interface deformation presented in (Friedman and Katz, The flow and mixing mechanisms caused by the impingement of an immiscible interface with a vertical jet). This was because of the natural instability of the deformation due to the highly turbulent flow. This momentum fluctuation can be seen moving from the left to the right side of the deformation in Figure 7.

For fluids discharged directly at the interface, these flow regimes have been found to be entirely a function of the Richardson number, for turbulent jets, and with a minor dependence on Re, for laminar flows. It has been found experimentally that mingling of the fluids occurs around the transition from flow regime 2 to regime 3. In these experiments we investigated the effects of separation from the interface.

### 2.2.3 Previous Experiments with No Separation

Previous experiments were conducted with a sharp density interface located at the jet exit. (Friedman and Katz, The flow and mixing mechanisms caused by the impingement of an immiscible interface with a vertical jet) determined the flow regimes and defined the AR as a function of the Richardson number. The results of their experiments were used as the benchmark for these experiments. Other research has also been done with immiscible fluids that relates to the sharp density interface of the present experiments. (Longmire, Norman and Gefroh) discussed the pinch-off of a dense fluid injected into the top of a lighter fluid at low Reynolds numbers. Previous research by (Friedman, Vandakoot and Meyer Jr.) summarizes the parametric relationship, of many of the dimensionless groups in Equation 2 shown here in Equation 3.

$$\left(\frac{h}{D}, Bo\right) = F\left(Ri, Re, We, \phi, \frac{\mu_F}{\mu_S}\right)$$

**Equation 3 Previously Developed Relationships**

## 2.3 Jets Impinging on Separated Interface

For the jets studied in the present experiments, the jet fluid passes through a similar ambient fluid, acting as a pure jet; thus having the constant spreading rate and constant decrease of centerline velocity as discussed in 2.1.2. However, after the fluid has traveled a given distance from the jet exit, the density interface has an effect on both the velocity and the spreading. It then continues to affect the fluid with the addition of buoyant forces until the forces overcome the momentum and the flow reverses to a neutrally buoyant state. Both (Banks and Chandrasekhara) and (Qian, Mutharasan and Farouk) performed experiments using an air jet impinging a water interface at varying separation distances in both laminar and turbulent flows. Another study of air impinging water mixed with fast drying cement was performed by (Cheslak, Nicholls and Sichel) to map the geometry of the cavity/deformation. Further study of an air jet expansion inside a confined tube on to a liquid interface was performed by (Evans, Jameson and Rielly). This study also confirmed that the interface jet diameter increased linearly with separation from the jet exit as discussed in section 2.1.1.

We hypothesized that the flow regimes mentioned in Section 2.2.2 are governed by the local Richardson number where the jet interacts with the interface. We will designate this $Ri_i$. Since $U_i$ and $D_i$ are impossible to measure in the SPR caverns, we would like to relate them to known values at the jet exit, $U_p$ and $D_p$. Therefore, to go from a Richardson number based on properties at the jet exit ($Ri_p = \frac{g\Delta\rho D_p}{\rho_2 {U_p}^2}$) to a Richardson number based on properties at the fluid interface, $Ri_i$, the following geometric considerations are applied. A turbulent round jet spreads linearly (Lee and Chu), therefore: $C = \frac{D_p}{D_i}$. A jet spreading factor was introduced by (Friedman and Katz, Rise height for negatively buoyant fountains and depth of penetration for negatively

buoyant jets impinging an interface), $F = \frac{U_i}{U_p}$, where F = 1 in the near field and is self similar in the far field, as stated previously, the centerline velocity decays linearly. It has also been explained in (Friedman and Katz, Rise height for negatively buoyant fountains and depth of penetration for negatively buoyant jets impinging an interface) that F = C, by use of a balance of kinetic and potential energy or momentum balance, and therefore $Ri_i = \frac{Ri_p}{F^3}$

# 3 Experiments

The experiments were conducted at the University of Massachusetts Dartmouth in the Mechanical Engineering Fluids Laboratory. They focused on the effect of flow regime changes due to spreading from a top issuing, negatively buoyant jet impinging a sharp density interface.

The experiments were designed to define a relationship between the separation of the interface and the Richardson number for different flow regime transitions. Different visualization techniques were implemented in the execution of the experiments. Video of the flow was taken to document flow regimes and to estimate spreading. PIV (Particle Image Velocimetry) was used to map the nearly instantaneous velocity measurements in a cross-section of the fluid. Along with those, LIF (Laser Induced Fluorescence) was used to visualize the density interface. The experimental equipment consists of experimental fluids, mechanical system, and data acquisition equipment.

## 3.1 Test Facility

### 3.1.1 Experimental Fluids

Using experimental techniques discussed by (Budwig) we used a water/glycerin mixture to represent the salt water and silicone oil to represent the crude oil. The test fluids used in these experiments are 5 and 0.65 centistokes silicone oil. The 5 cSt silicone oil was used for early laminar experiments. The 0.65 cSt fluid provided turbulent conditions under all but the slowest flow rates. The majority of the relevant data was obtained using the 0.65 cSt oil in the turbulent experiments. Because fluid properties vary with temperature, the laboratory, and thus the ambient exposed fluids, was maintained at 77°F during all experiments.

#### 3.1.1.1 Refractive Index Matching

The index of refraction is a measure of the change in speed at which light travels through a substance when compared to the speed of light in a vacuum. For instance, water has a refractive index of 1.33; therefore light would travel 1.33 times faster in a vacuum as it would in water. According to Snell's Law when light passes from one medium to another it also changes its propagation direction, causing the light to "bend". Due to the immiscible nature of the fluids being used in these experiments, light would bend when passing between the fluids causing the light plane and therefore the images and video to seem distorted. To avoid this instead detrimental effect, the brine substitute was a mixture of glycerin and water mixed to match their respective indices of refraction to within ±0.001 of the silicone oil. The refractive indices were measured using a Misco Palm Abbe™ digital refractometer model #PA202. The Properties of the fluids used can be seen in Table 1.

**Table 1 Experimental Fluids Properties**

| ***Fluid*** | ***Density*** ***($kg/m^3$)*** | ***Viscosity*** ***(cSt)*** | ***Refractive Index*** |
|---|---|---|---|
| *Silicone Oil* | *910* | *5.0* | *1.3970* |
| *Water/Glycerin (49% wt. Glycerin)* | *1125* | *6.0* | *1.3966* |
| *Silicone Oil* | *760* | *0.65* | *1.3769* |
| *Water/Glycerin (33% wt. Glycerin)* | *1083* | *3.2* | *1.3765* |

#### 3.1.1.2 Fluid Clarity

Problems with fluid clarity have been noted in the beginning of the experiments as well as previous experiments. To improve the clarity of the fluids mechanical filters were added to both fluid loops. These along with regular circulation of the fluids helped to remove impurities. Microorganisms in the water were feeding on the oil causing a biological growth that created problems for visualization. It was eliminated by adding a small amount of hydrochloric acid to the water/glycerin mixture to lower the pH to slightly below 7, thus killing current growth and inhibiting future growth. This required adding 20 ml of 20° Baume (31.45%) acid to 10 gallons of mixture.

#### 3.1.1.3 Additives

PIV measurements require a "seed particle" to be added to the fluid. For good measurements there are three characteristics that are weighed in the selection of the seed used.

1. Seed particles should be as close as possible to the density of the fluid to minimize the rate of separation.
2. Seed particles should be as large as possible to provide visibility.
3. Seed particles should be as small as possible so the actual flow of the fluid is not affected.

Essentially points 2 and 3 contradict each other and compromise must be met. Lab grade, titanium dioxide powder particles were used as seed in the water/glycerin and 4μm nylon particles were used in the silicone oil. Because both fluids are transparent, LIF was used to visualize the interface. LIF is a method of analysis and visualization where a substance is excited by a fixed laser wavelength and, after a few nanoseconds to microseconds, de-excites and emits a larger wavelength light. Water-soluble Rhodamine 6G dye was added to the water/glycerin mixture to provide this effect. 15ml of a 0.005 g/l dye concentration was added. The fluids were distinguishable because the dye is insoluble in the silicone oil; this made the oil dark and the water/glycerin mixture bright.

### 3.1.2 Mechanical System

The mechanical hardware consists of the test chamber, a recirculating oil loop, an open water/glycerin loop, and frame/alignment structure. The intent of the design was to discharge a negatively buoyant, top-issuing jet against an interface with varying separation from the jet exit. The setup was built to simulate the flow of crude oil into a void of saltwater and as the oil displaces the saltwater the interface separation would change. Jet exit diameters were exchangeable allowing variations in the Richardson number.

#### 3.1.2.1 Test Chamber

The fluid chamber, shown in Figure 8, is approximately 12" x 12" x 28" internally. The bottom is a 2" thick gray PVC with four holes close to the corners threaded for 1" PVC pipe fittings. As shown in Figure 9, two of these holes are used for the water/glycerin loop, one is used with a stand-pipe in the oil loop, and the last hole is used as a drain. There is also a hole in the center for a 3" PVC pipe that was plugged for these experiments. The walls and lid are ½" thick cast acrylic for optical clarity. The lid has a bulkhead fitting for 2" pipe and a ¾" hole for adding chemicals/particles directly to the tank.

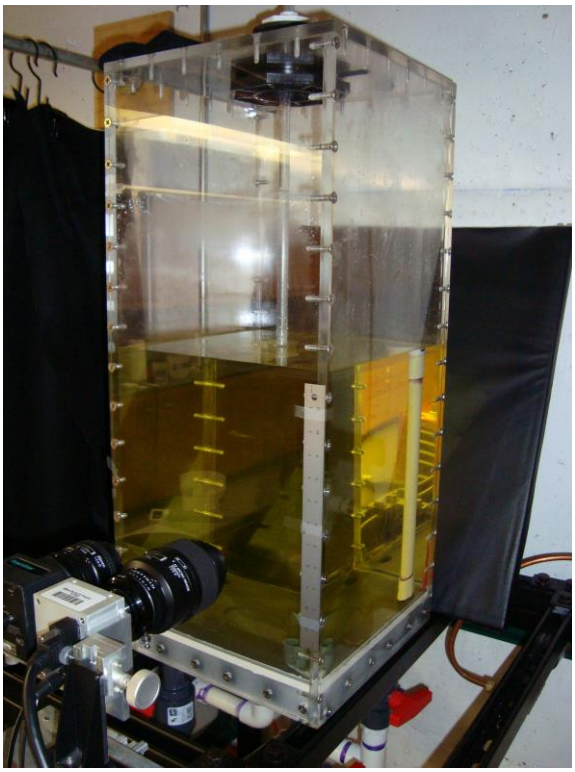

**Figure 8 Test Chamber**

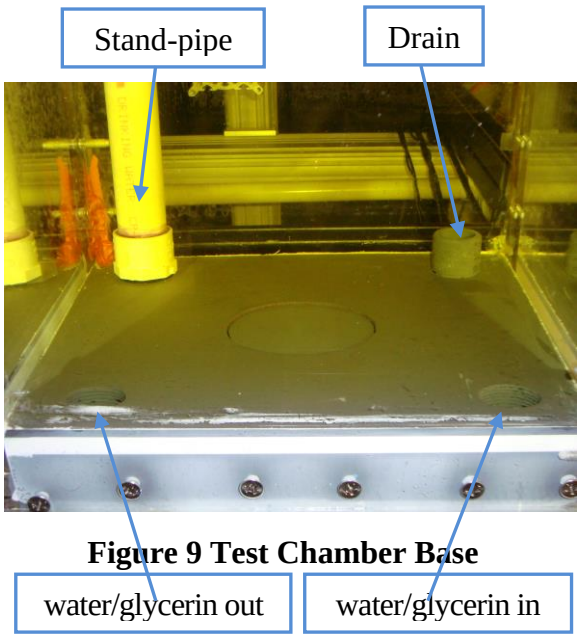


**Figure 9 Test Chamber Base**

### 3.1.2.2 Recirculating Oil Loop

The circulating loop draws the oil from above the interface inside fluid chamber, via a standpipe and out one of the holes in the base of the fluid chamber. The piping then tees to go to a storage tank or into the main circulating pump. The storage tank is a 10 gallon square conical PVC tank. This tank is only used to store extra oil and for adding particles. The other branch of the tee goes to the main circulating pump that is a Little Giant® Model TE-4-MD-HC. The flow exits the circulating pump and enters a Whirlpool® filtration system 5 micron filter; this filter can be placed on bypass for some experiments. The oil flow exits the filter and enters a throttle valve and calibrated flow meter combination shown in Figure 10. Depending on the experiment being performed, the flow meter and throttle valve can be replaced with different capacity instruments. The Great Plains Industries® flow meters were capable of measuring either from .3 to 3 gallons per minute or from 3 to 30 gallons per minute. The smaller flow meter had minor inaccuracies so a calibration curve was used. The data in the Appendix (not included here – see original thesis) shows both display flow rate and actual flow rate for this flow meter. The flow then leaves the flow meter and passes through a section of clear PVC pipe for the inspection of air bubbles. The pipe is supported by a hanger on the ceiling and connects to the jet exit pipe with a threaded union. There are four possible jet exit pipes; ¼", ½", ¾" and 1", these are nominal pipe sizes, not true internal diameters, the measured diameters are given in Table 2. The jet pipes have approximately 36" of undisturbed flow prior to jet exit to allow profile development. The piping schematic in Figure 11 shows both the recirculating oil loop and the open water/glycerin loop.

**Figure 10 Exchangeable Throttle Valve and Calibrated Flow Meter Combination**

**Table 2 Pipe Size Diameters**

| ***Nominal pipe size*** | *¼"* | *½"* | *¾"* | *1"* |
|---|---|---|---|---|
| ***Measured Diameter*** *(in)* | *0.354* | *0.619* | *0.8185* | *1.054* |

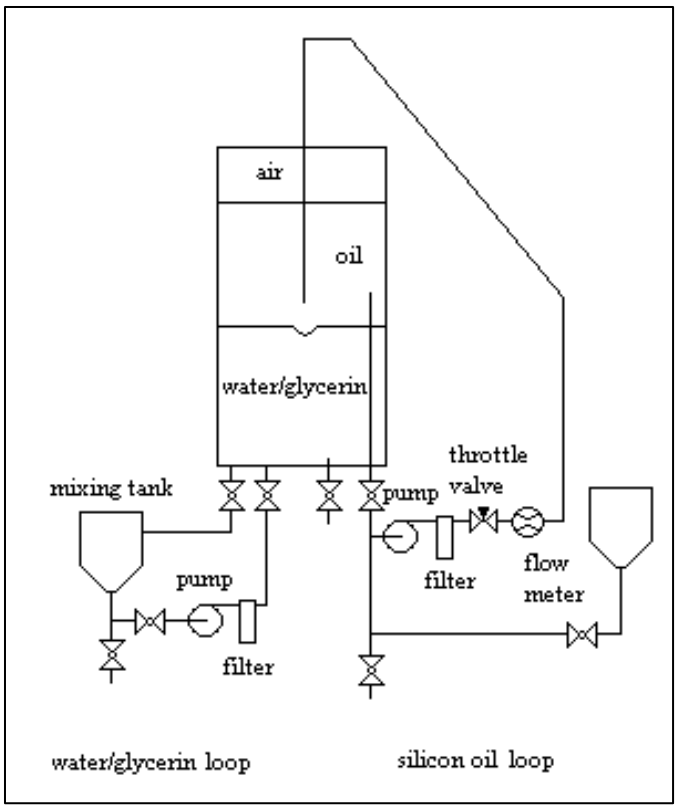


**Figure 11 Fluid Piping Schematic**

#### 3.1.2.3 Open Water/Glycerin Loop

The open water/glycerin loop draws the mixture from the bottom of the fluid chamber, through one of the holes in the base. The piping goes directly into another storage tank. Using gravity to drain into this tank, the interface is lowered away from the jet exit. This storage tank is another 10 gallon square conical PVC tank and is used to mix the water and glycerin and to store extra water/glycerin. A second Little Giant® Model TE-4-MD-HC pump is used to draw the mixture from the tank through another Whirlpool® filtration system 5 micron filter. The mixture then returns to the bottom of the fluid chamber through another one of the holes in the bottom. Using the pump and filter, the mixture can be circulated to maintain clarity or increase the interface closer to the jet exit.

#### 3.1.2.4 Frame and Alignment Structure

The test chamber and all supporting plumbing are mounted on a Unistrut® frame. The frame is built in an "L" shape allowing the laser light sheet to maintain a perpendicular geometry to the cameras. The frame is attached to a concrete wall to prevent vibration and motion. The frame also supports sections of X-rail which allow for X-Y-Z adjustments of the laser and cameras. The design of the frame and X-rail system are shown in Figure 12. Under the frame is an emergency catch basin to collect any potential leaks from the fluid chamber of any of the plumbing. The unit is surrounded by an enclosure, which serves as a laser safety shield and also improves image quality by reducing stray light in the images.

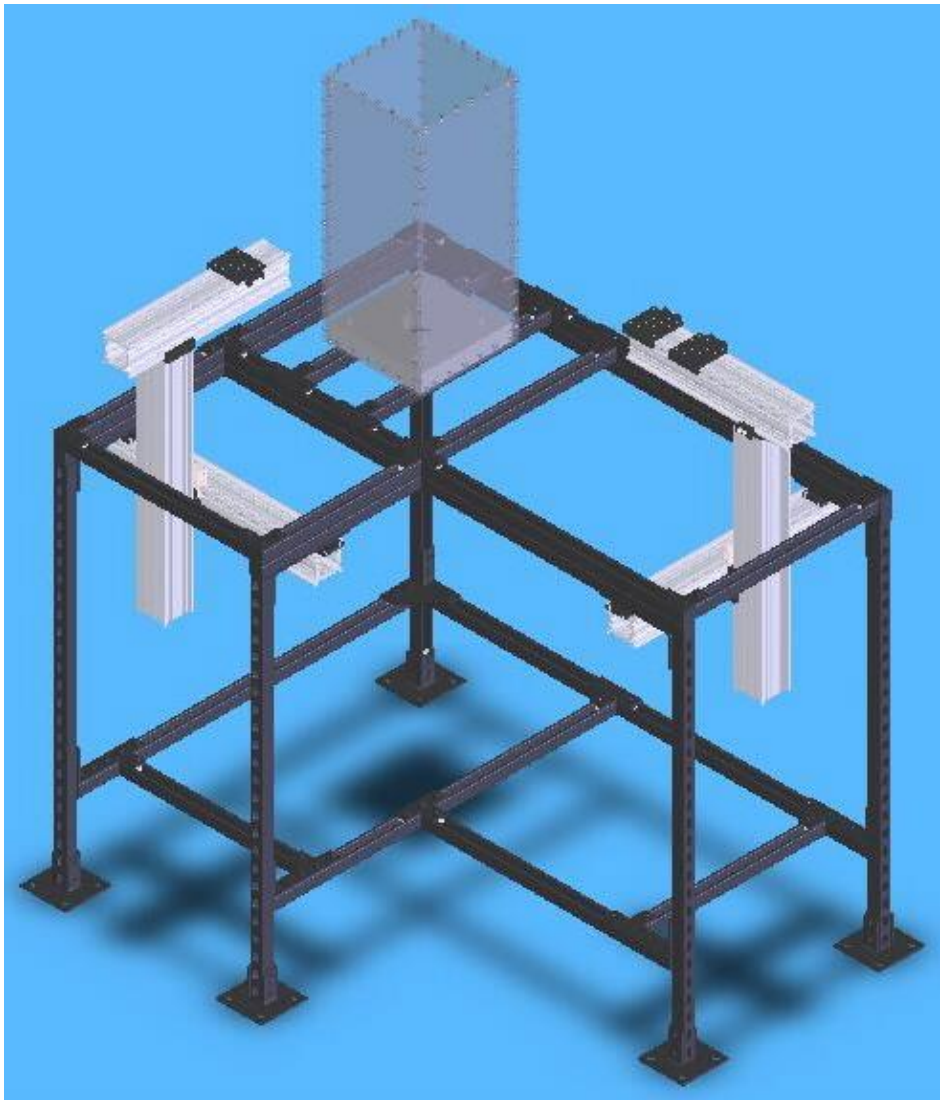

**Figure 12 Test Chamber and Framing Design**

### 3.1.3 Data Acquisition Equipment

There are three parts to the data acquisition equipment: illumination equipment, image capture equipment, and data processing equipment. The acquisition equipment was used in various combinations for the desired function, depending on the data to be captured. The data was collected in three forms; PIV images and measurements, laser synchronized video, LIF enhanced measurements. The data acquisition equipment and its orientation to the test chamber are shown in Figure 13.

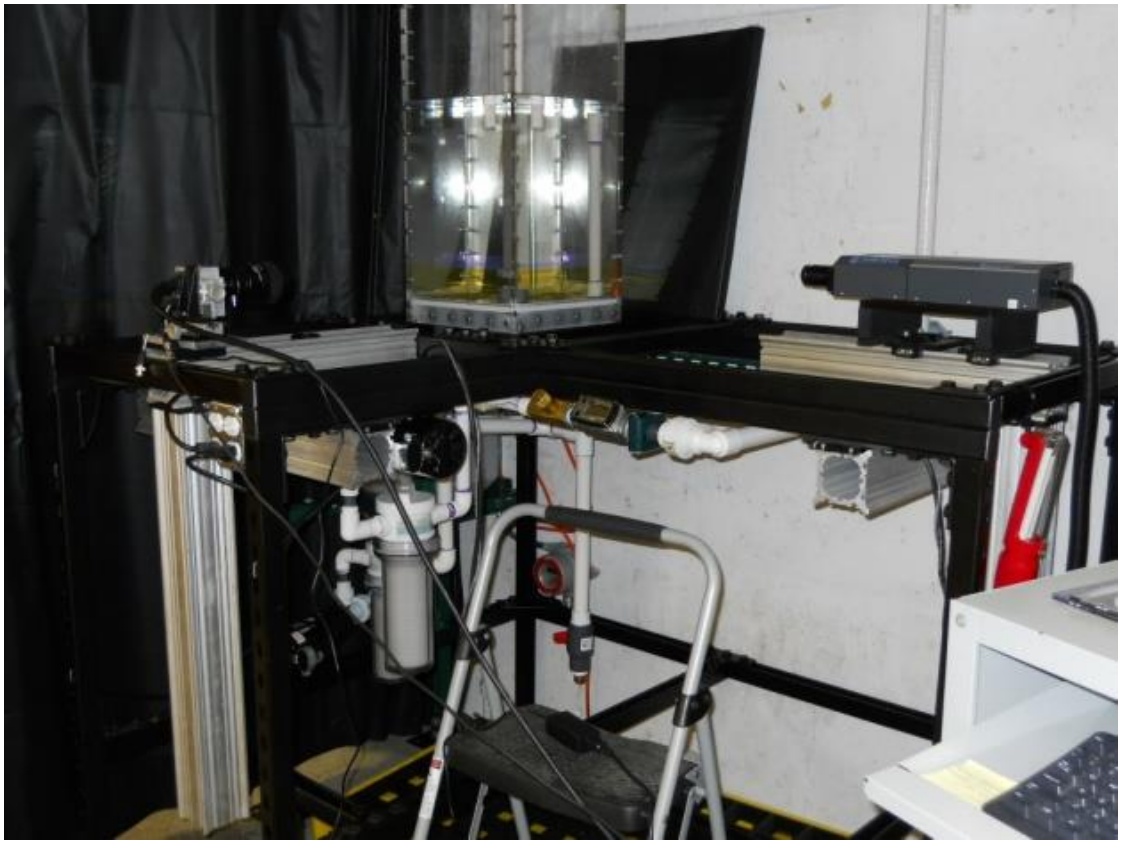

**Figure 13 Test Chamber and Data Acquisition Equipment on the Frame**

#### 3.1.3.1 Illumination Equipment

The illumination system consisted of a New Wave Research® Solo II PIV©, dual head Nd:YAG laser along with various optical lenses. The laser produces 30mJ light at 532nm with pulse duration of 4±1 ns, and a variable pulse repetition rate with a maximum of 15Hz. The laser produces an approximately 4.5mm diameter beam of light. It then passes through various cylindrical and a spherical lens to produce a light sheet approximately 1.0mm thick and has a width to the scale of the desired size. For PIV the laser is pulsed by the Laser Pulse ™ synchronizer to produce two rapid pulses used for cross-correlation with the TSI® camera disclosed below. For video capture, in order to increase the frame rate possible, the two laser heads are used alternately by a custom designed flip-flop circuit purchased from Steve King of Kingdom Electronics and The John Hopkins University for laser synchronized video, or the internal variable pulse rate switch. The illumination controlling equipment is shown in Figure 14.

#### 3.1.3.2 Image Capture Equipment

The image acquisition was through two different cameras. A TSI® Model# 630057 PowerView™ plus 2Megapixel digital Charge Coupled Device (CCD) camera was used to capture images for PIV. For video, an Imperx® 1 megapixel CCD camera along with an Active Silicon® Framegrabber was used. 28mm, 55mm, and 105mm lenses were used with both cameras to capture the desired field of view. Both cameras are mounted on a translation stage for fine X-Y axis adjustments beyond the coarse adjustment capability of the X-rail system.

#### 3.1.3.3 Data Processing Equipment

The data was processed on two Dell™ Vostro™ workstations with Intel® Core™ i5 750 CPUs with 4GB of Ram operating Windows XP. Another Dell™ Vostro™ workstation with Intel® Core™ i5 750 CPUs with 16GB of Ram operating Windows XP x64 was used to stream video. PIV images were processed using TSI® Insight 3G™ PIV software to produce velocity vector maps. Video Capture was processed using NorPix© Streampix 3™ at a maximum frame rate of 30Hz. The data processing station is shown in Figure 14.


**Figure 14 Data Processing Station and Illumination Controlling Equipment**

## 3.2 Experimental Procedures

The first step, after building the test setup, was to calibrate the measurement devices. Both flow meters were calibrated with water as well as with the test fluid, silicone oil. A calibration curve was fitted and used with one of the flow meters. Mixing the water/glycerin to match the refractive index of the Silone oil and recording the fluid properties followed. Prior to any data acquisition a scale shot is taken for velocity and distance correlation. Table 3 shows the experiments that were performed and the experimental parameters used.

**Table 3 Experiments and Experimental Parameters**

| | ***Experiment 1*** | ***Experiment 2*** | ***Experiment 3*** | ***Experiment 4*** |
|---|---|---|---|---|
| ***Purpose*** | *Relationship between AR and Ri* | *Relationship between AR and regime transitions* | *Relationship between Ri and regime transitions* | *Determining spreading factor* |
| ***Visualization*** | *LIF, PIV images* | *LIF, PIV images* | *LIF, PIV images, Video* | *LIF, PIV images, Video* |
| ***Jet Diameters*** | *1"* | *1"* | *¼", ½", ¾", 1"* | *¼", ½", ¾", 1"* |
| ***silicone oil viscosity*** | *5 cSt* | *5 cSt* | *0.65 cSt* | *0.65 cSt* |
| ***Flow type*** | *Laminar* | *Laminar* | *Turbulent* | *Turbulent* |
| ***Re range*** | *200-1300* | *550-1100* | *2690-31200* | *2690-31200* |
| ***Ri range*** | *.10-30* | *1.3-5.3* | *.02-10* | *.02-11* |

### 3.2.1 Experiment 1

The purpose of experiment 1 was to develop a relationship between the aspect ratio (AR) and the Richardson number for laminar flows. PIV images were used to record maximum depth of penetration of the jet fluid in pixels for specified flow rates. The pixel height was converted to a scaled length and then normalized using the jet diameter to determine the AR. The flow rate determined the average jet exit velocity, the only free parameter of the Richardson number. This was repeated over a range of interface separations.

### 3.2.2 Experiment 2

The purpose of experiment 2 was to develop a relationship between the aspect ratio and the transition points of the defined flow regimes for laminar flows. LIF techniques and transition indicators were used to determine the flow regime transition points; this was not difficult due to the laminar flow. Again, PIV images were used to record maximum depth of penetration of the jet fluid in pixels but at the regime transition flow rates. The pixel height was converted to the aspect ratio (AR) in the same means. The flow rate for the transition point determined the Richardson number. This was repeated at over a range of interface separations.

### 3.2.3 Experiment 3

The purpose of experiment 3 was to develop a relationship between the Richardson number and the transition points of the defined flow regimes for turbulent flows. LIF techniques and transition indicators were used to determine the flow regime transition points again; however this was not as easy as the in laminar flow due to the turbulence causing fluctuations in the flow. The flow rate for the transition point determined the Richardson number. This was repeated over a range of interface separations and using multiple jet diameters. Due to inconsistencies in identifying transition points, numerous repetitions with several independent observers were required. Experiment 3 provided the most important data in this study.

### 3.2.4 Experiment 4

The purpose of experiment 4 was to determine the spreading factor relating the Richardson number of the jet to a Richardson number located at the interface for turbulent flows. Previous data from experiment 3 was used compared to additional PIV Data and Video images. PIV and video was repeated over a range of interface separations and using multiple jet diameters. Experiment 4 was also used to determine possible values of the virtual origin and the empirical jet spreading coefficient. Data from experiment 4 was useful in correlating data from experiment 3.

# 4 Results

A summary of the results for the experimentation that was conducted is presented in this section. The tabulated data collected from the experiments is located in the Appendix (not included – see original thesis).

## 4.1 Laminar Flow Experiments

Experiments one and two were conducted with laminar flow patterns. It has been shown by (Friedman and Katz, The flow and mixing mechanisms caused by the impingement of an immiscible interface with a vertical jet) that a corrected Richardson number, based on the root mean square velocity, can be applied to laminar flows to a momentum equivalent turbulent flow. Therefore, a laminar flow with the same average velocity based on volumetric flow as a turbulent flow has a Richardson number that is twice as large.

### 4.1.1 Experiment 1

The data taken falls close to the $AR = Ri^{-1}$ curve. This correlates closely with previous data and the momentum analysis by (Friedman and Katz, The flow and mixing mechanisms caused by the impingement of an immiscible interface with a vertical jet). However, this does deviate from previous data at high Ri numbers, low flow rates. Beyond a Ri of approximately 2, previous data followed $AR = 0.72\ Ri^{-1/3}$.

The graph in Figure 15 shows, as one would predict, the AR decreases as the interface separates from the jet exit for a fixed flow rate or Richardson number. It is also of interest that the decrease due to separation also decreases as the Richardson number increases.

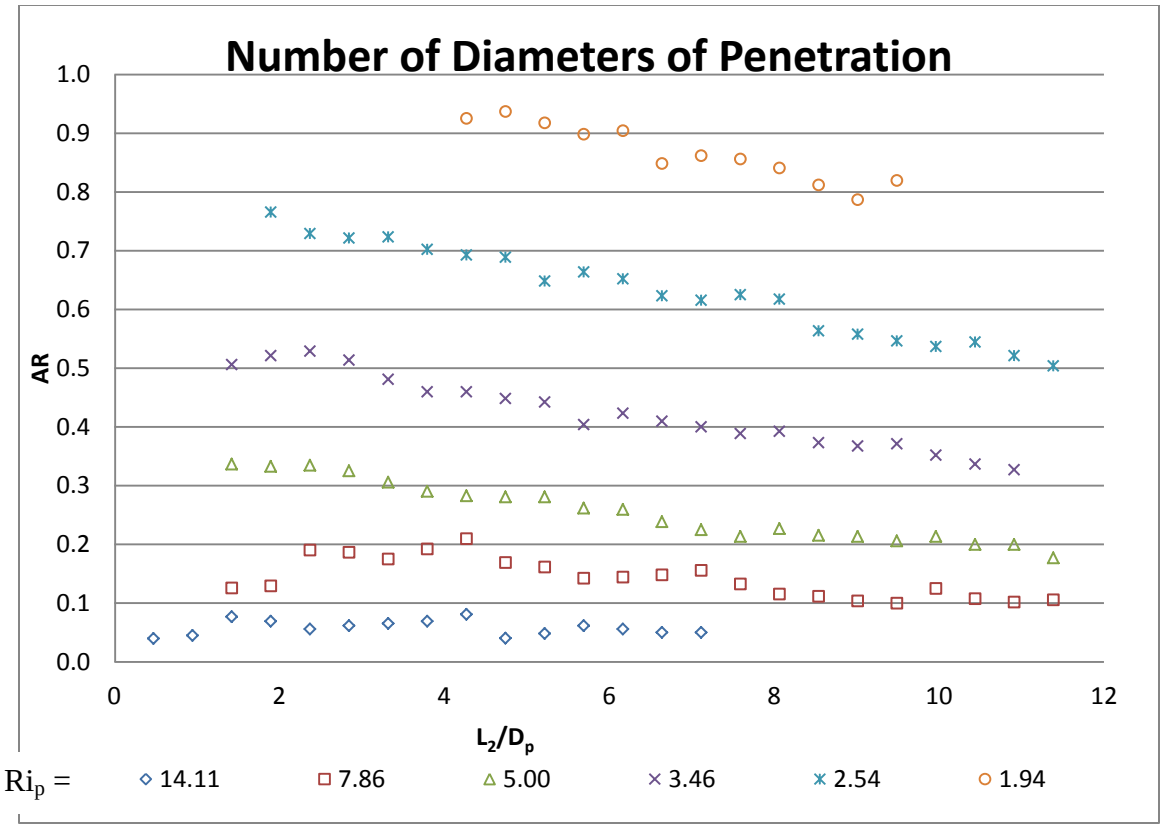


**Figure 15 AR vs. Separation for Various Ri**

### 4.1.2 Experiment 2

The graph in Figure 16 shows the aspect ratio at the transition of flow regimes at various separations from the jet exit along with linear trend lines fitted to the data. It is of interest that the aspect ratio for the 2-3 flow regime transition has a rapidly increasing trend, reaching a maximum just over a value of 1 at around 6-7 diameters of separation, and then slowly decreasing or even remaining constant. Meanwhile, the aspect ratio for the 1-2 flow regime transition remains constant in the 0.33-0.34 range over the 12 diameters used in the experiment.

The data collected was also used to determine the transition Richardson numbers for laminar flow as seen in Figure 17. The data shows the direct correlation between the Richardson number for regime transition and the separation between the interface and the jet exit.

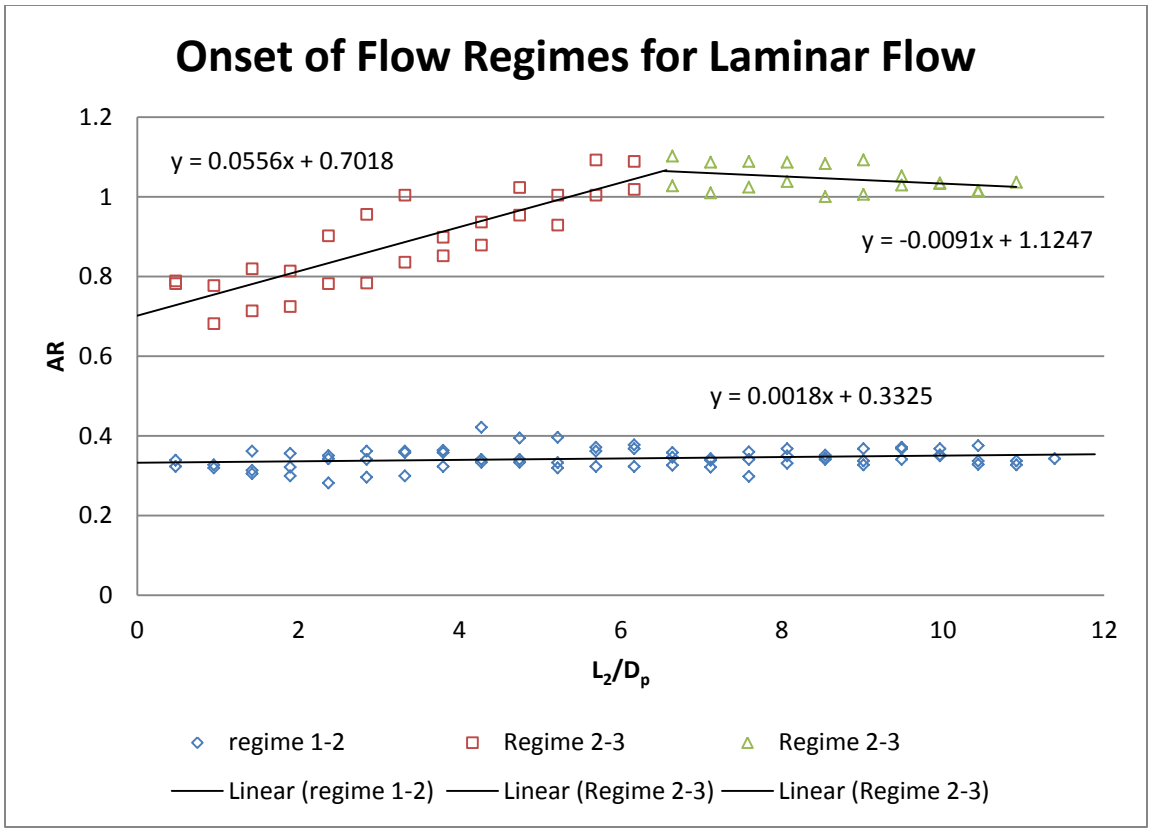


**Figure 16 Flow Regime Transition AR**

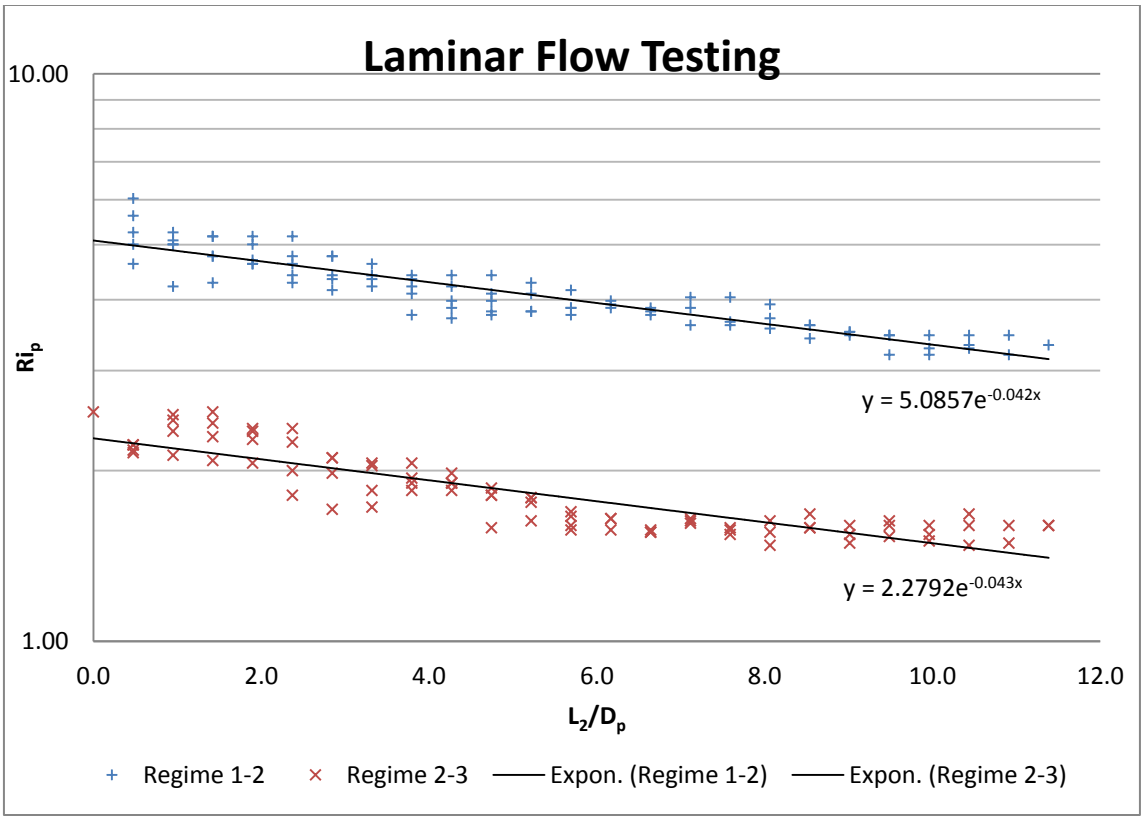


**Figure 17 Ri vs. Separation for Laminar Flows**

## 4.2 Turbulent Flow Experiments

### 4.2.1 Experiment 3

Experiment 3 determined the transitions between flow regimes for various separations from the interface with turbulent flow. Figure 18 and Figure 19 show the transition Richardson numbers for 4 different pipe diameters used in the experiment as a function of dimensionless separation from the interface. Although minor diameter dependence seems to exist from the graph for the flow regime 1-2 transition data, this may be due to measuring inaccuracies or transition ambiguities mentioned in section 3.2.3; however, the 2-3 flow regime transition data appears to independent of diameter. The data has been combined in Figure 20 to show the overall trends. The exponential trend does not seem to represent the physics of the situation so another possibility will be discussed in section 5.

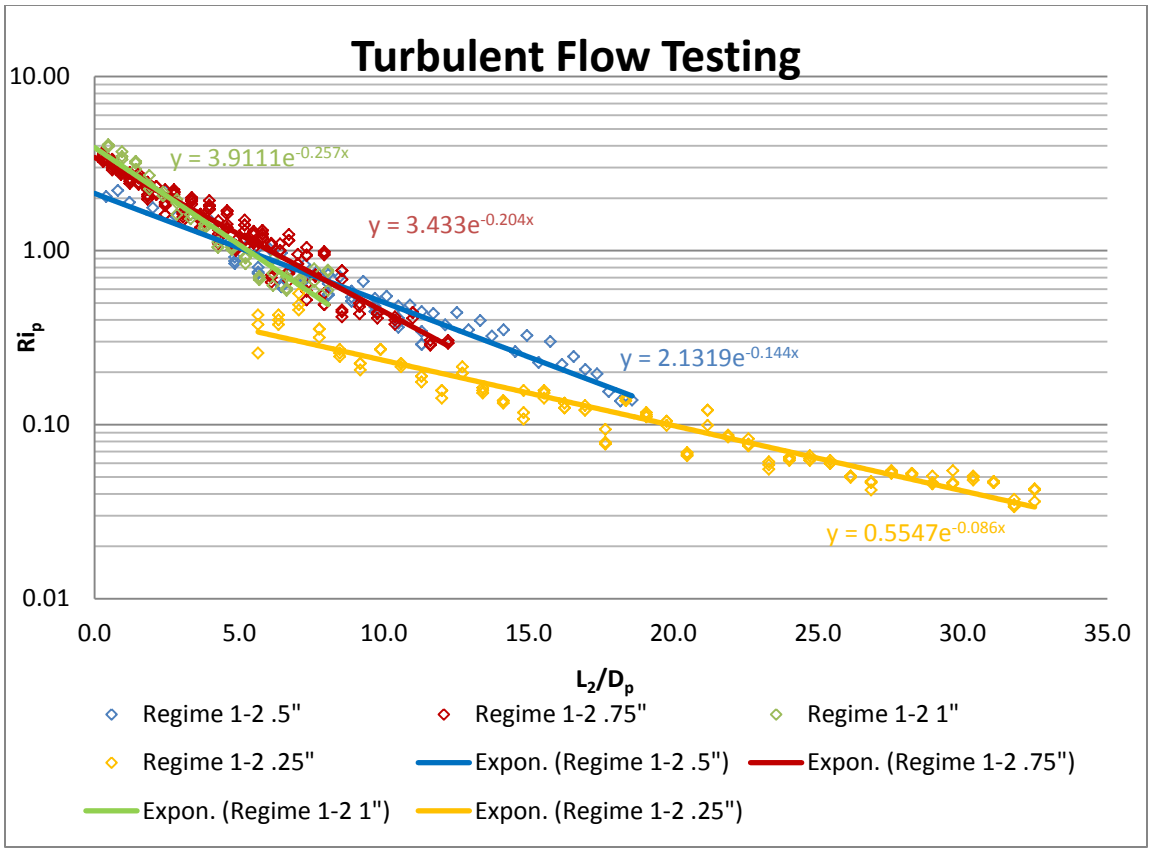


**Figure 18 Ri vs. Separation for Flow Regime Transition 1-2**

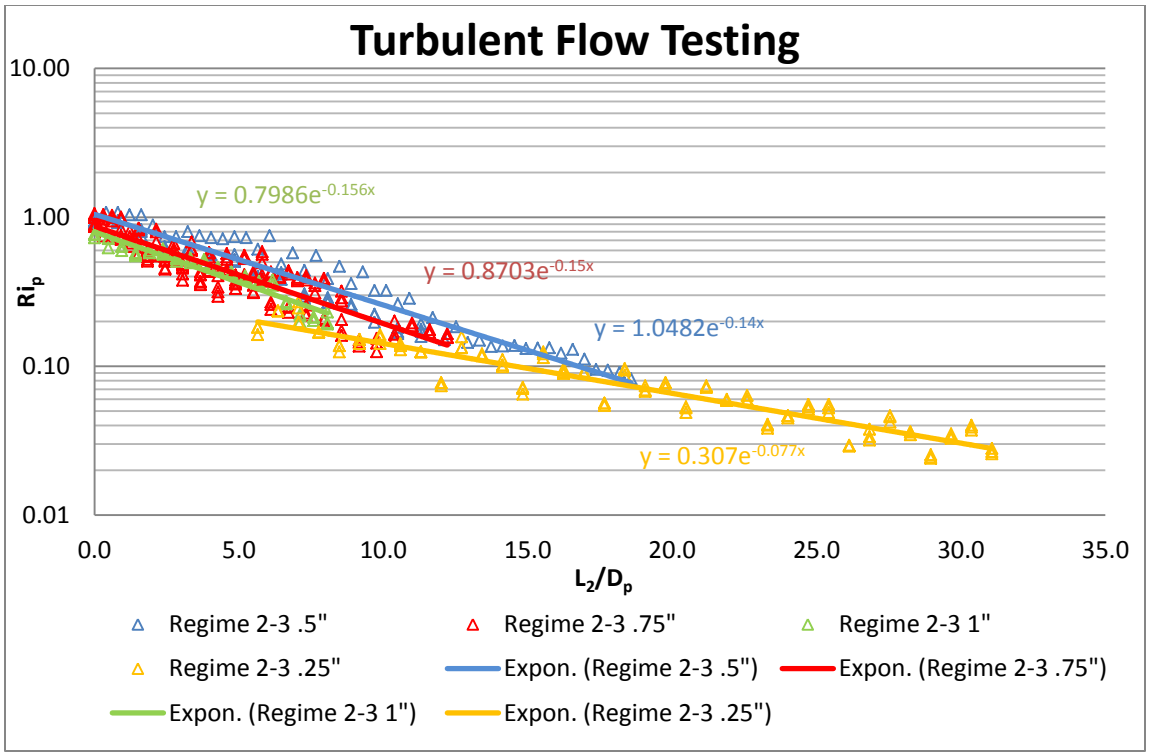


**Figure 19 Ri vs. Separation for Flow Regime Transition 2-3**

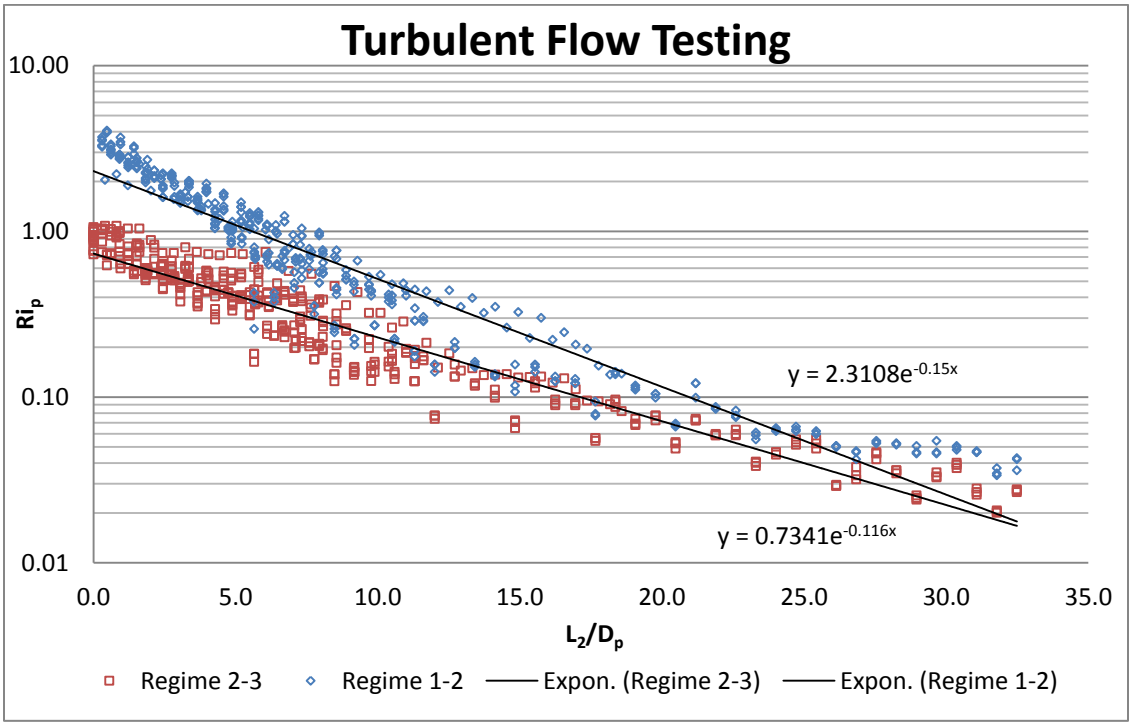


**Figure 20 Combined Ri vs. Separation Data**

### 4.2.2 Experiment 4

176 PIV images taken at various exit diameters, flow rates, and interface separations were manually analyzed using Adobe® Photoshop© and plotting the location in which the edges of the jet intersected to determine the location of the virtual origin. Four image data points were removed as outliers using Chauvenet's criterion (Coleman and Steele). The mean virtual origin location out of remaining 172 images was -7.413 (7.413 diameters upstream of the pipe exit) with a standard deviation of 3.048 diameters. Binned data (binned to the nearest full diameter) is shown in Figure 21 along with a best fit Gaussian distribution. Statistical analysis based on the data results in a virtual origin located at $7.413 \pm 0.465$ (95% uncertainty) diameters upstream of the pipe exit.

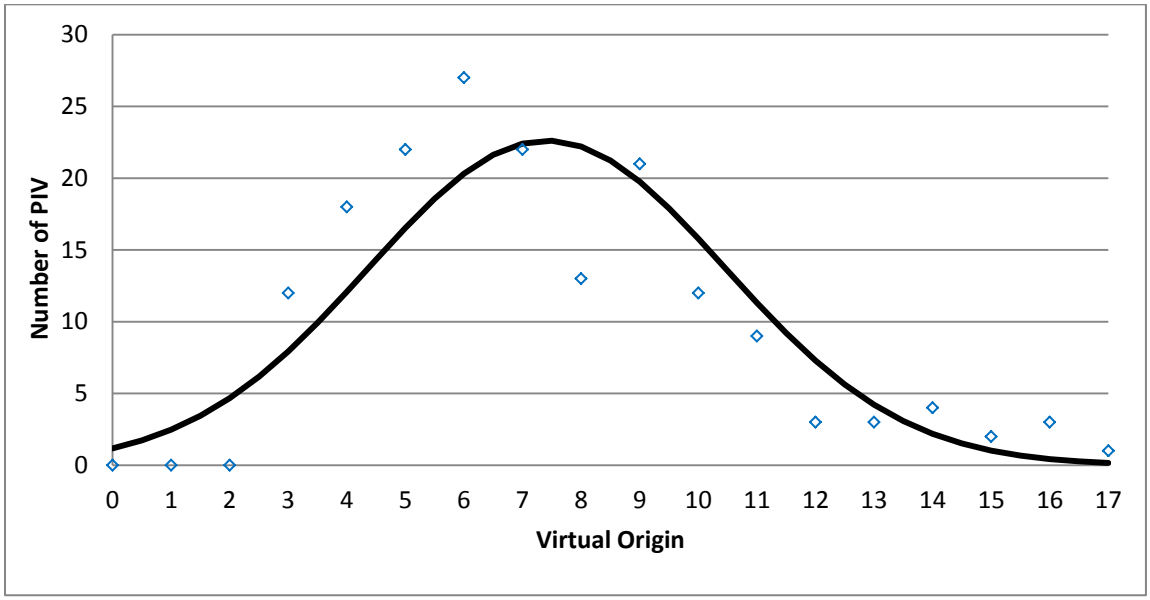


**Figure 21 Binned Virtual Origin PIV Data**

# 5 Discussion and Analysis

## 5.1 Differences Between Laminar and Turbulent Flow Patterns

In the case of laminar flow, the flow regimes were very easily distinguishable with the use of transition indicators, as discussed in section 2.2.2. The change from regime 1-2 was indicated due to the formation of a rise, or "lip", at the edge the deformation due to the high shear of the jet fluid pulling the impinged fluid up as the flow separated from the interface. The change from regime 2-3 was indicated when the stable deformation began to become unstable and collapse in upon itself. An example of this laminar flow can be seen in the PIV vector map shown in Figure 22.

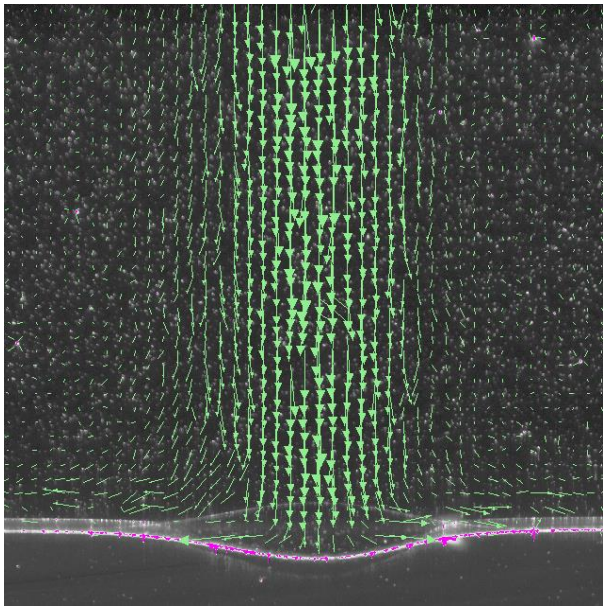

**Figure 22 Laminar Flow in Regime 1**

In the case of turbulent flow, on the other hand, the results were not as easy to interpret. A new set of transition indicators needed to be developed and even with the use of these new indicators there was still ambiguity in deciding when the transition occurred. Due to the turbulent flow the deformation was always unstable and the "lip" would occasionally form and disappear repeatedly. As a result, the indicator for the 1-2 regime transition was the occurrence of the "lip" as the dominant feature. The deformation was shifting location, size and shape in the plane of view, therefore, the 2-3 regime transition indicator was also changed to note when large momentum fluctuated from one side to the other. An example of the turbulent flow can be seen in the PIV vector map shown in Figure 23.

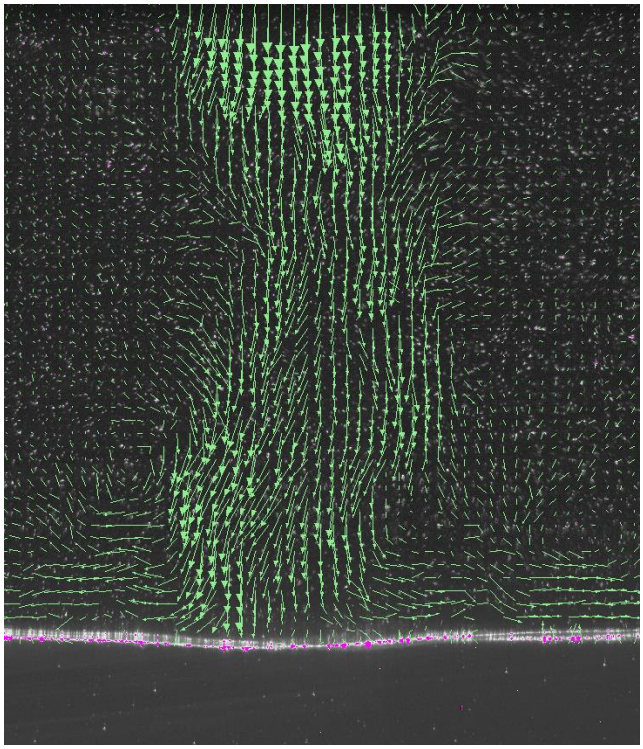

**Figure 23 Turbulent Flow Regime 1**

## 5.2 Analysis of Laminar Experiments

A proposed calculation, Equation 4, shown in Figure 24 as the "calc," for the AR as a function of both the Richardson number and the dimensionless separation.

$$AR = (0.0141 \ln(Ri) - 0.0379)\frac{L_2}{D_p} + \frac{2.25}{Ri} - 0.1$$

**Equation 4 Proposed Equation for AR ($Ri, L_2/D_p$)**

This equation is based purely on this data collection. More data, varying the pipe diameter and fluids used would be needed to verify the equation and what the functional dependencies of the coefficients.

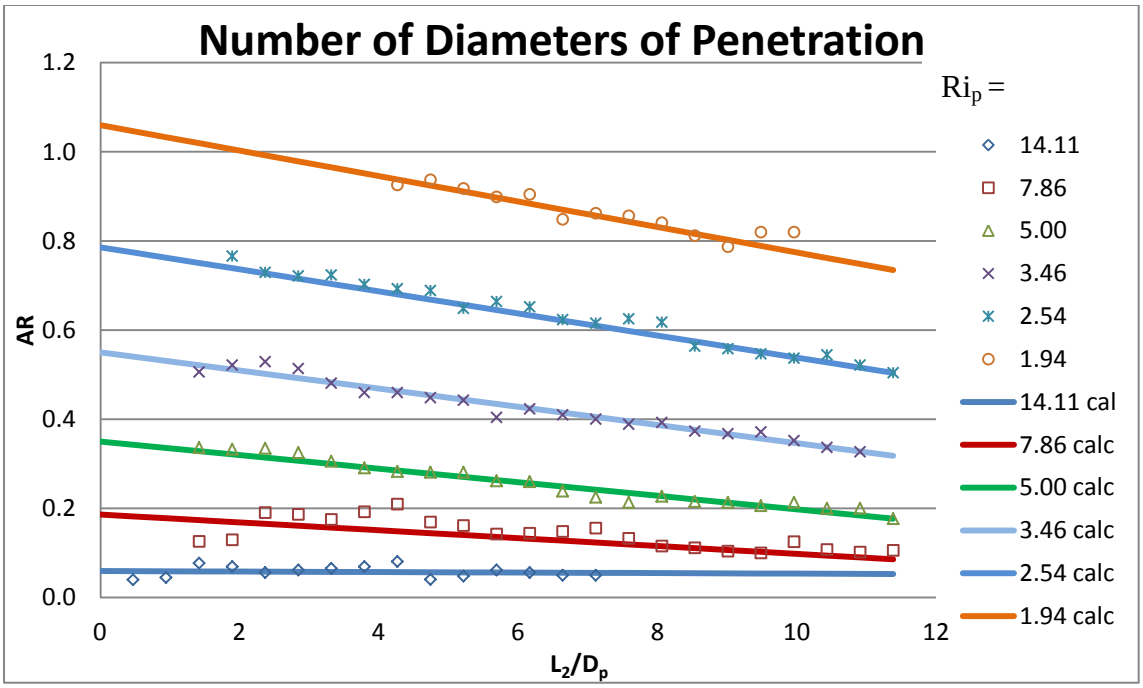


**Figure 24 AR vs. Separation for Various Ri with Calculate Function**

## 5.3 Accuracy of Flow Regime Interpretation for Turbulent Flow

The unsteady deformation and adjusted transition indicators for the turbulent flow experiments led to some ambiguity and personal interpretation differences as to the exact flow rate of the transition. Figure 25 shows the difficulty in determining the flow regime. On the right side of the Figure, flow regime 1 appears to be present as the flow is attached to the interface; however, the left side shows characteristics of flow regime 2, in that it separates from the interface. This lead to a spread in the data due to interpretation, to overcome these difficulties, experiments were independently repeated a large number of times using several operators and the results were statistically analyzed.

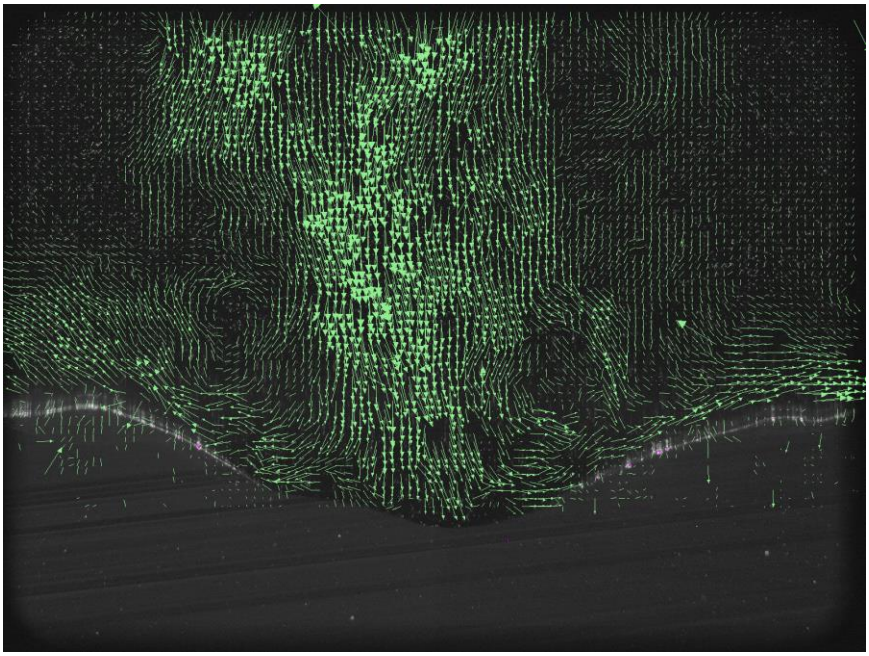

**Figure 25 Example of Flow Regime Uncertainty**

## 5.4 Dimensional Analysis of Constant Richardson Number

For a given Richardson number based on jet exit parameters, the local Richardson number increases with distance from the jet exit as a result of spreading. The interface Richardson number is defined as the local Richardson number when the jet reaches the interface. Assuming that the jet diameter spreads linearly and the velocity decreases linearly, then the exit velocity increases as a cubic to maintain a constant interface Richardson number as distance from the interface is increased.

## 5.5 Spreading Factor

Assuming the Richardson number at the interface dictates the flow regime, it would be of use to use the jet spreading velocity decay factor, F, discussed in section 2.3 to relate the interface Richardson number to the Richardson number at the pipe exit. Assuming, with no separation from the jet exit, flow regime 1-2 transitions at $Ri_i = 3$ and flow regime 2-3 transitions at $Ri_i = 1$ which correlates with previous data taken. By taking the cube root of the ratio of the assumed critical Richardson numbers at the interface to the Richardson number based on parameters at the pipe exit gives the jet spreading velocity decay factor, F. Using this method on the data from experiment 3 provides the resultant data shown in Figure 26.

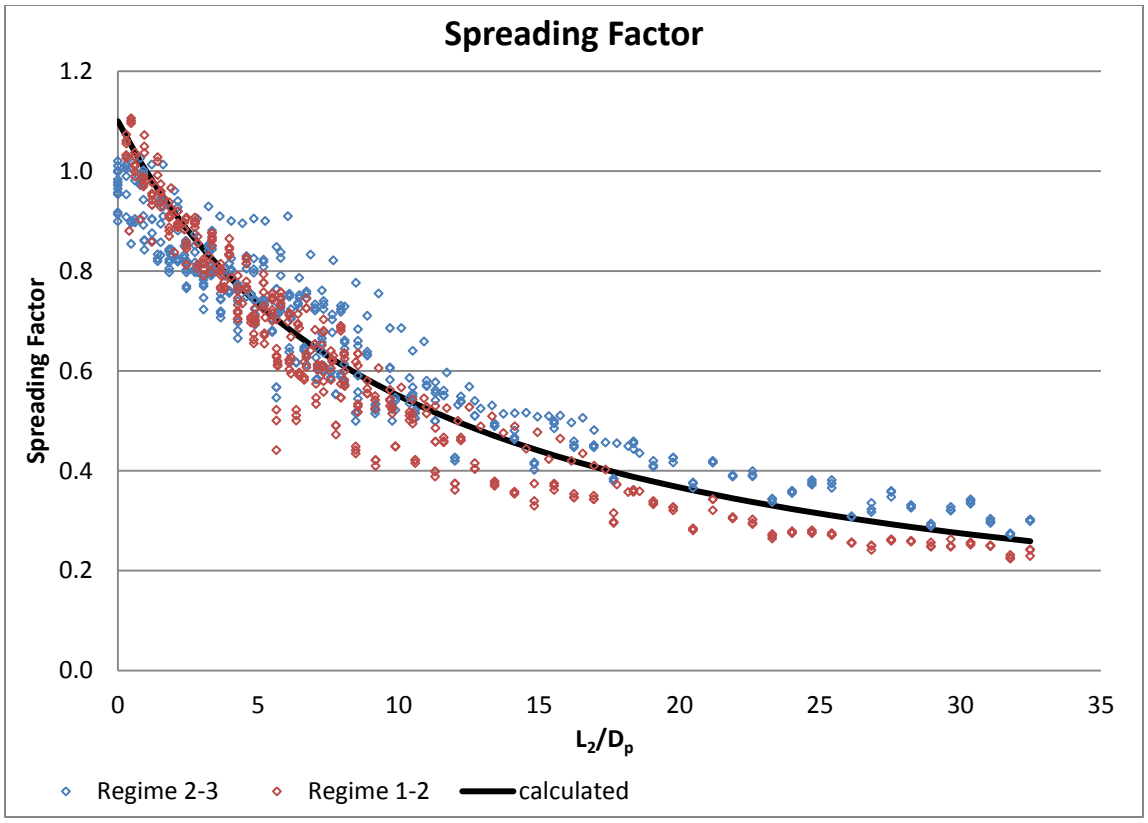


**Figure 26 Spreading Factor Data**

The "calculated" curve is obtained by fitting a calculated spreading factor in the form of Equation 5, based on linear velocity decay in the self-similar region, where $x_0$ and $K_2$ are the only variables. Note that $K_2$, the empirical jet spreading coefficient, is the inverse of $\alpha$, the jet spreading rate, discussed in 2.1.1.

$$F = \frac{D_p K_2}{l - x_0}$$

**Equation 5 (White)**

The best fit over the range of data from the exit to the location 33 diameters downstream is the curve shown in the Figure with $x_0/D_p = -10$ and $K_2 = 11$. These values were chosen due to the best fit of the data over the entire curve. This virtual origin location differs slightly from the 7.41 $\pm$ 0.47 diameters determined in section 4.2.2. The virtual origin is only applicable to the self-similar region, generally assumed to be greater than about 10-15 diameters downstream. However, Table 4 shows the corresponding jet spreading coefficient that is the best fit for each possible virtual origin and some of these are plotted in Figure 27.

**Table 4 Virtual Origins and Jet Spreading Coefficients**

| *Possible $X_0/D_p$* | *-4* | *-5* | *-6* | *-7* | *-8* | *-9* | *-10* |
|---|---|---|---|---|---|---|---|
| *Corresponding $K_2$* | *9.5* | *9.5* | *10* | *10.5* | *10.5* | *11* | *11* |

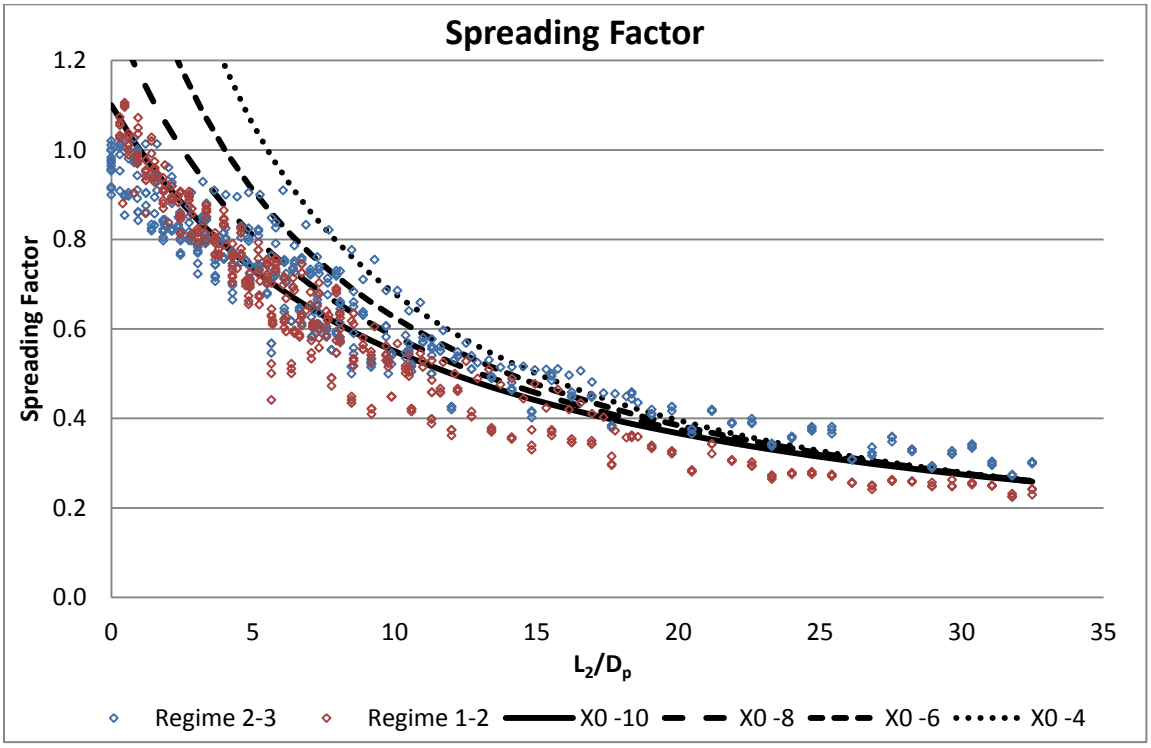


**Figure 27 Spreading Factor Data For Various $X_0$**

## 5.6 Usability in the Caverns

The jet flow in the cavern can be modeled as a free flow as long as the edge effects are not significant. A good approximation of when edge effects become significant is when the downward flowing velocity is equal to the upward flowing velocity, thus by conservation of energy, having equivalent cross sectional areas. This occurs when the jet radius is equal the cavern radius divided by .the square root of 2 (0.707). Using the approximate dimensions of the cavern (100 feet radius and 2000 feet height) this would occur when the jet radius is 70.7 feet. Therefore using Equation 1, the concept of the uniform jet spreading, an empirical jet spreading coefficient of 11, using a 10 inch fill pipe, and a virtual origin located 10 diameters upstream of the pipe exit, the depth of the cavern that can be modeled as free flow can be calculated.

$$b(x) = \frac{1}{K_2}(x - \frac{x_0}{D_p}D_p)$$

$$70.7' = \frac{1}{11}(x - (-10 * 0.83') \therefore x \sim 770'$$

Then approximately only the top 1/3 of the cavern can be modeled as a free flow, assuming the pipe is near the top of the cavern. After that the edges play a role in the flow pattern as well as the mingling characteristics. However during the filling process it is possible that edge effects are not significant until the jet actually reaches the edges of the cavern. This would occur at a depth of approximately 1017 feet and therefore the top ½ of the cavern could be analyzed as a free flow.

# 6 Conclusions

Experiments were performed to investigate the effects of jet spreading on phase mingling at a sharp density interface by downward directed, laminar and turbulent, silicone oil jets. In these experiments jet diameter, flow rate, and separation from the interface were individually varied. Two different silicone oils of differing viscosity were used to form laminar and turbulent exit conditions.

The effects of separation from the interface were quantified. The important results are as follows:

1. The interaction of the jet with the interface falls into distinct regimes that are governed almost entirely by the jet exit Richardson number, defined using the parameters at the jet exit, and distance from the interface.
2. Alternatively, transitions can be based on a critical interface Richardson number, which is based on properties of the jet as it reaches the sharp density interface. The critical transition for regime 1-2 occurs at $Ri_i = 3$ and for regime 2-3 occurs at $Ri_i = 1$
3. The interface Richardson number is related to the jet exit Richardson number by a jet spreading factor, defined as the characteristic centerline velocity divided by the velocity at the pipe exit. Based on conservation of momentum, the interface Richardson number varies inversely with the cube of the spreading factor, or $Ri_i = Ri_p/F^3$. This jet spreading factor was empirically determined for turbulent jets (see Figure 26).
4. For turbulent jets, a curve fit to the experimental data for the jet spreading factor closely matches the classical decay of a self-similar jet with a virtual origin located 10 diameters upstream of the exit and an empirical jet spreading coefficient of 11. The fitted curve is valid from the pipe exit to a distance of about 35 diameters downstream of the pipe exit or $F = 11D_p/(1-(-10\ D_p))$.
5. Laminar jets spread with a higher spreading factor (closer to unity), indicating that the jet spreads more slowly. This results in reducing the effect of separation from the interface on the transition.

These results are limited to cases where there is no interference from the edges of the test chamber. In the case of the research application, recirculation and filling of the strategic petroleum reserves, this free flow analysis is only valid for the top ½ of the caverns at a maximum. Further research could include a tank setup more to the scaling of the caverns, this would allow the study of the edge effects on phase mingling deeper into the cavern. This research does however provide a good basis as a control for the flow rate when filling the new tanks to prevent phase mingling when the fluid interface is near the top.

## 11.3 Application to SPR

Experiments were conducted at UMass – Dartmouth to quantify the behavior of a downward-directed turbulent oil jet impinging on the interface separating two immiscible fluids such as the oil-brine interface in an SPR cavern. The transition between various flow regimes, which indicate the potential amount of mixing between the two layers, has been quantified as a function of the jet exit Richardson number and the dimensionless distance from the interface.

For SPR, a typical jet exit Richardson number is 0.07 based on a pipe ID of 9.75 inches, an outlet velocity of 12.5 ft/s, and oil and brine specific gravities of 0.85 and 1.2, respectively. Based on this value, and the correlation equations presented in Figure 11-5 (also given earlier), the distances for Flow Regime transitions 1-2 and 2-3 are 19 ft and 16.5 ft, respectively. Therefore, if the distance from the pipe exit to the interface is greater than 20 ft, no mixing between the downward-directed oil jet and the underlying brine is expected.

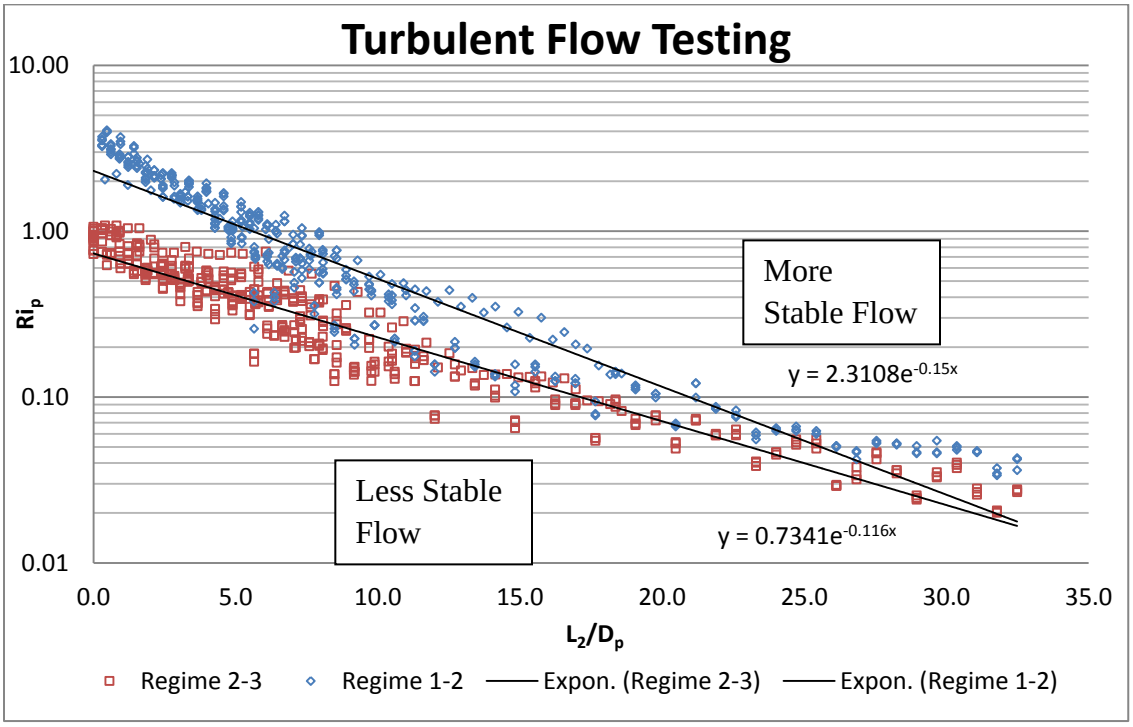


**Figure 11-5. Combined Ri vs. Separation Data**

# 12 Selective Withdrawal

Selective withdrawal, or the withdrawal of fluid from a layered fluid system, has been widely studied. Situations include the withdrawal of fluid from a certain level in a water reservoir for water quality reasons. For SPR, there are two application situations 1) withdrawal of oil with the withdrawal pipe just above the oil-brine interface, and 2) withdrawal of brine with the pipe just below the oil-brine interface. In both cases, when the withdrawal rate reaches or exceeds a critical value, fluid will be withdrawn both from the target layer but also from the other layer.

## 12.1 Oil Withdrawal

Webb (2003) looked at the generic problem of selective withdrawal and evaluated the critical withdrawal rate for typical SPR conditions for oil withdrawal near the oil-brine interface as given in the rest of this section.

### 12.1.1 Turner Correlation

Turner (1973) summarizes results for selective withdrawal in a two-layer system such as SPR. As shown in Figure 12-1, for a withdrawal location in the upper layer (oil), the critical Froude number for incipient withdrawal of fluid from the lower (brine) layer for a large tube above the interface is

$$F_{crit} = 4.5\left(\frac{D}{h}\right)^{1/2}$$

where

$$F_{crit} = \frac{Q}{g'^{1/2}\, h^{5/2}}$$

$$g' = g\,\frac{\rho_{lower} - \rho_{upper}}{\rho_{lower}}$$

and Q is the volumetric outlet flow rate, D is the outlet pipe diameter, and h is the height of the outlet above the undisturbed interface as developed by Rouse (1956).

Rearranging the above equations gives the critical withdrawal rate as a function of geometry and fluid conditions, or

$$Q = 4.5\, g'^{1/2}\, h^{2}\, D^{1/2}$$

or the critical height as

$$h = \left( \frac{Q}{4.5 g'^{1/2} D^{1/2}} \right)^{1/2}$$

For typical SPR conditions of a withdrawal rate of 100,000 bbl/day, an outlet pipe inner diameter of 9 ¾ inches, and oil and brine with specific gravities of 0.85 and 1.20, respectively, the critical height is about 0.72 ft.

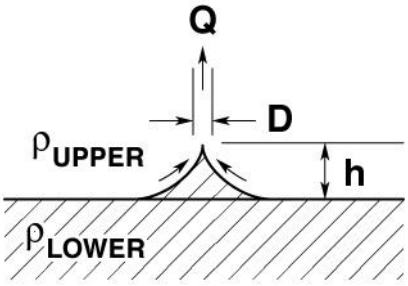


**Figure 12-1. Schematic of Selective Withdrawal (after Turner, 1973)**

While these results are interesting, certain fluid parameters that are obviously important, such as the surface tension and the fluid viscosities, are not included in the above relationship. Lister (1989) performed a more recent analysis considering surface tension effects. His analysis assumes equal fluid viscosities. The case of unequal fluid viscosities is discussed and justified based on the experimental data of Blake and Ivey (1986) that suggests the results are only weakly dependent on the viscosity ratio of the fluids. Lister's results are presented in terms of a stability diagram with coordinates $Q_L$ and $\Gamma$ (capillary number), which are defined as

$$Q_L = \frac{Q\mu}{\rho_{lower} g' h^4}$$

$$\Gamma = \frac{\sigma}{\rho_{lower} g' h^2}$$

The stability diagram is shown in Figure 12-2. Unfortunately, the relationships can't be solved directly for h. Assuming a surface tension of 50 dynes/cm, a fluid viscosity of 10 centistokes, and a height of 1 ft, the dimensionless parameters are

$$Q_L = 5.\text{x}10^{-5};\ \Gamma = 1.6\text{x}10^{-4} \rightarrow \Gamma^{1/2} = 0.0125$$

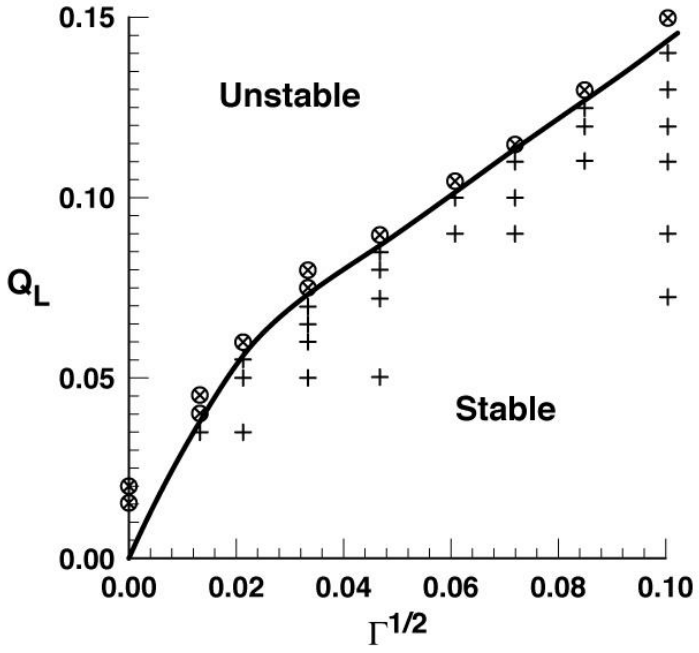


**Figure 12-2. Stability Diagram (after Lister, 1989)**

From Figure 12-2, the 1 ft height is very stable such that there will be no flow of the underlying brine through the outlet similar to the previous results.

### 12.1.2 FLUENT Results

The above analyses are for infinite lateral dimension fluids. In the case of SPR, the fluids are confined by the cavern walls. Preliminary simulations were performed for oil over water using the two-phase Volume of Fluids (VOF) formulation in FLUENT for a uniform cavern radius of 100 ft, a water depth of 100 ft, and a 1 ft radius outlet pipe 20 feet above the oil-water interface. For an outlet flow rate of 500,000 bbl/day, which is 5 times higher than expected, the deflection of the oil-water interface toward the outlet pipe is less than 1 foot compared to no flow conditions, confirming the results of the two models discussed above.

### 12.1.3 Application to SPR

The problem of selective withdrawal of oil in an oil-brine layer system was analyzed for typical SPR conditions. The correlation of Rouse (1956) (as presented by Turner, 1973), the model of Lister (1989), and FLUENT calculations were performed. The above analyses confirm that withdrawal of brine through a hanging string in the oil is unlikely even if the outlet is located within 1 foot of the oil-brine interface.

## 12.2 Brine Withdrawal

Lab-scale experiments for selective withdrawal in the brine layer were conducted by Hartenberger and O'Hern (2011). As mentioned by Hartenberger and O'Hern (2011), Turner (1973) has presented a situation similar to this condition where fluid is withdrawn from the lower layer of a layer system through an orifice in the bottom of the vessel with a critical Froude number of 1.6. For typical SPR conditions as given earlier, the critical height is 0.34 m, or about 1.1 ft. The brine withdrawal string must be a minimum of 1.1 ft below the oil-brine interface to prevent oil being drawn into the brine string. In this situation, the fluid from the bottom layer only flows from locations higher than the withdrawal location. In SPR, the bottom layer is deep, and fluid flows from locations much deeper than the withdrawal location. A much higher critical Froude number is expected for SPR than the situation presented by Turner (1973). Therefore, lab-scale experiments were conducted to determine the critical Froude number for the SPR configuration.

A summary of the experiments and application to SPR by Lord (2011) is given below with minor editing. Note that a couple of figures are not included in this summary due to copyright issues.

### Executive Summary

Laboratory-scale experiments were conducted at Sandia National Laboratories in order to determine the critical flowrates and offset distances allowable for selective fluid withdrawal from an oil-brine fluid system containing a hanging string near the oil-brine interface. This system has direct application to the U.S. Strategic Petroleum Reserve during final oil fill when the oil-brine interface is near the end of the brine string and runs the risk of overfill and subsequent oil contamination of the brine handling system. The laboratory experiments comprised a layered system with silicone oil on top and calcium chloride brine or fresh water underneath. Brine was withdrawn from a hanging string positioned at measured distances from the oil-brine interface to include conditions where the oil was entrained. Critical submergence depth "$S_{crit}$" was measured for the onset of light-layer entrainment over a range of geometries, fluid pairs, and flowrates. The results were non-dimensionalized and found to correspond to a critical Froude number of $F_{crit}$ = 5.5 to 16 for Reynolds numbers (Re) greater than 30,000. The Froude number represents a ratio of inertial to buoyancy forces, and when the ratio is sufficiently high, onset of entrainment is possible. In the current synopsis, the laboratory findings were scaled to SPR typical operating conditions and a range of critical submergence depths were calculated for oil injection/brine withdrawal scenarios, and were found to be a half foot or less. The standard offset distance between the oil-brine interface and end of hanging string required at SPR is currently 10 feet, or about (10 ft ÷ 0.5 ft) = 20 times further than required to protect against entrainment due to liquid inertia during brine withdrawal. In light of the many factors contributing to the uncertainty in actual distance between the end of hanging string and oil-brine interface in an SPR cavern (wireline measurement uncertainty, creep closure, salt falls, hanging string failure), this current

safety factor is appropriate and no change from the 10-foot offset is recommended as a result of this work.

### 12.2.1 Problem Statement

Oil fill at SPR runs the risk of oil entrainment in the brine string as the oil-brine interface descends to near the end of the hanging string due to a number of factors, which include uncertainty in the submergence depth "S" of the hanging string in the oil, as well as the depth over which oil may cone down and become entrained in the brine due to the balance between inertial and buoyancy forces. A conceptual drawing of an SPR cavern in oil fill mode is shown in Figure 12-3. As oil is injected and brine is withdrawn and the oil-brine interface approaches the end of the hanging string, a cone of depression may develop as shown in Hartenberger and O'Hern (2011).

The work presented by Hartenberger and O'Hern (2011) sought to determine the critical submergence depth $S_{crit}$ marking onset of entrainment associated with a variety of withdrawal configurations. The data were then non-dimensionalized to find an associated critical Froude number.

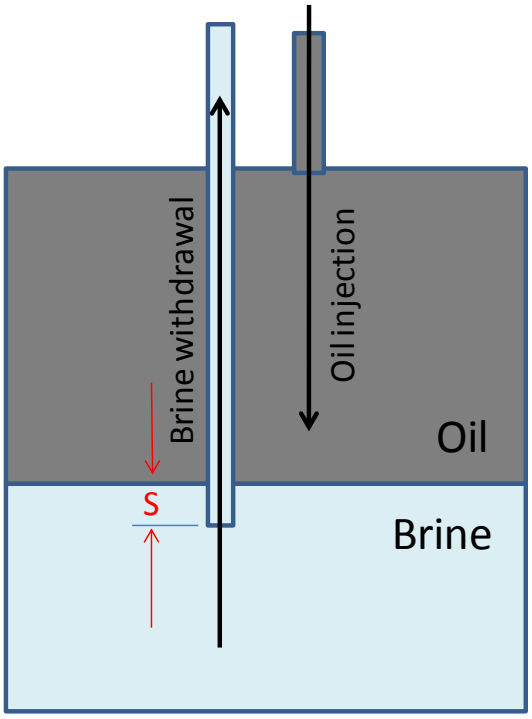


**Figure 12-3. Conceptual drawing of an SPR cavern showing oil fill and concurrent brine withdrawal. "S" is the submergence depth of the hanging string in the brine.**

### 12.2.2 Discussion

The laboratory work comprised over 350 experimental trials, varying liquid pairings, pipe geometry, and flowrate. For each trial, brine or fresh water was drawn up the pipe while the pipe position was slowly raised toward the oil-brine interface until oil entrainment was observed, and a critical submergence depth $S_{crit}$ was noted. The data were non-dimensionalized and plotted as critical Froude number against Reynolds number as shown in Hartenberger and O'Hern (2011). The data generally collapse around $F_{crit} \sim 16$ for Re > 30,000 for the standard pipe hanging down configuration and $F_{crit} \sim 5.5$ for the pipe pointing up secondary configuration.

### 12.2.3 Application of Results to SPR

The critical Froude number utilized in Hartenberger and O'Hern is defined as:

$$F_{crit} = \frac{Q}{\left[\frac{g(\rho_1-\rho_2)}{\rho_1}S^5\right]^{0.5}} \quad \text{(Eq. 1)}$$

where Q is the volumetric flowrate, g is gravitational acceleration, ρ is fluid density, subscripts 1 and 2 denote the heaver and lighter fluids, respectively, and S is the submergence depth associated with the onset of entrainment. Eq. 1 may be rearranged and solved for S for given conditions of known $F_{crit}$, Q, $\rho_1$, and $\rho_2$:

$$S = \left[\left(\frac{Q}{F_{crit}}\right)^2\left(\frac{\rho_1}{g(\rho_1-\rho_2)}\right)\right]^{1/5} \quad \text{(Eq. 2)}$$

Typical parameter values for an SPR oil fill scenario are given in Table 12-1 in both oilfield and SI units. These values were then used to compute $Re=\rho Ud/\mu$ and $S_{crit}$ for 12,000 – 96,000 bbl/d brine production, which are summarized in Table 12-1. Note Re for SPR cases shown here ranges from 100,000-1,000,000, which corresponds well with the region where $F_{crit}$ ~ 16 for the downward-facing tube and ~5.5 for the upward facing tube.

**Table 12-1. Typical parameters for SPR oil fill configuration**

| Parameter description | Value | Units | Value | Units |
|---|---|---|---|---|
| Hanging string inner diameter | 9.85 | In | 0.250 | m |
| Brine density ($\rho_1$) | 1.2 | g/cc | 1200 | $kg/m^3$ |
| Oil density ($\rho_2$) | 0.85 | g/cc | 850 | $kg/m^3$ |
| Volumetric flowrate - low end | 12,000 | bbl/d | 0.022 | $m^3/s$ |
| Volumetric flowrate - high end | 96,000 | bbl/d | 0.177 | $m^3/s$ |
| Brine absolute viscosity ($\mu_1$) | 1 | cP | 0.001 | Pa·s |

The downward facing tube (Figure 12.3) is geometrically more representative of the SPR configuration, but the tube itself may affect the experiment, which could be significant in the small scale experiment, but probably negligible for SPR. Therefore, using $F_{crit} \sim 5.5$ applicable to the upward facing tube experiment may be more appropriate in the limit of negligible tube effects. Both values of $F_{crit} = 5.5$ and 16 are used here to illustrate the range of effects.

Computed $S_{crit}$ values for $F_{crit} = 16$ are summarized in Table 12-2, and shown graphically for $F_{crit} = 5.5$ and 16 in Figure 12-4. Critical submergence depth thus ranges from ~0.2-0.7 ft according this analysis, indicating that oil entrainment is unlikely to occur as long as the pipe extends into the brine by more than 0.7 feet.

**Table 12-2. *Re* and $S_{crit}$ calculated for typical SPR oil fill conditions with $F_{crit}$ = 16.**

| GIVEN | | | | COMPUTED | | |
|---|---|---|---|---|---|---|
| Q | Q | U | $F_{crit}$ | Re | Scrit | Scrit |
| [b/d] | [$m^3$/s] | [m/s] | [-] | [-] | [m] | [ft] |
| 12,000 | 0.022 | 0.449 | 16 | 1.35E+05 | 0.06 | 0.19 |
| 24,000 | 0.044 | 0.898 | 16 | 2.69E+05 | 0.08 | 0.25 |
| 36,000 | 0.066 | 1.346 | 16 | 4.04E+05 | 0.09 | 0.30 |
| 48,000 | 0.088 | 1.795 | 16 | 5.39E+05 | 0.10 | 0.33 |
| 60,000 | 0.110 | 2.244 | 16 | 6.74E+05 | 0.11 | 0.36 |
| 72,000 | 0.132 | 2.693 | 16 | 8.08E+05 | 0.12 | 0.39 |
| 84,000 | 0.154 | 3.142 | 16 | 9.43E+05 | 0.13 | 0.41 |
| 96,000 | 0.177 | 3.590 | 16 | 1.08E+06 | 0.13 | 0.44 |

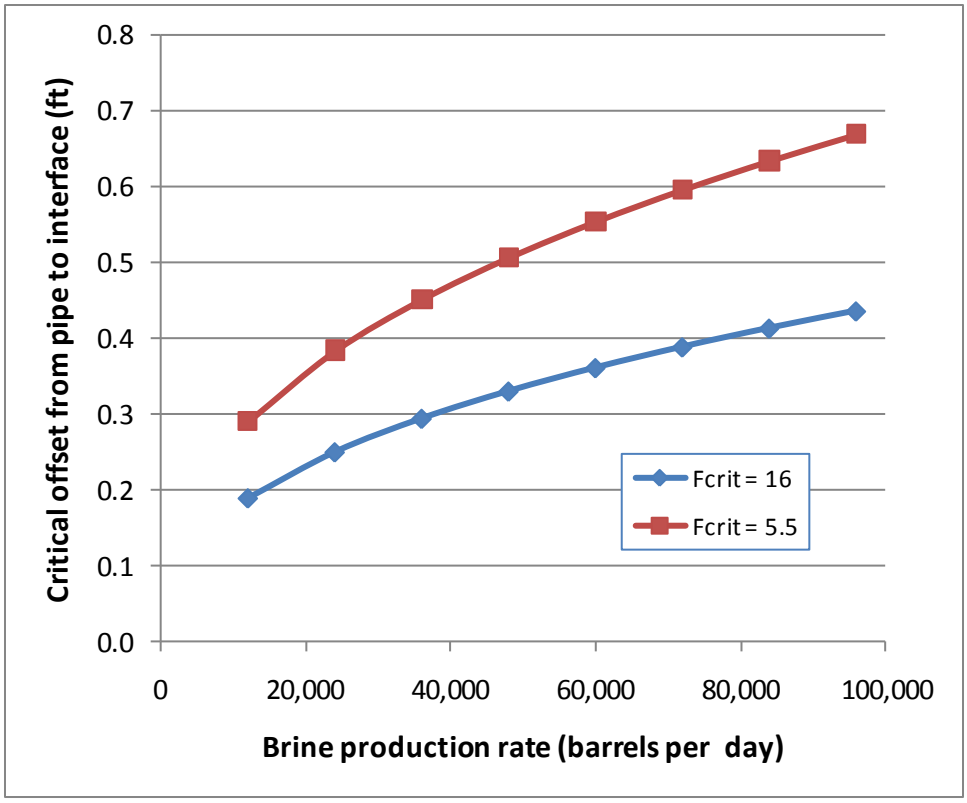


**Figure 12-4. Critical offset from pipe to interface for typical SPR configuration calculated from two values of critical Froude number ($F_{crit}$ = 5.5 and 16).**

Note current SPR practice is to bring the oil-brine interface no closer than 10 feet from the end of the hanging string. It is therefore unlikely that the local cone of depression caused by the balance between fluid inertia and buoyancy forces during a brine withdrawal will lead to unexpected oil entrainment. From an SPR operations standpoint, uncertainty in the actual offset "S" between the end of the hanging string and the oil-brine interface is on the order of several feet, hence several times larger than the critical S determined from the Froude number. This implies that there are a number of factors more likely to lead to oil entrainment in the brine than the fluid inertia near the end of the pipe Such factors include uncertainty in depth measurements as well as cavern creep closure and salt falls that change cavern geometry and may sever the hanging string.

## Sensitivity to fluid densities

$F_{crit}$ and $S_{crit}$ are functions of the ratio of inertial to buoyancy forces. Varying flowrate in the prior section demonstrated the system sensitivity to inertial forces with constant buoyancy forces. Table 12-3 below demonstrates the system sensitivity to buoyancy forces by changing the oil density. Note typical SPR oil density is around 850 kg/m$^3$, but can vary from about 800-900 kg/m$^3$. The heavier phase was assumed to be saturated brine at 1200 kg/m$^3$. Very little sensitivity to $\rho_2$ was observed here, with $S_{crit}$ varying by only several hundredths of a foot.

**Table 12-3. $S_{crit}$ calculated for a range of oil densities for $F_{crit}$ = 5.5 and 16. Q was fixed at 48,000 bbl/d and brine density $\rho_1$ = 1200 kg/m$^3$.**

| | $F_{crit}$ = 5.5 | $F_{crit}$ = 16 |
|---|---|---|
| $\rho_2$ | $S_{crit}$ | $S_{crit}$ |
| [kg/m$^3$] | [ft] | [ft] |
| 800 | 0.50 | 0.32 |
| 811 | 0.50 | 0.33 |
| 822 | 0.50 | 0.33 |
| 833 | 0.50 | 0.33 |
| 844 | 0.51 | 0.33 |
| 856 | 0.51 | 0.33 |
| 867 | 0.51 | 0.34 |
| 878 | 0.52 | 0.34 |
| 889 | 0.52 | 0.34 |
| 900 | 0.53 | 0.34 |

# 13 **Immiscible jet mixing**

O'Hern et al. (2003, 2004) conducted lab-scale experiments at Sandia National Laboratories for oil injection into brine. The experiments conducted by O'Hern et al. (2003) used simulant fluids (silicon oil and sodium-nitrate brine). Image-processing techniques are applied to quantify the penetration depth of the oil jet, the width of the buoyant plume, and the interface deflection. The experiments conducted by O'Hern et al. (2004) used real SPR fluids including the sludge layer.

These experiments were performed to investigate oil injection into brine for the Strategic Petroleum Reserve (SPR) after degassing of the resident oil at the surface as depicted in Figure 13-1. The present approach for returning the degassed oil to the cavern involves cutting off a part of the brine pipe in the oil layer, pumping the degassed oil back through this shortened pipe in the oil-filled region, and replacing the shortened pipe with a new full-length pipe into the brine layer. Considerable time and expense could be saved if the oil could be injected without modifying the brine pipe. However, this new approach involves injecting the oil below the oil-brine interface and allowing the oil to float up through the brine. One concern involves the degree of emulsification that occurs during this process, including the thickness and properties of the oil-brine layer that forms at the boundary between the oil and brine regions. A critical issue of the proposed process is whether the oil and brine form a stable emulsion at the oil-brine interface after the oil droplets rise through the more dense brine and reach the interface.

These experiments will only be summarized in this section because there are full SAND reports available.

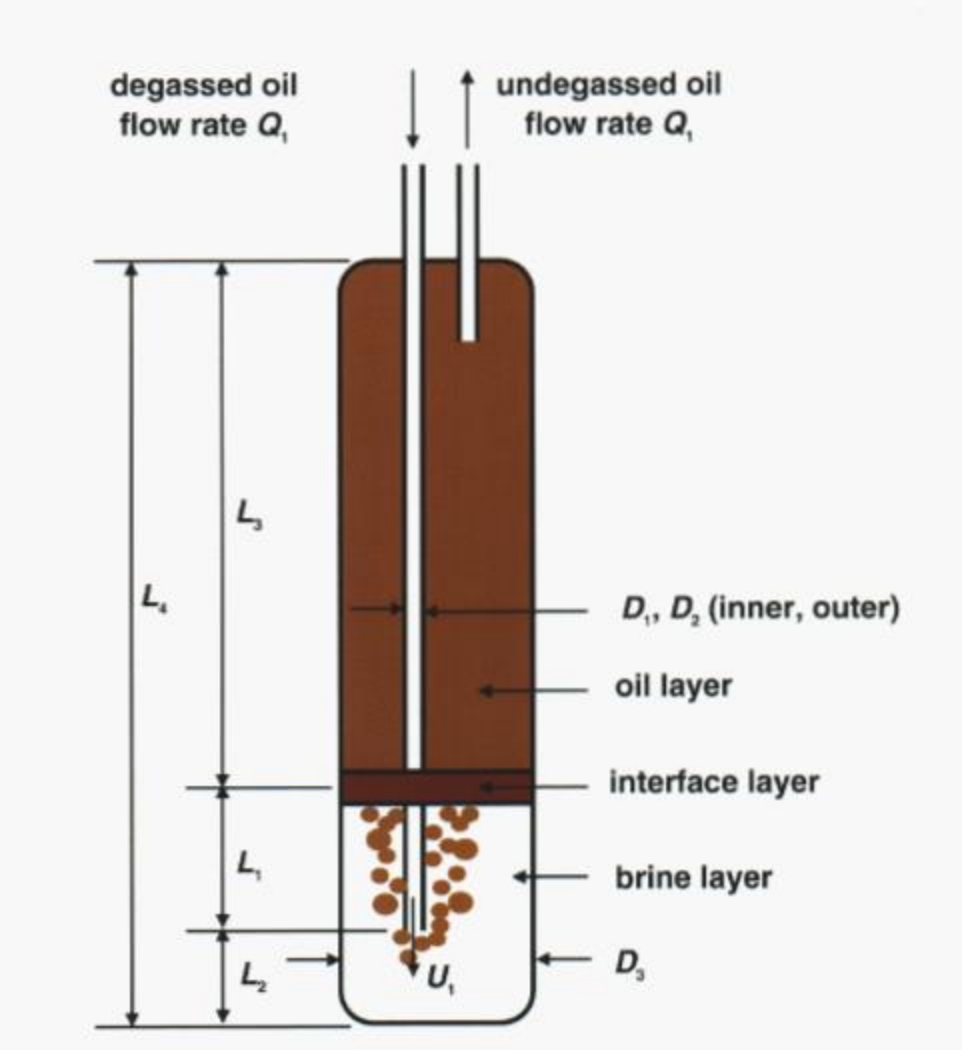


**Figure 13-1. Schematic for Proposed New Approach for Oil Reintroduction to Cavern**

## 13.1 Experiments with Simulant Fluids

Details are given in O'Hern et al., 2003. Excerpts from O'Hern et al. (2003) are given below.

An experiment has been performed to investigate oil injection into brine for the Strategic Petroleum Reserve (SPR). The goal is to investigate a new approach to oil reintroduction in SPR. Oil in an SPR cavern must be periodically brought to the surface for degassing. The present approach for returning the degassed oil to the cavern involves cutting off a substantial length of the brine pipe so that it terminates well above the oil-brine interface, pumping the degassed oil back through this shortened pipe so that it reenters the oil-filled region of the cavern, removing the shortened brine pipe, and installing a new full-length brine pipe. Considerable time and expense could be saved if the oil could be injected without modifying the brine pipe. However, this new approach involves injecting the oil below the oil-brine interface and allowing the oil to float up through the brine. One concern involves the degree of emulsification that occurs during this process, including the thickness and properties of the oil-brine layer that forms at the boundary between the oil and brine regions.

A critical issue of the proposed process is whether the oil and brine form a stable emulsion at the oil-brine interface after the oil droplets rise through the more dense brine and reach the interface. The experiment is a scale-model flow system (1:10 and 1:20 scale) that maintains the same ratio of buoyancy to momentum as in SPR caverns. The experiment uses silicon oil (Dow Corning 200® Fluid, 5 cSt) and a sodium nitrate solution to simulate the crude oil and brine (saturated sodium chloride solution) in SPR caverns. Image-processing techniques are applied to quantify the penetration depth of the oil jet, the width of the buoyant plume, and the interface deflection. The oil is injected downward through a tube into the brine at a prescribed depth below the oil-brine interface. Flow rates are determined by scaling to match the ratio of buoyancy to momentum between the experiment and the SPR. Initially, the momentum of the flow produces a downward jet of oil below the tube end. Subsequently, the oil breaks up into droplets due to shear forces, buoyancy dominates the flow, and a plume of oil droplets rises to the interface. The interface is deflected upward by the impinging oil-brine plume.

Two different diameter injection tubes were used (½-inch and 1-inch OD) to vary the scaling. Use of the 1-inch injection tube also assured that turbulent pipe flow was achieved, which was questionable for lower flow rates in the ½-inch tube. In addition, a ½-inch J-tube was used to direct the buoyant jet upwards rather than downwards to determine whether flow redirection could substantially reduce the oil-plume size and the oil-droplet residence time in the brine. Reductions of these quantities would inhibit emulsion formation by limiting the contact between the oil and the brine.

Videos of this flow were recorded for scaled flow rates that bracket the equivalent pumping rates in an SPR cavern. Image-processing analyses were performed to quantify the penetration depth of the oil jet, the width of the jet, and the deflection of the interface. The measured penetration

depths are shallow, as predicted by penetration-depth models, in agreement with the assumption that the flow is buoyancy-dominated, rather than momentum-dominated. The turbulent penetration depth model provided a good estimate of the measured values for the 1-inch injection tube but overpredicted the penetration depth for the ½-inch injection tube. Adding a virtual origin term would improve the prediction for the ½-inch tube for low to nominal injection flow rates but could not capture the rollover seen at high injection flow rates.

As expected, the J-tube yielded a much narrower plume because the flow was directed upward, unlike the downward-oriented straight-tube cases where the plume had to reverse direction, leading to a much wider effective plume area. Larger surface deflections were caused by the narrower plume emitted from the J-tube. Although velocity was not measured in these experiments, the video data showed that the J-tube plume was clearly faster than those emitted from the downward-oriented tubes. These results indicate that oil injection tube modifications could inhibit emulsion formation by reducing the amount of contact (both time and area) between the oil and the brine.

To support the development of these experiments, an analysis is performed to determine the scaling behavior of the flow. This flow is driven by the downward injection of a buoyant liquid (oil) into an immiscible liquid (brine). The following observations result from this analysis. The oil jet penetrates only a few pipe diameters downward (i.e., a very small distance with respect to cavern length scales) before buoyant forces overwhelm the jet momentum and turn the flow upward. Far from the injection point, the oil volumetric fraction becomes small, indicating that the flow field can be described approximately as a zero-momentum buoyant plume of a single liquid, with oil concentration analogous to temperature. Under this assumption, oil injection 50 feet below the brine layer produces a buoyant plume with a 10-foot diameter at the oil-brine interface, within which the maximum (centerline) oil volume fraction is about 0.03 (3%). Based on the turbulent shear stress of a buoyant plume, oil droplets with diameters in the millimeter range are expected close to the oil-brine interface.

### 13.1.1 Experimental Setup

The experiments were conducted in a 35-inch (0.89 m) diameter acrylic tank filled with a 12-inch (0.3 m) oil layer over a 78-inch (1.98 m) brine layer. The ½-inch string for oil injection is centered in the tank and terminates 24 inches below the oil-brine interface in a downward direction as shown in Figure 13-2. The experimental setup for the ½-inch J-Tube is similar except that the oil injection direction is upward rather than downward as shown in Figure 13-3.

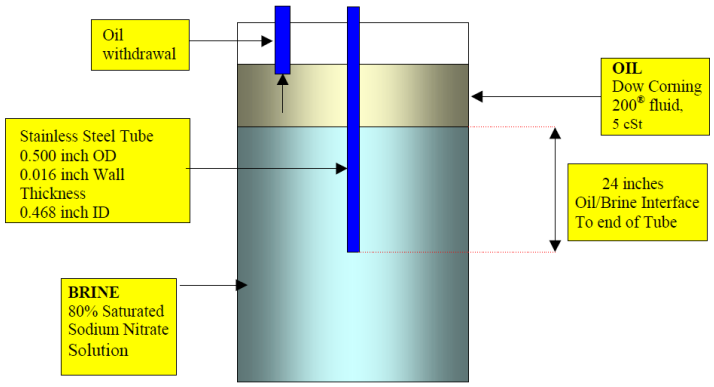


**Figure 13-2. Experimental Setup with ½-inch Straight Tube**

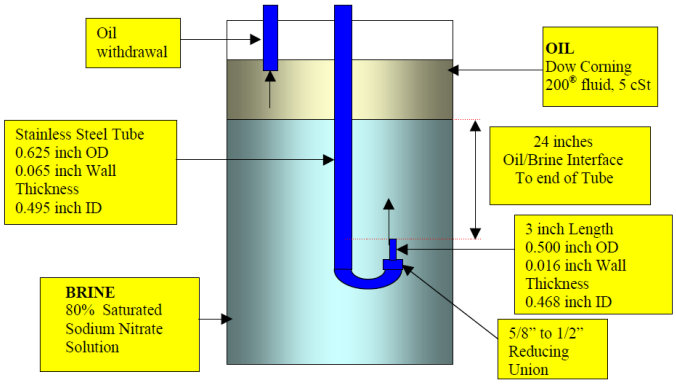


**Figure 13-3. Experimental Setup with ½-inch J-Tube**

The experimental setup for the1-inch straight tube is similar to the ½-inch straight tube except that the tube terminates 48 inches below the oil-brine interface rather than 24 inches below as shown in Figure 13-4.

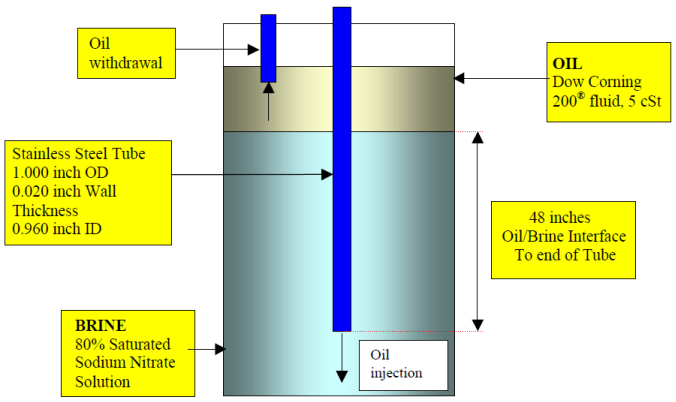


**Figure 13-4. Experimental Setup with 1-inch Straight Tube**

### 13.1.2 General Behavior

The oil injection behavior is shown in Figure 13-5 at the oil injection and at the oil-brine interface at the maximum velocity for each configuration. These views are split screen views showing the plume and interface simultaneously; there is a 24-inch section (1/2-inch tubes) or a 48-inch section (1-inch tube) of the vessel between the tube end and the interface not included in these images.

Figure 13-6 shows the normalized jet penetration depth (depth / pipe diameter) for the ½-inch straight tube, while Figure 13-7 shows the results for the 1-inch straight tube. In both cases, equation (1) on the figures is the original Turner (1966) correlation. Equation (2) is a simplified plume penetration model as discussed in O'Hern et al. (2003). The data are generally in agreement with the Turner (1966) correlation except at the higher flow rates for the ½-inch straight tube.

Note that as discussed by O'Hern et al. (2004), the normalized and scaled penetration depths for the 1-inch tube are too large by a factor of 1.92. Corrected data are shown in the next section.

Plume width and interface disturbance results are also discussed by O'Hern et al. (2003).

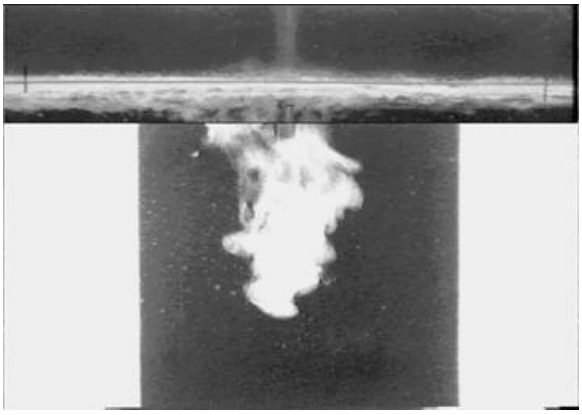

(a) ½-inch Straight Tube – 1.78 m/s

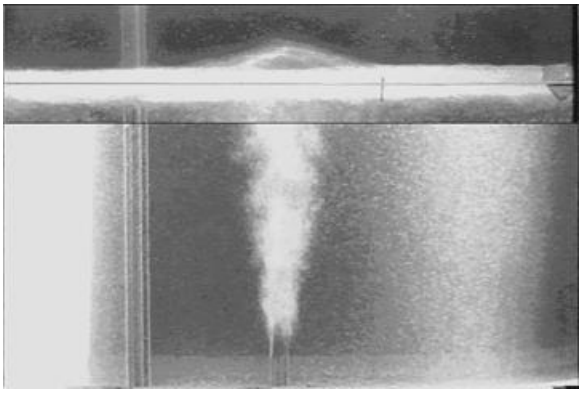

(b) ½-inch J-Tube – 1.76 m/s

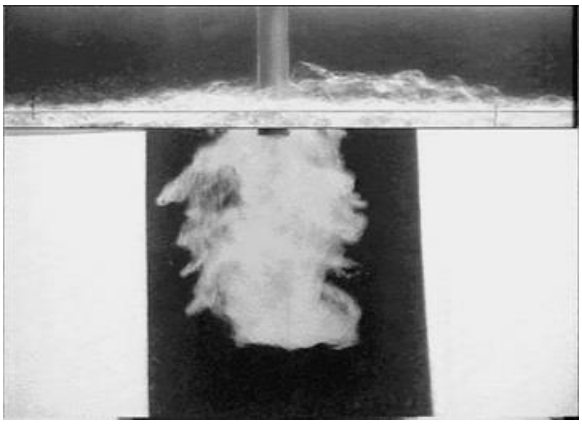

(c) 1-inch Straight Tube – 1.72 m/s

**Figure 13-5. Photographs of oil injection behavior**

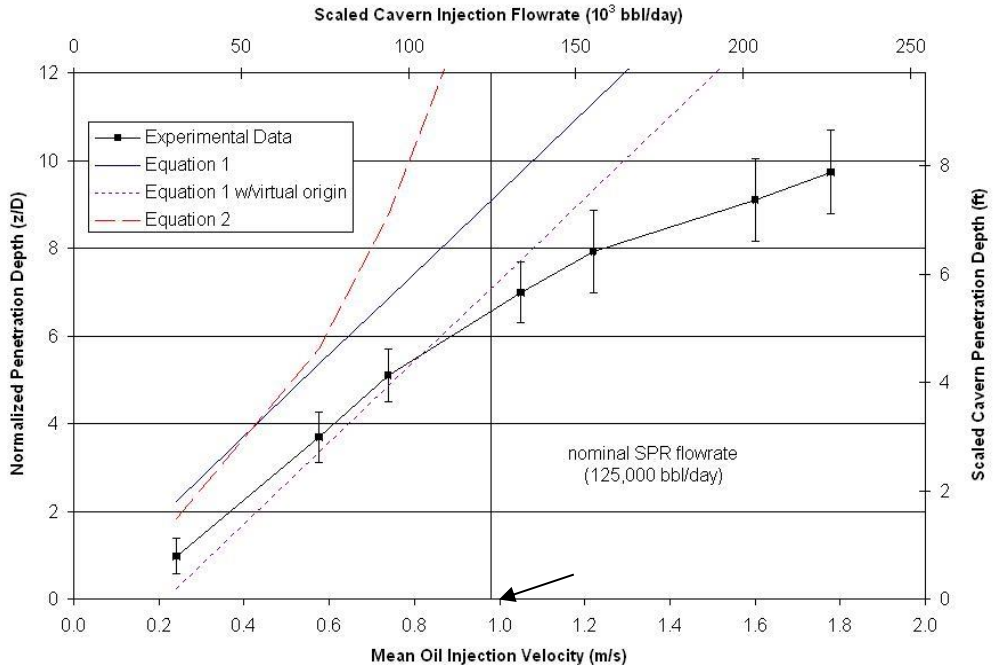


**Figure 13-6. Normalized Penetration depth as a function of oil flow rate for the ½-inch straight tube. Cavern flow rate and penetration depth are scaled from laboratory data. Bars indicate ± one standard deviation of the penetration depth.**

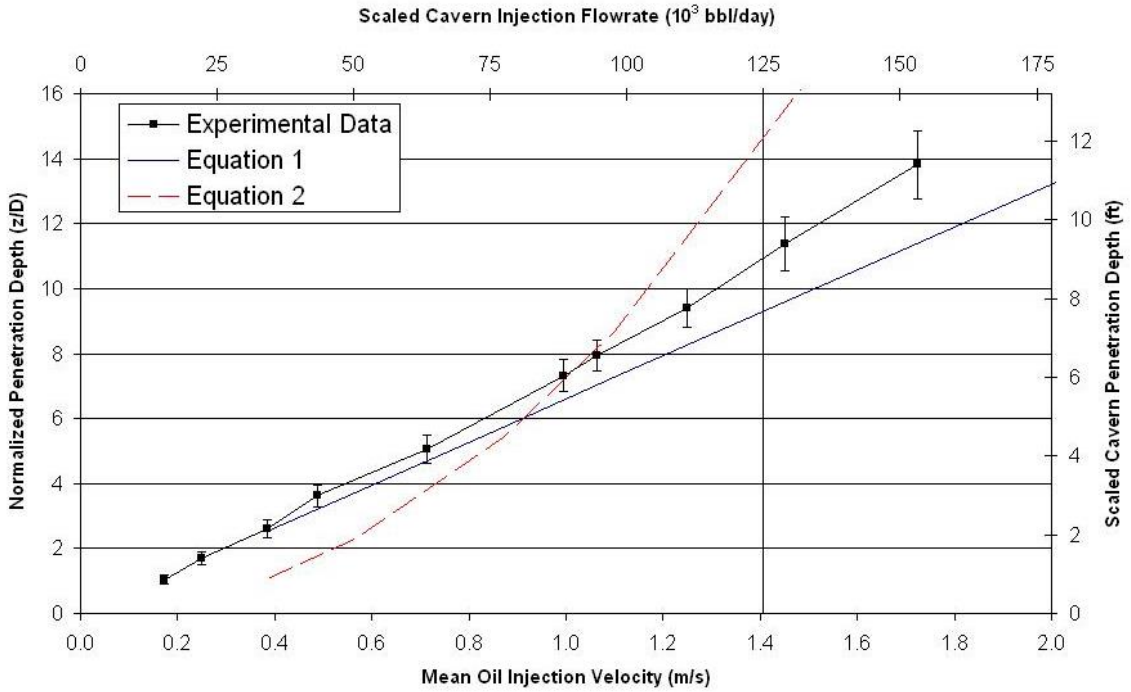


**Figure 13-7. Normalized Penetration Depth as a function of oil flow rate for the 1-inch straight tube. Bars indicate ± one standard deviation of the penetration depth. The data are too large by a factor of 1.92 as discussed in the text and in the next section.**

## 13.2 Experiments with SPR Fluids

Details are given in O'Hern et al., 2004. Excerpts from O'Hern et al. (2004) are given below.

O'Hern et al. (2004) conducted plume experiments similar to those for simulant fluids with acual SPR oil, brine and sludge using the 1-inch straight tube for injection.

### 13.2.1 Experimental Setup

The setup without sludge is shown in Figure 13-8. The oil and brine layer thickness as well as the injection tube depth are the same as for the simulant fluid experiments.

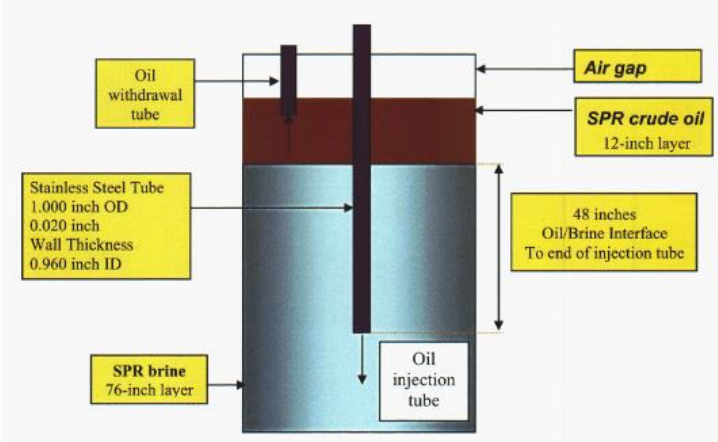


**Figure 13-8. Experimental Setup Using SPR Fluids Without Sludge**

The setup with sludge is shown in Figure 13-9. Note that the oil, brine, and submergence depths are all slightly different than the experiments without sludge.

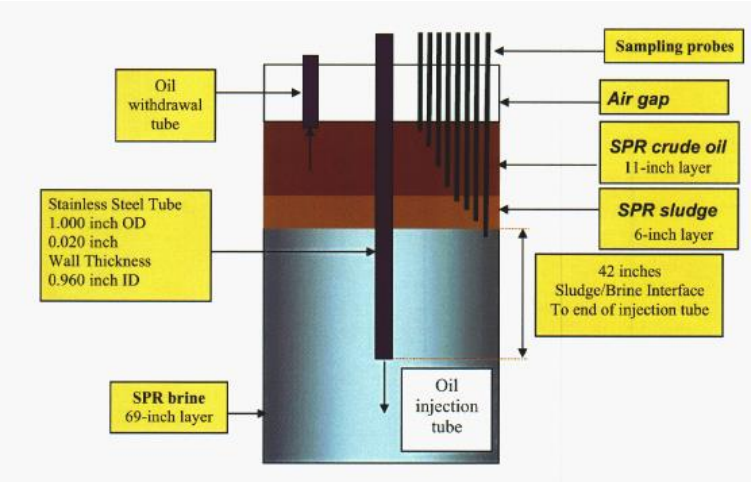


**Figure 13-9. Experimental Setup Using SPR Fluids With Sludge**

### 13.2.2 General Behavior

The crude oil injection plumes into the brine layer are shown in Figure 13-10 for the maximum velocities of the experiments. The plume shapes are similar with and without sludge.

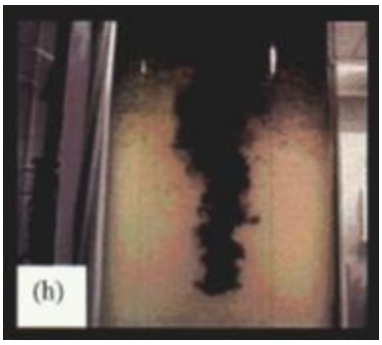


(a) Overall Oil Plume for 1.66 m/s Velocity Without Sludge

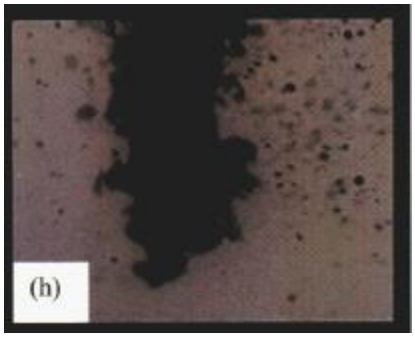


(b) Close-up of Oil Plume for 1.66 m/s Velocity Without Sludge

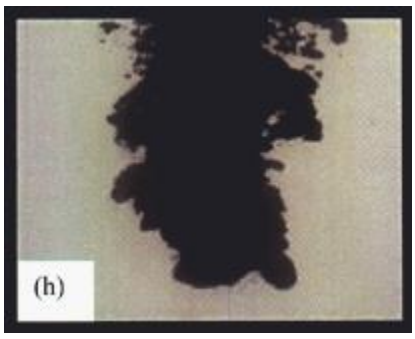


(c) Close-up of Oil Plume for 1.74 m/s Velocity With Sludge

**Figure 13-10. SPR Crude Oil Injection Plumes**

**Plume Hydrodynamics Experiments – General Observations**

The oil jet exiting the tube end breaks up into oil droplets as expected and as observed with the simulant fluids in O'Hern et al., (2003). However, a new phenomenon was observed with the real fluids: bubbles consisting of an oil shell surrounding brine were formed during this jet breakup process. Formation of such bubbles occurred especially strongly at the higher flow rates. The previous experiments with simulant fluids showed very few such bubbles being formed. Figure 13-11 shows photographs of some of these bubbles suspended in the brine during a run. After each run, these bubbles would rise to the interface, and the oil and brine would separate. A fairly wide range of bubble sizes on the order of 1 cm was observed, but the precise size distribution was not measured.

The formation of these bubbles was less pronounced in the presence of sludge. The bubbles often clumped together and rose to produce a foamy emulsion layer at the sludge-brine interface. This foamy layer was especially noticeable at higher injection flow rates.

**Interface Disturbance**

Previous experiments used transparent simulant fluids to allow measurement of the interface deflection caused by the rising oil (O'Hern et al., 2003). Similar measurements could obviously not be made with the opaque SPR fluids.

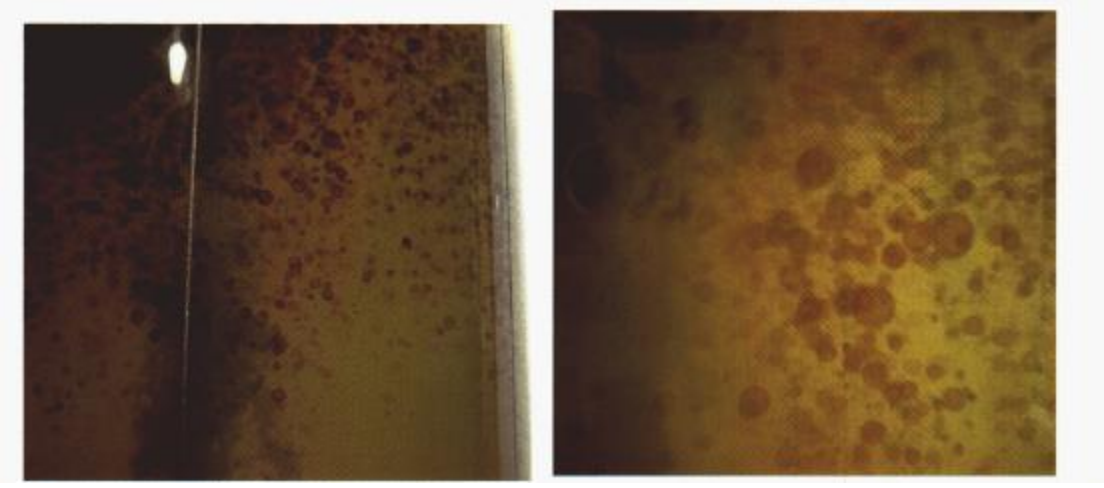

**Figure 13-11. Photographs of oil-brine bubbles**

## Jet Penetration

Figure 13-12 presents the jet penetration depth from the experiments. The jet penetration depth is typically about 5-10% longer than for the simulant fluids. The penetration-depth data in Figure 13-12 was normalized by the pipe diameter and scaled to cavern units. Unfortunately, an error in the normalization performed for the 1-inch line for the simulant fluids (O'Hern et al., 2003) was uncovered such that the depths for the 1-inch line are too large by a factor of 1.92. The corrected data are shown in Figure 13-12. Equation (1) in the plot is the original Turner (1966) correlation, which overpredicts the experimental data even if a virtual origin is added. Adding sludge to the flow system did not have a significant effect on the plume characteristics.

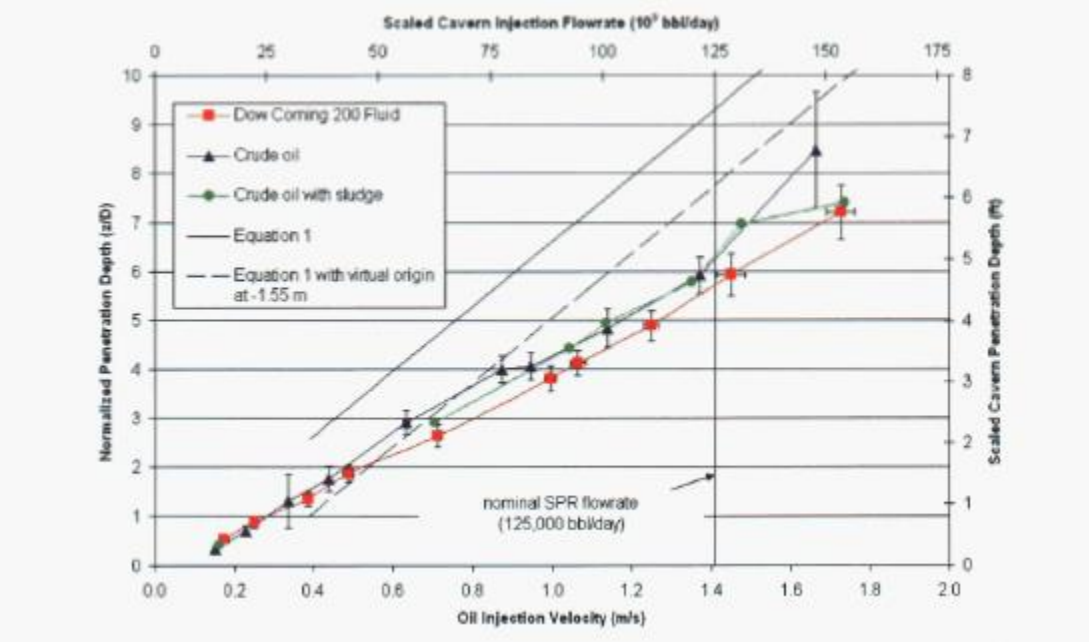


**Figure 13-12. Normalized Penetration Depth Results and Data-Model Comparison Including Corrected Data for Simulant Fluids**

Emulsification experiments and data were also obtained during these experiments through the sampling probes in the oil, sludge and brine layers. The results show that strong mixing caused the water content in the oil layer to increase sharply during oil injection but that the water content in the oil dropped back to less than 0.5% within 16 hours after injection was terminated. In contrast, the sludge and oil appeared to be well mixed, and the oil had not returned to the baseline value after 3 months. More details are given in O'Hern et al. (2004).

# 14 **Weeks Island**

In 1989, an investigation into brine-oil mixing in the near-horizontal Fill-hole drift at Weeks Island SPR site was initiated by Sandia National Laboratories in the Department of Petroleum Engineering at the Louisiana State University (LSU). In the Weeks Island configuration, brine was seeping into the Fill-hole drift that was used for oil injection into the mine. Mixing between the oil and the brine is important for oil quality.

Later it was discovered that brine was leaking into the mine from a sinkhole above Weeks Island, and the oil was pumped out of the mine and Weeks Island was decommissioned. In any event, these historical studies of brine-oil mixing including emulsion studies are of potential interest. These reports are in the SPR Library.

Modeling and experimental components were included. Five reports were completed including

Part 1: Literature Survey (Wojtaniwicz, A., 1989a)

Review of Turbulent mixing in immiscible flow, gravity segregation analysis, inclined drift hydrodynamics review, and proposed experiments.

Part 2: Design of the Laboratory Analog (Wojtaniwicz, A., 1989b)

Review of fill-hole hydrodynamics, inclined drift scaling, and experimental pressure calculations

Part 3: Laboratory Study of Crude Oil/Brine System Including Emulsions (Barton, D., 1990)

M.S. Thesis of David R. Barton, "An Experimental Investigation Into the Mixture Stability of Crude Oil and Brine within the Weeks Island Strategic Petroleum Reserve" including modeling and experimental data on oil-brine mixing and emulsion stability.

Part 4: Visual Analog Study of Fill-Hole Drift (Bourgoune, Jr., A.T., 1990)

Video of Weeks Island analog experiments conducted at LSU.

Part 5: Evaluation of Fill-hole Completions (Wojtaniwicz, A., 1991)

Simulation results for oil-brine transport including the M.S. Thesis of Mladen Ruzic, "Effect of Oil Injection Dynamics on Brine Movement in a Strategic Petroleum Reserve Storage Facility", a Project Report by Bernard M. Franklin, "Multiple Regression Model of Oil/Water Mixture in Weeks Island (SPR), and a Project Report by Murali Kadaveru, "Tank-in-Series Model for the Analysis of Brine Transport though the Inclined Drift".

No detailed review will be undertaken for this report because the geometry and conditions were specific to Weeks Island and do not exist elsewhere at SPR.

# 15 Discussion of SPR Data and Evaluation of Models

As in the main part of this report, this section will be split into miscible and immiscible sections.

## 15.1 Miscible Fluid Mixing

Miscible fluid mixing, such as water and brine mixing or the mixing of different oils, has been discussed above in the general context of SPR oil degasification in which a jet of degassed oil is injected into a cavern and undegassed oil is withdrawn from another location. Lord and Rudeen (2007) developed the simple degas cavern mixing model (SDM) to try to understand the various processes important during degas operations including ideal plug flow and complete and partial mixing models.

In the ideal plug flow model, the degassed oil that is introduced at the top of the cavern simply displaces the resident undegassed oil with little or no mixing. This situation is the most efficient for degas because all the oil is degassed in a single cavern volume. In the complete mixing model, the degassed oil mixes completely with the undegassed oil. In this scenario, degassing is not very efficient as previously degassed oil is processed a number of times. In the partial mixing model, the mixing is incomplete, and the behavior is between plug flow and complete mixing.

Based on data-model comparisons, the ideal plug flow and mixing models discussed above capture many of the features of cavern mixing. Perhaps the most useful feature of the ideal models is that they can set bounds for the expected performance of the real degas systems, with plug flow rendering the highest efficiency, and complete mixing rendering the lowest efficiency. However, an important limitation in the SDM is that it cannot predict when a change will occur or how a system will respond to changes in operational parameters like string configuration or pumping rates.

### 15.1.1 Literature Review

In order to understand the important physical processes occurring during degas and the state of predictive methods, a literature review was conducted for jet and plume mixing in uniform and stratified fluids including different jet and resident fluid densities. The quantitative behavior of the injected jet for unconfined flow has been discussed as a function of the Froude number, which includes the density difference between the injected oil and the resident oil, the injection velocity and the pipe diameter. The influence of stratification was also reviewed. Simple ODE entrainment models have been discussed to predict the jet and resident fluid behavior along with literature values for the entrainment coefficient. Entrainment across density interfaces, such as density interfaces in the oil layer, is also discussed. Integral models that describe the development of flow in open and closed volumes as well as the entrainment across density

interfaces are described. In general, these models are limited to container aspect ratio of about 1.0, which is much different than the SPR cavern dimensions.

A recently discovered study by Barnett (1991) investigated jet mixing in confined regions including a vertical circular cylinder very similar to the SPR cavern aspect ratio (H/D ~ 14.6). Barnett (1991) split the problem into 3 regions – a plume region, a mixing region, and a convective region. He developed a numerical model for the plume region based on the entrainment equations including the development of stratification. Models for the mixing and convective regions were also developed. In the mixing region, conservation of buoyancy equation was used to get buoyancy, which is uniform in mixing region, versus time. The convective region is simply convection with a constant eddy diffusivity. Data-model comparisons show encouraging results especially given the similar geometry to SPR caverns.

Other physical processes such as the Rayleigh-Taylor instability due to a heavier fluid over a lighter fluid in a confined geometry are discussed as well as the Coriolis force. As confirmed by the reviewed literature, fluid mixing by the Rayleigh-Taylor instability is rapid and essentially complete. The Coriolis force has been found to be negligible as expected.

There are obviously potential scaling issues regarding the application of lab-scale experiments and models to full-size SPR caverns. However, in most situations, the effects of scaling are thought to be minimal. Geometry scaling can be done, and dimensionless scaling for the buoyancy forces through the Froude number can be accomplished. The dimensionless number Reynolds number scaling can not be met, although as long as the Reynolds number is greater than about 10,000, turbulence is expected to be fully developed with similar behavior to larger Reynolds number values.

### 15.1.2 SNL Work

Computational fluid dynamics (CFD) simulations have also been performed to investigate the oil mixing processes in simplified SPR caverns. Depending on the conditions, the mixing results may follow the plug flow or the complete mixing limits outlined in the SDM developed by Lord and Rudeen (2007) or be in between these limits. Mixing due to various conditions was evaluated numerically.

A simplified Mixing Layers Model (MLM) was developed by Webb (2010) based on Rayleigh-Taylor instability that showed good comparison with SPR cavern degas data. This model could be combined with model for cavern oil mixing to predict cavern degas behavior.

Details of the jet / plume mixing behavior have been investigated at SNL for application to the leaching problem. O'Hern et al. (2005) conducted laboratory-scale experiments for water injected downward into brine where he looked at the plume dynamics and the resulting stratified flow along the top of the brine layer. Khalil and Webb (2006) performed detailed CFD

simulations of the processes involved. These details can not be included in any cavern model but they can be used to evaluate integral approaches.

### 15.1.3 Arizona State University

Preliminary jet mixing studies were performed at Arizona State University in 2009. The configuration consisted of a container with an aspect ratio similar to a simplified SPR geometry. A jet of water was introduced at the top of the container, which contained an initially water-brine stratified fluid. Fluid was withdrawn from the bottom of the container, and the salinity of the withdrawn fluid was measured.

This experiment would be very useful to quantify mixing across density layers from the inlet jet. Unfortunately, the initial density stratification in the container was only estimated, not measured, and the data for similar conditions show significantly different and unrealistic behavior. While these data may be qualitatively interesting, quantitative use is limited.

### 15.1.4 University of Notre Dame

Comprehensive jet mixing studies were performed at the University of Notre Dame. Experiments were conducted that detail the behavior of a confined jet. A neutral jet completely dissipates in a confined geometry at about 3.6 container diameters. Note that this value is similar to that given by Risso and Fabre (1997) as well as that of Barnett (1991), who came up with a value of 2.79. Detailed mean flow and turbulence information were also obtained. The experiments are summarized in Voropayev, et al., 2011.

Mixing between the jet and the resident fluid was also investigated for a uniform resident fluid using water and water-brine mixtures. Cases of a lighter and heavier density jet compared to the uniform resident fluid were experimentally investigated. A simple mathematical model was developed that compared well to the data. These results are given in Voropayev, et al., 2012.

The impact of the jet being off-center wall also investigated. For offsets from the center less than about 0.2 enclosure diameters, the jet behavior is similar to that of a center jet. For larger offsets, the jet behavior changes and the jet penetration depth increases. These results are given in Nath, et al., (2014).

Other studies looking at the combined effects of a jet with natural convection in the resident fluid and the pressure distribution in confined jet flow were also conducted.

### 15.1.5 Application to SPR Caverns

Miscible fluid mixing, such as water and brine mixing or the mixing of different oils, has been discussed above in the general context of SPR oil degasification in which a jet of degassed oil is injected into a cavern and undegassed oil is withdrawn from another location. The physical processes for mixing in confined regions due to jet mixing have been investigated and are understood.

A model for oil mixing in SPR caverns including the jet processes and oil stratification has not been fully developed. A potential approach is based on the simplified Mixing Layers Model (MLM) was developed by Webb (2010) based on Rayleigh-Taylor instability that showed good comparison with SPR cavern degas data. This model could be combined with an ODE model similar to that of Barnett (1991) to predict cavern degas behavior.

The general behavior should be able to be reasonably well modeled using the knowledge developed in this investigation. Various approaches to oil mixing behavior are available including the approach of Voropayev et al. (2012) as discussed in Chapter 10 of this report, the solution of ODE equations using the entrainment approach, and the 3-region model of Barnett (1991). These approaches should be able to predict oil mixing in SPR caverns.

## 15.2 Immiscible Fluid Mixing

Immiscible fluid mixing, or mixing between the oil and brine layers, may occur near the oil-brine interface.

A number of situations have been investigated including

- Oil and brine withdrawal near oil-brine interface, or selective withdrawal;
- Oil injection into brine layer; and
- Oil injection just above oil-brine interface.

as discussed below.

### 15.2.1 Sandia Labs

Selective withdrawal is of concern near the oil-brine interface. If the oil withdrawal pipe is located too close to the oil-brine interface, oil plus brine could be withdrawn into the pipe. Similarly, if the brine withdrawal pipe is located too close to the oil-brine interface, oil could be withdrawn in addition to the brine.

For the oil withdrawal scenario, the selective withdrawal correlation of Rouse (1956) as presented by Turner (1973) is appropriate. For typical SPR conditions, the pipe should be located 1 foot or more above the oil-brine interface.

For brine withdrawal, no applicable data exist for the SPR configuration. Therefore, laboratory-scale selective withdrawal experiments were conducted for a downward facing brine string. Experimental data were obtained for various liquids, flow rates, and geometries, which were correlated as a function of Froude number. From these data, the brine withdrawal pipe needs to be at least 0.5 ft below the oil-brine interface.

Oil-brine mixing has also been investigated for the case of oil degassing where the degassed oil is injected into the brine layer so the brine string does not need to be cut off and replaced. The general oil plume behavior is similar to the miscible behavior discussed in this report. Oil injection into brine leads to emulsion formation.

LSU also investigated oil injection into brine as part of a study of processes occurring in the Weeks Island mine. An oil-brine emulsion was also studied.

### 15.2.2 University of Massachusetts - Dartmouth

If oil is injected downward in the oil layer just above the oil-brine interface, the oil jet from the injection location may impact the oil-brine interface and cause entrainment of brine into the oil and possibly form an emulsion.

Simulant experiments performed at the University of Massachusetts – Dartmouth investigated this possibility. Various mixing flow regimes at the interface were identified, and laminar and turbulent flow experiments were conducted. The transition between mixing regimes was identified as a function of normalized distance from the pipe exit. A general correlation based on the Richardson number across the interface was developed for the mixing regime transitions. Based on typical SPR conditions, for downward oil injection, the pipe should be a minimum of about 20 feet above the oil-brine interface.

# 16 Recommendations for Future Work

## 16.1 Miscible

The work conducted at SNL, Arizona State University, and the University of Notre Dame has formed a good base of knowledge about oil mixing in SPR caverns. As discussed below, there are still a few items that need to be addressed, but the knowledge gained to date can be used to evaluate oil mixing due to jets.

The prediction of degas performance, and modification of degas operations as a result, can have a significant impact on SPR operations. For example, it may be possible to change some of the degas parameters and change degas performance from complete mixing to plug flow.

In order to accomplish this goal, development of a degas simulation program similar to CaveMan (Hart, 2014; Ehgartner, 2004) is proposed. Various approaches to oil mixing behavior are available including the approach of Voropayev et al. (2012) as discussed in Chapter 10 of this report, the solution of ODE equations using the entrainment approach, and the 3-region model of Barnett (1991). These approaches combined with a model for oil property changes that occur in the degas plant could be used to predict degas performance, which could be compared to actual degas data from various caverns.

Additional lab-scale jet mixing data similar to the experiments used by Voropayev et al. (2012) could be obtained for additional validation of any of these approaches with initial internal layer stratification. The initial fluid stratification should be measured to avoid the problems with similar data obtained at Arizona State University.

Preliminary investigation of jet behavior in the presence of natural convection was conducted at the University of Notre Dame. This behavior should be studied further including proper scaling to ascertain the importance of natural convection effects during jet mixing especially after jet penetration stops.

## 16.2 Immiscible

Work conducted into selective withdrawal and jet mixing at the oil-brine interface resulted in SPR criteria that can be used to avoid immiscible mixing in these situations. Preliminary investigation of oil-brine mixing for oil injected into the brine layer has been performed, but additional study is needed to develop any predictive models.

# References


Abraham, G. "Jet diffusion in stagnant ambient fluid." Technical Report 29. Delft Hydraulics Lab, 1963.

—. "Jets with negative buoyancy in homogeneous fluids." Journal of Hydraulic Research 1967: 235-248.

Adrian, R.J. "Particle-imaging techniques for experimental fluid mechanics." Annu. Rev. Fluid Mech. (1991): 261-304.

Albertson, M. L., et al. "Diffusion of submerged jets." Transactions of ASCE 1950: 639-697.

Ansong, J. K. "Plumes in Stratified Environments." 2009.

Baines, W. D. and V. H. Chu. "Jets and Plumes." Environmental Hydraulics. Ed. Vijay P. Singh and Willi H. Hager. Dordrecht, The Netherlands: Kluwer Academic Publishers, 1996.

Baines, W.D. "Entrainment by a plume or jet at a density interface." Journal of Fluid Mechanics (1975): 309-320.

Baines, W.D., and Turner, J.S. "Turbulent buoyant convection from a source in a confined region." Journal of FLuid Mechanics (1969): 51-80.

Baines, W.D., Corriveau, A.F., and Reedman, T.J. "Turbulent fountains in a closed chamber." Journal of FLuid Mechanics (1993): 621-646.

Baines, W.D., Turner, J.S., and Campbell, I.H. "Turbulent fountains in an open chamber." Journal of Fluid Mechanics (1990): 557-592.

Banks, R. B. and D. V. Chandrasekhara. "Experimental investigation of the penetration of a high-velocity gas jet through a liquid surface." Journal of Fluid Mechanics 1963: 13-34.

Barenblatt, G.I. Scaling, Self-similarity, and Intermediate Asymptotics. Cambridge University Press, 1996.

Barnett, S.J. "The Dynamics of Buoyant Releases in Confined Spaces." 1991.

Barton, D. Fluid Dynamics of Oil Storage and Production Cycles at the Weeks Island Strategic Petroleum Reserve - Part 3: Laboratory Study of Crude Oil/Brine System. Baton Rouge, LA: Petroleum Engineering Research and Technology Transfer Laboratory, Lousiana State University, 1990.

Batchelor. Introduction to Fluid Mechanics. Cambridge University Press, 1970.

Blake, S., and Ivey, G.N. "Magma-mixing and the dynamics of withdrawal from stratified reservoirs." Journal of Vocanology and Geothermal Research (1986): 153-178.

Blake, W.K., and Powell, A. "The development of contemporary views of flow-tone generation." Krothapali, A., and Smith, C.A. Recent advances in aeroacoustics. New York: Springer, 1986. 247-325.

Bourgoyne, Jr., A.T. Fluid Dynamics of Oil Storage and Production Cycles at the Weeks Island Strategic Petroleum Reserve - Part 4 - Visual Analog Study of Fill-hole Drift. Baton Rouge, LA: Petroleum Engineering Research and Technology Transfer Laboratory, Lousiana State University, 1990.

Bourque, C., and Newman, B.G. "Reattachment of a two-dimensional incompressible jet to an adjacent flat plate." Aeronaut Q 11 (1960): 201-232.

Broderson, S., Metzger, D.E., and Fernando, H.J.S. "Flows Generated by the Impingement of a Jet on a Rotating Surface: Part I - Basic Flow Patterns." J. Fluids Eng. (1996): 62-67.

Brown, J.S., Khoo, B.C., and Sonin, A.A. "Rate correlation for condensation of pure vapor on turbulent subcooled liquid." Int. J. Heat Mass Transfer (1990): 2001-2008.

Budwig, R. "Refractive index matching methods for liquid flow investigations." Experiments in Fluids 1994: 350-355.

Cantwell, B.J. "Viscous starting jets." J. Fluid Mech. (1986): 159-189.

Carazzo, G., Kaminski, E., and Tait, S. "On the dynamics of volcanic columns: A comparison of field data with a new model of negatively buoyant jets." Journal of Volcanology and Geothermal Research (2008a): 94-103.

—. "On the rise of turbulent plumes: Quantitative effects of variable entrainment for submarine hydrothermal vents, terrestrial and extra terrestrial explosive volcanism." Journal of Geophysical Reserach (2008b): B09201.

—. "The rise and fall of turbulent fountains: a new model for improved quantitative predictions." Journal of Fluid Mechanics (2010): 1-20.

—. "The roue to self-similarity in turbulent jets and plumes." Journal of FLuid Mechanics (2006): 137-148.

Cardoso, S.S.S., and Woods, A.W. "Mixing by a turbulent plume in a confined stratified region." J. Fluid Mech. (1993): 277-305.

Chen, C.J., and Rodi, W. Vertical turbulent buoyant jets: A review of experimental data. New York: Oxford, 1980.

Cheslak, F. R., J. A. Nicholls and M. Sichel. "Cavities formed on liquid surfaces by impinging gaseous jets." Journal of Fluid Mechanics 1969: 55-63.

Coleman, H. W. and W. G. Steele. Experimentation and uncertainty analysis for engineers. Ed. second. New York: John Wiley & Sons, 1999.

Cook, A.W., and Dimotakis, P.E. "Transition stages of Rayleigh-Taylor instability between miscible fluids." Journal of FLuid Mechanics (2001): 69-99.

Corporation, C TECH Development. C TECH Development Corporation: Sandia National Labratories. 2006-2010. <http://www.ctech.com/?page=sandia>.

Dalziel, S.B., Patterson, M.D., Caulfield, C.P., and Coomaraswamy, I.A. "Mixing efficiency in high-aspect-ratio Rayleigh-Taylor experiments." Physics of Fluids (2008): 065106.

Davidson, P.A. Turbulence: An Introduction for Scientist and Engineers. Cambridge University Press, 2004.

Denisikhina, D.M., Bassina, I.A., Nikulin, D.A., and Strelets, M.Kh. "Numerical simulation of self-excited oscillation of a turbulent jet flowing into a rectangular cavity." High Temperature (2005): 568-579.

Department of Energy. DOE - Fossil Energy: Environmental Imapct Statement Information for Expanding the SPR. 21 May 2010. Fossil Energy Office of Communications. <http://www.fossil.energy.gov/programs/reserves/spr/expansion-eis.html>.

—. DOE - Fossil Energy: The Strategic Petroleum Reserve Storage Sites. 08 September 2010. Fossil Energy Office of Communications. <http://www.fossil.energy.gov/programs/reserves/spr/spr-sites.html>.

—. DOE - Fossil Energy: U.S. Petroleum Reserves. 29 June 2010. Fossil Energy Office of Communications. <http://www.fossil.energy.gov/programs/reserves/>.

Dimotakis, P.E. "The mixing transition in turbulent flows." J. Fluid Mech. (2000): 69-98.

Dimotakis, P.E., Miake-Lye, R.C., and Papatoniou, D.A. "Structure and dynamics of round turbulent jets." Phys. Fluids (1983): 3185-3192.

Ehgartner, B., Webb, S.W., and Lord, D.L. Future degas behavior at Big Hill. Albuquerque, NM: Sandia National Laboratories Technical Memo, 2005.

Evans, G. M., G. J. Jameson and C. D. Rielly. "Free jet expansion and gas entrainment characteristics of a plunging liquid jet ." Experimental Thermal and Fluid Science 2 February 1996: 142-149.

Fernando, H.J.S. "Oil Mixing in Confined Low Aspect Ratio Cylinders - Report on Work Performed October 1, 2006 - Dewcember 31, 2011." May 28, 2012.

—. "Private Communication." 2011.

Fischer, Hugo B., List, E. John, Koh, Robert C.Y., Imberger, Jorg, and Brooks, Norman H. MIXING in Inland and Coastal Waters. San Diego: Academic Press, 1979.

Frick, T.C., editor. Petroleum Production Handbook, Vol. I, pg. 16-8. Dallas, Tx: Soceity of

Petroleum Engineers of AIME, 1962.

Friedman, P. D. and J. Katz. "Rise height for negatively buoyant fountains and depth of penetration for negatively buoyant jets impinging an interface." Journal of Fluids Engineering December 2000: 779-782.

—. "The flow and mixing mechanisms caused by the impingement of an immiscible interface with a vertical jet." Physics of Fluids September 1999: 2598-2606.

Friedman, P. D., et al. "Instability threshold of a negatively-bouyant fountain." Experiments in Fluids 2007: 751-759.

Gebert, B.M., Davidson, M.R., and Rudman, M.J. "Computed oscillations of a confined submerged liquid jet." Appl. Math. Modelling (1998): 843-850.

Gu, R. "Modeling two-dimensional turbulent offset jets." J. Hydraulic Eng. (1996): 617-624.

Hartenberger, J.D., and O'Hern, T.J. "Experimental Investigation of Selective Withdrawal and Light Layer Entrainment of Stratified Immiscible Liquids." ASME IMECE. Denver, CO, 2011. IMECE2011-66278.

Hartenberger, J.D., O'Hern, T.J., Webb, S.W., and James, D.L. "Transition from Selective Withdrawal to Light Layer Entrainment in an Oil-Water System." APS DFD 63rd Annual Meeting. Long Beach, CA, 2010.

Hussein, H.J., S.P. Capp, and W.K. George. "Velocity measurements in a high-Reynolds-number, momentum-conserving, axisymmetric, turbulent jet." Journal of Fluid Mechanics (1994): 31-75.

Jirka, G.H. "Integral Model for Turbulent Buoyant Jets in Unbounded Stratified Flows. Part 1: Single Round Jet." Environmental FLuid Mechanics (2004): 1-56.

Kaminski, E., Tait, S., and Carazzo, G. "Turbulent entrainment in jets with arbitrary buoyancy." Journal of FLuid Mechanics (2005): 361-376.

Keane, R.D., and Adrian, R.J. "Theory of cross-correlation analysis of PIV images." Appl. Sci. Res. (1992): 191-215.

Khalil, I., and Webb, S.W. "Numerical Simulations of Lab-Scale Brine-Water Mixing Experiments." 2006.

Khoo, B.C., Chew, T.C., Heng, P.S., and Kong, H.K. "Turbulence characterization of a confined jet using PIV." Exp. Fluids (1992): 350-356.

Konig, O., and Fiedler, H.E. "The Structure of Round Turbulent Jets in Counterflow: A Flow Visualization Study." Adv. in Turbulence (1991): 61-66.

Konstantinidou, K., and Papanicolaou, P.N. "Vertical round and orthogonal buoyant jets in a

linear density-stratified fluid." Proc. 30th IAHR Congress on Water Engineering and Research in a Learning Society. 2003. 293-300.

Kumagai, Mikio. "Turbulent buoyant convection froma source in a confined two-layered region." Journal of Fluid Mechanics (1984): 105-131.

Launder, B.E., and Rodi, W. "The turbulent wall jet measurements and modeling." Annual Rev. Fluid Mech., Vol 15 (1983): 429-459.

Lawson, N.J. "Self-sustained oscillation of a submerged jet in a thin rectangular cavity." J. Fluid and Structures (2001): 59-81.

Lee, J. H.W. and V.H. Chu. Turbulent buoyant jets and plumes: A langrangian approach. Kluwer Academic Publishers, 2003.

Liberzon, D., and Fernando, H.J.S. "Pressure Distribution in Confined Jet Flow." J. Fluids Eng. (2014): 031202:1-6.

Linden, P.F., Redondo, J.M., and Youngs, D.L. "Molecular mixing in Rayleigh-Taylor instability." Journal of Fluid Mechanics (1994): 97-124.

List, E.J. "Turbulent Jets and Plumes." Annual Review of Fluid Mechanics, Vol. 14. 1982. 189-212.

List, E.J., and Imberger, J. "Turbulent Entrainment in Buoyant Jets and Plumes." ASCE - Journal of the Hydraulics Division (1973): 1461-1474.

Lister, J.R. "Selective withdrawal from a viscous two-layer system." J. FLuid Mech. (1989): 231-254.

Liu, H., Winoto, S.H., Dilip, A., and Shah, D.A. "Velocity measurements within confined turbulent jets: application to cardiovalvular regurgitation." Annals Biomedical Eng. (1997): 939-948.

Longmire, E. K., T. L. Norman and D. L. Gefroh. "Dynamics of pinch-off in liquid/liquid jets with surface tension." International Journal of Multiphase Flow October 2001: 1735-1752.

Lord, D.L. "Experimental Investigation of Selective Withdrawal and Light Layer Entrainment of Stratified Immiscible Fluids." 2011.

Lord, D.L., and Rudeen, D.K. Summary of Degas II Performance at the US Strategic Petroleum Reserve Big Hill Site. Albuquerque, NM: SAND2007-5564, Sandia National Laboratories, 2007.

Manins, P.C. "Turbulent buoyant convection from a source in a confined region." J. Fluid Mech. (1979): 765-781.

Mataoui, A. and Schiestel, R. "Unsteady phenomena of an oscillating turbulent jet flow inside a cavity: effect of aspect ratio." J. Fluids & Structures (2009): 60-79.

Mataoui, A., Schiestel, R., and Salem, A. "Study of the oscillatory regime of a turbulent plane jet impinging in a rectangular cavity." App. Math. Modelling (2003): 89-144.

McKeon, C.D., James, D.L., O'Hern, T.J., and Webb, S.W. "Predicting transition from selective withdrawal to entrainment in a liquid-liquid system." 2013.

Meng, A., Jaworski, A.J., and White, N.M. "Composition measurements of crude oil and process water emulsions using thick-film ultrasonic transducers." Chemical Engineering and Processing (2006): 383-391.

Milojevic, D. "Lagrangian stochastic-deterministic (LSD) predictions of particle dispersion in turbulence." Part. Syst. Charact. (1990): 181-190.

Miozzi, M., Lalli, F., and Romano, G.P. "Experimental investigation of a free-surface turbulent jet with Coanda effect." Exp. Fluids (2009): 341-353.

Molloy, N.A., and Taylor, P.L. "Oscillatory flow of a jet into a blind cavity." Nature (1969): 1192-1194.

Morton, B. R. "Forced plumes." Journal of Fluid Mechanics 1959: 151-163.

Nathan, G.J., Hill, S.J., and Luxton, R.R. "An axisymmetric ‘fluidic’ nozzle to generate jet precession." J. Fluid Mech. (1998): 347-380.

Office of Petroleum Reserves, U.S. Department of Energy. Strategic petroleum reserve plan expansion to onebillion barrels. Washington D.C., June 2007.

O'Hern, T.J. "Leaching Plume Studies in Lab-Scale Vessel - Experimental Analysis Completed." 2005.

O'Hern, T.J., and Oelfke, J.B. "Leaching Plume Studies in Lab-Scale Vessel - Experiments Completed." 2005.

O'Hern, T.J., Cote, R.O., Webb, S.W., and James, D.L. "Preliminary Investigations of the Oil-Brine Interface Stability during Brine Withdrawal." April 7, 2010.

O'Hern, T.J., Oelfke, J.B., and Webb, S.W. "Preliminary Results of and Analysis Plan for Leaching Plume STudies in Lab-Scale Vessel." 2005.

O'Hern, T.J., Torczynski, J.R., Barney, J., Castaneda, J., Cote, R.O., and Shollenberger, K.A. "Investigation of Oil Injection into Brine for the Strategic Petroleum Reserve - Hydrodynamics Experiments with Simulant Liquids." 2003.

O'Hern, T.J., Torczynski, J.R., Cote, R.O., and Castaneda, J.N. "Investigation of Oil Injection into Brine for the Strategic Petroleum Reserve - Hydrodynaics and Mixing Experiments

with SPR Liquids." 2004.

O'Hern, T.J., Webb, S.W., and Ehgartner, B.L. "Experimental Plan for Leaching Plume Studies in Lab-Scale Vessel." 2004.

Pantzlaff, L., and Lueptow, R.M. "Transient positively and negatively buoyant turbulent round jets." Experiments in Fluids (1999): 117-125.

Papanicolaou, P. and E. J. List. "Investigations of round vertical turbulent buoyant jets." Journal of Fluid Mechanics 1988: 341-391.

Papanicolaou, P.N., and Stamoulis, G. "Spreading of buoyant jets and fountains in a calm, linearly density-stratified fluid." Environmental Hydraulics. London: Taylor and Francis Group, 2010. 123-128.

Papanicolaou, P.N., Papakonstantis, I.G., and Christodoulou, G.C. "On the entrainment coefficient in negatively buoyant jets." Journal of Fluid Mechanics (2008): 447-470.

Papanicolaou, P.N., "Figures." email to Kayla Streit (SNL), October 31, 2015.

Pol, S.U. "Evolution of Convection and Turbulent Jets in Stratified Low Aspect Ratio Containers." 2010.

Pol. S., Nath, C., Gest, D., Voropayev, S., Fernando, H.J.S, and Webb, S. "Evolution of Turbulent Jets in Low Aspect Ratio Containers." B. Am Phys. Soc. (2009).

Qian, F., R. Mutharasan and B. Farouk. "Studies of interface deformations in single- and multi-layered liquid baths due to an impinging gas jet." Metallurgical and Materials Transactions B 1996: 911-920.

Raffael, M., Willert, C., Wereley, S., and Kompenhans, J. Particle Image Velocimetry: A Practical Guide. Berlin Heidelberg: Springer-Verlag, 2007.

Rajaratnam, N., and Subramanian, N. "Plane turbulent reattachment wall jets." ASCE, J. Hydraulic Div (1968): 95-112.

Revuelta, A., Martinez-Bazan, C., Sanchez, A.L., and Linan, A. "Laminar Craya-Curtet jets." Physics of FLuids (2004): 208-211.

Risso, F., and Fabre, J. "Diffusive turbulence in a confined jet experiment." J. Fluid Mech. (1997): 233-261.

Rouse, H. "Seven exploratory studies in hydraulics I. Development of the non-circulatory waterspout." J. Hydr. DIv. ASCE (1956): 1038-2 - 1038-7.

Schlichting, H. Boundary Layer Theory. McGraw-Hill, 1979.

Sonin, A.A., Shimko, M.A., and Chun, J.H. "Vapor condensation onto a turbulent liquid - I. The steady condensation rate as a function of liquid-side turbulence." Int. J. Heat Mass

Transfer (1986): 1319-1332.

Turner, J. S. "Jets and plumes with negative or reversing buoyancy." Journal of Fluid Mechanics 1966: 779-792.

Turner, J.S. Buoyancy Effects in Fluids. Cambridge: Cambridge University Press, 1973.

—. "Jets and plumes with negative or reversing buoyancy." Journal of Fluid Mechanics 26.4 (1966): 779-792.

—. "The influence of molecular diffusivity on turbulent entrainment across a density interface." Journal of FLuid Mechanics (1968): 639-656.

Ungate, C.D., Harleman, D.R.F., and Jirka, G.H. "Stability and Mixing of Submerged Turbulent Jets at Low Reynolds Numbers." 1975.

van Sommeren, D.D.J.A., Caulfield, C.P., and Woods, A.W. "Advection and buoyancy-induced turbulent mixing in a narrow vertical tank." J. Fluid Mech. (2013): 450-479.

—. "Spatially varying mixing of a passive scalar in buoyancy-driven turbulent flow." J. Fluid Mech. (2014): 701-719.

—. "Turbulent buoyant convection from a maintained source of buoyancy in a narrow vertical tank." J. Fluid Mech. (2012): 278-303.

Villermaux, E., and Hopfinger, E.J. "Self-sustained oscillations of a confined jet: a case study for the non-linear delayed saturation model." Physica D (1994): 230-243.

Voropayev, S.I., Nath, C., and Fernando, H.J.S. "Mixing by turbulent buoyant jets in slender containers." Phys. Letters A (2012): 3213-3218.

Voropayev, S.I., Sanchez, X., Nath, C., Webb, S., and Fernando, H.J.S. "Evolution of a confined turbulent jet in a long cylindrical cavity: Homogeneous fluids." Physics of Fluids (2011): 1151-6:1-11.

—. "Evolution of a confined turbulent jet is a long cylindrical cavity: Homogeneous fluids." Physics of Fluids (2011): 115106, 1-11.

Wang, H., and Law, A.W-K. "Second-order integral model for a round turbulent buoyant jet." Journal of Fluid Mechanics (2002): 397-428.

Webb, S.W. "Selective Withdrawal in SPR Caverns." 2003.

—. "Simple Degas Mixing Model Results - Comparison of Star and luent Results." 2009.

—. "Simple Degas Mixing Model Results Including Stratification." 2009.

Webb, S.W., and Lord, D. "Prediction of BM106 Degas Performance." 2010.

White, F. M. Viscous fluid flow. Boston: McGraw-Hill, 1991.

Whitman, G.B. Linear and Nonlinear Waves. New York: John Wiley & Sons, Inc., 1974.

Wojtaniwicz, A. Fluid Dynamics of Oil Storage and Production Cycles at the Weeks Island Strategic Petroleum Reserve - Part 5: Evaluation of Fill-hole Completions. Baton Rouge, LA: Petroleum Engineering Research and Technology Transfer Laboratory, Lousiana State University, 1991.

Wojtanowicz, A. Fluid Dynamics of Oil Storage and Production Cycles at the Weeks Island Strategic Petroleum Reserve - Part 1: Literature Study. Baton Rouge, LA: Petroleum Engineering Research and Technology Transfer Laboratory, Lousiana State University, 1989.

—. Fluid Dynamics of Oil Storage and Production Cycles at the Weeks Island Strategic Petroleum Reserve - Part 2: Design of the Laboratory Analog. Baton Rouge, LA: Petroleum Engineering Research and Technology Transfer Laboratory, Lousiana State University, 1989.

Worster, M.G., and Huppert, H.E. "Time-dependent density profiles in a filling box." Journal of Fluid Mechanics (1983): 457-466.

Wygnanski, I, and H. Fieldler. "Some measurements in the self-preserving jet." Journal of Fluid Mechanics (1969): 577-612.

# APPENDIX: Webb Memos

# Simple Degas Mixing Model Results Including Stratification

Stephen W. Webb
Sandia National Laboratories
June 29, 2009

## I. Introduction

A simple 2-d axisymmetric model of a full-scale cavern has been developed in the Fluent computational fluid dynamics (CFD) code to investigate the effect of the inlet oil density on mixing and degas efficiency including uniform initial oil density and oil stratification. The model developed in this report is simple by design. The geometry and fluid properties will be modified in the future to better represent actual caverns. Nevertheless, these initial results provide some insight into cavern mixing processes during degas.

## II. Numeric Model

The modeled cavern is 2000 ft high with a uniform diameter of 200 ft as shown in Figure 1 with a total capacity of 11.2 MMB. No brine layer is assumed to be present so the entire volume is oil. The injection is located 100 ft from the top of the cavern while the outlet is 200 ft from the bottom. The inlet and outlet strings are concentric with the cavern with radii of 1.0 ft (bottom inlet/outlet) and 1.5 ft (top inlet/outlet). For this study, properties of diesel (density = 730 kg/m$^3$ (45.6 lb/ft$^3$), dynamic viscosity = 0.0024 Pa-s, kinematic viscosity = 3.3cSt, molecular diffusivity = $10^{-9}$ m$^2$/s) are used. The degas inlet mass flow rate is 175 kg/s (130,000 BBL/day) for a cavern turnover time of 85.9 days.

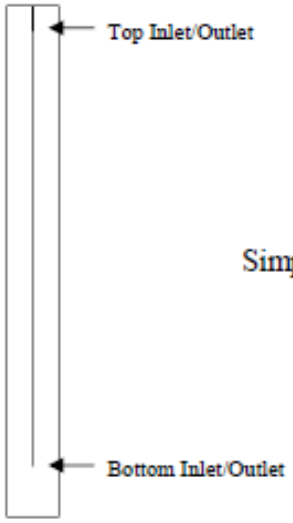


Figure 1
Simplified Cavern Geometry

The model is a two-dimensional R-Z model with variable mesh point spacing in both directions in order to concentrate the mesh near the inlet and outlet locations and the outer wall. The mesh near the top is shown in Figure 2a, while the mesh near the bottom is given in Figure 2b. Note that the mesh shown is mirrored around the centerline at R=0 as indicated by the yellow vertical line in Figure 2b. The concentric hanging strings are clearly shown in these figures.

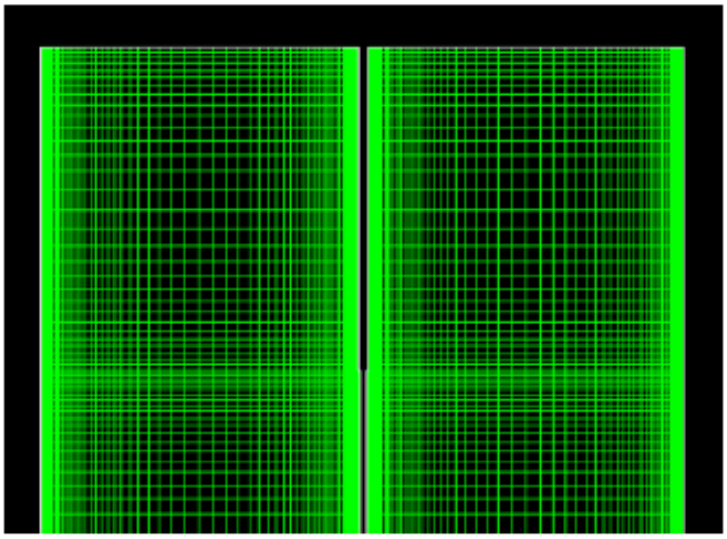

(a) Mesh Near the Top Inlet/Outlet

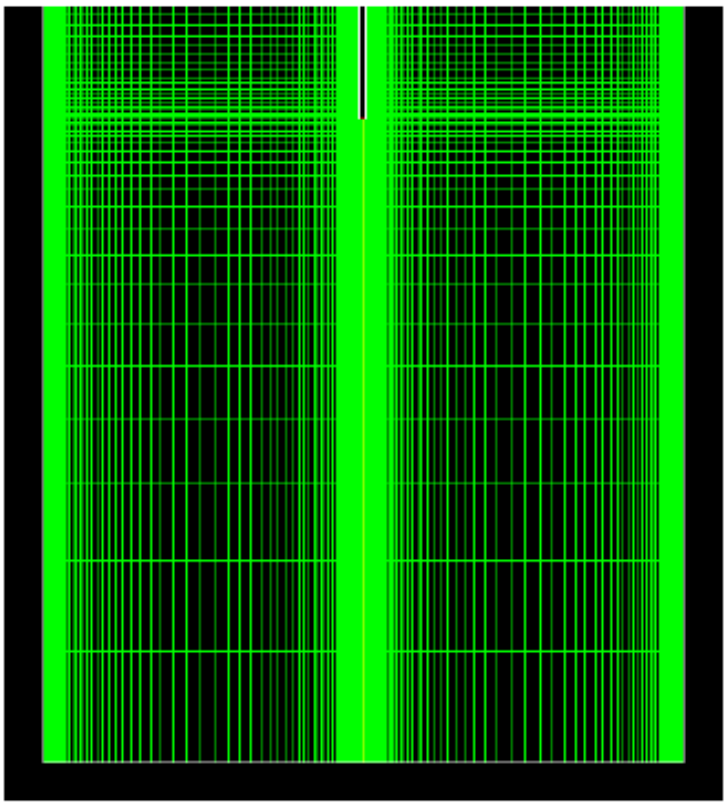

(b) Mesh Near Bottom Inlet/Outlet

Figure 2
Details of Meshing in Fluent R-Z Model

## III. Cavern Mixing and Degas Performance

Cavern mixing is dominated by two processes – mixing from the fluid jet as it enters the cavern at the inlet and mixing due to the buoyancy of the incoming fluid. As the fluid jet enters the cavern, mixing in the region just downstream of the inlet will occur. The length of this jet mixing region is affected by the buoyancy of the incoming fluid relative to the resident fluid. If the incoming fluid is lighter than the resident fluid, the incoming jet will reverse direction at some point and become a plume, and the mixed fluid will rise toward the top of the cavern as shown in Figure 3. Conversely, if the incoming fluid is heavier than the resident fluid, the jet will continue downward toward the bottom of the cavern even when the jet momentum is dissipated. If the fluid densities are the same, the jet will continue downward until it's momentum is dissipated, and mixing will occur in the region between the inlet and the position of jet momentum dissipation. Additional mixing may or may not occur if the jet/plume encounters a stratification boundary depending on the momentum of the jet/plume and the density difference across the stratification boundary. Mixing may also occur if the outlet location is located near a stratification boundary, which is often referred to as selective withdrawal, in which flow from the lower layer is "pulled up" into the outlet through the upper layer.

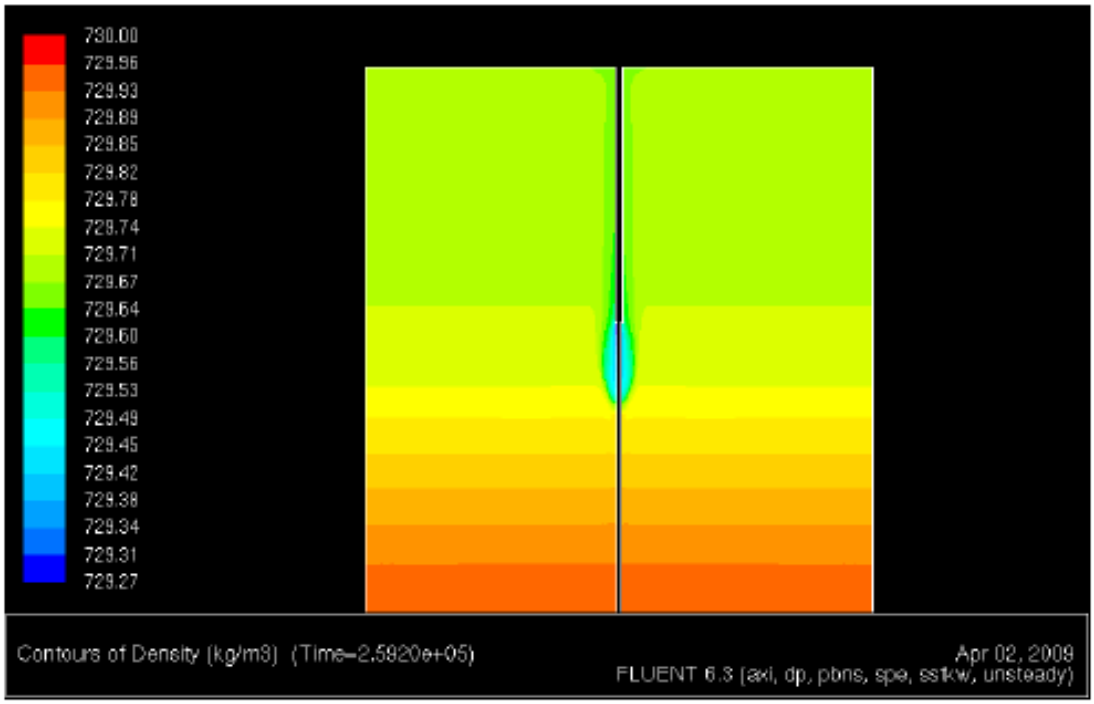


Figure 3
Jet/Plume Processes at the Inlet for Injection of a Lighter Fluid

All of these mixing processes may affect the efficiency of any degas operation. Note that these processes are only approximated in this simple cavern degas mixing model. The geometry and inlet/outlet radii are greatly simplified as are the fluid properties. In

addition, the nodalization used in the numerical model is not fine enough to capture all the details of the jet/plume mixing processes or the interactions between the fluid velocity and the stratification because the stratification boundary is often smeared by the numerics. Nevertheless, the present numerical model should give general trends and insight into degas operations. Further development of the model including using actual cavern geometry and fluid properties and comparison to actual degas data is needed to provide confidence in the model. Data-model comparisons are scheduled to be performed and reported later in 2009.

The density of the injected fluid was kept constant during these simulations so the impact could be easily studied. Two types of plots are presented.

1. The first plot shows the normalized bubble point (BP) at the outlet of the model, or at the degas plant. A normalized value of 1.0 is indicative of the pre-degas BP value, while a normalized value of 0.0 corresponds to the outlet BP value from the degas plant. A higher value of normalized BP indicates less mixing and better degas performance.
2. The second plot shows the fraction of processed oil in the entire cavern. If the value is 0.9, that indicates that 90% of the original oil in the cavern has been degassed. This value should increase as rapidly as possible, which indicates less mixing and better degas performance.

Lord and Rudeen (2007) have developed two cases for degas operations that tend to bound the results as shown in Figure 4. The best case for degas operations is plug flow. The injected oil pushes the initial resident fluid to the outlet, so the resident oil is processed first with no mixing between the two oils, so only a single cavern volume needs to be processed as shown by the "plug flow" line in Figure 4. The other limit is complete mixing of the injected fluid with the resident fluid. In this case, the withdrawn fluid includes some of the injected fluid, so the degas operation is less efficient than plug flow. This limit is shown in Figure 4 as the "complete mixing" line. In general, degas results should be between these two limits. Due to dead zones in the cavern and fluid stratification, degas performance can be below the complete mixing limit, but in general, complete mixing is the minimum degas performance. The difference is significant as can be seen for the time to process 80% of the oil. For the plug flow case, the time is 0.80 cavern volumes, while the time is 1.6 cavern volumes for the complete mixing case, or twice as long.

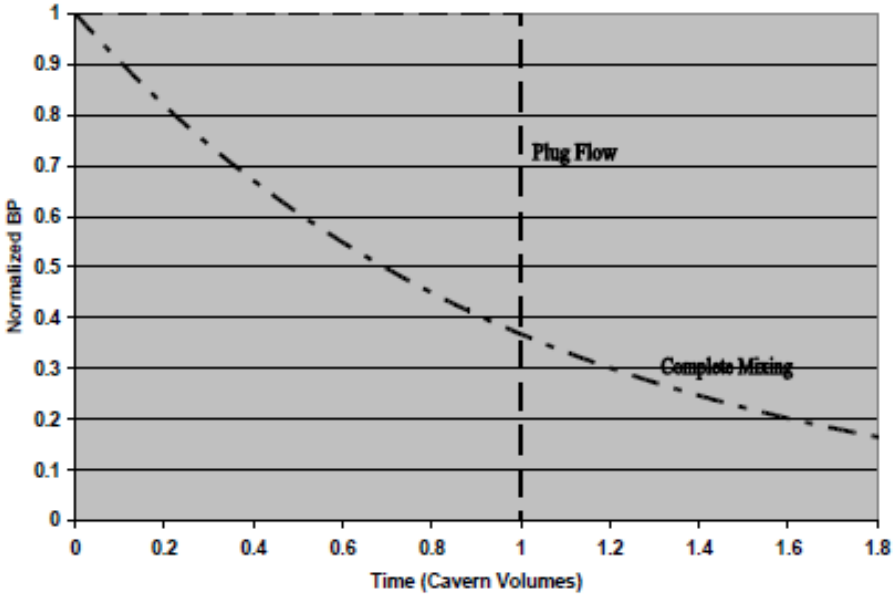


(a) Normalized Bubble Point (BP) Pressure Limits

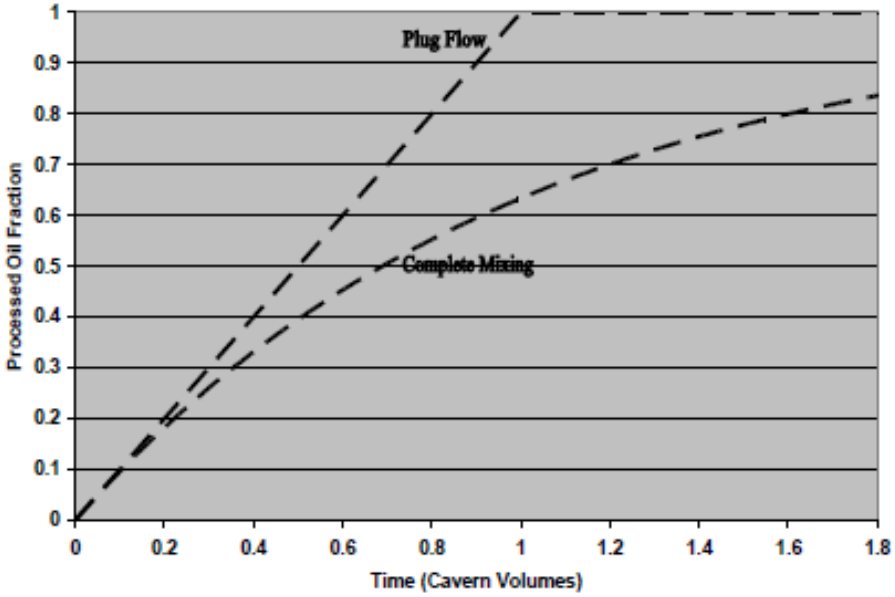


(b) Processed Oil Fraction Limits

Figure 4
Plug Flow and Complete Mixing Limits for Degas Performance Curves

## IV. Simulation Results

Simulated degas performance results are shown below for the following cases:

1. Uniform Density Initial Conditions – all the oil initially in the cavern is at the same density with no stratification.
    a. Lighter oil injection at the top inlet – oil that is lighter than the original oil is added to the cavern near the top. Oil is withdrawn near the bottom of the cavern.
    b. Neutral density oil injection at the top inlet – the oil injected and the oil originally in the cavern are at the same density. Oil is added near the top of the cavern and withdrawn near the bottom of the cavern.
    c. Heavier oil injection at the top inlet – the oil injected near the top of the cavern is heavier than that initially in the cavern. Oil is withdrawn near the bottom.
    d. Heavier oil injection at the bottom inlet – this case confirms that heavier oil injected near the bottom is essentially the same as lighter oil injected near the top. In this case, heavier oil is injected near the cavern bottom, and oil is withdrawn near the top.
2. Stratified Density Initial Conditions – the cavern is assumed to consist of equal volumes of a lighter oil over a heavier oil with a density difference of 0.1%.
    a. Injection of bottom layer oil at the top inlet – oil is withdrawn near the bottom of the cavern and injected near the top with no change in density. Because the oil in the bottom of the cavern is heavier than that in the top, the injected oil is heavier than the oil in the cavern at the injection location.
    b. Injection of top layer oil at the bottom inlet – the reverse of case a. Oil is withdrawn near the top of the cavern and injected into the cavern near the bottom. Because the oil in the top of the cavern is lighter than that in the bottom, the injected oil is lighter than the oil in the cavern at the injection location.
    c. Injection of lighter oil at the top inlet – oil that is lighter than either of the oil layers in the cavern is injected near the top of the cavern. Oil is withdrawn near the bottom of the cavern.
    d. Degas in two phases – degas occurs in two stages. In the first stage, the top layer is degassed, while in the second stage, the bottom layer is degassed. Oil is injected near the top of the cavern.
        i. Phase 1 – top layer degas – oil is withdrawn just above the initial density interface between the two fluids.
        ii. Phase 2 – bottom layer degas – the withdrawal location is changed from just above the initial density interface to near the bottom of the cavern after 40 days. The injection location in unchanged.
3. Viscosity Effect – Fluid Viscosity Increased by Factor of 10
    Uniform Density Initial Conditions
    Lighter, Neutral, and Heavier Oil Injected Near Top of Cavern
    0.01% Density Difference for Lighter and Heavier Cases
    Similar to Cases 1a, 1b, and 1c

## 1. Uniform Density Initial Conditions

### 1a - Lighter Oil Injection

The normalized BP and processed oil fraction results for injection of a lighter fluid at the top inlet are shown as a function of time in Figure 5. The difference between the density of the injected fluid and the resident fluid varies from 0.01% lighter, 0.1% lighter, to 1.0% lighter. The injected oil creates a jet that initially descends downward in the cavern. Due to the density difference, however, the jet turns around and rises to the top of the cavern as a plume as shown earlier in Figure 3. The processed oil fraction is relatively insensitive to the density difference as long as the injected fluid is lighter than the resident fluid.

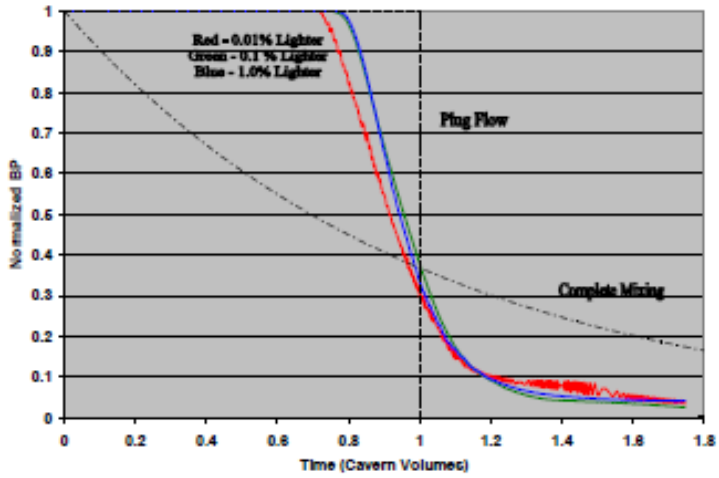


(a) Normalized BP Results

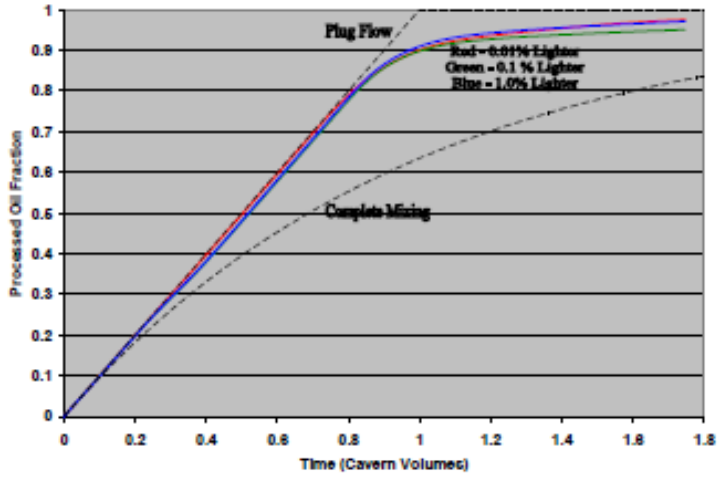


(b) Processed Oil Fraction Results

Figure 5
Degas Performance Curve Results For Lighter Oil Injection – Top Inlet

Both plots indicate a very efficient degas operation until about 80-85% of the resident fluid is processes similar to the plug flow case of Lord and Rudeen (2007). The difference after 0.85 cavern volumes is related to the outlet elevation and the fact that there is 90% of the resident fluid is above the outlet as well as dispersion of the plug flow "front" as seen in Figure 6.

Figure 6 shows contours of the injected oil mass fraction in the cavern as a function of time for the 0.1% lighter case. The mass fraction of initially resident oil to be degassed is simply 1.0 minus the injected oil fraction. Injection occurs near the top of the cavern while withdrawal occurs near the bottom. For the most efficient degas operation, the injected oil fraction should be minimized at the outlet in order to process the maximum amount of initially resident oil. The injected fluid is seen to rise to the top of the cavern, which pushes the resident oil to the outlet similar to plug flow conditions.

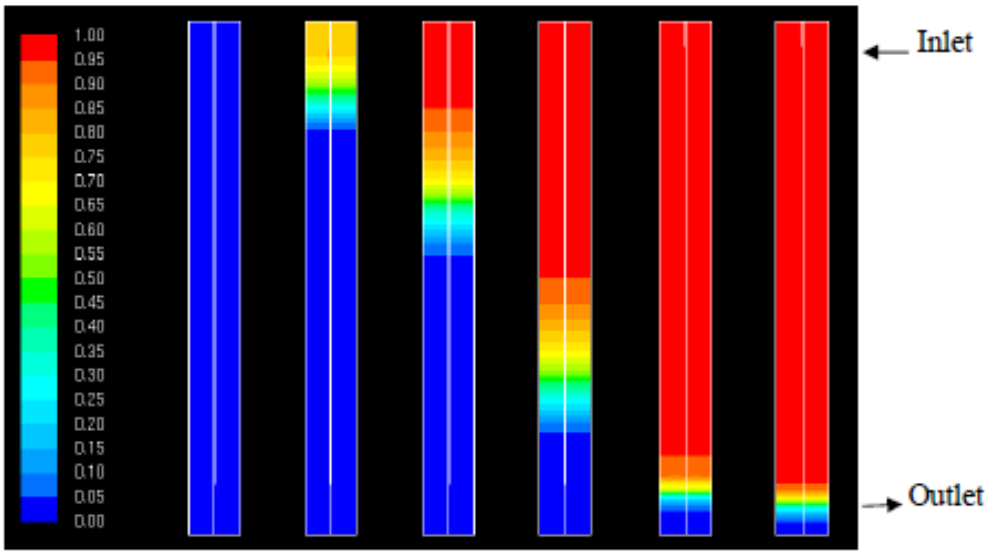


| Time | 0 days | 10 days | 30 days | 60 days | 90 days | 120 days |
|---|---|---|---|---|---|---|
| Cavern Vols | 0. | 0.12 | 0.35 | 0.70 | 1.05 | 1.4 |

Figure 6
Contours of Mass Fraction of Injected Fluid in Cavern
(Lighter Oil Injection, Top Inlet)

### 1b - Neutral Density Oil Injection

This case corresponds to the situation where the injected oil and the resident oil are at exactly the same density. The normalized BP and processed oil fraction results as a function of time for injection of a neutral density fluid at the top inlet are shown in Figure 7. The initial results are similar to plug flow up until about 0.5 cavern volumes; after that time, the results are about mid-way between plug flow and complete mixing.

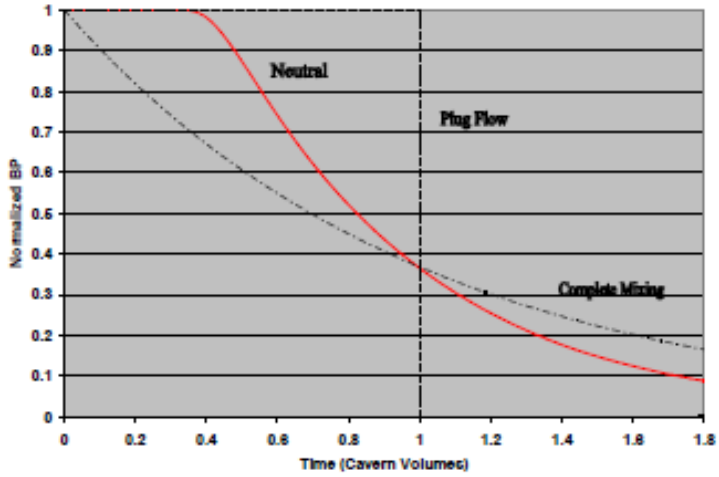


(a) Normalized BP Results

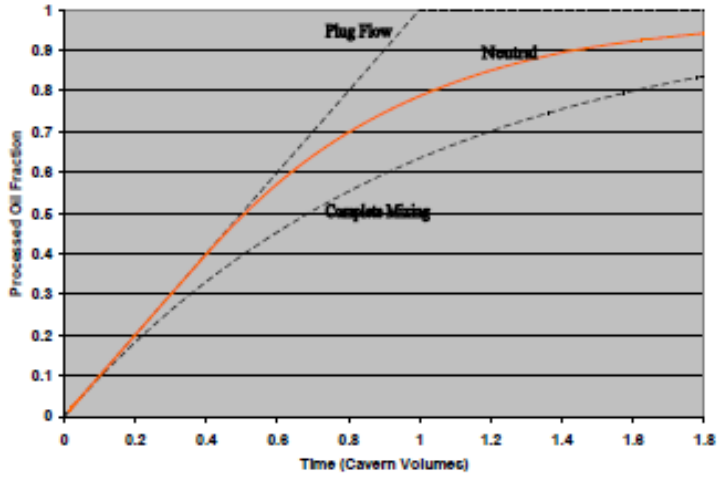


(b) Processed Oil Fraction Results

Figure 7
Degas Performance Curve Results For Neutral Density Oil Injection – Top Inlet

Figure 8 shows contours of the injected oil mass fraction in the cavern as a function of time for the neutral case. The initial jet of neutral density oil mixes about 1/3 of the cavern oil below the injection location. Below this location is a diffuse front of mixed oil. The front becomes more diffuse with time because there is no density difference between the injected and resident oil.

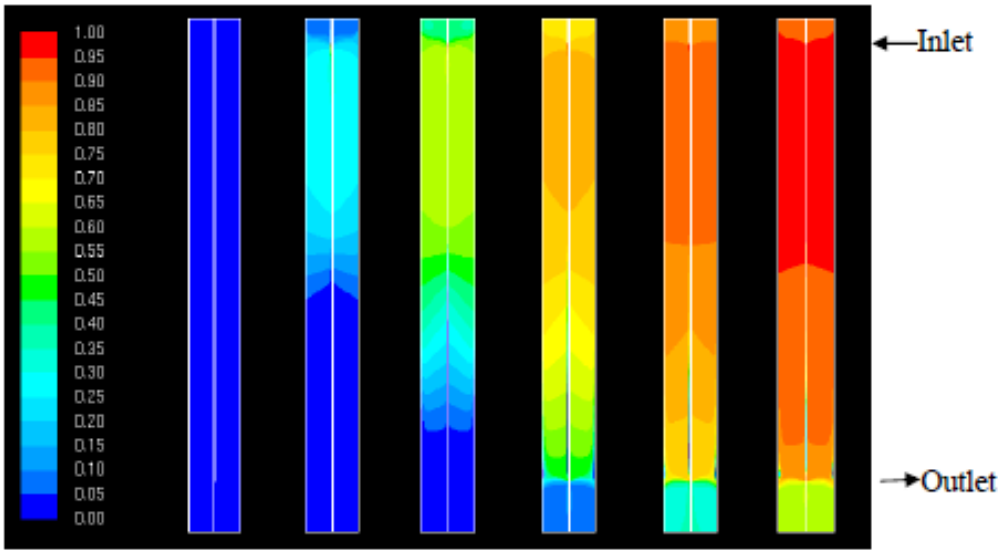


| Time | 0 days | 10 days | 30 days | 60 days | 90 days | 120 days |
|---|---|---|---|---|---|---|
| Cavern Vols | 0. | 0.12 | 0.35 | 0.70 | 1.05 | 1.4 |

Figure 8
Contours of Mass Fraction of Injected Fluid in Cavern
(Neutral Density Oil Injection, Top Inlet)

### 1c - Heavier Oil Injection – Top Inlet

The normalized BP and processed oil fraction results for injection of a heavier fluid are shown in Figure 9. The difference between the density of the injected fluid and the resident fluid varies from 0.01% heavier, 0.1% heavier, to 1.0% heavier. As shown in Figure 9, the results are similar to the complete mixing case with a minor influence on the density difference. The heavier injected fluid flows down to the bottom in the cavern promoting large scale mixing.

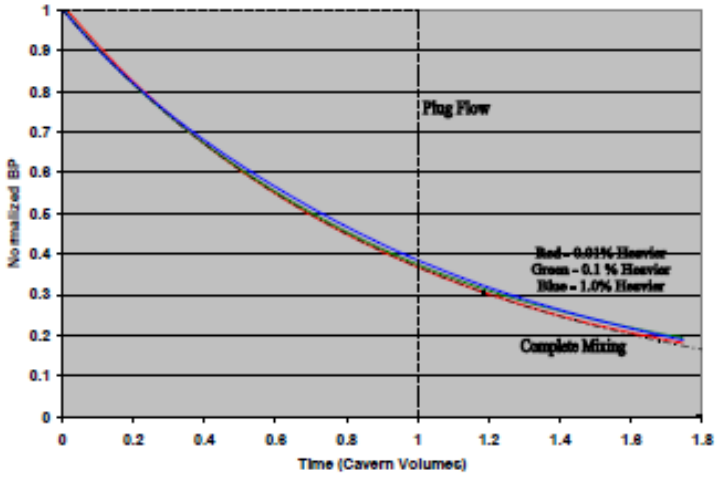


(a) Normalized BP Results

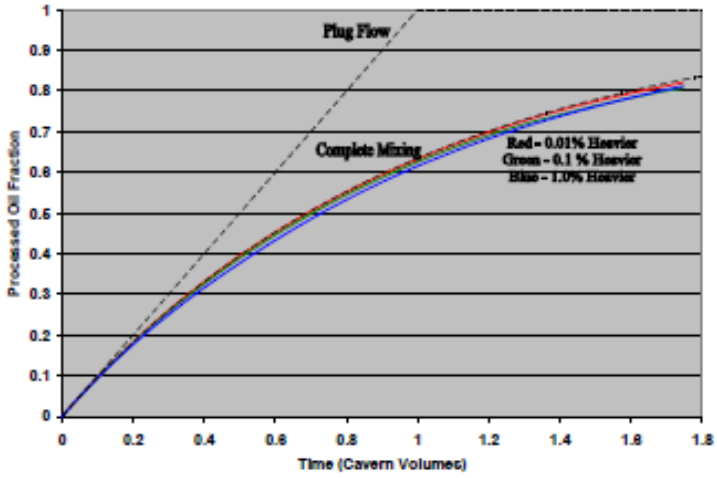


(b) Processed Oil Fraction Results

Figure 9
Processed Oil Fraction vs. Time For Heavier Oil Injection – Top Inlet

Figure 10 shows contours of the injected oil mass fraction in the cavern as a function of time for the 0.1% heavier case. The injected oil mixes with the resident oil immediately after injection. The results show an essentially uniform distribution of the injected oil below the inlet, or complete mixing in this region consistent with the degas performance curves shown above.

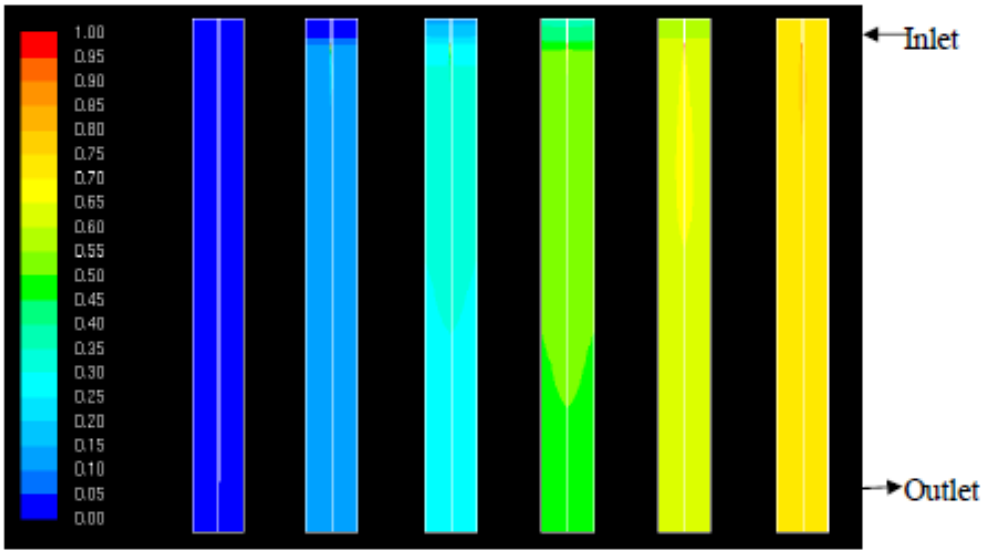


| Time | 0 days | 10 days | 30 days | 60 days | 90 days | 120 days |
|---|---|---|---|---|---|---|
| Cavern Vols | 0. | 0.12 | 0.35 | 0.70 | 1.05 | 1.4 |

Figure 10
Contours of Mass Fraction of Injected Fluid in Cavern
(Heavier Oil Injection, Top Inlet)

### 1d - Heavier Oil Injection – Bottom Inlet

Previous results for lighter oil injection at the top showed good degas performance similar to plug flow, and heavier oil injection at the top showed poor degas performance similar to complete mixing. The present case of heavier oil injection at the bottom was chosen to confirm that injecting heavier oil at the bottom is essentially the same as injecting lighter oil at the top. In both cases, the injected oil would go to the bottom or top of the cavern depending on the density difference, although the jet dynamics would obviously be different due to the direction of the inlet jet. The injected oil would then push the resident oil toward the outlet in a plug flow situation. The degas performance curves for this case given in Figure 11 show exactly that, similar to the lighter oil injection at the top case. Degas proceeds similar to plug flow until about 80% of the oil is processed.

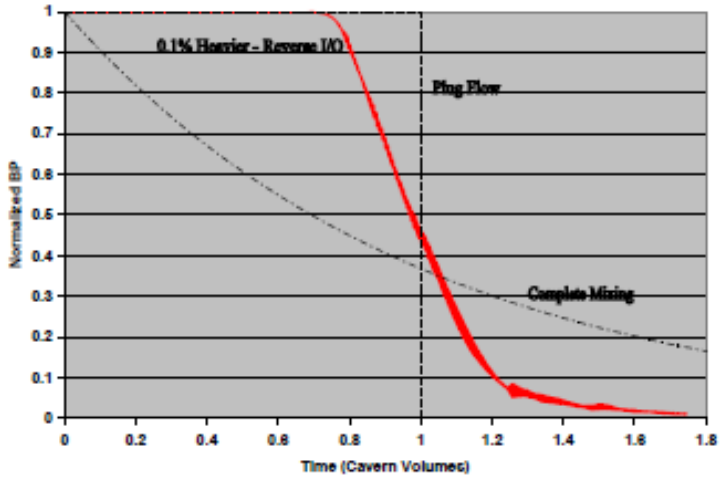


(a) Normalized BP Results

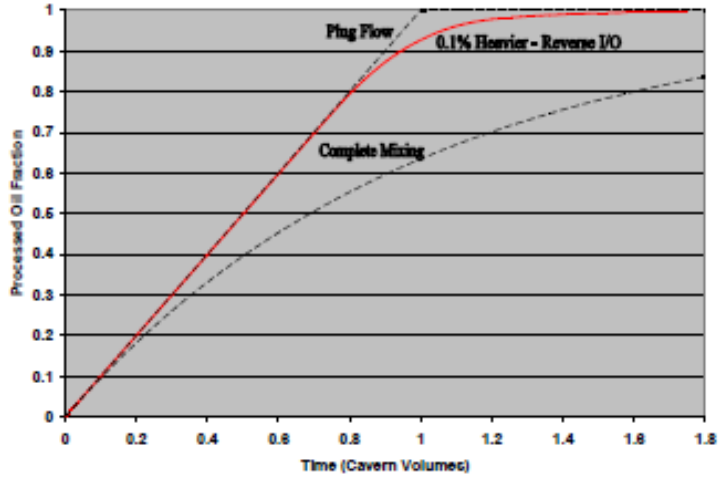


(b) Processed oil Fraction Results

Figure 11

Degas Performance Curve Results For Heavier Oil Injection – Bottom Inlet

Figure 12 shows the injected oil mass fraction contours for this case. As expected, the results are similar to the lighter oil injection at the top inlet in that the injected oil accumulates at the bottom (top for lighter oil injection) that then pushes the resident oil to the outlet in a plug flow situation.

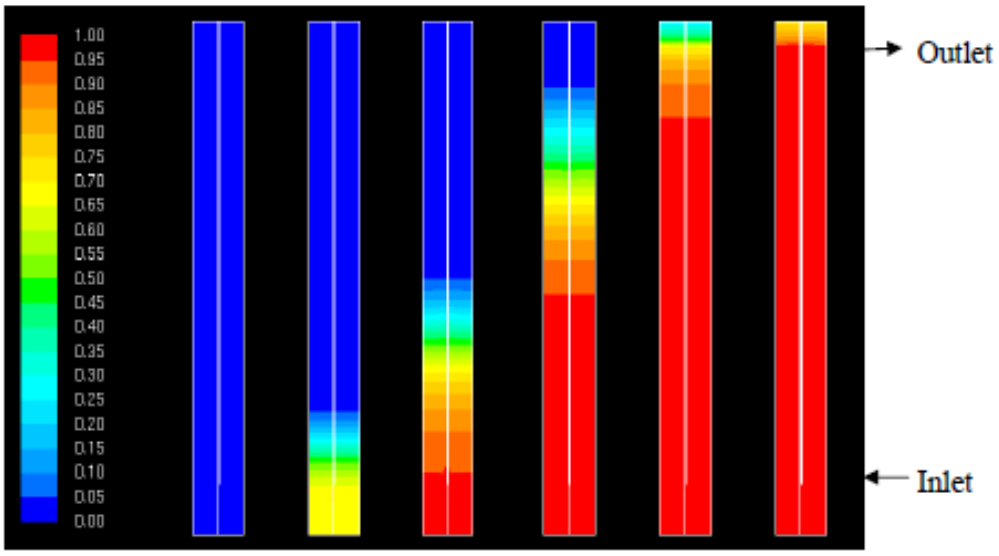


| Time | 0 days | 10 days | 30 days | 60 days | 90 days | 120 days |
|---|---|---|---|---|---|---|
| Cavern Vols | 0. | 0.12 | 0.35 | 0.70 | 1.05 | 1.4 |

Figure 12
Contours of Mass Fraction of Injected Fluid in Cavern
(Heavier Oil Injection, Bottom Inlet)

## 2. Stratified Density Initial Conditions

### 2a / 2b - Inject Bottom Layer Into Top Inlet / Inject Top Layer Into Bottom Inlet

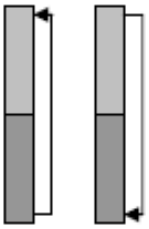

In the first case, the oil is taken out of the bottom of the cavern and injected into the top with the injected density equal to the initial withdrawal density. In this case, the influence of the initial density stratification on degas performance is evaluated. As seen in Figure 13, the degas performance curves are initially similar to plug flow until about 35% of the oil is processed and then they go to the complete mixing curve, or when the stratification interface gets to the outlet location. The red curve shows the case of injecting the bottom layer oil into the top inlet. The green curve shows the reverse situation where the strings are simply reversed so the top layer oil is injected into the bottom inlet. Both curves give similar results.

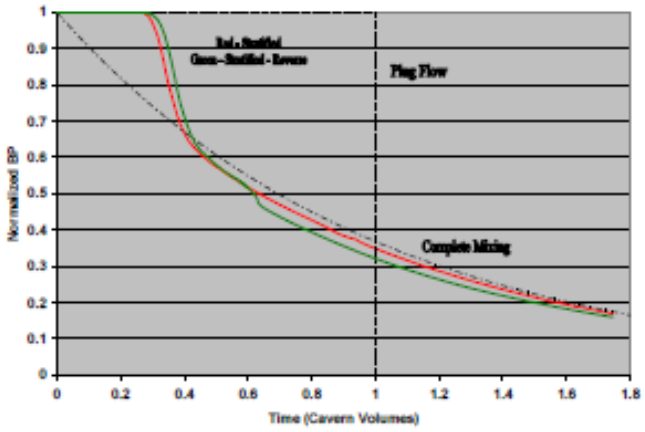


(a) Normalized BP Results

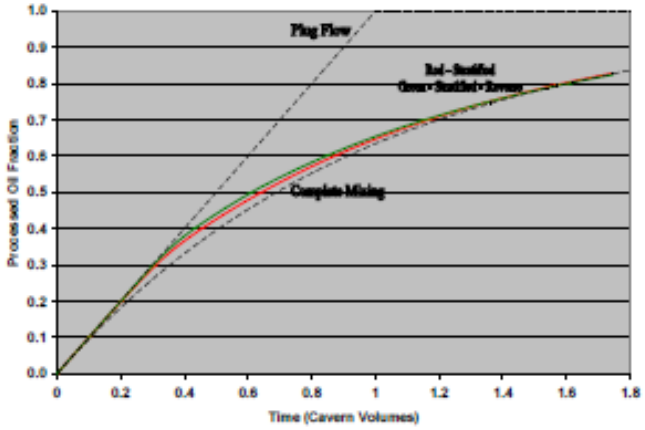


(b) Processed Oil Fraction Results

Figure 13
Degas Performance Curve Results For Stratified Case
Inject Bottom Layer Into Top Inlet (Red) / Inject Top Layer Into Bottom Inlet (Green)

Figure 14 shows the injected fluid mass fraction and density contours as a function of time for injection of the bottom layer oil into the top inlet (Red Curve above). The upper layer is well mixed but remains separate from the bottom layer. The bottom layer is withdrawn similar to plug flow until the well-mixed upper layer gets to the outlet; after that, the performance is similar to complete mixing.

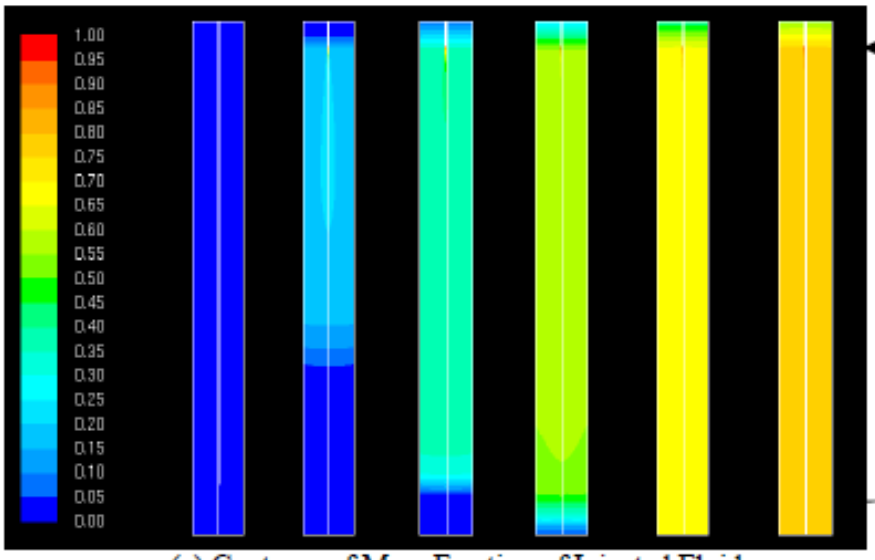


(a) Contours of Mass Fraction of Injected Fluid

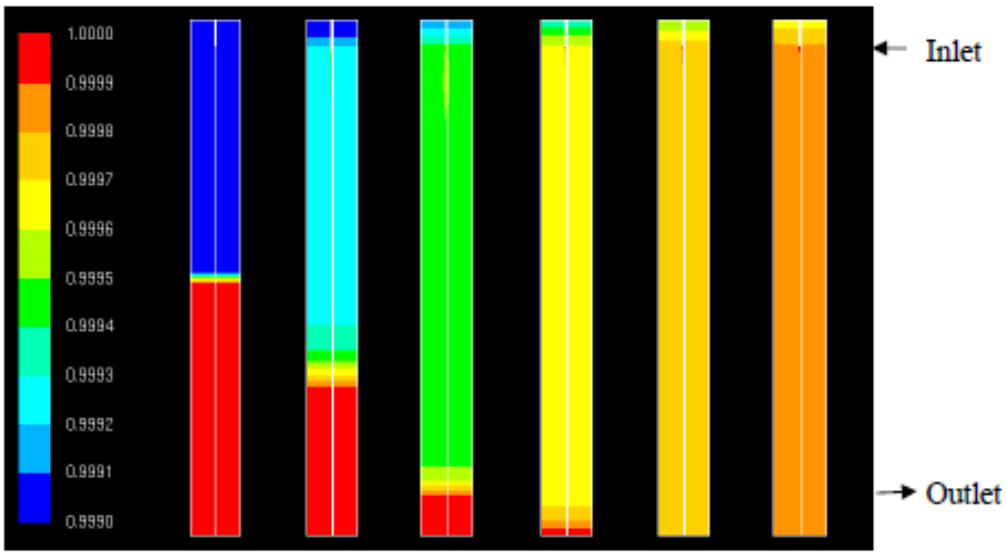


(b) Density Contours

| Time | 0 days | 10 days | 30 days | 60 days | 90 days | 120 days |
|---|---|---|---|---|---|---|
| Cavern Vols | 0. | 0.12 | 0.35 | 0.70 | 1.05 | 1.4 |

Figure 14
Cavern Contours for Injection of Bottom Layer Into Top Inlet

Figure 15 shows the injected fluid mass fraction and density contours as a function of time for injection of the top layer oil into the bottom inlet (Green Curve above). The bottom layer is well mixed but remains separate from the top layer. The top layer is withdrawn similar to plug flow until the well-mixed bottom layer gets to the outlet; after that, the performance is similar to complete mixing.

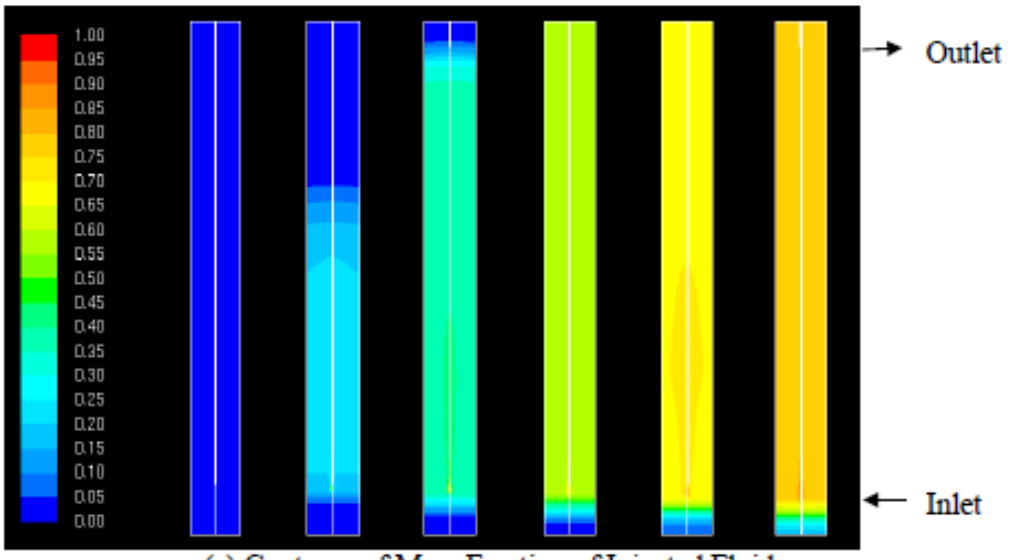


(a) Contours of Mass Fraction of Injected Fluid

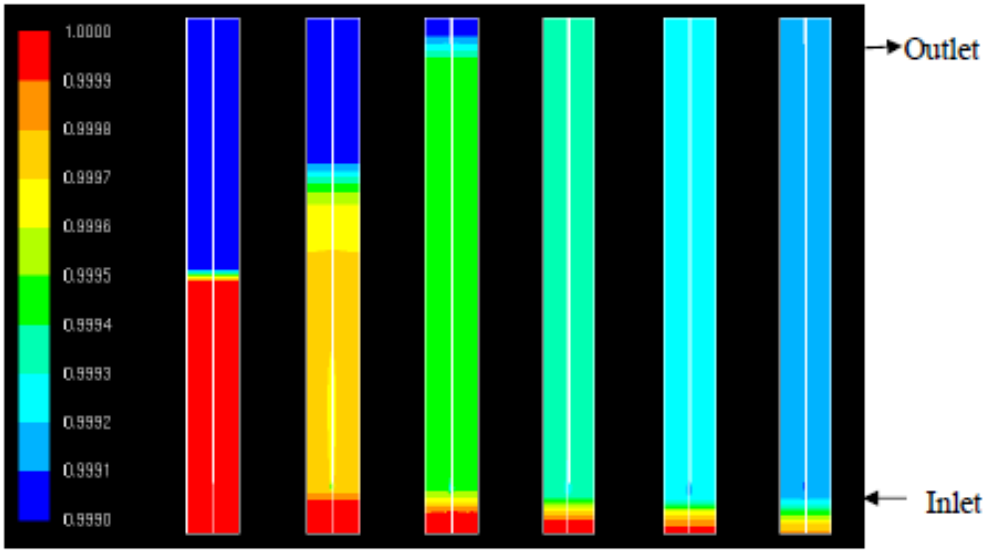


(b) Density Contours

| Time | 0 days | 10 days | 30 days | 60 days | 90 days | 120 days |
|---|---|---|---|---|---|---|
| Cavern Vols | 0. | 0.12 | 0.35 | 0.70 | 1.05 | 1.4 |

Figure 15
Cavern Contours for Injection of Top Layer Into Bottom Inlet

## 2c - Inject Lighter Fluid Into Top Inlet

In this case, an oil lighter than either the top or bottom oil layers is injected into the top inlet. The inlet oil is 0.1% lighter than the oil in the top layer, or 0.2% lighter than the bottom layer. As expected, the degas performance curves shown in Figure 16 are very similar to those for a lighter oil injection into a uniform density cavern. The degas performance is similar to plug flow until about 80% of the oil in the cavern has been processed.

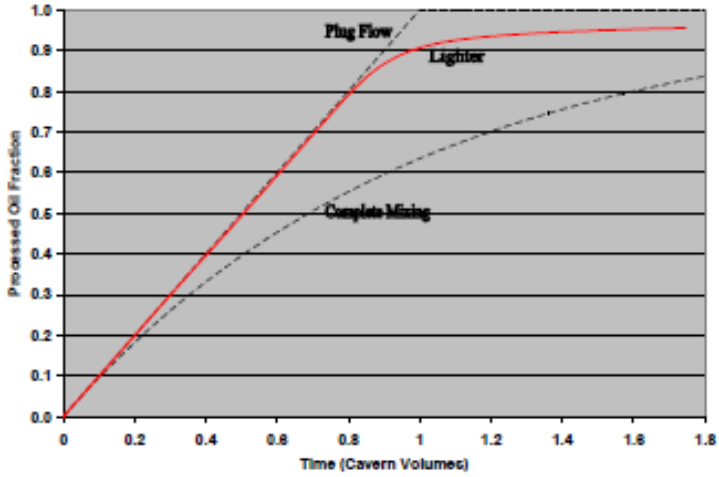


(a) Normalized BP Results

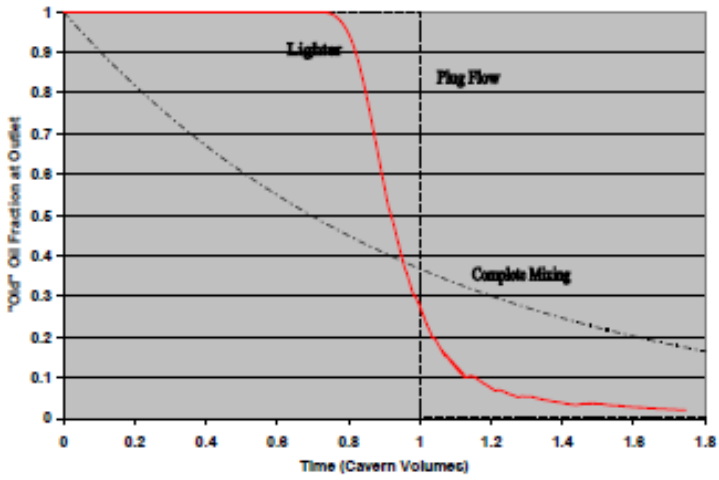


(b) Processed Oil Fraction Results

Figure 16
Degas Performance Curve Results For Stratified Case
Inject Lighter Oil Into Top Inlet

Figure 17 shows the contours of the injection mass fraction in the cavern as well as the fluid density. The cavern acts like plug flow for most of the time consistent with the earlier case of lighter oil injection into a uniform density cavern.

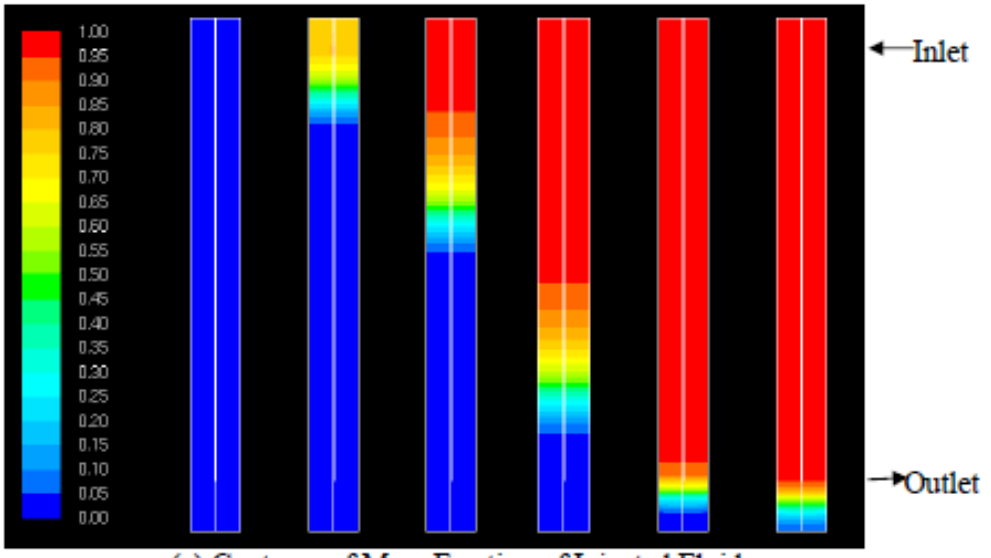


(a) Contours of Mass Fraction of Injected Fluid

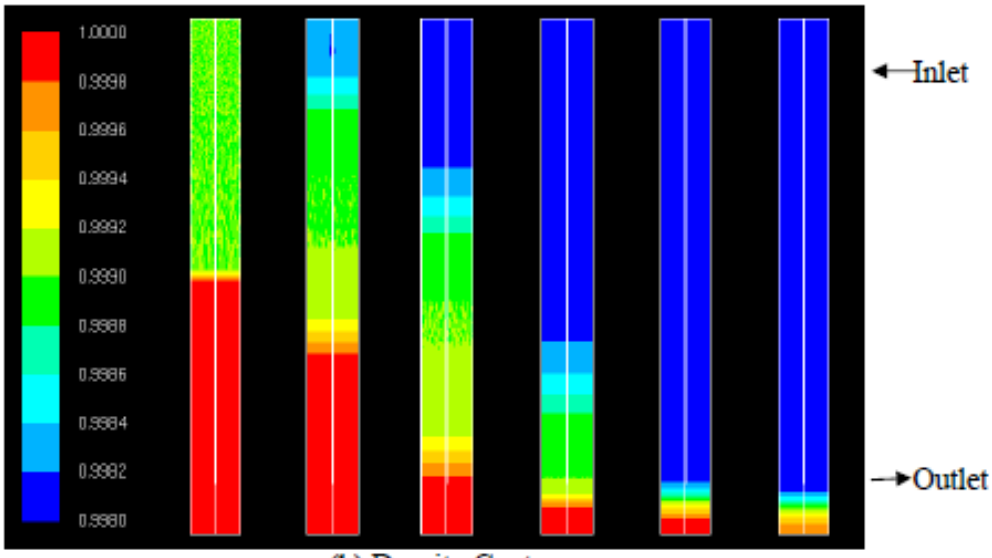


(b) Density Contours

| Time | 0 days | 10 days | 30 days | 60 days | 90 days | 120 days |
|---|---|---|---|---|---|---|
| Cavern Vols | 0. | 0.12 | 0.35 | 0.70 | 1.05 | 1.4 |

Figure 17
Cavern Contours for Injection of Light Oil Into Top Inlet

**2c – Degas In Two Phases**

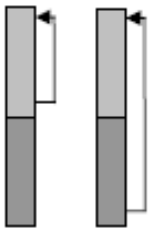

Previous results for injection of a fluid into another location (Inject Bottom Layer Into Top Inlet / Inject Top Layer Into Bottom Inlet) produced inefficient degas results that approach the complete mixing case. Only when the fluid density injected is lighter than any fluid in the cavern (Inject Lighter Fluid Into Top Inlet) were efficient degas results obtained. If the cavern density difference is large, injecting a lighter density fluid could be difficult. In this case, the density of the withdrawn fluid is decreased by 0.1% before it is injected into the cavern (initial density stratification is 0.1%). Degas is done in two phases. In Phase 1, the outlet is near the bottom of the top layer, while fluid injection is near the top of the cavern, and the top layer is degassed. In Phase 2, the outlet from the cavern is moved to be near the bottom of the cavern after a time period, 40 days in this case, while

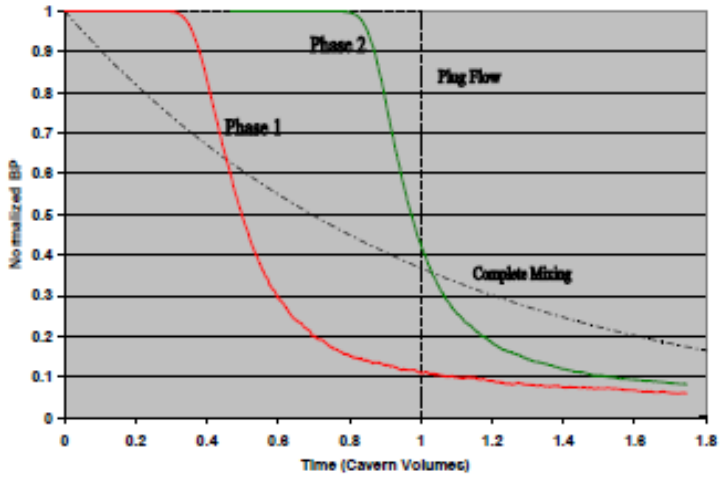


(a) Normalized BP Results

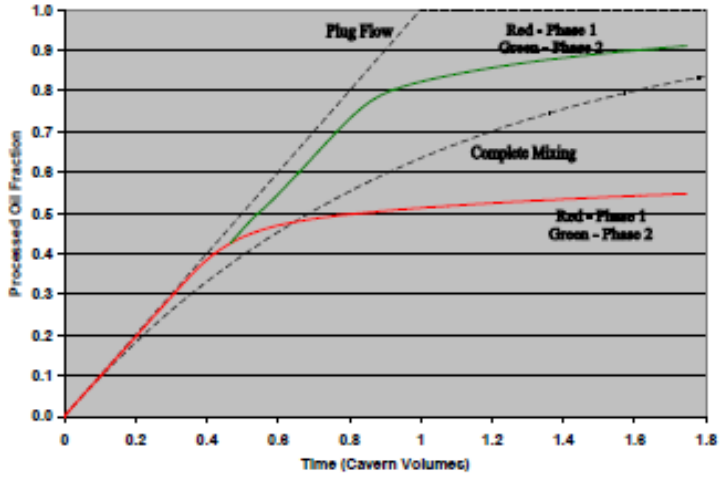


(b) Processed Oil Fraction Results

Figure 18

Degas Performance Curve Results For Stratified Case
Degas In Two Phases

the injection location is unchanged, and the bottom layer is degassed. Figure 18 shows the degas performance results. The transition from Phase 1 to Phase 2 is at 40 days. The Phase 1 simulation was continued to show the significant effect of changing the outlet location at 40 days. The overall degas performance as shown by the Phase 2 curve approaches plug flow conditions until about 80% of the cavern has been degassed. Figures 19 and 20 present the mass fraction and density contours for Phases 1 and 2, respectively. Phase 1 is essentially plug flow in the top layer, while Phase 2 is similar to neutral flow conditions in the entire cavern. The result is an efficient degas operation for initial cavern stratification.

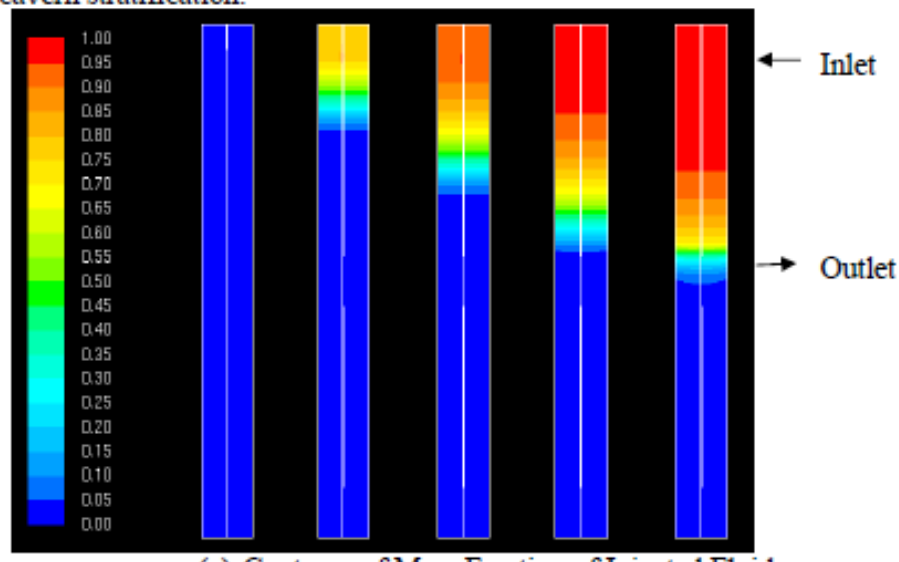


(a) Contours of Mass Fraction of Injected Fluid

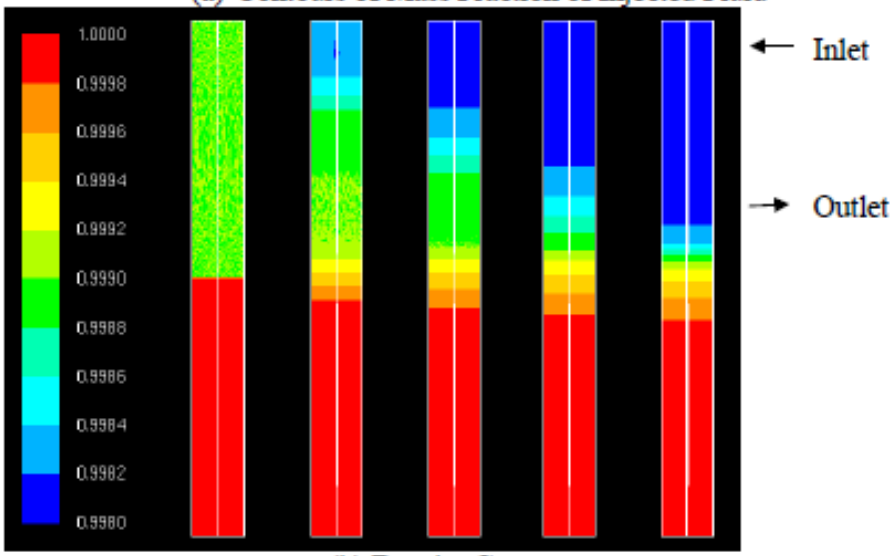


(b) Density Contours

| Time | 0 days | 10 days | 20 days | 30 days | 40 days |
|---|---|---|---|---|---|
| Cavern Vols | 0. | 0.12 | 0.24 | 0.35 | 0.47 |

Figure 19
Cavern Contours for Phase 1 Degas

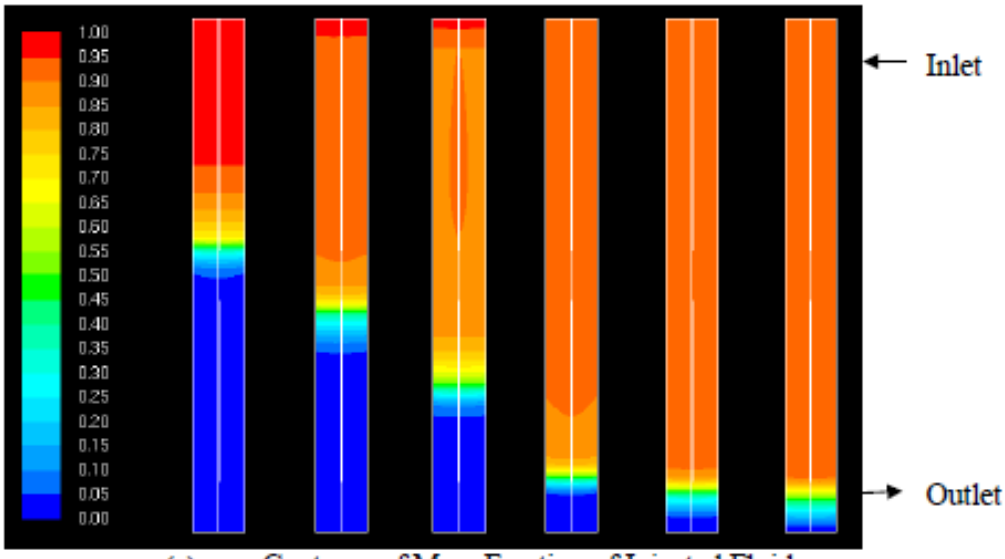


(a) Contours of Mass Fraction of Injected Fluid

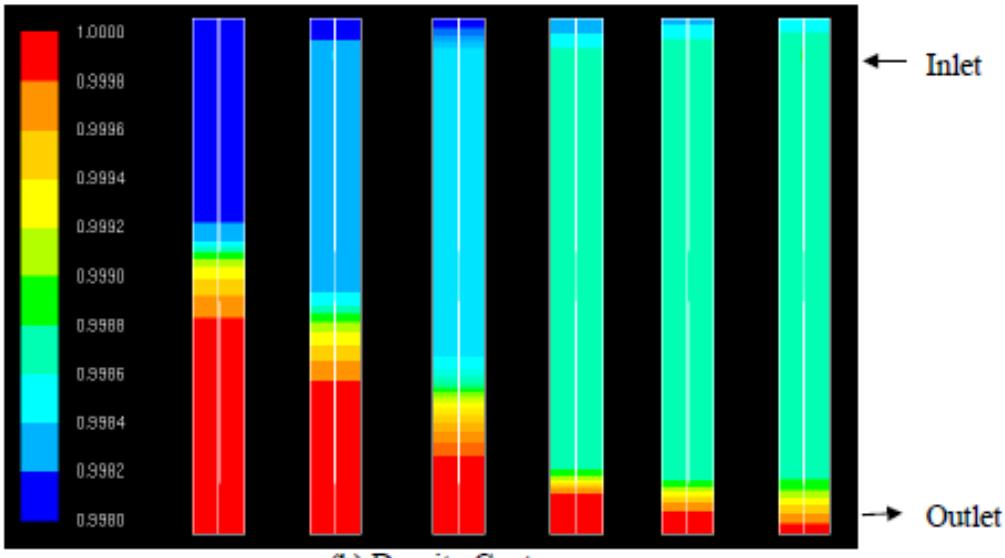


(b) Density Contours

| Time | 40 days | 50 days | 60 days | 80 days | 100 days | 120 days |
|---|---|---|---|---|---|---|
| Cavern Vols | 0.47 | 0.58 | 0.70 | 0.93 | 1.16 | 1.4 |

Figure 20
Cavern Contours for Phase 2 Degas

### 3. Viscosity Effect

Because the viscosity of the diesel fluid used in these simulations is low (dynamic viscosity = 0.0024 Pa-s, kinematic viscosity = 3.3cSt) compared to crude oil, cases have been simulated where the viscosity was increased by a factor of 10. Uniform density initial conditions have been used for lighter, neutral, and heavier injection cases. For the lighter and heavier cases, the density difference is 0.01%. These results are compared to those in cases 1a, 1b, and 1c.

Figures 21, 22, and 23 show the degas performance curves for lighter, neutral, and heavier oil injection, respectively. As can be seen, there is only a small influence of the results on fluid viscosity.

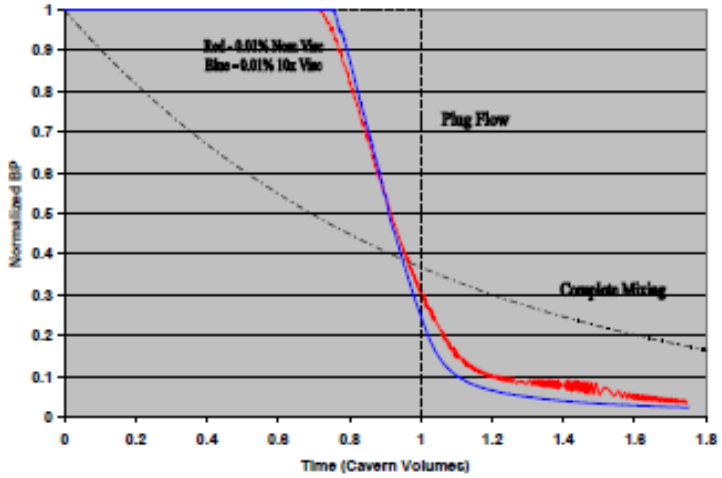


a) Normalized BP Results

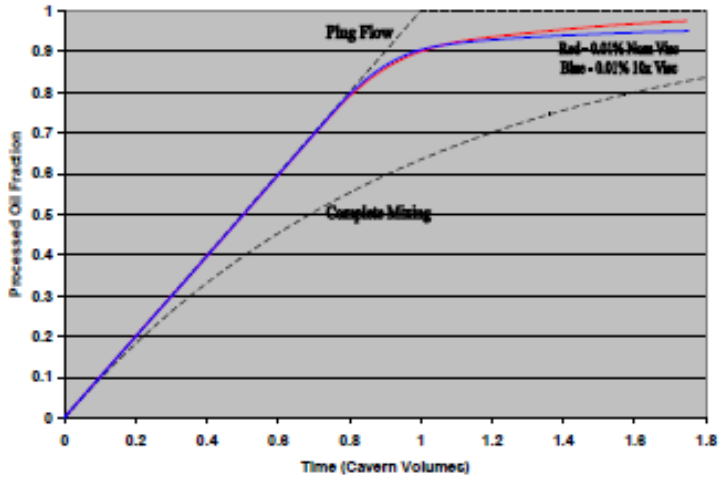


(b) Processed Oil Fraction Results

Figure 21
Degas Performance Curve Results For Lighter Density Oil Injection
Effect of Viscosity

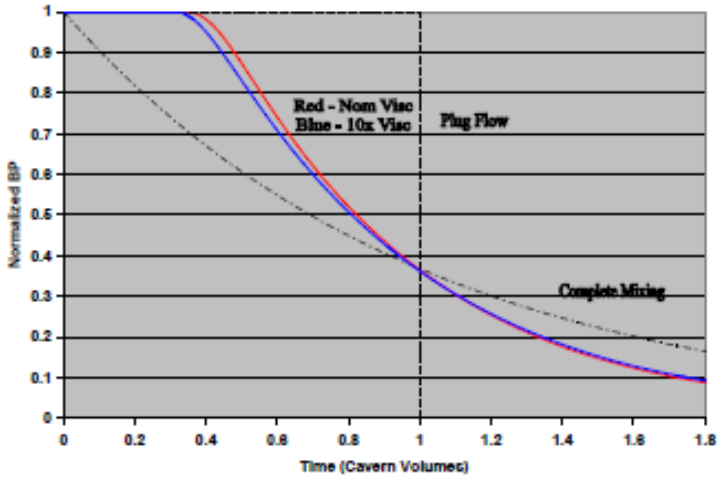


a) Normalized BP Results

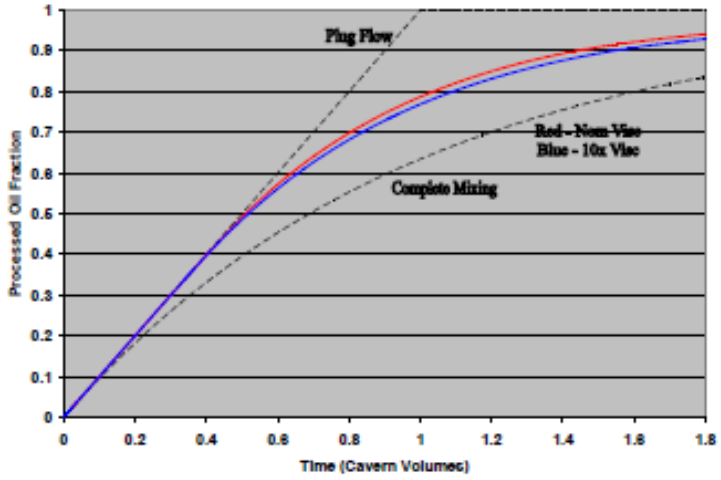


(b) Processed Oil Fraction Results

Figure 22
Degas Performance Curve Results For Neutral Density Oil Injection
Effect of Viscosity

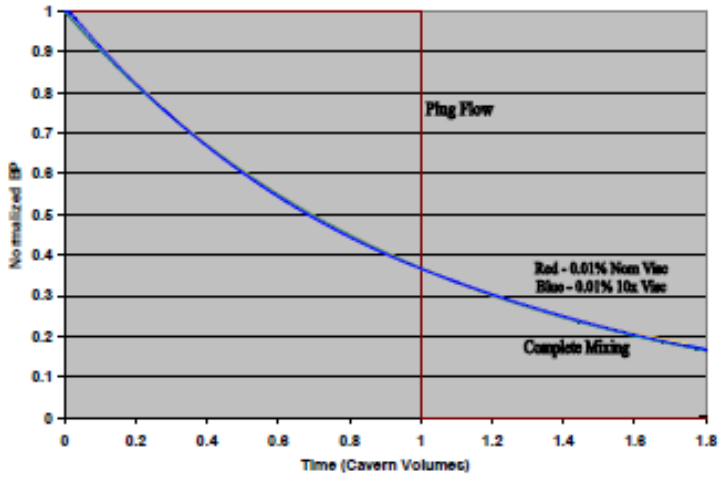


a) Normalized BP Results

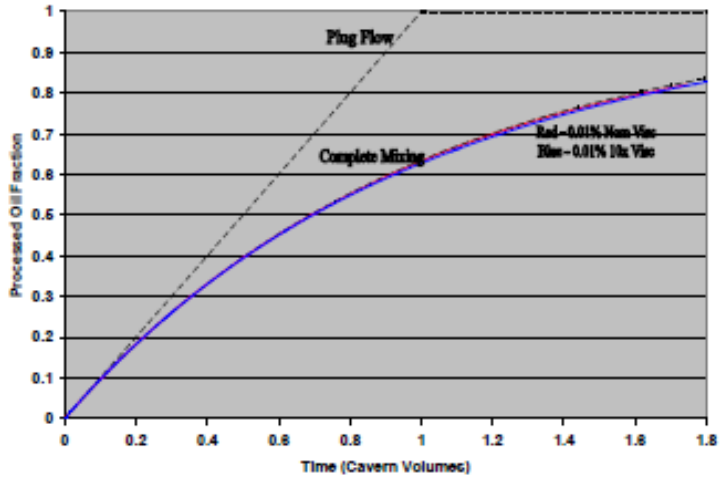


(b) Processed Oil Fraction Results

Figure 23
Degas Performance Curve Results For Heavier Density Oil Injection
Effect of Viscosity

## V. Discussion and Conclusions

Degas performance has been investigated as a function of density difference between the injected fluid and the resident fluid. The results for a uniform density initial condition can be converted from a density difference to a temperature difference by using an approximate oil thermal expansion coefficient of 5. x $10^{-4}$/°F (Meng et al., 2006, Frick, 1962). Therefore, a 0.01% density difference corresponds to a temperature difference of about 0.2 °F. The degas performance curves for uniform density initial conditions have been replotted in Figure 24 below.

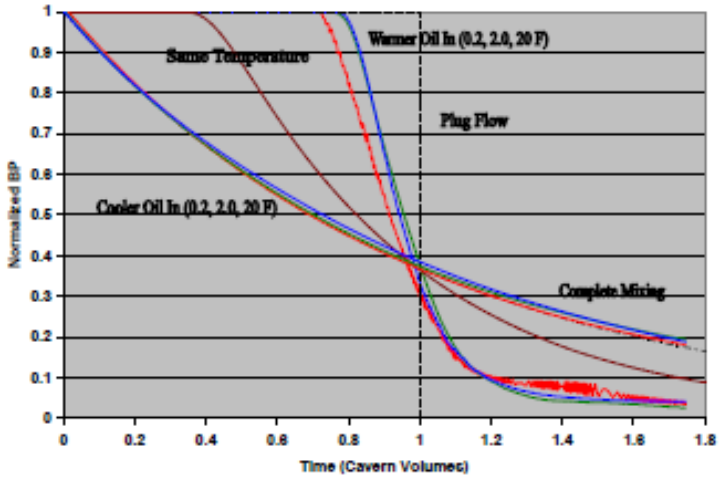


a) Normalized BP Results

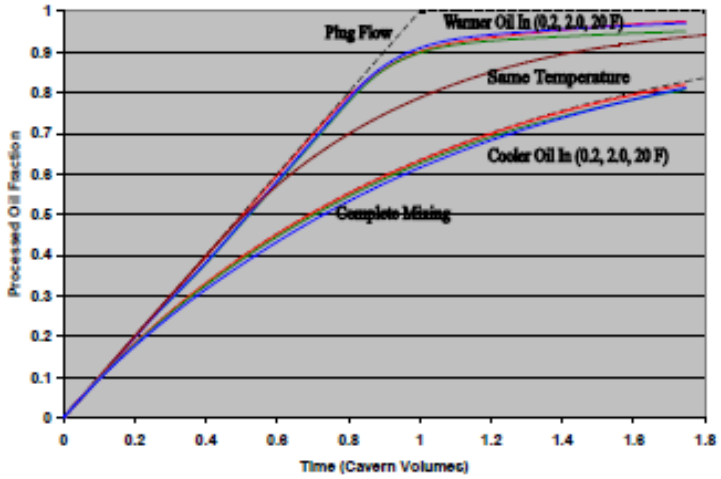


(b) Processed Oil Fraction Results

Figure 24
Degas Performance Curves vs. Inlet Oil Temperature

Calculated degas performance of a simplified cavern geometry with uniform initial density (no stratification) is strongly dependent on the density/temperature of the injected fluid. If the injected fluid is lighter/warmer than the resident fluid, degas proceeds similar to the plug flow model from Lord and Rudeen (2007). If the injected fluid is heavier/cooler than the resident fluid, large-scale mixing occurs and degas is similar to the complete mixing model of Lord and Rudeen (2007).

For initially stratified caverns, the degas performance is a little more complicated because it depends on the density stratification. If the fluid is simply withdrawn from the bottom part of the cavern and injected directly near the top (or withdrawn near the top and injected near the bottom), with no change in density due to degas, the degas performance curves are similar to complete mixing with poor degas performance. If the fluid is withdrawn near the bottom and the density is decreased so it is lighter than the fluid at the top of the cavern, the degas performance is good similar to plug flow conditions.

In some instances, however, it may be impractical to decrease the density of the bottom oil to be below the top oil, especially if the density difference is large. In this case, a two phase degas operation may prove useful in which the top layer is degassed first followed by the rest of the cavern. This procedure leads to an efficient degas operation wile limiting the decrease in oil density. However, the procedure does involve the movement of the withdrawal string midway through the degas procedure.

While these simulations are informative, the ultimate test of the model is comparison to actual cavern degas data. These comparisons, which will involve actual cavern geometries and fluid properties, are scheduled to be performed later in 2009.

## VI. References


Frick, T.C., editor, 1962, Petroleum Production Handbook, Vol. I, Soceity of Petroleum Engineers of AIME, Dallas, Texas, pg. 16-8.

Lord, D.L., and D.K. Rudeen, 2007, "Summary of Degas II Performance at the US Strategic Petroleum Reserve Big Hill Site," SAND2007-5564, Sandia National Laboratories, October 2007.

Meng, A., A.J. Jaworski, and N.M. White, 2006, "Composition measurements of crude oil and process water emulsions using thick-film ultrasonic transducers," Chemical Engineering and Processing, Vol. 45, pp. 383–391.

**Simple Degas Mixing Model Results – Comparison of Star and Fluent Results**

Stephen W. Webb
Sandia National Laboratories
November 17, 2009

## I. Introduction

Webb (2009) developed a simple 2-d axisymmetric model of a full-scale cavern in the Fluent computational fluid dynamics (CFD) code to investigate the effect of the inlet oil density on mixing and degas efficiency including uniform initial oil density and oil stratification. Due to contractual issues, the Fluent CFD code is being replaced by the Star-CD code from CD-adapco. The purpose of this report is to compare the results from the two codes for some selected cases to ascertain any differences in the results due to things such as the numerical scheme, differencing approaches, and numerical convergence criteria.

In order to make the comparison as clean as possible, the exact same mesh has been used in both codes. The Fluent mesh used by Webb (2009) was imported into Star-CD. In addition, the fluid properties and inlet boundary conditions are the same in the two simulations.

## II. Numeric Model

As discussed by Webb (2009), the modeled cavern is 2000 ft high with a uniform diameter of 200 ft as shown in Figure 1 with a total capacity of 11.2 MMB. No brine layer is assumed to be present so the entire volume is oil. The injection is located 100 ft from the top of the cavern while the outlet is 200 ft from the bottom. The inlet and outlet strings are concentric with the cavern with radii of 1.0 ft (bottom inlet/outlet) and 1.5 ft (top inlet/outlet). For this study, properties of diesel (density = 730 kg/m$^3$ (45.6 lb/ft$^3$), dynamic viscosity = 0.0024 Pa-s, kinematic viscosity = 3.3cSt, molecular diffusivity = $10^{-9}$ m$^2$/s) are used. The degas inlet mass flow rate is 175 kg/s (130,000 BBL/day) for a cavern turnover time of 85.9 days.

The model is a two-dimensional R-Z geometry with variable mesh point spacing in both directions in order to concentrate the mesh near the inlet and outlet locations and the outer wall. Due to the two-dimensional geometry, the inlet and outlet strings are concentric in these simulations.

The processed oil fraction plot is used in this comparison. As discussed by Webb (2009), this type of plot shows the fraction of processed oil in the entire cavern. If the value is 0.9, this indicates that 90% of the original oil in the cavern has been degassed. This value should increase as rapidly as possible, which indicates less mixing and better degas performance.


Figure 1
Simplified Cavern Geometry

Four cases have been selected for this comparison as follows:

1. Uniform Density Initial Conditions – all the oil initially in the cavern is at the same density with no stratification.
    a. Lighter oil injection at the top inlet – oil that is lighter than the original oil is added to the cavern near the top. Oil is withdrawn near the bottom of the cavern.
    b. Neutral density oil injection at the top inlet – the oil injected and the oil originally in the cavern are at the same density. Oil is added near the top of the cavern and withdrawn near the bottom of the cavern.
    c. Heavier oil injection at the top inlet – the oil injected near the top of the cavern is heavier than that initially in the cavern. Oil is withdrawn near the bottom.
2. Stratified Density Initial Conditions – the cavern is assumed to consist of equal volumes of a lighter oil over a heavier oil with a density difference of 0.1%.
    Injection of bottom layer oil at the top inlet – oil is withdrawn near the bottom of the cavern and injected near the top with no change in density. Because the oil in the bottom of the cavern is heavier than that in the top, the injected oil is heavier than the oil in the cavern at the injection location.

## 1. Uniform Density Initial Conditions

### 1a - Lighter Oil Injection

The processed oil fraction results for injection of a lighter fluid at the top inlet are shown as a function of time in Figure 2. The density of the injected fluid is 0.1% less than the original resident fluid. The injected oil creates a jet that initially descends downward in the cavern. Due to the density difference, however, the jet turns around and rises to the top of the cavern as a plume as shown earlier in Webb (2009).

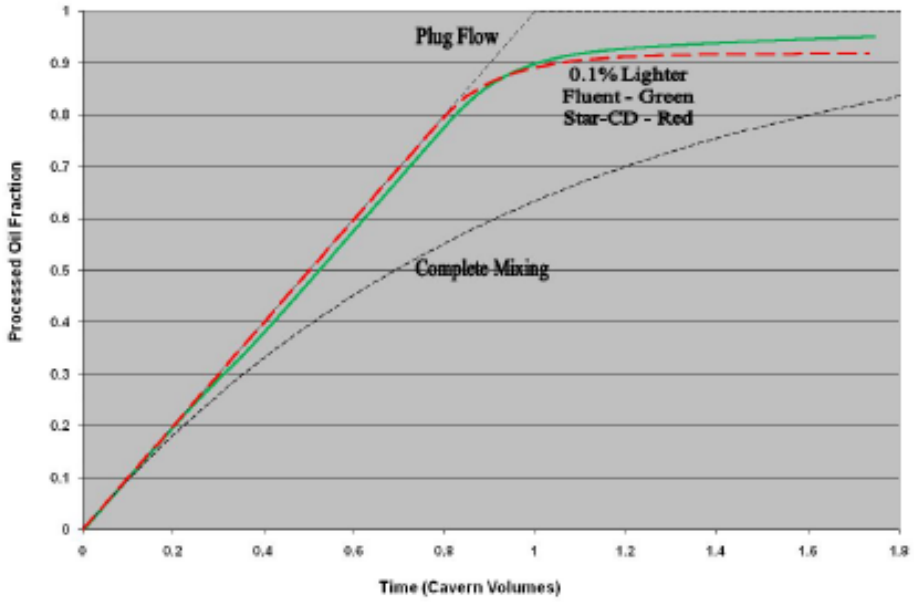


Figure 2
Processed Oil Fraction Results For Lighter Oil Injection – Top Inlet

Both codes (Fluent and Star-CD) indicate a very efficient degas operation until about 80-85% of the resident fluid is processes similar to the plug flow case of Lord and Rudeen (2007). The difference after 0.85 cavern volumes is related to the outlet elevation and the fact that there is 90% of the resident fluid is above the outlet as well as dispersion of the plug flow "front" as noted by Webb (2009).

The Star-CD results follow the plug flow limit more closely than Fluent. The plug flow limit is expected to be the initial behavior of this configuration. Based on these results, the predictions of Star-CD may be marginally better than those of Fluent for this case, but in general the results from the two codes are essentially equivalent.

### 1b - Neutral Density Oil Injection

This case corresponds to the situation where the injected oil and the resident oil are at exactly the same density. The processed oil fraction results as a function of time for injection of a neutral density fluid at the top inlet are shown in Figure 3. There are significant differences between the Fluent and Star-CD results. The Fluent predictions for the processed oil fraction are considerably greater than for Star-CD. The two curves for Star-CD are for different turbulence models. The effect of different turbulence models is minor.

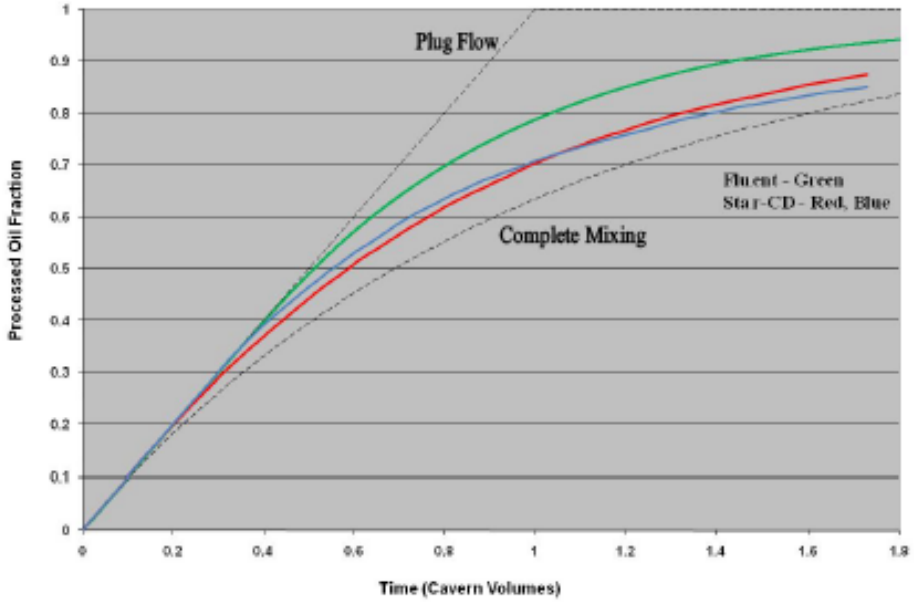


Figure 3
Processed Oil Fraction Results For Neutral Density Oil Injection – Top Inlet

The reason for the difference in the predictions is that Star-CD predicts that the inlet flow will finger down and "short-circuit" to the outlet as shown in Figure 4a for the two turbulence models (k- ε High Reynolds number and k-ε RNG) investigated. In contrast, Fluent predicts a flat oil interface as shown in Figure 4b.

Physically, the results from Star-CD seem to be more realistic. The interface shape is not expected to be flat as predicted by Fluent. Experiments currently being conducted at Arizona State University as part of the oil mixing program may shed more light on the interface shape. In any event, the influence of neutral density oil injection is probably small. As shown in the other comparisons, essentially any density difference will change the mixing pattern dramatically.

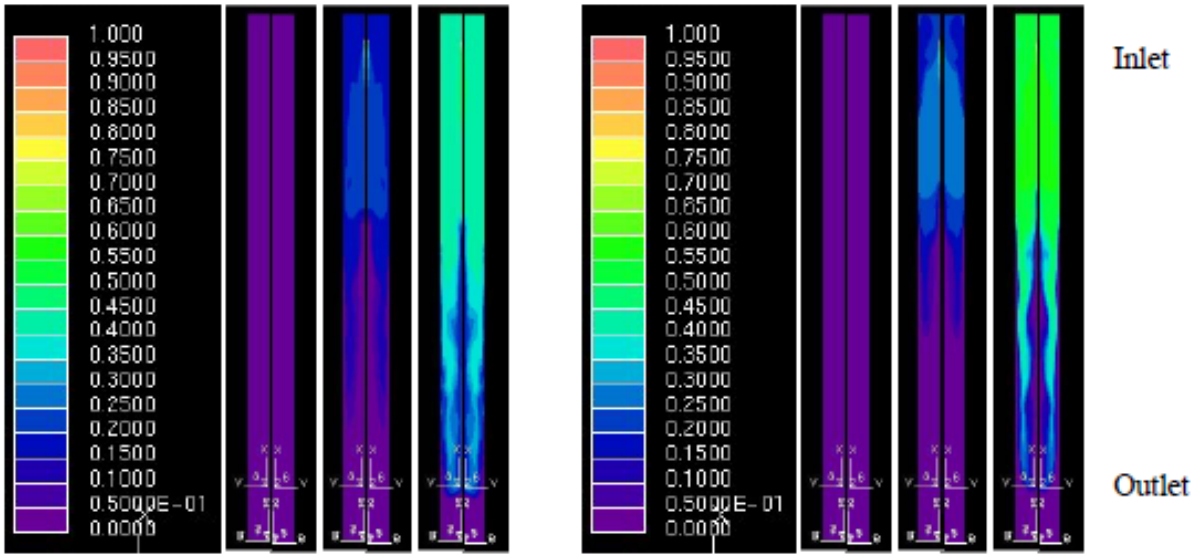


Time 0 days 10 days 30 days
Cavern Vols 0. 0.12 0.35
k- ε High Reynolds Number Model

0 days 10 days 30 days
0. 0.12 0.35
k- ε RNG Model

(a) Star-CD Results

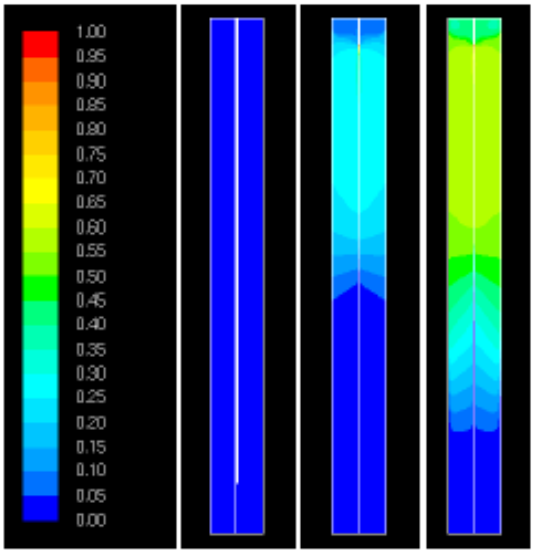


Time 0 days 10 days 30 days
Cavern Vols 0. 0.12 0.35

(b) Fluent Results

Figure 4
Mixing Flow Patterns For Neutral Density Oil Injection – Top Inlet

### 1c - Heavier Oil Injection – Top Inlet

The processed oil fraction results for injection of a heavier fluid are shown in Figure 5. The injected fluid is 0.1% heavier than the initial resident fluid. The heavier injected fluid flows down to the bottom in the cavern promoting large scale mixing. Both codes predict essentially the same behavior of complete mixing.

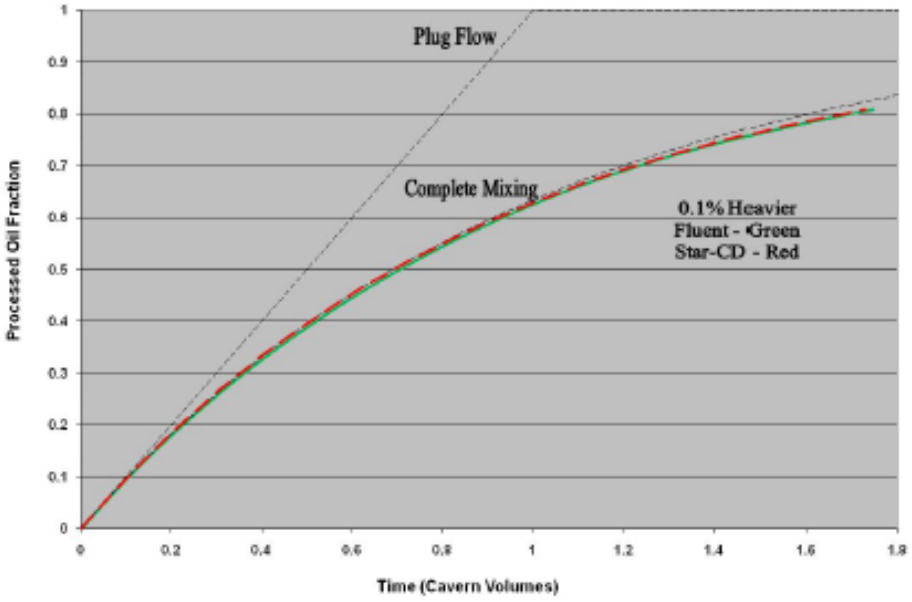


Figure 5
Processed Oil Fraction vs. Time For Heavier Oil Injection – Top Inlet

## 2. Stratified Density Initial Conditions

### 2a - Inject Bottom Layer Into Top Inlet

In this case, the oil is taken out of the bottom of the cavern and injected into the top with the injected density equal to the initial withdrawal density. As seen in Figure 6, the processed oil fraction curve for both CFD codes are initially similar to plug flow until about 35% of the oil is processed. The results then go toward the complete mixing curve when the stratification interface gets to the outlet location. There is minimal difference in the results from the two codes.

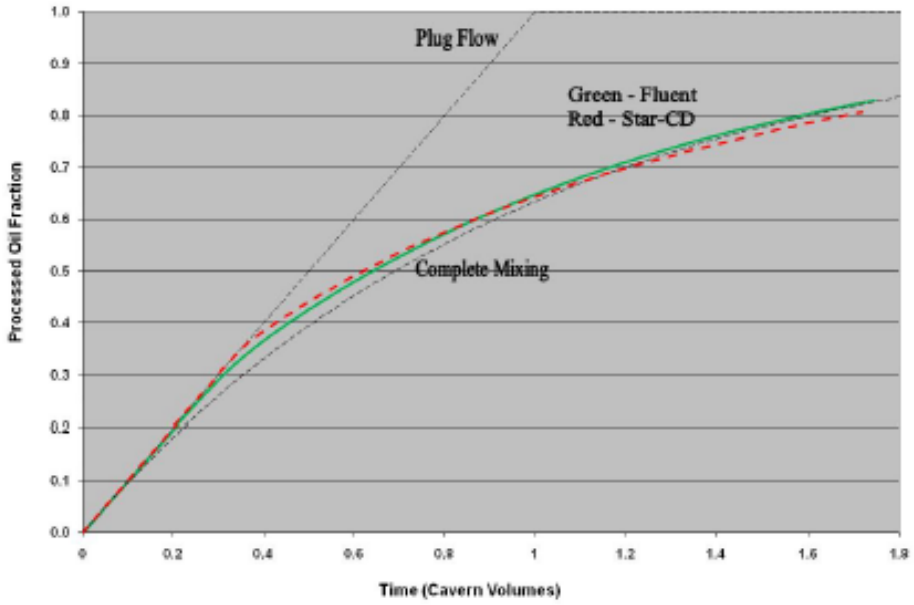


Figure 6
Processed Oil Fraction Results For Stratified Case
Inject Bottom Layer Into Top Inlet

## V. Discussion and Conclusions

Cavern mixing and degas performance has been simulated by the Fluent and Star-CD computer codes for a number of cases given by Webb (2009). The results from both codes are essentially the same except for neutral density case. In this situation, the Star-CD results seem more physically realistic. Experiments being performed at Arizona State University may shed more light on the actual interface shape. In any event, the impact of this difference is probably small because any small density difference will significantly change the mixing behavior.

## VI. Reference

Webb, S.W., 2009, "Simple Degas Mixing Model Results Including Stratification," June 29, 2009.

# Distribution

External Distribution

Electronic copies to:

Wayne Elias (wayne.elias@hq.doe.gov) for distribution to DOE SPR Program Office, Washington, DC

Diane Willard (diane.willard@spr.doe.gov) for distribution to DOE and DM SPR Project Management Office, New Orleans, LA

Lisa Eldredge (lisa.eldredge@spr.doe.gov) for distribution to FLUOR, New Orleans, LA

Sandia Distribution

Print copies to:

| | | | |
|---|---|---|---|
| 5 | MS0706 | David Lord | 6912 |
| 5 | MS0750 | Carolyn Kirby | 6913 |

Electronic Copies:

MS0899 Technical Library, 9536 (electronic copy)

[This page intentionally blank]


Sandia National Laboratories